

THÈSE

Pour obtenir le grade de
Docteur

Délivré par l'**ÉCOLE NATIONALE SUPÉRIEURE
DE CHIMIE DE MONTPELLIER**

Préparée au sein de l'école doctorale des Sciences Chimiques
(ED 459), et de l'unité de recherche de l'Institut de Chimie
Moléculaire et des Matériaux Charles Gerhardt Montpellier

Spécialité : **Chimie des Matériaux**

Présentée par **Jonas Croissant**

**NANOMÉDECINE THÉRANOSTIQUE
ACTIVÉE À DEUX-PHOTONS
POUR LE TRAITEMENT DU CANCER**

Soutenue le 21 juillet 2014 devant le jury composé de

M. Jean-Olivier DURAND, Dr., Université de Montpellier II

Co-Directeur

M. Michel WONG CHI MAN, Dr., Ecole Nationale
Supérieure de Chimie de Montpellier

Co-Directeur

Mme Marie Joëlle MENU, Pr., Université de Toulouse III

Rapporteur

M. Vincent SOL, Pr., Université de Limoges

Rapporteur

Mme Mireille BLANCHARD-DESCE, Dr., Université de
Bordeaux

Examineur

M. Jeffrey I. ZINK, Pr., University of California, Los Angeles

Examineur

ÉCOLE NATIONALE SUPÉRIEURE DE CHIMIE DE MONTPELLIER

PhD Dissertation

**TWO-PHOTON-ACTUATED THERANOSTIC NANOMEDICINE
FOR CANCER TREATMENT**

Jonas CROISSANT

Submitted to the graduate faculty
in fulfillment of the requirements for the degree of :
DOCTOR OF PHILOSOPHY
July 21st 2014

Approved by

M. Jean-Olivier Durand	Université de Montpellier II	Co-Advisor
M. Michel Wong Chi Man	Ecole Nationale Supérieure de Chimie de Montpellier	Co-Advisor
Mme Marie Joëlle Menu	Université de Toulouse III	Thesis referee
M. Vincent Sol	Université de Limoges	Thesis referee
Mme Mireille Blanchard-Desce	Université de Bordeaux	Examinator
M. Jeffrey I. Zink	University of California Los Angeles	Examinator

2011-2014

DEDICATION

*“Oh, the depth of the riches both of the wisdom and knowledge of God!
How unsearchable are His judgments and His ways past finding out!
“For who has known the mind of the Lord?
Or who has become His counselor?”
“Or who has first given to Him
And it shall be repaid to him?”
For of Him and through Him and to Him are all things, to whom be glory forever. Amen.”*

Romans 11:33-36, The Holy Bible

(New King James Version).

ACKNOWLEDGMENTS

I would like to express all the gratitude I have for my co-advisors professors Jean-Olivier Durand and Michel Wong Chi Man first and foremost. It has been a great privilege to work under their supervision during my PhD, the time and energy they devoted to teach me the art and science of being a researcher is very dear to me.

I am also very grateful to Xavier Cattoën and Laurence Raehm for their time to read and revise research articles, and the helpful discussions and insights they shared. I give thanks to Clarence Charnay as well.

The collaboration with Jeffrey Zink in the University of California Los Angeles (UCLA) has been very enriching, and I am thankful for the opportunity to learn from him and his team members such as Min Xue, Derrick Tarn, Daniel Ferris, and Bryana Anderson.

Many thanks to the biologist team members in Montpellier without whom the essential biomedical applications could not have been studied. I would like to thank Magali Gary-Bobo, Marie Maynadier, Audrey Gallud, and Marcel Garcia. Thanks also to the biology team of Fuyu Tamanoi in UCLA, especially to Jie Lu.

The photophysical studies led by Olivier Mongin, Vincent Hugues, and Mireille Blanchard-Desce were of a great value and importance for the understanding and demonstration of the mechanism behind the effect of the nanomaterials. Many thanks for their work.

I acknowledge Christine Biolley for the solid state nuclear magnetic resonance and inductively-coupled plasma analyses, and Xavier Dumail for his collaboration in the organic synthesis of photosensitive precursors. Thanks to Hubert Mutin for the opportunity to work in the Chimie Moléculaire et Organisation du Solide (CMOS) laboratory in the University of Montpellier II. I appreciated the friendship of the CMOS and SIKEMIA teams as well as the NJC members, and I would like to acknowledge Mathieu Meyer, Saad Sene, Celine Schmitt, Charlene Presti, Guillaume Gracy, Karim Bouchmella, Gilles Guerrero, Christian Guerin, Yannick Guari, and Denise Parent for their kindness, not forgetting Serge Bertrand in this regard and for his technical support. I would also like to thank Jérôme Long, Sébastien Clément, Arnaud Chaix, and Chiara Mauriello Jimenez for their enthusiasm and collaborations.

I acknowledge the Architecture Moléculaire et Matériaux Nanostructurés (AM2N) team members, especially Nouredine Achraf and Simon Giret for their kindness and collaboration.

I give thanks to the interns and follow workers that I was given to supervise who helped to advance the research: Christian Qi, Damien Salles, Celia Garnier, Jean-Baptiste Tissot, and Martina Serric. Thanks also to Sonia Dib, Siham Chelouaou, and Makhlouf Boufatit from Algeria University who collaborated on the pollutant removal project.

I would like to thank the Agence Nationale de la Recherche for their financial support with the ANR Mechanano.

The last but not the least, I am extremely grateful to my family: my wife and our child, my father, my mother, my two sisters, and extended families for their faithful love, tender care, and continuous support. Great thanks as well to all my dear friends.

ABSTRACT

Two-photon actuated nanomedicine has become one of the main proponents for the achievement of the spatiotemporal selectivity needed for nanomedicine. Indeed, the *raison d'être* of the medical application of nanotechnology in the field of cancer treatment is to lower and suppress the side effects caused by current techniques such as chemotherapy and radiotherapy, due to their lack of selectivity. Among various nanoparticles (NPs), mesoporous silica nanoparticles (MSN) have attracted increasing attention over the past decade for their low cytotoxicity, cellular internalization and excretion, and the ability to carry multiple features for both the *diagnosis* and *therapy* of cancers in a single nanovehicle: the so-called *theranostic* nanomedicine.

In this dissertation, I will describe MSN for one and/or two-photon-actuated fluorescence imaging, drug-delivery, gene delivery and photodynamic therapy (PDT). First, plasmonically-triggered cargo delivery via MSN nanovalves and designed mesoporous silica photodegradation is presented. Then, *in-vitro* two-photon-triggered drug delivery with azobenzene-functionalized MSN such as nanoimpellers and fluorescent nanovalves, along with preliminary studies of gene delivery via ammonium-functionalized nanoimpellers are discussed. Multifunctional MSN incorporating a two-photon photosensitizer are systematically studied in terms of the resulting optical and photophysical properties of the NPs, and then used for *in-vitro* biomedical applications.

Furthermore, two kinds of emerging nanomaterials are also designed for two-photon actuated nanomedicine, bridged silsesquioxane (BS) and periodic mesoporous organosilica (PMO) NPs. These nanomaterials are elaborated without silica precursor (e.g. tetraethoxysilane) and solely with bis- or tetra-organoalkoxysilanes, thus providing materials with the highest organic content for the targeted applications. Consequently, disulfide-based hybrid BS and PMO NPs were elaborated as biodegradable nanomedical tools, and photosensitizer-based BS and PMO NPs were used for efficient *in-vitro* PDT. BS and gold-BS core-shells NPs are constructed for ultrabright two-photon imaging and efficient PDT, while two-photon functionalized PMO NPs serve as theranostic nanocarriers. Besides, versatile multipodal ethylene-benzene PMO NPs with very high surface areas are presented as a promising strategy for the design of structural complexities at the nanoscale.

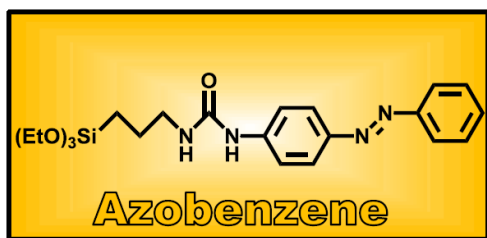
Finally, iron oxide core MSN shell ($\text{Fe}_3\text{O}_4@\text{MSN}$) nanocontainers are described for versatile applications. The design of two-photon-sensitive magnetic MSN and PMO core-shell nanovehicles is presented as a perspective for gene delivery and magnetic resonance imaging. Furthermore, $\text{Fe}_3\text{O}_4@\text{MSN}$ containers are constructed for heavy metal removal of twelve of the most toxic metal ions through the diethylene triamine pentaacetic acid (DTPA) ligand. The enhancement of the pollutant removal efficiency is studied by selective surface and/or porous DTPA functionalizations.

TABLE OF CONTENTS

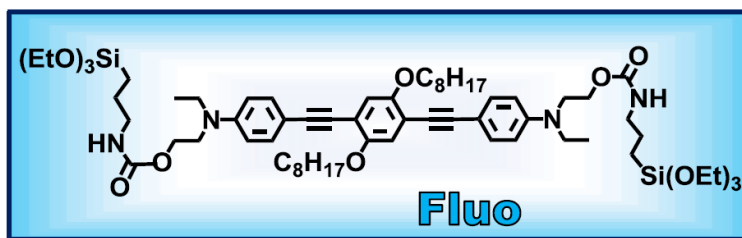
Acknowledgments.....	4
Abstract.....	5
Schematic main list of organic molecules and nanomaterials.....	7
CHAPTER 1. Introduction to mesoporous silica nanoparticles in nanomedicine.....	11
CHAPTER 2. Nanovalve-controlled cargo release activated by plasmonic heating.....	36
CHAPTER 3. Controllable photodegradation of mesoporous silica encapsulating gold cores for remote cargo release.....	50
CHAPTER 4. Two-photon-actuated drug and nucleic acid deliveries via azobenzene-functionalized mesoporous silica nanovehicles.....	64
<i>A. Two-photon-triggered drug delivery in cancer cells via nanoimpellers.....</i>	65
<i>B. Two-photon-triggered drug delivery via fluorescent nanovalves.....</i>	86
<i>C. Two-photon-actuated siRNA delivery via ammonium-azobenzene-functionalized mesoporous silica nanoparticles.....</i>	104
CHAPTER 5. Two-photon-actuated photodynamic and/or photothermal therapies via photosensitizer-functionalized mesoporous silica nanovehicles on cancer cells.....	119
<i>A. Influence of the synthetic method on the properties of two-photon-sensitive mesoporous nanoparticles for in-vitro fluorescence imaging.....</i>	120
<i>B. Multifunctional gold-mesoporous nanoplatform for synergetic two-photon photodynamic and photothermal therapies in cancer cells.....</i>	141
<i>C. Two-photon synergetic cell killing via multifunctional mesoporous nanogates.....</i>	160
CHAPTER 6. Versatile synthesis of biodegradable disulfide hybrid bridged silsesquioxane nanoparticles: two-photon photodynamic therapy on cancer cells.....	178
CHAPTER 7. From two-photon photosensitizer to bridged silsesquioxane and periodic mesoporous organosilica nanoparticles: application to cancer theranostic.....	192
CHAPTER 8. Design of periodic mesoporous organosilica hybrid nanoparticles.....	216
<i>A. Biodegradable ethylene-bis(propyl)disulfide-based periodic mesoporous organosilica nanorods and nanospheres for efficient in-vitro drug delivery.....</i>	217
<i>B. Multipodal hybrid periodic mesoporous organosilica nanoparticles with crystal-like architectures.....</i>	239
CHAPTER 9. Versatile heavy metals removal via magnetic mesoporous nanocontainers...	257
Conclusion.....	283
French summary.....	285

ORGANIC MOLECULES

Chap. 4A

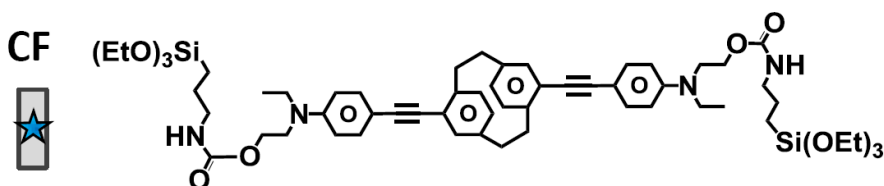


Nanoimpeller



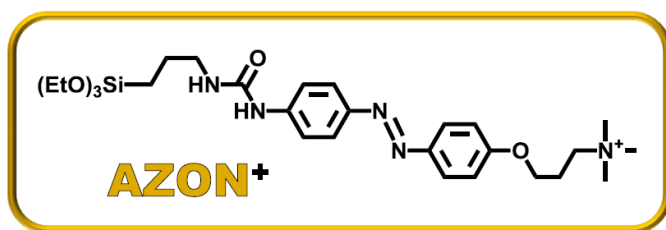
Two-photon Fluorophore

Chap. 4B

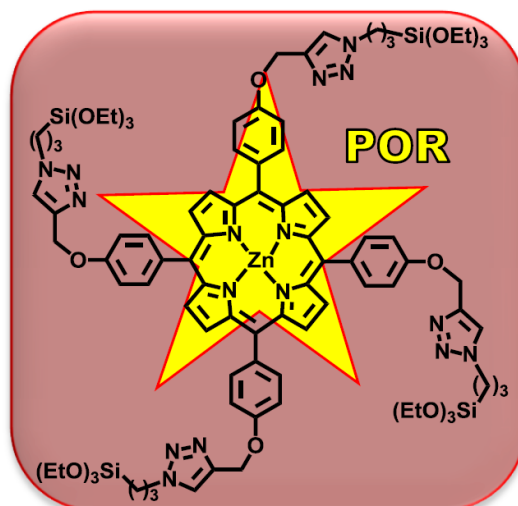


Two-photon paraCyclophane-Fluorophore

Chap. 4C



Ammonium-nanoimpeller



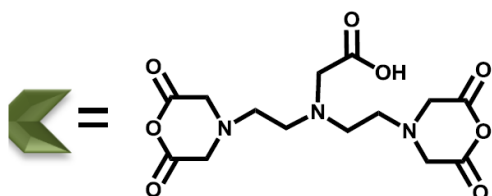
Porphyrin photosensitizer

Chap. 5-7



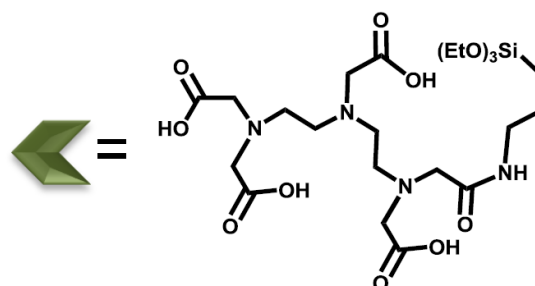
Two-Photon Photosensitizer

Chap. 9



L Ligand precursor

DTPA Ligand

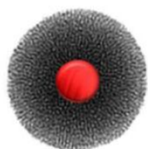


L Ligand

Alkoxysilylated Ligand

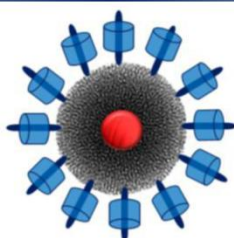
NANOMATERIALS

Chap. 2-3



Au@MSN

Gold@Mesoporous Silica

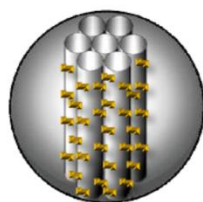


Au@MSN@Valve



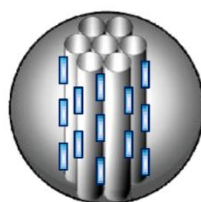
Au@MSN@Polymer

Chap. 4A



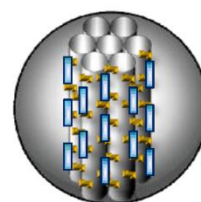
MA NPs

Mesoporous Azobenzene-silica



MF NPs

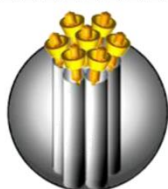
Mesoporous Fluorophore-silica



MAF NPs

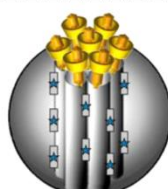
Mesoporous Azobenzene-Fluorophore-silica

Chap. 4B



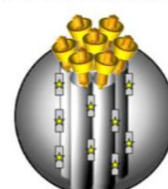
MSN-AZO@βCD

Mesoporous silica-Azobenzene@β-Cyclodextrine



MCF-AZO@βCD

Mesoporous paraCyclophane-Fluorophore-silica-Azobenzene@β-Cyclodextrine



MFITC-AZO@β-CD

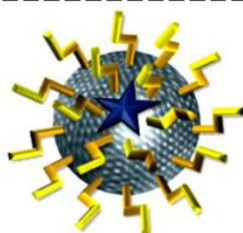
Mesoporous Fluorescein-silica Azobenzene@β-Cyclodextrine

Chap. 4C



MCF

Mesoporous paraCyclophane-Fluorophore-silica



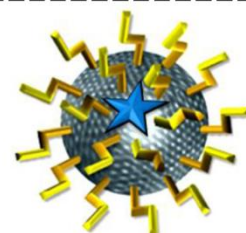
MCF-AZON⁺

Mesoporous paraCyclophane-Fluorophore-silica-Ammonium-Azobenzene



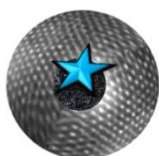
MF

Mesoporous Fluorophore-silica



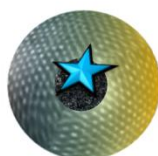
MF-AZON⁺

Mesoporous Fluorophore-silica-Ammonium-Azobenzene



Fe₃O₄@MF

Iron oxide@Mesoporous Fluorophore-silica



Fe₃O₄@MFAZON⁺

Iron oxide@Mesoporous Fluorophore-Ammonium-Azobenzene-silica



Fe₃O₄@EF

Iron oxide@Ethylene-Fluorophore Periodic mesoporous organosilica

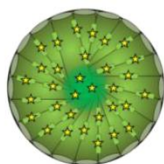


Fe₃O₄@EFAZON⁺

Iron oxide@Ethylene-Fluorophore-Ammonium-Azobenzene Periodic mesoporous organosilica

NANOMATERIALS

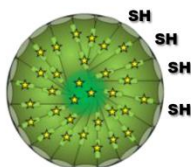
Chap. 5



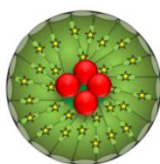
M2PS
Mesoporous Two-Photon-Photosensitizer-silica



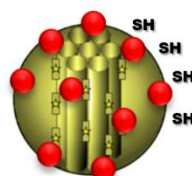
M2PS-Nanogates
Mesoporous Two-Photon-Photosensitizer-silica-Disulfide Nanogates



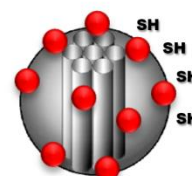
M2PS-SH
Mesoporous Two-Photon-Photosensitizer-mercapto-silica



Au@M2PS
Gold@Mesoporous Two-Photon-Photosensitizer-silica

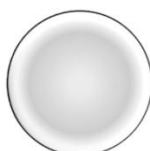


M2PS-SH@Au
Mesoporous Two-Photon-Photosensitizer-mercapto-silica@Gold

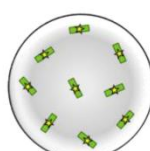


MSN-SH@Au
Mesoporous mercapto-silica@Gold

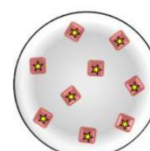
Chap. 6



DIS NPs
Disulfide Bridged-Silsesquioxane



DIS2 NPs
Disulfide-Two-Photon-Photosensitizer Bridged-Silsesquioxane



DISP NPs
Disulfide-Porphyrin Photosensitizer Bridged-Silsesquioxane

Chap. 7



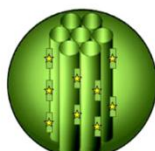
BSNPs
Two-Photon Photosensitizer Bridged-Silsesquioxane



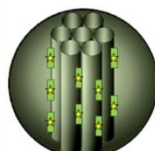
BS@AuNPs
Two-Photon Photosensitizer Bridged-Silsesquioxane@Gold



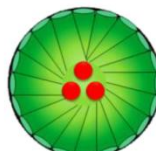
Au@BSNPs
Gold@Two-Photon Photosensitizer Bridged-Silsesquioxane



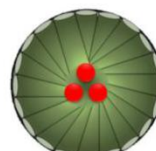
E2



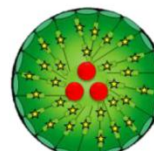
B2



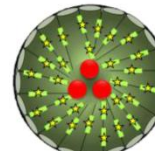
AE



AB



AE2



AB2

Ethylene (or **B**enzene)
-Two-Photon Photosensitizer
periodic mesoporous organosilica

Gold@**E**thylene (or **B**enzene)
periodic mesoporous organosilica

Gold@**E**thylene (or **B**enzene)
-Two-Photon Photosensitizer
periodic mesoporous organosilica

NANOMATERIALS

Chap. 8A



E PMO

Ethylene Periodic Mesoporous Organosilica



EDIS MPMO

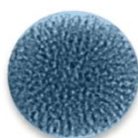
Ethylene-Disulfide Mixed Periodic Mesoporous Organosilica



DIS BS

Disulfide Bridged-Silsesquioxane

Chap. 8B



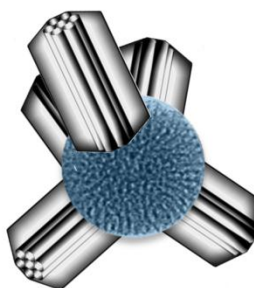
B PMO

Benzene Periodic Mesoporous Organosilica



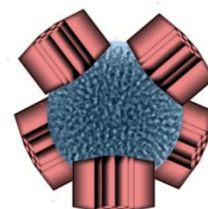
E PMO

Ethylene Periodic Mesoporous Organosilica



BE mp-PMO

Benzene-Ethylene Multipodal Periodic Mesoporous Organosilica



BEDIS mp-PMO

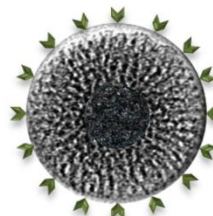
Benzene-Ethylene-Disulfide Multipodal Periodic Mesoporous Organosilica

Chap. 9



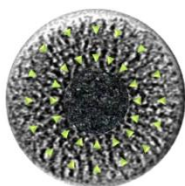
Fe₃O₄@MSN

Iron oxide@ Mesoporous Silica



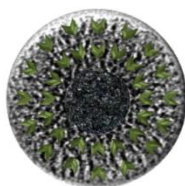
Fe₃O₄@MSN-L

Iron oxide@ Mesoporous Silica-Ligand



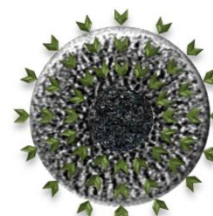
Fe₃O₄@MSN₂

Iron oxide@ Mesoporous amino-Silica



Fe₃O₄@MSL

Iron oxide@ Mesoporous Ligand-Silica

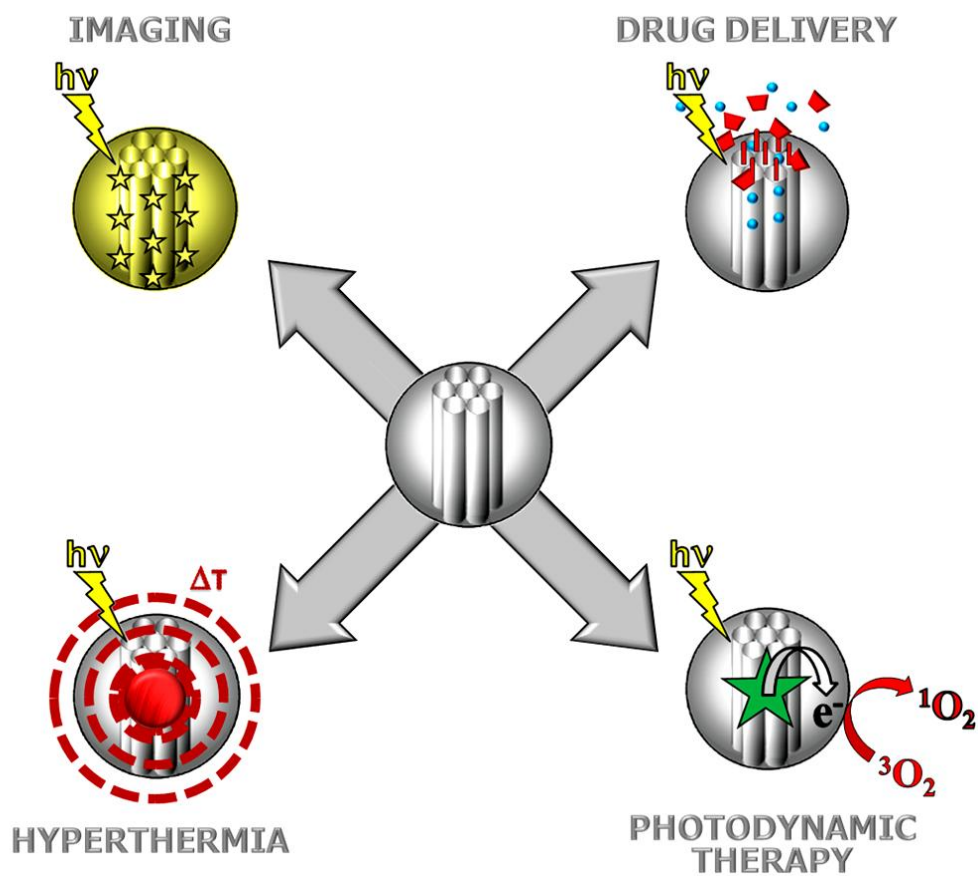


Fe₃O₄@MSL-L

Iron oxide@ Mesoporous Ligand-Silica-Ligand

CHAPTER 1

Introduction to Mesoporous Silica Nanoparticles in Nanomedicine



1.1 Definitions and a short history of mesoporous silica materials

Silica, also known as silicon dioxide (SiO_2), is constituted of the two most abundant elements of the earth's crust, the oxygen being the most. Thus, it is a very common mineral on earth, composing for instance the majority of the sand of the planet. Silica is found in amorphous state in opals, or Kieselguhr, and in crystalline state, with minerals such as α -quartz and β -quartz.

Porous materials are generally differentiated as microporous, mesoporous, and macroporous compounds, from the Greek prefixes *micro* (small) which stands for pores comprised between 0 to 2 nm, *meso* (middle) for pores of 2 to 50 nm, and *macro* (large) for pores larger than 50 nm.

Natural mesoporous silica materials are also found on earth. In fact, nature has been filled with such minerals from long ago, some of them called *diatoms* and *radiolarians* come from the bio-chemical interface of plants and animals respectively. Besides, these two types of porous silica really are of fantastic beauty and complexity (see Figure 1), which humbles the chemist who simply tries to design ordered mesoporous silica materials.

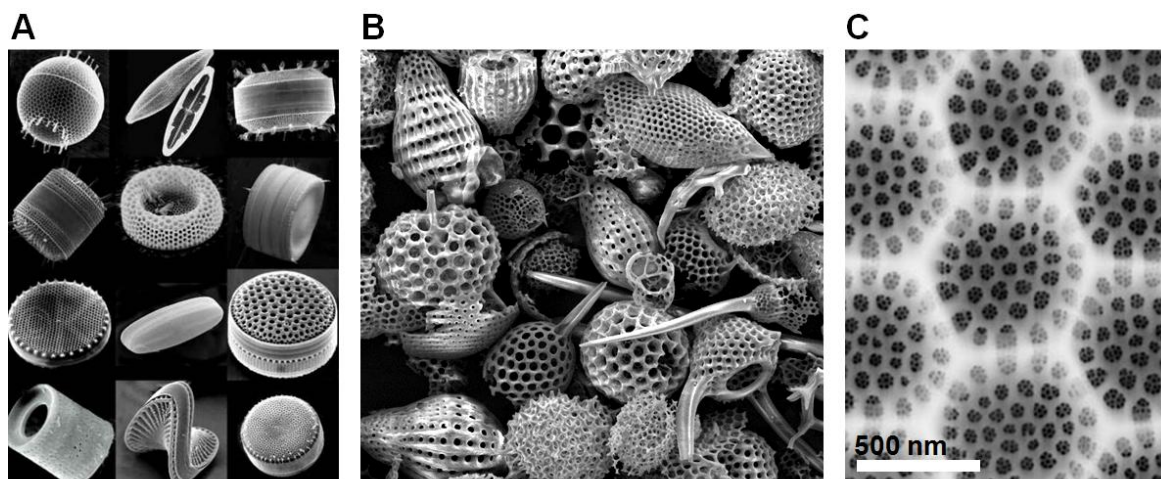


Figure 1. Scanning electron micrographs of diatoms (A, objects ranging from 1 to 2000 μm) and radiolarians (B, objects ranging from 50 to 500 μm). High magnification electron micrograph of the hierarchical porosity found at the nanoscale of diatoms (C).

Synthetic mesoporous silica materials were first patented in the late sixties by American researchers,^[1-3] and went almost unnoticed until 1990 when Kuroda *et al.* published synthetic mesoporous silica for the first time,^[4] and, in 1992, when the researchers from Mobil Oil corporation produced the so-called MCM-41 mesoporous material, standing for Mobil

Crystalline Materials.^[5] Afterwards, one of the American patents was reproduced in 1997 by F. Di Renzo *et al.* in an article entitled: “A 28-year-old synthesis of micelle-templated mesoporous silica”.^[6] At that time, mesoporous silica was solely obtained from cetyltrimethylammonium micellar template, typically leading to pores of 2 nm. In the year 1998 in the University of Santa Barbara in California, a new kind of mesoporous silica known as SBA-15 (Santa-Barbara Amorphous) was first described by G. D. Stucky *et al.* from a triblock copolymer template, thus achieving larger pores ranging from 5 to 30 nm.^[7] Nowadays, MCM-41 and SBA-15 are the most common synthetic mesoporous silica materials; this thesis will focus on the former type of mesoporous compounds.

MCM-41 nanomaterials were described by S. Mann *et al.* in 2002 from a CTAB-templated diluted system,^[8] and then used as drug delivery nanocarriers by Lin *et al.* in 2003.^[9] This pioneering study was based on the idea of the controllable closing and re-opening of the pores. The drug was first loaded in the porous framework, then 2 nm CdS quantum dots were chemically grafted at the entrance of the pores, thus preventing the drug leaking. Given that the CdS grafting was based on disulfide linkage, the cleavage of these bonds was chemically triggered in solution with a dithiothreitol reducer, as well as autonomously in the cells with the glutathione reducer they naturally contain. A wide variety of drug delivery systems was designed to transport various cargo molecules and macromolecules, and to release them on-demand with many different kinds of stimuli,^[10] which will be presented hereafter.

1.2 Nanomedicine: the biological and pharmaceutical contexts

The human body is a very complex organism which is composed of 65 percent of water and close to 50 trillion cells, which are the basic units of life. These cells are organized biologically to form the whole body. Although each cell is an amazingly complex universe in and of itself, their stability can be threatened by various illnesses. Unfortunately, many harsh diseases like hemophilia, asthma and cancers are currently affecting a very significant part of the world population.

Cancers form a “group of more than 100 distinct diseases characterized by the uncontrolled growth of abnormal cells in the body. In the early 21st century some 12 million new cancer cases were diagnosed worldwide each year, and the disease affected one in every three persons born in developed countries. Hence, cancer is a major cause of sickness and death throughout the world” (Encyclopedia Britannica). Various treatments were thus developed to cure cancers, such as selective surgery, radiation therapy, and chemotherapeutic drugs. The latter, commonly known as chemotherapy, is nonetheless limited in its efficacy due to both a lack of *spacial selectivity*, causing side effects on non-cancerous tissues, and of *temporal selectivity*, diluting or concentrating uncontrollably the effect in time.

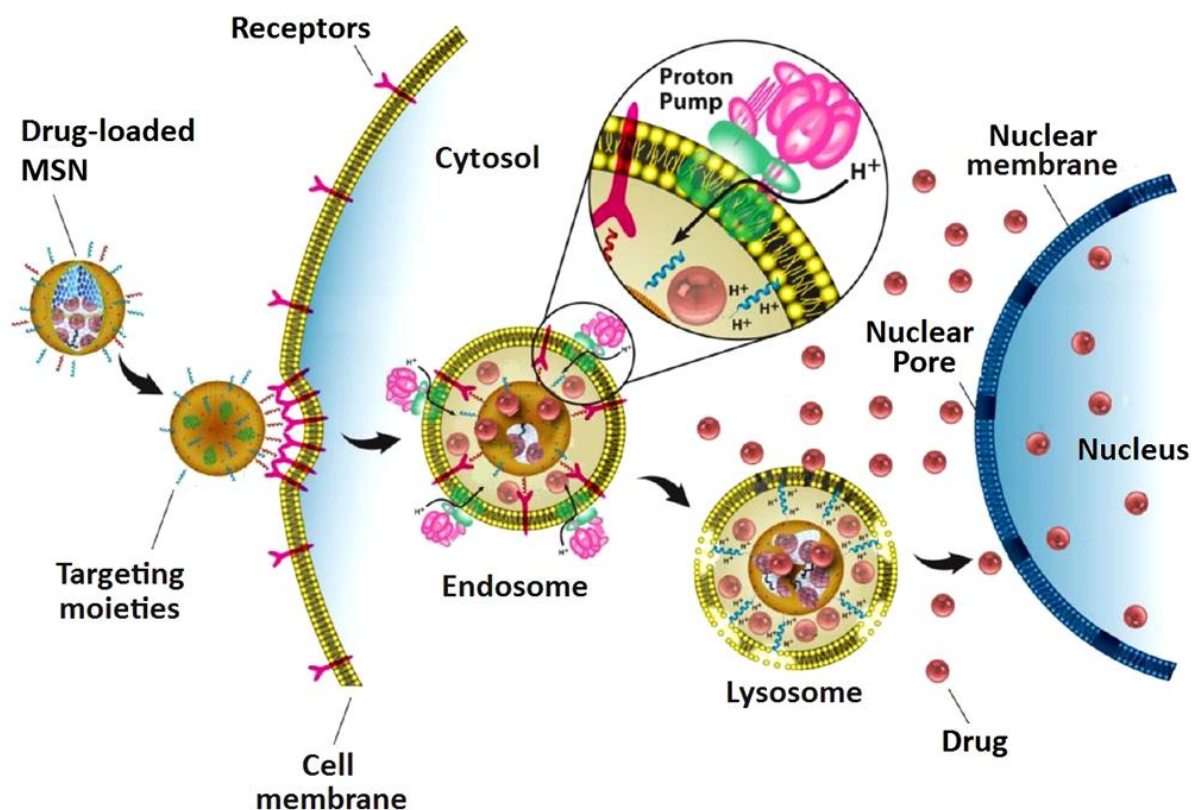
Therefore, extensive efforts have been made to create in the so-called *nanomedicine* to prevent and reduce both acute and chronic unwanted side-effects. Nanomedicine is the medical application of nanotechnology to achieve diagnosis and/or therapy of pathologies.

The term theranostics has recently been coined for systems that combine both diagnostic and therapeutic features. Current research has shown the potential of nanoparticles (NPs) to decrease the side effects caused by the lack of selectivity of the chemotherapeutic strategy. Given that both the cancer cells and the normal cells are in the specific targeted location, the goal is to induce *apoptosis* or *necrosis* which are the death of these pathogenic cells, without causing the death of the normal cells. To manage such control, one of the strategies of nanomedicine, called *drug-delivery*, is used to carry, retain, and deliver on-demand chemotherapeutic drugs selectively in the tumor.

Cell membranes are composed of a phospholipid bilayer with embedded proteins and receptors used for the permeability of chemicals and ions. The transport of biochemicals or NPs through the phospholipid bilayer in and out of the cell is called the endocytosis and exocytosis, respectively. An endocytosed entity is then encapsulated in a vesicle called endosome, which through the proton pump effect will become more acidic (see Scheme 1). This phenomenon is based on a specific membrane protein that is capable of selective proton transport in the endosome. The pH of the vesicles will go down to 5.5 as opposed to the 7.4 in the blood stream, and the endosome will be called a lysosome. The pH variation as well as the final disruption of the lysosome have inspired “Trojan horse” nanosystems for intracellular drug delivery.

The aim of drug delivery is to first encapsulate a hydrophobic drug via NPs, to transport and protect it until the ill organs. Indeed, only 10% of the commercialized drugs are hydrophilic, and more than 40% of substances found via combinatorial screening programs display poor solubility in water.^[11] Moreover, the ability to carry hydrophobic drugs in the hydrophilic blood stream through soluble nanovehicles is a major advantage of NPs, since it is very difficult to change the solubility of a drug without losing its therapeutic effect. The drug transport step is highly dependent on the route of administration of drug. Indeed, the oral route involves a first-pass effect (i.e. drug metabolism through the liver and the gut wall), and various acidic, ionic, and enzymatic conditions in the stomach, which reduce the efficacy of the treatment. Nevertheless, such hurdles could be circumvented by the intravenous injection which appears to be an efficacious route for nanodevices, since it allows an instantaneous biodisponibility into the systemic circulatory system.^[12]

The next step is to specifically deliver the drug to the tumor cells. The selectivity of NPs towards tumor cells is induced by the enhanced permeability and retention (EPR) effect, which is a consequence of the properties of neovasculature. In fact, endothelial cells forming the interior surface of blood vessels and lymphatic vessels become poorly-aligned and defective, thus wide fenestrations are found close to tumors. These characteristics induce a high permeation of smaller molecules and NPs smaller than 200 nm, preferentially in cancerous than in normal cells. Hence, versatile nano-objects can take advantage of the EPR phenomenon, such as liposomes, proteins, macromolecules, and many kinds of nanoparticles amongst which are mesoporous silica nanoparticles (MSN). The nanovehicles are first uptaken into the cell (endocytosis), which then leads to the lysosome compartment. Finally, cargo molecules are released from the NPs towards the cell nucleus (Scheme 1).



Scheme 1. Representation of drug-loaded MSN endocytosed by a cell (entering the cytosol), then transported in the endosome and the lysosome to release their drug content via acid stimuli (through the intracellular the proton pump effect). The anticancer drugs are finally reaching the cell nucleus. Adapted from reference 10.

Second generation nanomedicine has been developed to enhance the spacial selectivity of the drug delivery via biochemical targeting of the cancerous cells. The targeting feature is pictured by the famous *lock and key* analogy first postulated in 1894 by Emil Fischer. The idea is basically to find out the biochemical structural correspondence between a chemical entity (the key) and specific substrate (the lock), in this case cellular receptors (see Scheme 1). Targeting moieties such as the folate receptor, peptides, genes, and integrins are being extensively studied towards specific receptors of cancerous cells.^[13]

1.3 Significance of mesoporous silica and organosilica NPs in nanomedicine

The MCM-41 mesoporous silica framework has attracted much attention in nanomedicine over the past years due to their high surface areas, ordered pores, and the well-known silicon chemistry which virtually offers unlimited functionalities. At the nanoscale, these platforms provide numerous advantages, such as the low cytotoxicity of silica,^[14] NPs endocytosis and exocytosis, long term blood circulation, NPs excretion, cargo transportation

and protection, post-synthetic surface grafting for targeting, controlled drug delivery, or enhanced endocytosis, and tailored delivery pharmacokinetics.^[11]

Mesoporous silica and organosilica NPs have been rightly called a “universal platform for drug delivery”.^[15] As previously mentioned, the size and loading capacity of the NPs have a critical influence in the treatment efficiency. Hence, the ability to tune both the NPs particle size (15 to 1000 nm),^[16-17] and pore diameter (1 to 30 nm),^[18-20] enables the tuning of the surface area (from 150 to 1200 m².g⁻¹) in order to benefit high loading capacities (from 3 to 50 wt%) depending on the size and physico-chemistry of the cargo and the characteristics of the NPs. Moreover, the controlled-release of a large range of guests such as dendrimers,^[21] DNA,^[21] siRNA,^[12] proteins,^[22] smaller nanoparticles (Au, CdS, Fe₃O₄),^[23-25] fluorescent labels, hydrophobic drugs (ibuprofene, camptothecin, paclitaxel, doxorubicin),^[12,24,26-27] and chemicals reagents have been demonstrated.

Besides, the syntheses of MSN with versatile size, morphology, and functionalization could be controlled by means of precise experimental conditions and post-treatments in view of nanomedicine. Mesoporous silica and organosilica spherical particles from 10 nm to few hundreds nanometers,^[28,29] as well as MSN nanorods, hollow spheres, hollow nanorods have been prepared.^[30,31] Indeed, it has been shown that the NPs size and shape modify the cellular uptake and the metabolism.^[19,32] Typically, MSN nanorods of 1.5 to 3 aspect ratio (AR) are more readily up-taken in the cells than nanospheres, supposedly for their close mimic of the shape of bacteria.^[30] Also, short nanorods (AR=1.5) are excreted faster than long NRs (AR=5).^[31] In addition, the third generation of nanocarriers have been elaborated via surface functionalization of the NPs inducing a biological “stealthiness”. The resulting NPs are said to be stealthy particles in the sense that the proteins-NPs interaction is reduced, generally through polymer coating (e.g. polyethyleneglycol), and thus circulate longer in the blood stream with lesser accumulation in the liver.^[31] Moreover, it should be noticed that certain pathologies, such as those related to the brain (brain cancers) or the eyes (retinoblastoma cancers), require ultra small NPs (< 25 nm) to cross the blood-brain and blood-ocular barriers. Thus according to the targeted biomedical application, the ability to vary the size, the shape, and the surface functionalization of MSN is particularly useful.

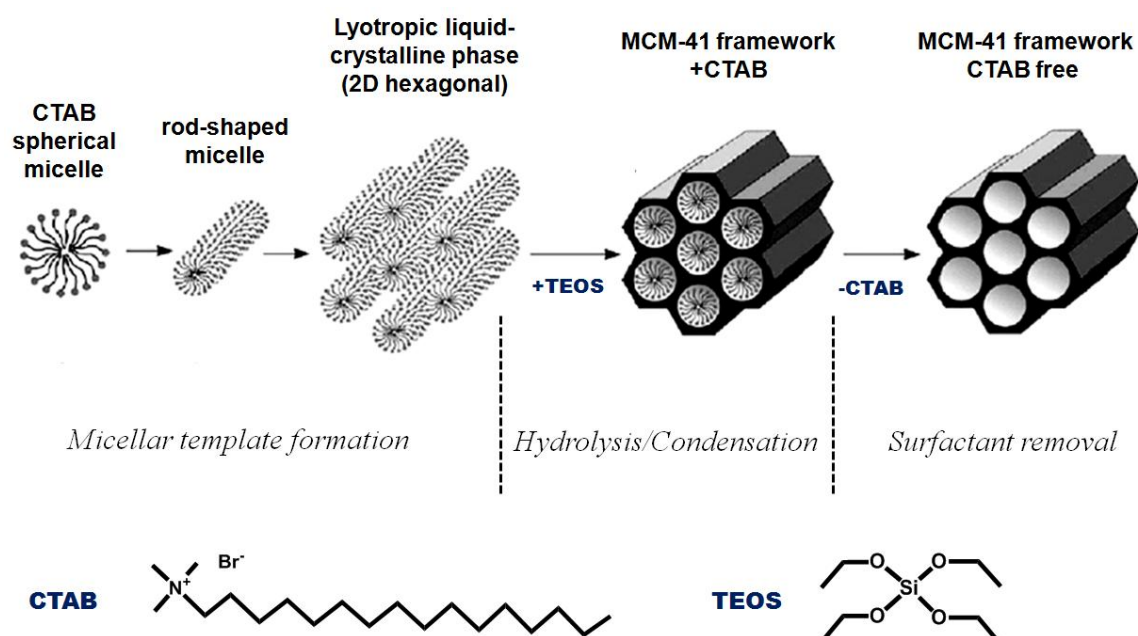
Furthermore, the sol-gel process provides a powerful tool to combine organic fragments within the inorganic silica framework by co-condensation. Hence, multifunctional nanomaterials tailored with –to name a few– fluorescent imaging, photodynamic therapy, drug delivery, and photothermal therapy features from the added fragment, could be gathered in a single device. Also, the properties of other NPs could be combined in the MSN structure, to form NPs core MSN shell nanosystems.

MSN nanomaterials have been employed in order to provide “smart nanocontainers” capable of releasing their content on-command, thanks to the rich silicon chemistry that allow surface molecular, supramolecular, and macromolecular mechanization of the pores. According to the drug delivery strategy employed (see section 1.5 *MSN applications in theranostic nanomedicine*), the cargo release could be reversibly or irreversibly triggered, which may in turn allow the treatment of chronic diseases with the use of a long-term

medication, as well as the treatment of infections. In the latter case, delivering a precise amount of drug in tumor cells is essential. It is noteworthy that many systems have high loading capacities, but the robustness of the carriers is often not trustworthy. On the contrary, the MSN platform can be designed so as to avoid any premature leakage of the cargo, thus preventing side effects and delivering a precise and predetermined amount of drug. For instance, camptothecin loaded MSN nanovalve (see section 1.5) are biocompatible in human cancer cells (PANC-1, and SW48) until the actuation of the release.^[32]

1.4 Design and characterization of mesoporous silica and organosilica nanoparticles

To take advantage of the assets of MSN in view of nanomedical applications, the sol-gel elaboration of the nanocarriers should be precisely controlled. In this section, a typical synthesis and characterization of MSN is presented. MSN are synthesized by the hydrolysis-condensation of a silica precursor such as tetraethylorthosilicate (TEOS) in a micellar template solution, in most cases of cetyltrimethylammonium bromide (CTAB) (Scheme 2).^[33] The reaction is catalyzed by sodium hydroxide ($\text{pH}_0=12$), and the temperature is accurately controlled at $T=80^\circ\text{C}$ under vigorous stirring (700 rpm). After two hours, the mixture is cooled down to room temperature, and the surfactant is extracted to recover the porosity. There are several available extraction processes, some able to modify the integrity of the framework, and provoke the aggregation of the sample. To avoid such drawbacks as well as the degradation of co-condensed organic fragments, calcination methods are not used and extractions in solution based on positive repulsive electrostatic interactions with CTAB are performed (e.g. NPs refluxed in MeOH/HCl).



Scheme 2. Representation of the cetyltrimethylammonium bromide (CTAB) templating effect, and the sol-gel hydrolysis-condensation of tetraethylorthosilicate (TEOS) to produce MCM-41 materials. Scheme adapted from reference 33.

a) Preparation of MSN

A mixture of CTAB (250 mg), distilled water (120 mL), and sodium hydroxide (875 μ L, 2 M) is typically stirred at 80°C for 50 minutes at 700 rpm in a three neck 250 mL round bottomed flask. The sol-gel process being kinetically-controlled, the basicity, temperature, and stirring speed (not to mention the geometry, size, and cleanness of the glassware) have a crucial impact on the resulting material. Then, a silica precursor such as TEOS (1.2 mL) is added to the aforementioned solution, and the condensation process is conducted for 2 hours. The solution is cooled to room temperature while stirring to prevent the aggregation of the NPs, and collected by centrifugation during 15 minutes at 21 krpm. Two acidic extractions of CTAB are generally performed by refluxing the NPs powder in a mixture of methanol (60 mL) and concentrated hydrochloric acid (3.2 mL). Finally, the sample is washed three times with ethanol, water, and ethanol. The collection of the material is carried out by centrifugation after extraction and washing steps. The as-prepared material is eventually dried under vacuum for few hours.

In the case of hybrid organic-inorganic materials, the organoalkoxysilane is co-condensed by addition along with the TEOS precursor. In this manner, amino-functionalized mesoporous organosilica (MSN-NH₂) NPs could be fabricated by APTMS addition. Note that, the chemistry of amines is at this point available on the NPs for further functionalization.

b) Nanomaterials characterization

A complete characterization of nanomaterials requires a complementary panel of techniques. On the one hand, techniques focusing on the properties of few NPs, such as transmission electron microscopy (TEM) down to the nanoscale accuracy; and, on the other hand, the confirmation and completion of the material properties on tens or hundreds of milligrams of the sample via dynamic light scattering (DLS), X-ray diffraction (XRD), scanning electron microscopy (SEM), nitrogen-adsorption-desorption, etc. Specific functionalities could be also characterized by techniques such as Fourier Transform Infrared (FTIR) spectroscopy, and solid state nuclear magnetic resonance (NMR), etc.

Transmission Electron Microscopy. An accurate characterization of any nanomaterials requires electron micrographs to visually determine the shape and size of the synthesized compound. The TEM analysis is, however, particularly needed for the characterization of the mesostructures of the siloxane network. Figure 2 displays the TEM images of MSN-NH₂ and reveals nearly monodisperse nanospheres with a diameter of 90 to 110 nm. Besides, a well ordered honey-comb-like hexagonal array of the pores is readily visible at high magnification. To further confirm these conclusions on the whole compound, the X-ray diffraction and the dynamic light scattering analysis were performed.

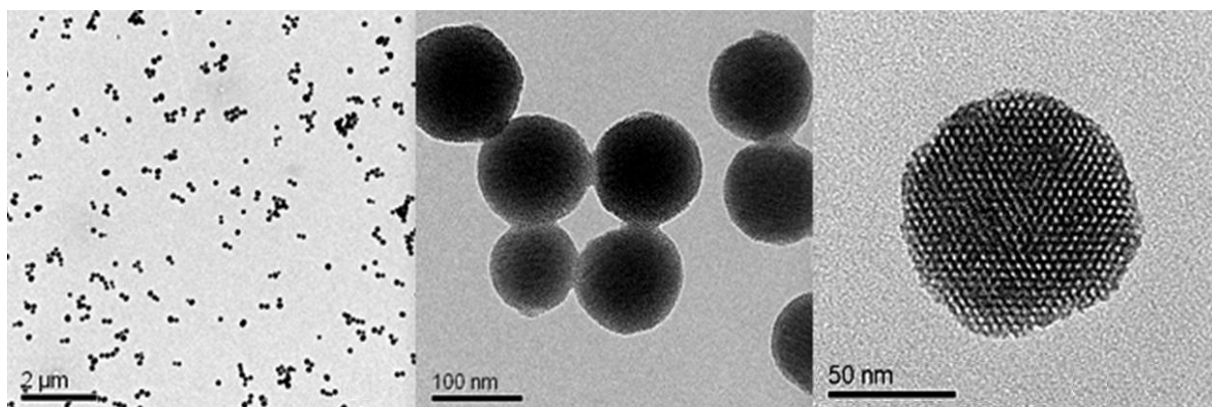


Figure 2. TEM micrographs of MSN-NH₂ at different magnifications.

X-Ray Diffraction. The organization of the porous framework is then controlled by XRD. Small angle diffraction peaks confirm the two-dimensional hexagonal symmetry ($p6m$) in the MSN (Figure 3A). The MSN d spacing (d_{100}) was calculated from the law of Bragg to be 4.1 nm, which led to the pore-to-pore distance of 4.7 nm (a_0 lattice parameter). The latter value can be used to approximate a pore diameter of 2.5-3 nm. Besides, the sharpness of the d_{100} peak and the presence of the well defined harmonics at $\sqrt{3}a_0$ ($2\theta = 3.7^\circ$) and $2a_0$ ($2\theta = 4.3^\circ$) demonstrates the long distance structural order in the nanomaterial.

Dynamic Light Scattering. The size distribution of the MSN is confirmed via DLS analysis (Figure 3B) on a solution of NPs sonicated for half an hour. The main size distribution (117 nm) corresponds to the non-aggregated nanoparticles, whereas the second population (374 nm) is related to irreversibly fused MSN (3 in average). These small nanoparticles could be used for biological applications.

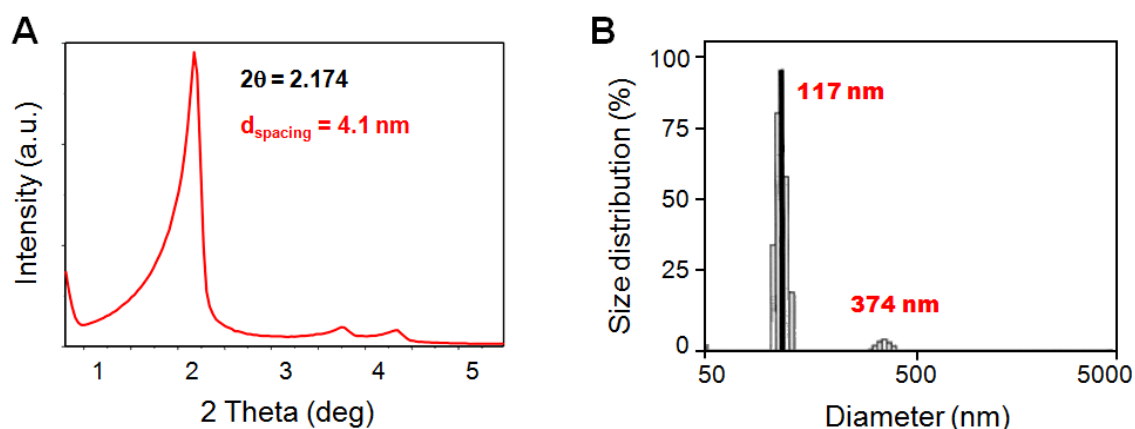


Figure 3. XRD pattern (A), and the DLS size distribution of the MSN-NH₂ (B).

N₂-adsorption-desorption. The adsorption-desorption of nitrogen in the mesopores, followed by the Brunauer–Emmett–Teller (BET) and Barrett–Joyner–Halenda (BJH) theories of calculation enables the determination of the surface area (S_{BET} in $\text{m}^2\cdot\text{g}^{-1}$) and the pore size distribution respectively (Figure 4). The surface area of MSN is calculated to be of $1075 \text{ m}^2\cdot\text{g}^{-1}$ with 2.5 nm pores. Note that, the mesoporous range of the pores confirms by the hysteresis in the adsorption-desorption cycles (Figure 4A).^[34]

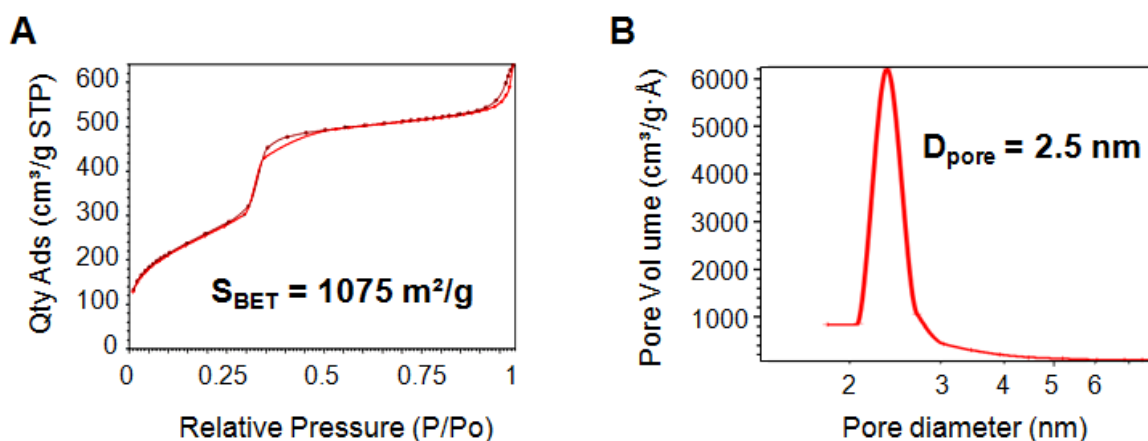


Figure 4. N_2 -adsorption-desorption isotherm (A), and pore size distribution of MSN (B).

Fourier Transform Infrared spectroscopy. Since the CTAB surfactant is highly cytotoxic, the use of MSN for biological applications requires the complete CTAB removal. The confirmation of the successful extraction of the surfactant is commonly performed via FTIR spectroscopy. The next figure shows the FTIR spectra of the MSN before and after CTAB acidic extraction. The vibration stretching modes $\nu_{\text{Si-O}} \approx 1000\text{--}1150 \text{ cm}^{-1}$ and $\nu_{\text{Si-C}} \approx 1200 \text{ cm}^{-1}$ validated the organosilica framework, and the aliphatic alkyl chains of CTAB could be observed with the $\nu_{\text{C-H}}$ mode around 2900 cm^{-1} .

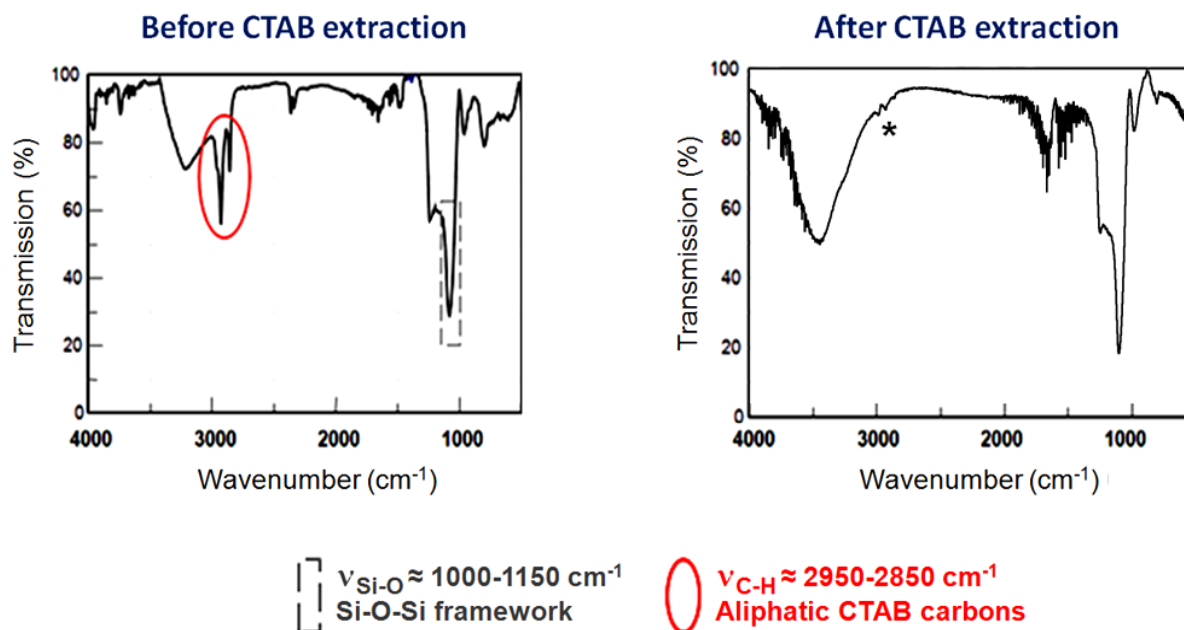


Figure 5. FTIR spectra before and after the acidic extraction of CTAB from MSN. *CTAB residues trapped in inaccessible pores.

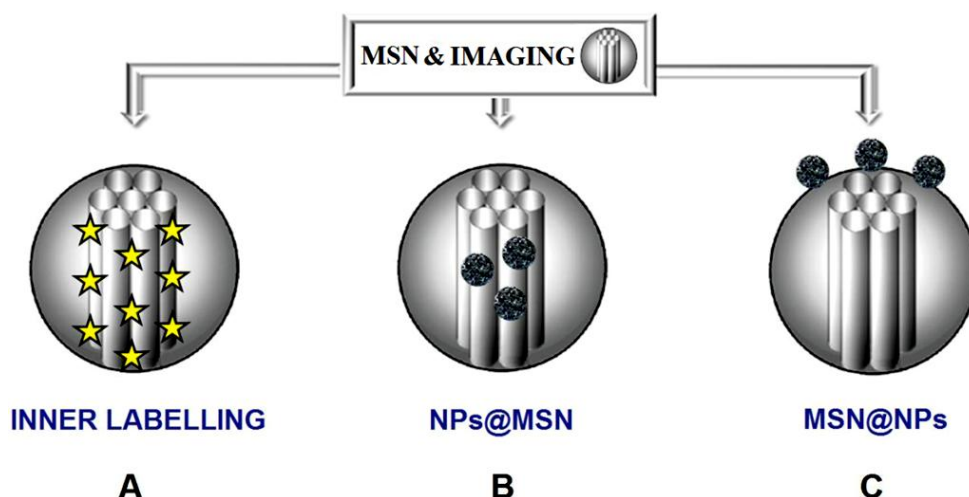
The post-extraction spectrum of the sample shows nearly complete extraction of the surfactant from the pores. Biological studies revealed no cytotoxicity of such NPs, which suggests that few remaining CTAB molecules are located within inaccessible pores.

1.5 MSN applications in theranostic nanomedicine

MSN are particularly attracting as theranostic nanocarriers. Indeed, the MSN platform allows the combination of several properties in a single device, such as cellular imaging, drug delivery, photodynamic and photothermal therapies.^[35] The former three features will be presented, along with the two-photon-actuated MSN in nanomedicine.

a) Imaging via MSN

The following scheme is a representation of the main strategies available to obtain MSN for imaging. The first approach is the inner-functionalization of the mesoporous silica with a fluorescent label (Scheme 3A), whereas the second and third approaches involve core shell systems with fluorescent or magnetic resonance imaging (MRI) active NPs (Scheme 3B-C). The reason for these three strategies is that it is generally easily feasible (though not always) to co-condense an alkoxysilylated dye with a silica precursor to have an external surface accessible for post-functionalization, whereas the stabilization of NPs within silica is much more challenging. As a result, when the porosity could not be maintained in NPs@MSN, or when the NPs encapsulation revealed either unsuccessful or insufficient, the surface functionalization was chosen.



Scheme 3. Representation of the diverse strategies of MSN suited for intracellular imaging (A-C): the inner functionalization of MSN with fluorescent labels (A), fluorescent NPs core MSN shell (B), and fluorescent NPs grafted on the surface of the MSN (C).

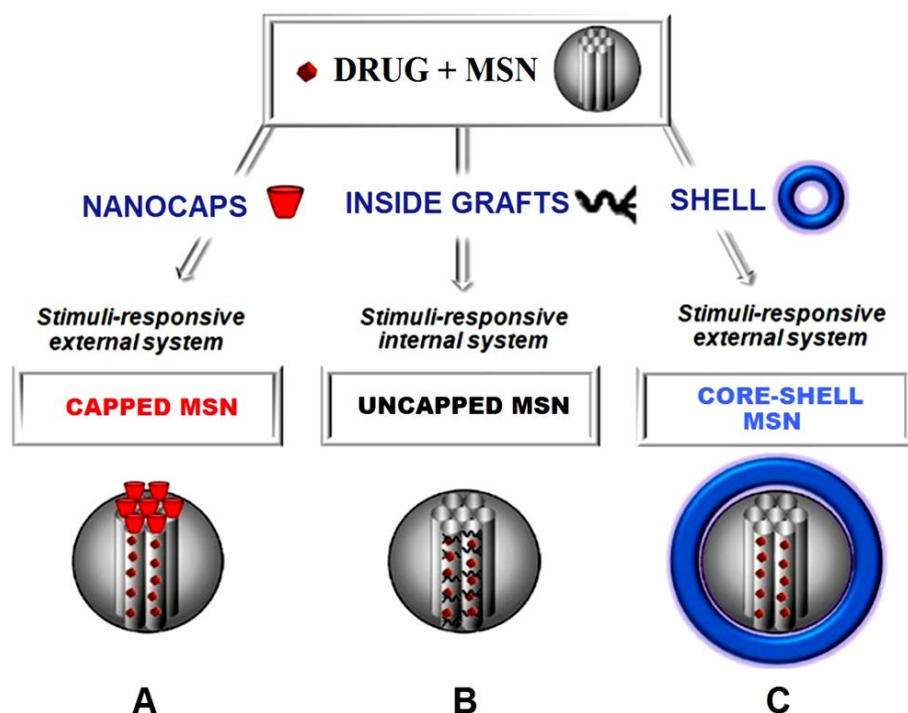
The earliest study on MSN as a nanomedical tool for imaging was published by Mou *et al* in 2004 in an article entitled “*Gadolinium(III)-Incorporated Nanosized Mesoporous Silica as Potential Magnetic Resonance Imaging Contrast Agents*”,^[36] which corresponds to Scheme 3B and will be presented hereafter.

Practically, the most straightforward and simple way to muster the imaging feature in the MSN matrix is based on the covalent functionalization of fluorescent dyes. Fluorescent MSN were also first reported the group Mou in 2005.^[37,38] They used the henceforth landmark of an alkoxysilylated fluorescein co-condensed with TEOS during the sol-gel reaction.^[39] In the case of a two photon fluorescence, Durand *et al.* developed two-photon fluorescent MSN,^[40] from complex organic molecules designed by and Blanchard-Desce *et al.*^[41-43] Recently, this feature has become more complex with multifluorescent MSN under a single excitation wavelength,^[44] dual colored MSN with pH activable rhodamine-lactam fluorescence for the sensing of the lysosomal acidity,^[45] and real time monitoring of intracellular drug delivery.^[46]

Secondly, various types of NPs could be either encapsulated within the silica, or coated on its surface (Scheme 3B and C respectively). Iron oxide nanospheres and nanorods, as well as hollow manganese oxide nanoparticles were developed as novel T1 magnetic resonance imaging (MRI) contrast agent within the silica framework.^[47-50] Gold nanospheres and nanorods were used as cores within MSN shells in order to track the nanoplatform via dark field microscopy.^[49,51] Recently, NaYF₄ nanocrystals were also coated with mesoporous silica for bimodal imaging and proved to be suitable for cell labeling,^[52] as were nanodiamond core MSN shells, successfully prepared for bioimaging and drug delivery.^[53] Finally, surface functionalization could be performed, for instance via gold nanorods to obtain the tracking of the nanodevices as well as photothermal properties.^[54]

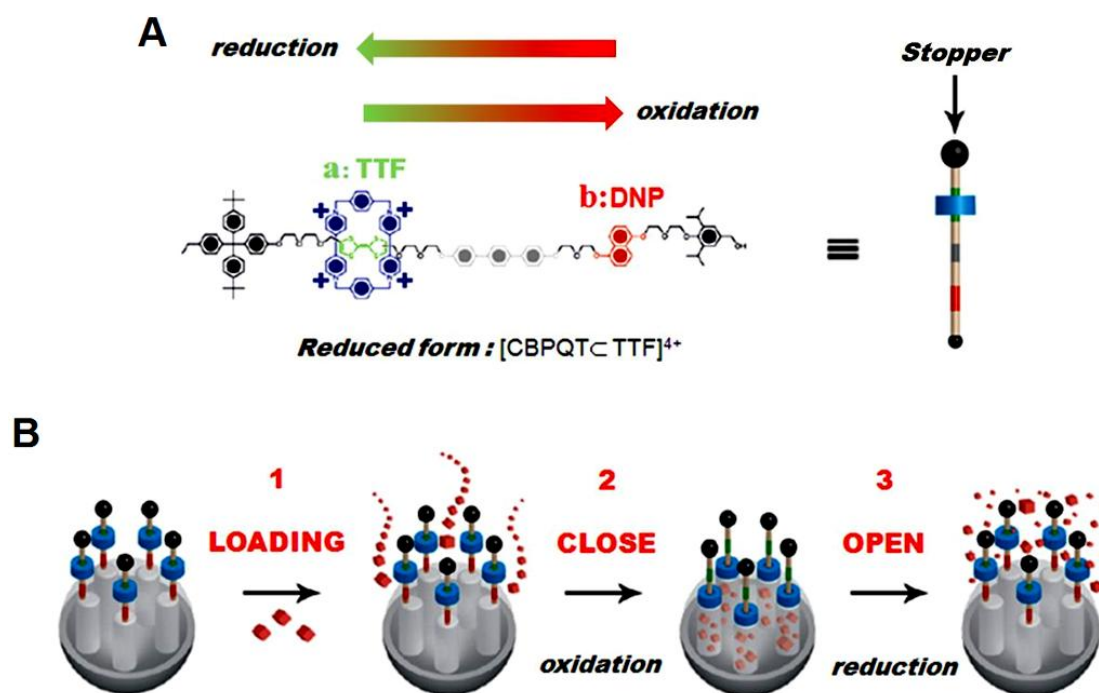
b) Drug delivery via MSN

Recent studies on MSN have explored three main strategies of encapsulation and delivery of cargo molecules (Scheme 4). Herein, we do not pretend to furnish an exhaustive overview in this wide and constantly progressing field. Indeed, from 2005 to 2008 and 2011 the production of research articles in that field has more than doubled every three year, with up to 350 publications in 2011, and the topic still flourishes up to this day.^[33]



Scheme 4. Versatile strategies of drug encapsulation in mesoporous silica nanomaterials: capped MSN (A), uncapped MSN (B), and core-shell MSN.

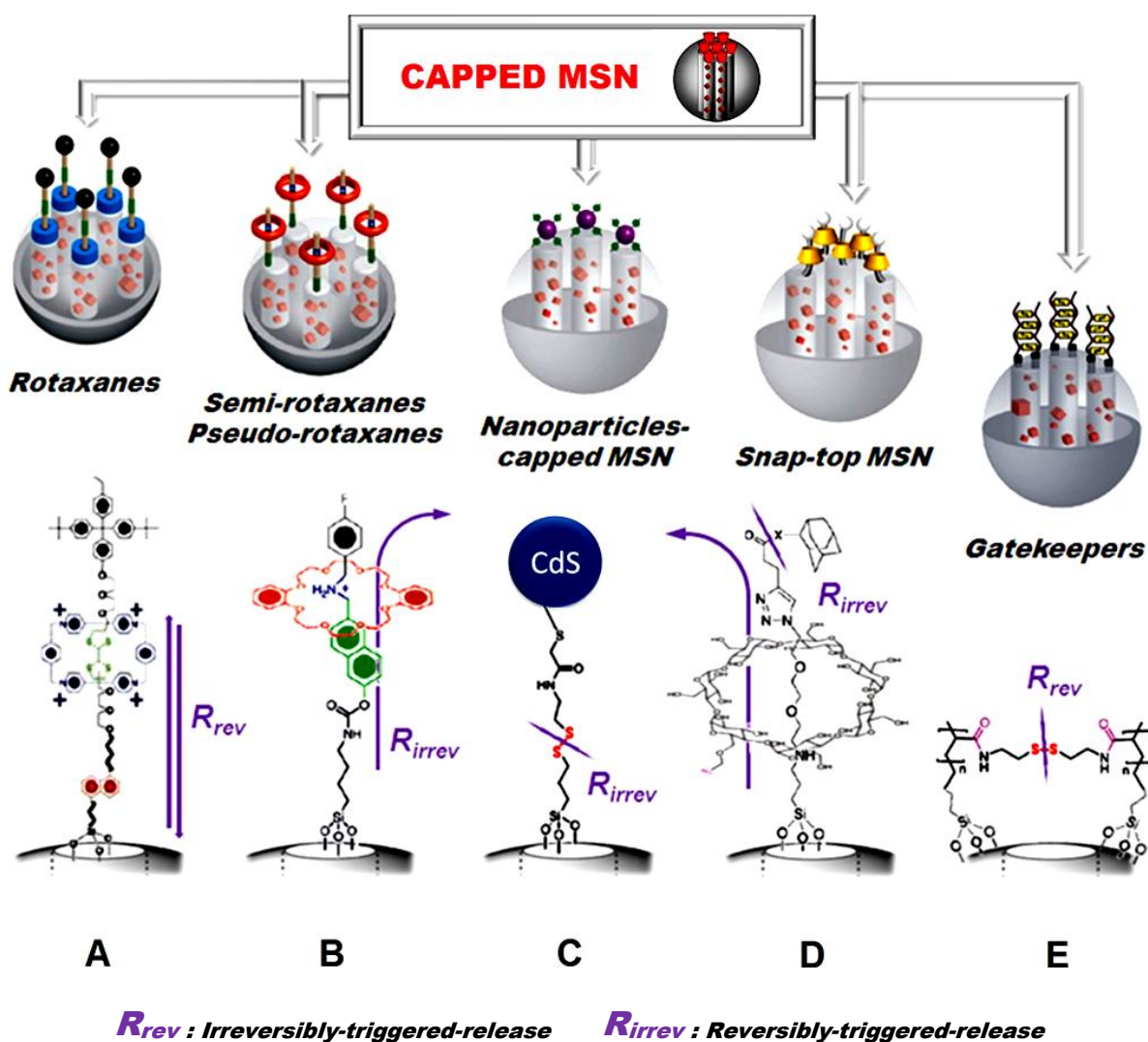
Capped MSN. As discussed earlier, historically the first drug delivery strategy involved “nanocaps” of CdS nanocrystals grafted via disulfide linkage on the MSN surface.^[19] This idea was then utilized with various other nanocaps to encapsulate and deliver cargo molecules (Scheme 4B). One such nanocarrier based on the “load-close-open” procedure, is the bistable rotaxane created by J. F. Stoddart and transformed as MSN-nanovalves along with J. I. Zink (Scheme 5).^[56,57] The nanovalve was constituted of a stalk of tetrathiafulvalene-1,5-dioxynaphthalene (TTF-DNP), and the mobile part was a molecular ring of [cyclobis(paraquat-*p*-phenylene)]⁴⁺ (CBPQT⁴⁺) (see Scheme 5A). In this study, the steps of closing and opening were induced by a redox process, which changed the affinity of the CBPQT⁴⁺ ring from the TTF to the DNP extremity of the stalk (Scheme 5B). Besides, the presence of bulky groups at the extremity of the stalk, called stoppers, offers a switchable ability to these mechanized MSN.



Scheme 5. Concept of the redox-triggered supramolecular affinities of the rotaxane (A), and representation of the loading-closing procedure for MSN nanovalves, along with the redox-actuated release of cargos from the pores (B). Adapted from reference 58.

Furthermore, at least five different nanocaps could be classified under the following designation: rotaxanes,^[56,57,59] nanovalves,^[60,61] semi-rotaxanes or pseudo-rotaxanes,^[62] NPs-capped MSN,^[19,63,64] snap-top MSN,^[65-67] and gatekeepers (see Scheme 6A-E).^[68-71] The cargo release could be either irreversible or reversible, according to the design of the nanocaps. Surface grafted NPs and snap-top systems are both based on the irreversible cleavage of a bulky object preventing the cargo release, therefore they (along with pseudo-rotaxanes) produce an irreversible release. On the contrary, rotaxanes do act as nanovalves *per se*, since they can be opened and closed reversibly. Such is also a feature of gatekeepers, which are typically polymeric system with switchable chemical binding or solubility.^[70] For instance, polyethyleneimine gatekeepers bonded to DNA were constructed on the MSN surface to trap cargo molecules.^[71]

Many stimuli have been used like oxidation and/or reduction with rotaxanes, semi-rotaxanes, pseudo-rotaxanes, nanoparticles-capped MSN.^[23-25] Gatekeepers were opened chemically,^[71] biochemically,^[68] electrochemically,^[72] thermally,^[69] and photochemically.^[73] Competitive binding have been equally harnessed in the case of semi-rotaxanes, which are also pH-responsive due to the electrostatic interactions involved in certain types of molecular rings as crown ethers (Scheme 6B),^[12] or cucurbituril.^[74] Cyclodextrin snap-tops were cleaved via light or enzyme stimuli (Scheme 6D).^[75]

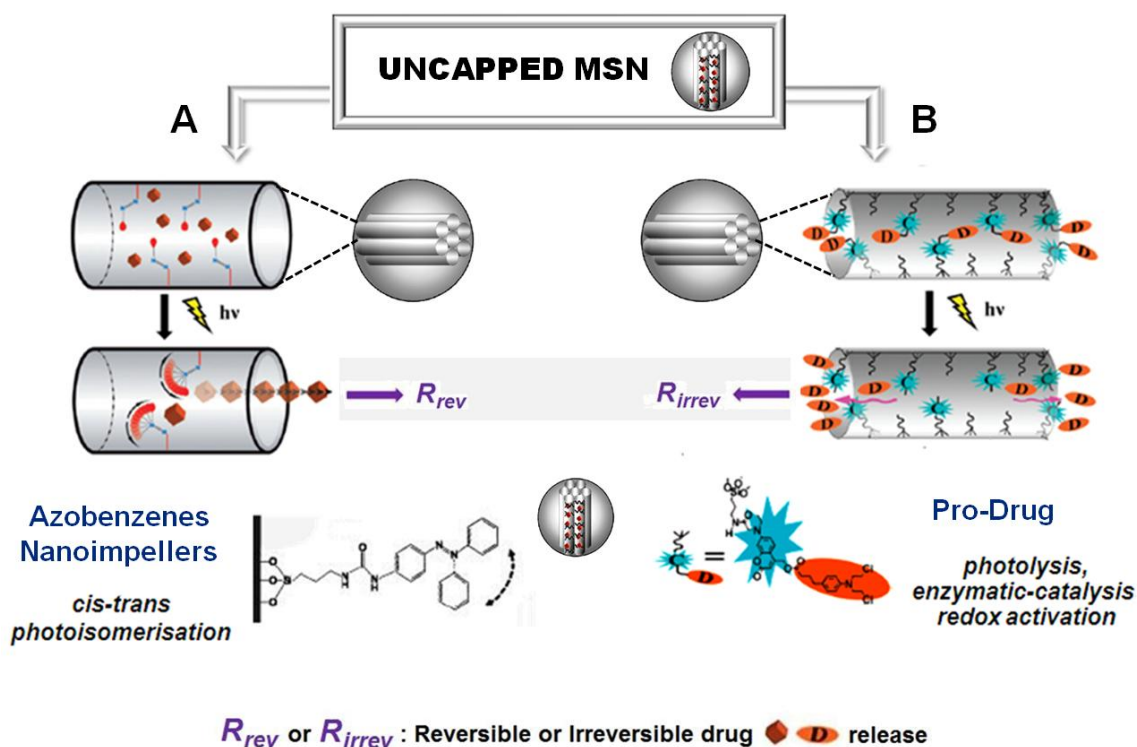


Scheme 6. Representation of five types of capped-MSN for cargo delivery (A-E).

Uncapped MSN. The simplest way to encapsulate cargos in MSN is by taking advantage of selective pore-cargo interactions, which correlates the solubility of the transported molecules. In this manner, J. Zink and F. Tamanoi used the hydrophobic camptothecin anticancer drug loaded in the MSN pores and transported towards cancer cells.^[76] The doxorubicin could also be transported and autonomously released in the lysosome through the electrostatic interactions involved with the silanols, which cease at pH 5.5 with the protonating of the drug.^[77] Nonetheless, the limitation of this strategy lies in the fact that there is always a premature release of the drug, especially in the biological media. Thus there is often neither a satisfactory temporal nor spacial selectivity of the drug release which is *la raison d'être* of nanovehicles.

As a result, more robust uncapped MSN were designed containing internal grafts which are elaborated to physically or chemically entrap drugs, as well as to release this payload on-demand (Scheme 7). The first challenge is to design mesostructures with a

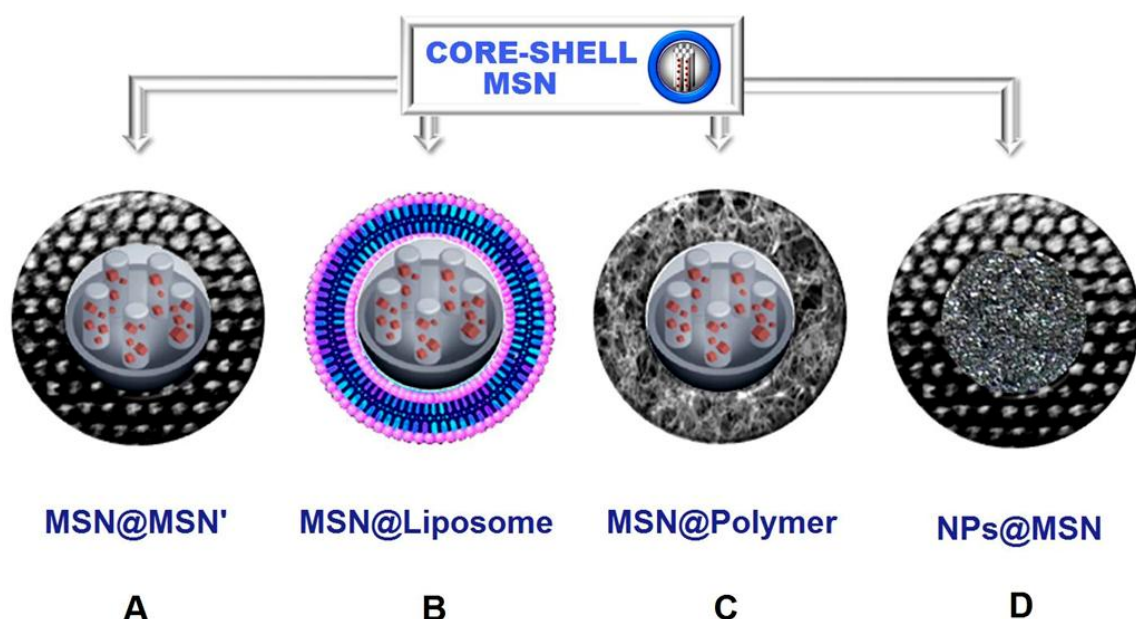
controlled density of the reactive functions *inside* the pores. Bein *et al* have demonstrated the specific functionalization of the pores through the passivation of the external MSN surface, by taking advantage of the presence of the template to functionalize aminopropyl groups, and then removing the template.^[78]



Scheme 7. Representation of the uncapped MSN smart nanovehicles strategies: azobenzene nanoimpellers (A),^[32] and pro-drug MSN (B).^[87]

Azobenzene nanoimpellers were incorporated in the silica mesopores in order to physically entrap camptothecin, and release it through light-induced photoisomerization in cancer cells.^[32] The wavelength of irradiation was 413 nm, which is close to the isobestic point at which the azobenzene cis-to-trans and trans-to-cis photoisomerizations constantly occur. Besides, in 2010 Zhu *et al.* reported a light actuated pro-drug strategy which managed to protect covalently linked drugs within the MSN.^[79] Note that these two strategies differ in that the former produces a reversible release feature via the on/off nanoimpeller photoisomerization, whereas the latter induces an irreversible drug release via instantaneous-photocleavage.

Core-shell MSN. In this case, the MSN are combined with various types of shells in order to confer additional properties or to regulate the rate of the release (Scheme 8). Thus the surface properties of the nanocarriers become those of the materials (or the molecules) which compose the shell.



Scheme 8. Representation of diverse core-shell nanocarrier strategies: hierarchical porosity in MSN (A) liposome, and polymer coated MSN NPs (B and C respectively), NPs core MSN shell (D).

Owing to correlation of the diffusion rate with the MSN pore diameter, multilayer MSN with hierarchical porosity (Scheme 8A) are both useful to control the release, and to deliver different molecules or biomolecules.^[80] Such structures could be also mechanized on their surface in order to trigger the delivery.

Moreover, a remarkable study on liposome fused on MSN nanocarriers (Scheme 8B) had shown their ability to deliver their content upon the destabilization of the phospholipids induced by enzymes inside the cells.^[81] In addition, various types of polymer coatings have been explored (Scheme 8C), such as the coating with poly(N-isopropylacrylamide) for pH and temperature-responsive MSN drug delivery.^[82]

Finally, another route which leads to a wide panel of materials is to design mesoporous silica shell on various nanoparticles (Scheme 8D). This idea had inspired versatile multifunctional materials such as $\text{Fe}_3\text{O}_4\text{@MSN}$ which combines superparamagnetic properties of Fe_3O_4 NPs with drug delivery of MSN,^[83] extensive research on Au@MSN , Ag@MSN , $\text{TiO}_2\text{@MSN}$, $\text{ZrO}_2\text{@MSN}$, to name a few. Silver NCs were embedded to provides antimicrobial properties on MSN nanocarriers, as time allowed the release of Ag^+ ions in the cell culture.^[84] Theranostic nanosystems have abounded in the literature compiling diagnostic and therapeutic properties: intracellular NPs tracking, magnetic resonance imaging (MRI), magnetic hyperthermia, plasmonic photothermal therapy, drug delivery, photodynamic therapy, and so on.

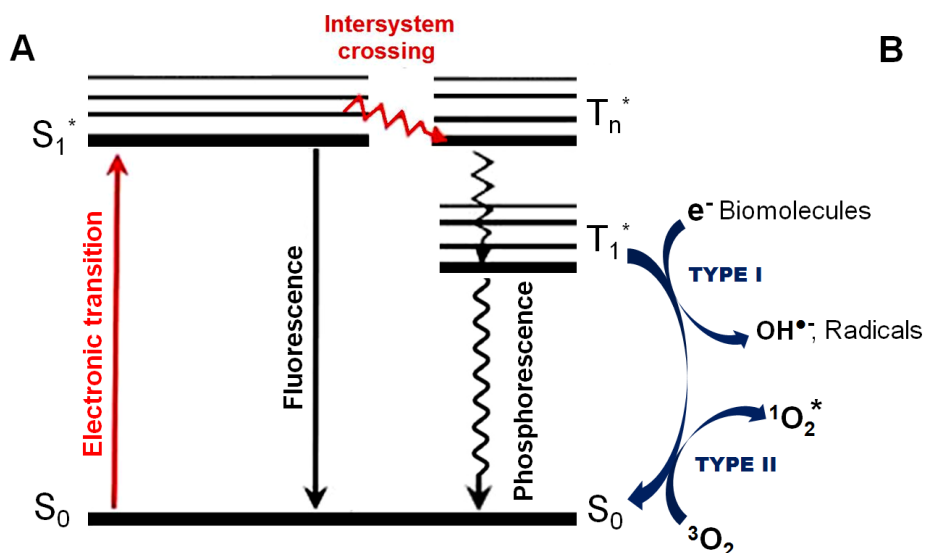
c) Photodynamic therapy via MSN

A brief history. The first observation of chemical sensitization of tissue via light stimuli was reported in 1900 by Raab.^[85] However, this was nothing new since the Egyptians were already using the sun light to treat skin diseases with natural substances, but, the idea of using light to treat cancer started in 1903 when Tappeiner and Jesionek used the eosin and the sunlight to treat skin cancer.^[86] Besides, it was not until the early eighties that a photoactive moiety (or photosensitizer) of a hematoporphyrin derivative was isolated and partially identified. They were later on known as “photofrins”. Today, photofrins have been approved by health organizations in the United States, Canada, Europe, and Japan for the treatment of various types of cancers.^[86]

Nowadays, photodynamic therapy (PDT) has emerged as an important method in biomedical research and clinical practice in cancerous pathologies. In fact, it is a less invasive technique due to the possibility to limit the treatment to the irradiated area, leaving the surrounding healthy tissues and cells undamaged.^[87,88] The most commonly used photosensitizers are derivatives of porphyrins, unfortunately many of them are hydrophobic which limits their potential applications in physiological conditions.^[89] Moreover, even with hydrophilic porphyrins, the selective accumulation in cells or tissues is usually too low for clinical use. Hence, the necessity of an adequate scaffold to overcome such disadvantages and carry the photosensitizer to the desired location has become a crucial point.

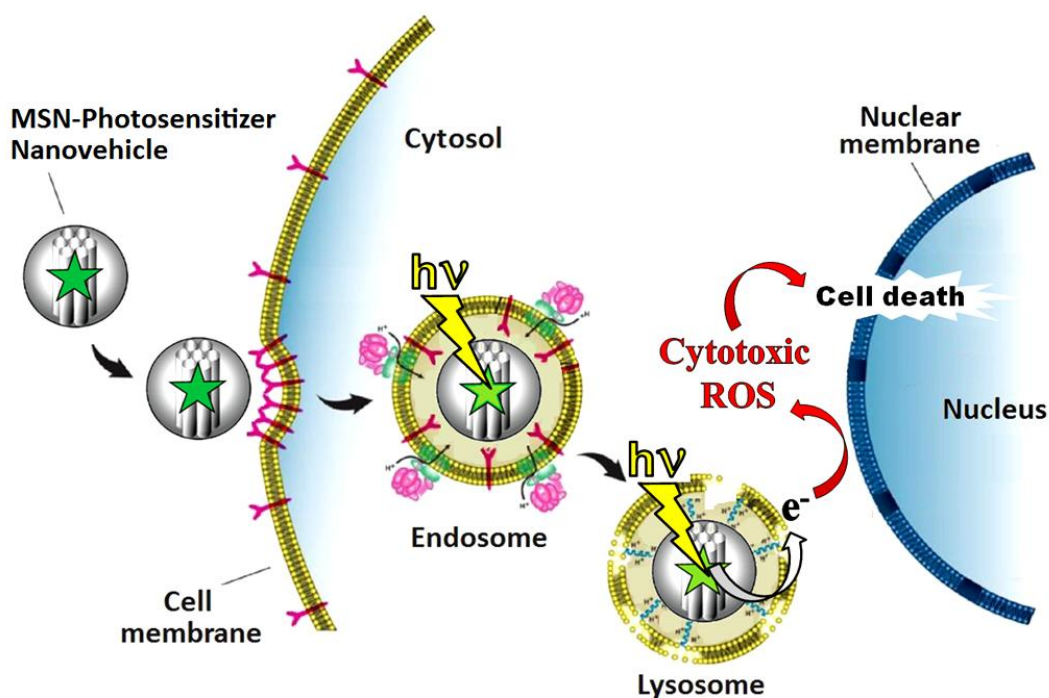
Mechanism. Following the absorption of light, the photosensitizer is excited from its ground singlet state (S_0) into an electronically excited singlet state (S_1^* , see Scheme 9A). At this point, fluorescence de-excitation generally occurs with a lifetime of 5 to 20 nanoseconds. However, intersystem crossing into a triplet state (T_n^* , T_1^*) can occur, followed by emission of a photon (phosphorescence) with a much longer half life in the order of milliseconds (sometimes even minutes or hours), which accounts for the remarkable optical properties of phosphorescent substances.

Furthermore, the T_1^* state can be followed by two kinds of reaction as shown in the Jablonski diagram (Scheme 9B). First, it can participate in an electron-transfer process with a biological substrate to form radicals and radical ions (type I mechanism), which may also interact with oxygen to form reactive oxygen species (ROS), such as OH^\bullet or O_2^\bullet . Alternatively, a type II mechanism resulting in the conversion of stable triplet oxygen (3O_2) leads to the short-lived cytotoxic and highly reactive singlet oxygen ($^1O_2^*$). In summary, since the diameter of human cells ranges from 10 to 100 μm , and the diffusion range of $^1O_2^*$ is limited to approximately 45 nm in cellular media,^[90] the PDT effect is *spatiotemporally controlled* according to the irradiation parameters.



Scheme 9. Modified Jablonski energy diagram (A) and the formation of cytotoxic ROS (B).

Application with MSN. The nanomedicine strategy thus came into play by incorporating photosensitizers in mesoporous silica frameworks to induce *in-vitro* and *in-vivo* PDT.^[92-94] The first study on MSN for PDT was published in by Mou *et al.* in 2009.^[95] They demonstrated the cancer therapy of a porphyrin derivative on HeLa cells. The MSN platform is indeed most suitable for a PDT mediated treatment via their capacity to transport specific photosensitizers, physically or chemically trapped in NPs. As expected, the light-actuated cancer cell killing was determined to be based on the generation of reactive cytotoxic ROS (See scheme 10).^[95]



Scheme 10. MSN-Photosensitizer as PDT agent *in-vitro*.

The following study of porphyrin-based nanoparticles for PDT has been reported and demonstrates the efficiency of the MSN scaffold. Human breast cancer cells were treated with MSN-Porphyrin functionalized with mannose targeting moieties on the NPs surface (see Figure 6A-B), then submitted to irradiation at 680 nm under low fluence (6 mW.cm^2) for 40 min, and caused a complete apoptosis (Figure 6C).^[96]

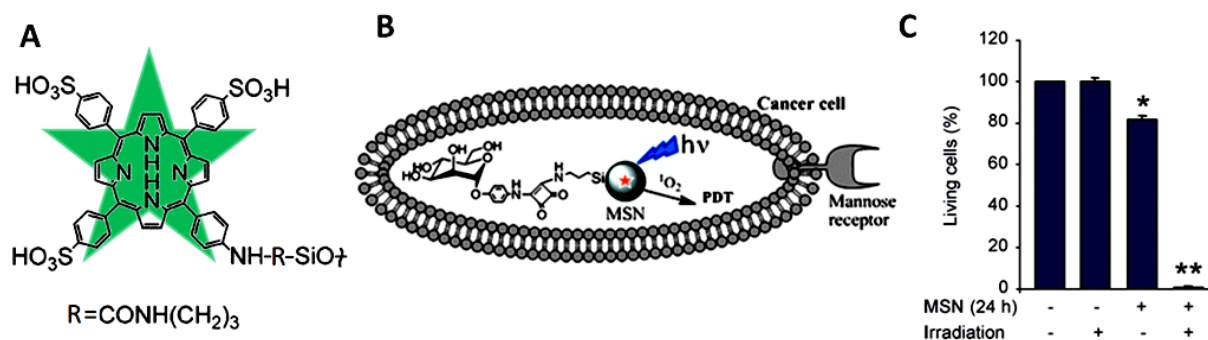
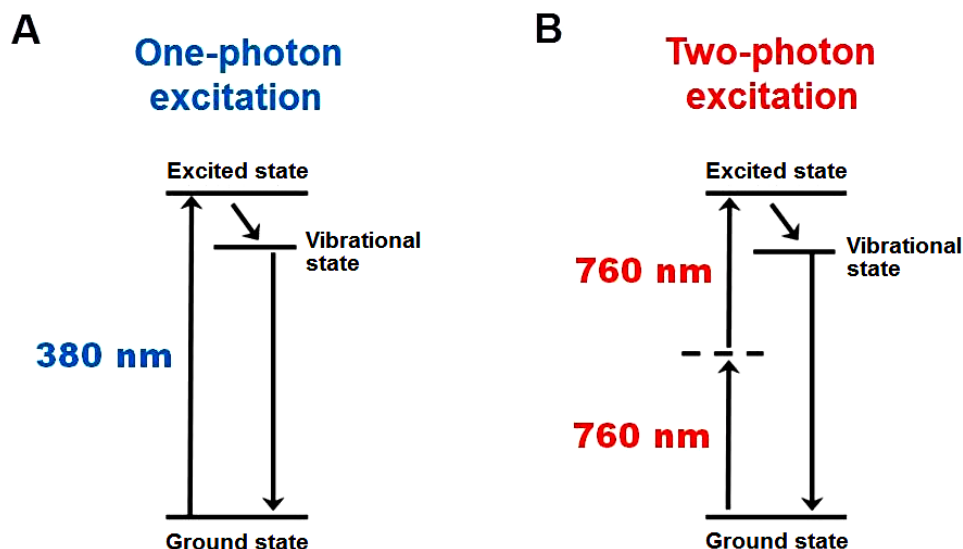


Figure 6. A porphyrin derivative (A) grafted on MSN capped with a mannose receptor for cancer treatment (B). Cancer cell survival study with and without NPs and laser light (C). Adapted from reference 104.

d) Two-photon nanomedicine relevance via MSN

Two-photon excitation principle. The two-photon absorption is a rare phenomenon of non-linear optics when one photon plus one photon equals one photon. In a two-photon absorption, two photons of same energy (though not always) are added to produce an energy transition equal to the sum of the energy of the two photons. It differs from linear absorption in that the strength of absorption depends on the square of the light intensity. Such a phenomenon involves two photons of comparably lower energy than needed for one photon excitation. Each photon carries approximately half of the energy necessary to excite a molecule (Scheme 11B).^[97] The probability of the near-simultaneous absorption of two photons is extremely low. The enhancement of the absorption can be reached either by means of high-power continuous wave lasers or short-pulse of femtosecond lasers.^[98] To further increase the two-photon excitation (TPE) probability, the two-photon laser has been combined with confocal microscopy to “concentrate” the photons in space and in time.



Scheme 11. Jablonski diagram of one (A) and two-photon excitations (B). Fluorescent absorption and emission transitions between the ground and excited states are depicted by vertical arrows.

Furthermore, the reason why two-photon absorption is rare is that most fluorescent molecules have low maximum two-photon cross sections (σ_2^{max}), calculated per chromophore in Goeppert-Mayer units (GM). The σ_2 varies according to the wavelength, and basically corresponds to the probability of a two-photon event. Hence, the mastering of organic synthesis and photophysics is necessary to design novel and powerful two-photon sensitive molecules, either fluorophores or photosensitizers.^[99-101]

Relevance of two-photon nanomedicine. As mentioned earlier, the medical application of nanotechnology in the field of cancer therapy requires both a *timely* and a *spatially*-controlled therapeutic effect. The non-fulfillment of these criteria would seriously diminish the efficacy of the treatment and produce unpredictable and unacceptable side effects on the patient. That is why the use of a two-photon near-infrared (NIR) irradiation is particularly relevant in nanomedicine, since it is a noninvasive three dimensional spatiotemporally-controlled irradiation of the order of one micron. Thus the tumor can be screened by the laser beam with the precision towards a single cell. Photographs made from the group of K. D. Belfield display the spacial resolution of two-photon (2 $h\nu$, 760 nm) versus one-photon (1 $h\nu$, 380 nm) irradiations with 200 femtosecond pulsed laser beams (Figure 7A and B).^[102]

On the other hand, another key point comes from the NIR light which minimizes the scattering and attenuation of the irradiation in the living tissues. Figure 7C represents the penetration depth in the human skin of the laser as a function of the wavelength. The so-called biological window is the wavelength range that is most appropriated for a safe laser treatment, the best results being obtained at 740 nm with a 3 cm penetration depth.^[103] The variation of the laser penetration is related to the different refractive indices and molar extinction coefficients of the components present in human tissues (skin layer, blood, water, fat

tissues).^[104] Moreover, the scattering coefficient of human tissue decreases as the wavelength increases, which further accounts for the interests of two-photon NIR-actuated nanomedicine.

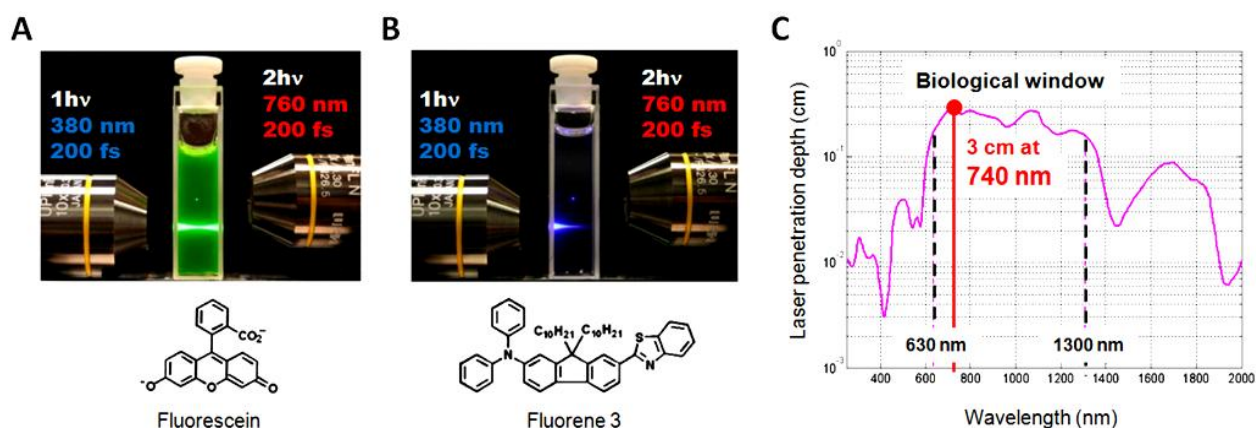


Figure 7. One-photon versus two-photon irradiation of fluorescein and fluorene 3 displaying the 3D-spatial resolution of TPE (A and B respectively). Laser penetration depth in the human skin as a function of the wavelength (C).

In summary, TPE nanomedicine in the NIR is particularly relevant for cancer therapy. Pathologies involving short laser penetrations such as skin and retinoblastoma cancers could greatly benefit from efficient medical nanodevices using NIR TPE. To further increase the penetration depth threshold, surgery and optical fibers could be alternatives, but from today's knowledge standpoint, it is likely that some pathologies would need different actuations.

REFERENCES

- [1] "Process for producing silica in the form of hollow spheres", Application No. US 342525 A filed on 04-Feb-1964; Publication No. US 3383172 A published on 14-May-1968.
- [2] "Porous silica particles containing a crystallized phase and method", Application No. US 3493341D A filed on 23-Jan-1967; Publication No. US 3493341 A published on 03-Feb-1970.
- [3] Chiola, V.; Ritsko, J. E. and Vanderpool, C. D. "Process for producing low-bulk density silica", Application No. US 3556725D A filed on 26-Feb-1969; Publication No. US 3556725 A published on 19-Jan-1971.
- [4] T. Yanagisawa, T. ShimizuK. Kuroda, C. Kato, *Bull. Chem. Soc. Jpn.* **1990**, 63, 988.
- [5] S. Beck, J. C. Vartuli, W. J. Roth, M. E. Leonowicz, C. T. Kresge, K. D. Schmitt, C. T.-W. Chu, D. H. Olson, E. W. Sheppard, S. B. McCullen, J. B. Higgins, and J. L. Schlenkert, *J. Am. Chem. Soc.* **1992**, 114, 10834.
- [6] F. Drenzo, H. Cambon, R. Dutartre, *Micro. Mater.* **1997**, 10, 283.
- [7] D. Zhao, J. Feng, K. Huo, N. Melosh, G. H. Fredrickson, B. F. Chmelka, G. D. Stucky, *Science* **1998**, 279, 548.
- [8] S. Sadasivan, C. E. Fowler, D. Khushalani, S. Mann, *Angew. Chem. Int. Ed.* **2002**, 41, 2151.
- [9] C.-Y. Lai, B. G. Trewyn, D. M. Jeftinija, K. Jeftinija, S. Xu, S. Jeftinija, V. S. Y. Lin, *J. Am. Chem. Soc.* **2003**, 125, 4451.
- [10] D. Tarn, C. E. Ashley, M. Xue, E. C. Carnes, J. I. Zink, C. J. Brinker, *Acc. Chem. Res.* **2013**, 46, 792.
- [11] V. Mamaeva, C. Sahlgren, M. Lindén, *Adv. Drug Del. Rev.* **2013**, 65, 689.
- [12] C. Hom, J. Lu, F. Tamanoi, *J. Mater. Chem.* **2009**, 19, 6308.
- [13] S. Palantavida, N. V. Guz, C. D. Woodworth, I. Sokolov, *Nanomedicine: NBM* **2013**, 9, 1255.
- [14] H. Zhang, D. R. Dunphy, X. Jiang, H. Meng, B. Sun, D. Tarn, M. Xue, X. Wang, S. Lin, Z. Ji, R. Li, F. L. Garcia, J. Yang, Ma. L. Kirk, T. Xia, J. I. Zink, A. Nel, C. J. Brinker, *J. Am. Chem. Soc.* **2012**, 134, 1579.
- [15] C. Argyo, V. Weiss, C. Bräuchle, T. Bein, *Chem. Mater.* **2014**, 26, 435.
- [16] H. Yamada, C. Urata, H. Ujiie, Y. Yamauchi, K. Kuroda, *Nanoscale* **2013**, 5, 6145.
- [17] I. I. Slowing, J. L. Vivero-Escoto, C. W. Wu, V. S. Y. Lin, *Adv. Drug Deliv. Rev.* **2008**, 60, 1278.
- [18] F. Gao, P. Botella, A. Corma, J. Blesa, L. Dong, *J. Phys. Chem. B*, **2009**, 113, 1796.
- [19] B. G. Trewyn, S. Giri, I. I. Slowing, V. S. Y. Lin, *Chem. Commun.* **2007**, 31, 3236.
- [20] D. Niu, Z. Liu, Y. Li, X. Luo, J. Zhang, J. Gong, J. Shi, *Adv. Mater.* **2014**, DOI: 10.1002/adma.201400815.
- [21] D. R. Radu, C.-Y. Lai, K. Jeftinija, E. W. Rowe, S. Jeftinija, V. S. Y. Lin, *J. Am. Chem. Soc.* **2004**, 126, 13216.
- [22] I. I. Slowing, B. G. Trewyn, V. S. Y. Lin, *J. Am. Chem. Soc.* **2007**, 129, 884.
- [23] C. Y. Lai, B. G. Trewyn, D. M. Jeftinija, K. Jeftinija, S. Xu, S. Jeftinija, V. S. Y. Lin, *J. Am. Chem. Soc.* **2003**, 125, 4451.
- [24] E. Aznar, M. D. Marcos, R. Martinez-Máñez, F. Sancenón, J. Soto, P. Amorós, C. Guillem, *J. Am. Chem. Soc.* **2009**, 131, 6833.
- [25] S. Giri, B. G. Trewyn, M. P. Stellmaker, V. S. Y. Lin, *Angew. Chem. Int. Ed.* **2005**, 44, 5038.
- [26] C. Charnay, S. Bégu, C. Tourné-Péteillh, L. Nicole, D. A. Lerner, J.-M. Devoiselle, *Eur. J. Pharm. Biopharm.* **2004**, 57, 533.
- [27] J. Lu, M. Liong, S. Sherman, T. Xia, M. Kovochich, A. E. Nel, J. I. Zink, F. Tamanoi, *Nanobiotechnol.* **2007**, 3, 89.
- [28] G. V. Rama Rao, G. P. López, J. Bravo, H. Pham, A. K. Datye, H. F. Xu, T. L. Ward, *Adv. Mater.* **2002**, 14, 1301.
- [29] K. Ma, U. Werner-Zwanziger, J. Zwanziger, U. Wiesner, *Chem. Mater.* **2013**, 25, 677.
- [30] X. Huang, X. Teng, D. Chen, F. Tang, J. He, *Biomaterials* **2010**, 31, 438.
- [31] X. Huang, L. Li, T. Liu, N. Hao, H. Liu, D. Chen, F. Tang, *ACS Nano* **2011**, 5, 5390.
- [32] J. Lu, E. Choi, F. Tamanoi, J. I. Zink, *Small* **2008**, 4, 421.
- [33] F. Tang, L. Li, D. Chen, *Adv. Mater.* **2012**, 24, 1504.
- [34] Sing, *Pure Appl. Chem.* **1985**, 63, 612.
- [35] N.-T. Chen, S.-H. Cheng, J. S. Souris, C.-T. Chen, C.-Y. Mou, L.-W. Lo, *J. Mater. Chem. B* **2013**, 1, 3128.
- [36] F. Tang, L. Li, D. Chen, *Adv. Mater.* **2012**, 24, 1504.
- [37] D.-M. Huang, Y. Hung, B.-S. Ko, S.-C. Hsu, W.-H. Chen, C.-L. Chien, C.-P. Tsai, C.-T. Kuo, J.-C. Kang, C.-Y. Mou, Y.-C. Chen, *FASEB.* **2005**, 19, 2014.
- [38] V. S. Y. Lin, C.-P. Tsai, H.-Y. Huang, C.-T. Kuo, Y. Hung, D.-M. Huang, Y.-C. Chen, C.-Y. Mou, *Chem. Mater.* **2005**, 17, 4570.
- [39] I. Slowing, B. G. Trewyn, V. S. Y. Lin, *J. Am. Chem. Soc.* **2006**, 128, 14792.
- [40] M. Gary-Bobo, Y. Mir, C. Rouxel, D. Brevet, O. Hocine, M. Maynadier, A. Gallud, A. Da Silva, O. Mongin, M. Blanchard-Desce, S. Richeter, B. Looock, P. Maillard, A. Morère, M. Garcia, L. Raehm, J.-O. Durand, *Int. J. Pharma.* **2012**, 432, 99.
- [41] O. Mongin, L. Porrès, M. Charlot, C. Katan, M. Blanchard-Desce, *Chem. Eur. J.* **2007**, 13, 1481.

- [42] E. Beaumont, J.-C. Lambry, A.-C. Robin, P. Martasek, M. Blanchard-Desce, A. Slama-Schwok, *ChemPhysChem* **2008**, 9, 2325.
- [43] A.-C. Robin, S. Gmouh, O. Mongin, V. Jouikov, M. H. V. Werts, C. Gautier, A. Slama-Schwok, M. Blanchard-Desce, *Chem. Commun.* **2007**, 13, 1134.
- [44] L. Wang, J. Lei, J. Zhang, *Chem. Commun.* **2009**, 16, 2195.
- [45] J. Lai, B. P. Shah, E. Garfunkel, K.-B. Lee, *ACS Nano* **2013**, 7, 2741.
- [46] S. Wu, Z. Li, J. Han, S. Han, *Chem. Comm.* **2011**, 47, 11276.
- [47] S.-H. Wu, Y.-S. Lin, Y. Hung, Y.-H. Chou, Y.-H. Hsu, C. Chang, C.-Y. Mou, *ChemBioChem* **2008**, 9, 53.
- [48] J. Kim, H. S. Kim, N. L., T. Kim, H. Kim, T. Yu, I. C. Song, W. K. Moon, T. Hyeon, *Angew. Chem. Int. Ed.* **2008**, 47, 8438.
- [49] Y. Chen, H. Chen, D. Zeng, Y. Tian, F. Chen, J. Feng, J. Shi, *ACS Nano* **2010**, 10, 6001.
- [50] T. Kim, E. Momin, J. Choi, K. Yuan, H. Zaidi, J. Kim, M. Park, N. Lee, M. T. McMahon, A. Quinones-Hinojosa, J. W. M. Bulte, T. Hyeon, A. A. Gilad, *J. Am. Chem. Soc.* **2011**, 133, 2955.
- [51] X. Huang, P. K. Jain, I. H. El-Sayed, M. A. El-Sayed, *Nanomedicine*, **2007**, 2, 681.
- [52] X. Lui, H. Qian, Y. Ji, Z. Li, Y. Shao, Y. Hu, G. Tong, L. Li, W. Guo, H. Guo, *RSC Adv.* **2012**, 2, 12263.
- [53] N. Prabhakarab, T. Näreoja, E. von Haartmana, D. Ş. Karamana, H. Jiange, S. Kohod, T. A. Dolenkof, P. E. Hänninend, D. I. Vlasovg, V. G. Ralchenkog, S. Hosomih, I. I. Vlasovg, C. Sahlgrenbci, J. M. Rosenholm, *Nanoscale* **2013**, 5, 3713.
- [54] Z. Zhang, L. Wang, J. Wang, X. Jiang, X. Li, Z. Hu, Y. Ji, X. Wu, C. Chen, *Adv. Mater.* **2012**, 24, 1418.
- [55] H. Li, L.-L. Tan, P. Jia, Q.-L. Li, Y.-L. Sun, J. Zhang, Y.-Q. Ning, J. Yuc, Y.-W. Yang, *Chem. Sci.* **2014**, DOI: 10.1039/C4SC00198B.
- [56] R. Hernandez, H.-R. Tseng, J. W. Wong, J. F. Stoddart, J. I. Zink, *J. Am. Chem. Soc.* **2004**, 126, 3370.
- [57] T. D. Nguyen, K. C.-F. Leung, M. Liong, C. D. Pentecost, J. F. Stoddart, J. I. Zink, *Org. Lett.* **2006**, 8, 3363.
- [58] K. K. Coti, M. E. Belowi, M. Liong, M. W. Ambrogio, Y. A. Lau, H. A. Khabib, J. I. Zink, N. M. Khashab, J. F. Stoddart, *Nanoscale*, **2009**, 1, 16.
- [59] S. Angelos, E. Johanson, J. F. Stoddart, J. I. Zink, *Adv. Funct. Mater.* **2007**, 17, 2261.
- [60] D. P. Ferris, Y.-L. Zaho, N. M. Khashab, H. A. Khabib, J. F. Stoddart, J. I. Zink, *J. Am. Chem. Soc.* **2009**, 131, 1686.
- [61] C. R. Thomas, D. P. Ferris, J.-H. Lee, E. Choi, M.-H. Cho, E. S. Kim, J. F. Stoddart, J.-S. Shin, J. Cheon, J. I. Zink, *J. Am. Chem. Soc.* **2010**, 132, 10623.
- [62] S. Angelos, Y.-W. Yang, N. Khashab, J. F. Stoddart, J. I. Zink, *J. Am. Chem. Soc.* **2009**, 131, 11344.
- [63] R. Liu, Y. Zhang, X. Zhao, A. Agarwal, L. J. Mueller, P. Feng, *J. Am. Chem. Soc.* **2010**, 132, 1500.
- [64] F. Muhammad, M. Guo, W. Qi, F. Sun, A. Wang, Y. Guo, G. Zhu, *J. Am. Chem. Soc.* **2011**, 133, 8778.
- [65] K. Patel, S. Angelos, W. R. Dichtel, A. Coskun, Y. W. Yang, J. I. Zink, J. F. Stoddart, *J. Am. Chem. Soc.* **2008**, 130, 2382.
- [66] M. W. Ambrogio, T. A. Pecorelli, K. Patel, N. M. Khashab, A. Trabolsi, H. A. Khatib, Y. Y. Botros, J. I. Zink, J. F. Stoddart, *Org. Lett.* **2010**, 12, 3304.
- [67] Z. Luo, K. Cai, Y. Hu, L. Zhao, P. Liu, L. Duan, W. Yang, *Angew. Chem. Int. Ed.* **2011**, 50, 640.
- [68] C. Park, K. Lee, C. Kim, *Angew. Chem. Int. Ed.* **2009**, 48, 1275.
- [69] E. Aznar, L. Mandragón, J. V. Ros-Lis, F. Sancenón, M. D. Marcos, R. Martínez-Máñez, J. Soto, E. Pérez-Payá, P. Amorós, *Angew. Chem. Int. Ed.* **2011**, 123, 11368.
- [70] R. Liu, X. Zhao, T. Wu and P. Y. Feng, *J. Am. Chem. Soc.* **2008**, 130, 14418.
- [71] R. Casasús, E. Climent, M. D. Marcos, R. Martínez-Máñez, F. Sancenón, J. Soto, P. Amorós, J. Cano, E. Ruiz, *J. Am. Chem. Soc.* **2008**, 130, 1903.
- [72] N. M. Khashab, A. Trabolsi, Y. A. Lau, M. W. Ambrogio, D. C. Friedman, H. A. Khatib, J. I. Zink, J. F. Stoddart, *Eur. J. Org. Chem.* **2009**, 11, 1669.
- [73] C. Park, K. Lee, C. Kim, *Angew. Chem. Int. Ed.* **2009**, 121, 1301.
- [74] S. Angelos, Y.-W. Yang, K. Patel, J. F. Stoddart, J. I. Zink, *Angew. Chem. Int. Ed.* **2008**, 47, 2222.
- [75] A. Bernardos, E. Aznar, M. D. Marcos, R. Martínez-Máñez, F. Sancenón, J. Soto, J. M. Barat, P. Amorós, *Angew. Chem. Int. Ed.* **2009**, 48, 5884.
- [76] J. Lu, M. Liong, J. I. Zink, F. Tamanoi, *Small* **2007**, 3, 1341.
- [77] M. Ma, H. Chen, Y. Chen, X. Wang, F. Chen, X. Cui, J. Shi, *Biomaterials* **2012**, 33, 989.
- [78] J. Kecht, A. Schlossbauer, T. Bein, *Chem. Mater.* **2008**, 20, 7207.
- [79] Q. Lin, Q. Huang, C. Li, C. Bao, Z. Liu, F. Li, L. Zhu, *J. Am. Chem. Soc.* **2010**, 132, 10645.
- [80] V. Cauda, A. Schlossbauer, J. Kecht, A. Zürner, T. Bein, *J. Am. Chem. Soc.* **2009**, 131, 11361.
- [81] J. Liu, X. Jiang, C. Ashley and C. J. Brinker, *J. Am. Chem. Soc.* **2009**, 131, 7567.
- [82] Q. Fu, G. V. Rama Rao, L. K. Ista, Y. Wu, B. P. Andrzejewski, L. A. Sklar, T. L. Ward, G. P. Lopez, *Adv.*

Mater. **2003**, 15, 1262.

[83] C. Vogt, Toprak, T. Muhammet, S. Laurent, J.-L. Bridot, R. Müller, M. Muhammed, *J. Nanopart. Res.* **2010**, 12, 1137.

[84] M. Liong, B. France, K. A. Bradley, J. I. Zink, *Adv. Mater.* **2009**, 21, 1684.

[85] O. Raab, *Z. Biol.* **1900**, 39, 524.

[86] D. E. Dolmans, D. Fukumura and R. K. Jain, *Nat. Rev. Cancer*, **2003**, 3, 380.

[87] B. W. Henderson, S. M. Waldow, T. S. Mang, W. R. Potter, P. B. Malone, T. J. Dougherty, *Cancer Res.* **1985**, 45, 572.

[88] M. Ochsner, *J. Photochem. Photobiol. B* **1997**, 39, 1.

[89] Y. N. Konan, R. Gurny, E. Allémann, *J. Photochem. Photobiol. B* **2002**, 66, 89.

[90] W. M. Sharman, C. M. Allen and J. E. Van Lier, *Methods Enzymol.*, **2000**, 319, 376.

[91] M. Sadasivam, P. Avci, G. K. Gupta, S. Lakshmanan, R. Chandran, Y-Y. Huang, R. Kumar, M. R. Hamblin, *Eur. J. Nanomed.* **2013**, 5, 115.

[92] D. Bechet, P. Couleaud, C. Frochot, M. L. Viriot, F. Guillemin, M. Barberi-Heyob, *Trends Biotechnol.* **2008**, 26, 612.

[93] P. Couleaud, V. Morosini, C. Frochot, S. Richeter, L. Raehm, J.-O. Durand, *Nanoscale* **2010**, 2, 1083.

[94] M. Gary-Bobo, Y. Mir, C. Rouxelb, D. Brevet, O. Hocinec, M. Maynadier, A. Gallud, A. Da Silva, O. Mongin, M. Blanchard-Desce, S. Richeter, B. Looock, Philippe Maillard, A. Morère, M. Garcia, Laurence Raehm, J.-O. Durand, *Inter. J. Pharma.* **2012**, 432, 99.

[95] H.-L. Tu, V. S. Y. Lin, H.-Y. Lin, Y. Hung, L.-W. Lo, Y.-F. Chen, C.-Y. Mou, *Adv. Mater.* **2009**, 21, 172.

[96] D. Brevet, M. Gary-Bobo, L. Raehm, S. Richeter, O. Hocine, K. Amro, B. Looock, P. Couleaud, C. Frochot, A. Morère, P. Maillard, M. Garcia, J.-O. Durand, *Chem. Commun.* **2009**, 12, 1475.

[97] M. Oheim, D. J. Michael, M. Geisbauer, D. Madsen, R. H. Chow, *Adv. Drug Deliv. Rev.* **2006**, 58, 788.

[98] A. Diaspro, G. Chirico, M. Collini, *Quart. Rev. Biophys.* **2005**, 38, 97.

[99] B. A. Reinhardt, L. L. Brott, S. L. Clarson, A. G. Dillard, J. C. Bhatt, R. Kannan, L. Yuan, G. S. He, P. N. Prasad, *Chem. Mater.* **1998**, 10, 1863.

[100] M. Pawlicki, H. A. Collins, R. G. Denning, H. L. Anderson, *Angew. Chem.Int. Ed.* **2009**, 48, 3244.

[101] C. B. Milojevic, D. W. Silverstein, L. Jensen, J. P. Camden, *J. Am. Chem. Soc.* **2011**, 133, 14590.

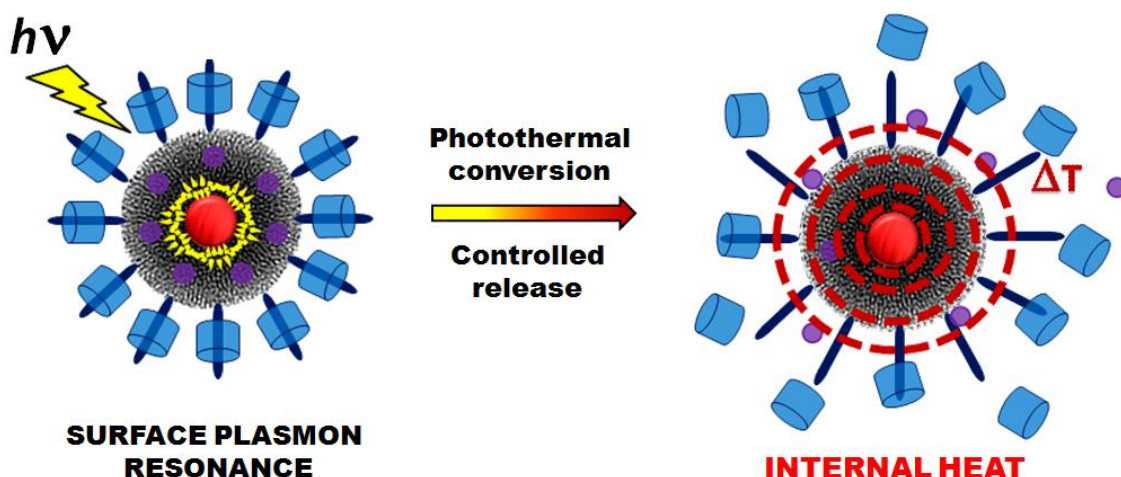
[102] K. D. Belfield, M. V. Bondar, F. E. Hernandez, O. V. Przhonska, S. Yao, *J. Phys. Chem. B* **2007**, 111, 12723.

[103] A. M. Smith, M. C. Mancini, S. Nie, *Nat. Nanotechnol.* **2009**, 4, 710.

[104] C. L. Tsai, J. C. Chen, W. J. Wang, *J. Med. Biol. Eng.* **2001**, 21, 7.

CHAPTER 2

Nanvalve-Controlled Cargo Release Activated by Plasmonic Heating[†]



Abstract

The synthesis and operation of a light-actuated nanvalve that controls the pore openings of mesoporous silica nanoparticles containing gold nanoparticle cores is described. The nanoparticles, composed of 20 nm gold cores inside 150 nm mesoporous silica spheres, were synthesized using a unique one-pot method. The nanovalves consist of cucurbit[6]uril rings encircling stalks that are attached to the 2 nm pore openings. Plasmonic heating of the gold core raises the local temperature and decreases the ring–stalk binding constant, thereby unblocking the pore and releasing the cargo molecules that were preloaded inside. Bulk heating of the suspended particles to 60 °C is required to release the cargo, but no bulk temperature change was observed in the plasmonic heating release experiment. High-intensity irradiation caused thermal damage to the silica particles, but low-intensity illumination caused a local temperature increase sufficient to operate the valves without damaging the nanoparticle containers. These light-stimulated, thermally activated, mechanized nanoparticles represent a new system with potential utility for on-command drug release.

This work was realized during a master 2 internship and the beginning of the PhD in the laboratory of Pr. Zink.

[†] J. Croissant, J. I. Zink,* *J. Am. Chem. Soc.* **2012**, *134*, 7628.

Introduction

Multifunctional drug delivery systems are currently being studied intensively because of their potential to combine multiple essential properties in a single nanovehicle.^[1-4] The ability to control the location, time, and amount of drug released are important in nanomedicine.^[5,6] In the specific case of photothermal control of the release, multifunctional nanoparticles (NPs) combining the photothermal heating of metal particles that have plasmonic properties with core or shell NPs that have drug-carrying capability as specific remote triggered-release have been exploited with bare gold NPs,^[7,8] core@shell Au@liposome,^[9,10] Au@polyelectrolytes-multilayers@lipid,^[11] polymer@Au,^[12] and silica nanorattle@mesoporous-silica@Au.^[13] None of these systems are robust nanocarriers that prevent premature release because of drug leakage through phospholipid membranes, polymer irregularities, and shell imperfections respectively. Very recently, gold nanorods were coated with mesoporous silica to photothermally release doxorubicin electrostatically trapped in the pores, but premature leakage from the uncapped pores before irradiation was severe.^[13]

Mesoporous silica nanoparticles (MSN) have been shown to be non-toxic,^[14,15] are taken up (endocytosed) by cells,^[16-18] and are able to transport various drugs.^[19,20] Many gate-keeping mechanisms have been developed and attached to MSN pore openings to trap the drug payload.^[21,22] As a result, a remarkable variety of mesoporous silica nanocarriers have been designed with both autonomous activation (pH or redox opening of nanovalves),^[23-25] and external (light or magnetic field) control.^[26-28] Note that in most of these on-command release systems, precise spatial control cannot be achieved.

In this study we considered the synthesis and successful operation of nanovalves on MSN that are remotely controlled by light by using a photothermal mechanism involving plasmonic properties of a gold NPs core. During the course of this study we discovered a facile one-pot synthesis of gold NPs embedded in the mesoporous silica matrix (Au@MSN), through the autoreduction of tetrachloroaurate ions in the presence of cetyltrimethylammonium bromide (CTAB) that also induces the template directed assembly. This one-pot synthesis is a faster and greener preparation of such nanovehicles than the multistep methods previously reported.^[29] Irradiation of the Au@MSN that are mechanized with nanovalves at wavelengths corresponding to the plasmon resonance of the gold core causes internal heating and subsequent opening of the nanovalve that allow the contents of the pore to escape. Investigation of the state of the particles after release showed that they remain intact at moderate light intensities but that some degradation occurs at high intensity.

Results and discussion

The nearly monodisperse Au@MSN were obtained through the condensation of tetraethoxysilane on freshly prepared gold NPs (21 ± 4 nm) in a basic water/ethanol mixture as displayed by transmission electron microscopy (TEM) images (Fig. 1A-D, and S1A-B). The nanomaterial had a high surface area of $1014 \text{ m}^2 \cdot \text{g}^{-1}$ calculated from the nitrogen-adsorption-desorption isotherm with the BET theory (Fig. S2A), with an average of BJH pore diameter of 2.4 nm (Fig. S2B), consistent with the low angles x-ray diffraction (XRD) pattern (Fig. S2C). The formation of the gold NPs was surprising because no additional reducing agent was provided. The reduction of the gold precursor was sensitively dependent on the precise experimental conditions (basic pH, order of introduction of the reactants, and temperature, see table S1). Interestingly, the injection of sodium hydroxide was found to be necessary to obtain the gold NPs. Previously studies reported the reduction of tetrachloroaurate ions via quaternary ammonium ions under γ -irradiation,^[30] and the encapsulation of gold NPs via a similar autoreduction in the presence of a cross-linked tertiary amine polymer.^[31]

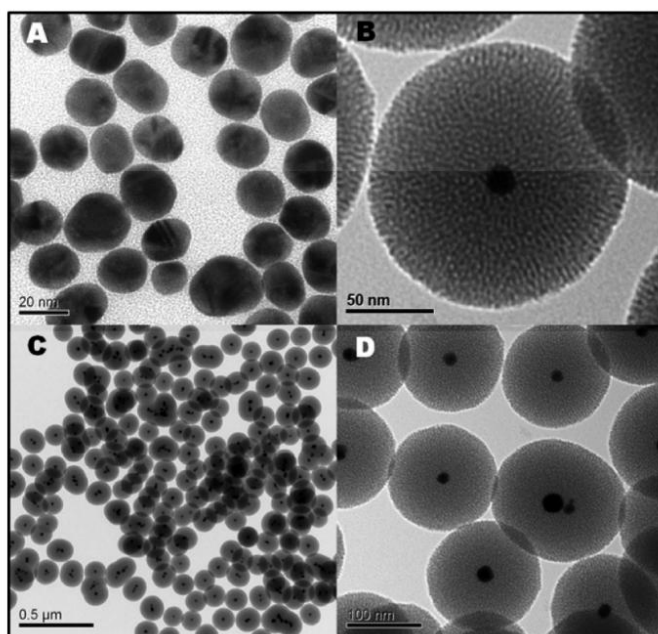


Figure 1. TEM images of gold NPs prepared by the CTAB-mediated autoreduction of tetrachloroaurate ions (A), and the final Au@MSN from the one-pot synthesis (B–D).

The mechanism of operation of the molecular machine involves temperature-dependent non-covalent interactions between the stalk and the cucurbit[6]uril ring (Fig. 2). The two ammonium groups of the stalk interact with the carbonyl groups of the cucurbituril via hydrogen bonds, while the alkyl chain of the thread interacts with the hydrophobic cucurbit[6]uril core through London forces. The stalk-ring binding constant decreases exponentially with the temperature, so that at 25°C the cucurbit[6]uril rings dwell on the threads, but at 60°C these rings slip off and open the pores (Fig. 2A).

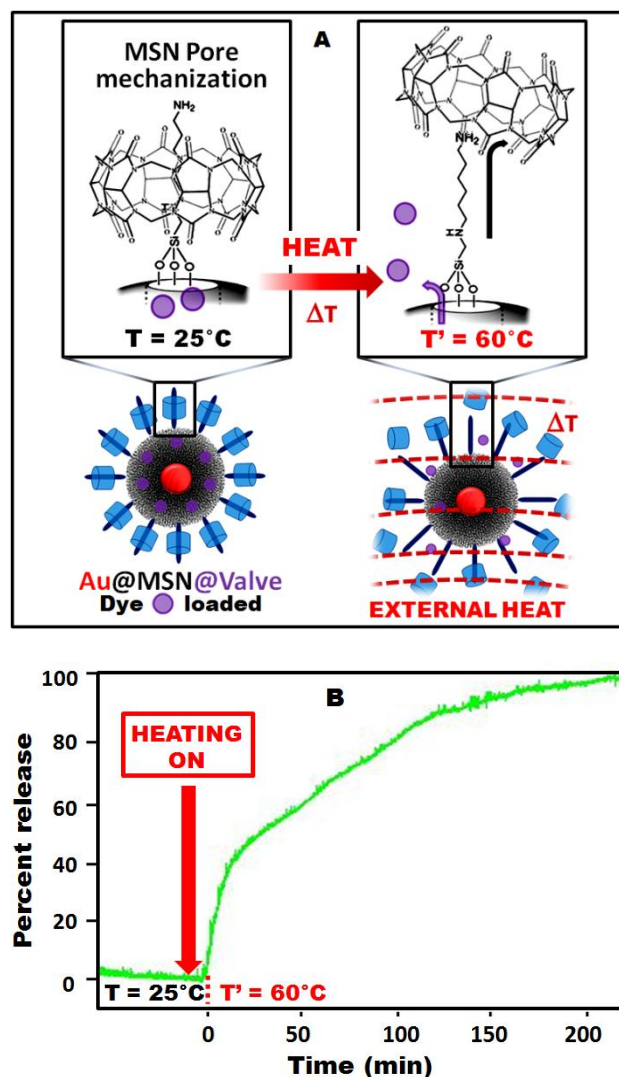


Figure 2. External heating of a suspension of Au@MSN@Valve to 60°C causes dissociation of the cucurbituril caps from the stalks and release of the cargo molecules from the pores (A). The release profile caused by bulk thermal activation of the nanomachines (B).

The molecular mechanization was performed by condensing N-(6-N-aminohexyl)-aminomethyltriethoxysilane stalks on the porous silica surface in dried toluene (see solid state NMR ^{13}C and ^{29}Si Fig. S3).^[28] Then the rhodamine B cargo was loaded by soaking the CTAB-extracted Au@MSN-thread NPs in a concentrated aqueous solution. Finally the pores were closed by complexing cucurbit[6]uril on the stalks (Scheme S1). This step was performed by adding cucurbit-6-uril (and sodium chloride to increase its solubility) to the previous rhodamine loading solution in order to avoid the loss of cargo molecules during the pore capping process.

The thermal operation of the machine was assessed in a control experiment (without light) by heating the solution. The dye loaded Au@MSN@Valve nanomachines were placed in the bottom of a glass cuvette filled with water and heated on a hot-plate (Scheme S2). The

release of cargo molecules was monitored by a probe diode laser (448 nm, 18 mW) irradiating the upper part of the cuvette and a CCD detector to measure the fluorescence of the dye that escaped from the pores. This experiment showed that a temperature of 60°C or higher was required to induce the release by disrupting the supramolecular temperature-dependant thread-ring interactions (Fig. 2A-B). At room temperature the release profile exhibits a flat baseline characteristic of a non-leaky carrier, which validates its usefulness as a robust drug delivery system without premature leakage of the cargo.

Operation of the system by photo-induced internal heating was studied in a similar manner except that no external heating of the solution occurred. Figure 3A illustrates schematically the surface plasmon effect induced by an appropriate laser irradiation on the Au@MSN@Valve, which produces a photothermal conversion of the laser energy. The mechanism involves the internal temperature increase inside the particle that is produced by the photothermal effect in order to disrupt the thread-ring interactions and release the cargo. The dye loaded particles were placed in a corner of a glass cuvette as was done in the bulk external heating control experiments, but the sample was irradiated at 514 nm (100 mW) to excite the gold cores at their plasmon band maximum at 530 nm (see extinction spectrum Fig. S1C). The release of cargo molecules was monitored by a probe diode laser (448 nm, 18 mW) irradiating the upper part of the cuvette, and a CCD detector to measure the dye fluorescent emission. The release profile displays the laser triggered instantaneous release of rhodamine B under irradiation (Fig. 3B), thus demonstrating the control of a temporal remote-photothermal release of cargo molecules encapsulated in Au@MSN nanocarriers.

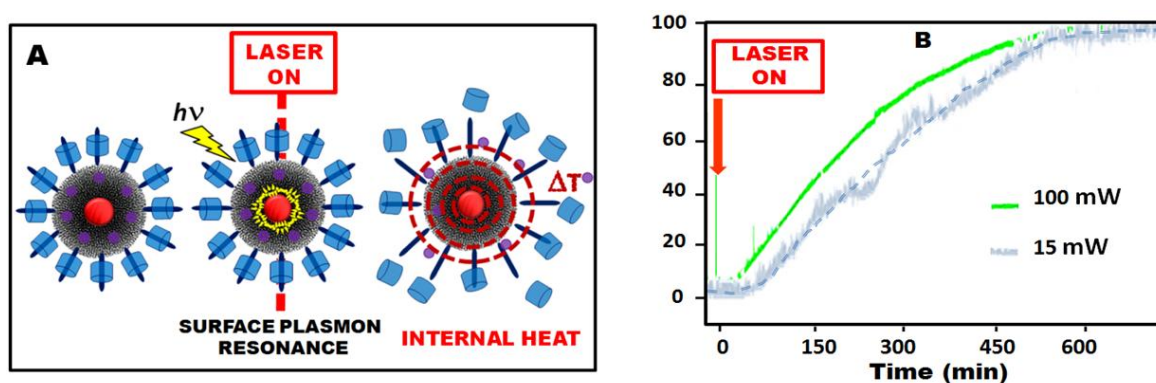


Figure 3. Photothermal-induced internal heating of Au@MSN@Valve through the surface plasmon effect (A) of the gold cores releases dye molecules under power-dependant laser actuation (B). The release profiles were normalized to the plateaus representing the maximum amount of released dye. The maximum varied according to the geometry of the experiments and the laser power. The rate of release increased with laser power.

To verify that the local temperature increase in the NPs (rather than an increase of the temperature of the bulk solvent) is responsible for the cargo release, the solvent temperature was monitored during the photothermal-induced release experiment. The solution temperature remained unchanged within experimental error during experimental runs as long as ten hours.

These results show that the heat necessary for uncapping the pore and releasing the cargo was provided by the very local heating of the NPs by photothermal conversion of the laser electromagnetic energy. Local temperatures in the vicinity of the stalk and cap must reach at least 60 °C in Au@MSN. Besides, Rho B-loaded MSN@Valves control (no gold core) did not release their content upon irradiation, thus the nanovalve complexes were not photo-sensitive in these conditions (Fig. S4). Note that, the addition of sodium hydroxide (pH' 10.5) to the former nanomaterial induced an instantaneous release of the cargo, as expected with the thread deprotonation (pK_A 9.5) leading to repulsive negative stalk-cucurbit[6]uril interactions (see Fig. S4). Such a local temperature increase should be very useful to apply these nanomachines for spatially controlled dual therapy: by delivering the cargo to cells, and by necrosis through hyperthermia. This dual use of plasmonic heating distinguishes this light sensitive nanomachine from others based on chromophores alone and may be advantageous for increasing killing efficiency.^[32, 26-27]

An alternative mechanism for releasing the cargo could be thermal damage to the silica shell itself. The nanocarriers were analyzed after photo-irradiation and cargo release by TEM (Fig. 4 A-B). Under the highest irradiation intensity (100 mW), some of the particles were severely degraded. Thus some of the cargo release could have been produced by cracking the silica rather than by the opening of the nanovalves. As a control, bare MSN (no gold core) were irradiated at 514 nm (100 mW for 14 h), and no silica damage was observed, confirming that only the gold embedded NPs were light-sensitive (Fig. S5). Release experiments were carried out at lower power (15 mW), with equal irradiation times, and the release profiles were characterized similarly (Fig. 3B). The release was slower at lower power as expected. The particles were undamaged (Fig. 4B). Thus it is clear that plasmonic heating at high light intensities produces enough heat or a rapid enough temperature change to degrade the silica, but that lower powers do not damage the silica but do cause enough of a local temperature change to open the valves and release the contents.

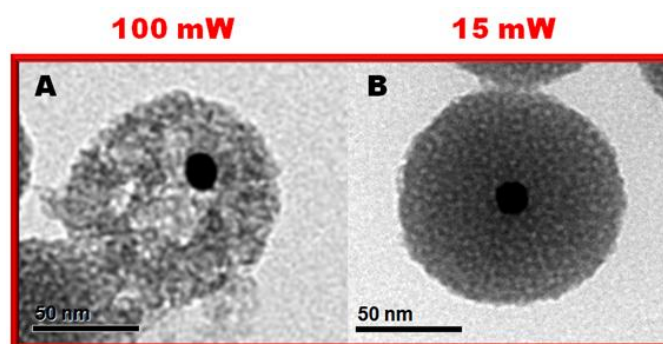


Figure 4. TEM images of Au@MSN irradiated with 100 mW (A), and 15 mW (B) for 14 h, and bare MSN as a control, under 100 mW for 14 h.

Conclusions

In summary, we have demonstrated that novel gold-core mesoporous silica nanomachines are effective in actuating a thermosensitive nanovalve under exposure to laser irradiation. The release mechanism was demonstrated to be caused by local internal heat produced by the photothermal conversion of the light energy, and not a bulk temperature increase. A novel one-pot synthesis of the Au@MSN was presented. The mechanized Au@MSN enabled remotely controlled triggered release of the cargo molecules “on command” via a robust matrix without premature leaking. This novel nanocarrier fulfills the strict criterion of controlled release of cargo molecules at a desired time in a specified spatial location that is a significant advancement for nanomedicine. It is envisioned that Au@MSN nanomachines would be efficient to kill cancer cells through hyperthermia, as well as synergistically enhancing the drug cytotoxicity under such conditions of medicine such as docetaxel.^[33]

REFERENCES

- [1] Torchilin, V. P. *Adv. Drug Delivery Rev.* **2006**, 58, 1532.
- [2] Sanvicens, N.; Marco, M. P. *Trends Biotechnol.* **2008**, 26, 425.
- [3] Liu, H.; Chen, D.; Li, L.; Liu, T.; Tan, L.; Wu, X.; Tang, F. *Angew. Chem. Int. Ed.* **2011**, 50, 891.
- [4] Li, Z.; Barnes, J. C.; Boscoy, A.; Stoddart, J. F.; Zink, J. I. *Chem. Soc. Rev.* **2012**, 41, 2590.
- [5] Liu, Y.; Miyoshi, H.; Nakamura, M. *Int. J. Cancer* **2007**, 120, 2527.
- [6] De Jong, W. H.; Borm, P. J. *Int. J. Nanomed.* **2008**, 2, 133.
- [7] Jones, M. R.; Millstone, J. E.; Giljohann, D. A.; Seferos, D. S.; Young, K. L.; Mirkin, C. A. *ChemPhysChem* **2009**, 10, 1461.
- [8] Poon, L.; Zandberg, W.; Hsiao, D.; Erno, Z.; Sen, D.; Gates, B. D.; Branda, N. R. *ACS Nano* **2010**, 4, 6395.
- [9] Anderson, L. J. E.; Hansen, E.; Lukianova-Hleb, Y. E.; Hafner, J. H.; Lapotko, O. D. *J. Control. Release* **2010**, 144, 151.
- [10] Paasonen, L.; Laaksonen, L.; Johans, C.; Yliperttula, M.; Kontturi, K.; Urtti, A. *J. Control. Release* **2007**, 122, 86.
- [11] Angelatos, S. A.; Radt, B.; Caruso, F. *J. Phys. Chem. B* **2005**, 109, 3071.
- [12] Park, H.; Yang, J.; Seo, S.; Kim, K.; Suh, J.; Kim, D.; Haam, S.; Yoo, K.-H. *Small* **2008**, 4, 192.
- [13] Zhang, Z.; Wang, L.; Wang, J.; Jiang, X.; Li, X.; Hu, Z.; Ji, Y.; Wu, X.; Chen, C. *Adv. Mater.* **2012**, 24, 1418.
- [14] Lin, Y.-S.; Wu, S.-H.; Hung, Y.; Chou, Y.-H.; Chang, C.; Lin, M.-L.; Tsai, C.-P.; Mou, C.-Y. *Chem. Mater.* **2006**, 18, 5170.
- [15] Liong, M.; Lu, J.; Kovochich, M.; Xia, T.; Ruehm, S. G.; Nel, A. E.; Tamanoi, F.; Zink, J. I. *ACS Nano* **2008**, 2, 889.
- [16] Slowing, I.; Trewyn, B. G.; Lin, V. S.-Y. *J. Am. Chem. Soc.* **2006**, 128, 14792.
- [17] Lu, J.; Liong, M.; Zink, J. I.; Tamanoi, F. *Small* **2007**, 3, 1341.
- [18] Trewyn, B. G.; Slowing, I. I.; Giri, S.; Chen, H. T.; Lin, V. S. Y. *Acc. Chem. Res.* **2007**, 40, 846.
- [19] Slowing, I. I.; Trewyn, B. G.; Giri, S.; Lin, V. S.-Y. *Adv. Funct. Mater.* **2007**, 17, 1225.
- [20] Meng, H.; Liong, M.; Xia, T.; Li, Z.; Ji, Z.; Zink, J. I.; Nel, A. E. *ACS Nano* **2010**, 4, 4539.
- [21] Vallet-Regí, M.; Francisco, B.; Daniel, A. *Angew. Chem. Int. Ed.* **2007**, 46, 7548.
- [22] Ambrogio, M. W.; Thomas, C. R.; Zhao, Y. L.; Zink, J. I.; Stoddart, J. F. *Acc. Chem. Res.* **2011**, 44, 903.
- [23] Angelos, S.; Khashab, N. M.; Yang, Y.-W.; Trabolsi, A.; Khatib, H. A.; Stoddart, J. F.; Zink, J. I. *J. Am. Chem. Soc.* **2009**, 131, 12912.
- [24] Meng, H.; Xue, M.; Xia, T.; Zhao, T.; Tamanoi, T.; Stoddart, J. F.; Zink, J. I.; Nel, A. E. *J. Am. Chem. Soc.* **2010**, 132, 12690.
- [25] Liu, R.; Zhao, X.; Wu, T.; Feng, P. *J. Am. Chem. Soc.* **2008**, 130, 14418.
- [26] Lu, J.; Choi, E.; Tamanoi, F.; Zink, J. I. *Small* **2008**, 4, 421.
- [27] Angelos, S.; Choi, E.; Vogtle, F.; De Cola, L.; Zink, J. I. *J. Phys. Chem. C* **2007**, 111, 6589.
- [28] Thomas, C. R.; Ferris, D. P.; Lee, J.-H.; Choi, E.; Cho, M. H.; Kim, E. S.; Stoddart, J. F.; Shin, J. S.; Cheon, J.; Zink, J. I. *J. Am. Chem. Soc.* **2010**, 132, 10623.
- [29] Liu, S.; Han, M.-Y. *Chem. Asian J.* **2010**, 5, 36.
- [30] Chen, S.; Liu, Y.; Wu, G. *Nanotechnology* **2005**, 16, 2360.
- [31] Oishi, M.; Hayashi, H.; Uno, T.; Ishii, T.; Iijima, M.; Nagasaki, Y. *Macromol. Chem. Phys.* **2007**, 208, 1176.
- [32] Mal, N. K.; Fujiwara, M.; Tanaka, Y. *Nature* **2003**, 421, 350.
- [33] Mohamed, F.; Marchettini, P.; Stuart, A.; Urano, M.; Sugarbaker, P. H. *Ann. Surg. Oncol.* **2003**, 10, 463.

APPENDIX: SUPPLEMENTARY INFORMATION

Materials. Cetyltrimethylammonium bromide (CTAB, H5882, 98%+), tetraethylorthosilicate (98%+), toluene (99.5%+), and cucurbit[6]uril hydrate (CB[6]) were purchased from Sigma-Aldrich. Sodium hydroxide (NaOH, beads) and concentrated hydrochloric acid (12N) were purchased from Fisher Chemical. N-(6-aminohexyl)aminomethyltriethoxysilane, 95%, was purchased from Gelest. Rhodamine B was purchased from Exciton. Toluene was distilled before usage, and deionized water was used.

One-pot synthesis of Au@MSN NPs. A mixture composed of water (100 mL), ethanol (40 mL), and CTAB (0.640 g) was stirred at 70 °C in a three neck 250 mL round bottom flask. Then, an aqueous solution of tetrachloroaurate (55 mg in 5 mL) was injected and stirred 5 minutes. Finally, sodium hydroxide (200 μ L, 2 M) was injected to produce the NPs nucleation instantaneously. The NPs growth was led during 30 minutes under a 600 rpm stirring. Afterwards, tetraethylorthosilicate (1000 μ L) was added by dropwise additions to the stirred aforementioned solution. After 1 minute 30 seconds, the typical purple color of thin coated Au@MSN particles was observed, and the sol-gel process was lead for 2 h. The filtrate was gathered through centrifugation at 7830 rpm 15 minutes. Each fraction was washed with 40 mL of MeOH and centrifuged 10 minutes, three times. Note that, the order of the reactant injected was found to be crucial, as depicted by the following table:

CTAB MEDIATED REDUCTION OF KAuCl_4 IN GOLD NPs								
Batch mixture			Injected reactants			Reduction	Size range	Temp.
CTAB	KAuCl_4	NaOH	x	x	x	✓	polydisperse	RT
CTAB	KAuCl_4	x	x	x	x	x	x	RT to 80°C
x	KAuCl_4	NaOH	x	x	x	x	x	RT to 80°C
CTAB	x	NaOH	x	KAuCl_4	x	x	x	80°C
CTAB	x	NaOH	x	KAuCl_4	x	✓	polydisperse	RT
CTAB	KAuCl_4	x	x	x	NaOH	✓	polydisperse	80°C
CTAB	x	x	x	1- KAuCl_4	2-NaOH	✓	21 \pm 4 nm	70°C

Table S1. Truth table of the one-pot synthesis procedure.

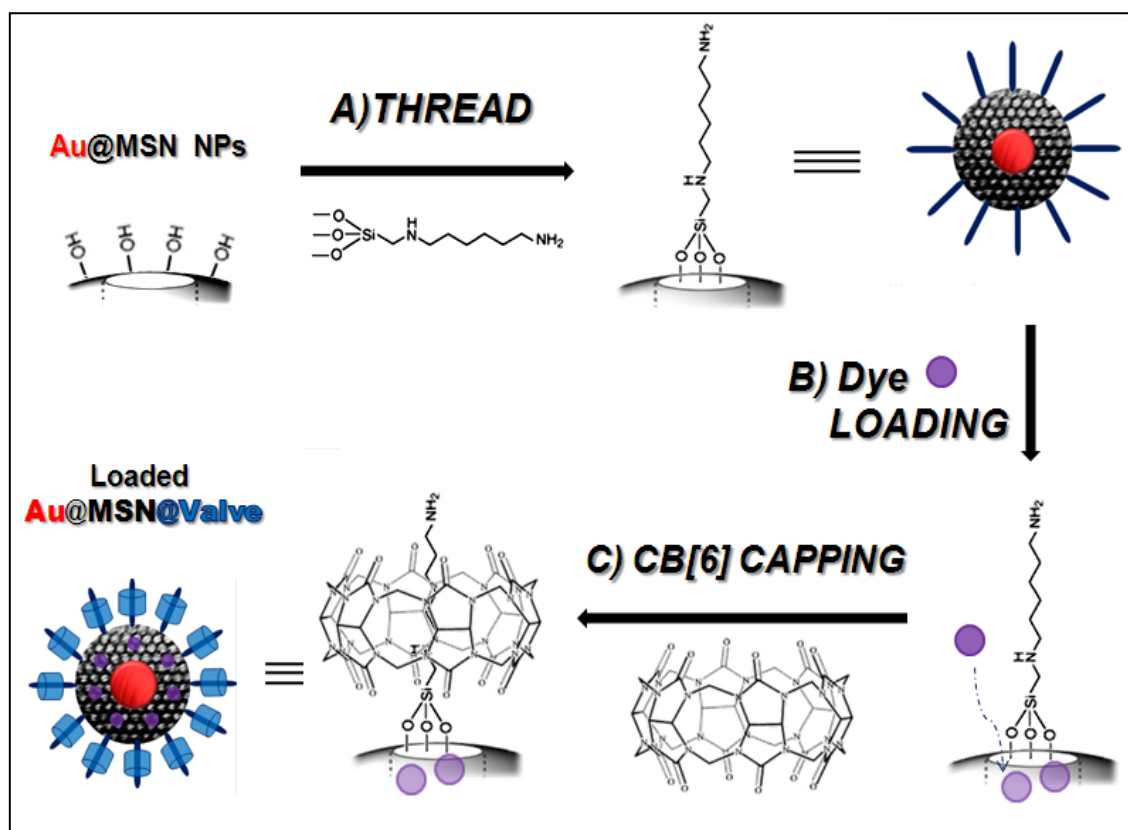
Acidic extraction of CTAB. The CTAB acidic extraction of the Au@MSN was performed according to the method of Lang *et al.*^[1] The filtrate was mixed and sonicated with ethanol (50 mL), and then ammonium nitrate (33 mg). The solution was stirred 20 minutes at 60°C, cooled down at RT. Finally, the extracted Au@MSN were washed with ethanol and water two times each (40 mL each time).

Stalk mechanization of Au@MSN. The reported thermosensitive nanovalve of Thomas *et al.* was used on the core@shell NPs.^[2] A solution of dried toluene and Au@MSN was prepared (40 mg in 10 mL) and stirred at room temperature under nitrogen. Then, N-(6-aminohexyl)aminomethyltriethoxysilane (30 μ L of stalk, see Scheme S1 step A) was added

by drop wise consecutive additions. The reaction was led for 10 h, and the solution was centrifuged during 20 minutes to gather the as-functionalized Au@MSN-Stalk. Afterwards, two aqueous washings (30 mL) were performed with sonication between the centrifugation separations.

Dye loading of Au@MSN-Stalk. An aqueous solution Au@MSN-Stalk (40 mg in 1.5 mL of water) was mixed with the rhodamine B dye (2 mg, 3 mM) and stirred at room temperature during 2 days (see Scheme S1 step B).

Pores closing of loaded Au@MSN-Stalk. Ultimately, a sonicated aqueous solution (2.5 mL) of sodium chloride (35 mg, NaCl) and CB[6] (40 mg) was stirred during 5 hours, and was added to the loaded NPs to cap the pores (see Scheme S1 step C). The resulting Au@MSN@Valve nanomachine involves supramolecular interactions between the molecular thread and the cucurbituril rings called Valve



Scheme S1. Representation of the valve mechanization. First the threads have been reacted on the silica surface of Au@MSN (A), followed by the dye loading (rhodamine B) (B), and ultimately CB[6] rings were complexed with the stalks (C).

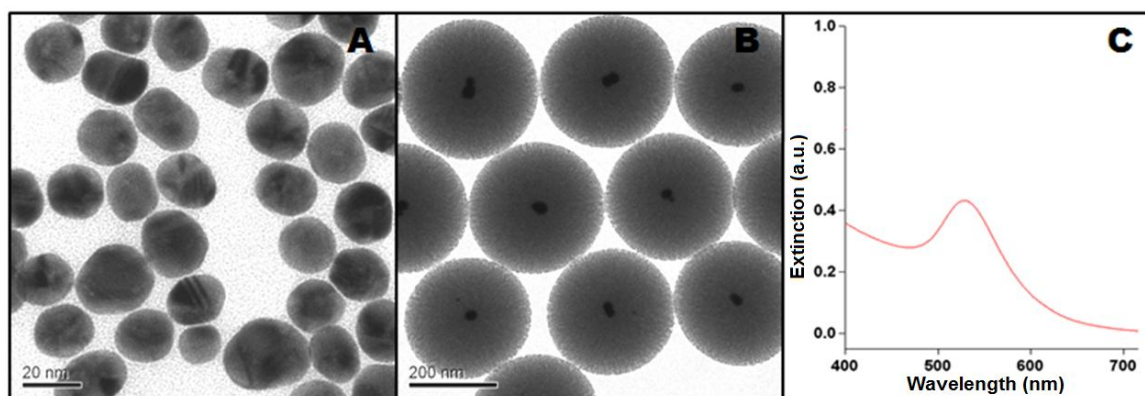


Figure S1. TEM images of gold NPs (A), and Au@MSN (B). Extinction spectrum of Au@MSN (C).

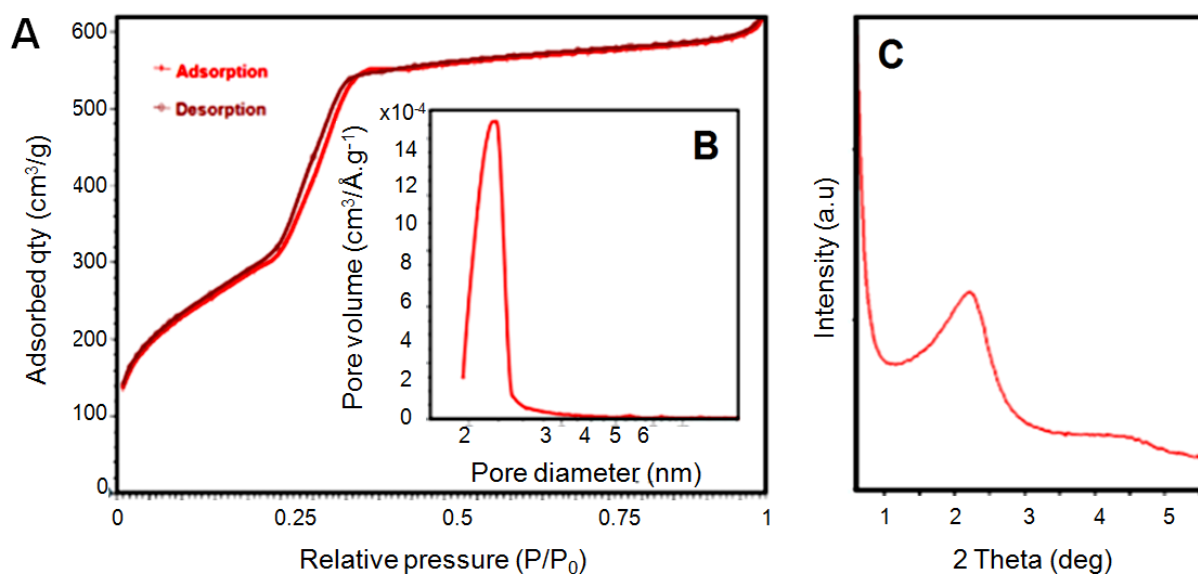


Figure S2. N_2 -adsorption-desorption isotherm (A), BJH pore size distribution (B), and XRD pattern of the one-pot Au@MSN NPs (C).

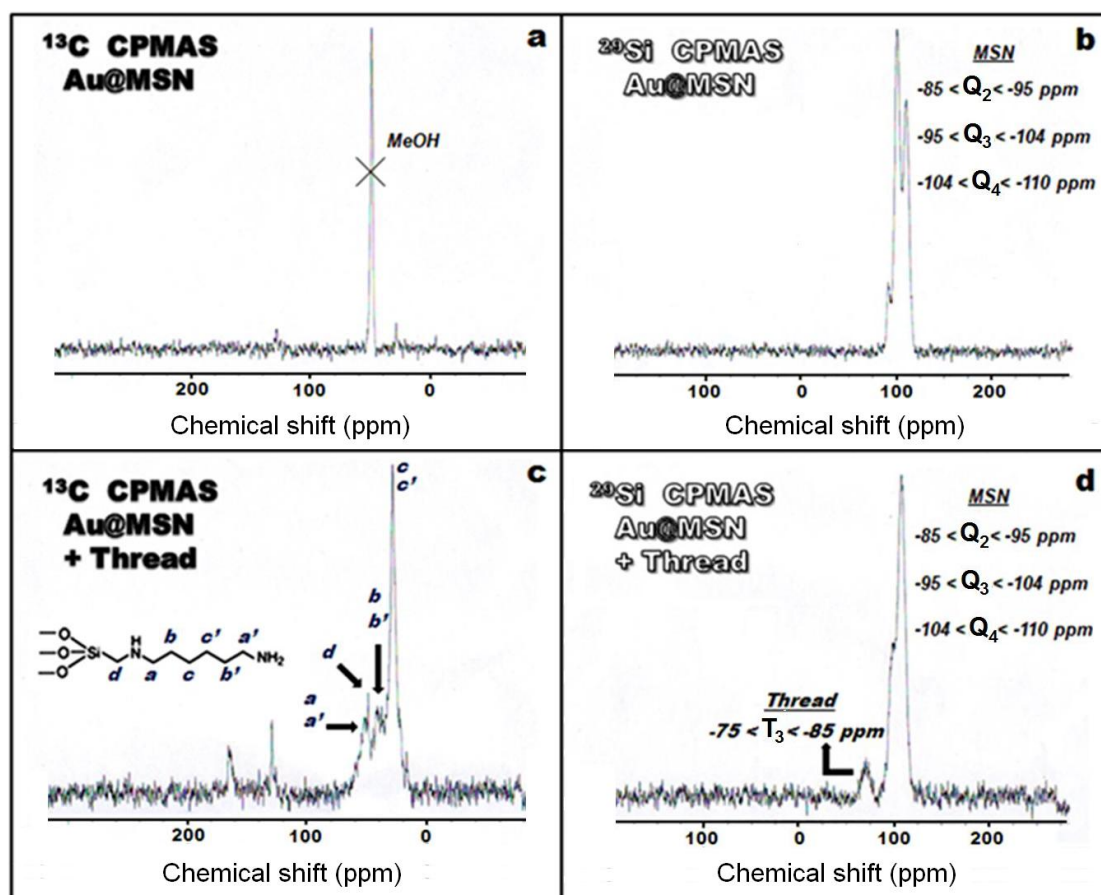
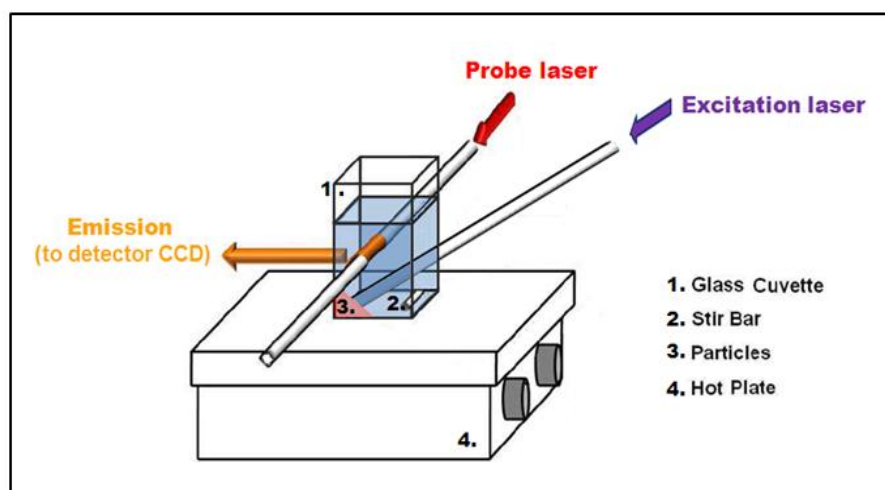


Figure S3. Solid state NMR spectra on Au@MSN particles before (a,b) and after (d,c) thread mechanization. CP-MAS sequences on ^{13}C (a,c) and ^{29}Si (b,d).

Laser experiment setup. The experimental setup for the photothermal triggered release experiment is depicted in scheme S2. The particles are placed in one corner of a glass cuvette and few milliliters of solvent (typically water or methanol) are added carefully to prevent particles from mixing into the solution. A stir bar is added and allowed to stir gently to increase the diffusion of the dye. A probe diode laser (448 nm, 18 mW) is trained on the cuvette solution to excite the released dye (Rhodamine B), for detection by the CCD (charge coupled device) detector. The argon ion laser (515 nm, 100 mW or 15 mW) was used to excite the loaded cargo-loaded Au@MSN@Valve.



Scheme S2. Experimental setup for the photothermal-induced release experiments.

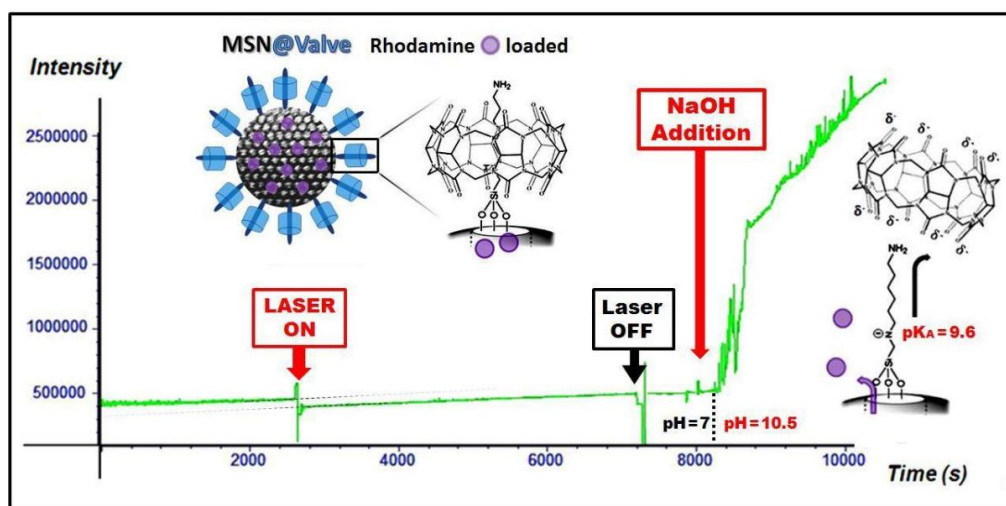


Figure S4. Control release experiment on MSN@Valve with rhodamine B in water. Laser (514, 100 mW) irradiation alone did not trigger the release, while sodium hydroxide aliquots triggered the release confirming the successful loading and valve functionalization, as well as the necessity to have a gold core to design a light-sensitive nanocarrier.

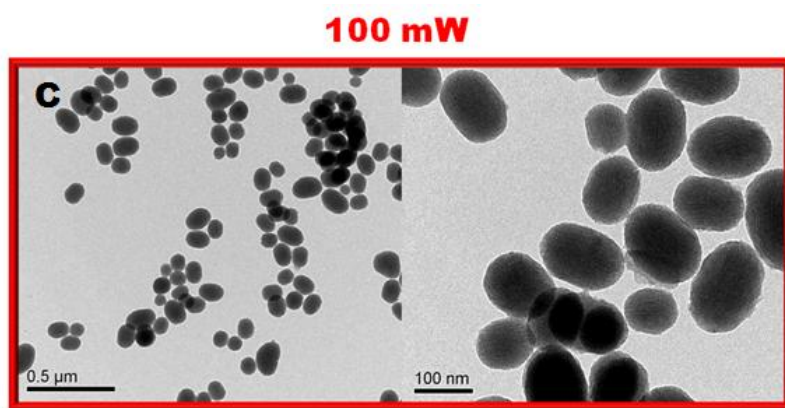


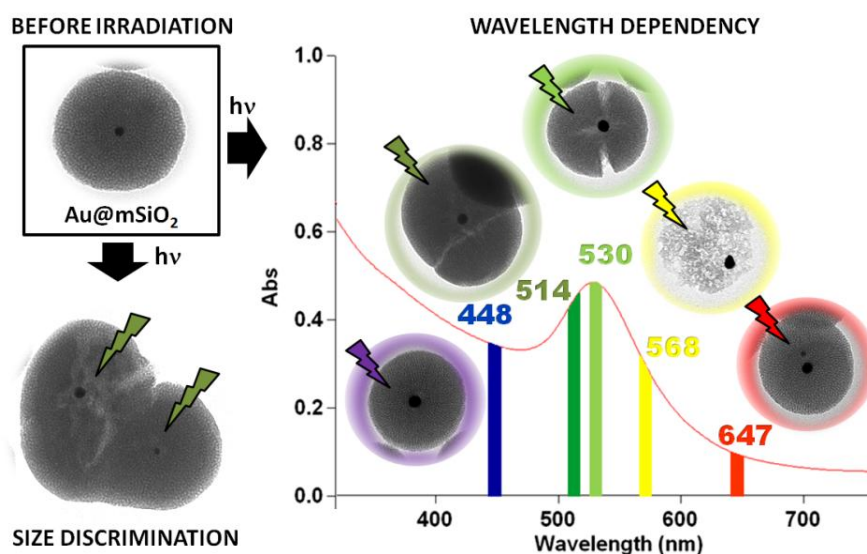
Figure S5. TEM images of MSN irradiated with 100 mW during 14 h, which were shown intact as a control.

REFERENCES

- [1] Lang, N.; Tuel, A., *Chem. Mater.* **2004**, 16, 1961.
- [2] Thomas, C. R.; Ferris, D. P.; Lee, J.-H.; Choi, E.; Cho, M. H.; Kim, E. S.; Stoddart, J. F.; Shin, J. S.; Cheon, J.; Zink, J. I., *J. Am. Chem. Soc.* **2010**, 132, 10623.

CHAPTER 3

Controllable Photodegradation of Mesoporous Silica Encapsulating Gold Cores for Remote Cargo Release



Abstract

Designed photothermal degradation of mesoporous silica shells is performed via the plasmonic properties of gold encapsulated nanoparticles. The photodegradation dependence on the power of the irradiation, the wavelength tuning, and the size of the gold core is assessed. Selective nanoparticle photodegradation based on the size of the core is demonstrated. The application of this feature is performed for remote cargo release from polymer-coated nanovehicles.

This work was realized during the beginning of the PhD in the laboratory of Pr. Zink.

J. Croissant, and J. I. Zink : *Photodegradation studies.*

J. Croissant, T. M. Guardado-Alvarez, and J. I. Zink: *Polymer design and release experiment.*

Introduction

Plasmonic nanoparticles (NPs) are being increasingly utilized as photothermal (PT) transducers for a wide variety of applications in colloidal and surface sciences.¹⁻⁵ The control of the PT efficacy of various metal NPs has numerous potential applications, as witnessed by the increasing number of theoretical and experimental studies made on such systems.⁶⁻¹² Detailed studies of the PT efficacies of gold NPs revealed the high-energy bleaching of NIR resonant bands for gold shells and rods (relative PT efficacy decreased by 16–22 times), which was not observed for gold spheres.¹³ Gold nanospheres are thus transducers that can produce very high local temperature. In this context, the PT properties of such NPs are often used via embedding them in various shells or matrices. In the biomedical field, gold NPs are often coated with polymers (e.g. polyethyleneglycol), in order to maintain a long circulation time in the bloodstream and to accumulate them in cancer cells.¹⁴ Liposomes,¹⁵ polyelectrolytes,¹⁶ and mesoporous silica shells have been placed on gold NPs to combine the loading properties of such matrices with those of the metal cores.¹⁷ It has also been reported that a powerful near-infrared femtosecond pulsed irradiation (90 fs pulses at 1 kHz repetition rate with energy up to 1 mJ/pulse for a total energy of 180 μ J), could remove the silica on silica core (112 nm)/gold shell (18 nm), and disrupt the gold shell at higher power (300 μ J).¹⁸ These studies demonstrate that PT effects can be used to photodegrade the various nanocarriers and enhance their biodegradability, and in addition can be used as a novel release actuation that may be useful in nanotherapy.

In this study we report surprisingly powerful PT cracking and destruction of gold NPs embedded within mesoporous silica shells (Au@MSN) caused by low power continuous wave irradiation (20 to 100 mW) in the visible region. Such a behaviour was found in the framework of our recently reported study involving a novel drug delivery system composed of cargo loaded Au@MSN NPs, which were functionalized on their porous surface in order to deliver their payload on demand through PT actuation.¹⁹ In those studies, a plasmonically-induced local temperature increase reaching a least 60°C was demonstrated on the Au@MSN surface by thermally-induced dissociation of a supramolecular complex that acted as a nanovalve over the pores. The power of the irradiation was limited in order to avoid degradation of the carriers and demonstrate actuation of the nanovalves. Herein, we present new insights on how to use the PT properties of embedded gold NPs to deliberately control the physical degradation of the mesoporous silica matrix, as well as its application for remote cargo release. We demonstrate control of the PT efficiency by varying the wavelength, the power, and the time of the laser irradiation. In addition, we study the size effect of the embedded gold NPs on the photodegradation under various conditions. The knowledge of such a PT impact is important not only in order to take advantage of externally controllable degradation for novel researches on controlled delivery, plasmonic heating, and photolithography, but also to prevent negative impacts on thermo-sensitive systems where it is desirable for the nanocarrier to remain intact.

Results and discussion

The PT efficacy on the photodegradation was studied by monitoring the mesoporous silica framework stability using transmission electron microscopy (TEM) before and after irradiation of the samples. The nanomaterials were composed of monodisperse 15 nm gold nanospheres embed in mesoporous silica for an overall size of 150 nm (see Figures S1-3). The laser experiments were carried out by directing a laser beam on nanoparticle powders that were placed on the bottom of sample tubes filled with water.

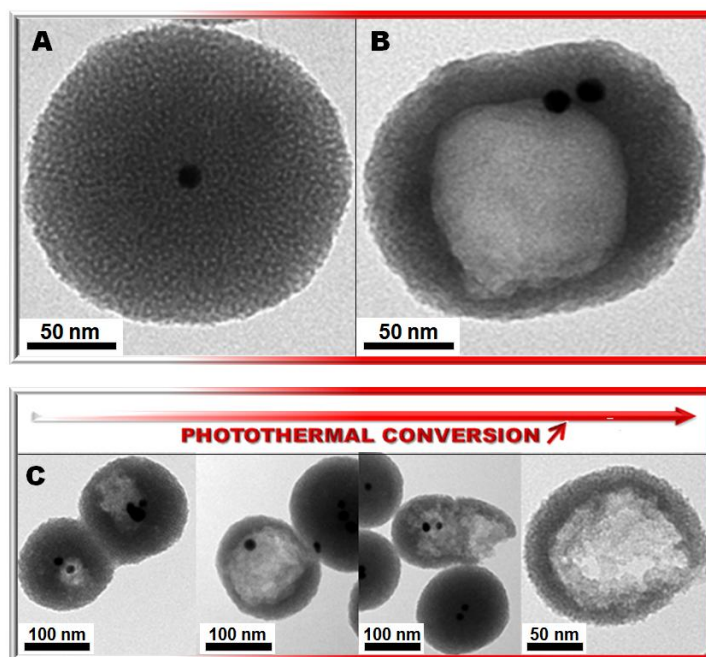


Figure 1. TEM images of Au@MSN before irradiation (A), and after 7 h of irradiation through an argon ion laser at 514 nm under 50 mW (B). Impact of the PT conversion of the gold cores on the MSN matrix under 50 mW (C).

The remarkable silica photodegradation is shown by TEM micrographs before and after 7 h of irradiation (514 nm, 50 mW) of Au@MSN (Figure 1A and B respectively). The PT conversion evolution (Figure 1C) is the result of the experimental fact that all the NPs are not receiving the same treatment under the irradiation geometry used. As a result, such qualitative PT conversion impacts have been deduced from different NPs having received a different energy. Moreover, the cause of the silica cracking was the PT effect from the gold NPs, since the damage occurs from the inside out; the TEM images in Figure 1B, and 1C revealed a growing internal hole which eventually led to the opening of the particles. Furthermore, the observation that the holes or cracks present on Au@MSN did not always match the spatial position of the gold cores (see Figures 1B-C, 3A at 530 nm) suggested that the destruction of the silica was not due to gold particle vibration under irradiation, but rather to the thermo-degradation of the weakest part of the porous framework. In order to take advantage of the externally-stimulated photodegradation of the mesoporous silica, it is important to be able to control its extent. Hence, to achieve a designed photodegradation three parameters were assessed to regulate the PT efficacy: the power, the wavelength, and the gold NPs size dependences.

The power dependence of the PT effect was studied in order to determine the parameters that at one extreme cause heating without particle destruction and at the other extreme lead to severe degradation. The particles were irradiated at 514 nm for 14 h under 15 and 100 mW (Figure 2A and 2B respectively), and whereas the former one did not show any photodegradation, the latter displayed a complete silica photodegradation. However, in a control experiment, bare MSN without gold cores were irradiated at 514 nm under 100 mW for 14 h, and none of the NPs were damaged (see Figure 2C). Note that, we reported a plasmonically-actuated cargo delivery via Au@MSN nanovalves under an irradiation of 15 mW at 514 nm.¹³ Besides, between 15 and 100 mW, the modulation of the power produced intermediated types of photodegradation; at 30 mW the silica photo-cracking was observed for a given time of 7 h (Figure 7F), whereas for higher power of 50 mW the photodegradation is much more severe for the same duration (Figure 1B,C).

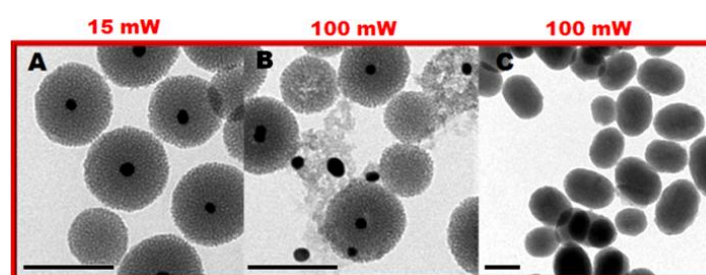


Figure 2. TEM images of Au@MSN irradiated 14 h at 514 nm under 15 mW (A), and 100 mW (B) displaying the power dependency of PT effect. Bare mesoporous silica NPs irradiated separately for 14 h at 514 nm under 100 mW (C). Scale bars of 100 nm (A-C).

The dependence of the photodegradation on the wavelength of the irradiation was also assessed. The plasmonic heating is expected to correlate with the extinction by the nanoparticles, that in turn is correlated with the particle size. Both the extinction coefficient and the wavelength of maximum extinction increase as the particle size increases, but the extinction coefficient is much more sensitive to the size than to the wavelength. For example the plasmon band maximum (λ_{max}) and molar extinction coefficient (ϵ) have been reported to be $\lambda_{\text{max}} = 524$ nm and $\epsilon = 7 \cdot 10^7$ L.mol⁻¹.cm⁻¹, $\lambda_{\text{max}} = 524$ nm and $\epsilon = 78 \cdot 10^7$ L.mol⁻¹.cm⁻¹, and $\lambda_{\text{max}} = 530$ nm and $\epsilon = 540 \cdot 10^7$ L.mol⁻¹.cm⁻¹, for 7.5, 16, and 35 nm gold NPs respectively.²⁰ Thus, Au@MSN were irradiated at three different wavelengths (448, 530, and 568 nm) under 20 mW for 30 minutes to study the wavelength-dependence of the photodegradation (Figure 3A). A clear dependence on the irradiation wavelength on the mesoporous silica photodegradation was observed, since at 530 nm the silica shell was cracked, while at 568 nm the core induced a hollow mesoporous silica nanostructure, whereas the silica was intact at 448 nm under the same power. Besides, the photodegradation was obtained after a relatively short time of irradiation (30 minutes), which demonstrates the efficiency of the process previously observed after 14 h of irradiation at 514 nm (Figure 1C). Then, the photodegradation for a selection of Au@MSN nanoparticles with three different gold nanoparticle diameters (Figures S4,5) at five different wavelengths under 20 mW light irradiation for 30 minutes was performed (See Figure 3B-D). The gold nanoparticle sizes are 5-10, 15-20, and 25-35 nm in Figure 3B, C, and D respectively. The mesoporous silica shells

were in average of 150 nm. The 5 to 10 nm size range showed a slight degradation of the silica matrix from 448 to 568 nm, with a maximum at 514 nm (Figure 3B). Conversely, the particles of the 25 to 35 nm size range did not exhibit silica degradation at these lower wavelengths, but the cracking and the destruction of the silica was observed at higher wavelengths (530 and 568 nm, see Figure 3D). Moreover, the second size range (15-20 nm, see Figure 3C) produced the deterioration of the silica in an intermediated window of wavelength from 514 nm to 568 nm respectively, and the silica matrix was almost totally photodegraded at 568 nm. Such a behavior is consistent with the plasmonic properties of gold nanocrystals of different sizes. In all cases no degradation occurred at the highest irradiation wavelength (647 nm).

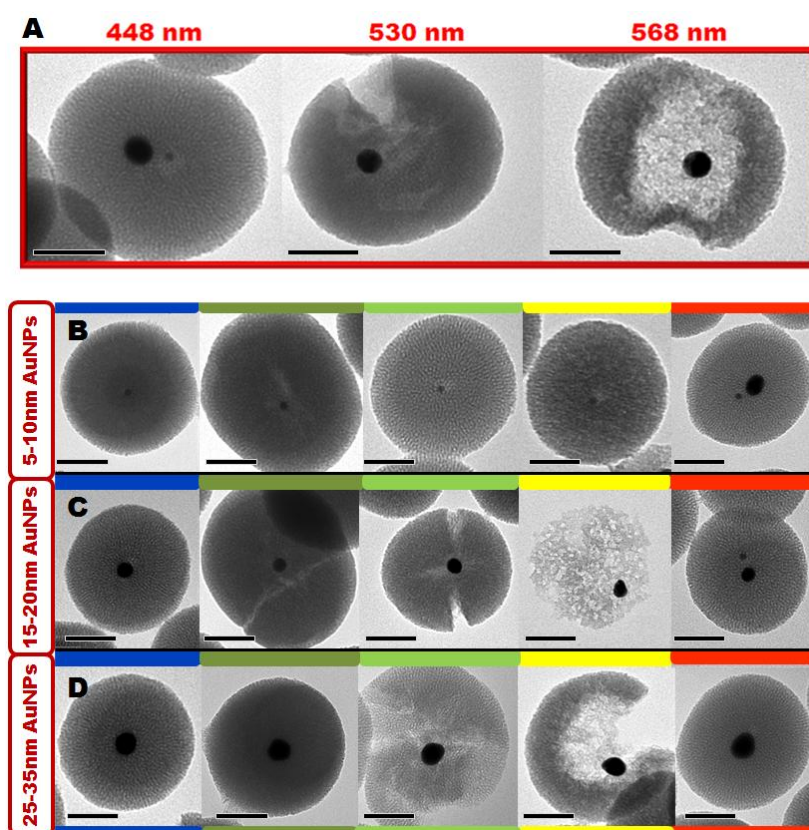


Figure 3. Wavelength dependency of the PT effect demonstrated by the TEM images of irradiated NPs under 20 mW for 30 minutes at different wavelengths: 448 nm, 530 nm, 568 nm (A). TEM images of three ranges of gold sizes in the mesoporous silica shells: 5-10 nm (B), 15-20 nm (C), and 25-35 nm (D) irradiated 30 minutes under 20 mW at various wavelengths (448, 514, 530, 568, 647 nm). The most damaged NPs are presented for each size and wavelength. Scale bar of 50 nm (A-D).

The variation of the gold nanoparticles size within the silica shells for a given wavelength and power displayed interesting results, which highlighted the origin of the degradation evolution as well. Note that, the silica degradation could have been either purely energetic, that is solely correlated to the laser power, or due to the different SPR band of the NPs. For a given wavelength the size of the gold NPs affects drastically the PT efficacy (as displayed by the matrix thermo-degradation, see vertically the TEM images in Figure 3B-D),

and such behavior is not linear with the size at 514 nm and 568 nm. The photodegradation of all Au@MSN at 530 nm correlates the overlapping of the SPR bands of the three size ranges of gold NPs, as reported for 5 to 40 nm bare gold NPs.^{11, 12} Besides, the higher half width of the 5 to 10 nm NPs accounts for their slight excitation up to 568 nm.²⁰ These experiments verify that the origin of the photodegradation evolution is thus due to the plasmonic properties of the sample, rather than a thermal effect of the laser. Thus these studies demonstrate the high dependence of the PT efficiency with gold NPs size, and such a size effect could be utilized to design remarkably different photodegradation of mesoporous silica shells.

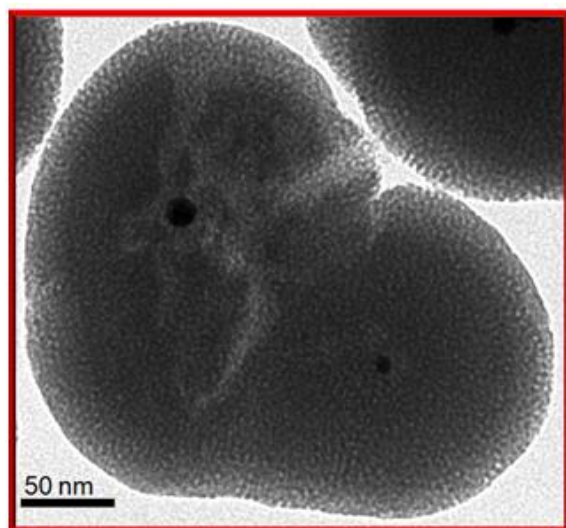


Figure 4. Gold core size discrimination of the PT photodegradation displayed by a unique TEM image of Au@MSN after 7 h of irradiation through an argon ion laser at 514 nm under 30 mW.

Consequently, the discrimination of the gold NPs according to their size via tuning the wavelength, to control the silica damaging through a strong PT conversion, was envisioned for wavelength apart from the SPR maximum of 530 nm. Such a size discrimination was demonstrated in Figure 4, where the very unique case of two fused particles containing 15 and 5 nm cores sufficiently separated to be considered independent, displayed solely silica degradation around the 15 nm core when irradiated at 514 nm. The reverse situation was found in Figure 3A at 448 nm, where 5 and 15 nm gold cores were mustered within one silica shell, and the 448 nm irradiation revealed a slight local degradation around the 5 nm core. This opens new horizons in selective photolithography, as well as in dual cargo release based on the size discrimination design of the PT degradation.

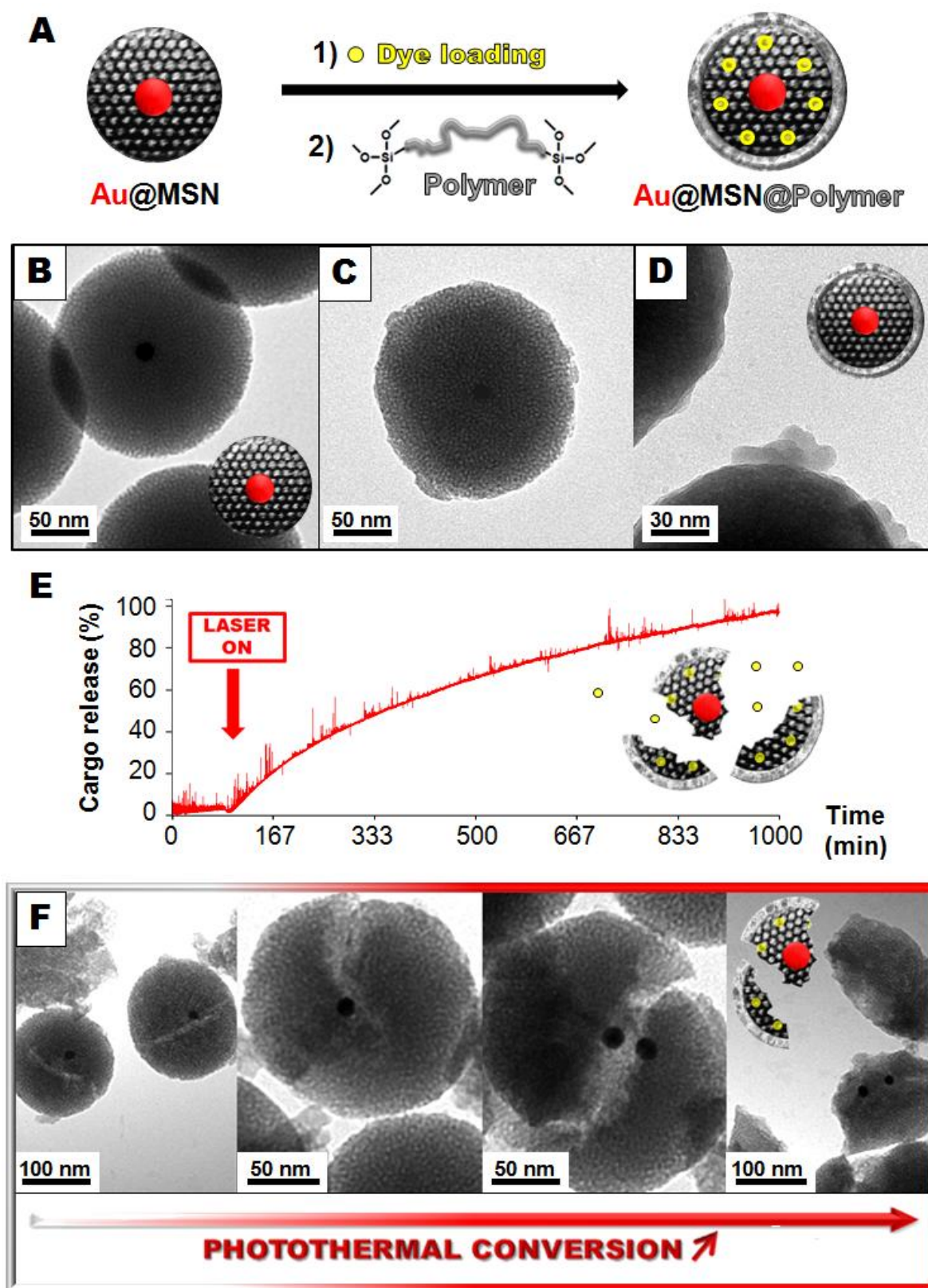


Figure 5. Schematic representation of the dye loading and polymer coating of Au@MSN (A). TEM micrographs before (B) and after polymer coating (C-D). Light-triggered cargo release in solution (514 nm, 30 mW) (E). TEM photodegradation of the dye-loaded Au@MSN@Polymer nanoparticles after 7 h of release experiment (F).

The controlled photodegradation feature was then harnessed for remote cargo release. Au@MSN nanomaterial with 15 nm cores were loaded with the rhodamine B dye in aqueous solution, and then coated with an alkoxysilylated polycaprolactone polymer of 2000 g.mol⁻¹ (see Figure S6A) to prevent the dye leakage (see Figure 5A). The alkoxysilylated polycaprolactone was obtained from the coupling of the commercial polycaprolactone diol with 3-isocyanatopropyltrimethoxysilane in toluene (see ESI). The successful polymer coating on the NPs was readily visible by TEM image before (Figure 5B) and after functionalization (Figure 5C,D and S7), and confirmed by Fourier transform infrared (FTIR) spectroscopy with the ν_{C-H} vibration modes between 2950 and 2850 cm⁻¹ as well as the carbonyl vibration at 1692 cm⁻¹ of the polymer (Figure S6B). A rhodamine B payload of 3 wt% was determined via UV-visible analysis of the loading supernatant. Then, dye-loaded Au@MSN@Polymer were placed at the bottom of a glass cuvette filled with water, and irradiated at 514 nm under 30 mW (see Figure 5E). It is noteworthy that the flat baseline before laser irradiation is characteristic of a robust nanocarrier avoiding premature leakage of cargo molecules. Besides, when the laser was turned on an instantaneous release of the rhodamine B cargo was observed; after 1000 minutes nearly all the dye content was released (Figure 5E). Furthermore, TEM analysis of the irradiated Au@MSN@Polymer nanocarriers revealed that the release of the cargo was due to the remarkable controlled photo-cracking of the carriers (see Figures 5F, and S8). Thus, the gold yolk mesoporous silica shell could be used as “nanoeggs” for on-demand cargo delivery via photo-cracking.

In summary, we reported a surprisingly powerful PT conversion of continuous excitation laser energy in heat via gold NPs embedded in a mesoporous silica shell, leading to its controlled photodegradation. The PT efficacy was found to be a complex sum of the power and wavelength of irradiation, as well as the gold NPs size in the Au@MSN platform. The silica shell degradation was controlled through lowering or increasing the laser power, or tuning the wavelength of the laser. Furthermore, the release of cargo molecule encapsulated in Au@MSN@Polymer was achieved via the controlled photodegradation of mesoporous silica shells through the plasmonic PT effect. The designed photodegradation of the silica shells should enhance the biodegradability of such nanocarriers, and decrease their excretion time, thus extending their efficacy in the nanomedicine field. The wavelength control of the particle cracking may be used as a dual drug delivery system, where 15 and 30 nm Au@MSN particles containing a different type of drug in their pores, would be irradiated separately (i.e. the 15 nm at 514 nm, and then the 30 nm at 568 nm). Additionally, novel drugs such as docetaxel have an enhancement of cytotoxicity under hyperthermia.²¹ As a result, this particular case illustrates the synergetic potentialities of a regulated PT conversion with surrounding molecules or materials for drug delivery.

REFERENCES

1. P. K. Jain, X. Huang, I. H. El-Sayed and M. A. El-Sayed, *Acc. Chem. Res.*, 2008, **41**, 1578-1586.
2. L. Dykman and N. Khlebtsov, *Chem. Soc. Rev.*, 2012, **41**, 2256-2282.
3. M. E. Stewart, C. R. Anderton, L. B. Thompson, J. Maria, S. K. Gray, J. A. Rogers and R. G. Nuzzo, *Chem. Rev.*, 2008, **108**, 494-521.
4. X. Lu, M. Rycenga, S. E. Skrabalak, B. Wiley and Y. Xia, *Annu. Rev. Phys. Chem.*, 2009, **60**, 167-192.
5. J. Homola, S. S. Yee and G. Gauglitz, *Sensors Actuat. B-Chem.*, 1999, **54**, 3-15.
6. G. L. Liu, J. Kim, Y. Lu and L. P. Lee, *Nature Mater.*, 2006, **5**, 27-32.
7. M. Rycenga, Z. Wang, E. Gordon, C. M. Cobley, A. G. Schwartz, C. S. Lo and Y. Xia, *Angew. Chem. Int. Ed.*, 2009, **48**, 9924-9927.
8. V. Raji, J. Kumar, C. S. Rejiya, M. Vibin, V. N. Sheno and A. Abraham, *Exp. Cell Res.*, 2011, **317**, 2052-2058.
9. M. R. Jones, J. E. Millstone, D. A. Giljohann, D. S. Seferos, K. L. Young and C. A. Mirkin, *ChemPhysChem.*, 2009, **10**, 1461-1465.
10. N. Zeng and A. B. Murphy, *Nanotechnology*, 2009, **20**, 375702.
11. W. Haiss, N. T. K. Thanh, J. Aveyard and D. G. Fernig, *Anal. Chem.*, 2007, **79**, 4215-4221.
12. P. K. Jain, K. S. Lee, I. H. El-Sayed and M. A. El-Sayed, *J. Phys. Chem. B*, 2006, **110**, 7238-7248.
13. E. Y. Hleb and D. O. Lapotko, *Nanotechnology*, 2008, **19**, 355702.
14. G. Zhang, Z. Yang, W. Lu, R. Zhang, Q. Huang, M. Tian, L. Li, D. Liang and C. Li, *Biomaterials*, 2009, **30**, 1928-1936.
15. L. Paasonen, T. Laaksonen, C. Johans, M. Yliperttula, K. S. Kontturi and A. Urtti, *J. Control. Release*, 2007, **122**, 86-93.
16. A. S. Angelatos, B. Radt and F. Caruso, *J. Phys. Chem. B*, 2005, **109**, 3071-3076.
17. S. Liu and M. Y. Han, *Chem. Asian J.*, 2010, **5**, 36-45.
18. V. Prasad, A. Mikhailovsky and J. A. Zasadzinski, *Langmuir*, 2005, **21**, 7528-7532.
19. J. Croissant and J. I. Zink, *J. Am. Chem. Soc.*, 2012, **134**, 7628-7631.
20. N. R. Jana, L. Gearheart and C. J. Murphy, *Langmuir*, 2001, **17**, 6782-6786.
21. F. Mohamed, P. Marchettini, O. A. Stuart, M. Urano and P. Sugarbaker, *Ann. Surg. Oncol.*, 2003, **10**, 463-468.

APPENDIX: SUPPLEMENTARY INFORMATION

I- EXPERIMENTAL SECTION

Laser irradiation. A COHERENT CUBE 445-40C diode laser was used to irradiate the Au@MSN NPs at 448 nm. A COHERENT Argon Innova 90C-5 ion laser was used to irradiate the Au@MSN NPs at 514 nm. A COHERENT Ar/Kr⁺ laser was used to irradiate the Au@MSN NPs at 530, 568, and 647 nm. The powers of irradiations specified in the manuscript (15, 20, 30, 50, and 100 mW) take into account the different mirrors, lenses, and glass objects in the path of the laser beam. The laser spot was half of a centimeter in diameter, thus the Au@MSN were submitted to 0.06, 0.08, 0.12, 0.2, and 0.4 W/cm² for the aforementioned laser powers.

Materials and methods. Potassium tetrachloroaurate (99%+) was purchased from Alfa Aesar. Sodium citrate tribasic dihydrate (99%+), cetyltrimethylammonium bromide (CTAB, 99%+), tetraethylorthosilicate (TEOS), ammonium nitrate (NH₄NO₃), rhodamine B, polycaprolactone diol, (Mn=2000 g.mol⁻¹), 3-(trimethoxysilyl)propylisocyanate, and 3-aminopropyl-trimethoxysilane (APTMS) were purchased from Sigma-Aldrich, sodium hydroxide (beads), was purchased from Fisher Chemical.

Au NPs 15 nm. Monodisperse Au NPs of 15 nm in diameter were obtained from the reported Turkevich method involving the reduction of potassium tetrachloroaurate complexes (55 mg, 11 mM) via the injection of sodium tribasic citrate reducing agent (120 mg, 40 mM) in boiling water (100 mL) for 5 minutes.^[1] The resulting solution **A** was utilized without further preparation.

Au@MSN with 15 nm cores. An aqueous solution (90 mL) of sodium hydroxide (875 μ L, 2 M), and CTAB (250 mg) were stirred vigorously at 80 °C. Then, a solution of 15 nm Au NPs (30 mL of **A**) was added to the aforementioned mixture. Finally, TEOS (1200 μ L) was added by consecutive dropwise additions. The sol-gel process was conducted 2 h. Afterwards, the solution was cooled at room temperature while stirring; fractions were gathered in propylene tubes and collected by centrifugation during 15 minutes at 21 krpm. The sample was then extracted twice with an alcoholic solution of NH₄NO₃ (6 g.L⁻¹), and washed three times with ethanol, water, and ethanol. Each extraction involved a sonication step of 30 minutes at 50°C in order to remove the CTAB surfactant; the collection was carried out in the same manner. The as-prepared material was dried under air flow for few hours.

Au@MSN with the three gold core diameters. Such a procedure was adapted from a reported one-pot process of Au@MSN NPs.^[2] A mixture of water (100 mL), ethanol (40 mL), and CTAB (640 mg), and potassium tetrachloroaurate (55 mg) was stirred at 70 °C in a three neck 250 mL round bottom flask. Secondly, sodium hydroxide (200 μ L, 2 M) was injected to produce the nucleation of the NPs nucleation instantaneously. The NPs growth was conducted during 30 minutes under 600 rpm. Afterwards, TEOS (1000 μ L) was added by dropwise additions to the stirred aforementioned solution. Then, the condensation process was triggered

by a second addition of sodium hydroxide (400 μL , 2 M). After 1 minute 30 seconds, the typical purple color of thin coated Au@MSN particles was observed, and the sol-gel process was lead for 2 h. The material was collected through centrifugation at 7830 rpm for 15 minutes. Each fraction was washed with MeOH (40 mL) and centrifuged 10 minutes, three times. Extraction and the following steps were identical as those described for Au@MSN with monodisperse cores.

Polymer alkoxysilylation. A mixture of toluene (40 mL), polycaprolactone diol (65 mg, $3.24 \cdot 10^{-5}$ mole, $M_n = 2000 \text{ g} \cdot \text{mol}^{-1}$) and 3-(trimethoxysilyl)propylisocyanate (16 μL , $6.48 \cdot 10^{-5}$ mole) was stirred at 50°C during 36 h under nitrogen flow. The solution (**B**) was used without further purification.

Loading and polymer coating of Au@MSN. Au@MSN particles (40 mg) were soaked in water (5 mL) with rhodamine B (5 mM) for one day at room temperature. The solution was then centrifuged at 7000 rpm for 8 minutes, the supernatant was removed, and the material was dried through air flow. Dried rhodamine B-loaded Au@MSN nanoparticles were crushed and dissolved in dried toluene (10 mL). Finally, this solution was quickly poured out in a stirring solution **B** (10 mL) of alkoxysililated polymer under nitrogen flow. The coating was led during 36 h, and the nanoparticles were centrifuged at 7000 rpm for 8 minutes. The supernatant was removed and the material was washed with water three times, each step being followed by centrifugation. The dye-loaded Au@MSN@Polymer nanoparticles were dried under air flow for 1 h. The as-prepared nanocarriers were used for the release experiment.

II-NANOMATERIALS CHARACTERIZATIONS

Au@MSN with 15 nm cores

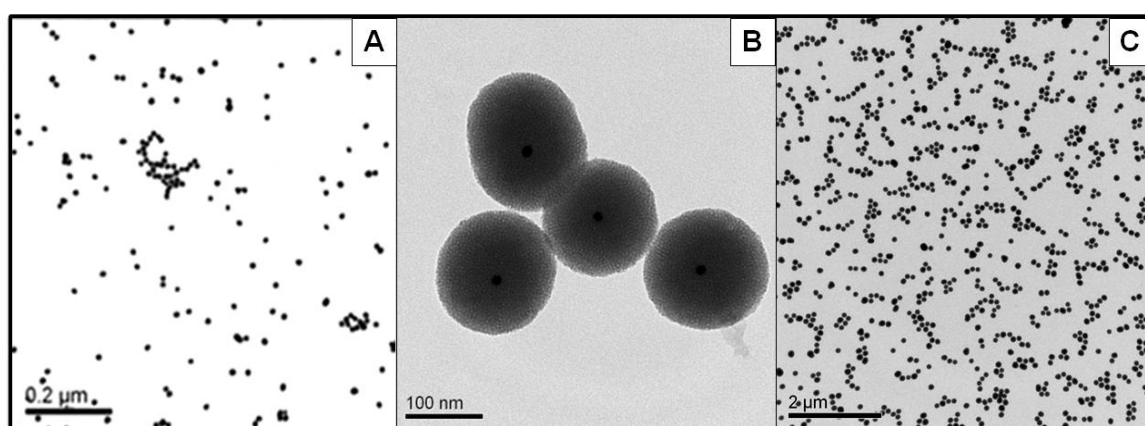


Figure S1. TEM images of gold-citrate NPs (A) and Au@MSN (B-C).

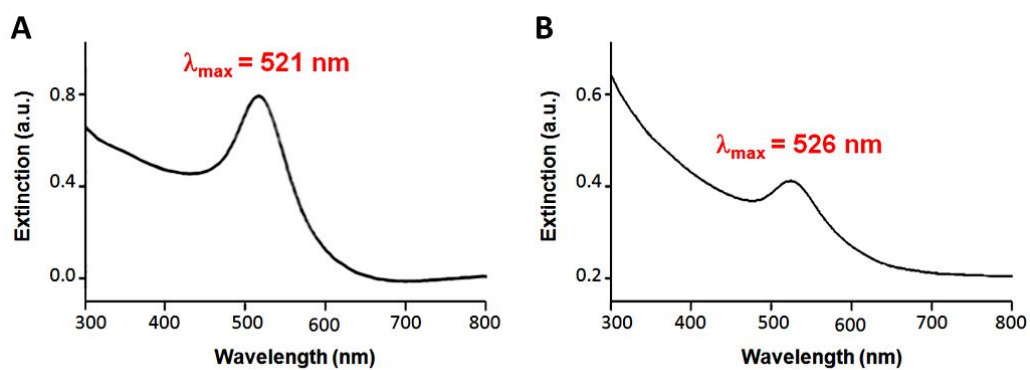


Figure S2. Extinction of gold nanospheres (A) and Au@MSN (B).

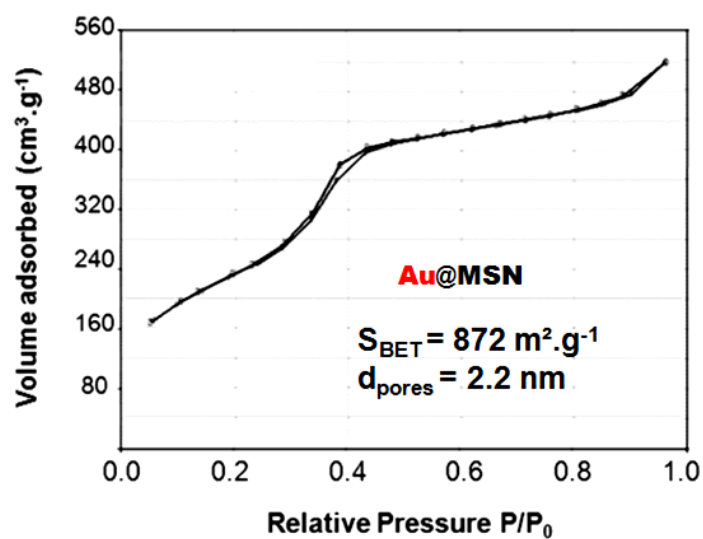


Figure S3. N_2 -adsorption-desorption of Au@MSN NPs containing 15 nm gold cores.

Au@MSN with the three gold core diameters

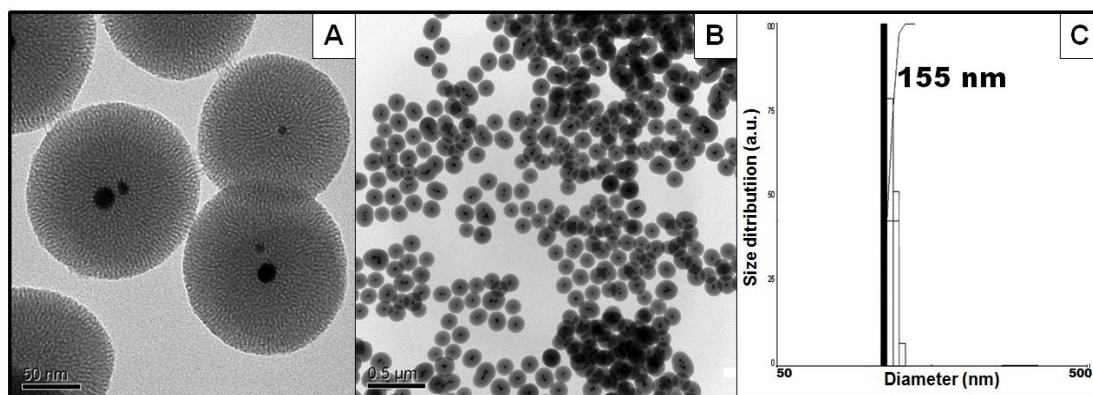


Figure S4. TEM images of Au@MSN (A-B), and the corresponding DLS size distribution (C).

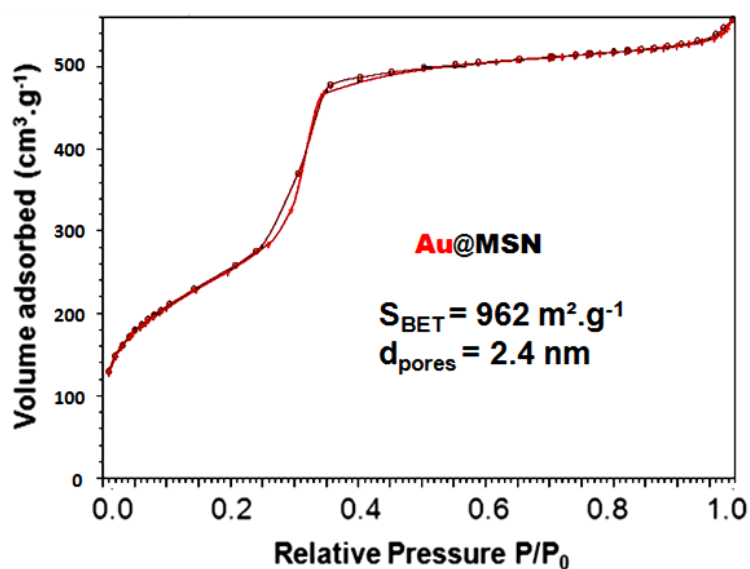


Figure S5. N₂-adsorption-desorption of Au@MSN containing the three gold core diameters.

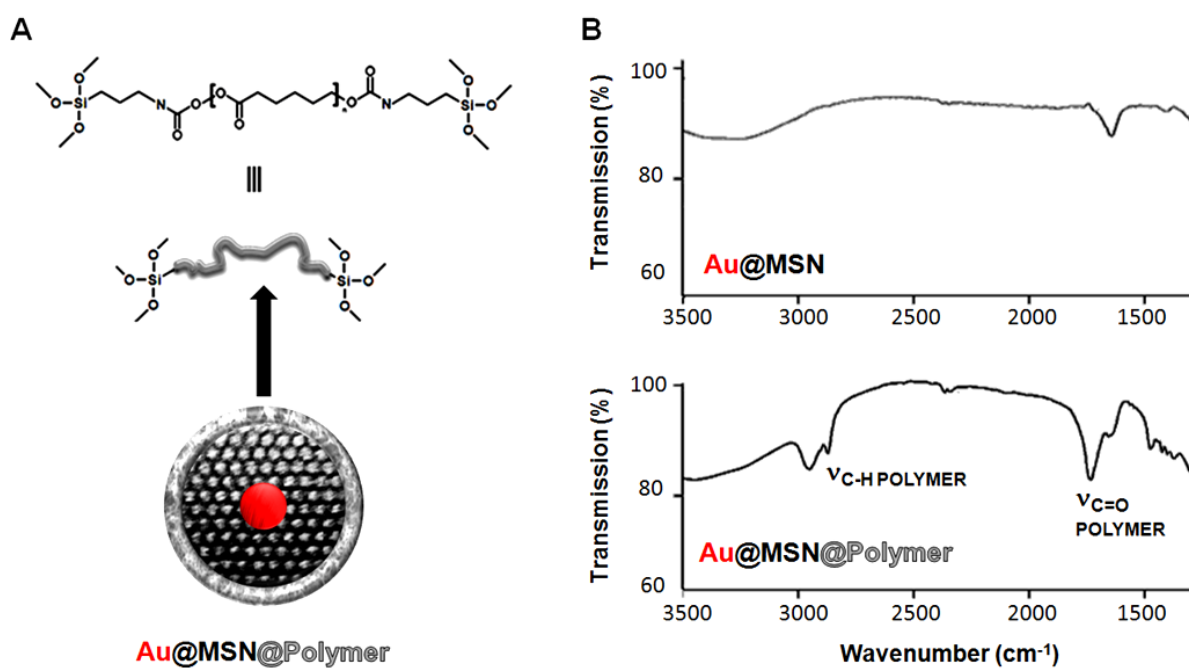


Figure S6. Representation of the alkoxy-sililated polycaprolactone polymer coated (A). FTIR spectra of Au@MSN and Au@MSN@Polymer NPs, confirming the successful coating.

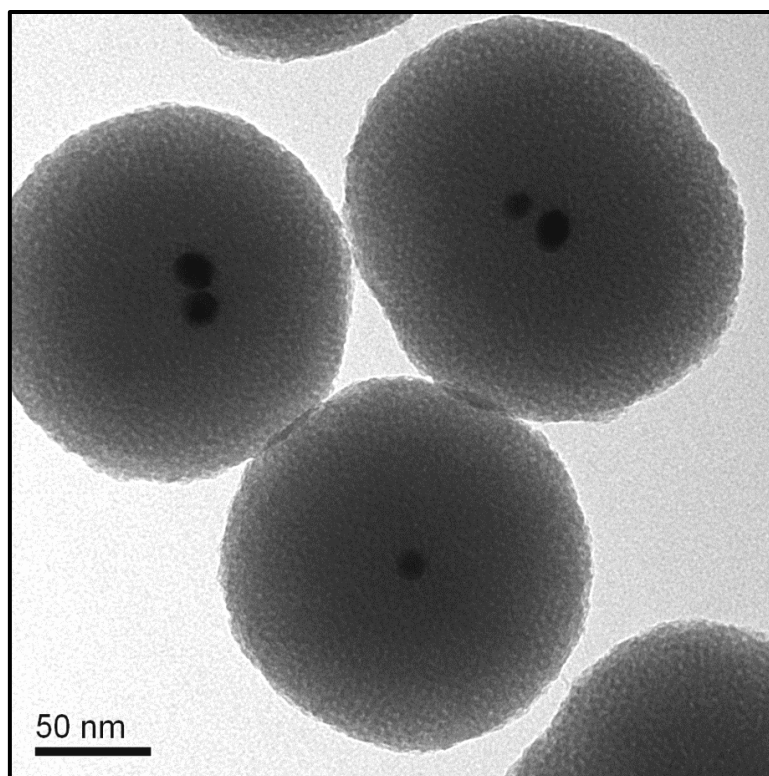


Figure S7. TEM micrograph of Au@MSN@Polymer.

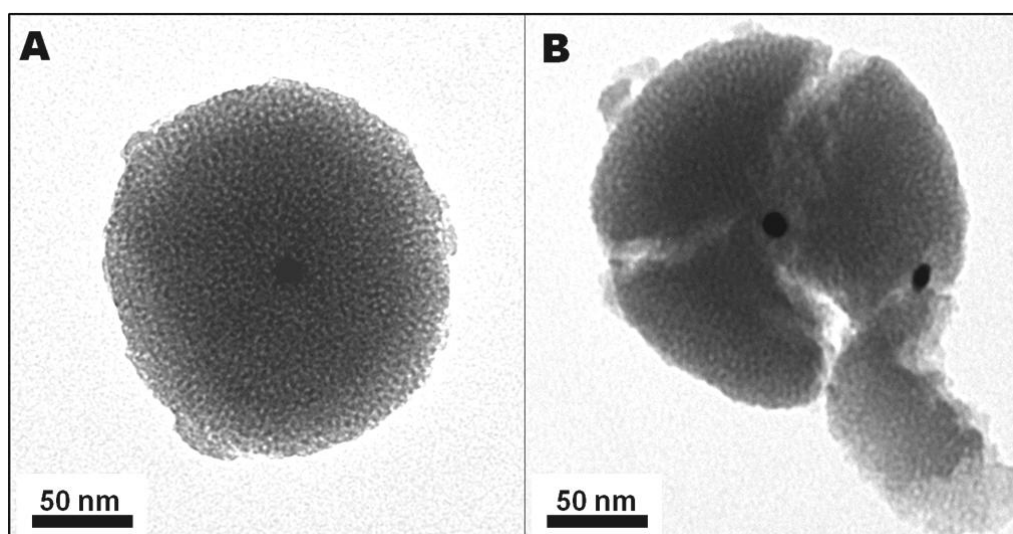


Figure S8. TEM micrographs of Au@MSN@Polymer before (A) and after 7 h of photodegradation (B).

REFERENCES

-
- [1] Turkevich, J.; Stevenson, P. C.; Hillier, J., *Discuss. Faraday Soc.* **1951**, 11, 55. Enüstün, B. V.; Turkevich, J., *J. Am. Chem. Soc.* **1963**, 85, 3317.
- [2] Croissant, J.; Zink, J. I., *J. Am. Chem. Soc.* **2012**, 134, 7628.

CHAPTER 4

Two-Photon-Actuated Drug and Nucleic Acid Deliveries via Azobenzene-Functionalized Mesoporous Silica Nanovehicles

INTERDISCIPLINARY COLLABORATION

J. Croissant, A. Chaix, H. P. N'Dongo, J. L. Nyalosaso, G. Derrien, C. Charnay, J-O. Durand, L. Raehm, J. I. Zink: *Nanomaterial concept, synthesis, physico-chemical characterizations, and applications in solution.*

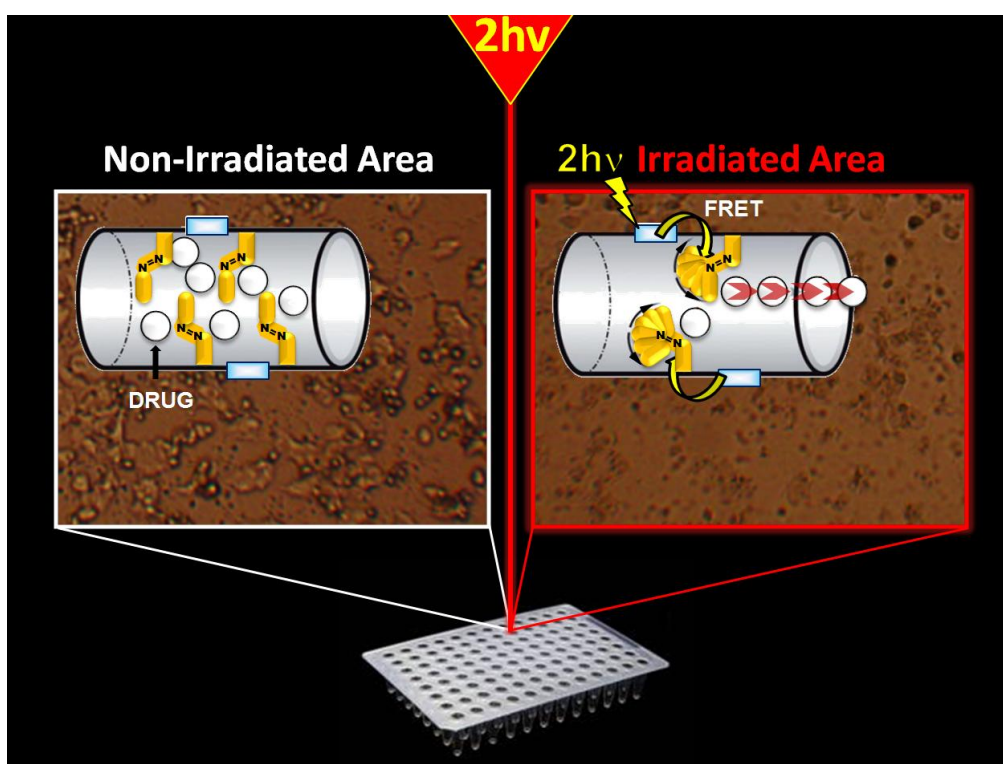
O. Mongin, V. Hugues, M. Blanchard-Desce: *Nanomaterial and fluorophore photophysical characterizations.*

J. Croissant, F. Serein-Spirau, N. Cheminet, T. Jarrosson, S. Clément: *Fluorophores synthesis and physico-chemical characterizations.*

M. Gary-Bobo, M. Maynadier, A. Gallud, M. Garcia, J. Lu, F. Tamanoi, D. Tarn, T. M. Guardado-Alvarez: *Two-photon cell studies.*

CHAPTER 4

A. Two-Photon-Triggered Drug Delivery in Cancer Cells via Nanoimpeller[†]

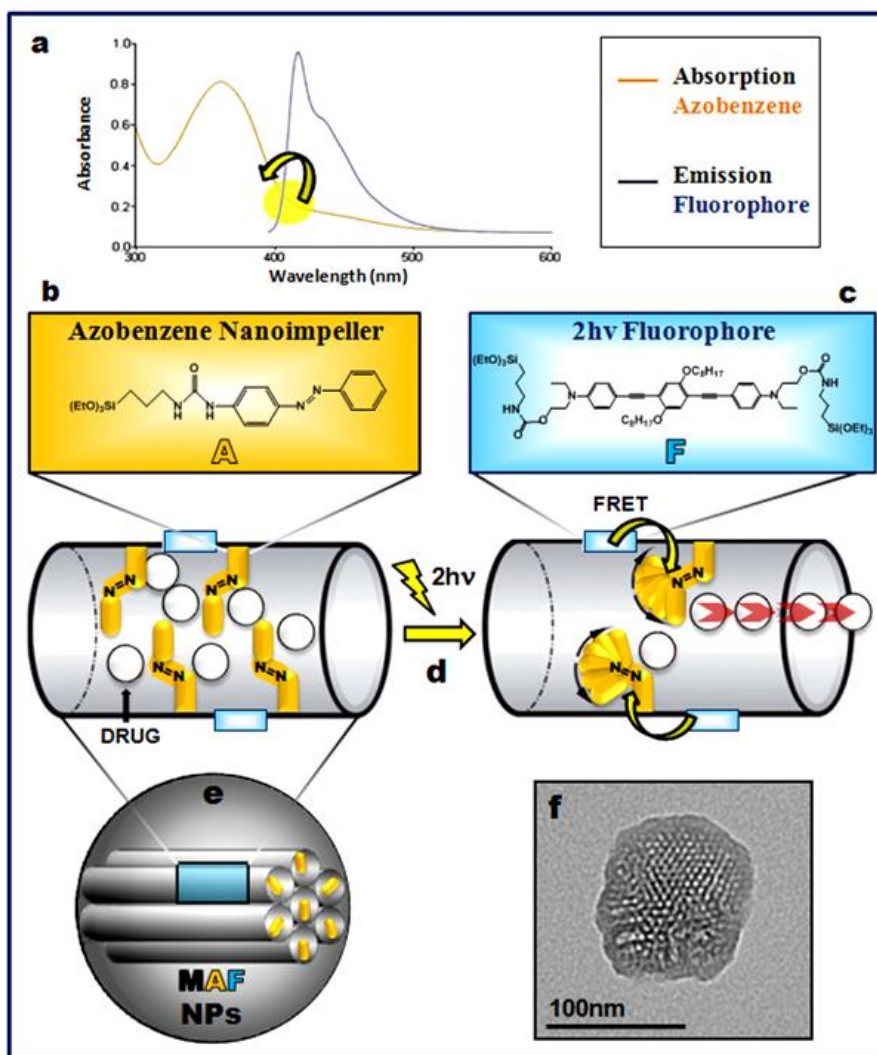


[†] J. Croissant, M. Maynadier, A. Gallud, H. P. N'Dongo, J. L. Nyalosaso, G. Derrien, C. Charnay, J.-O. Durand,* L. Raehm, F. Serein-Spirau, N. Cheminet, T. Jarrosson, O. Mongin, M. Blanchard-Desce, M. Gary-Bobo,* M. Garcia, J. Lu, F. Tamanoi, D. Tarn, T. M. Guardado-Alvarez, J. I. Zink,* **Angew. Chem. Int. Ed.** 2013, 125, 14058.

Introduction

Nowadays, remote activation of nanoparticles (NPs) by light for biomedical applications has become an important area of research.^[1] Among the different nano-objects, mesoporous silica nanoparticles (MSN) for light-triggered drug delivery applications have recently emerged and the field is expanding. Since the pioneering works of Zink,^[2, 3] Kim,^[4] Lin,^[5] and co-workers, many different systems have been described so far involving photo-cleavage,^[4-11] photo-dissociation,^[12] photo-isomerization,^[13-21] photo-release,^[22] photo-thermal,^[23, 24] photo-plasmonic heating,^[25-28] and up-conversion-photo-isomerization.^[29] Except for up-conversion, plasmonic and photo-thermal heating systems which can be activated with near infrared (NIR) light, the majority of the works is proof of concepts and was performed with UV-Vis light. Therefore the applications are limited because UV-Vis light can damage cells^[30] and does not penetrate deep inside tissues. Using two-photon excitation (TPE) in the NIR region instead of UV-Vis light has many advantages such as deeper penetration in tissues (down to 2 cm), lower scattering losses, and three dimensional spatial resolution. TPE is therefore highly suitable for applications in nanomedicine. Indeed nanomedicine aims at suppressing the side-effects of chemotherapeutic drugs, but the challenge to deliver on-demand such drugs with spatial and temporal accuracy remains unsolved. A two-photon actuated nanovehicle would provide an excellent spatial and temporal control of the release in tumors, which is not achieved with classical NIR systems. Only one example of photo-cleavage with MSN was described using TPE.^[10] The drug was covalently attached to the MSN through the photo-cleavable linker, which necessitated the functionalization of the drug. Moreover, the MSN were tested on cancer cells with UV-Vis light.

In this communication, we report the synthesis of nanoimpellers^[20] functionalized with a two-photon fluorophore **F** with a high two-photon absorption cross-section, suitable for the Förster Resonance Energy Transfer (FRET) to photoisomerize azobenzene **A** moieties in the NIR region (see Scheme 1). The nanoimpeller groups pending in the porous framework allow the physical entrapment of the anticancer drug camptothecin, which is then kicked out of the pores via two-photon-triggered photoisomerization, and finally leads to *in-vitro* cancer cell killing.



Scheme 1. Organically modified mesoporous silica NPs combining a two-photon fluorophore (c) and azobenzene moieties (b). The design of the so-called MAF NPs allows a 2-photon activated release of drug molecules via the Förster Resonance Energy Transfer (FRET) towards the azobenzene groups for the photoisomerization (d). Schematic representation of such NPs (e), and their transmission electron microscopy image (f).

Results and discussion

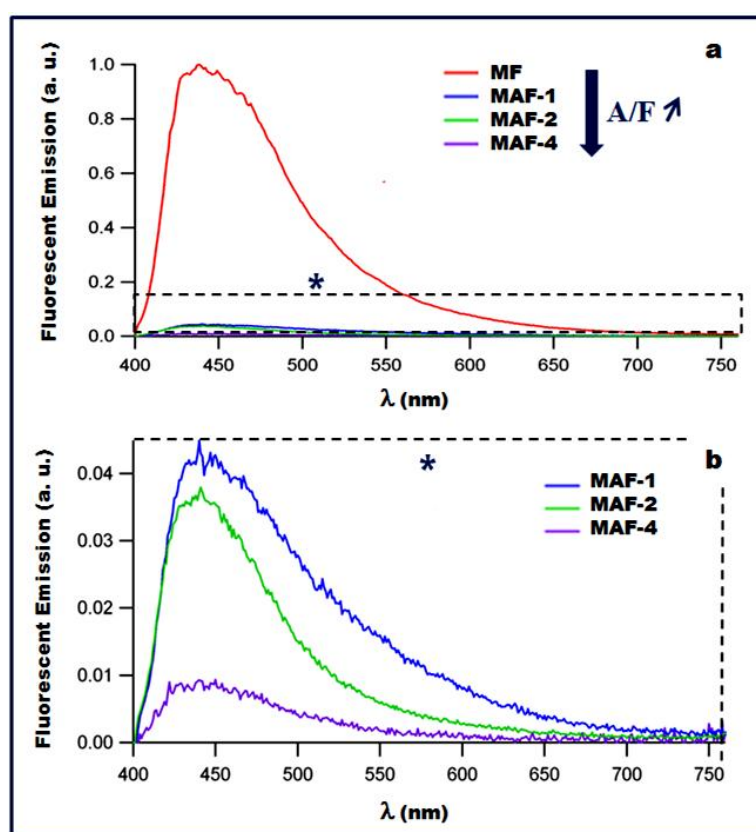
First, a novel fluorophore for TPE possessing two triethoxysilane moieties was designed and fully characterized (see ESI). The maximum fluorescence emission ($\lambda_{\text{ex}} = 385$ nm) of the fluorophore was 420 nm in THF, with a quantum yield of 88%.

The fluorophore or/and mono-triethoxysilylated azobenzene were co-condensed with tetraethoxysilane (TEOS) in basic media with cetyltrimethylammonium bromide (CTAB) following our synthesis procedure of MSN.^[31] The as-prepared nanomaterials were labeled **MA** and **MF**, respectively for the Mesoporous silica-Azobenzene and Mesoporous silica-Fluorophore modification, whereas the co-condensation of both the azobenzene and the fluorophore with different proportions led to **MAF-x** (see Table 1).

Table 1. Characteristics of MA, MF, and MAF nanoimpellers.

NPs	Ratio A/F	n_0 Azo (mol)	n_0 Fluo (mol)	S_{BET} ($\text{m}^2\cdot\text{g}^{-1}$)
MA	0	$3.7 \cdot 10^{-4}$	0	1144
MF	0	0	$1.0 \cdot 10^{-5}$	991
MAF-1	0.8	$4.0 \cdot 10^{-5}$	$5.0 \cdot 10^{-5}$	1066
MAF-2	2.2	$2.2 \cdot 10^{-4}$	$1.0 \cdot 10^{-4}$	851
MAF-3	4.4	$2.2 \cdot 10^{-4}$	$5.0 \cdot 10^{-5}$	658
MAF-4	17.0	$1.7 \cdot 10^{-4}$	$1.0 \cdot 10^{-5}$	745

The characterizations of the nanoimpellers after surfactant removal confirmed the nanosized mesoporous organosilicas (see Scheme 1d and Fig. S1-S7) with high specific surface areas suitable for cargo transportation.

**Figure 1.** Photophysical properties of MF and MAF NPs, the fluorescent emissions demonstrate the energy transfer.

FRET between the fluorophore and azobenzene moieties with **MAF** nanoimpellers was then studied by steady state fluorescence experiments. First the quantum yield fluorescence emission (Φ_F) of the fluorophore inside the MSN (**MF** sample) was determined to be 58%. The fluorescence emission of the **MAF** materials was quenched when the azobenzene groups were co-condensed with the fluorophore showing the FRET mechanism from the fluorophore to the azobenzene with **MAF** nanoimpellers (see Fig. 1). When the ratio

A/F increased the fluorescence quantum yield Φ_F decreased accordingly. The energy transfer quantum yield (Φ_{ET}) increased and was maximum for **MAF-4** (Table 2). The same trend was observed in the work of Lo and co-workers^[32] where fluorescein isothiocyanate was able to transfer its energy with a high quantum yield to a porphyrin photosensitizer, in MSN, for TPE-photodynamic therapy. The two-photon absorption cross-sections σ_2 of the fluorophore and of **MF** and **MAF** samples were determined (Fig. 2) and reached a maximum at 700 nm. The two-photon absorption properties of the fluorophore were retained in the materials and no decrease of σ_2 was noticed after encapsulation. The nanoimpellers **MA** and **MAF** were then loaded with rhodamine B (2 to 5% in mass), to give **MA+R** and **MAF+R** respectively, in water to study cargo release under one-photon excitation. After centrifugation and extensive washing, the nanoparticles were put at the bottom of a quartz cell and the cell was carefully filled with water. The release of the cargo was monitored by UV-Vis spectroscopy (see Fig. 3 and Fig. S8). No release was noticed without irradiation. UV irradiation at 365 nm triggered the release of the cargo showing the efficiency of all the nanoimpellers in water.

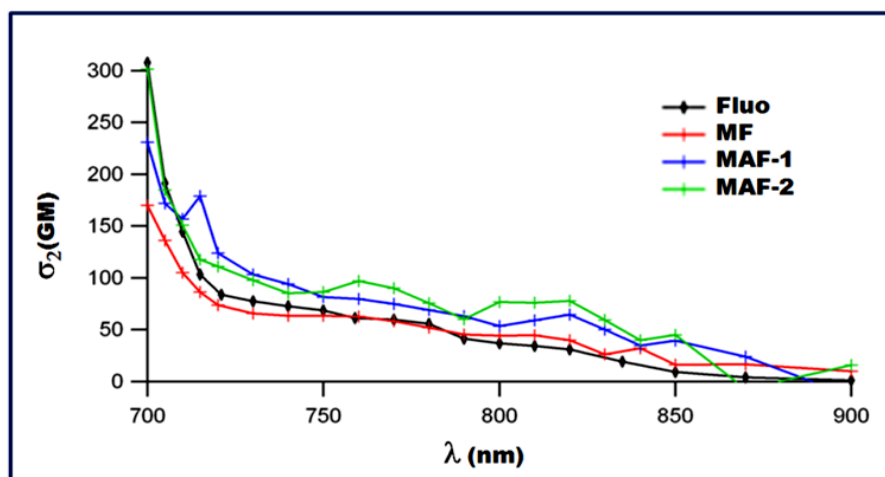


Figure 2. Two-photon absorption cross sections of **MF** and **MAF**, compared with the fluorephore in ethanol.

Table 2. Photophysical properties of **MA**, **MF**, and **MAF** nanoimpellers.

NPs	$\lambda_{abs}/\lambda_{em}$ (nm)	Φ_F ^[a]	Φ_{ET} ^[a]	$\sigma_2^{max[b]}$ (GM)
MA	368/-	0	-	-
MF	385/441	0.58	-	170
MAF-1	382/441	0.025	0.95	230
MAF-2	378/441	0.022	0.96	300
MAF-4	370/441	0.005	0.99	-

[a] Quinine bisulfate standard at 0,5M in H₂SO₄. [b] per chromophore.

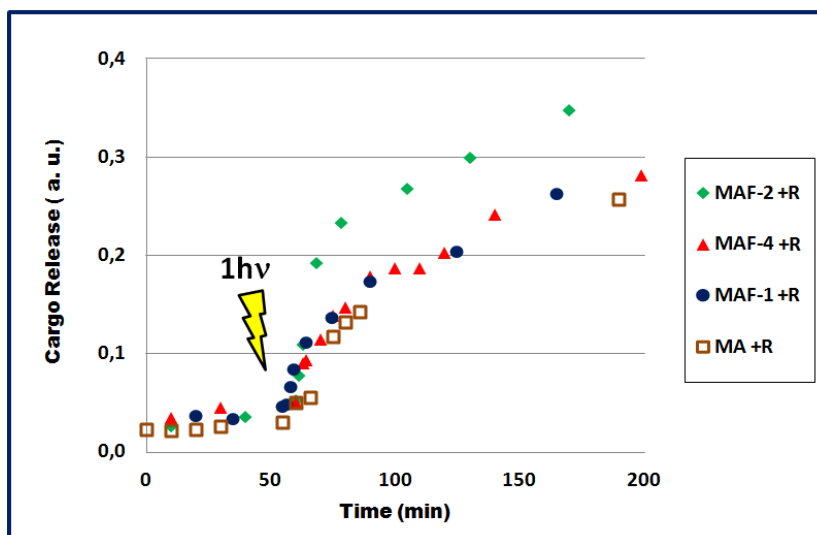


Figure 3. One-photon-triggered rhodamine B delivery in water, comparison between nanoimpellers **MA** and **MAF-1, 2, 4**.

The nanoimpellers were configured for two-photon activation, therefore an *in vitro* study was led on MCF-7 breast cancer cell line, and the laser excitation was performed with a Carl Zeiss two-photon confocal microscope. The cellular uptake was assessed via two-photon fluorescence imaging. The cell walls were stained with a cell mask 15 min before the imaging experiments. The remaining fluorescence of the fluorophore (Φ_F : 2.5 to 0.5 %, see Table 2) was taken into advantage to localize the **MAF** nanoimpellers. The slight emission of **MAF-3** and **MAF-4** was localized within the cells thus demonstrating the successful internalization of the nanoimpellers (see Fig. 4 and Fig. S9). The nanoimpellers loaded with camptothecin (**MA+C**, **MAF+C**) were then screened under TPE in MCF-7 cancer cells. Cells were incubated with nanoimpellers in a 384 multiwell plate. Irradiation was performed with a Carl Zeiss microscope at very short time, with a focused laser beam and at maximum laser power (laser power input 3 W, laser power output before the objective 900 mW.cm⁻²). The well was irradiated with three scans of 1.57 s each per irradiated area, in four different areas, without overlaps between irradiated areas, with an objective: Carl Zeiss NA 0.3, 10 X. Half of the well was irradiated with this technique. The MTT assay was performed two days after irradiation. **MA**, **MF**, and **MAF-4** nanoparticles did not induce cell death, with or without irradiation in the absence of camptothecin (see Fig. S11). We further verify the safety of these nanoparticles by a 4-day incubation time with increasing dose of **MAF-4** on normal fibroblasts and MCF-7 cancer cells (Fig. S10). Nanoimpellers were thus not toxic for cells and direct cancer cell killing (photothermal effect or ROS generation) was not observed. When loaded with camptothecin, **MAF-1+C** and **MAF-2+C** did not induce more cancer cell killing under TPE than without irradiation which is probably correlated to the low A/F ratio (Fig. 5a). By contrast, when the A/F ratio increased, more cancer cell death was observed with **MAF-3+C** and **MAF-4+C** nanoimpellers under TPE than without irradiation, and the best result was obtained with **MAF-4+C** nanoimpeller possessing an A/F ratio of 17 and a high energy transfer quantum yield (see Fig. S9).

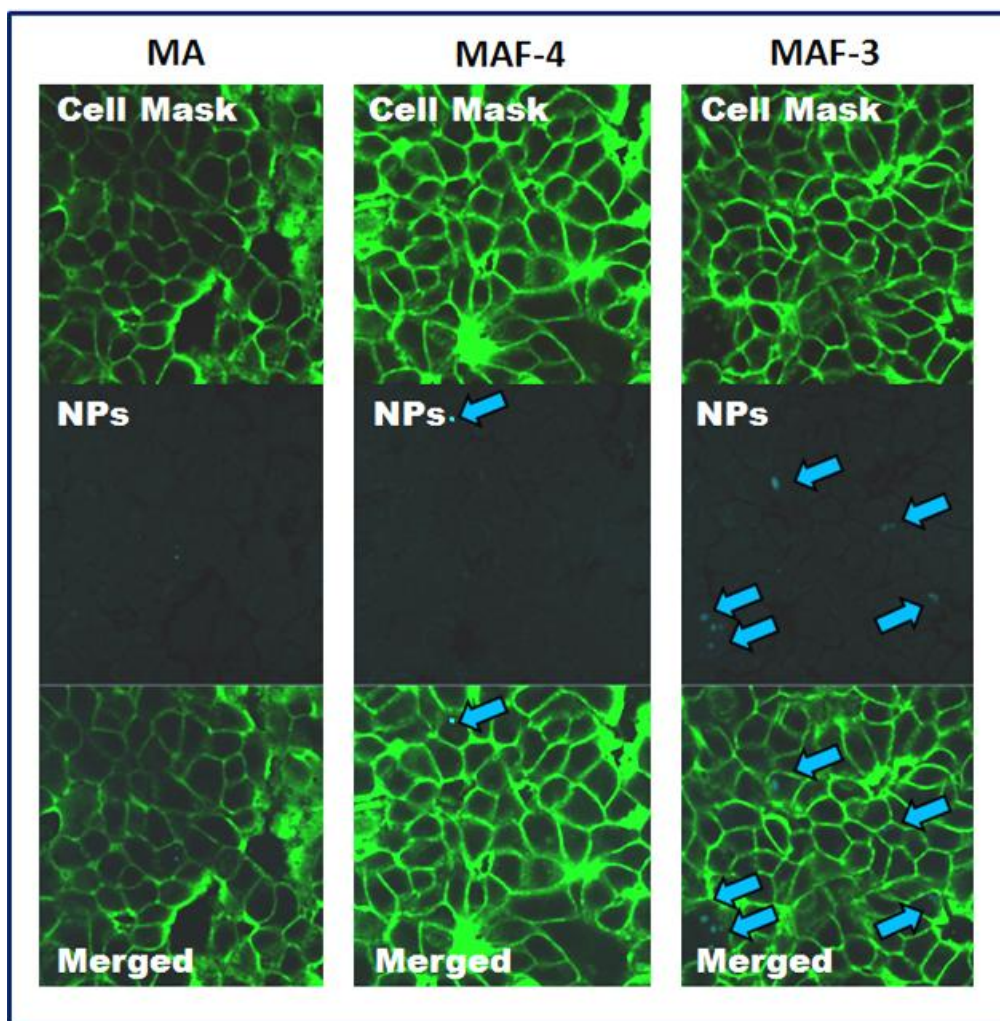


Figure 4. Two-photon imaging of MA, MAF-3, and MAF-4 confirming the NPs cellular uptake.

Hence, further *in vitro* experiments were led at different concentrations (from 20 to 80 $\mu\text{g.mL}^{-1}$) with **MA+C** and **MAF-4+C** nanoimpellers (Fig. 5b). **MA+C** nanoimpeller which does not possess the two-photon fluorophore did not kill cancer cells under TPE (see Figure 5b) at 20 $\mu\text{g.mL}^{-1}$ and no difference was observed between irradiated and non irradiated cells with **MA+C** nanoimpeller at higher concentration. By contrast **MAF-4+C** nanoimpeller was efficient in killing cancer cells at 20 and 40 $\mu\text{g.mL}^{-1}$, under TPE and up to 40% of cancer cell death was observed. At 80 $\mu\text{g.mL}^{-1}$ **MAF-4+C** nanoimpeller induced 30% of cancer cell death without irradiation and 75% cell death with irradiation. These results demonstrate that the fluorophore was necessary to observe cancer cell death with nanoimpellers under TPE at short time of irradiation, focused laser beam and high power. Note that **MA+C** and **MAF-4+C** were both efficient in inducing cancer cell killing under TPE with different conditions (Fig. S12-S13). Furthermore, premature release of camptothecin was not observed in aqueous solution without irradiation (Fig. S14).

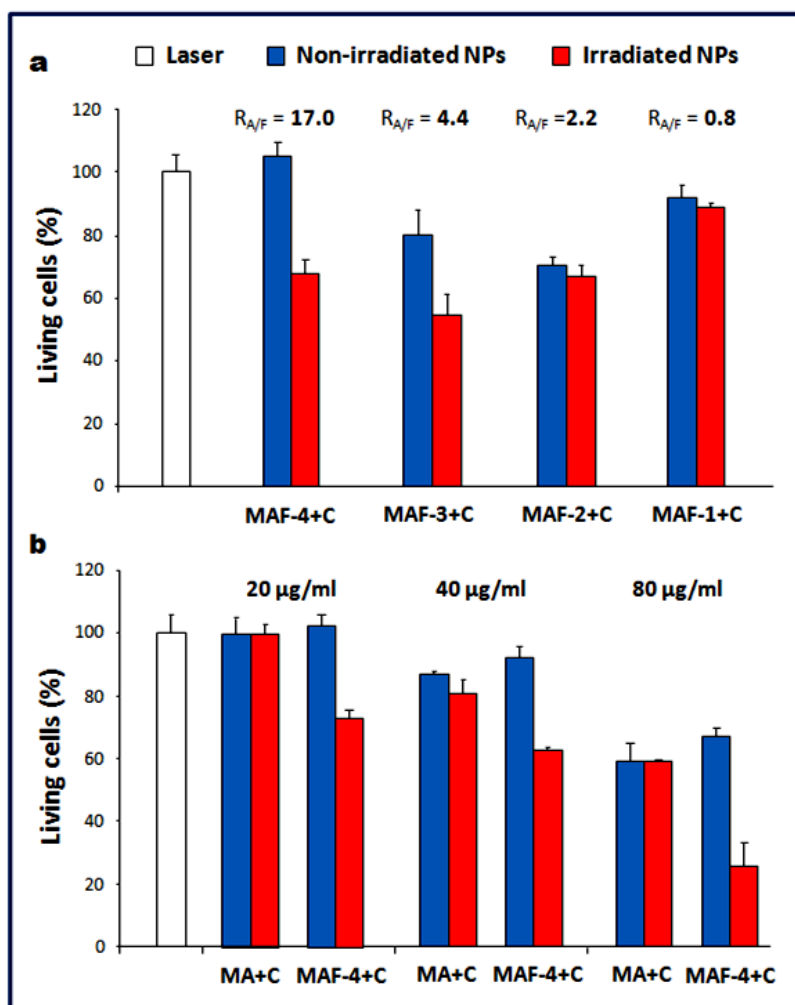


Figure 5. Two-photon-triggered *in-vitro* delivery of camptothecin, comparison between nanoimpellers MAF-1, 2, 4, 5, at $20 \mu\text{g.mL}^{-1}$ (a), and between MA and MAF 4 at various concentrations of NPs (b).

Conclusion

In summary, we have designed nanoimpellers with a two-photon fluorophore possessing a high two-photon absorption cross-section, leading to nanoimpellers configured for TPE with FRET from the fluorophore to the azobenzene. The residual fluorescence of the nanoimpellers allowed to perform TPE fluorescence imaging in cancer cells demonstrating the internalization of the nanoimpellers. Nanoimpeller **MAF-4+C** with a high energy transfer quantum yield from the fluorophore to the azobenzene moiety was able to induce cancer cell death under these TPE conditions and was not toxic to cells without irradiation at low concentration. Work is in progress to further extend the scope and applications of this methodology.

REFERENCES

- [1] R. Tong, D. S. Kohane, *Wires Nanomed. Nanob.* **2012**, *4*, 638-662.
- [2] E. Johansson, E. Choi, S. Angelos, M. Liong, J. I. Zink, *J. Sol-Gel Sci. Technol.* **2008**, *46*, 313-322.
- [3] T. D. Nguyen, K. C. F. Leung, M. Liong, Y. Liu, F. Stoddart, J. I. Zink, *Adv. Funct. Mater.* **2007**, *17*, 2101-2110.
- [4] C. Park, K. Lee, C. Kim, *Angew. Chem. Int. Ed.* **2009**, *48*, 1275-1278.
- [5] J. L. Vivero-Escoto, Slowing, I. I., C. W. Wu, V. S. Y. Lin, *J. Am. Chem. Soc.* **2009**, *131*, 3462-3463.
- [6] N. Z. Knezevic, V. S. Y. Lin, *Nanoscale* **2013**, *5*, 1544-1551.
- [7] D. He, X. He, K. Wang, J. Cao, Y. Zhao, *Langmuir* **2012**, *28*, 4003-4008.
- [8] A. Agostini, F. Sancenon, R. Martinez-Manez, M. D. Marcos, J. Soto, P. Amoros, *Chem. Eur. J.* **2012**, *18*, 12218-12221.
- [9] N. Z. Knezevic, B. G. Trewyn, V. S. Y. Lin, *Chem. Eur. J.* **2011**, *17*, 3338-3342.
- [10] Q. N. Lin, Q. Huang, C. Y. Li, C. Y. Bao, Z. Z. Liu, F. Y. Li, L. Y. Zhu, *J. Am. Chem. Soc.* **2010**, *132*, 10645-10647.
- [11] J. Lai, X. Mu, Y. Xu, X. Wu, C. Wu, C. Li, J. Chen, Y. Zhao, *Chem. Commun.* **2010**, *46*, 7370-7372.
- [12] D. He, X. He, K. Wang, J. Cao, Y. Zhao, *Adv. Funct. Mater.* **2012**, *22*, 4704-4710.
- [13] Y. Wang, B. Li, L. Zhang, H. Song, L. Zhang, *ACS Appl. Mater. Inter.* **2013**, *5*, 11-15.
- [14] Q. Yuan, Y. Zhang, T. Chen, D. Lu, Z. Zhao, X. Zhang, Z. Li, C.-H. Yan, W. Tan, *ACS Nano* **2012**, *6*, 6337-6344.
- [15] H. Yan, C. Teh, S. Sreejith, L. Zhu, A. Kwok, W. Fang, X. Ma, N. Kim Truc, V. Korzh, Y. Zhao, *Angew. Chem. Int. Ed.* **2012**, *51*, 8373-8377.
- [16] Y. Wen, L. Xu, W. Wang, D. Wang, H. Du, X. Zhang, *Nanoscale* **2012**, *4*, 4473-4476.
- [17] X. Mei, S. Yang, D. Chen, N. Li, H. Li, Q. Xu, J. Ge, J. Lu, *Chem. Commun.* **2012**, *48*, 10010-10012.
- [18] Y. A. Lau, B. L. Henderson, J. Lu, D. P. Ferris, F. Tamanoi, J. I. Zink, *Nanoscale* **2012**, *4*, 3482-3489.
- [19] D. P. Ferris, Y. L. Zhao, N. M. Khashab, H. A. Khatib, J. F. Stoddart, J. I. Zink, *J. Am. Chem. Soc.* **2009**, *131*, 1686-1688.
- [20] J. Lu, E. Choi, F. Tamanoi, J. I. Zink, *Small* **2008**, *4*, 421-426.
- [21] S. Angelos, E. Choi, F. Voegtle, L. De Cola, J. I. Zink, *J. Phys. Chem. C* **2007**, *111*, 6589-6592.
- [22] N. Z. Knezevic, B. G. Trewyn, V. S. Y. Lin, *Chem. Commun.* **2011**, *47*, 2817-2819.
- [23] A. K. Singh, M. A. Hahn, L. G. Gutwein, M. C. Rule, J. A. Knapik, B. M. Moudgil, S. R. Grobmyer, S. C. Brown, *Int. J. Nanomed.* **2012**, *7*, 2739-2750.
- [24] L. G. Gutwein, A. K. Singh, M. A. Hahn, M. C. Rule, J. A. Knapik, B. M. Moudgil, S. C. Brown, S. R. Grobmyer, *Int. J. Nanomed.* **2012**, *7*, 351-357.
- [25] Z. Jiang, B. Dong, B. Chen, J. Wang, L. Xu, S. Zhang, H. Song, *Small* **2013**, *9*, 604-612.
- [26] Z. Zhang, L. Wang, J. Wang, X. Jiang, X. Li, Z. Hu, Y. Ji, X. Wu, C. Chen, *Adv. Mater.* **2012**, *24*, 1418-1423.
- [27] X. Yang, X. Liu, Z. Liu, F. Pu, J. Ren, X. Qu, *Adv. Mater.* **2012**, *24*, 2890-2895.
- [28] J. Croissant, J. I. Zink, *J. Am. Chem. Soc.* **2012**, *134*, 7628-7631.
- [29] J. Liu, W. Bu, L. Pan, J. Shi, *Angew. Chem. Int. Ed.* **2013**, *52*, 4375-4379.
- [30] T. Kushibiki, T. Hirasawa, S. Okawa, M. Ishihara, *Photomed. Laser Surg.* **2013**, *31*, 95-104.
- [31] M. Gary-Bobo, Y. Mir, C. Rouxel, D. Brevet, I. Basile, M. Maynadier, O. Vaillant, O. Mongin, M. Blanchard-Desce, A. Morere, M. Garcia, J.-O. Durand, L. Raehm, *Angew. Chem. Int. Ed.* **2011**, *50*, 11425-11429.
- [32] S.-H. Cheng, C.-C. Hsieh, N.-T. Chen, C.-H. Chu, C.-M. Huang, P.-T. Chou, F.-G. Tseng, C.-S. Yang, C.-Y. Mou, L.-W. Lo, *Nano Today* **2011**, *6*, 552-563.

APPENDIX: SUPPLEMENTARY INFORMATION

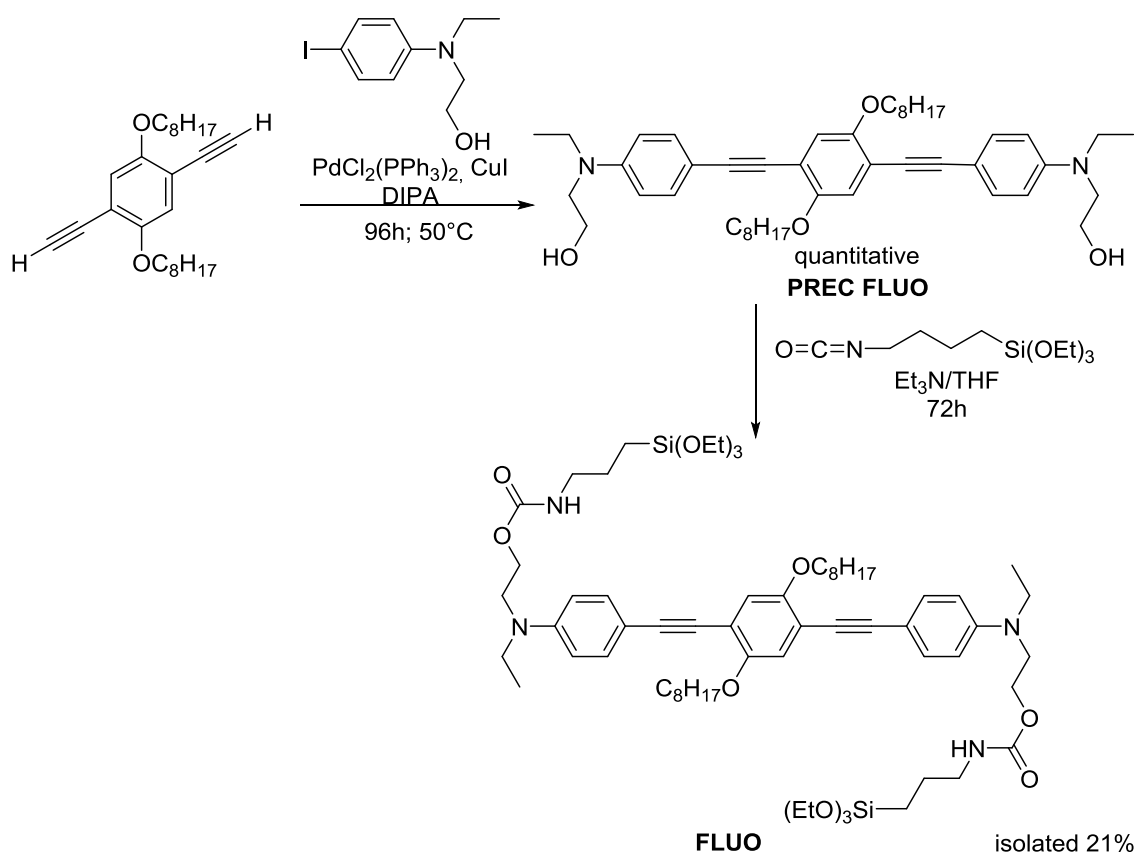
I- EXPERIMENTAL SECTION

General procedures. THF and diisopropylamine were dried over sodium/benzophenone or CaH_2 respectively. Triethylamine, triethoxy(3-isocyanatopropyl)silane, bis(triphenylphosphine) dichloro-palladium, copper iodide were purchased (Alfa and Aldrich) and used without further purification. 1,4-Diethynyl-2,5-bis(octoxy)benzene^[1] and 2-[ethyl(4-iodophenyl)amino]ethanol^[2] were prepared according to the literature. Flash chromatography purifications were carried out on an Armen Spot II Ultimate instrument. ^1H and ^{13}C NMR spectra were recorded with a Bruker AC 400 spectrometer. Chemical shifts (in δ units, ppm) are referenced to TMS using CHCl_3 ($\delta = 7.26$ ppm) and CDCl_3 ($\delta = 77.0$ ppm) as the internal standards, respectively, for ^1H and ^{13}C NMR spectra. IR spectra were recorded on a Perkin-Elmer 100 FT spectrophotometer. Absorption spectra were recorded on a Hewlett-Packard 8453 spectrophotometer and fluorescence data were collected on a Perkin-Elmer LS55 fluorimeter. Mass spectrometry was carried out at the Laboratoire de Spectrometrie de Masse (Lyon, France) with a Thermo-Finnigan MAT95 apparatus in electronic impact ionization mode.

II- SYNTHESIS AND CHARACTERIZATION OF ORGANIC COMPOUNDS

AZO precursor. The aminobenzene precursor (2.1 g) was placed in a 100 mL two necks round bottom flask with absolute ethanol (50 mL) and stirred under nitrogen flow at 54°C . Then, isocyanatopropyltriethoxysilane (2800 μL) was added through micropipette. Finally, the mixture was stirred overnight. The compound was stored in the fridge. The concentration was 4.2 mg of AZO per 100 μL EtOH (50 mL EtOH for 2.1 g of AZO).

FLUO precursor. FLUO was prepared according to a Pd(0) catalyzed double Sonogashira cross-coupling between 1,4-diethynyl-2,5-bis(octyloxy)benzene with two equivalents of 2-[ethyl(4-iodophenyl)amino]ethanol, giving in quantitative yield crude bis(ethanolamine) FLUO precursor (FLUO PREC) after 96 h reaction at 50°C in diisopropylamine. Crude FLUO PREC was then reacted in triethylamine with triethoxy(3-isocyanatopropyl)silane in refluxing THF during 72 h. FLUO was obtained in 21% yield after a flash chromatography purification over a $15\mu\text{m}$ spherical silica column with CH_2Cl_2 -AcOEt solvent mixture according to the (1:0 v:v) to (1:1 v:v) elution gradient (Scheme 1)



Scheme 1. Synthesis of FLUO.

PREC FLUO. In a 25 mL round-bottomed two-necked flask, 500 mg (1.307 mmol) of 1,4-diethynyl-2,5-bis(octyloxy)benzene, 0.836 mg (2.875 mmol) of 2-[ethyl(4-iodophenyl)amino]ethanol, 36 mg (0.052 mmol) of bis(triphenylphosphine)dichloropalladium and 9 mg (0.052 mmol) of copper iodide were introduced under nitrogen and dissolved into 6 mL of freshly distilled and degassed diisopropylamine. The mixture was stirred at 50°C for 96 hours and filtered after cooling to room temperature over a silica gel plug eluted with dichloromethane-ethylacetate solvent mixture according to the (1:0 v:v) to (1:1 v:v) gradient. The filtrate was concentrated *in vacuo* and 970 mg of PREC FLUO was obtained in 99% yield as a black solid and will be used without further purification in the following step.¹H NMR (400 MHz, CDCl₃) : δ = 7.38 (d, J = 9 Hz, 4H, H_{Ph}), 6.96 (s, 2 h, H_{Ph} (central)), 6.67 (d, J = 9 Hz, 4H, H_{Ph}), 4.01 (t, J = 6.5 Hz, 4H, OCH₂), 3.79 (t, J = 6.0 Hz, 4H, N-CH₂), 3.48 (t, J = 6.0 Hz, 4H, CH₂-OH), 3.43 (d, J = 7.1 Hz, 4H, CH₂ of Et), 1.83 (dt, J = 14.6, 6.5 Hz, 4H, O-CH₂-CH₂), 1.28-1.25 (m, 20 h, CH₂ alkyl), 1.16 (t, J = 7.1 Hz, 6H, CH₃ of Et), 0.87 (t, J = 6.9 Hz, 6H, CH₃) ; ¹³C NMR (101 MHz, CDCl₃) : δ = 153.7, 148.3, 133.3, 117.1, 114.4, 112.25 (4C) 110.8, 96.2, 85.5, 70.0, 60.5, 52.6, 45.9, 32.2, 29.85 (4 C), 29.7; 26.5 23.1, 19.6, 14.54 (2C). IR (neat KBr) $\nu_{\text{max}}/\text{cm}^{-1}$ = 3064, 2921, 2869, 2850, 2154, 2026, 1704, 1596, 1538, 1503, 1488, 1466, 1409, 1387, 1274, 1260, 1248, 1213, 1192, 1164, 1127, 1102, 1064, 1042, 1003, 889, 849, 790, 753, 725; UV/Vis λ_{max} (CHCl₃): 385 nm ; Emission (CHCl₃): λ_{max} =428 nm ($\lambda_{\text{excitation}}$ =385 nm) ; MS (EI) m/z (%) : 709 (50) [M⁺], 355 (100) ; HRMS (EI) : m/z calcd for C₄₆H₆₄N₂O₄ : 709.4939, found 709.4929.

FLUO. In a 50 mL round-bottomed two-necked flask equipped with a condenser and a magnetic stirrer were introduced, under nitrogen, 500 mg (0.712 mmol) of PREC FLUO, 10 mL of THF and 1 mL of triethylamine, both being freshly distilled and degassed. The mixture was refluxed for 72 hours under stirring. After cooling, solvents were removed *in vacuo* and the product was purified under flash chromatography over a 15 μ m spherical silica column eluted with CH₂Cl₂-AcOEt solvent mixture according to the (1:0 v:v) to (1:1 v:v) gradient. FLUO was obtained in 21% yield (180 mg) (purification not optimized). ¹H NMR (400 MHz, CDCl₃): δ = 7.37 (d, *J* = 8.9 Hz, 4H, H_{Ph}), 6.95 (s, 2 h, H_{Ph (central)}), 6.65 (d, *J* = 8.9 Hz, 4H, H_{Ph}), 4.96- 4.93 (m, 2 h, NH), 4.19 (t, *J* = 6.4 Hz, 4H, N-CH₂-CH₂-O), 4.00 (t, *J* = 6.4 Hz, 4H, OCH₂), 3.81 (q, *J* = 7.0 Hz, 12 h, Si-O-CH₂), 3.54 (t, *J* = 6.4 Hz, 4H, N-CH₂-CH₂-O), 3.41 (q, *J* = 6.9 Hz, 4H, N-CH₂-CH₃), 3.17 (t, *J* = 6.5 Hz, 4H, NH-CH₂), 1.85-1.79 (m, 4H, O-CH₂-CH₂), 1.65-1.57 (m, 4H, NH-CH₂-CH₂-CH₂-Si), 1.57-1.49 (m, 4H, O-CH₂-CH₂-CH₂-), 1.40-1.25 (m, 16H, CH₂), 1.22 (t, *J* = 7.0 Hz, 18H, Si-O-CH₂-CH₃), 1.17 (t, *J* = 7.1 Hz, 6H, N-CH₂-CH₃), 0.86 (t, *J* = 6.9 Hz, 6H, CH₃ alkyle), 0.62 (t, *J* = 8.1 Hz, 4H, Si-CH₂); UV/Vis λ_{\max} (CHCl₃): 388 nm; Emission (CHCl₃): λ_{\max} = 426 nm ($\lambda_{\text{excitation}}$ = 388 nm); MS (EI) *m/z* (%): 1203 (100) [M⁺], 602 (35); HRMS (EI): *m/z* calcd for C₆₆H₁₀₆N₄O₁₂Si₂: 1203.7419, found 1203.7446.

III- SYNTHESIS AND CHARACTERIZATION OF THE NANOMATERIALS

MA NPs. A mixture of cetyltrimethylammonium bromide (690 mg, CTAB), and sodium hydroxide (40 mL, 0.2 M) was stirred at room temperature during 50 minutes at 700 rpm in a 500 mL three necks round bottom flask. Then, an alcoholic solution of the alkoxysilylated AZO ($n_0 = 3.7 \cdot 10^{-4}$ mol, in 1.8 mL EtOH) was added to elaborate MA NPs, and the stirring speed was changed to 1000 rpm. One minute later, tetraethoxysilane (3.6 mL, TEOS) was added to the aforementioned solution, and after 40 seconds, an aqueous solution (260 mL) was poured out. The solution was then heated through a hair drier ($T_0 = 25^\circ\text{C}$, $T' = 28-30^\circ\text{C}$ in 1-2 min), in order to trigger the condensation process. After 5 minutes 30 seconds of reaction, a solution of hydrochloric acid (36 mL + aliquots of HCl 0.2 M) was added to quench the reaction by reaching a pH of 6.9. Fractions were gathered in propylene tubes and collected by centrifugation during 15 minutes at 21 krpm. The sample was then extracted twice with an alcoholic solution of ammonium nitrate (6 g.L⁻¹, NH₄NO₃), and washed three time with ethanol, water, and ethanol. Each extraction involved a sonication step of 30 minutes at 50°C in order to remove the CTAB surfactant; the collection was carried out in the same manner. The as-prepared material was dried under air flow for few hours.

MF NPs. A mixture of CTAB (690 mg), and sodium hydroxide (40 mL, 0.2 M) was stirred at room temperature during 50 minutes at 700 rpm in a 500 mL three necks round bottom flask. Then, an alcoholic solution of the alkoxysilylated FLUO ($n_0 = 1.0 \cdot 10^{-5}$ mol, in 0.4 mL THF), and the stirring speed was changed to 1000 rpm. One minute later, TEOS (3.6 mL) was added to the aforementioned solution, and after 40 seconds, an aqueous solution (260 mL) was poured out. The solution was then heated through a hair drier ($T_0 = 25^\circ\text{C}$, $T' = 28-30^\circ\text{C}$ in 1-2

min), in order to trigger the condensation process. After 5 minutes 30 seconds of reaction, a solution of hydrochloric acid (36 mL + aliquots of HCl 0.2 M) was added to quench the reaction by reaching a pH of 6.9. Fractions were gathered in propylene tubes and collected by centrifugation during 15 minutes at 21 krpm. Extraction and the following steps were identical as those described for MA NPs.

MAF NPs. A mixture of CTAB (690 mg), and sodium hydroxide (40 mL, 0.2 M) was stirred at room temperature during 50 minutes at 700 rpm in a 500 mL three necks round bottom flask. Then, the alcoholic solution of the alkoxysilylated AZO (n_0 mol of AZO, see Table 1, in 0.8 mL EtOH), as well as the tetrahydrofuran solution of the alkoxysilylated FLUO (n_0 mol of FLUO, see Table 1) were added, and the stirring speed was changed to 1000 rpm. One minute later, TEOS (3.6 mL) was added to the aforementioned solution, and after 40 seconds, an aqueous solution (260 mL) was poured out. The solution was then heated through a hair drier ($T_0=25^\circ\text{C}$, $T'=28-30^\circ\text{C}$ in 1-2 min), in order to trigger the condensation process. After 5 minutes 30 seconds of reaction, a solution of hydrochloric acid (36 mL + aliquots of HCl 0.2 M) was added to quench the reaction by reaching a pH of 6.9. Fractions were gathered in propylene tubes and collected by centrifugation during 15 minutes at 21 krpm. Extraction and the following steps were identical as those described for MA NPs.

RHODAMINE B LOADING OF MA and MAF NPs. A mixture of surfactant free MA or MAF NPS (40 mg), rhodamine B (12 mg), and deionized water (12 mL) was sonicated during 30 minutes and then stirred two days at room temperature. Afterwards, the sample was collected by centrifugation during 15 minutes at 21 krpm. Several aqueous washings were performed (30 mL each), and the sample was centrifugated to remove the unloaded rhodamine cargos. Eventually, the NPs were dried under vacuum for few hours. Note that, the various steps following the dye loading were all done in the absence of light.

CAMPTOTHECIN LOADING OF MA and MAF NPs. A mixture of surfactant free MA or MAF NPS (24 mg), camptothecin (3 mg), and dimethyl sulfoxide (1.5 mL) was sonicated during 30 minutes and then stirred two days at 30°C in a 5 mL round bottom flask with a $\frac{1}{2}$ cm stir bare. Afterwards, the sample was collected by centrifugation during 15 minutes at 21 krpm. One washing was performed with dimethylsulfoxide (5 mL), and two aqueous washings were performed as well (30 mL each), and the sample was centrifugated. Eventually, the NPs were dried under vacuum for few hours. Note that, the various steps following the drug loading were all done in the absence of light.

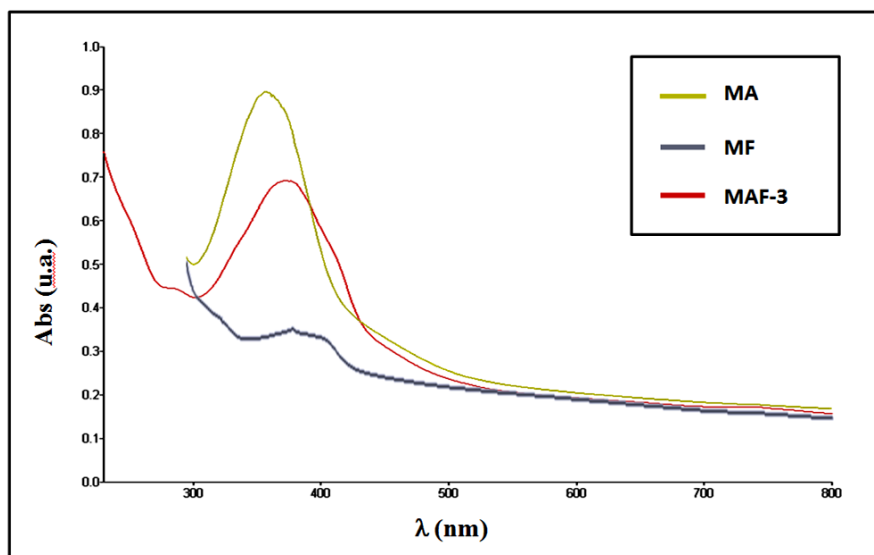


Figure S1. UV-visible spectra of **MA**, **MF**, and **MAF-3** nanoimpellers, demonstrating the incorporation of both the azobenzene and the fluorophore species.

For each nanomaterials (**MA** **MF** **MAF-1** to **MAF-4**), Transmission Electron Microscopy (TEM), UV-visible spectroscopy (UV-Vis), Dynamic Light Scattering (DLS), X-Ray Diffraction (XRD), and Nitrogen-Adsorption-Desorption (N₂ Ads) characterizations are presented in the following pattern:

TEM	TEM
UV-Vis	DLS
XRD	N ₂ Ads

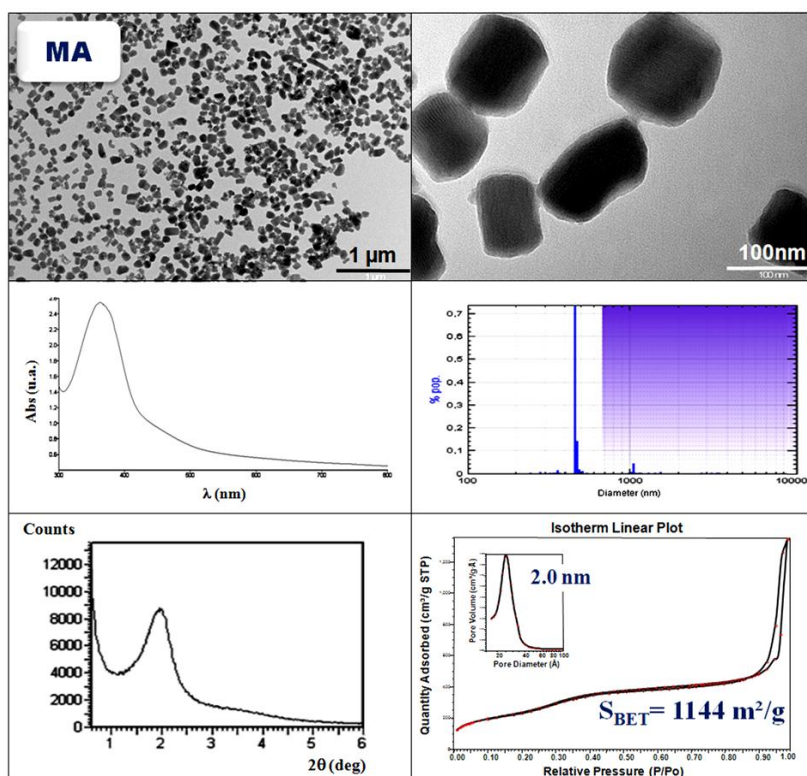


Figure S2. TEM, UV-Vis, DLS, XRD, and N₂ Ads characterizations of MA NPs.

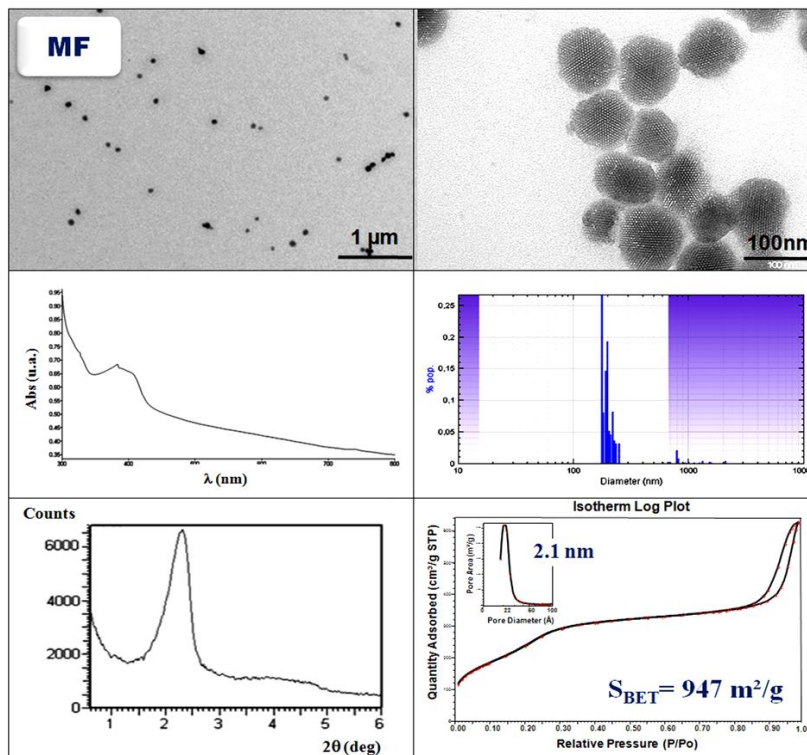


Figure S3. TEM, UV-Vis, DLS, XRD, and N₂ Ads characterizations of MF NPs.

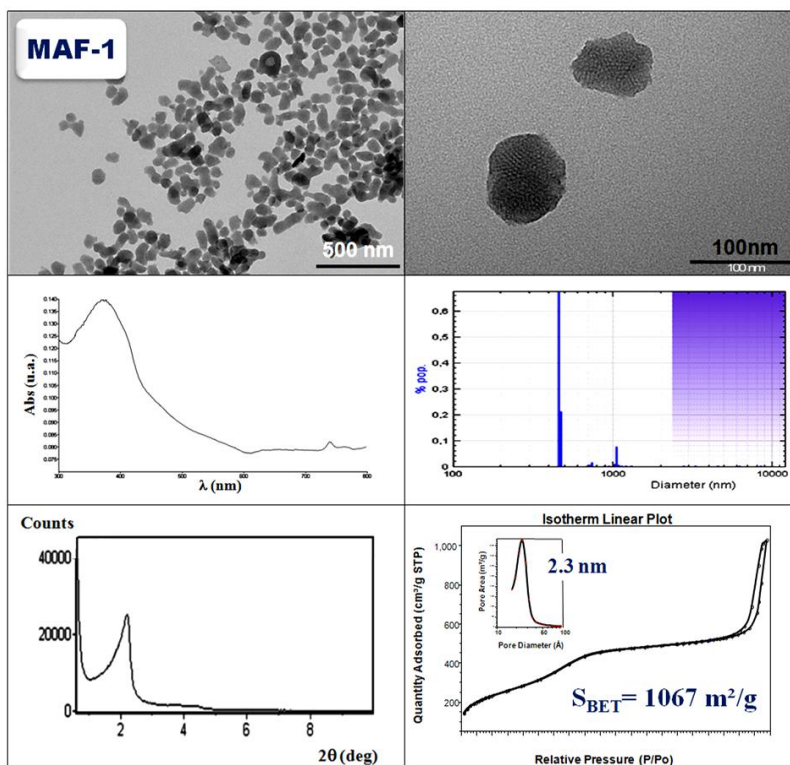


Figure S4. TEM, UV-Vis, DLS, XRD, and N₂ Ads characterizations of MAF-1 NPs.

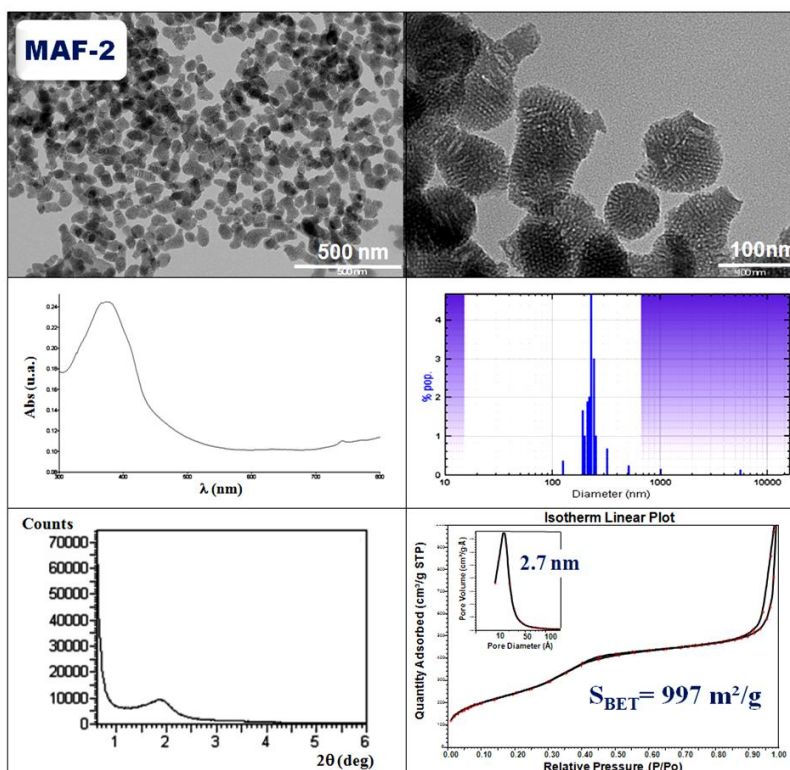


Figure S5. TEM, UV-Vis, DLS, XRD, and N₂ Ads characterizations of MAF-2 NPs.

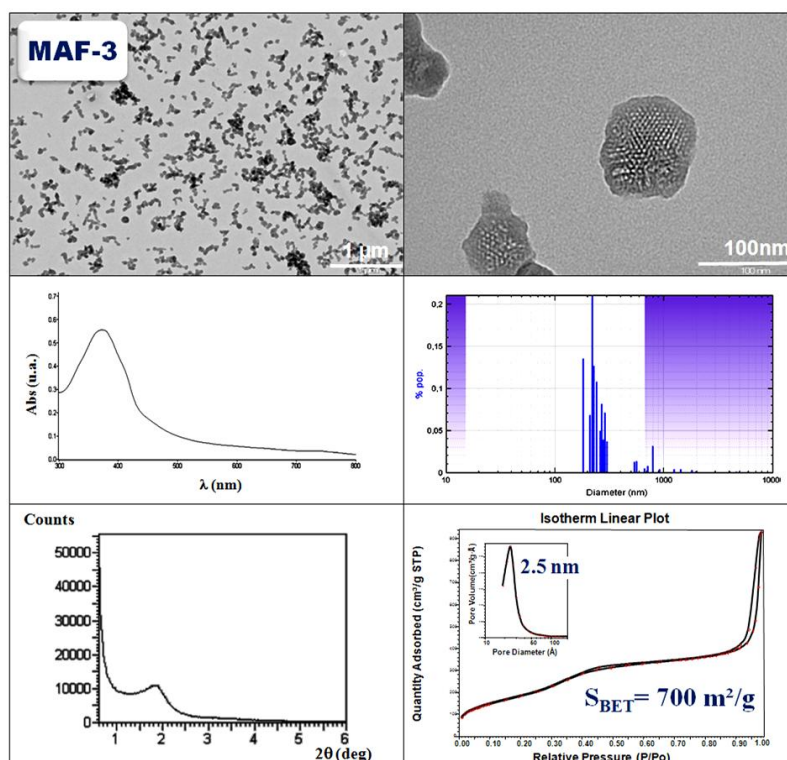


Figure S6. TEM, UV-Vis, DLS, XRD, and N₂ Ads characterizations of MAF-3 NPs.

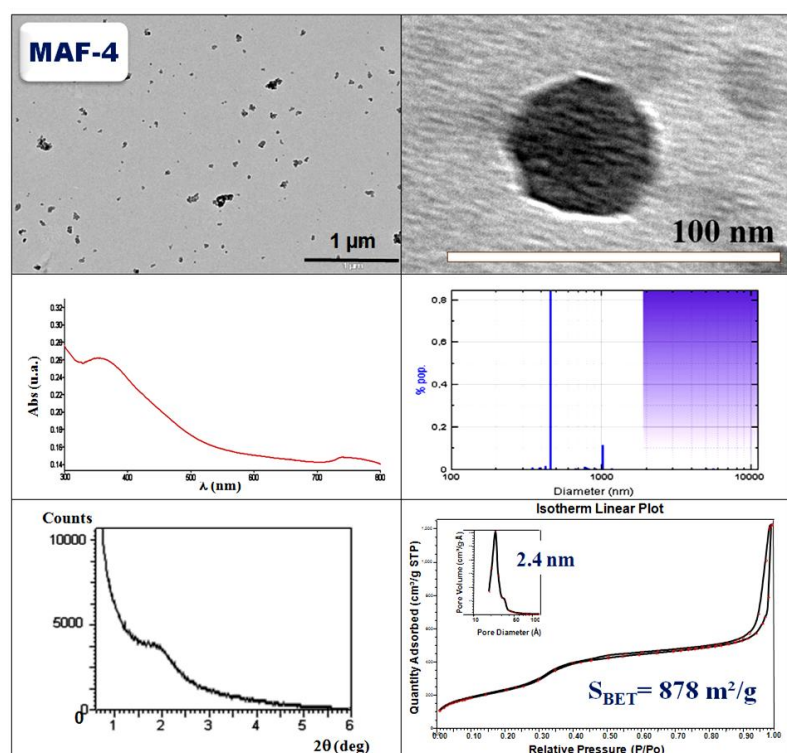


Figure S7. TEM, UV-Vis, DLS, XRD, and N₂ Ads characterizations of MAF-4 NPs.

IV- ONE-PHOTON RELEASE OF RHODAMINE B LOADED MA AND MAF NPs

The one-photon-triggered release of rhodamine B was performed according to the following figure:

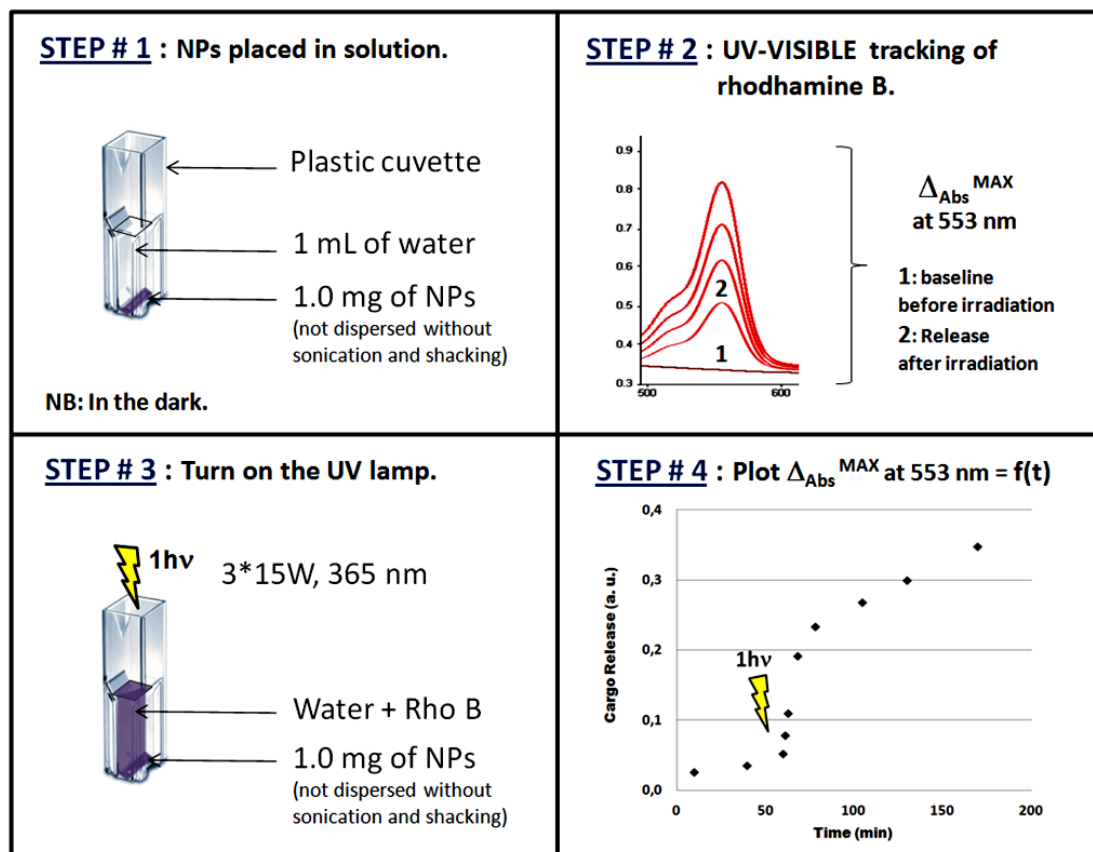


Figure S8. One-photon-triggered release of rhodamine B on MA and MAF NPs.

V- TWO-PHOTON FLUORESCENCE IMAGING

The day prior to the experiment, MCF-7 human breast cancer cells (purchased from ATCC) were seeded onto bottom glass dishes (World Precision Instrument, Stevenage, UK) at a density of 10^6 cells.cm⁻². Adherent cells were then washed once and incubated in 1 mL medium containing nanoimpellers at a concentration of 40 $\mu\text{g.mL}^{-1}$ for 20 h. 15 minutes before the end of incubation, cells were loaded with Cell Mask (Invitrogen, Cergy Pontoise, France) for membrane staining at a final concentration of 5 $\mu\text{g.mL}^{-1}$. Before visualization, cells were washed gently with phenol red-free Dulbecco's modified Eagle's medium (DMEM). Cells were then scanned with a LSM 780 LIVE confocal microscope (Carl Zeiss, Le Pecq, France), at 760 nm with a slice depth (Z stack) of 0.62 μm .

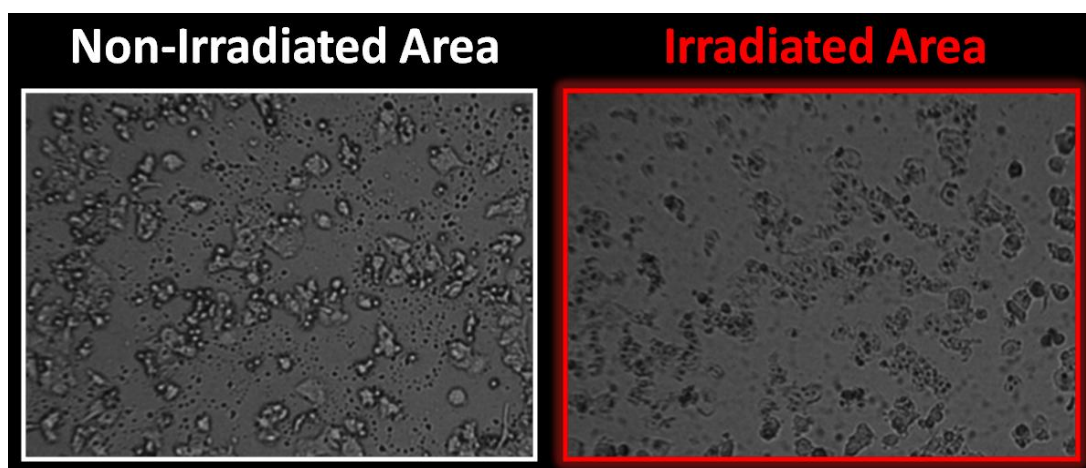


Figure S9. Two-photon-triggered drug delivery with **MAF-4+C** on the MCF-7 cells before and after laser irradiation.

VI- UNLOADED NANOCARRIERS IN-VITRO CONTROL: TPE with the Carl Zeiss microscope

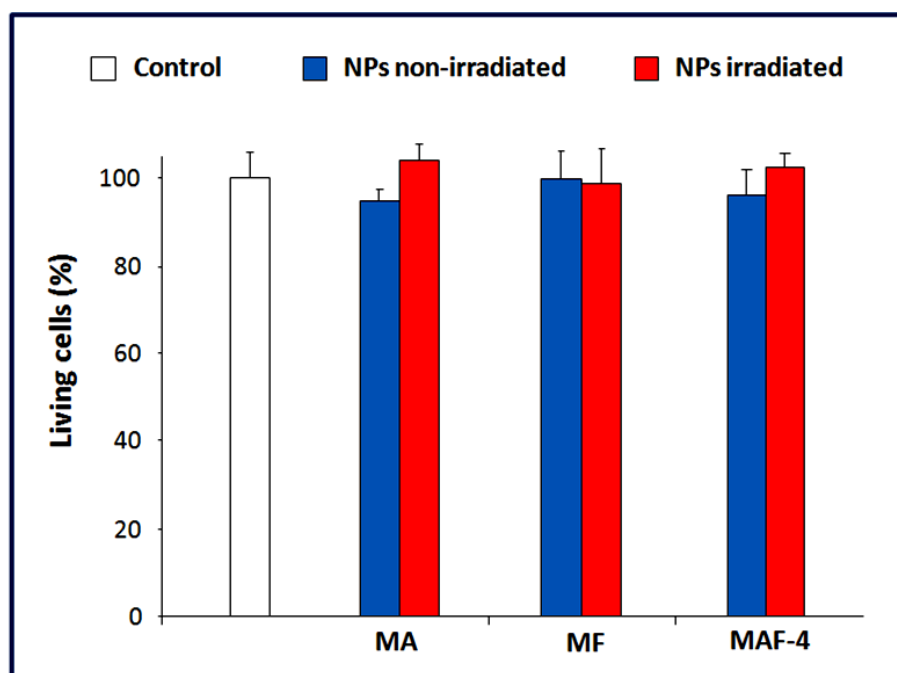


Figure S10. Two-photon *in-vitro* control with **MA**, **MF**, and **MAF-4** nanoimpellers ($40 \mu\text{g.mL}^{-1}$) not loaded with camptothecin. The irradiation did not produce any cell death. Conditions: with a focused laser beam and at maximum laser power (laser power input 3 W, laser power output before the objective 900 mW.cm^{-2}). The well was irradiated with three scans of 1.57 s each per irradiated area, in four different areas, without overlaps between irradiated areas, with an objective: Carl Zeiss NA 0.3, 10x.

VII- UNLOADED NANOCARRIERS IN-VITRO CONTROL: Cytotoxicity for 4 days

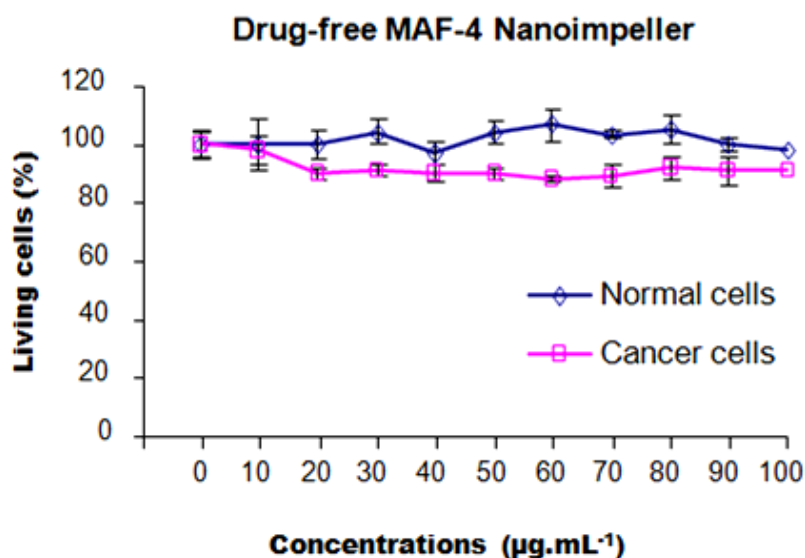


Figure S11. Absence of toxicity of free drug nanocarrier. Cancer (MCF-7) and normal (fibroblasts) cells were incubated with increasing concentrations of **MAF-4** (from 10 to 100 $\mu\text{g.mL}^{-1}$). After 4 days treatment, a MTT assay was performed and data are mean \pm SD of 3 experiments.

VIII- DRUG-LOADED NANOIMPELLERS IN-VITRO CONTROL: TPE with the Leica microscope

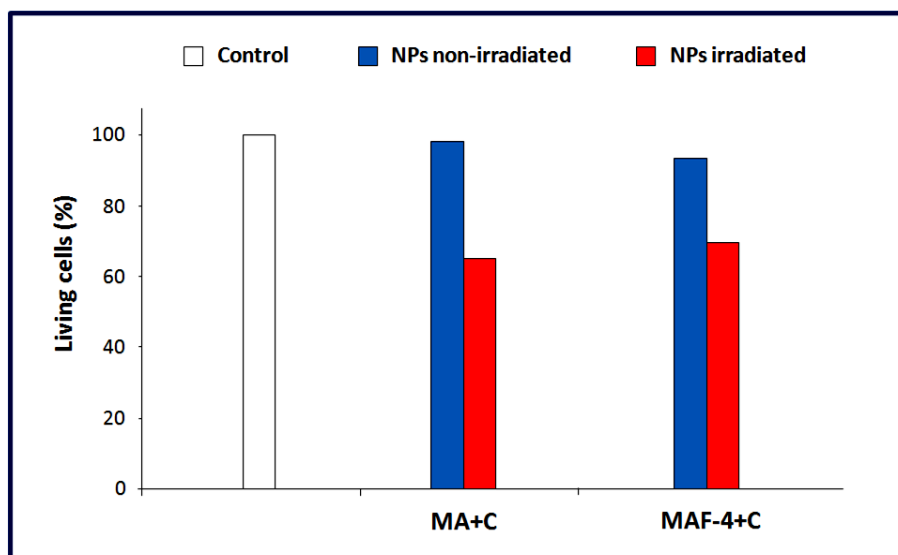


Figure S12. Two-photon-triggered *in-vitro* delivery of camptothecin, comparison between nanoimpellers **MA+C** and **MAF-4+C**, incubated at 80 $\mu\text{g.mL}^{-1}$. MCF-7 cells were submitted (or not) to laser irradiation; with a Leica Microscope (laser power input 1.5 W, objective lens 10x, NA 0.4). 4 different areas were irradiated for 3 min each, leading to 90% of the well surface irradiated at 760 nm. 35% of cancer cell death was observed with **MA+C** in these conditions (long irradiation time, lower power, less focused laser beam than with the Carl Zeiss microscope), which is probably due to the photothermal isomerization of the azobenzene moiety under these conditions.

VIII- UNLOADED NANOIMPELLERS IN-VITRO CONTROL: TPE with the Leica microscope

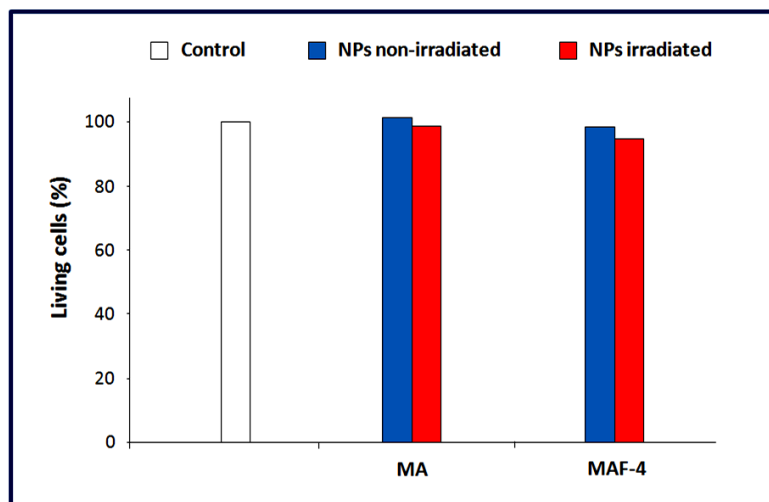


Figure S13. Two-photon *in-vitro* control with MA, and MAF-4 nanoimpellers ($80 \mu\text{g.mL}^{-1}$) not loaded with camptothecin. The irradiation (same conditions as Figure S10) did not produce any cell death.

IX- PREMATURE RELEASE CONTROLS OF THE NANOIMPELLERS IN SIMULATED BIOLOGICAL MEDIA

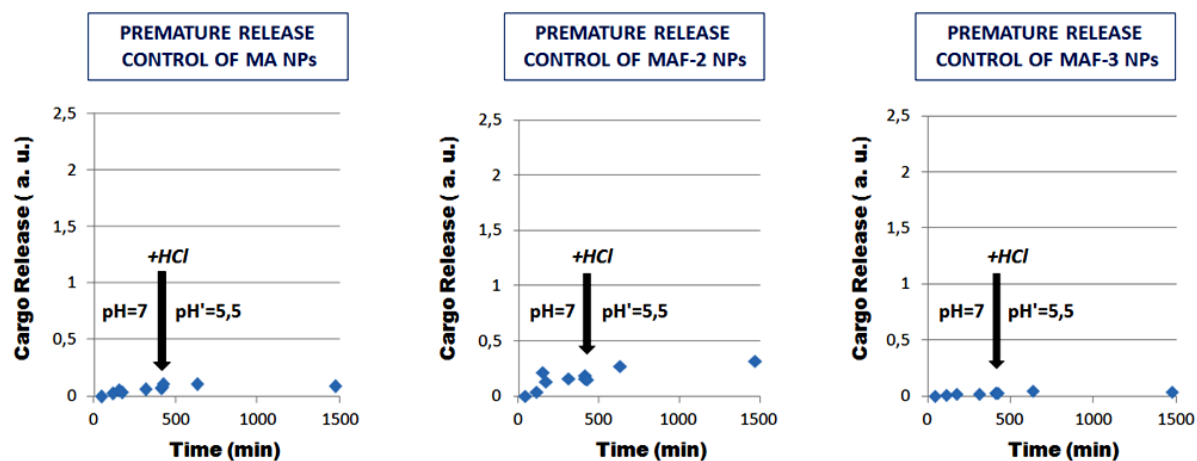


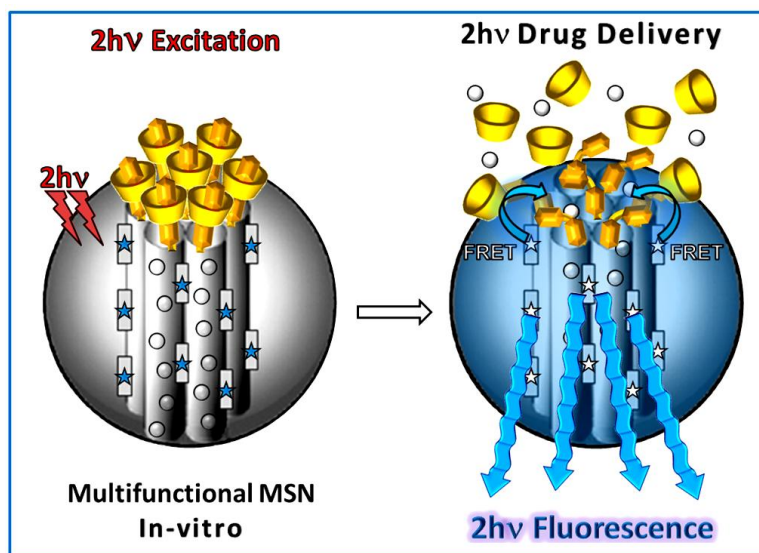
Figure S14. Control of the premature release of camptothecin-loaded nanoimpellers in aqueous media at pH 7 and 5.5.

REFERENCES

- [1] C. Weder, M. S. Wrighton, *Macromolecules* **1996**, 29, 5157-5165.
- [2] C. Monnereau, E. Blart, F. Odobel, *Tetrahedron Lett.* **2006**, 46, 5421-5423.

CHAPTER 4

B. Two-Photon-Controlled Drug Delivery via Fluorescent Nanovalves[†]



Abstract

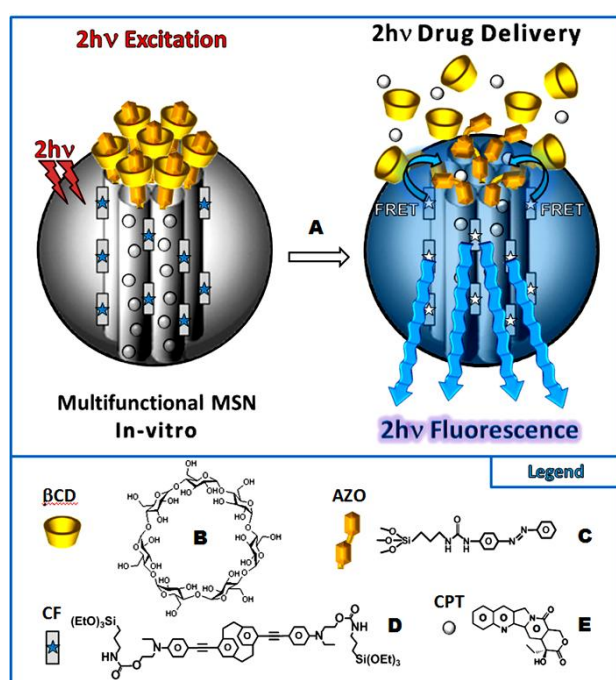
In this communication, we describe the synthesis of azovalve-based mesoporous silica nanoparticles (MSN), in order to deliver anticancer drugs in cancer cells by two-photon activation. An original two-photon paracyclophane-based fluorophore was synthesized and incorporated inside the framework of the MSN during the sol-gel procedure. Then the MSN were functionalized on the surface with azobenzene, the pores were loaded with camptothecin and the system was cap with beta cyclodextrin in order to avoid the premature release of the cargo. Förster resonance energy transfer (FRET) from the fluorophore to the azobenzene was studied and a very high FRET quantum yield was obtained. Breast cancer cells were then treated with the nanovalve and two-photon fluorescence imaging at low power of the laser allowed to show the endocytosis of the nanovalve inside the cells. Two-photon irradiation at high power triggered the delivery of camptothecin and led to cancer cell death.

[†] J. Croissant, A. Chaix, O. Mongin, M. Wang, S. Clément, L. Raehm, J-O. Durand,* V. Hugues, M. Blanchard-Desce, M. Maynadier, A. Gallud, M. Gary-Bobo,* M. Garcia, J. Lu, F. Tamanoi, D. P. Ferris, D. Tarn, J. I. Zink,* **Small**, 2014, sml.201400042.

Introduction

Mesoporous silica nanoparticles (MSN) for theranostic applications in nanomedicine have attracted considerable attention the last decade.^[1-8] Among the gated-MSN systems for drug release,^[9-11] light-activated nanovalves based on azobenzene isomerization are very promising.^[12-15] However, the systems described so far require UV-Vis light which limits their applications. Two-photon excitation (TPE) in the near-infrared region is a promising alternative to UV-Vis light due to the many advantages TPE provides such as three dimensional spatial resolution, lower scattering losses, and deeper penetration in tissues.^[16] Very few TPE-triggered MSN-based drug delivery systems have been described in the literature,^[17, 18] and only two very recent examples were reported with cytotoxic drug delivery in cancer cells. The first example is based on coumarin cleavage and needed very high material concentration (1 mg.mL⁻¹) in cells and long time of irradiation (1 h) to observe a cancer cell killing effect.^[19] The second was described by us and concerned nanoimpellers reconfigured for TPE.^[20] The system was efficient in inducing cancer cell death under TPE.

In this communication, we report an alternative MSN-azobenzene-based system with a high specific surface area and pore volume for TPE-triggered drug delivery in cancer cells. Furthermore, two-photon fluorescence imaging *in-vitro* was also performed (see Scheme 1). First of all, a novel two-photon paracyclophane-based fluorophore (CF) possessing a high two-photon absorption cross-section was designed and fully characterized (see ESI). The maximum emission of the fluorophore was 415 nm in THF, with a quantum yield of 68% suitable for FRET with azobenzene (Fig. 1).



Scheme 1. Schematic representation of the two-photon-triggered multifunctional nanovalve (A). The two-photon irradiation triggers the release of the camptothecin anticancer drugs (E), via the photo-isomerization of azobenzene moieties (C) grafted on the surface of so-called CF fluorophore (D)-modified MSN, and bonded with β -cyclodextrin (B).

Results and discussion

The silylated fluorophore (CF) was co-condensed with tetraethoxysilane (TEOS) and cetyltrimethylammonium bromide (CTAB) in basic media to lead to the two-photon fluorescent MSN (MCF NPs). Mono-triethoxysilylated azobenzene was then grafted on the surface of the nanoparticles (MCF-AZO NPs). Then, the cargo was loaded in the pores of the MCF-AZO NPs. The supramolecular complexation of β -cyclodextrin was performed in ice-cooled conditions, in order to cap the porous surface to lead to the nanovalve (MCF-AZO@ β CD NPs). As a control MCM-41 type MSN NPs were functionalized with azobenzene (MSN-AZO NPs) and β -cyclodextrin MSN-AZO@ β CD NPs using the same procedure.

The characterizations of the MCF NPs after surfactant removal confirmed the monodispersity and mesoporosity of the nanoparticles (Fig. 1A and S1), with a high specific surface area of $1072 \text{ m}^2\text{g}^{-1}$ and a 2.4 nm pore size, thus enabling cargo transportation. Besides, a UV-visible spectroscopic comparison (Fig. 1B) of MSN-AZO@ β CD NPs, MCF NPs, MCF-AZO@ β CD NPs and their characterizations by UV-visible and IR spectroscopies, ^{29}Si and ^{13}C solid state NMR, and dynamic light scattering (see Fig. S5-S8) revealed both the successful encapsulation of the fluorophore, as well as the azobenzene grafting and the complexation of β CD. The two-photon absorption cross-section of the fluorophore (CF) was measured by the TPE fluorescence technique (Table S1, Fig. S4). After encapsulation of the fluorophore in the MCF NPs, the biphotonic properties of the fluorophore were retained in the material (Table S1, Fig. 1D). After grafting of the azobenzene moieties, Förster resonance energy transfer (FRET) from the fluorophore to the azobenzene was studied (Fig. 1C). The fluorescence emission of MCF NPs overlaps with the absorption of MSN-AZO@ β CD NPs showing that FRET is possible. The fluorescence quantum yield Φ_F dropped from 39% for MCF NPs to 0.2% for MCF-AZO@ β CD NPs indicating an important quenching effect of the azobenzene moieties. The FRET quantum yield Φ_{ET} was very high (99%).

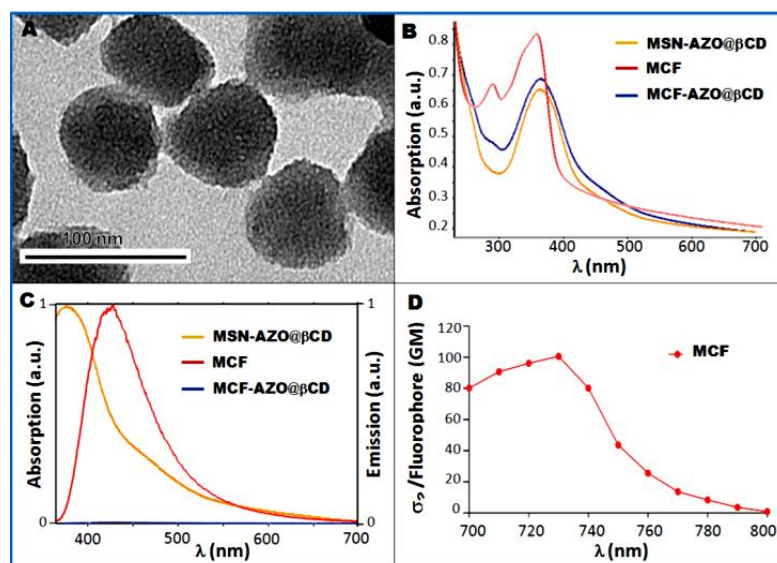


Figure 1. Transmission electron microscopy image of the organically modified mesoporous silica nanoplateform (A). UV-visible spectroscopy of MSN-AZO@ β CD, MCF, and MCF-AZO@ β CD NPs (B). Absorption spectrum of MSN-AZO@ β CD and emission spectra of MCF and MCF-AZO@ β CD NPs in EtOH, the fluorescence emission quenching demonstrates the FRET (C). Two-photon absorption cross-sections of MCF NPs in ethanol (D).

The nanovalves MCF-AZO@ β CD NPs were then loaded with propidium iodide (3% in mass) in water to study the cargo release. After centrifugation and several washings, the nanoparticles were put at the bottom of a quartz cell and the cell was carefully filled with water. The release of the cargo was monitored by UV-Vis spectroscopy, while the UV irradiation at 365 nm was activated (Fig. 2, and Fig. S3). No release was noticed without irradiation, whereas the irradiation actuated the release of the cargo, which demonstrated the efficiency of the nanovalve in water.

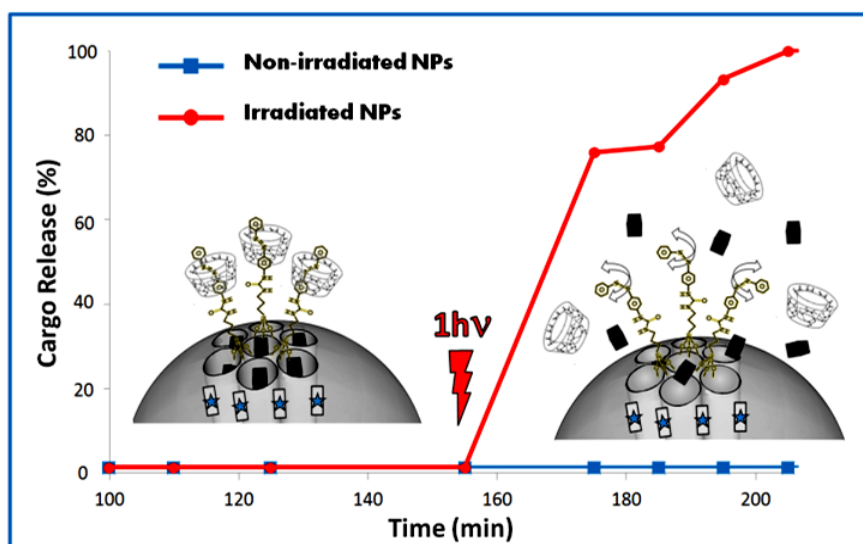


Figure 2. One-photon-triggered propidium iodide release in water, comparison between irradiated and non-irradiated nanovalves MCF-AZO@ β CD NPs at 365 nm (2-3 wt% or dye released).

The *in-vitro* two-photon imaging studies were then performed with MCF-7 breast cancer cell line with camptothecin (CPT) anticancer drug loaded NPs. Three nanovalves were used, camptothecin loaded MSN-AZO@ β CD+CPT NPs, MCF-AZO@ β CD+CPT NPs and unloaded MCF-AZO@ β CD NPs. The nanovalves were incubated for 20 h with MCF-7 cells. The membranes of the cells were stained with a membrane marker (cell mask) 15 min. before two-photon imaging experiments. Two-photon imaging was performed with a Carl Zeiss confocal microscope (Laser input 3W) at low power (3% of the laser input) at 760 nm.

The two-photon imaging of loaded and unloaded MCF-AZO@ β CD nanovalves confirmed the successful cellular uptake of the NPs (Fig. 3B and 3C). The blue dots in the cytoplasm correspond to the residual fluorescence of the fluorophore in MCF-AZO@ β CD NPs ($\Phi_F = 0.2\%$). Since MSN-AZO@ β CD+CPT NPs do not possess the two-photon fluorophore; they were not detected in cells (Fig. 3A). Note that endocytosis was also observed with one-photon fluorescence using fluorescein-based nanovalves (MFITC-AZO@ β CD) in cancer cells (Fig. S9).

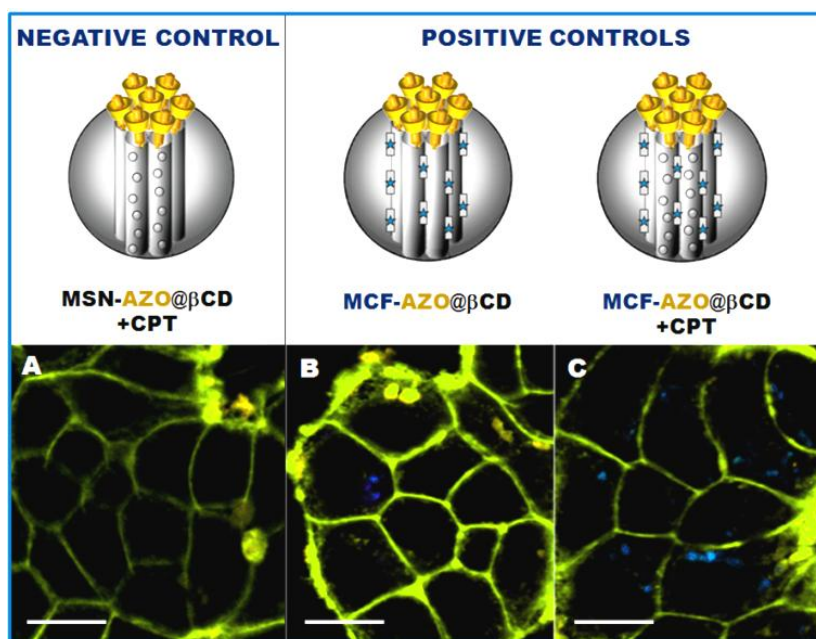


Figure 3. Two-photon imaging of MSN-AZO@ β CD loaded with camptothecin (A), MCF-AZO@ β CD with and without camptothecin (B-C), confirming the cellular uptake of the nanovalves, as well as their potential for two-photon intra-cellular tracking. Scale bar of 10 μ m.

Two-photon cancer cell killing experiments were then performed with the nanovalves. The nanovalves were incubated at 40 μ g.mL⁻¹ for 24 h with MCF-7 cancer cells, in 384 multiwell glass bottomed plate. Afterwards, the cells were irradiated or not with a confocal Carl Zeiss two-photon microscope (laser input power 3 W). The well was irradiated with three scans of 1.57 s each in four different areas without overlaps between irradiated areas, with the smallest objective (Carl Zeiss 10-fold magnification/objective 0.3 EC Plan-Neofluar) at 760 nm and maximum power of the laser. This experiment led to 50% of surface irradiation. The MTT assay was performed two days after irradiation. (Fig. 4). Camptothecin loaded MSN-AZO@ β CD+CPT NPs (2-3 wt% released in 50 minutes), which do not possess the two-photon fluorophore and unloaded MCF-AZO@ β CD NPs showed no significant cytotoxicity when they were irradiated or not. Therefore heating effects, reactive oxygen species generation and direct isomerisation of azobenzene by two-photon irradiation are not observed. By contrast, cancer cell death was observed with camptothecin loaded MCF-AZO@ β CD+CPT NPs, with up to 30 percent of two-photon selective cell killing. These experiments show that the fluorophore was necessary for the isomerisation of the azobenzene moiety through a FRET mechanism under two-photon excitation. Without irradiation, no premature release of the drug was observed with MCF-AZO@ β CD+CPT.

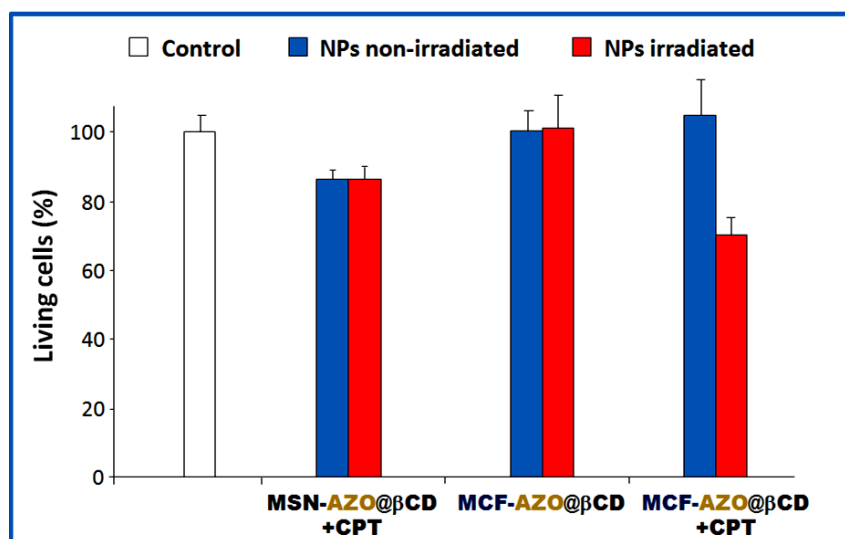


Figure 4. Two-photon-triggered *in-vitro* delivery of camptothecin, comparison between MSN-AZO@βCD+CPT, MCF-AZO@βCD, MCF-AZO@βCD+CPT at 40 μg.mL⁻¹.

Conclusion

In summary, we have described a MSN-nanvalve based on azobenzene, and original two-photon fluorophore moieties. The nanvalve was efficient for two-photon imaging of cancer cells due to the residual fluorescence of the fluorophore, at low power of the laser. No premature release of anticancer drugs in cells was observed when the nanvalves were loaded. When incubated with cancer cells and irradiated at short time and high laser power with a focused laser beam, the nanvalves showed efficient two-photon triggered drug delivery in cancer cells and cancer cell killing. Work is in progress to further extend the scope of these nanvalves.

REFERENCES

- [1] V. Mamaeva, C. Sahlgren, M. Linden, *Adv. Drug. Deliv. Rev.* **2013**, *65*, 689-702.
- [2] W. X. Mai, H. Meng, *Integr Biol-UK* **2013**, *5*, 19-28.
- [3] Y. Chen, H. Chen, J. Shi, *Adv. Mater.* **2013**, *25*, 3144-3176.
- [4] N.-T. Chen, S.-H. Cheng, J. S. Souris, C.-T. Chen, C.-Y. Mou, L.-W. Lo, *J. Mater. Chem. B* **2013**, *1*, 3128-3135.
- [5] J. L. Vivero-Escoto, R. C. Huxford-Phillips, W. B. Lin, *Chem. Soc. Rev.* **2012**, *41*, 2673-2685.
- [6] F. Tang, L. Li, D. Chen, *Adv. Mater.* **2012**, *24*, 1504-1534.
- [7] Z. Li, J. C. Barnes, A. Bosoy, J. F. Stoddart, J. I. Zink, *Chem. Soc. Rev.* **2012**, *41*, 2590-2605.
- [8] T. Asefa, Z. Tao, *Chem. Res. Toxicol.* **2012**, *25*, 2265-2284.
- [9] C. Coll, A. Bernardos, R. Martinez-Manez, F. Sancenon, *Acc. Chem. Res.* **2013**, *46*, 339-349.
- [10] Y.-W. Yang, *Med. Chem. Commun.* **2011**, *2*, 1033-1049.
- [11] K. K. Coti, M. E. Belowich, M. Liong, M. W. Ambrogio, Y. A. Lau, H. A. Khatib, J. I. Zink, N. M. Khashab, J. F. Stoddart, *Nanoscale* **2009**, *1*, 16-39.
- [12] Q. Yuan, Y. Zhang, T. Chen, D. Lu, Z. Zhao, X. Zhang, Z. Li, C.-H. Yan, W. Tan, *ACS Nano* **2012**, *6*, 6337-6344.
- [13] H. Yan, C. Teh, S. Sreejith, L. Zhu, A. Kwok, W. Fang, X. Ma, N. Kim Truc, V. Korzh, Y. Zhao, *Angew. Chem. Int. Ed.* **2012**, *51*, 8373-8377.
- [14] X. Mei, S. Yang, D. Chen, N. Li, H. Li, Q. Xu, J. Ge, J. Lu, *Chem. Commun.* **2012**, *48*, 10010-10012.
- [15] D. P. Ferris, Y. L. Zhao, N. M. Khashab, H. A. Khatib, J. F. Stoddart, J. I. Zink, *J. Am. Chem. Soc.* **2009**, *131*, 1686-1688.
- [16] M. Gary-Bobo, Y. Mir, C. Rouxel, D. Brevet, I. Basile, M. Maynadier, O. Vaillant, O. Mongin, M. Blanchard-Desce, A. Morere, M. Garcia, J.-O. Durand, L. Raehm, *Angew. Chem. Int. Ed.* **2011**, *50*, 11425-11429.
- [17] T. M. Guardado-Alvarez, L. Sudha Devi, M. M. Russell, B. J. Schwartz, J. I. Zink, *J. Am. Chem. Soc.* **2013**, *135*, 14000-14003.
- [18] Q. N. Lin, Q. Huang, C. Y. Li, C. Y. Bao, Z. Z. Liu, F. Y. Li, L. Y. Zhu, *J. Am. Chem. Soc.* **2010**, *132*, 10645-10647.
- [19] W. Ji, N. Li, D. Chen, X. Qi, W. Sha, Y. Jiao, Q. Xu, J. Lu, *J. Mater. Chem. B* **2013**, *1*, 5942-5949.
- [20] J. Croissant, M. Maynadier, A. Gallud, H. Peindy N'Dongo, J. L. Nyalosaso, G. Derrien, C. Charnay, J.-O. Durand, L. Raehm, F. Serein-Spirau, T. Jarrosson, O. Mongin, M. Blanchard-Desce, M. Gary-Bobo, M. Garcia, J. Lu, F. Tamanoi, D. Y. Tarn, T. M. Guardado-Alvarez, J. I. Zink, *Angew. Chem. Int. Ed.* **2013**, *125*, 14058-14062.

APPENDIX: SUPPLEMENTARY INFORMATION

I- EXPERIMENTAL SECTION

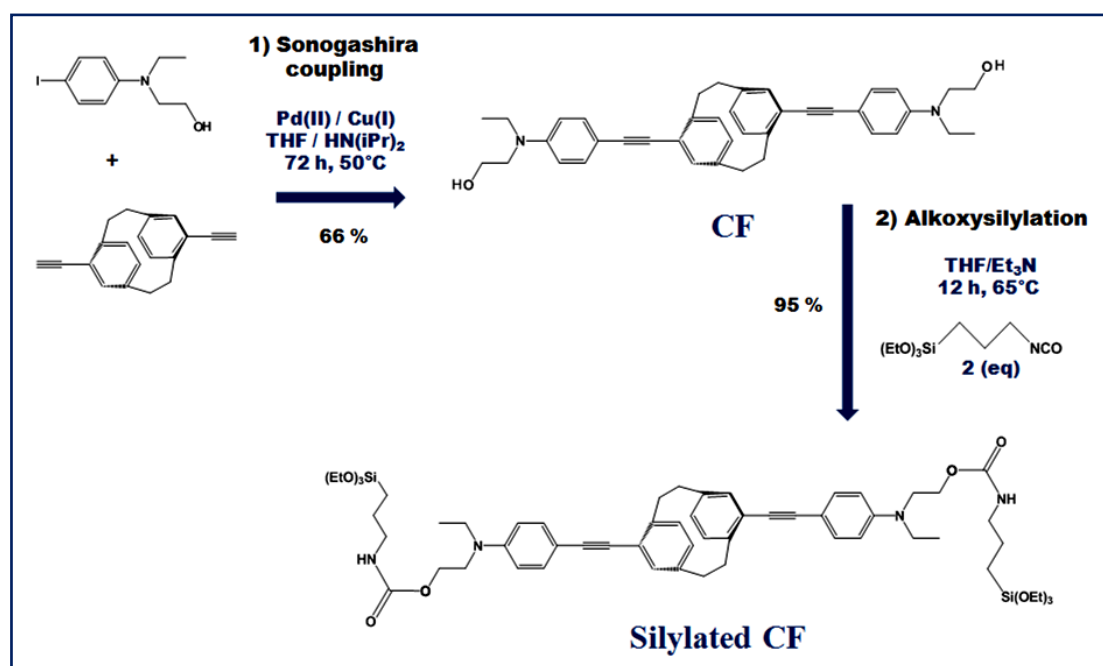
Two-photon Induced drug delivery. Human breast cancer cells MCF-7 (purchased from ATCC) were cultured in DMEM supplemented with 10% fetal bovine serum and 50 $\mu\text{g.mL}^{-1}$ gentamycin. All cells were allowed to grow in humidified atmosphere at 37°C under 5% CO_2 . For *in vitro* phototoxicity, MCF-7 cells were seeded into a 384 multiwell glass-bottomed plate (thickness 0.17 mm), with a black polystyrene frame, 2,000 cells per well in 50 μL of culture medium, and allowed to grow for 24 h. Nanovalves loaded with camptothecin were then dispersed under ultrasounds in PBS at a concentration of 1 mg.mL^{-1} and cells were then incubated for 20 h with or without nanovalves at a final concentration of 40 $\mu\text{g.mL}^{-1}$ in DMEM. After incubation with nanovalves, cells were washed twice, maintained in fresh culture medium, and then submitted (or not) to laser irradiation; with the Carl Zeiss Microscope (laser power input 3W). Half of the well was irradiated at 760 nm by three scans of 1.57 s duration in 4 different areas of the well. The laser beam was focused by a microscope objective lens (Carl Zeiss 10x/0.3 EC Plan-Neofluar). The scan size does not allow irradiating more areas without overlapping. After 2 days, the MTS assay was performed (as previously described^[33,34]) and was corrected according to the following formula $\text{Abs}_{\text{control}} - 2 \times (\text{Abs}_{\text{control}} - \text{Abs}_{\text{nanoimpellers}})$.

General Procedures. THF and diisopropylamine were dried over sodium/benzophenone or CaH_2 respectively. Triethylamine, 3-isocyanatopropyltriethoxysilane, bis(triphenylphosphine) dichloro-palladium(II), copper(I) iodide were purchased (Alfa and Aldrich) and used without further purification. 1,4-diethynyl-2,5-bis(octoxy)benzene,^[1] 4,16-diethynyl[2.2]paracyclophane^[2] and 2-[ethyl(4-iodophenyl)amino]ethanol^[3] were prepared according to the literature. Flash chromatography purifications were carried out on an Armen Spot II Ultimate instrument. ^1H and $^{13}\text{C}\{^1\text{H}\}$ NMR spectra were recorded with a Bruker AC 400 spectrometer. Chemical shifts (in δ units, ppm) are referenced to TMS using CHCl_3 ($\delta = 7.26$ ppm) and CDCl_3 ($\delta = 77.0$ ppm) as the internal standards, respectively, for ^1H and $^{13}\text{C}\{^1\text{H}\}$ NMR spectra. IR spectra were recorded on a Perkin-Elmer 100 FT spectrophotometer. Absorption spectra were recorded on a Hewlett-Packard 8453 spectrophotometer and fluorescence data were collected on a Perkin-Elmer LS55 fluorimeter. Mass spectrometry was carried out at the Laboratoire de Spectrometrie de Masse (Lyon, France) with a Thermo-Finnigan MAT95 apparatus in electronic impact ionization positive mode. Dynamic light scattering analysis were performed using a Cordouan Technologies DL 135 Particle size analyzer instrument. ^{29}Si and ^{13}C CPMAS solid state NMR sequences were recorded with a VARIAN VNMRS300, using Q8MH8 and adamantane references respectively.

II- SYNTHESIS AND CHARACTERIZATION OF ORGANIC COMPOUNDS

AZO. The aminobenzene precursor (2.1 g) was placed in a 100 mL two-neck round bottom flask with absolute ethanol (50 mL) and stirred under nitrogen flow at 54°C. Then, 3-isocyanatopropyltriethoxysilane (2800 μ L) was added through micropipette. Finally, the mixture was stirred overnight. The compound was stored in the fridge. The concentration was 4.2 mg of AZO per 100 μ L of EtOH (50 mL of EtOH for 2.1 g of AZO).

Silylated CF. The two-photon fluorophore (CF) was prepared according to a Pd catalyzed double Sonogashira cross-coupling reaction in diisopropylamine at 50°C between 4,16-diethynyl[2.2]paracyclophane with 2.4 equivalents of 2-[ethyl(4-iodophenyl)amino]ethanol for 72 h. The CF compound was obtained in 66% yield after a flash chromatography purification over a 15 μ m spherical silica column with CH₂Cl₂-AcOEt solvent mixture according to the (1:0 v:v) to (1:1 v:v) elution gradient. CF was then reacted in triethylamine with 3-isocyanatopropyltriethoxysilane in refluxing THF during 72 h. The silylated CF was obtained in 95% yield after evaporation of the solvent (Scheme 1).



Scheme S1. Synthesis of CF.

CF. In a 25 mL round-bottomed two-neck flask, 200 mg (0.781 mmol) of 4,16-diethynyl[2.2]paracyclophane, 500 mg (1.718 mmol) of 2-[ethyl(4-iodophenyl)amino]ethanol, 36 mg (0.052 mmol) of bis(triphenylphosphine)dichloropalladium (II) and 9 mg (0.052 mmol) of copper(I) iodide were introduced under nitrogen and dissolved into 6 mL of freshly distilled and degassed diisopropylamine. The mixture was stirred at 50°C for 72 hours and filtered after cooling to room temperature over a silica gel plug eluted with dichloromethane-ethylacetate solvent mixture according to the (1:0 v:v) to (1:1 v:v) elution

gradient. The filtrate was concentrated *in vacuo* and 298 mg of **CF** was obtained in 66% yield as a right green solid and will be used without further purification in the following step.

Silylated CF. In a 10 mL round-bottomed flask, 90 mg (0.155 mmol) of **CF**, 5 mL of freshly distilled THF, and 78 μ L of 3-isocyanatopropyltriethoxysilane (0.309 mmol) were stirred 3 days at 65°C under nitrogen conditions. After cooling, solvents were removed *in vacuo* and the product was used without further purification. Yield: 95% (158 mg). ^1H NMR (400 MHz, CDCl_3): δ = 7.48 (d, $^3J_{\text{H-H}}$ = 21.2 Hz, 2 h, H_{Ph}), 7.03 (d, $^3J_{\text{H-H}}$ = 8.3 Hz, 2 h, H_{Ph}), 6.79 (d, $^3J_{\text{H-H}}$ = 8.4 Hz, 2 h, $\text{H}_{\text{Ph (central)}}$), 6.56 (s, 2 h, $\text{H}_{\text{Ph (central)}}$), 6.50 (d, $^3J_{\text{H-H}}$ = 14.1 Hz, 2 h, $\text{H}_{\text{Ph (central)}}$), 3.86 (q, $^3J_{\text{H-H}}$ = 7.0 Hz, 12 h, $\text{O-CH}_2\text{-CH}_3$), 3.63 (t, $^3J_{\text{H-H}}$ = 9.0 Hz, 4H, COOCH_2), 3.58-3.49 (m, 8H, $\text{CH}_2\text{-CH}_2$ (central)), 3.32 (t, $^3J_{\text{H-H}}$ = 6.72 Hz, 6H, OCN-CH_2), 3.21 (t, $^3J_{\text{H-H}}$ = 6.4 Hz, 4H, $\text{N-CH}_2\text{-CH}_2\text{-O}$), 3.05 (q, $^3J_{\text{H-H}}$ = 6.9 Hz, 6H, $\text{N-CH}_2\text{-CH}_3$), 1.79-1.68 (m, 4H, $\text{Si-CH}_2\text{-CH}_2$), 1.28 (t, $^3J_{\text{H-H}}$ = 6.98 Hz, 18H, $\text{Si-O-CH}_2\text{-CH}_3$), 0.91 (t, $^3J_{\text{H-H}}$ = 6.4 Hz, 4H, $\text{N-CH}_2\text{-CH}_3$), 0.70 (t, $^3J_{\text{H-H}}$ = 8.0 Hz, 4H, $\text{Si-CH}_2\text{-CH}_2$); $^{13}\text{C}\{^1\text{H}\}$ NMR (300 MHz, CDCl_3): δ = 146.8, 140.6, 138.4, 135.7, 132.1, 131.8, 128.6, 124.4, 92.7, 86.9, 59.2, 57.5, 57.4, 51.3, 44.6, 44.4, 42.0, 33.2, 32.9, 24.1, 22.6, 17.4, 17.2, 11.2, 11.0, 6.5. UV/Vis λ_{max} (THF) : 365 nm ; Emission (THF): λ_{max} = 415 nm ($\lambda_{\text{excitation}}$ = 388 nm) ; MS (EI) m/z (%) : 1077 (100) [M^+], 540 (30) ; HRMS (EI) : m/z calcd for $\text{C}_{60}\text{H}_{84}\text{N}_4\text{O}_{10}\text{Si}_2$: 1077.5804, found 1077.5818.

III- SYNTHESIS OF THE NANOMATERIALS

MSN. A mixture of CTAB (250 mg), distilled water (120 mL), and sodium hydroxide (875 μ L, 2 M) was stirred at 80°C during 50 minutes at 700 rpm in a 250 mL three neck round bottom flask. Then, TEOS (1.2 mL) was added to the aforementioned solution, and the condensation process was conducted for 2 h. Afterwards, the solution was cooled at room temperature while stirring; fractions were gathered in propylene tubes and collected by centrifugation during 15 minutes at 21 krpm. The sample was then extracted twice with an alcoholic solution of ammonium nitrate (6 g.L⁻¹), and washed three times with ethanol, water, and ethanol. Each extraction involved a sonication step of 30 minutes at 50°C in order to remove the CTAB surfactant; the collection was carried out in the same manner. The as-prepared material was dried under air flow for few hours.

MCF NPs. A mixture of CTAB (345 mg), and sodium hydroxide (20 mL, 0.2 M) was stirred at room temperature during 50 minutes at 700 rpm in a 500 mL three necks round bottom flask. Then, an alcoholic solution of the silylated **CF** ($n_0 = 6.4 \times 10^{-5}$ mol, in 0.8 mL THF), and the stirring speed was changed to 1000 rpm. One minute later, TEOS (1.8 mL) was added to the aforementioned solution, and after 40 seconds, an aqueous solution (130 mL) was poured out. The solution was then heated through a hair drier ($T_0 = 25^\circ\text{C}$, $T' = 28\text{-}30^\circ\text{C}$ in 1-2 min), in order to trigger the condensation process. After 5 minutes 30 seconds of reaction, a solution of hydrochloric acid (18 mL + aliquots of HCl 0.2 M) was added to quench the reaction by reaching a pH of 6.9. Fractions were gathered in propylene tubes and collected by centrifugation during 15 minutes at 21 krpm. Extraction and the following steps were identical as those described for MSN.

MSN-AZO NPs. MSN NPs (55 mg) were mixed with the alkoxysilylated azobenzene (3.4×10^{-5} mol) in anhydrous toluene (10 mL), and stirred two days at 95°C. The sample was collected by centrifugation during 15 minutes at 21 krpm, and washed three times with ethanol, water, and acetone. The as-prepared material was dried under air flow for few hours. The yield of the grafting was determined to be of 82% via UV-visible azobenzene measurements of the supernatants.

MCF-AZO NPs. MCF NPs (55 mg) were mixed with the silylated azobenzene (3.4×10^{-5} mol) in anhydrous toluene (10 mL) and stirred overnight at 95°C. The sample was collected by centrifugation during 15 minutes at 21 krpm, and washed three times with ethanol, water, and acetone. The as-prepared material was dried under air flow for few hours. The yield of the grafting was determined to be of 92% via UV-visible azobenzene measurements of the supernatants.

PI LOADED MCF-AZO@ β CD NPs. MCF-AZO NPs (50 mg) were mixed with the propidium iodide dye (5.5×10^{-6} mol) in deionized water (1 mL), and stirred two days at room temperature. Then, an aqueous solution of β -cyclodextrine (8.8×10^{-3} mol) was added to the aforementioned preparation, and allowed to stir for 24 h. The nanomachines were collected by centrifugation for 15 minutes at 21 krpm, and washed three times with deionized water, and dried under air flow for few hours. The one-photon triggered release was performed on the as-prepared nanomaterials.

CPT LOADED MSN-AZO@ β CD NPs. MSN-AZO NPs (25 mg) were mixed with the camptothecin (8.6×10^{-6} mol) in dimethylsulfoxide (DMSO, 1 mL), and stirred two days at room temperature. Then, an aqueous solution of β -cyclodextrine (8.8×10^{-3} mol) was added to the aforementioned preparation, the mixture was then stirred and sonicated, and was allowed to stir on ice for 24 h to maximize the association of β -cyclodextrine and the formation of pseudorotaxanes. The nanomachines were collected by centrifugation for 15 minutes at 21 krpm, washed with DMSO (without sonication), deionized water twice, and finally dried under air flow for few hours.

CPT LOADED MCF-AZO@ β CD NPs. MCF-AZO NPs (25 mg) were mixed with the camptothecin (8.6×10^{-6} mol) in dimethylsulfoxide (DMSO, 1 mL), and stirred two days at room temperature. Then, an aqueous solution of β -cyclodextrine (8.8×10^{-3} mol, 2 mL) was added to the aforementioned preparation, and allowed to stir for 24 h. The nanomachines were collected by centrifugation for 15 minutes at 21 krpm, and washed with DMSO, and twice with deionized water, and dried under air flow for few hours.

MFITC NPs. First, 3-aminopropyltriethoxysilane (6 μ L, 3.9×10^{-5} mol) was added in an ethanol solution (3 mL) of fluorescein (FITC, 7×10^{-6} mol), and stirred for 2 hours. Then, tetraorthosilicate (1.2 mL) was added to the aforementioned preparation; the resulting mixture is called solution A. Secondly, in another container, cetyltrimethylammonium bromide (250 mg) was mixed with deionized water (120 mL), and sodium hydroxide (0.9 mL, 0.2 M). The solution was heated to 80°C while stirring and the solution A was added dropwise, and the condensation process was conducted for 2 h. Afterwards, the solution was cooled at room

temperature while stirring; fractions were gathered in propylene tubes and collected by centrifugation during 15 minutes at 21 krpm. The sample was then extracted twice with an alcoholic solution of ammonium nitrate (6 g.L^{-1}), and washed three times with ethanol, water, and ethanol. Each extraction involved a sonication step of 30 minutes at 50°C in order to remove the CTAB surfactant; the collection was carried out in the same manner. The as-prepared material was dried under air flow for few hours.

MFITC-AZO NPs. MFITC NPs (50 mg) were mixed with the alkoxysilylated azobenzene ($3 \times 10^{-5} \text{ mol}$) in anhydrous toluene (10 mL), and stirred two days at 95°C . The sample was collected by centrifugation during 15 minutes at 21 krpm, and washed three times with ethanol. The as-prepared material was dried under air flow for few hours.

MFITC-AZO@ β CD NPs. MFITC-AZO NPs were mixed with β -cyclodextrine ($4.4 \times 10^{-5} \text{ mol}$) in an aqueous solution (4 mL). Finally, the mixture was then stirred and sonicated, and was allowed to stir on ice for 12 h to maximize the association of β -cyclodextrine and the formation of pseudorotaxanes. The nanoparticles were separated from solution via centrifugation and were then washed with water three times. MFITC-AZO@ β CD NPs were dried overnight under vacuum.

IV- TWO-PHOTON EXPERIMENTAL SETTINGS

Two-photon fluorescence imaging. The day prior to the experiment, MCF7 cells were seeded onto bottom glass dishes (World Precision Instrument, Stevenage, UK) at a density of $10^6 \text{ cells.cm}^{-2}$. Adherent cells were then washed once and incubated in 1 mL medium containing nanovalves at a concentration of $40 \text{ }\mu\text{g.mL}^{-1}$ for 20 h. Fifteen min before the end of incubation, cells were loaded with Cell Mask (Invitrogen, Cergy Pontoise, France) for membrane staining at a final concentration of $5 \text{ }\mu\text{g.mL}^{-1}$. Before visualization, cells were washed gently with phenol red-free DMEM. Cells were then scanned with a LSM 780 LIVE confocal microscope (Carl Zeiss, Le Pecq, France), at 760 nm with a slice depth (Z stack) of $0.62 \text{ }\mu\text{m}$.

Two-photon induced drug delivery. MCF-7 human breast cancer cells were cultured in Dulbecco's modified Eagle's medium (DMEM) supplemented with 10% fetal bovine serum and $50 \text{ }\mu\text{g.mL}^{-1}$ gentamycin. All cells were allowed to grow in humidified atmosphere at 37°C under 5% CO_2 . For *in vitro* phototoxicity, MCF-7 cells were seeded into a 384 multiwell glass-bottomed plate (Thickness 0.17 mm), with a black polystyrene frame, 2000 cells per well in $50 \text{ }\mu\text{L}$ of culture medium, and allowed to grow for 24 h. Nanovalves loaded with camptothecin were then dispersed under ultrasounds in PBS at a concentration of 1 mg.mL^{-1} and cells were then incubated for 20 h with or without nanovalves at a final concentration of $40 \text{ }\mu\text{g.mL}^{-1}$ in DMEM. After incubation with nanovalves, cells were washed twice, maintained in fresh culture medium, and then submitted (or not) to laser irradiation; with the Carl Zeiss Microscope (laser power input 3W). Half of the well was irradiated at 760 nm by three scans of 1.57 s duration in 4 different areas of the well. The laser beam was focused by a

microscope objective lens (Carl Zeiss 10x , NA 0.4). After 2 days, the MTT assay was performed and was corrected.

V- MCF NANOMATERIAL FULL CHARACTERIZATION

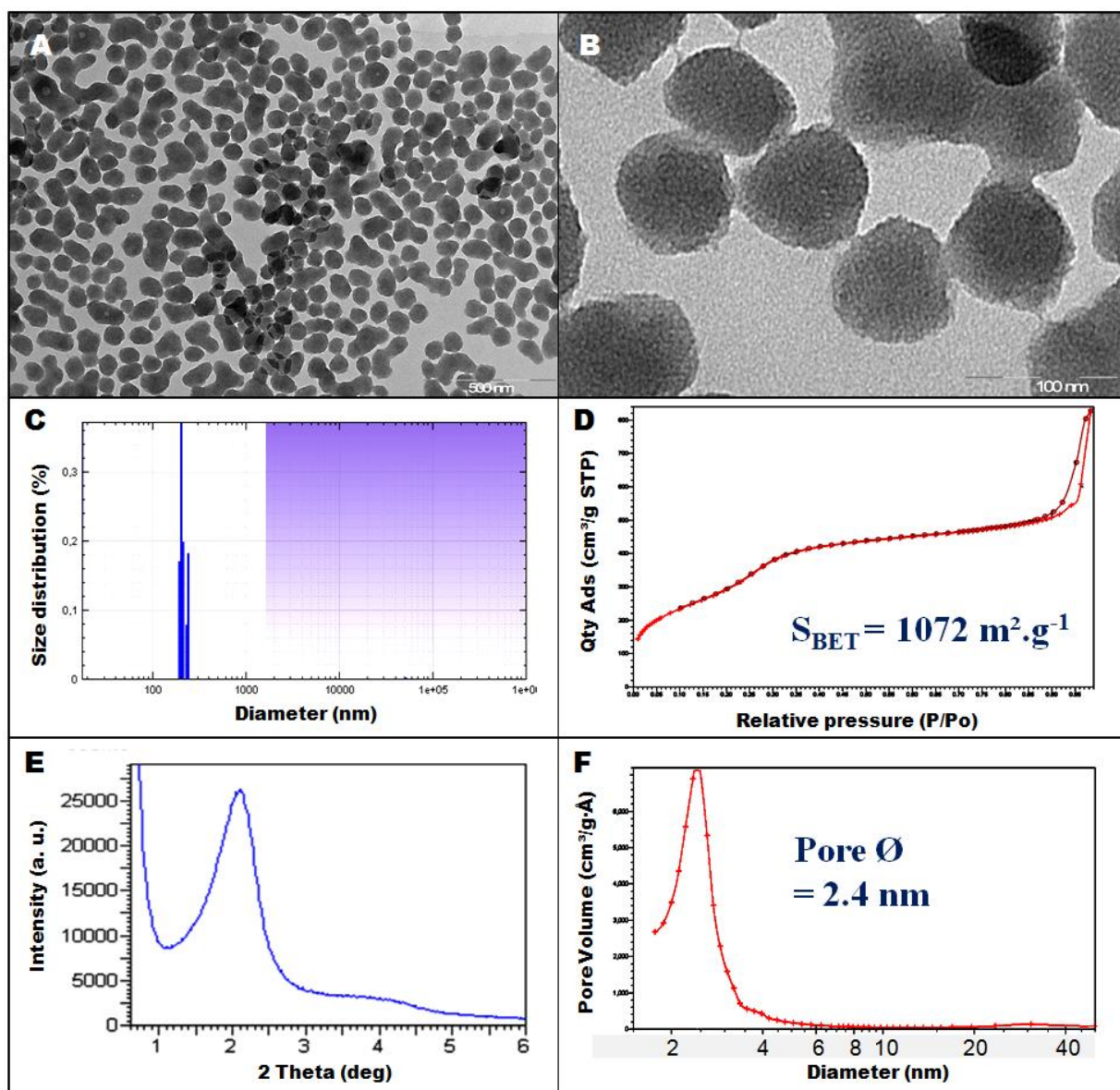


Figure S1. TEM images of MCF NPs (A-B). The size monodispersity of the sample is confirmed via DLS (C). The mesoporosity is demonstrated by N₂-adsorption-desorption (D,F), and small angle XRD (E).

VI- MSN NANOMATERIAL FULL CHARACTERIZATION

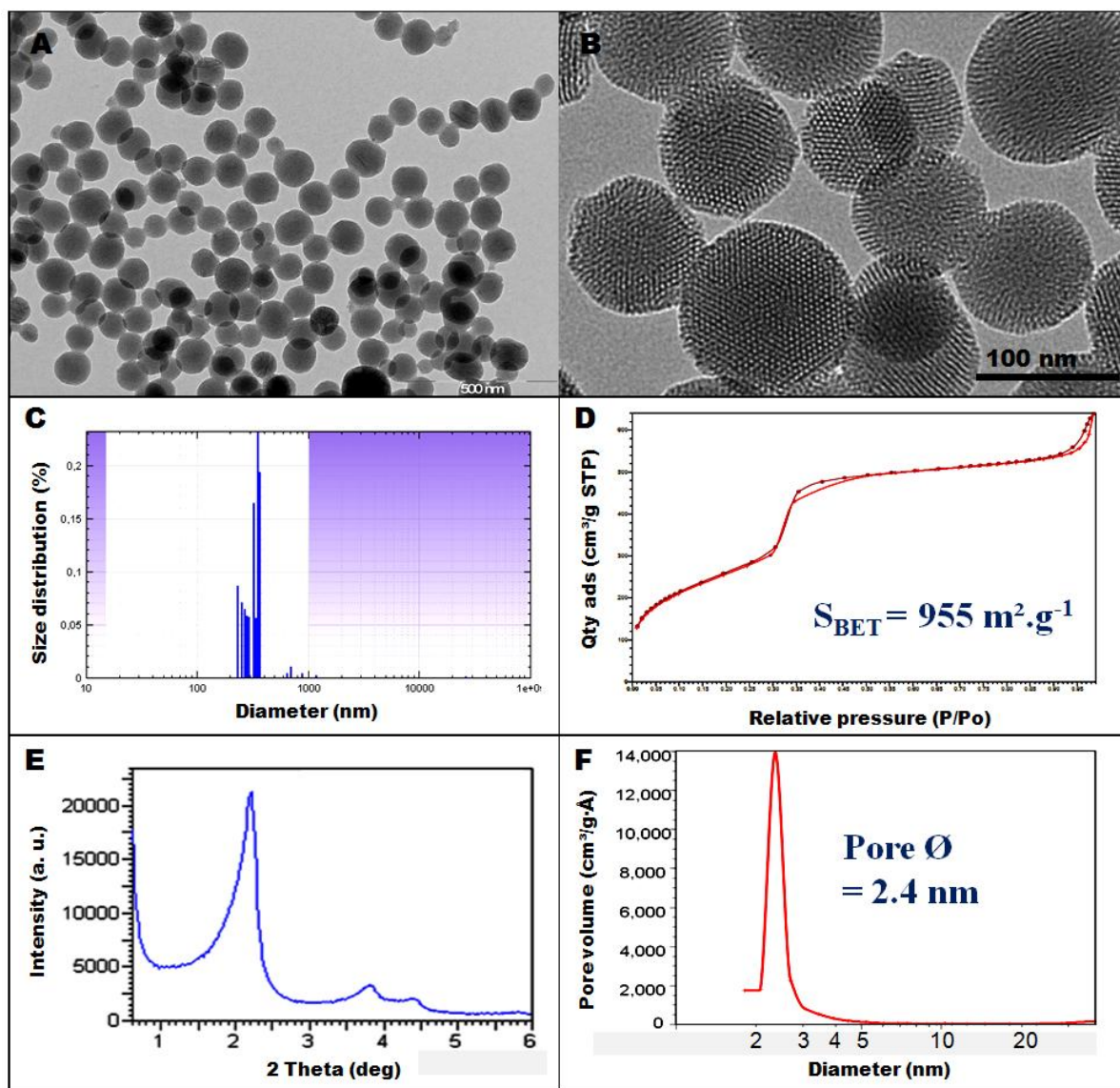


Figure S2. TEM images of MSN NPs (A-B). The size monodispersity of the sample is confirmed via DLS (C). The mesoporosity is demonstrated by N₂-adsorption-desorption (D,F), and small angle XRD (E).

VII- ONE-PHOTON RELEASE EXPERIMENT SETTINGS

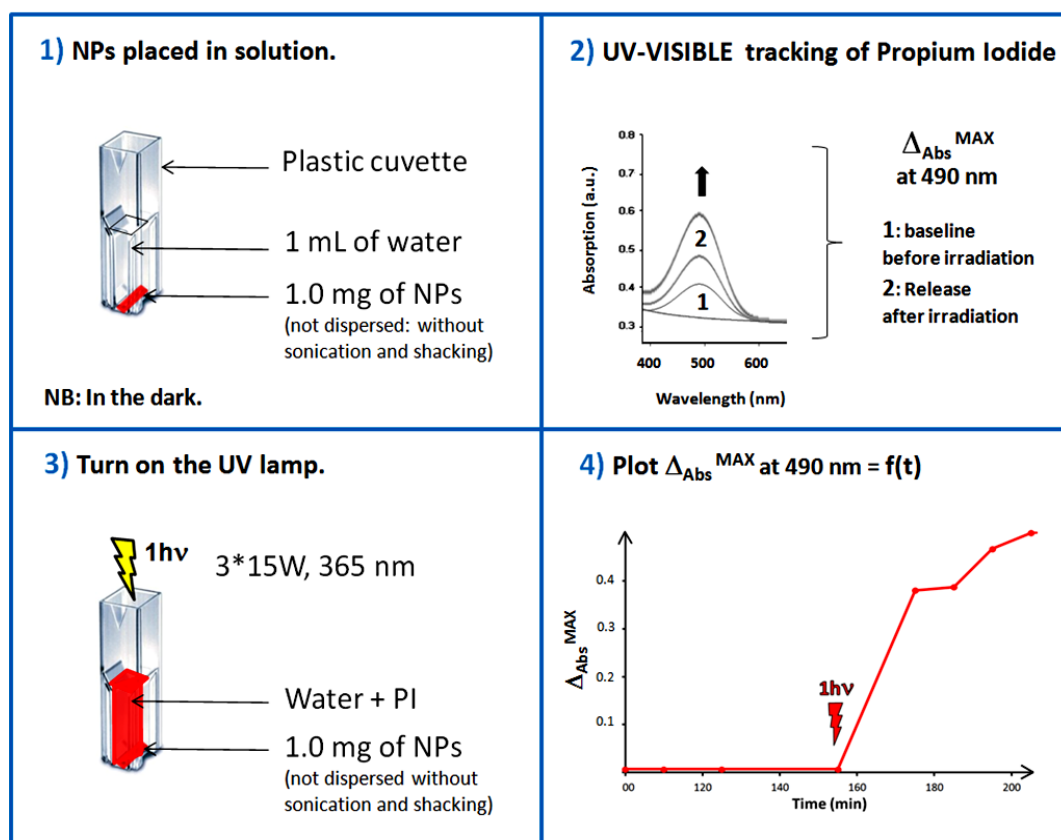


Figure S3. One-photon-triggered release settings of propidium iodide via nanovalves.

VIII- TWO-PHOTON PROPERTIES OF THE PRECURSOR AND THE MATERIALS

SAMPLE	λ_{abs} (nm)	λ_{em} (nm)	Φ_F^a (%)	Φ_{ET} (%)	$\sigma_2^{\text{max } b}$ (GM)
CF	385	415	68	-	130
MCF NPs	360	425	39	-	101
MCF-AZO@ β -CD NPs	360	428	0.2	99	—

Table S1. Photophysical properties of the CF precursor in THF, the MCF and the MCF-AZO@ β CD NPs in EtOH. The absorption and emission maxima are given along with the fluorescence quantum yield (Φ_F), the energy transfer quantum yield (Φ_{ET}), and the maximum two-photon cross section (σ_2^{max}). ^a Standard: quinine bisulfate in H₂SO₄ 0.5 M. ^b per fluorophore.

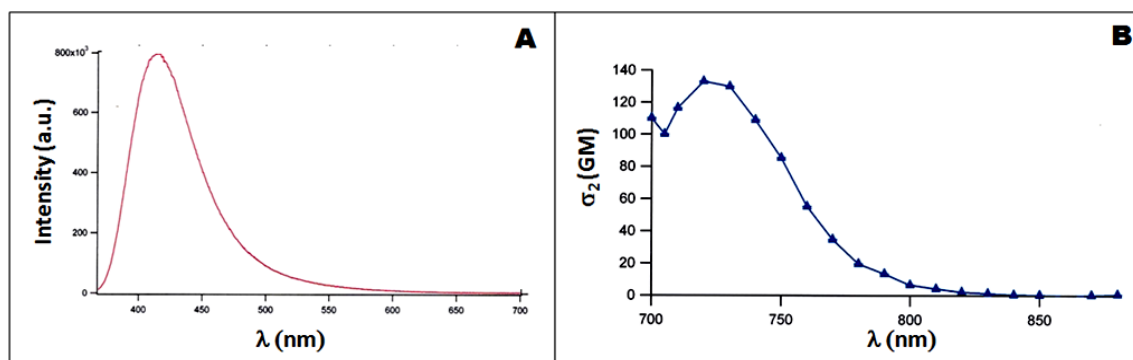


Figure S4. Fluorescent emission spectra of the CF precursor in tetrahydrofuran (A), as well as the two-photon cross section spectra in tetrahydrofuran (B).

IX- AZOBENZENE FUNCTIONALIZED NANOMATERIALS

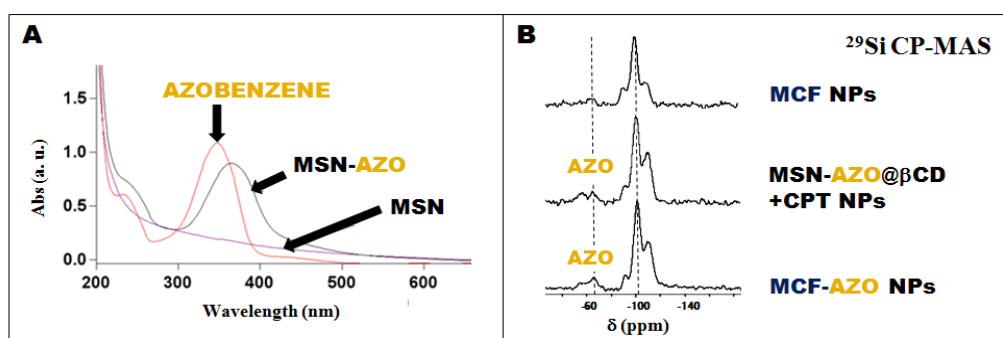


Figure S5. UV-visible spectra of MSN NPs, azobenzene precursor, and azobenzene functionalized MSN NPs in ethanol (A). Solid state nuclear magnetic resonance ²⁹Si CPMAS spectra on MCF, MSN-AZO@ β CD+CPT, and MCF-AZO@ β CD NPs.

X- BETA-CYCLODEXTRINE COMPLEXED NANOMATERIALS

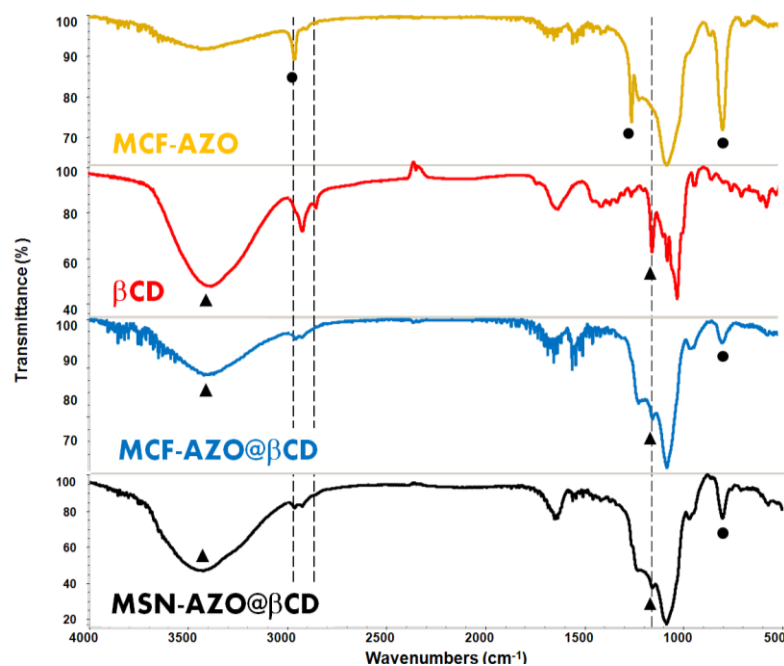


Figure S6. IR spectra of MCF-AZO NPs, β -cyclodextrine precursor, MCF-AZO@ β CD, and the MSN-AZO@ β CD. The β -cyclodextrine complexation is suggested by both the disappearance of some azobenzene vibration mode (■), as well as two additional modes of the β -cyclodextrine molecules (▼).

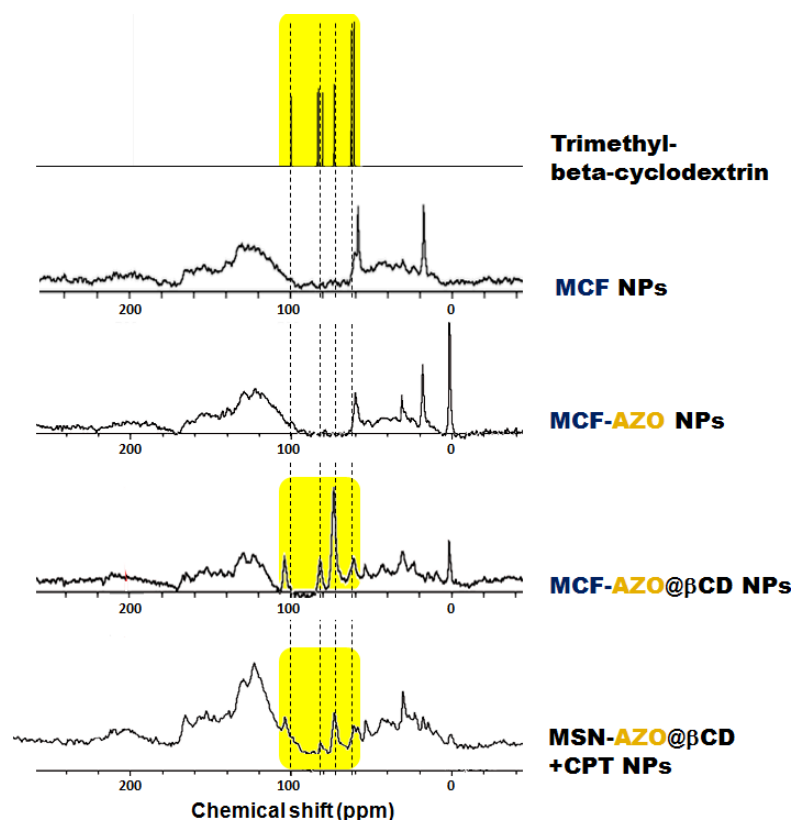


Figure S7. Solid state NMR ¹³C CPMAS spectra comparison demonstrating the β -cyclodextrine complexation on the MCF-AZO@ β CD, and the MSN-AZO@ β CD nanovalves.

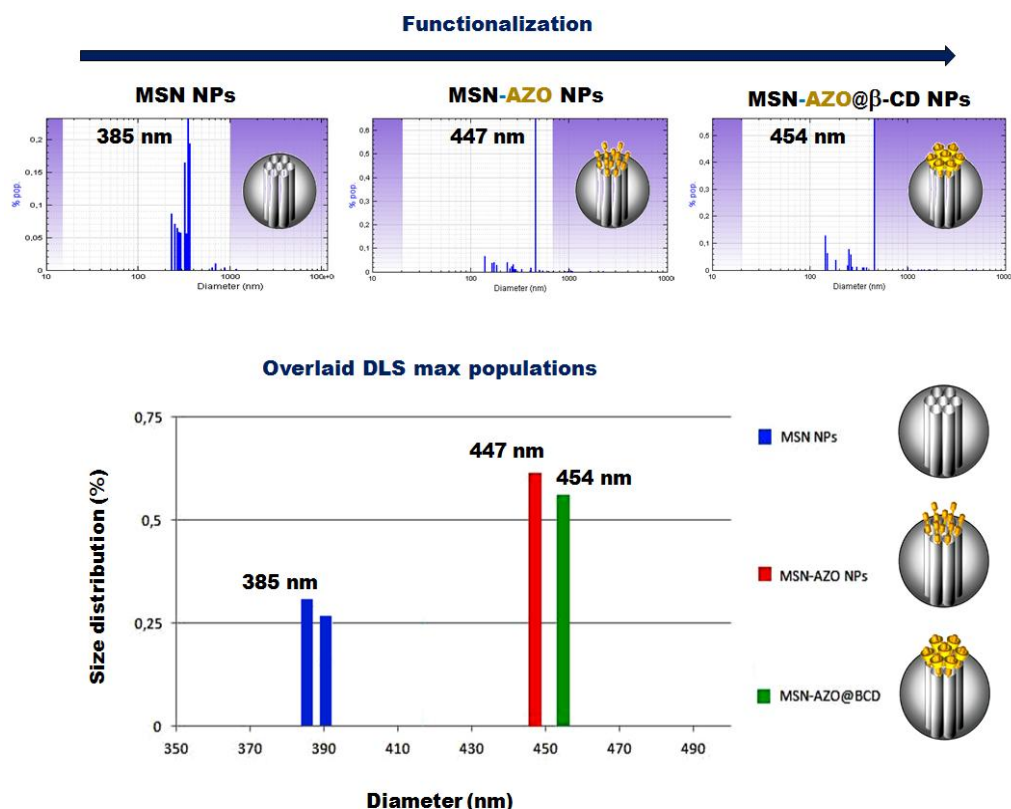


Figure S8. DLS analyses of MSN NPs, MSN-AZO NPs, and MSN-AZO@βCD +CPT NPs. The increasing trend of the maximum populations validated the β-cyclodextrine complexation of the grafted azobenzene moieties.

XI- ONE-PHOTON CELLULAR UPTAKE OF THE NANOVALVE

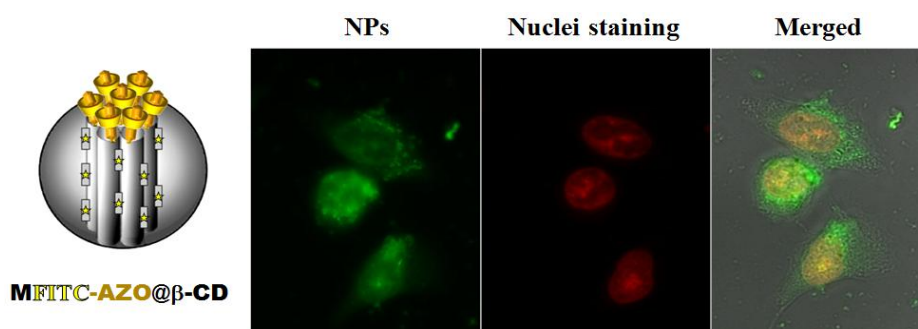


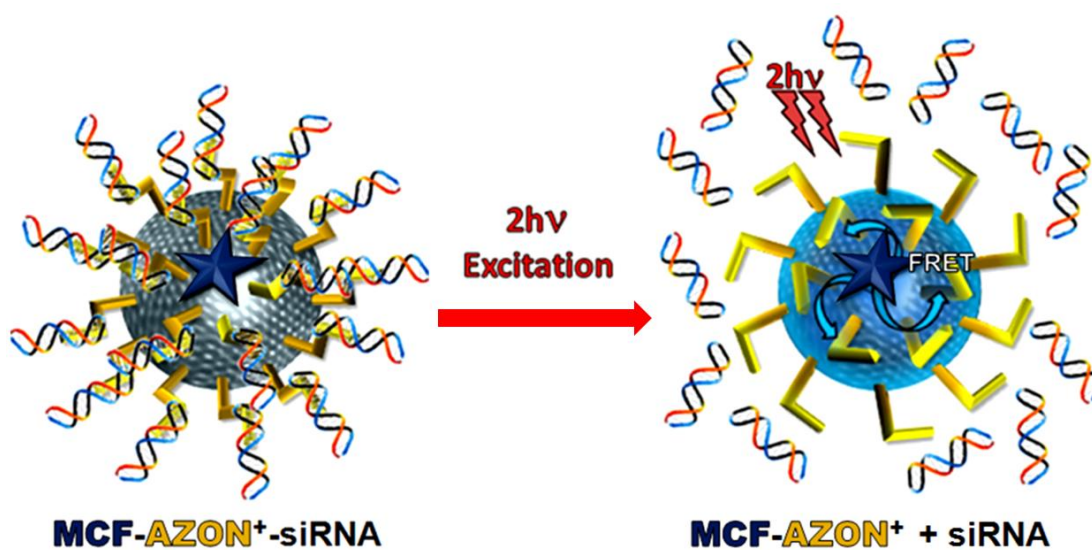
Figure S9. *In vitro* controls of fluorescein organosilica nanovalves (MFITC-AZO@βCD) in MiaPaca cells. Cells were incubated for 24 h with $30 \mu\text{g} \cdot \text{mL}^{-1}$ of MFITC-AZO@βCD, and fixed for one-photon fluorescence imaging.

REFERENCES

- [1] C. Weder, M. S. Wrighton, *Macromolecules* **1996**, *29*, 5157-5165.
- [2] S. Clément, L. Guyard, M. Knorr, S. Dilsky, C. Strohmann, M. Arroyo, *J. Organomet. Chem.* **2007**, *692*, 839-850.
- [3] C. Monnereau, E. Blart, F. Odobel, *Tetrahedron Lett.* **2006**, *46*, 5421-5423.

CHAPTER 4

C. Two-Photon-actuated siRNA Delivery via Ammonium-Azobenzene-Functionalized Mesoporous Silica Nanoparticles



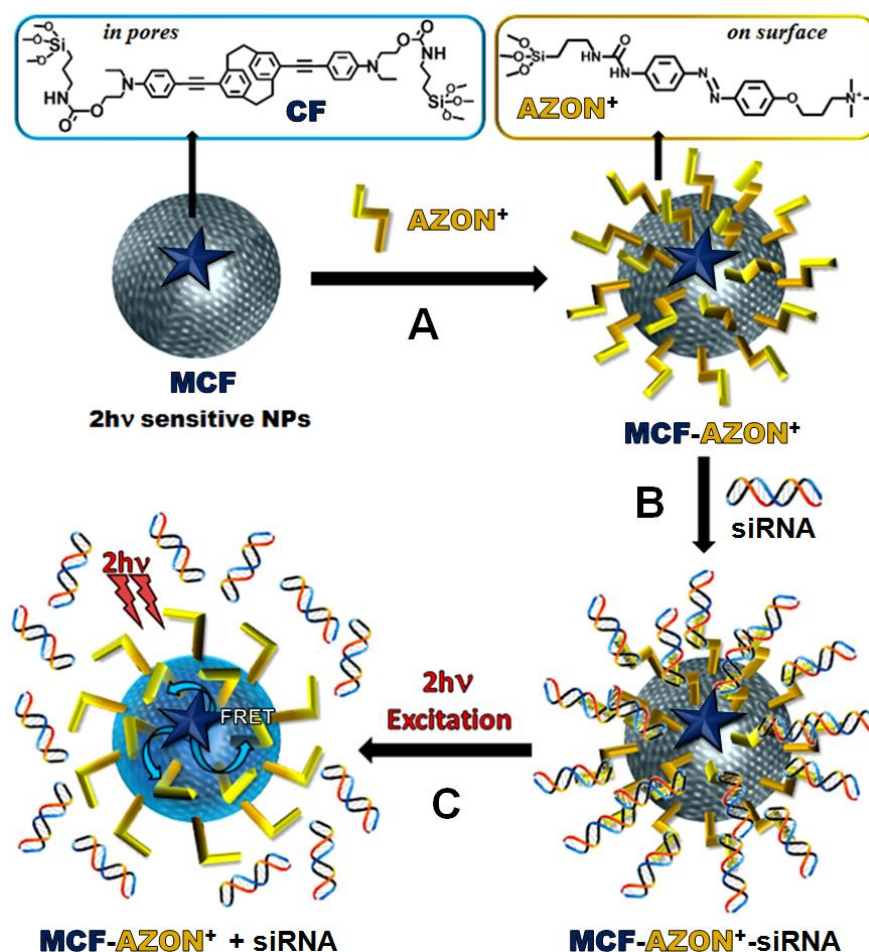
Introduction

Gene silencing via short interfering RNA (siRNA) has attracted much attention for therapeutic applications. Synthetic siRNA have been designed to efficiently and specifically silence the expression of a wide variety of genes,¹ which in turn provides treatments for viral infections,^{2, 3} hereditary disorders,⁴ and cancers.^{5, 6} Unfortunately, the direct biomedical translation of siRNA is often hindered for many reasons: (i) they are unstable in the blood stream, (ii) they can be immunogenic, (iii) their hydrophilicity and size prevents them to cross the cell membrane.⁷ Consequently, various nucleic acid delivery materials have been prepared to transport siRNA such as lipid nanoparticles (NPs),⁸ cyclodextrin NPs, peptides,⁹ antibodies, aptamers,¹⁰ nucleic acid NPs,¹¹ and polymer NPs.⁴ Another strategy involves the construction of conjugate-siRNA entities, when the siRNA part is conjugated with cholesterol, peptides, antibodies, aptamers, or small molecules.¹² Additionally, multifunctional mesoporous silica nanoparticles (MSN) have been used to transport siRNA via polyethylenimine-grafted MSN and drug delivery thanks to the high surface area of such materials. The main advantages of MSN NPs over other nanoformulations are (i) the robustness of the delivery it produced, along with (ii) the ease of functionalization for multifunctional and theranostic applications. MSN have been demonstrated to be biocompatible, endocytosed and exocytosed, excreted, and carrier of various cargos such as drugs and nucleic acids.^{13, 14}

Two-photon excitation (TPE) has become one of the main proponents for the achievement of the spatiotemporal selectivity needed in nanomedicine.¹⁵⁻¹⁹ Indeed, thanks to its three dimensional accuracy with a resolution of a single cell, the TPE screening of ill organs is very promising.²⁰ Besides, near infrared (NIR) two-photon irradiation allows safer and deeper laser penetration in living tissues.²¹ Light-triggered NIR delivery of siRNA has been reported with upconversion NPs,²² and shell-detachable NPs based on UV light-responsive amphiphile.²³ Consequently, two-photon siRNA delivery would be very relevant for efficient and localized gene silencing. The difficulty of the preparation of such NPs arises from the low two-photon cross-section of most dyes, which implies the organic design of efficient two-photon fluorophores ideally covalently linked with the nanomaterial.²⁴ To our knowledge no such delivery material has been reported to date.

Herein we report for the first time two-photon-actuated nucleic acid delivery via NPs. Mesoporous silica nanoparticles (MSN) were configured for NIR two-photon excitation through Förster resonance energy transfer (FRET) to transport siRNAs through phosphate-ammonium electrostatic interactions, and deliver them in MCF-7 breast cancer cells (Scheme 1). Sol-gel processes were used to incorporate a two-photon-sensitive fluorophore with a novel alkoxysilylated azobenzene containing an ammonium functional group (AZON⁺) in MSN. The nanomaterials structures and functionalizations were fully characterized, and the NPs were used for *in vitro* studies. Furthermore, two-photon fluorescence imaging inside the

cells demonstrated the internalization of the NPs, and TPE-triggered siRNA delivery caused more than 50% of gene expression decrease.



Scheme 1. Representation of two-photon sensitive MCF NPs grafted with AZON⁺ moieties (A) for siRNA complexation on MCF-AZON⁺ NPs (B), and NIR TPE-actuated nucleic acid delivery (C).

Results and discussion

The AZON⁺ was first designed and functionalized on two-photon-sensitive MSN nanomaterials. The AZON⁺ was obtained according to a modified Tochitsky *et al.* synthesis,²⁵ and the alkoxy-silylated derivative was then elaborated and characterized (see Scheme S1, ESI). The latter was then grafted on two types of fluorophore-functionalized 100 nm MSN nanospheres obtained by co-condensation of TEOS and the fluorescent moieties, previously reported and called MF and MCF NPs (see Scheme 1A, and S2).^{18, 26} The successful post-functionalization of MCF NPs was observed via UV-visible spectra comparison of MCF, AZON⁺, and MCF-AZON⁺ NPs (See Fig. 1A). The broadening of the absorption band present in the MCF-AZON⁺ NPs corresponds to the overlapping of the F and AZON⁺ moieties. Similar conclusions were drawn from UV-visible analysis of MF-AZON⁺ NPs (Fig. 1B). Besides, the zeta potential of the NPs was consistently modified with the positively charged azobenzene-ammonium groups incorporation, starting from -19 and -23 mV respectively for

MCF and MF materials, to +25 and +35 mV for MCF-AZON⁺ and MF-AZON⁺ NPs, respectively (Fig. 2C). This conclusion is also validated by the increase of the $\nu_{\text{Si-C}}$ vibration mode at 1154 cm⁻¹ in MF-AZON⁺ NPs, when compared to MF NPs (Fig. 2D, see Fig. S1 for the MCF equivalent). Thus, the positively charged MCF-AZON⁺ and MF-AZON⁺ NPs were good candidates for siRNA complexation.

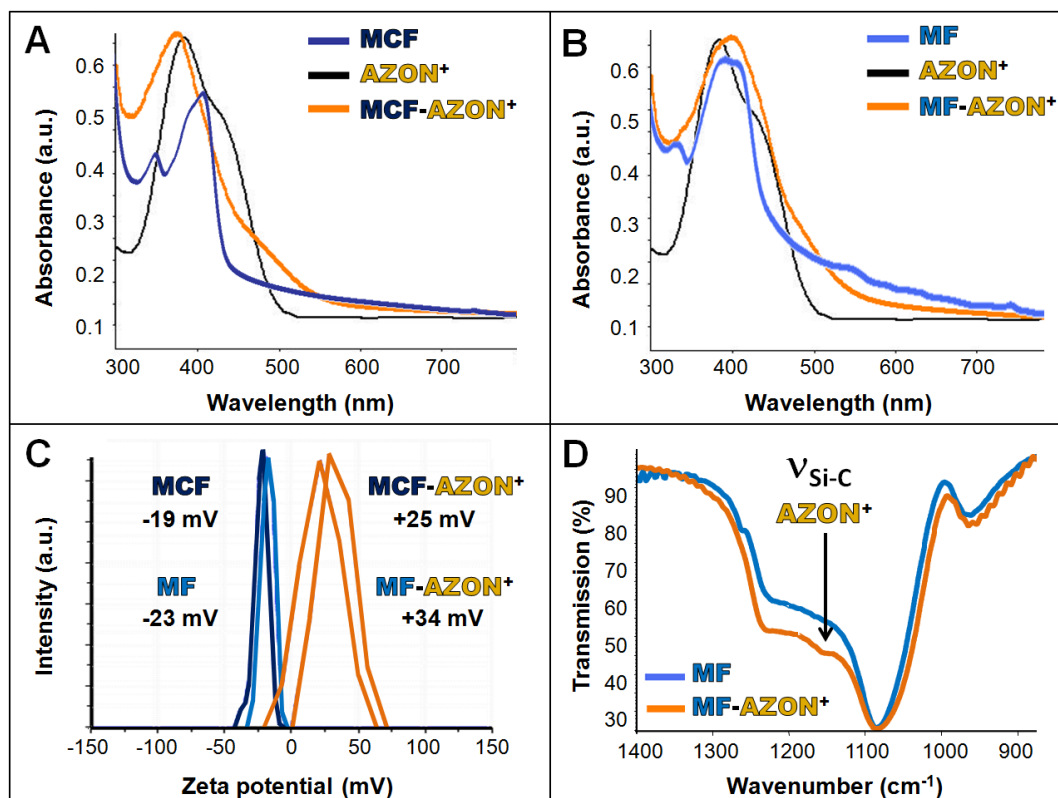


Figure 1. UV-visible spectra comparison demonstrating the AZON⁺ functionalization on MCF and MF NPs (A and B respectively). Zeta potential before and after AZON⁺ grafting on the MCF and MF NPs (C). FTIR spectra comparison of MF and MF-AZON⁺ NPs validating the grafting (D).

The endocytosis of the nanomaterial was then studied via two-photon fluorescence imaging on MCF-7 breast cancer cells. The MCF, MCF-AZO (containing azobenzene without ammonium groups), and MCF-AZON⁺ were incubated in cancer cells for 24 h at 40 $\mu\text{g/mL}$. The two-photon imaging was conducted with a Carl Zeiss two-photon confocal microscope. The successful endocytosis of MCF NPs was demonstrated by the bright blue dots readily visible inside the cells interior, revealed by Cell Mask (See Fig. 3A). Besides, both MCF-AZO and MCF-AZON⁺ NPs were internalized (Fig. 3B and C respectively), and the lower intensity of the blue dots was consistent with the FRET occurring between the CF and the AZO or AZON⁺ moieties. MF-AZON⁺ NPs were internalized as well (Fig. 3D), and the intensity of their remaining fluorescence was more important than in MCF-AZON⁺ NPs. Thus, the designed MF-AZON⁺ and MCF-AZON⁺ NPs can also be applied as diagnostic nanomedical tools.

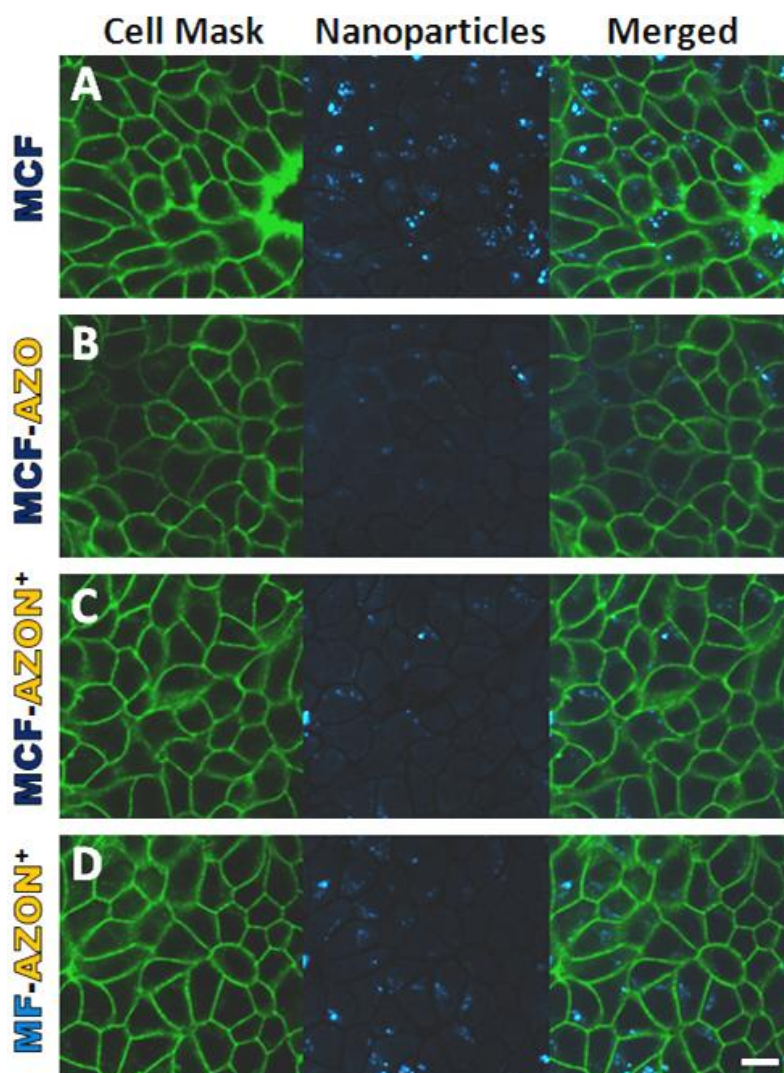


Figure 2. Two-photon fluorescence imaging of MCF-7 cells incubated with MCF (A), MCF-AZO (B), MCF-AZON⁺ (C), MF-AZON⁺ nanomaterials demonstrating the cellular uptake.

The siRNA delivery in MCF-7 cancer cells was finally assessed via TPE stimuli. The siRNA sequence targeting the luciferase gene (siLuc 5'-AACGTACGCGGAATACTTCGA-3') was chosen to complex the two-photon sensitive NPs, and the silencing efficiency was tested in stable luciferase-expressing MCF-7 cells. First, siRNAs were mixed 30 min at room temperature with MCF-AZON⁺ or MF-AZON⁺ NPs at weight ratio. Then, siRNA-NPs nanomaterials complexes were incubated for 24 h at 40 $\mu\text{g.mL}^{-1}$ with cells in 384 multiwell glass bottomed plate. Then, the cells were irradiated or not with a confocal Carl Zeiss two-photon microscope at 760 nm and maximum laser power (3W input). Three scans of 1.57s were carried out, each in four different areas without overlaps between irradiated areas, with the smallest objective (Carl Zeiss 10-fold magnification/objective 0.3 EC Plan-Neofluar). As a result, 50% of surface was irradiated, and the MTT assay (a yellow tetrazole reduced to a purple formazan in living cells) was performed two days after irradiation (Fig. 4). Several negative control experiments were first performed (Fig. 4A). The cells were not sensitive to the laser, while the siRNA and un-functionalized MCF NPs did not produce any gene

silencing effect. It is noteworthy, however, that non-positively charged MSN-AZO NPs were not able to transport the siRNA as well (Fig. 4A). Secondly, the non-irradiated MCF-AZON⁺ and MF-AZON⁺ were studied with and without siRNA mixing (blue and white bars respectively), and with laser irradiation when previously mixed with siRNA cargos (red bars, see Fig. 4B). Without siRNA, both nanoplateforms did not affect the luciferase expression. On the contrary, when MCF- AZON⁺ NPs were mixed in 1/5, 1/15, 1/30 weight ratio with siRNA, 27, 29, and 46% of luciferase luminescence decrease was observed. Additionally, MF-AZON⁺-siRNA NPs studied in the same conditions lead to 36% of gene silencing effect. Thus, both MCF-AZON⁺ and MF-AZON⁺ nanoplateforms enabled unprecedented two-photon triggered FRET-based siRNA in-vitro deliveries.

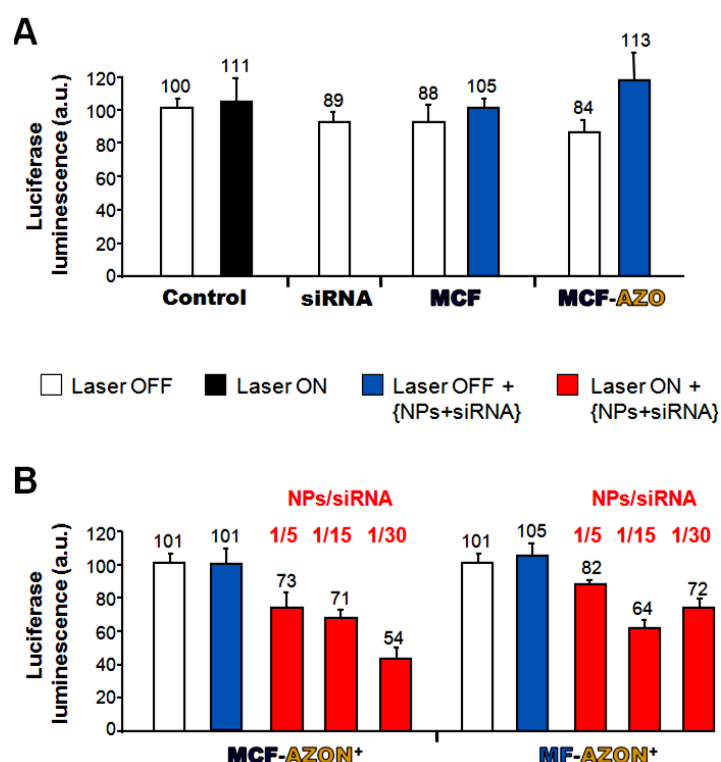


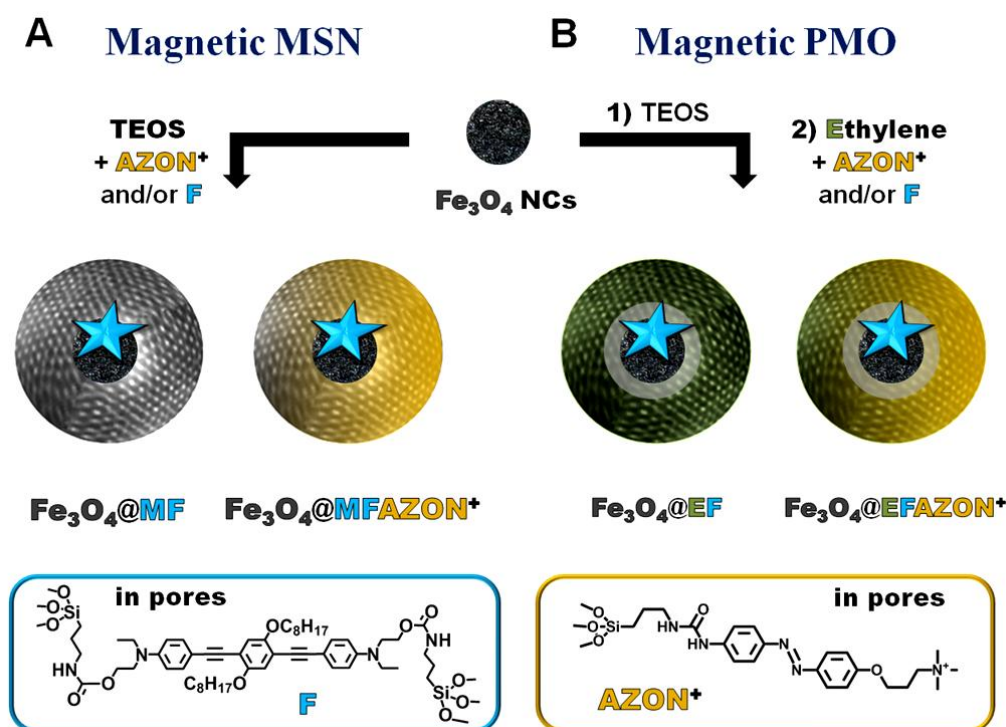
Figure 4. Two-photon-triggered siRNA delivery in MCF-7 breast cancer cells; negative (A) and positive controls (B).

Conclusion

In summary, MSN functionalized with azobenzene-ammonium moieties were designed and fully characterized for nucleic acid delivery application. The siRNA delivery principle was based on the FRET transfer between two types of two-photon fluorophores towards the nanoimpellers moieties. The fluorescence of MCF NPs and the remaining fluorescence of MCF-AZON⁺ and MF-AZON⁺ nanoplateforms demonstrated the cellular uptakes of the nanomaterials. Furthermore, unprecedented siRNA delivery causing 50% of gene silencing effect was observed. Two-photon-sensitive MSN nucleic acid nanocarriers are thus highly promising for gene therapy, and further investigation will be presented in the following perspectives.

Perspectives

Owing to this success with organically modified MSN, multifunctional magnetic MSN and magnetic periodic mesoporous organosilica (PMO, see chapter 8) nanocarriers were designed for siRNA delivery (see scheme 2). Iron oxide (Fe_3O_4) nanocrystals (NCs) were chosen for their well-known magnetic resonance imaging (MRI), as well as the active targeting that could be harnessed through the NCs magnetism. Conversely to the first AZON^+ post-grafting strategy, these NPs were designed via co-condensation of the AZON^+ fragments and/or the F fluorophore with TEOS for magnetic MSN (Scheme 2A), or with bis-(trimethoxysilane)ethylene for magnetic PMO NPs (Scheme 2B). Two controls containing only the F moiety were prepared, Fe_3O_4 core MSN-F shell ($\text{Fe}_3\text{O}_4@\text{MF}$), and Fe_3O_4 core ethylene-F PMO shell ($\text{Fe}_3\text{O}_4@\text{EF}$) NPs. The magnetic MSN and PMO for siRNA delivery were respectively $\text{Fe}_3\text{O}_4@\text{MFAZON}^+$ and $\text{Fe}_3\text{O}_4@\text{EFAZON}^+$ NPs. The aim of the co-condensation was to obtain AZON^+ fragments in the pores, so as to protect the siRNA within the nanocarriers. Consequently, the pore size was enhanced through the addition of the 1,2,4-trimethylbenzene (TMB) swelling agent to the cetyltrimethylammonium bromide micellar template, in order to enable the siRNA diffusion in the NPs.



Scheme 2. Design of magnetic MSN (A) and PMO (B) nanomaterials containing either the F fluorophore alone or the F fluorophore combined with the AZON^+ moiety.

First of all, two-photon-sensitive magnetic MSN were synthesized. Spherical Fe_3O_4 NCs of 21 ± 2 nm were synthesized *via* thermal decomposition at 340°C of hydrated iron oxide with oleic acid in docosane, as displayed with transmission electron microscopy images

(TEM, see Fig. S2). The NCs were redispersed in chloroform and stabilized with oleylamine. Then, an aqueous mixture of the cetyltrimethylammonium bromide template with the sodium hydroxide catalyst was prepared at 70°C, and the hydrophobic Fe₃O₄ NCs were added and stabilized in the micelles. A first thin mesoporous silica layer was grown in a sol-gel process at 80°C upon TEOS addition. Afterwards, the TMB swelling agent was added and the mixture was allowed to stir to homogenize the micellar nanorods sizes. Finally, TEOS was co-condensed with AZON⁺ fragments and/or the F fluorophore to obtain magnetic MSN with pores larger than 2 nm. A similar procedure was used to design magnetic PMO, thanks to the ethylene precursor (see ESI).

The morphological properties of the magnetic MSN and PMO compounds were then investigated. TEM micrographs clearly displayed the monodisperse core-shell structures of the Fe₃O₄@MF and Fe₃O₄@MFAZON⁺ nanomaterials (Fig. 5A-B). The NPs typically had one Fe₃O₄ core per particle, which was covered with a 30 nm mesoporous organosilica layer of radial porosity, for an overall size of 70 to 80 nm. Besides, Fe₃O₄@EF and Fe₃O₄@EFAZON⁺ PMO NPs were also found to be mesoporous core-shell nanostructures of 80 to 90 nm (Fig. 5C and D respectively), though the Fe₃O₄ stabilization was more challenging.

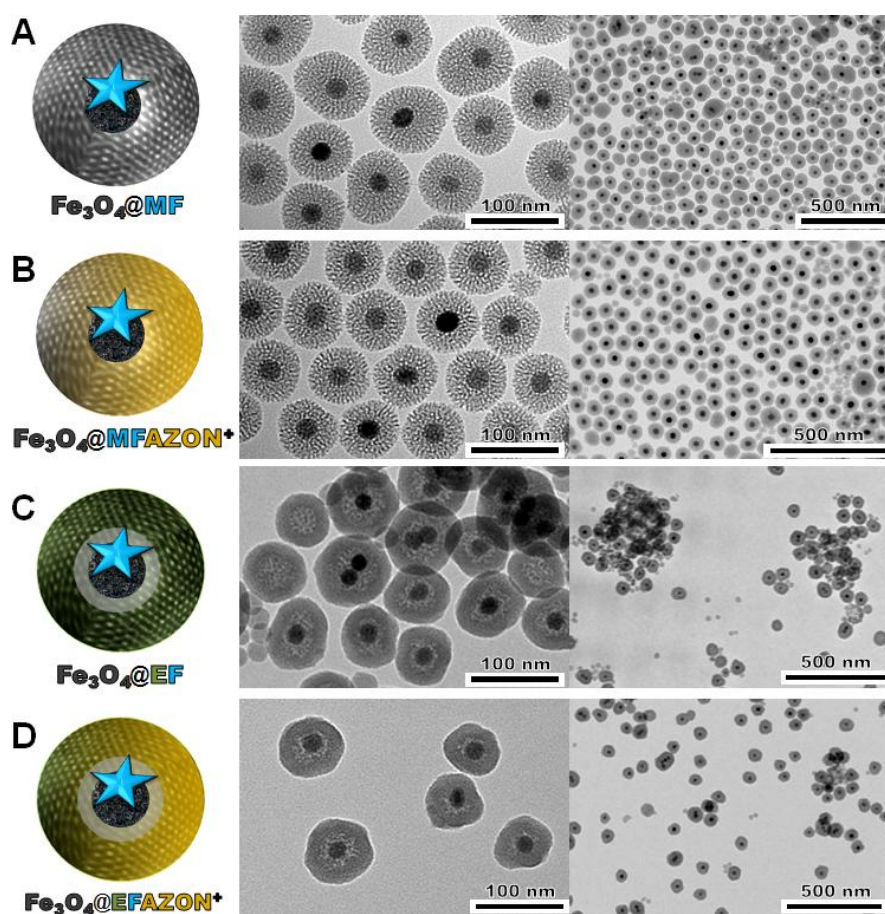


Figure 5. Schematic representation and TEM micrographs of the Fe₃O₄@MF (A), Fe₃O₄@MFAZON⁺ (B), Fe₃O₄@EF (C), and Fe₃O₄@EFAZON⁺ nanomaterials (D).

The functionalization and structure of the nanomaterials were then characterized. On the one hand, UV-visible spectroscopy demonstrated the co-condensation of the AZON⁺ and/or the fluorophore moieties in the NPs (Fig. 6A). The positive zeta potentials found in the Fe₃O₄@MFAZON⁺ and Fe₃O₄@EFAZON⁺ materials suggested that both the pores and the surface of the NPs were covered with the azobenzene derivative (Fig. 6B). On the other hand, nitrogen-adsorption-desorption technique coupled with the BET theory calculated a surface area of 650 m².g⁻¹ for Fe₃O₄@MFAZON⁺ with pores of 2.5 to 3.5 nm (Fig. 6C-D). Thus the magnetic MSN nanocarriers could be used for siRNA transportation. On the contrary, the surface area was not maintained in the magnetic PMO, since only 119 m².g⁻¹ were measured for Fe₃O₄@EFAZON⁺ (Fig. 6C). Note that, in a control sample containing neither the AZON⁺ nor the F fragments, Fe₃O₄@E NPs (see TEM Fig. S3A-B) did have 343 m².g⁻¹ (Fig. S3C-D). Consequently, magnetic MSN would be preferred for future work on siRNA delivery, and the stabilization of the porous framework of magnetic PMO NPs is still under investigation.

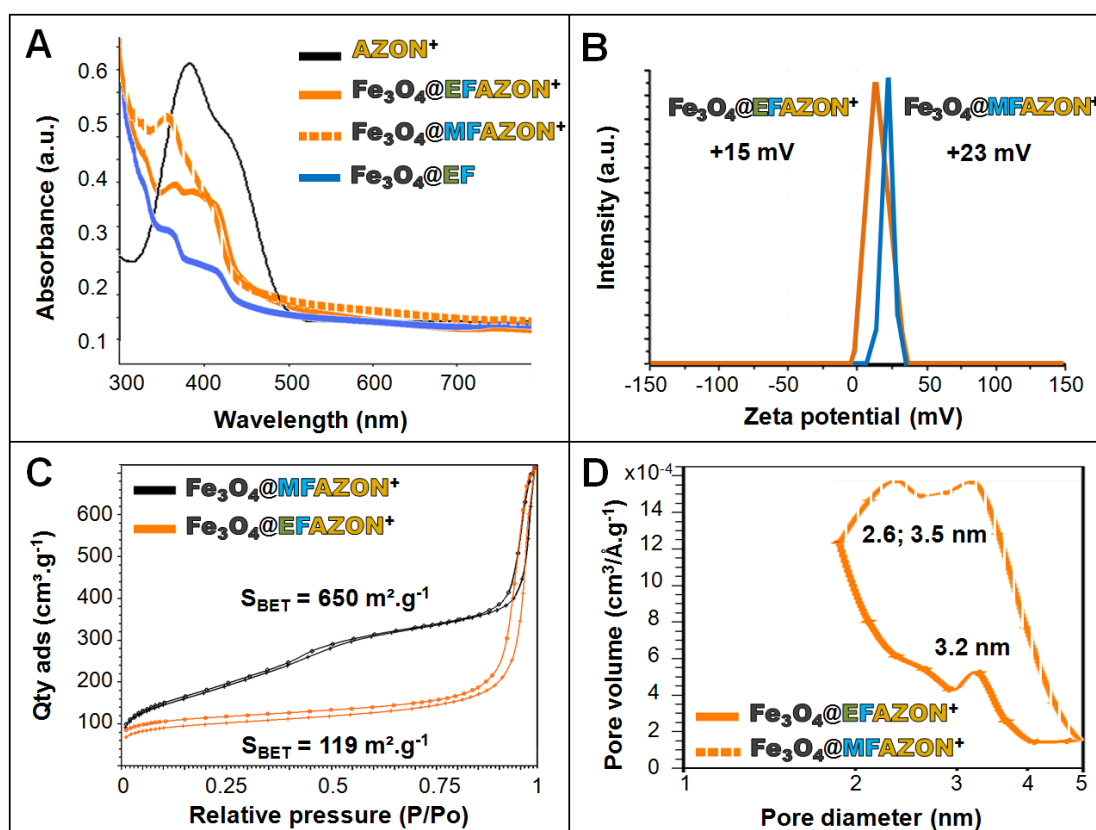


Figure 6. UV-visible spectra comparison of the AZON⁺, Fe₃O₄@MFAZON⁺, and Fe₃O₄@EFAZON⁺ NPs (A). Solid state NMR spectra of Fe₃O₄@EF and Fe₃O₄@EFAZON⁺ NPs (B). Zeta potential of the Fe₃O₄@EF and Fe₃O₄@EFAZON⁺ NPs (C). FTIR spectra comparison of the Fe₃O₄@EF and Fe₃O₄@EFAZON⁺ NPs (D).

REFERENCES

1. C. Huang, M. Li, C. Chen and Q. Yao, *Expert Opin. Ther. Tar.*, 2008, **12**, 637-645.
2. D. V. Morrissey, J. A. Lockridge, L. Shaw, K. Blanchard, K. Jensen, W. Breen, K. Hartsough, L. Machemer, S. Radka, V. Jadhav, N. Vaish, S. Zinnen, C. Vargeese, K. Bowman, C. S. Shaffer, L. B. Jeffs, A. Judge, I. MacLachlan and B. Polisky, *Nat Biotech*, 2005, **23**, 1002-1007.
3. A. Okumura, P. M. Pitha and R. N. Harty, *Proc. Natl. Acad. Sci.*, 2008, **105**, 3974-3979.
4. R. Kanasty, J. R. Dorkin, A. Vegas and D. Anderson, *Nat. Mater.*, 2013, **12**, 967-977.
5. H. Shen, T. Sun and M. Ferrari, *Cancer Gene Ther.*, 2012, **19**, 367-373.
6. M. E. Davis, J. E. Zuckerman, C. H. J. Choi, D. Seligson, A. Tolcher, C. A. Alabi, Y. Yen, J. D. Heidel and A. Ribas, *Nature*, 2010, **464**, 1067-1070.
7. K. A. Whitehead, R. Langer and D. G. Anderson, *Nat. Rev. Drug Discov.*, 2009, **8**, 129-138.
8. S. C. Semple, A. Akinc, J. Chen, A. P. Sandhu, B. L. Mui, C. K. Cho, D. W. Y. Sah, D. Stebbing, E. J. Crosley, E. Yaworski, I. M. Hafez, J. R. Dorkin, J. Qin, K. Lam, K. G. Rajeev, K. F. Wong, L. B. Jeffs, L. Nechev, M. L. Eisenhardt, M. Jayaraman, M. Kazem, M. A. Maier, M. Srinivasulu, M. J. Weinstein, Q. Chen, R. Alvarez, S. A. Barros, S. De, S. K. Klimuk, T. Borland, V. Kosovrasti, W. L. Cantley, Y. K. Tam, M. Manoharan, M. A. Ciufolini, M. A. Tracy, A. de Fougerolles, I. MacLachlan, P. R. Cullis, T. D. Madden and M. J. Hope, *Nat. Biotech.*, 2010, **28**, 172-176.
9. R. H. Mo, J. L. Zaro and W.-C. Shen, *Mol. Pharm.*, 2011, **9**, 299-309.
10. A. D. Keefe, S. Pai and A. Ellington, *Nat. Rev. Drug Discov.*, 2010, **9**, 537-550.
11. H. Lee, A. K. R. Lytton-Jean, Y. Chen, K. T. Love, A. I. Park, E. D. Karagiannis, A. Sehgal, W. Querbes, C. S. Zurenko, M. Jayaraman, C. G. Peng, K. Charisse, A. Borodovsky, M. Manoharan, J. S. Donahoe, J. Truelove, M. Nahrendorf, R. Langer and D. G. Anderson, *Nat. Nano.*, 2012, **7**, 389-393.
12. J. H. Jeong, H. Mok, Y.-K. Oh and T. G. Park, *Bioconjugate Chem.*, 2008, **20**, 5-14.
13. Z. Li, J. C. Barnes, A. Bosoy, J. F. Stoddart and J. I. Zink, *Chem. Soc. Rev.*, 2012, **41**, 2590-2605.
14. M. W. Ambrogio, C. R. Thomas, Y.-L. Zhao, J. I. Zink and J. F. Stoddart, *Acc. Chem. Res.*, 2011, **44**, 903-913.
15. Y. Chen, Y. Zhang, W. Liang and X. Li, *Nanomedicine: NBM*, 2012, **8**, 1267-1270.
16. S. S. Banerjee and D.-H. Chen, *Nanotechnology*, 2009, **20**, 185103.
17. J.-L. Li, H.-C. Bao, X.-L. Hou, L. Sun, X.-G. Wang and M. Gu, *Angew. Chem. Int. Ed.*, 2012, **51**, 1830-1834.
18. J. Croissant, M. Maynadier, A. Gallud, H. Peindy, N'Dongo, J. L. Nyalosaso, G. Derrien, C. Charnay, J.-O. Durand, L. Raehm, F. Serein-Spirau, N. Cheminet, T. Jarrosson, O. Mongin, M. Blanchard-Desce, M. Gary-Bobo, M. Garcia, J. Lu, F. Tamanoi, D. Tarn, T. M. Guardado-Alvarez and J. I. Zink, *Angew. Chem.*, 2013, **125**, *Angew. Chem. Int. Ed.*, 2013, **125**, 14058-14062.
19. H. M. Kim and B. R. Cho, *Acc. Chem. Res.*, 2009, **42**, 863-872.
20. M. Pawlicki, H. A. Collins, R. G. Denning and H. L. Anderson, *Angew. Chem. Int. Ed.*, 2009, **48**, 3244-3266.
21. M. Gary-Bobo, Y. Mir, C. Rouxel, D. Brevet, I. Basile, M. Maynadier, O. Vaillant, O. Mongin, M. Blanchard-Desce, A. Morère, M. Garcia, J.-O. Durand and L. Raehm, *Angew. Chem. Int. Ed.*, 2011, **123**, 11627-11631.
22. Y. Yang, F. Liu, X. Liu and B. Xing, *Nanoscale*, 2013, **5**, 231-238.
23. H.-J. Li, H.-X. Wang, C.-Y. Sun, J.-Z. Du and J. Wang, *RSC Adv.*, 2014, **4**, 1961-1964.
24. M. Gary-Bobo, Y. Mir, C. Rouxel, D. Brevet, I. Basile, M. Maynadier, O. Vaillant, O. Mongin, M. Blanchard-Desce, A. Morere, M. Garcia, J.-O. Durand and L. Raehm, *Angew. Chem. Int. Ed.*, 2011, **50**, 11425-11429.
25. I. Tochitsky, M. R. Banghart, A. Mourrot, J. Z. Yao, B. Gaub, R. H. Kramer and D. Trauner, *Nature Chem.*, 2012, **4**, 105-111.
26. J. Croissant, A. Chaix, O. Mongin, M. Wang, S. Clément, L. Raehm, J.-O. Durand, V. Hugues, M. Blanchard-Desce, M. Maynadier, A. Gallud, M. Gary-Bobo, M. Garcia, J. Lu, F. Tamanoi, D. P. Ferris, D. Tarn and J. I. Zink, *Small*, 2014, **n/a**, n/a.

APPENDIX: SUPPLEMENTARY INFORMATION

I- EXPERIMENTAL SECTION

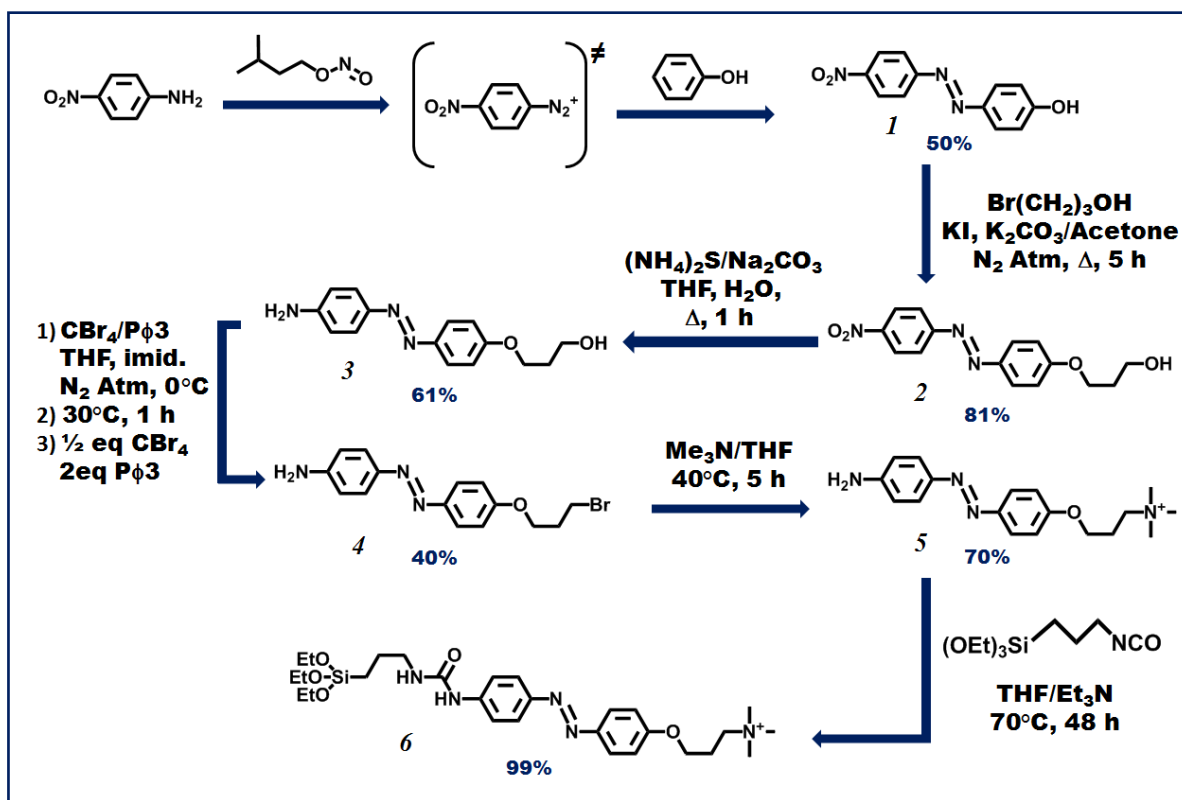
Materials. Tetraethoxysilane (TEOS), cetyltrimethylammonium bromide (CTAB), sodium hydroxide, hydrated iron oxide, oleic acid, ammonium nitrate, 1,2,4-trimethylbenzene, and ether were purchased from Sigma-Aldrich. Anhydrous ethanol, and chloroform were purchased from Fisher Chemicals. 1,2-bis(triethoxysilyl)ethylene was purchased from ABCR.

Methods. Dynamic light scattering analyses were performed using a Cordouan Technologies DL 135 Particle size analyzer instrument. ^{29}Si and ^{13}C CPMAS solid state NMR sequences were recorded with a VARIAN VNMRS300, using Q8MH8 and adamantane references respectively. TEM analyses were performed on a JEOL 1200 EXII instrument. SEM and EDS analyses were performed on a FEI Quanta FEG 200 instrument. ^1H and ^{13}C NMR spectra were recorded with a Bruker AC 400 spectrometer. Chemical shifts (in δ units, ppm) are referenced to TMS using CHCl_3 ($\delta = 7.26$ ppm) and CDCl_3 ($\delta = 77.0$ ppm) as the internal standards, respectively, for ^1H and ^{13}C NMR spectra. IR spectra were recorded on a Perkin-Elmer 100 FT spectrophotometer. Absorption spectra were recorded on a Hewlett-Packard 8453 spectrophotometer and fluorescence data were collected on a Perkin-Elmer LS55 fluorimeter. Mass spectrometry was carried out at the Laboratoire de Spectrometrie de Masse (Lyon, France) with a Thermo-Finnigan MAT95 apparatus in electronic impact ionization mode.

II- SYNTHESIS AND CHARACTERIZATION OF THE ORGANIC PRECURSOR

Compound 1 to 5. Reproduced from I. Tochitsky *et al.*, Nature Chem. **2012**, 4, 105 (see Scheme S1).

Compound 6 (AZON⁺). 4-(triethoxysilylpropyl)urea-4'-(trimethylammonium)propyloxyazobenzene was obtained by mixing 4-Amino-4'-(trimethylammonium)propyloxyazobenzene (50 mg, 1.6×10^{-1} mmol) with 3-isocyanatopropyltriethoxysilane (37 μL , 1.6×10^{-1} mmol) and triethylamine (50 μL), in THF (1 mL) for 3 days at 60°C under inert conditions. ^1H NMR (200 MHz, CDCl_3): δ 7.74 (d, $^3J = 7.0$ Hz, 2H, $\text{H}_{\text{Ph-N=N-Ph-O}}$), 7.61 (d, $^3J = 6.5$ Hz, 2H, $\text{H}_{\text{Ph-N=N-Ph-NHC=ONH}}$), 7.32 (d, $^3J = 8.0$ Hz, 2H, $\text{H}_{\text{Ph-NHC=ONH}}$), 6.62 (d, $^3J = 9.0$ Hz, 2H, $\text{H}_{\text{Ph-O}}$), 4.08 (t, $^3J = 4.0$ Hz, 2H, $\text{O-CH}_2\text{-CH}_2$), 3.75 (q, $^3J = 5.3$ Hz, 6H, $\text{O-CH}_2\text{-CH}_3$), 3.45 (t, 2H, $\text{CH}_2\text{-N}^+(\text{CH}_3)_3$), 3.27 (t, $^3J = 3.8$ Hz, 2H, $\text{CH}_2\text{-NH}$), 3.06 (s, 9H, N-CH_3), 2.93 (m, 2H, $\text{O-CH}_2\text{-CH}_2$), 1.42 (m, 2H, $\text{CH}_2\text{-CH}_2\text{-Si}$), 1.13 (t, $^3J = 7.2$ Hz, 9H, $\text{O-CH}_2\text{-CH}_3$), 0.50 (t, $^3J = 7.6$ Hz, 2H, $\text{CH}_2\text{-Si}$). IR (neat KBr) $\nu_{\text{max}}/\text{cm}^{-1} = 3373, 3313, 3203, 2974, 2930, 2886, 1707, 1629, 1600, 1548, 1501, 1485, 1442, 1390, 1299, 1245, 1192, 1151, 1106, 1084, 957, 844, 797, 724, 695, 543$. UV/Vis λ_{max} (EtOH): 382 nm. MS (ESI⁺) m/z (%): 313.2 (100), 423.2 (54), 560.3 (44) $[\text{MH}^+]$. HRMS (ESI⁺): m/z calcd for $\text{C}_{28}\text{H}_{46}\text{N}_5\text{O}_5\text{Si}$: 560.3268, found 560.3268.



Scheme S1. Multistep synthesis of the AZON⁺ precursor.

III- SYNTHESIS AND CHARACTERIZATION OF THE NANOMATERIALS

MCF-AZON⁺ and MF-AZON⁺. A mixture of MF or MCF NPs (15 mg), AZON⁺ (4 mg), and dried toluene (3 mL) was stirred overnight at 95°C. Then, the solution was centrifuged 5 min at 7 krpm in eppendorf tubes, washed twice with ethanol, twice with water, once with acetone, and dried under vacuum.

Fe₃O₄ NCs. A mixture of hydrated iron oxide (FeO(OH), 0.181 g), oleic acid (3.180 g), and docosane (5.016 g) was prepared in a 100 mL two neck round bottom flask, and stirred under vacuum for 30 minutes. Then, an argon atmosphere was applied and the mixture was refluxed at 340°C. As soon as the mixture reached 340°C, the reaction was conducted for 1 h 30 min. The solution was cooled down during 1 h without stirring. The resulting black solid was dissolved in pentane (14 mL), mixed with an ether/ethanol solution (30 mL, 2:1, v:v), and centrifuged 10 minutes at 21 krpm (27 krcf). The decomposed organic black solution was removed and the NCs were redispersed in pentane (2 mL), washed with the ether/ethanol solution, and centrifugated. The supernatant was removed, the NCs were stored in chloroform (15 mL), and stabilized with an addition of oleylamine (200 µL).

Fe₃O₄@MF. A mixture of CTAB (250 mg), distilled water (115 mL), and sodium hydroxide (875 µL, 2 M) was stirred at 70°C during 50 minutes at 700 rpm in a 250 mL three neck round bottom flask. Then, Fe₃O₄ NCs dispersed in chloroform were added stepwise (8*500 µL) during 20 minutes. Note that the chloroform is quickly evaporating from the mixture at this temperature, and 40 additional minutes were used at 80°C to stabilize the NCs in the micelles.

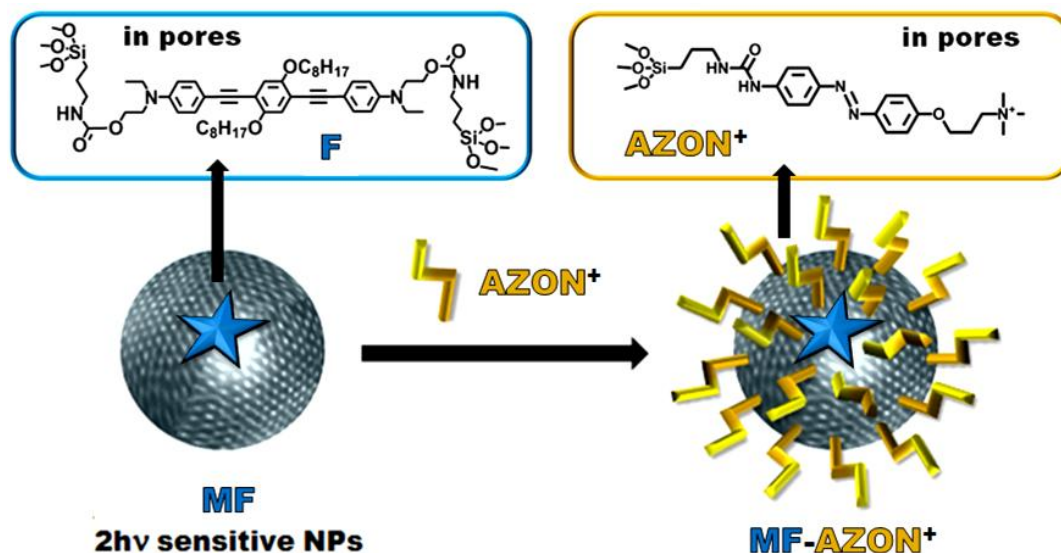
Then, TEOS (200 μL) was added to the solution, followed by the TMB swelling agent (750 μL), and the, mixture was allowed to stir for 50 min. Finally, TEOS (1 mL) and the FLUO precursor (20 mg) were added to the solution, and the condensation process was conducted for 2 h. Afterwards, the solution was cooled at room temperature while stirring; fractions were gathered in polypropylene tubes and collected by centrifugation during 15 minutes at 21 krpm (27 krcf). The sample was then extracted twice with an alcoholic solution of ammonium nitrate (6 g.L^{-1}), and washed three times with ethanol, water, and ethanol. Each extraction involved a sonication step of 30 minutes at 50°C in order to remove the CTAB surfactant; the collection was carried out in the same manner. The as-prepared material was dried under air flow for few hours.

$\text{Fe}_3\text{O}_4@\text{MFAZON}^+$. A mixture of CTAB (250 mg), distilled water (115 mL), and sodium hydroxide (875 μL , 2 M) was stirred at 70°C during 50 minutes at 700 rpm in a 250 mL three neck round bottom flask. Then, Fe_3O_4 NCs dispersed in chloroform were added stepwise (8*500 μL) during 20 minutes. Note that the chloroform is quickly evaporating from the mixture at this temperature, and 40 additional minutes were used at 80°C to stabilize the NCs in the micelles. Then, TEOS (200 μL) was added to the solution, followed by the TMB swelling agent (900 μL), and the, mixture was allowed to stir for 2 h 30 min. Finally, TEOS (1 mL), AZON^+ (12 mg), and the FLUO precursor (20 mg) were added to the solution, and the condensation process was conducted for 2 h. Afterwards, the solution was cooled at room temperature while stirring; fractions were gathered in polypropylene tubes and collected by centrifugation during 15 minutes at 21 krpm (27 krcf). Extraction and following steps were identical to those of $\text{Fe}_3\text{O}_4@\text{MF}$ material.

$\text{Fe}_3\text{O}_4@\text{EF}$. A mixture of CTAB (250 mg), distilled water (115 mL), and sodium hydroxide (875 μL , 2 M) was stirred at 70°C during 50 minutes at 700 rpm in a 250 mL three neck round bottom flask. Then, Fe_3O_4 NCs dispersed in chloroform were added stepwise (8*500 μL) during 20 minutes. Note that the chloroform is quickly evaporating from the mixture at this temperature, and 40 additional minutes were used at 80°C to stabilize the NCs in the micelles. Then, TEOS (200 μL) was added to the solution, followed by the TMB swelling agent (900 μL), and the, mixture was allowed to stir for 60 min. Finally, 1,2-bis(triethoxysilyl)ethylene (1 mL) and the FLUO precursor (20 mg) were added to the solution, and the condensation process was conducted for 2 h. Afterwards, the solution was cooled at room temperature while stirring; fractions were gathered in polypropylene tubes and collected by centrifugation during 15 minutes at 21 krpm (27 krcf). Extraction and following steps were identical to those of $\text{Fe}_3\text{O}_4@\text{MF}$ material.

$\text{Fe}_3\text{O}_4@\text{EFAZON}^+$. A mixture of CTAB (250 mg), distilled water (115 mL), and sodium hydroxide (875 μL , 2 M) was stirred at 70°C during 50 minutes at 700 rpm in a 250 mL three neck round bottom flask. Then, Fe_3O_4 NCs dispersed in chloroform were added stepwise (8*500 μL) during 20 minutes. Note that the chloroform is quickly evaporating from the mixture at this temperature, and 40 additional minutes were used at 80°C to stabilize the NCs in the micelles. Then, TEOS (200 μL) was added to the solution, followed by the TMB swelling agent (750 μL), and the, mixture was allowed to stir for 60 min. Finally, 1,2-bis(triethoxysilyl)ethylene (1 mL), AZON^+ (12 mg), and the FLUO precursor (20 mg) were added to the solution, and the condensation process was conducted for 2 h. Afterwards, the

solution was cooled at room temperature while stirring; fractions were gathered in polypropylene tubes and collected by centrifugation during 15 minutes at 21 krpm (27 krcf). Extraction and following steps were identical to those of $\text{Fe}_3\text{O}_4@\text{MF}$ material.



Scheme S2. AZON^+ alkoxyisilyls grafting on the MF NPs, leading to MF-AZON^+ nanomaterials.

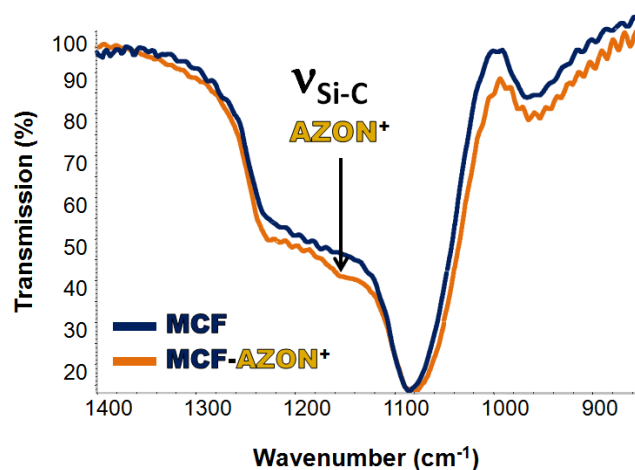


Figure S1. FTIR spectra comparison of MCF and MCF-AZON⁺ NPs, validating the AZON^+ grafting.

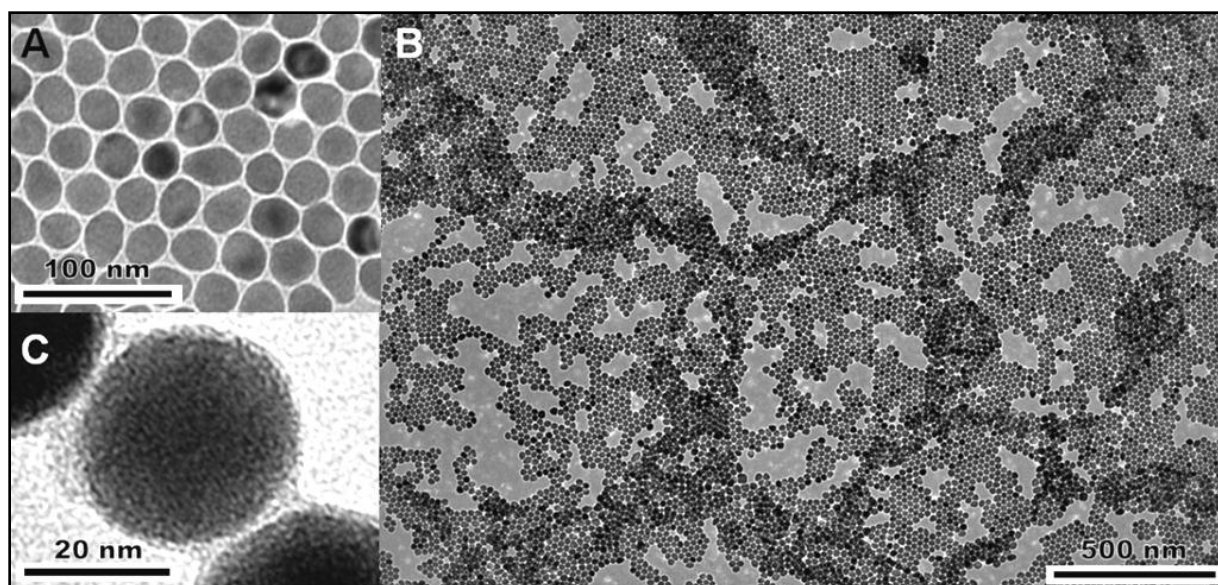


Figure S2. TEM images of Fe_3O_4 NCs (A-B). High Magnification TEM image of Fe_3O_4 NCs demonstrating the atomic organization.

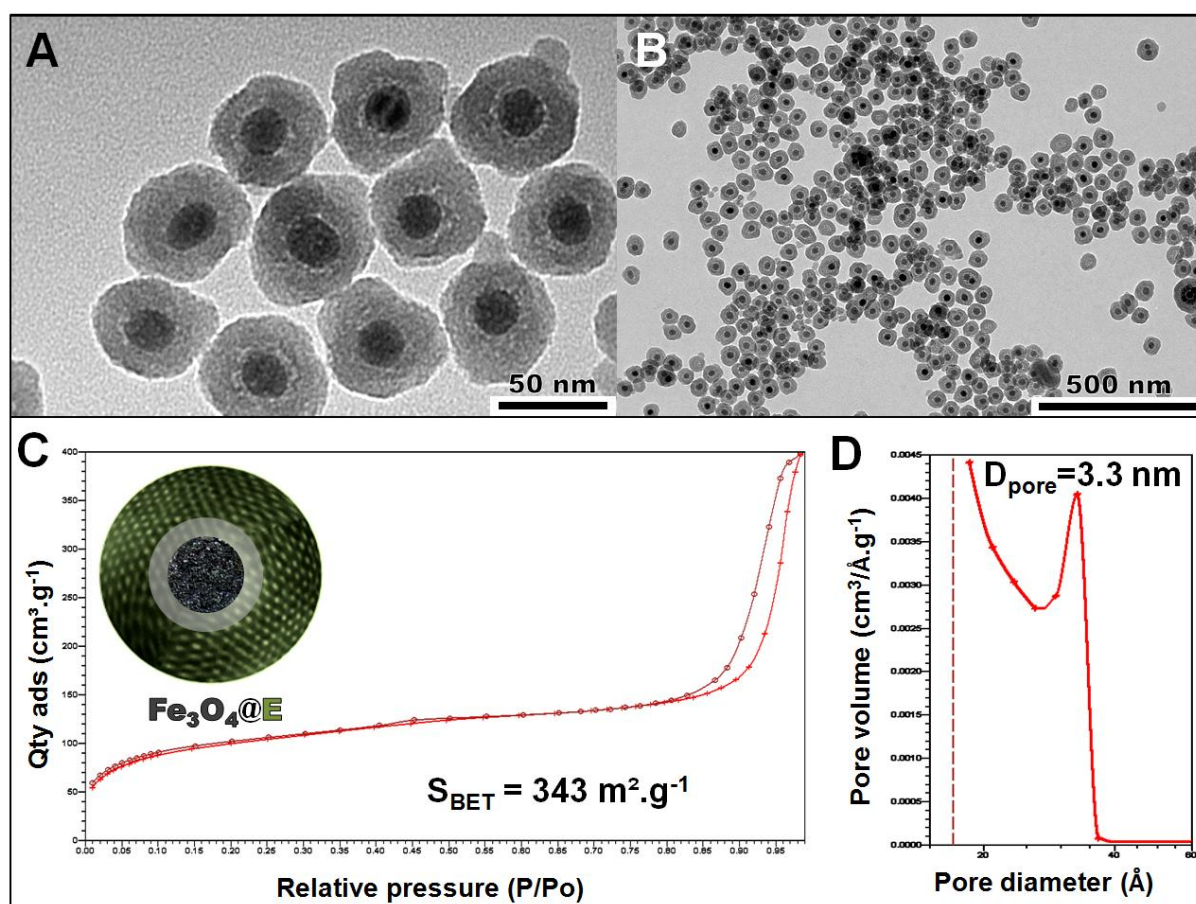


Figure S3. TEM images (A-B) and N_2 -adsorption-desorption isotherm (C) and BJH pore size distribution (D) of $\text{Fe}_3\text{O}_4@E$ NPs control.

CHAPTER 5

Two-Photon-Actuated Photodynamic and/or Photothermal Therapies via Photosensitizer-Functionalized Mesoporous Silica Nanovehicles on Cancer Cells

INTERDISCIPLINARY COLLABORATION

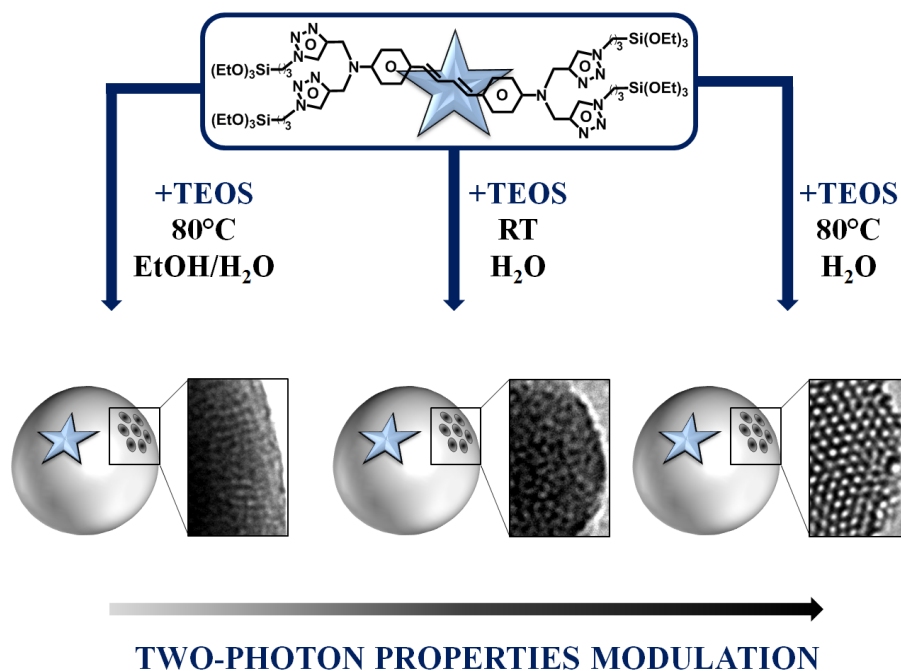
J. Croissant, X. Cattoën, M. Wong Chi Man, J-O. Durand, L. Raehm: *Photosensitizer synthesis and physico-chemical characterization, nanomaterial concept, synthesis, physico-chemical characterizations, and applications in solution.*

O. Mongin, V. Hugues, M. Blanchard-Desce: *Photosensitizer concept and two-photon photophysical characterizations. Nanomaterial two-photon photophysical characterizations.*

M. Gary-Bobo, M. Maynadier, A. Gallud, M. Garcia: *Two-photon cell studies.*

CHAPTER 5

A. Influence of the Synthetic Method on the Properties of Two-Photon-Sensitive Mesoporous Nanoparticles for *In-Vitro* Fluorescence Imaging



Abstract

Herein we report the modulation of the two-photon properties of mesoporous organosilica nanoparticles (NPs) via various synthetic approaches. Three types of elaborations were compared, one in aqueous media at 25 °C, and the other two at 80°C in water or in a water/ethanol mixture. For all these methods, an alkoxy-silylated two-photon photosensitizer (2PS) was co-condensed with tetraethylorthosilicate (TEOS), and five two-photon-sensitive mesoporous organosilica (M2PS) NPs were systematically studied. The M2PS NPs porous structure could be tuned from radial to worm-like and MCM-41 types of organization. Besides, the 2PS precursor spatial dispersion was found to be highly dependent of both the 2PS initial concentration and the elaboration process. As a result, two-photon properties were modulated by the choice of the synthesis, the best results being found in aqueous media at 25 or 80°C (Scheme 1). Finally, the M2PS material was demonstrated to be a suitable *in-vitro* two-photon fluorescent nanodevice.

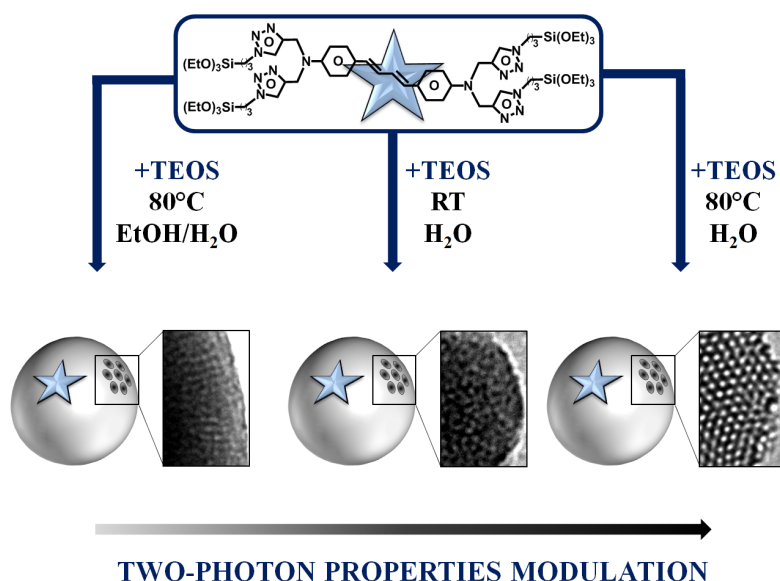
CHAPTER 5.A. INFLUENCE OF THE SYNTHETIC METHOD ON THE PROPERTIES OF TWO-PHOTON-SENSITIVE MESOPOROUS NANOPARTICLES FOR IN-VITRO FLUORESCENCE IMAGING

Introduction

Over the past few years, two-photon-sensitive NPs have attracted a lot of attention for theranostic nanomedicine.¹⁻⁸ Near-infrared (NIR) two-photon excitation is indeed very attractive for its deep-tissue penetration and 3D-spatiotemporal accuracy, which are crucial for site-specific cancer treatment.⁹ Among various nanoplatfroms, mesoporous silica nanoparticles (MSN) are particularly suited nanomedical devices for their low cytotoxicity, excretion, selective endocytosis through the enhanced permeability and retention effect (EPR), and multifunctionality.¹⁰⁻¹² The diversity of MSN features arises from their large surface areas, tunable pore size, controllable shape and morphology, and known silicon chemistry.^{13, 14} Besides, the sol-gel elaboration enables the co-condensation of versatile species with silica precursors to obtain mesoporous organosilica NPs.^{15, 16}

Hence, two-photon fluorophores and photosensitizers (2PS) could be either doped^{8, 17, 18} or covalently bound in the material¹⁸⁻²¹ to design M2PS NPs. The 2PS encapsulation could be physically performed during the sol-gel process if the fragments are mixed in the silica, or chemically via the prior alkoxysilylation of the 2PS. Phase segregation, low doping efficiency of 2PS moieties, as well as the photosensitizer diffusion out of the nanomaterial often make the chemical grafting more attractive.²² It should be noticed that the alkoxysilylation is not a trivial step since the conjugation and presence of donor groups must be maintained in the molecule to preserve its two-photon properties. Also, the alkoxysilylated 2PS fragments integrity and solubility should be compatible with the sol-gel temperature, pH, and solvent mixture. Secondly, the 2PS concentration and spatial distribution in the NPs will be crucial for the final two-photon properties of each chromophore.²³ The control of many different parameters is thus required for the construction of efficient M2PS NPs.

Herein, we report a systematic study on one type of M2PS NPs designed from three elaboration processes, in order to study their influence on the two-photon properties (Scheme 1). A novel two-photon photosensitizer (2PS) was designed and fully characterized. M2PS nanomaterials were elaborated via co-condensation of a tetraethoxysilane (TEOS) and 2PS moieties in various conditions. It was found that the choice of the synthetic approach is crucial and can induce either the enhancement or the collapse of the two-photon properties. The absorption and emission of fluorescence, two-photon cross-sections and fluorescence quantum yields are systematically compared in five M2PS nanocarriers. Finally, the performance of the designed M2PS NPs is demonstrated for *in-vitro* fluorescence imaging.



Scheme 1. Modulation of the two-photon properties of M2PS NPs via various synthetic pathways. Typical TEM images of the NPs porous framework are presented for each reaction.

Results and discussion

Firstly, a novel tetraalkoxysilylated two-photon photosensitizer was designed by multistep organic synthesis (Figure S1). The diaminodiphenylbutadiene core structure of the 2P was known to selectively photo-activate electron transfer in bio processes under TPE.²⁴ This 2PS molecule was elaborated using the $[\text{CuBr}(\text{PPh}_3)_3]$ -catalyzed CuAAC click reaction with (3-azidopropyl)triethoxysilane under mild conditions, was fully characterized via ^1H and ^{13}C NMR and mass spectroscopy (see ESI, Fig. S2). Besides, a stable two-photon reference of the 2PS (2PS ref) was elaborated for the photophysical and optical studies, according to a different click chemistry reaction at the last synthetic step (see ESI, Fig. S3). The 2PS ref was fully characterized with the aforementioned techniques (ESI, Fig. S4), as well as Fourier transform infrared (FTIR) spectroscopy (Fig. S5). Secondly, M2PS nanomaterials were designed via various synthetic approaches. Three procedures were compared which involved the co-condensation of the 2PS with the TEOS silica precursor, through sodium hydroxide catalysis in a template of cetyltrimethylammonium bromide. The first approach involved a modified Mann reaction,²⁵ the six minutes reaction in aqueous media at 25 °C. Two materials are compared from this procedure, **M2PS-1** and **M2PS-2**, with 9 and 18 weight percent (wt%) of 2PS respectively (see Table 1). In the second approach, the synthesis was carried out at 80°C in a water/ethanol mixture (5:2, v:v) for 30 minutes; the related compound will be called **M2PS-3**. The third approach is a modified Lin's reaction,²⁶ which was performed in aqueous media at 80°C for 1 hour 30 minutes. Higher concentrations of 2PS precursor were used in this procedure, with 50 and 25 wt% of 2PS were obtained for **M2PS-4** and **M2PS-5** respectively.

Secondly, the structure and morphology of the M2PS nanomaterials were characterized. Transmission electron microscopy (TEM) images depicted nearly 80 nm

nanospheres for all types of M2PS particles, except the 200 nm nanospheres obtained from the water/ethanol mixture for **M2PS-3** (Fig. 1A). Dynamic light scattering (DLS) size distributions showed that the best approaches to obtain monodisperse non-aggregated M2PS NPs were in aqueous media at 25 °C for low 2PS concentration, or in aqueous media at 80°C for higher concentrations (Fig. 1B). Besides, electron micrographs revealed different types of porous frameworks for each reaction (see Scheme 1 and Fig. 1A). Typically, worm-like structures were obtained with the aqueous route at 25 °C, and the pore organization is very sensitive to the 2PS content. Comparing the same procedure in **M2PS-1** and **M2PS-2**, the increase of the 2PS content from 9 to 18 wt% led to an important structural disorganization, as testified with the small angle X-ray diffraction (XRD) patterns (Fig. 1C). Conversely, the third strategy performed at 80°C did retain the MCM-41 hexagonal array of the pores even at high 2PS concentration, as displayed in both **M2PS-4** and **M2PS-5**. Alternatively, a well-defined radial porosity was obtained on **M2PS-3** NPs in the water/ethanol mixture. Moreover, the intense XRD peak at 2-theta 2 to 3° confirmed the typical 2 nm pores of M2PS NPs (Fig. 1C). Such an observation was validated by the nitrogen-adsorption-desorption technique. The BJH transform indicated pore diameters from 2.0 to 2.6 nm (see Table 2); high BET surface areas were found for all samples, ranging from 500 to 700 m².g⁻¹ (Fig. S6 to S10). Thus, both the size and the porosity of the M2PS nanomaterials make them suitable nanocarriers for nanomedicine.

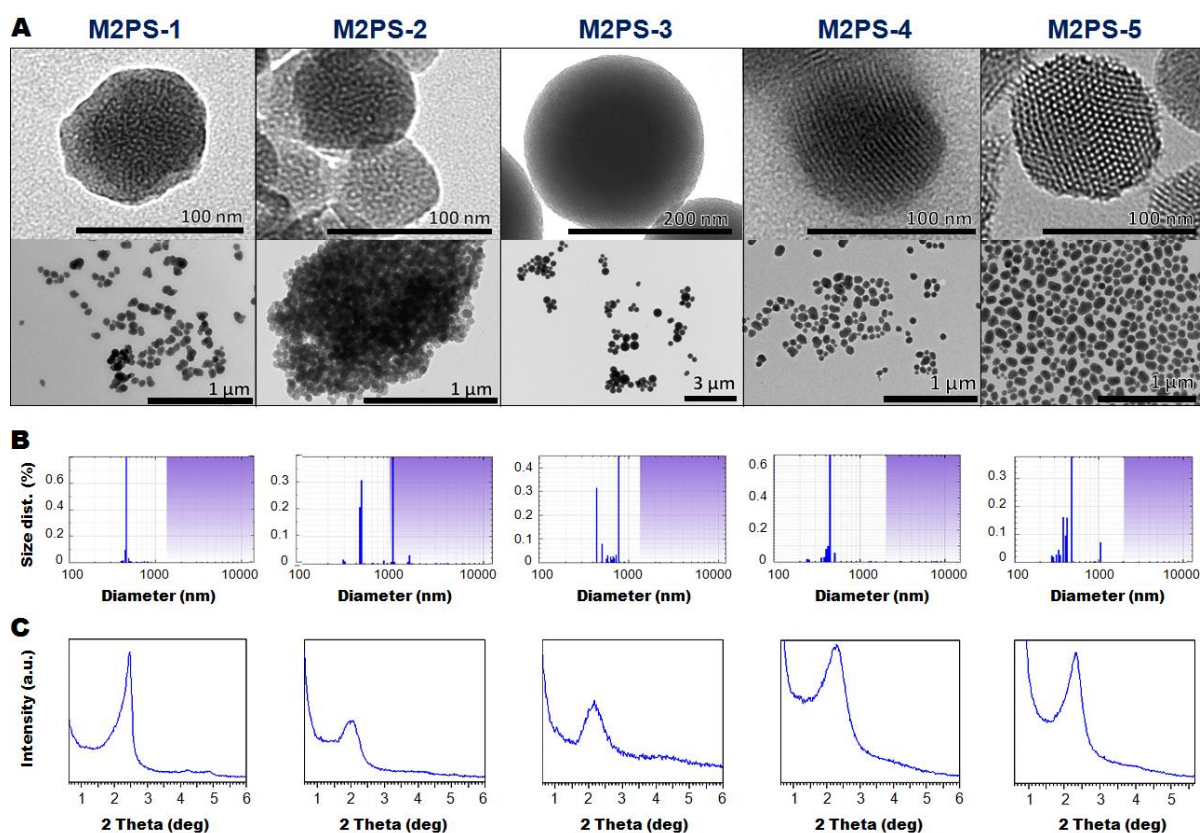


Figure 1. TEM images (A), DLS size distributions (B), and small angles XRD patterns of M2PS-1 to M2PS-5 NPs (C).

Table 1. 2PS weight percent determination in M2PS NPs.

Sample	Method	NPs N wt% ^[a]	NPs 2PS wt% ^[b]	Reactant 2PS wt%
M2PS-1	25 °C/H ₂ O	1.3	8.9	8
M2PS-2	25 °C /H ₂ O	2.7	18.7	12
M2PS-3	80 °C/H ₂ O:EtOH	3.5	24.9	13
M2PS-4	80 °C/H ₂ O	7.3	51.2	38
M2PS-5	80 °C/H ₂ O	3.4	23.7	10

[a] Elemental analysis by combustion measurements of the NPs.

[b] Determination based on the nitrogen wt% in the 2PS molecules.

Thirdly, the efficiency of the 2PS encapsulation in the nanomaterials was found to be highly dependent on the synthetic route. UV-visible spectroscopy demonstrated the successful encapsulation of the 2PS molecules in the silica framework of all M2PS NPs (Fig. S11 and S12). Solid state nuclear magnetic resonance (NMR) ²⁹Si and ¹³C CPMAS spectra (Fig. S13) further supported that assertion. Besides, as shown in Table 1 with the comparison of the 2PS wt% in the NPs and in the reactants, the efficacy of the 2PS condensation was higher than that of TEOS. Interestingly, highly organically functionalized M2PS NPs could be designed with both syntheses at 80 °C. However, the usefulness of the **M2PS-3** nanocarriers (water/ethanol mixture) is greatly impoverished, as we shall see with the photophysical properties.

Table 2. Textural properties of M2PS NPs.

Sample	M2PS-1	M2PS-2	M2PS-3	M2PS-4	M2PS-5
S_{BET} (m².g⁻¹)	713	647	603	503	677
D_{pore} (nm)	2.0	2.3	2.3	2.5	2.6

The 2PS spatial distribution in the silica was then studied by absorption and emission of fluorescence, since this factor affects directly the photophysical properties of the NPs. The emission spectra (Fig. 2A) and the fluorescence quantum yields (Table 3) of the M2PS compounds were measured and compared to those of the 2PS molecular reference (2PS-Ref, see structure Fig. S14). The most fluorescent NPs were found to be **M2PS-1**, **M2PS-4**, and **M2SP-5**, the latter having a quantum yield two to four times larger than the formers. A bathochromic effect was also observed on the 2PS band, as seen in the normalized spectra (Fig. 2B). The most red-shifted band corresponds to the synthesis performed in the water/ethanol mixture, with an absorption maximum at 469 nm; then follows the aqueous mixture at 25 °C ($\lambda_{\text{max}} = 453\text{-}455$ nm), and finally the aqueous reaction at 80°C ($\lambda_{\text{max}} \approx 448\text{-}450$ nm). Such an observation was consistent with the absorption spectra of the M2PS NPs (Fig. S7). These results are the direct outcome of the spatial dispersion of the 2PS molecules in the mesoporous silica matrices, thus we expected to obtain poorer two-photon properties on material having the most red-shifted 2PS emission bands. Indeed, the aggregation of 2PS moieties via $\pi\text{-}\pi$ stacking interactions or condensation generally leads to increased non-

radiative de-excitation rates and therefore to a quenching of the fluorescence, as well as to a decrease of the two-photon absorption properties.²⁷

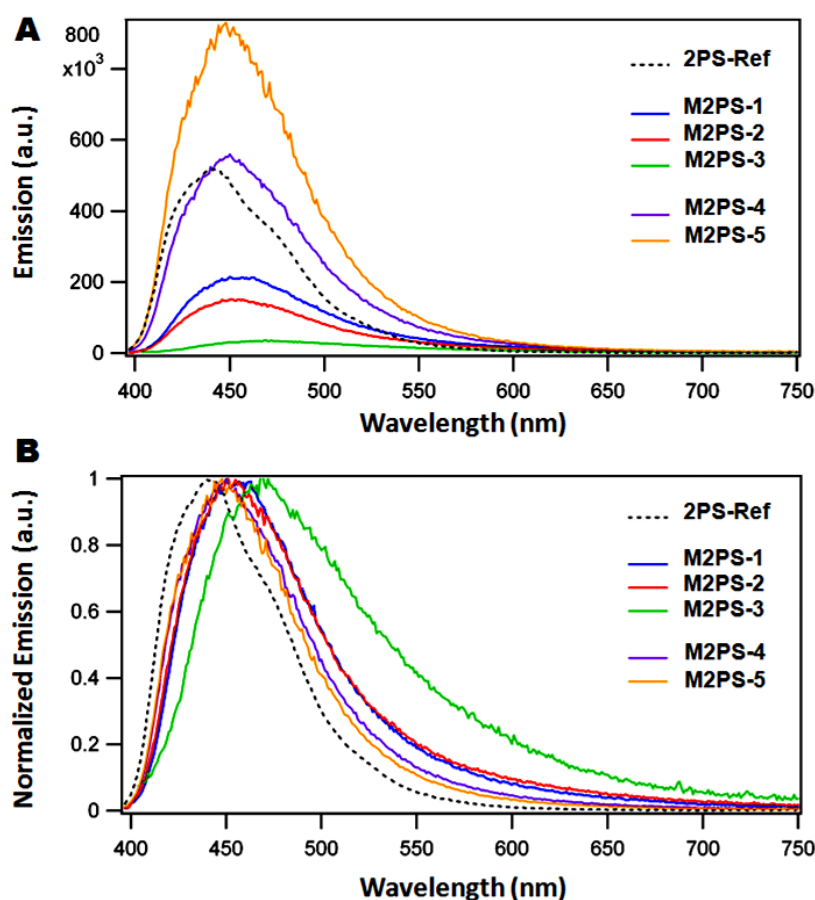


Figure 2. Fluorescence emission spectra of M2PS NPs (A), and the associated normalized spectra in ethanol (B).

Finally, the two-photon photophysical properties of the M2PS nanocarriers were investigated. The two-photon absorption cross-sections (σ_2) were determined between 700 and 900 nm by investigating their two-photon excited fluorescence, and as anticipated **M2PS-1**, **M2PS-4**, and **M2PS-5** displayed the highest cross-sections (see Table 3, and Fig. 3). It should be noticed that **M2SP-1**, **M2PS-4**, and **M2PS-5** also exhibit the largest quantum yields (11, 26, and 41%, respectively), while their maximum cross-sections ranged from 110 to 200 GM. In the case of the synthesis at 25 °C, the increase of the 2PS concentration from 8% (**M2PS-1**) to 19% in **M2PS-2** leads to a decrease of both the fluorescence and the two-photon absorption cross-section, from 11 to 8%, from 110 to 80 GM. On the other hand, comparing **M2PS-3** (reaction in water/ethanol) with **M2PS-5** (synthesis in water at 80 °C), which both have 24% of photosensitizer, drastically different properties were obtained. Indeed, the latter exhibits a two-photon brightness ($\sigma_2^{\max} \Phi_F$) of 82 GM, which is 40 times larger than that of the former (2 GM, see Fig. 3B). Furthermore, for a given reaction, the 2PS threshold for optimum properties was different, in the first synthetic approach, 8% was the maximum,

whereas in the third approach the 2PS content could be increased at least up to 25% without quenching the properties. Consequently, the modulation of the two-photon properties of M2PS NPs could be done by an appropriate choice of the elaboration process.

Table 3. Photophysical properties of M2PS NPs in ethanol.

Sample	$\lambda_{\text{abs}}/\lambda_{\text{em}}$ (nm)	Φ_F [a]	σ_2^{max} [b] (GM)	$\sigma_2^{\text{max}} \Phi_F$ (GM)
M2PS-1	386/455	0.11	110	12
M2PS-2	388/453	0.08	80	6
M2PS-3	420/469	0.03	60	2
M2PS-4	385/450	0.26	180	46
M2PS-5	384/448	0.41	200	82

[a] Quinine bisulfate standard at 0.5 M in H₂SO₄. [b] per chromophore.

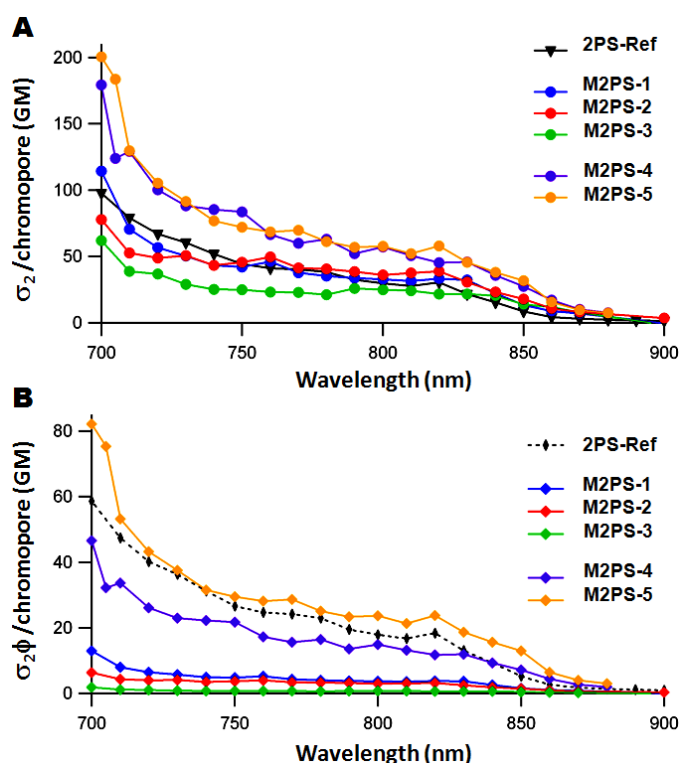


Figure 3. Two-photon absorption cross sections of M2PS NPs (A), and the corresponding two-photon brilliance spectra in ethanol (B).

The two-photon potential of our M2PS NPs for fluorescent imaging was eventually tested *in-vitro* on MCF-7 breast cancer cells. The two-photon laser excitation was carried out via a Carl Zeiss two-photon confocal microscope at low laser power and 760 nm. M2PS NPs were incubated for 24 h with MCF-7 cancer cells at 40 $\mu\text{g.mL}^{-1}$ in 384 multiwell glass

bottomed plate. On the one hand the fluorescence imaging confirmed the endocytosis of the M2PS NPs (Fig. 4), and on the other hand this experiment illustrated the multifunctionality of the two-photon-sensitive fluorescent M2PS nanocarriers for nanomedicine.

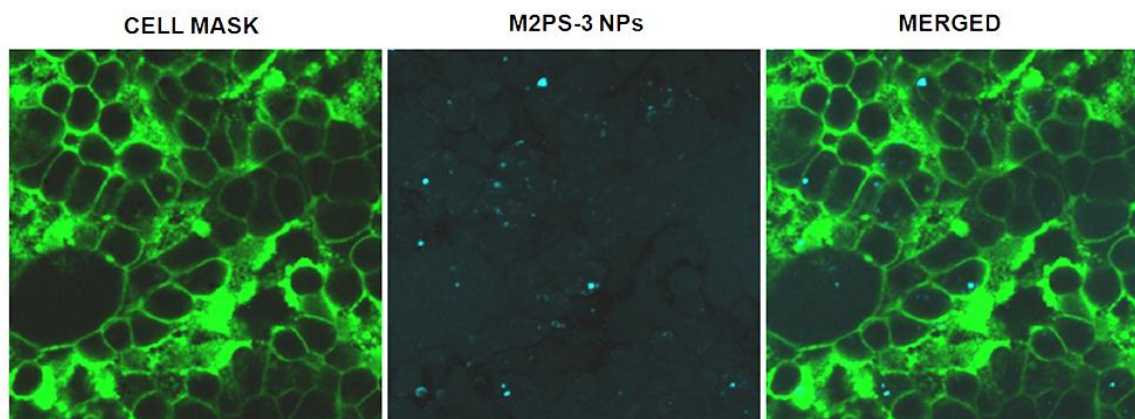


Figure S4. Two-photon *in vitro* imaging of M2PS-3 NPs, demonstrating the cellular uptake of the nanocarrier.

Conclusion

In summary, we report a systematic study of the properties of organically modified mesoporous silica NPs for two-photon excitation. The modulation of the two-photon properties was found to be highly dependent on the synthetic approach used, which directly affected the spatial distribution of the photosensitizers. Furthermore, the threshold of the photosensitizer maximum concentration varied according to the elaboration method, the best results being observed with a modified Mann's reaction in aqueous media at 25 °C for low concentration, whereas the Lin's method at 80°C in water was preferred at higher concentrations. Hence, M2PS nanomaterial was used for *in-vitro* two-photon fluorescence imaging. This study highlights the intricacies implied in the design of efficient NIR two-photon-sensitive nanomaterials for various applications such as nanomedicine.

REFERENCES

1. S. S. Banerjee and D.-H. Chen, *Nanotechnology*, 2009, **20**, 185103.
2. M. Gary-Bobo, Y. Mir, C. Rouxel, D. Brevet, I. Basile, M. Maynadier, O. Vaillant, O. Mongin, M. Blanchard-Desce, A. Morère, M. Garcia, J.-O. Durand and L. Raehm, *Angew. Chem. Int. Ed.*, 2011, **123**, 11627-11631.
3. J.-L. Li, H.-C. Bao, X.-L. Hou, L. Sun, X.-G. Wang and M. Gu, *Angew. Chem. Int. Ed.*, 2012, **51**, 1830-1834.
4. Y. Chen, Y. Zhang, W. Liang and X. Li, *Nanomedicine: NBM*, 2012, **8**, 1267-1270.
5. J. Croissant, A. Chaix, O. Mongin, M. Wang, S. Clément, L. Raehm, J.-O. Durand, V. Hugues, M. Blanchard-Desce, M. Maynadier, A. Gallud, M. Gary-Bobo, M. Garcia, J. Lu, F. Tamanoi, D. P. Ferris, D. Tarn and J. I. Zink, *Small*, 2014, n/a-n/a.
6. J. Croissant, M. Maynadier, A. Gallud, H. Peindy N'Dongo, J. L. Nyalosaso, G. Derrien, C. Charnay, J.-O. Durand, L. Raehm, F. Serein-Spirau, N. Cheminet, T. Jarrosson, O. Mongin, M. Blanchard-Desce, M. Gary-Bobo, M. Garcia, J. Lu, F. Tamanoi, D. Tarn, T. M. Guardado-Alvarez and J. I. Zink, *Angew. Chem. Int. Ed.*, 2013, **125**, 14058-14062.
7. R. Banerjee, Y. Katsenovich, L. Lagos, M. McIntosh, X. Zhang and C. Z. Li, *Curr. Med. Chem.*, 2010, **17**, 3120-3141.
8. S. Kim, T. Y. Ohulchanskyy, H. E. Pudavar, R. K. Pandey and P. N. Prasad, *J. Am. Chem. Soc.*, 2007, **129**, 2669-2675.
9. M. Pawlicki, H. A. Collins, R. G. Denning and H. L. Anderson, *Angew. Chem. Int. Ed.*, 2009, **48**, 3244-3266.
10. Z. Li, J. C. Barnes, A. Bosoy, J. F. Stoddart and J. I. Zink, *Chem. Soc. Rev.*, 2012, **41**, 2590-2605.
11. M. W. Ambrogio, C. R. Thomas, Y.-L. Zhao, J. I. Zink and J. F. Stoddart, *Acc. Chem. Res.*, 2011, **44**, 903-913.
12. P. Yang, S. Gai and J. Lin, *Chem. Soc. Rev.*, 2012, **41**, 3679-3698.
13. I. I. Slowing, J. L. Vivero-Escoto, B. G. Trewyn and V. S. Y. Lin, *J. Mater. Chem.*, 2010, **20**, 7924-7937.
14. K. K. Coti, M. E. Belowich, M. Liong, M. W. Ambrogio, Y. A. Lau, H. A. Khatib, J. I. Zink, N. M. Khashab and J. F. Stoddart, *Nanoscale*, 2009, **1**, 16-39.
15. B. G. Trewyn, I. I. Slowing, S. Giri, H.-T. Chen and V. S. Y. Lin, *Acc. Chem. Res.*, 2007, **40**, 846-853.
16. J. Kecht, A. Schlossbauer and T. Bein, *Chem. Mater.*, 2008, **20**, 7207-7214.
17. V. Lebre, L. Raehm, J. O. Durand, M. Smaïhi, M. H. V. Werts, M. Blanchard-Desce, D. Méthy-Gonnod and C. Dubernet, *J. Sol-Gel Sci. Technol.*, 2008, **48**, 32-39.
18. E. Chelebaeva, L. Raehm, J. O. Durand, Y. Guari, J. Larionova, C. Guerin, A. Trifonov, M. Willinger, K. Thangavel, A. Lascialfari, O. Mongin, Y. Mir and M. Blanchard-Desce, *J. Mater. Chem.*, 2010, **20**, 1877-1884.
19. T. M. Guardado-Alvarez, L. Sudha Devi, M. M. Russell, B. J. Schwartz and J. I. Zink, *J. Am. Chem. Soc.*, 2013, **135**, 14000-14003.
20. V. Lebre, L. Raehm, J.-O. Durand, M. Smaïhi, M. H. V. Werts, M. Blanchard-Desce, D. Méthy-Gonnod and C. Dubernet, *J. Biomed. Nanotechnol.*, 2010, **6**, 176-180.
21. T. M. Guardado-Alvarez, L. S. Devi, J.-M. Vabre, T. A. Pecorelli, B. J. Schwartz, J.-O. Durand, O. Mongin, M. Blanchard-Desce and J. I. Zink, *Nanoscale*, 2014, **6**, 4652-4658.
22. P. Couleaud, V. Morosini, C. Frochot, S. Richeter, L. Raehm and J. O. Durand, *Nanoscale*, 2010, **2**, 1083-1095.
23. X. Wang, A. R. Morales, T. Urakami, L. Zhang, M. V. Bondar, M. Komatsu and K. D. Belfield, *Bioconjugate Chem.*, 2011, **22**, 1438-1450.
24. E. Beaumont, J.-C. Lambry, M. Blanchard-Desce, P. Martasek, S. P. Panda, E. E. H. van Faassen, Brochon, E. Deprez, A. Slama-Schwok, *ChemBiochem.*, 2009, **10**, 690-701.
25. C. E. Fowler, D. Khushalani, B. Lebeau and S. Mann, *Adv. Mater.*, 2001, **13**, 649-652.
26. H.-P. Lin and C.-P. Tsai, *Chem. Lett.*, 2003, **32**, 1092-1093.
27. H. Y. Woo, B. Liu, B. Kohler, D. Korystov, A. Mikhailovsky and G. C. Bazan, *J. Am. Chem. Soc.*, 2005, **127**, 14721-14729.

APPENDIX: SUPPLEMENTARY INFORMATION

I- EXPERIMENTAL SECTION

Materials. Tetraethoxysilane (TEOS), cetyltrimethylammonium bromide (CTAB), sodium hydroxide, ammonium nitrate and tetrahydrofuran were purchased from Sigma-Aldrich. Absolute ethanol was purchased from Fisher Chemicals. R. Norma Pure

Apparatus. Absorption spectra were recorded on a Hewlett-Packard 8453 spectrophotometer and fluorescence data were collected on a Perkin-Elmer LS55 fluorimeter. Mass spectrometry was carried out at the Laboratoire de Spectrométrie de Masse (Lyon, France) with a Thermo-Finnigan MAT95 apparatus in electronic impact ionization mode. Dynamic light scattering analyses were performed using a Cordouan Technologies DL 135 Particle size analyzer instrument. ^{29}Si and ^{13}C CPMAS solid state NMR sequences were recorded with a VARIAN VNMRS300, using Q8MH8 and adamantane references respectively. TEM analysis performed on a JEOL 1200 EXII instrument. SEM analysis performed on a FEI Quanta FEG 200 instrument. ^1H and ^{13}C NMR spectra were recorded with a Bruker AC 400 spectrometer. Chemical shifts (in δ units, ppm) are referenced to TMS using CHCl_3 ($\delta = 7.26$ ppm) and CDCl_3 ($\delta = 77.0$ ppm) as the internal standards, respectively, for ^1H and ^{13}C NMR spectra. IR spectra were recorded on a Perkin-Elmer 100 FT spectrophotometer. Absorption spectra were recorded on a Hewlett-Packard 8453 spectrophotometer and fluorescence data were collected on a Perkin-Elmer LS55 fluorimeter. Mass spectrometry was carried out at the Laboratoire de Spectrométrie de Masse (Lyon, France) with a Thermo-Finnigan MAT95 apparatus in electrospray ionization mode.

II- TWO-PHOTON PHOTSENSITIZER SYNTHESIS AND CHARACTERIZATIONS

2PS synthesis. A general scheme of this multistep synthesis is presented in figure S1, each step is numbered and described as follows.

1) Wittig reaction: To a mixture composed of absolute ethanol (100 mL), 4-nitrocinnamadehyde (9.35 g, 52.7 mmol), and (4-nitrobenzyl)triphenylphosphonium bromide (25.35 g, 52.7 mmol) stirred in a 1 L round bottom flask, was added a solution of potassium tert-butoxide (17.1 g, 152.4 mmol) in absolute ethanol (300 mL) via cannula. The reaction mixture was stirred for 24 h at room temperature. Afterwards, deionized water (250 mL) was added to precipitate the product, which was collected through filtration and washed with an ethanol/water mixture (60:40 v:v).

2) Photoisomerization: The crude product was dissolved in anhydrous tetrahydrofurane (THF, 300 mL) in a 1 L round bottom flask to which an iodine (I_2 , 40 mg) solution in THF

(30 mL) was added. 365 nm irradiation (75 W) was applied for 42 h. A saturated aqueous solution of sodium thiosulfate (100 mL, 275 g) was then poured to induce the precipitation. The resulting mixture was stirred for 40 minutes, and filtered. The precipitate was dried under vacuum. The overall yield of these two reactions was of 99%, leading to (*E,E*)-bis(4-nitrophenyl)butadiene (15.4 g, 52 mmol).

3) Reduction of the nitro groups: The resulting (*E,E*)-photoisomerized compound (15.4 g, 52.0 mmol) was stirred overnight at 73 °C with tin chloride (93.1 g, 491 mmol) in absolute ethanol (200 mL) in a two necks 500 mL round bottom flask previously flushed with argon. Then, an aqueous solution of sodium hydroxide (10 g, 250 mmol, H₂O, 160 mL) was slowly added until the solution reached a pH of 8, which induced the precipitation of the tin by-products. The compound was mixed with ethyl acetate (600 mL) in a 1 L round bottom flask, and vigorously stirred for 12 h under reflux. Finally, the resulting mixture was filtered, and the solid was subjected again to a 12 h extraction at reflux. The operation was repeated several times until complete extraction. The yield of the reaction was of 92%, leading to the bis(4-aminophenyl)butadiene (11.3 g, 47.8 mmol).

4) Propargylation: To the as-prepared diamine (3.0 g, 12.7 mmol) dissolved in an ethanol/water mixture (80:20 v:v, 100 mL), was added potassium carbonate (12 g, 86.8 mmol), and the solution was stirred vigorously under reflux. Propargyl bromide (80% in toluene, 10 mL, 89.8 mmol) was added through micropipette, and the reaction mixture was refluxed for 3 days. The product was purified via chromatographic separation using a mixture of dichloromethane/pentane (80/20, v:v) as eluent. The yield of the reaction was of 75% (down to 55% when the reaction was scaled-up by 4), leading to the tetrapropargylylated compound (3.7 g, 9.5 mmol). ¹H NMR (200 MHz, CDCl₃): δ 7.42 (d, ³J = 8.75 Hz, 4H, H_{Ph}-butadiene), 6.97 (d, ³J = 8.78 Hz, 4H, H_{Ph}-amine), 6.82 (dd, ³J = 12.17, 2.89 Hz, 2H vinyl), 6.57 (dd, ³J = 11.9, 2.73 Hz, 2H, vinyl central), 4.17 (d, ⁴J = 2.27 Hz, 8H, N-CH₂), 2.30 (t, ⁴J = 2.2 Hz, 4H, CH₂-C≡CH). ¹³C NMR (400 MHz, CDCl₃): δ 131.2, 129.4, 129.1, 127.3, 127.2, 115.6, 79.1, 72.8, 40.4. IR (neat KBr) $\nu_{\text{max}}/\text{cm}^{-1}$ = 3257, 3014, 2827, 2105, 1636, 1601, 1560, 1541, 1511, 1457, 1418, 1365, 1346, 1323, 1292, 1256, 1237, 1215, 1185, 1145, 1117, 916, 894, 847, 804, 751, 700, 684, 597, 513, 450, 423. UV/Vis λ_{max} (EtOH): 368 nm. MS (ESI+) *m/z* (%): 350.2 (100) [trialkyl fragment], 388.2 (19) [M^{•+}], 389.2 (17) [MH⁺], 390.2 [MH⁺ ¹³C]. HRMS (ESI+): *m/z* calcd for C₂₈H₂₄N₂: 388.1939, found 388.1936. The rare phenomenon of the formation of the [M^{•+}] does occur in this ESI+ analysis due to the conjugated structure of the molecule (see also 2PS Ref). This is consistent with the intensities of the peaks of the [M^{•+}] (19), and [MH⁺] (17) which do not correspond to the isotopic proportions.

5) CuAAC coupling: To a mixture of the tetrapropargylylated precursor (200 mg, 5.15.10⁻¹ mmol) and [CuBr(PPh₃)₃] (15 mg, 1.6.10⁻² mmol) in anhydrous tetrahydrofuran (THF, 2.5 mL) placed in a 10 mL microwave sealable reactor was added (3-azidopropyl)triethoxysilane (510 mg, 2.06 mmol). The tube was flushed with argon, then microwave irradiation (max power 200 W, 100 °C, 15 min) was applied. After evaporation of the solvents, extraction with pentane and concentration, the 2PS was quantitatively obtained as a slightly brown solid (710 mg, 5.15.10⁻¹ mmol). ¹H NMR (200 MHz, CDCl₃): δ 7.48 (d, ³J = 6.0 Hz, 4H, H_{Ph}-butadiene),

7.30 (s, 4H, triazole), 6.89 (d, $^3J = 6.5$ Hz, 4H, $H_{\text{Ph-amine}}$), 6.78 (d, $^3J = 14.4$ Hz, 2H, vinyl), 6.53 (d, $^3J = 12.2$ Hz, 2H, vinyl central), 4.71 (s, 8H, N- CH_2 -triazol), 4.31 (t, $^3J = 7.0$ Hz, 8H, Triazol- CH_2), 3.80 (q, $^3J = 6.9$ Hz, 24H, O- CH_2 -CH $_3$), 1.99 (t, $^3J = 7.8$ Hz, 8H, Triazol-CH $_2$ -CH $_2$), 1.21 (t, $^3J = 6.8$ Hz, 36H, O-CH $_2$ -CH $_3$), 0.57 (t, $^3J = 7.9$ Hz, 8H, CH $_2$ -Si). ^{13}C NMR (400 MHz, CDCl_3): δ 147.3, 145.2, 130.9, 127.7, 127.5, 126.6, 122.1, 113.7, 58.6, 52.6, 47.0, 24.3, 18.4, 8.1. ^{29}Si NMR (400 MHz, CDCl_3): δ -46.9. IR (neat KBr) $\nu_{\text{max}}/\text{cm}^{-1} = 3117, 3068, 3013, 2950, 2929, 2857, 1604, 1562, 1521, 1457, 1374, 1337, 1299, 1261, 1213, 1186, 1102, 1053, 1025, 982, 941, 835, 808, 793, 577, 518$. UV/Vis λ_{max} (EtOH): 374 nm. Emission (EtOH): $\lambda_{\text{max}} = 416, 438$ nm ($\lambda_{\text{excitation}} = 388$ nm). MS (ESI+) m/z (%): 279.0 (100) [OPPh_3], 689.2 (7) [MH_2^{2+}], 1378.74 (1) [MH^+]. HRMS (ESI+): m/z calcd for $\text{C}_{64}\text{H}_{109}\text{N}_{14}\text{O}_{12}\text{Si}_4$: 1377.7427, found 1377.7426.

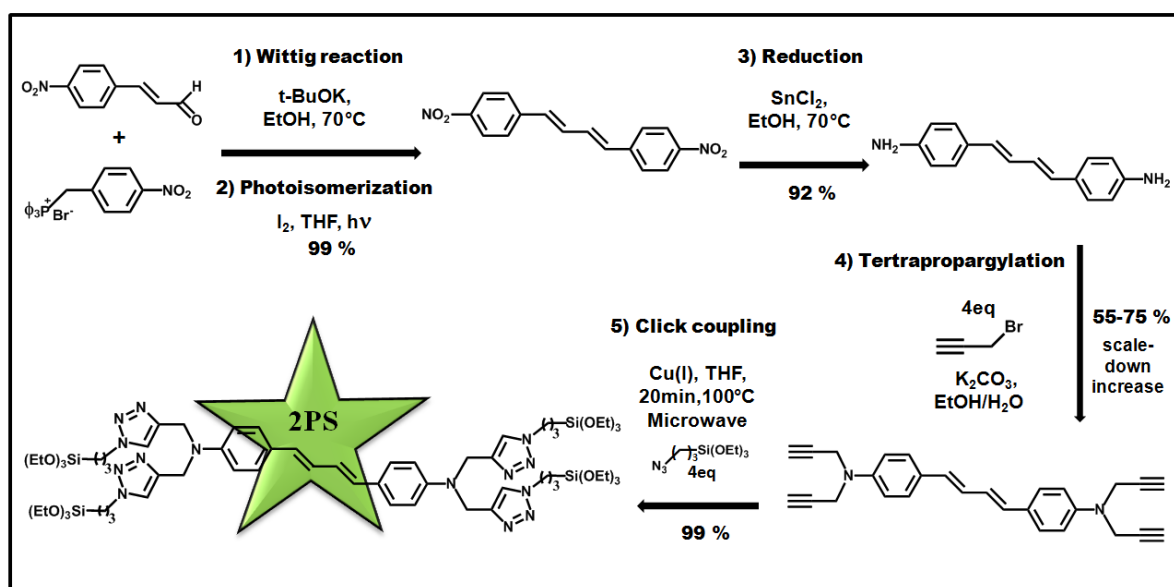


Figure S1. Multistep synthetic pathway to design the two-photon photosensitizer (2PS).

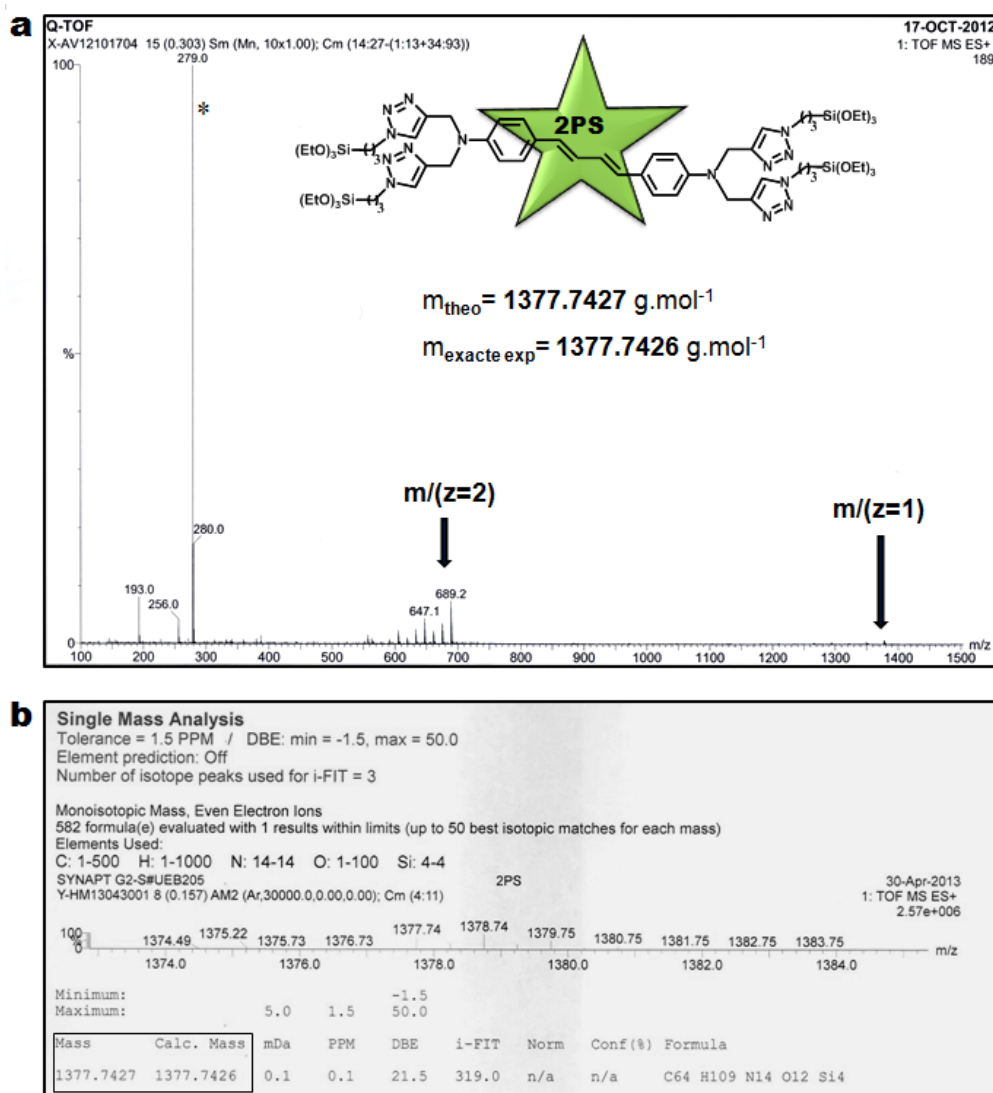


Figure S2. Q-TOF high resolution mass spectrum of the 2PS (a), and the high resolution single mass analysis (b). *Triphenylphosphine oxide.

III- TWO-PHOTON REFERENCE SYNTHESIS AND CHARACTERIZATIONS

2PS ref synthesis. The synthesis of the spectroscopic reference was done by modifying the fifth step of the 2PS procedure using hexylazide (262 mg, 2.06 mmol) as click partner through microwave irradiation (max power = 200 W, 100 °C, 14 min) (see Figure S3 below). The reaction was also quantitative (463 mg, 5.15.10⁻¹ mmol). ¹H NMR (200 MHz, CDCl₃): δ 7.49 (d, ³J = 6.5 Hz, 4H, H_{Ph}-butadiene), 7.33 (s, 4H, triazol), 6.94 (d, ³J = 7.4 Hz, 4H, H_{Ph}-amine), 6.78 (d, ³J = 14.2 Hz, 2H, vinyl), 6.51 (d, ³J = 13.8 Hz, 2H, vinyl central), 4.73 (s, 8H, N-CH₂), 4.31 (t, ³J = 7.2 Hz, 8H, Triazol-CH₂), 1.88 (m, 8H, Triazol-CH₂-CH₂), 1.30 (m, 24H, CH₂ alkyl), 0.90 (t, ³J = 7.9 Hz, 12H, CH₃ alkyl). ¹³C NMR (300 MHz, CDCl₃): δ 147.4, 145.5, 131.2, 130.8, 127.7, 127.0, 122.3, 114.2, 50.8, 47.4, 31.5, 30.6, 26.5, 22.8, 14.3. IR (neat KBr) $\nu_{\text{max}}/\text{cm}^{-1}$ = 3119, 3016, 2957, 2929, 2857, 1605, 1514, 1503, 1462, 1371, 1333, 1296, 1201, 1186, 1142, 1101, 1054, 1026, 981, 941, 835, 793, 512, 476. UV/Vis λ_{max} (EtOH): 378

nm. Emission (EtOH): $\lambda_{\text{max}} = 442 \text{ nm}$ ($\lambda_{\text{excitation}} = 388 \text{ nm}$). MS (ESI+) m/z (%): 279.1 (6) [OPPh₃], 449.3 (100) [MH₂²⁺], 732.5 (8) [trialkyl fragment], 897.7 (27) [M^{•+}], 898.7 (15) [MH⁺]. HRMS (ESI+): m/z calcd for C₅₂H₇₇N₁₄: 897.6457, found 897.6456.

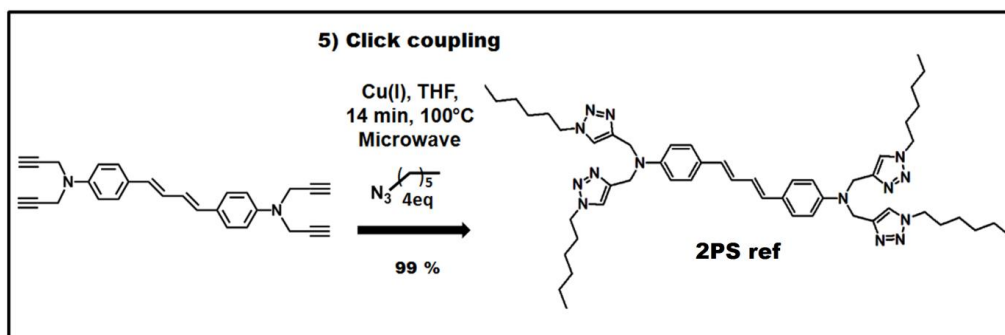


Figure S3. Modified CuAAC reaction to design the two-photon photosensitizer reference (2PS ref).

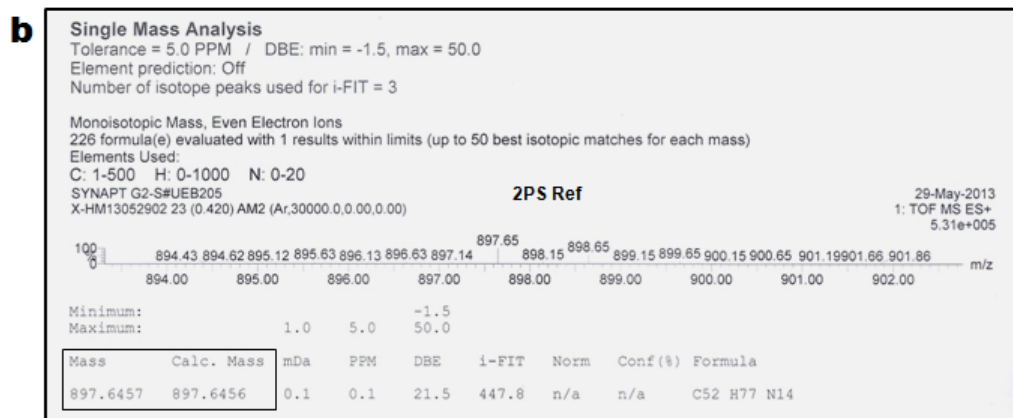
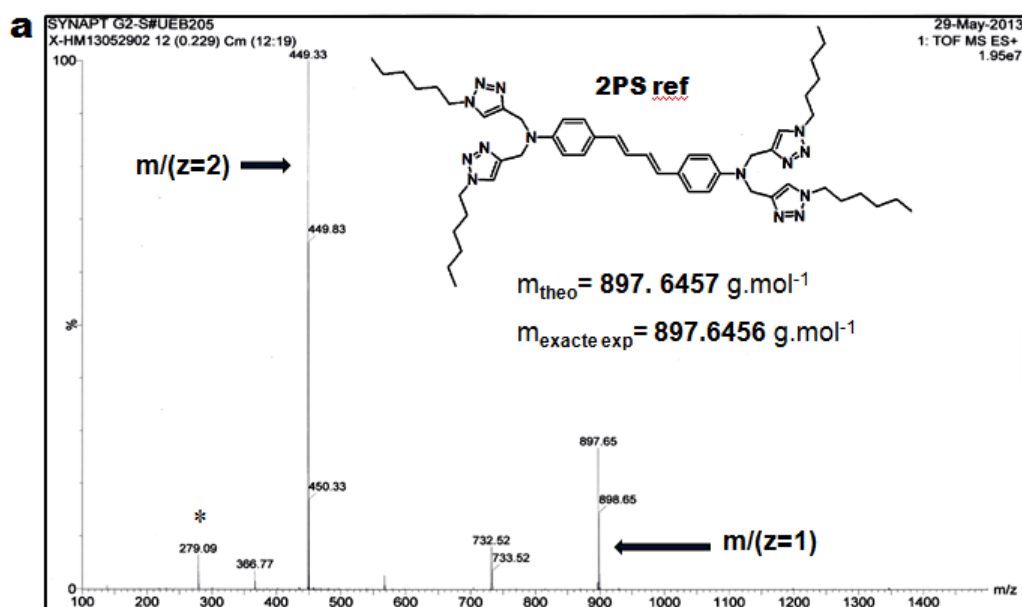


Figure S4. Q-TOF high resolution mass spectrum of the 2PS ref (a), and the high resolution single mass analysis (b). *Triphenylphosphine oxide.

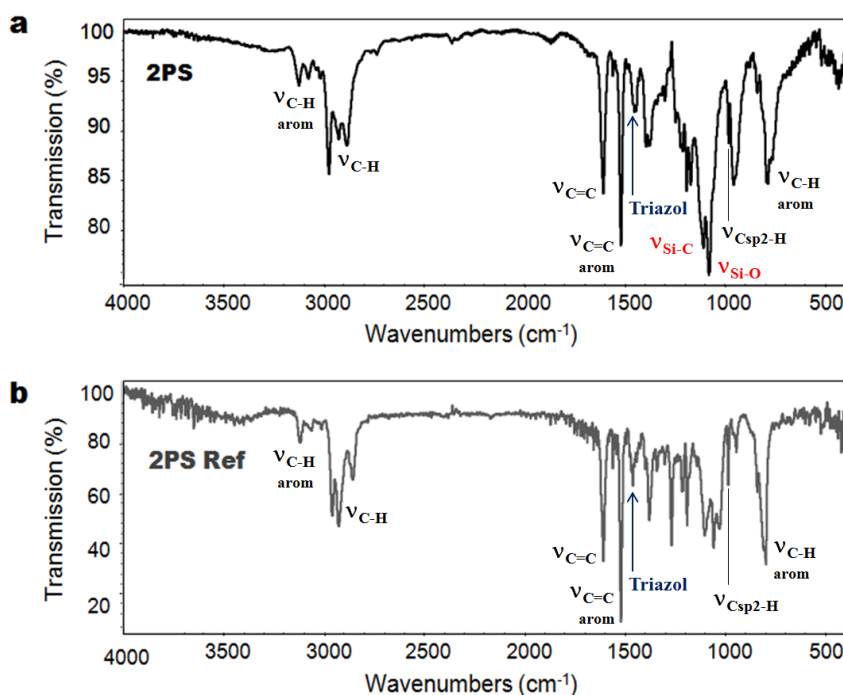


Figure S5. FTIR spectra comparison of the 2PS and the 2PS ref compounds (a and b respectively), validating the disappearance of the Si-O bonds ($1000\text{--}1100\text{ cm}^{-1}$) in the 2PS ref, while retaining the C=C conjugated structure ($1100\text{--}1650\text{ cm}^{-1}$).

IV- NANOMATERIALS SYNTHESSES AND CHARACTERIZATIONS

M2PS-1 NPs. A mixture of CTAB (345 mg), and sodium hydroxide (20 mL, 0.2 M) was stirred at room temperature during 50 minutes at 700 rpm in a 250 mL three neck round bottom flask. Then, the stirring speed was changed to 1000 rpm. TEOS (1.6 mL) was added and after 40 seconds water (260 mL) was poured out. Afterwards, an ethanolic solution of the 2PS precursor ($n_0 = 9.0 \cdot 10^{-5}$ mol, in 1 mL EtOH) was added. The solution was then heated using a hair drier (from $T_0=25\text{ }^{\circ}\text{C}$ to $T'=27\text{ }^{\circ}\text{C}$ over 1-2 minutes), in order to trigger the condensation process. After 5 minutes 30 seconds of reaction, a solution of hydrochloric acid (0.2 M, *ca* 36 mL) was added to reach pH 6.9. Fractions were gathered in polypropylene tubes and collected by centrifugation for 15 minutes at 21 krpm. The sample was then extracted twice with an ethanolic solution of ammonium nitrate (6 g.L^{-1}), and washed thrice with ethanol, water, and ethanol. Each extraction involved a sonication step of 30 minutes at $50\text{ }^{\circ}\text{C}$; the collection was carried out in the same manner. The as-prepared material was dried under air flow for few hours.

M2PS-2 NPs. A mixture of CTAB (345 mg), and sodium hydroxide (20 mL, 0.2 M) was stirred at room temperature during 50 minutes at 700 rpm in a 250 mL three neck round bottom flask. Then, the stirring speed was changed to 1000 rpm, TEOS (1.6 mL) was added along with an ethanolic solution of the 2PS precursor ($n_0 = 1.3 \cdot 10^{-4}$ mol, in 1 mL EtOH). After 40 seconds, water (260 mL) was poured out. The solution was then heated using a hair drier (from $T_0=25\text{ }^{\circ}\text{C}$ to $T'=27\text{ }^{\circ}\text{C}$ over 1-2 minutes), in order to trigger the condensation

process. After 5 minutes 30 seconds of reaction, a solution of hydrochloric acid (0.2 M, *ca* 36 mL) was added to reach a pH of 6.9. Fractions were gathered in polypropylene tubes and collected by centrifugation for 15 minutes at 21 krpm. Extraction and following steps were identical to those of M2PS-1 NPs.

M2PS-3 NPs. A mixture of CTAB (640 mg), deionized water (100 mL), and ethanol (40 mL) was stirred at 80°C for 40 minutes at 650 rpm in a 250 mL three neck round bottom flask. Then, an ethanolic solution of 2PS ($n_0 = 9.0 \times 10^{-5}$ mol, in 1 mL EtOH) was added to the stirred solution. A delay of 5 minutes was used to homogenize the solution, and TEOS (1.2 mL) was added via a syringe then the stirring speed was changed to 1000 rpm. The reaction was conducted for 30 minutes, then the solution was neutralized with hydrochloric acid (0.2 M), and the mixture was cooled down to room temperature. Fractions were gathered in polypropylene tubes and collected by centrifugation for 15 minutes at 21 krpm. Extraction and following steps were identical to those of M2PS-1 NPs.

M2PS-4 NPs. A mixture of CTAB (250 mg), distilled water (120 mL), and sodium hydroxide (875 μ L, 2 M) was stirred at 80°C for 50 minutes at 700 rpm in a 250 mL three neck round bottom flask. Then, TEOS (1.0 mL) was added along with the two-photon photosensitizer ($n_0 = 2.0 \times 10^{-4}$ mol, in 1 mL of dry THF), and the condensation process was conducted for 1 hour 30 minutes. Afterwards, the solution was cooled to room temperature while stirring; fractions were gathered in polypropylene tubes and collected by centrifugation for 15 minutes at 21 krpm. Extraction and following steps were identical to those of M2PS-1 NPs.

M2PS-5 NPs. A mixture of CTAB (250 mg), distilled water (120 mL), and sodium hydroxide (875 μ L, 2 M) was stirred at 80°C during 50 minutes at 700 rpm in a 250 mL three neck round bottom flask. Then, TEOS (1.0 mL) was added along with the two-photon photosensitizer ($n_0 = 6.4 \times 10^{-5}$ mol, in 1 mL of dry THF), and the condensation process was conducted for 1 hour 30 minutes. Afterwards, the solution was cooled to room temperature while stirring; fractions were gathered in polypropylene tubes and collected by centrifugation for 15 minutes at 21 krpm. Extraction and following steps were identical to those of M2PS-1 NPs.

TPE fluorescence and measurements of the two-photon absorption cross-sections. Two-photon excited fluorescence spectroscopy was performed using a mode-locked Ti:sapphire laser generating 150 fs wide pulses at a 76 MHz rate, with a time-averaged power of several hundreds of mW (Coherent Mira 900 pumped by a 5 W Verdi). The laser light is attenuated using a combination of half-wave plates and a Glan-laser polariser and the excitation power is further controlled using neutral density filters of varying optical density mounted in a computer-controlled filter wheel. After five-fold expansion through two achromatic doublets, the laser beam is focused by a microscope objective (10X, NA 0.25, Olympus, Japan) into a standard 1 cm stirred absorption cuvette containing the sample. The applied average laser power arriving at the sample was between 0.5 and 15 mW, leading to a time-averaged light flux in the focal volume on the order of 0.1-1 mW/ μm^2 . The generated fluorescence is collected in epifluorescence mode, through the microscope objective, and reflected by a dichroic mirror (675dcxru, Chroma Technology Corporation, USA). Residual excitation light

is removed using a barrier filter (e650-2p, Chroma) and the fluorescence is coupled into a 600 μm multimode fiber by an achromatic doublet. The fiber is connected to a compact CCD-based spectrometer (BTC112-E, B&W Tek, USA), which measures the two-photon excited emission spectrum. The emission spectra are corrected for the wavelength-dependence of the detection efficiency using correction factors established through the measurement of reference compounds having known fluorescence emission spectra. Briefly, the set-up allows for the recording of corrected fluorescence emission spectra under multiphoton excitation at variable excitation power and wavelength. Absolute values for the two-photon excitation action cross sections $\sigma_2\Phi_F$ were obtained according to the method described by Xu *et al.* (*J. Opt. Soc. Am. B* **1996**, 13, 481). using 10⁻⁴ M fluorescein in 10⁻² M aqueous NaOH as a reference, applying corrections for the refractive index of the solvent (M. H. V. Werts *et al.*, *Photochem. Photobiol. Sci.* **2005**, 4, 531). In the 700-720 nm excitation range, refined reference values for fluorescein were used. (C. Katan *et al.*, *J. Phys. Chem. B* **2007**, 111, 9468).

Two-photon imaging. The day prior to the experiment, MCF-7 human breast cancer cells (purchased from ATCC) were seeded onto bottom glass dishes (World Precision Instrument, Stevenage, UK) at a density of 10⁶ cells.cm⁻². Then, adherent cells were washed once and incubated in 1 mL medium containing M2PS NPs at a concentration of 40 $\mu\text{g.mL}^{-1}$ for 20 h. 15 minutes before the end of incubation, cells were loaded with Cell Mask (Invitrogen, Cergy Pontoise, France) for membrane staining at a final concentration of 5 $\mu\text{g.mL}^{-1}$. Before visualization, cells were washed gently with phenol red-free Dulbecco's modified Eagle's medium (DMEM). Cells were then scanned with a LSM 780 LIVE confocal microscope (Carl Zeiss, Le Pecq, France), at 760 nm with a slice depth (Z stack) of 0.62 μm .

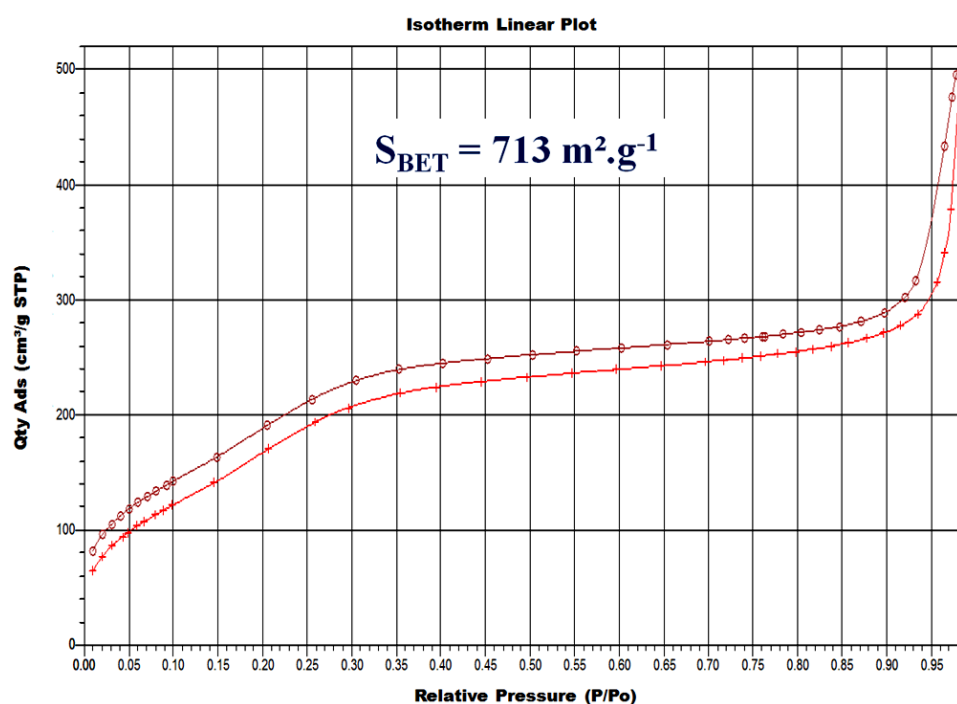


Figure S6. N₂-adsorption-desorption isotherm of M2PS-1 NPs.

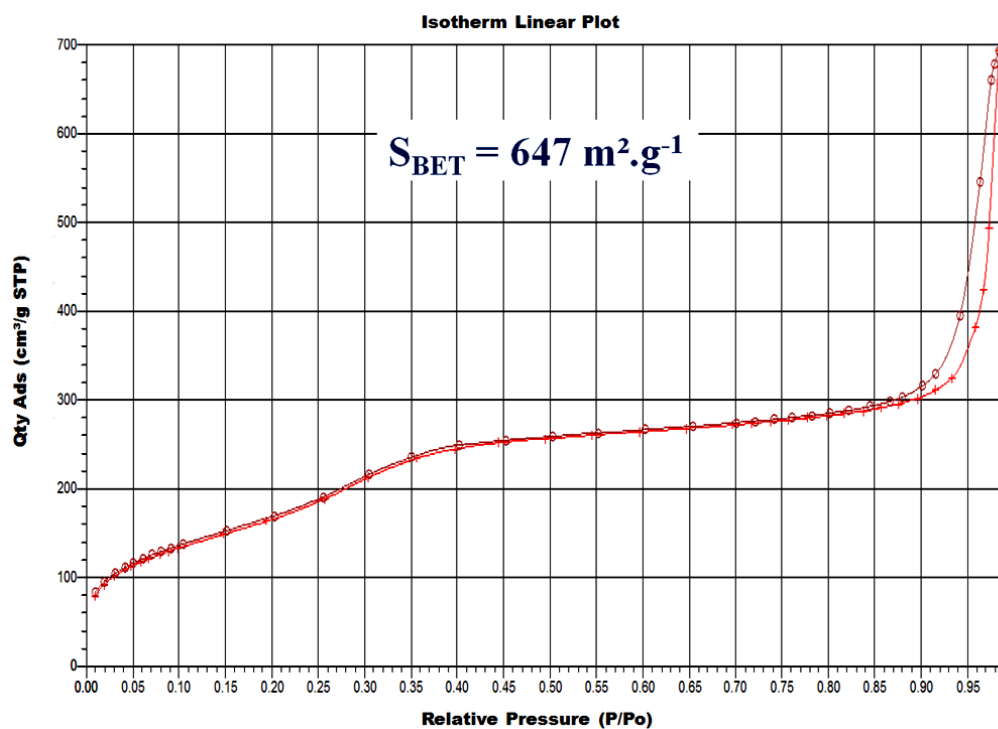


Figure S7. N₂-adsorption-desorption isotherm of M2PS-2 NPs.

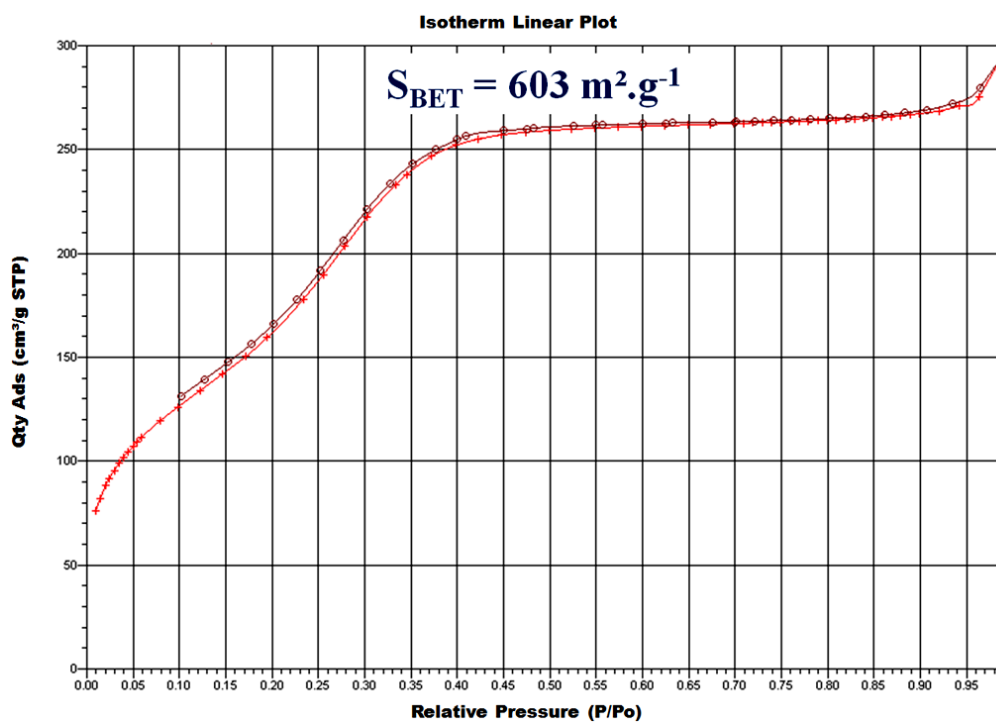


Figure S8. N₂-adsorption-desorption isotherm of M2PS-3 NPs.

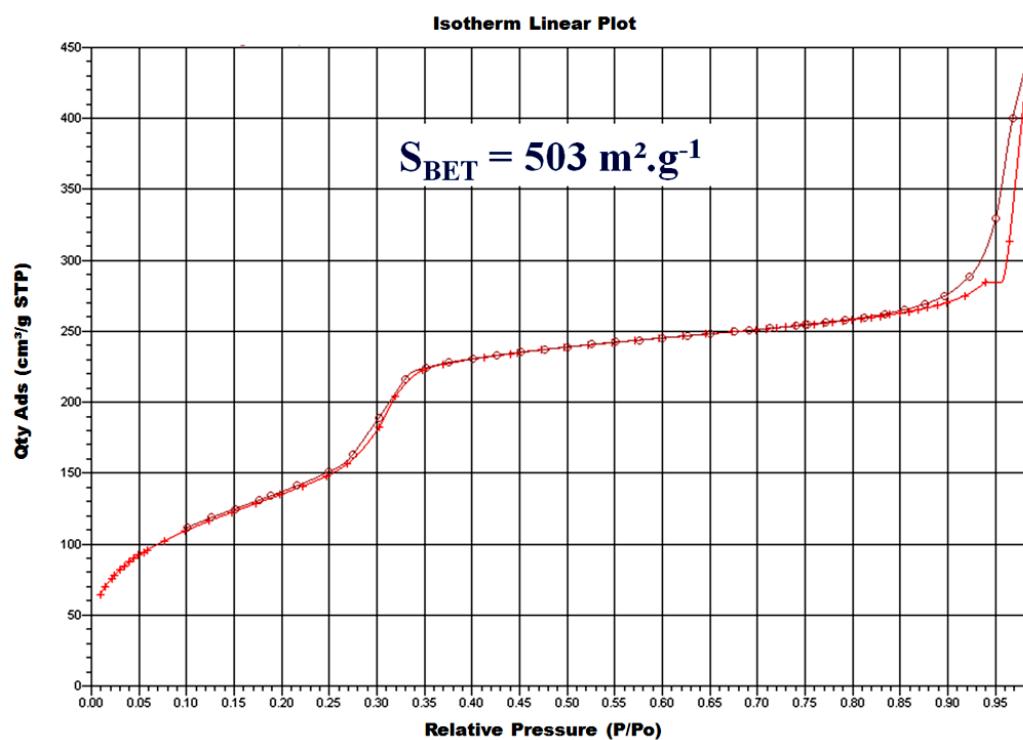


Figure S9. N₂-adsorption-desorption isotherm of M2PS-4 NPs.

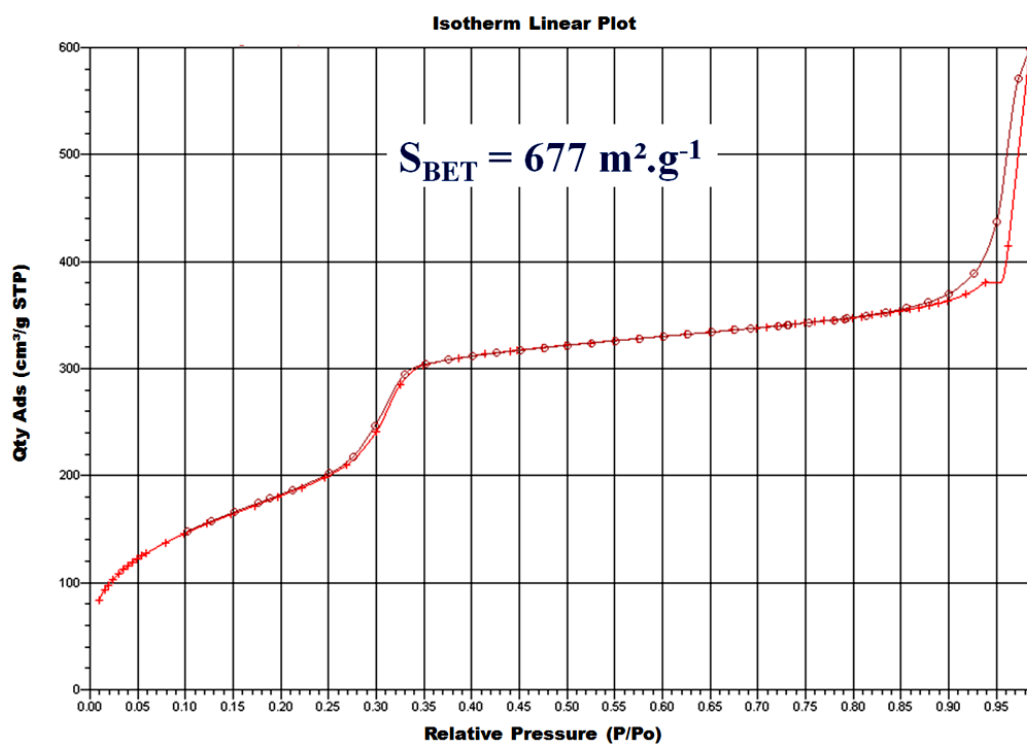


Figure S10. N₂-adsorption-desorption isotherm of M2PS-5 NPs.

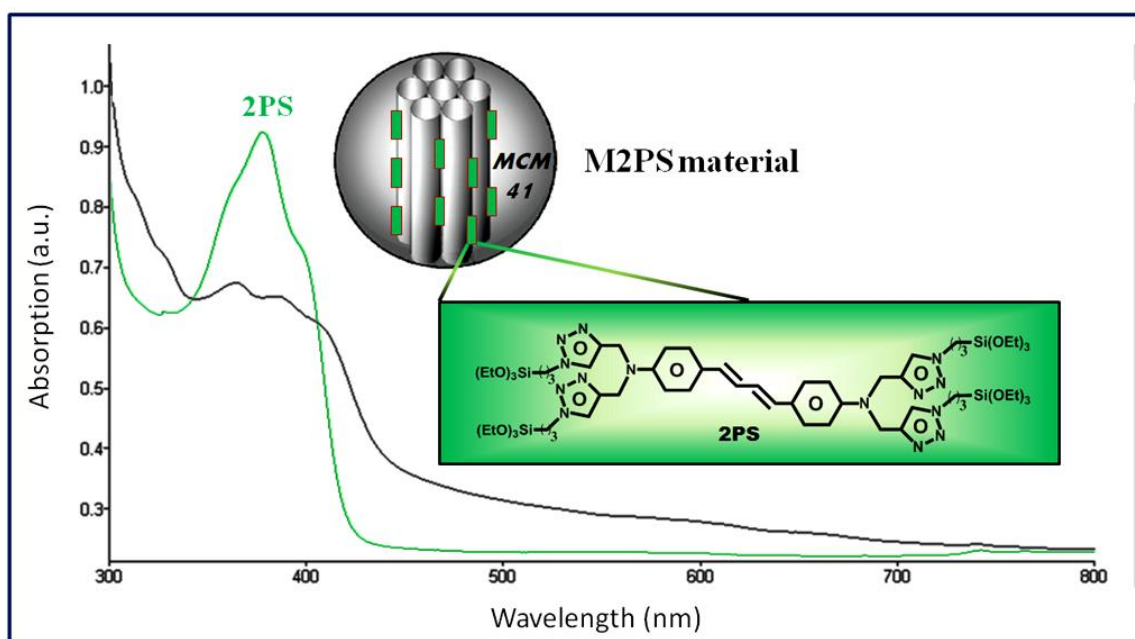


Figure S11. UV-visible spectra of the 2PS precursor and M2PS NPs in ethanol.

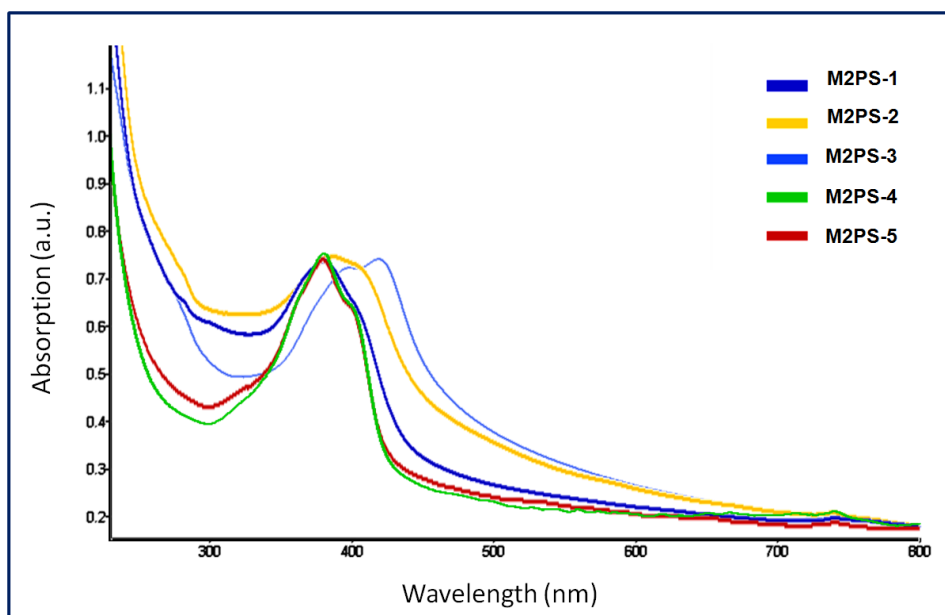


Figure S12. Overlaid UV-visible spectra of M2PS NPs in ethanol depicting the bathochromic effect involved in the 2PS moieties of M2PS-1 to M2PS-3 NPs.

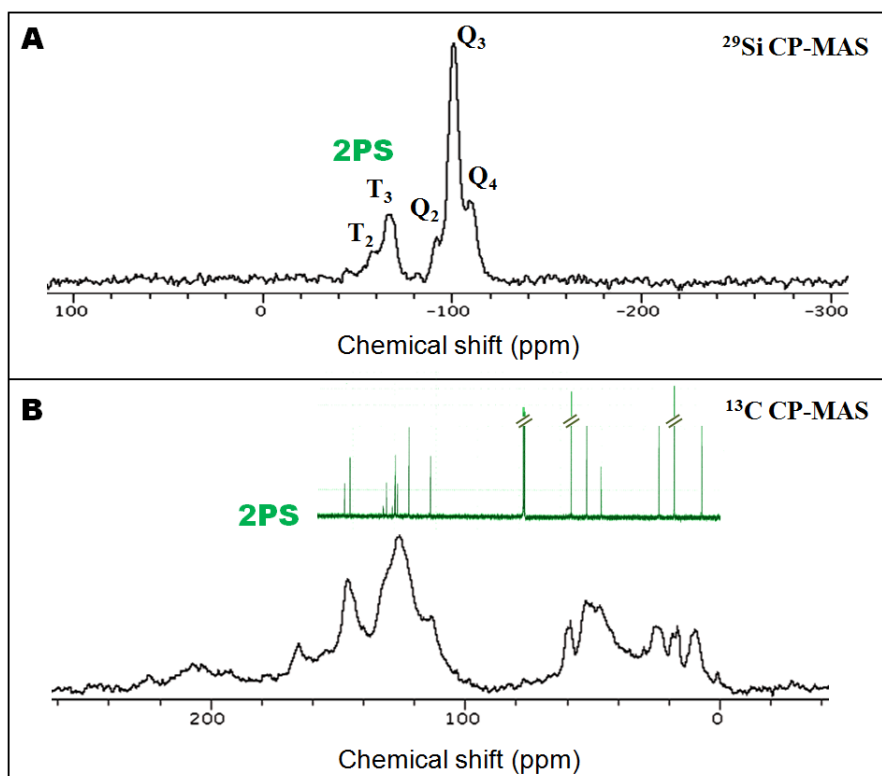


Figure S13. Solid state NMR ^{29}Si (A) and ^{13}C (B) CPMAS spectra on M2PS-4 NPs.

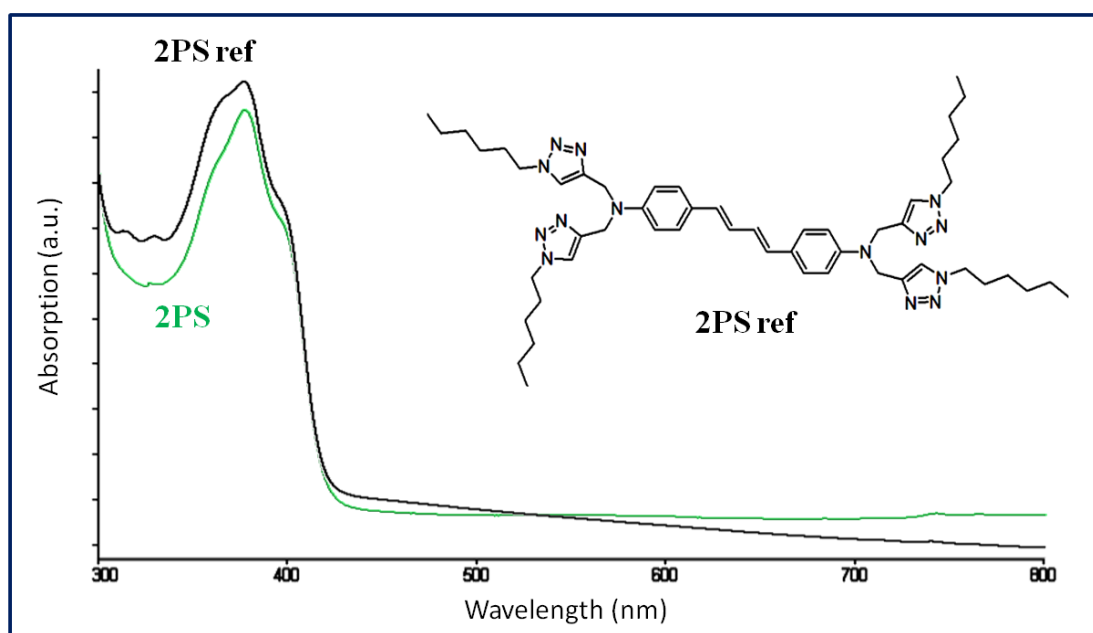


Figure S14. UV-visible spectra of the 2PS and 2PS ref fragments in ethanol.

CHAPTER 5

B. Multifunctional Gold-Mesoporous Nanoplatfom for Synergetic Two-Photon Photodynamic and Photothermal Therapies in Cancer Cells

Abstract

Thanks to its unique spatiotemporal accuracy, two-photon nanomedicine is emerging as a very promising nanomedical tool for cancer treatment. Although, two-photon photodynamic therapy has been achieved via mesoporous nanoscaffolds, the efficiency of the treatment still needs to be improved. Here, it is demonstrated that it is possible to enhance the efficiency of the treatment via synergetic two-photon photodynamic and photothermal therapies in cancer cells. The photothermal feature is harnessed and optimized via a comparative study of the shape and spacial position of gold nanoparticles (AuNPs) with the mesoporous silica nanoparticles (MSN). The resulting multifunctional nanocarriers showed better two-photon imaging properties when gold nanospheres (AuNSs) are encapsulated within the silica, whereas the photothermal and photodynamic synergy is the highest with the MSN surface was decorated with AuNSs. Thus, this study provides insights in the powerful two-photon synergetic potential that is available with gold nanospheres, as demonstrated with more than 60 percent of selective killing of MCF-7 breast cancer cell.

Introduction

Thanks to its unique spatiotemporal accuracy two-photon nanomedicine is emerging as a very promising nanomedical tool for cancer treatment as witnessed by the recently reported nanodevices with two-photon excitation (TPE).^[1-7] Intrinsic properties of this non-linear optical technology provide a three-dimensional resolution of the irradiation, while near-infrared (NIR) TPE enables a deeper tissue penetration (down to 2 cm), lower scattering, and safer treatment than UV-visible excitations.^[8] Recently, mesoporous silica nanoparticles (MSN) have been used *in-vitro* for two-photon fluorescence imaging,^[9, 10] two-photon photodynamic therapy (PDT),^[8, 11, 12] and two-photon-triggered drug delivery.^[13, 14] MSN are indeed excellent candidates for efficient nanomedicine since they are biocompatible, endocytosed and exocytosed by cells,^[15] excreted,^[16] and a suitable nanoplatform for multifunctional theranostics.^[17, 18] Nonetheless, the efficiency of the 2PE treatment often needs to be improved because of low two-photon cross sections. Besides, some studies only encapsulated the photosensitive fragments,^[19, 20] which in turns may decrease the biological efficacy with the leaking out of the dye from the NPs. To circumvent this problem, the photosensible moieties could be covalently attached to the mesoporous silica framework.^[8, 11] One-photon photothermal therapy (PTT), also known as hyperthermia, had been tailored *in-vitro* via gold nanorods (AuNRs) encapsulated in MSN NPs.^[21] To our knowledge, two-photon hyperthermia has not been achieved, and multiple therapeutic features have not been harnessed for cancer treatment with MSN.

Herein it is demonstrated that it is possible to enhance the efficiency of two-photon nanomedicine via synergistic two-photon photodynamic and photothermal therapies in cancer cells. The photothermal feature is harnessed and optimized via a comparative study of the shape and spacial position of gold nanoparticles (AuNPs), either on the surface or within of two-photon-sensitive mesoporous organosilica (M2PS). The resulting multifunctional nanocarriers showed better two-photon fluorescence imaging when gold nanospheres (AuNSs) were combined with MSN, and the synergetic PDT and PTT was most effective with M2PS decorated with AuNSs on their surface. This study provides insights in the powerful two-photon synergetic potential that is available with AuNSs, as demonstrated with 63 percent of selective killing of MCF-7 breast cancer cell.

Results and discussion

First of all, the influence of encapsulated AuNSs within M2PS NPs was assessed. Two types of nanocarriers were designed via sol-gel process and compared, M2PS and gold core M2PS shell (Au@M2PS) NPs (Fig. 1A-B). The M2PS nanomaterial was elaborated by co-condensation of tetraethoxysilane (TEOS) and a two-photon photosensitizer (2PS) (see chapter 5.A) at 80°C for 2 h in an water/ethanol mixture (5:2, v:v) with a sodium hydroxide

catalyst and cetyltrimethylammonium bromide (CTAB) template. The Au@M2PS NPs were constructed via a modified reported one-pot process involving *in-situ* production of monodisperse AuNSs and subsequent sol-gel process at 80°C for 2 h.^[22]

The M2PS and Au@M2PS nanocarriers were then characterized via transmission electron microscopy (TEM, Fig. 1C-D, Fig. S1A-B, S2A-B), which depicted 200 nm monodisperse spherical particles. The narrow size distributions of both systems were confirmed by dynamic light scattering measurement (DLS, Fig. S1C, S2C). Moreover, the successful encapsulation of the 2PS moieties was demonstrated by the absorption band of the 2PS ($\lambda_{\text{max}} = 385 \text{ nm}$) on the UV-visible spectra of the nanomaterials (Fig. S1D, S2D). The 2PS content in the M2PS and Au@M2PS NPs were determined to be of 25 and 31 weight percent (wt%) via elemental analysis of nitrogen atoms (14 per 2PS molecule, see Table S2). The gold core readily visible on the TEM images of Au@M2PS produced the plasmonic band from 500 to 600 nm on the UV-visible spectra (Fig. S2D). Nitrogen-adsorption desorption analysis calculated surface areas of 603 and 808 $\text{m}^2\cdot\text{g}^{-1}$ with the BET theory for M2PS and Au@M2PS respectively, with 2.0 to 2.3 nm BJH pore diameters (Fig. S1E, S2E). The gold core content was determined to be of 4.7% via energy dispersive spectroscopy (Table S1).

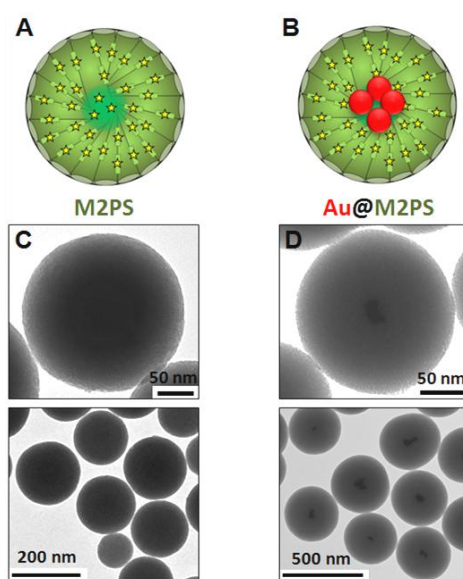


Figure 1. Schematic representation (A-B) and TEM images of M2PS (C), and Au@M2PS NPs (D) where the stars represent the 2PS fragments.

Two-photon *in-vitro* irradiation of M2PS and Au@M2PS was then conducted on MCF-7 breast cancer cells. The NPs were incubated at $40 \mu\text{g}\cdot\text{mL}^{-1}$ for 20 h with the cancer cells in 384 multiwell glass bottomed plate. Then, the cells were irradiated or not with a confocal Carl Zeiss two-photon microscope (laser input power 3 W). The well was irradiated at maximum power of the laser at 760 nm with the smallest objective (Carl Zeiss 10-fold magnification/objective 0.3 EC Plan-Neofluar). Three scans of 1.57 s each in four different areas without overlaps between irradiated areas. M2PS NPs caused 25% of selective cell-killing *via* two-photon PDT. Besides, the Au@M2PS NPs produced an impressive 50% of

selective cell killing under two-photon irradiation. Such an effect might have come solely from the 2PS-induced TPE-PDT, or from synergetic PDT of the 2PS and hyperthermia of AuNS.

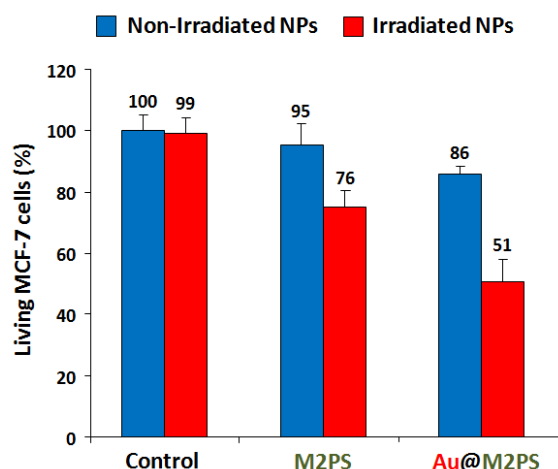


Figure 2. Two-Photon-triggered cancer cell killing via M2PS and Au@M2PS NPs.

The influence of AuNSs on surface of various silica nanocontainers was thus assessed. First, thiol groups were grafted in one-pot on the MSN and M2PS surfaces for their excellent capability to chelated AuNPs, leading to MSNSH and M2PSSH NPs respectively. The nanomaterial syntheses of MSNSH and M2PSSH were carried out via sol-gel process at 80°C for 2 h in a water/ethanol mixture (5:2, v:v) with CTAB template as well as sodium hydroxide catalysis. Both reactions were performed with an initial addition of TEOS (and of the 2PS moieties in the case of M2PSSH), and after 6 minutes of condensation, mercaptopropyltrimethoxysilane (1:10 TEOS, v:v) was added to cover the growing outer surface of the NPs. Surfactant-free MSHSH and M2PSSH NPs were fully characterized by TEM and DLS (Fig. S3A-C, and S4A-C), which showed nanoporous 60 to 80 nm spherical particles. This procedure typically led to excellent surface areas in the order of 1200 m².g⁻¹ (Fig. 3.D, and 4D). UV-visible spectroscopy and elemental analysis confirmed the encapsulation of 13 wt% of 2PS fragments. The presence of thiol groups was confirmed by the ν_{C-H} vibration modes at 2927 and 2856 cm⁻¹ in MSHSH and M2PSSH, and the 2PS encapsulation was also validated by the ν_{Si-C} vibration at 1156 cm⁻¹ and the aromatic ν_{C-H} modes at 3021 and 3062 cm⁻¹ (Fig. S5). Afterwards, the resulting thiol functionalized NPs were mixed with AuNSs to elaborate surface decorated MSNSH@Au and M2PSSH@Au nanocarriers (see Fig. 3A-B, and Fig. S6, S7). The grafted AuNSs were readily visible on the surfaces of the porous MCM-41 nanomaterial by TEM images (Fig. S7A-B, and S8A-B), and caused the appearance of the plasmonic band of gold nanocrystals (λ_{max} = 525 nm, see Fig. S6C, and 7C). Inductively-coupled-plasma measurements of the gold weight percent, provided comparable values of grafted nanocrystals (Au wt%_{MSNSH@Au} = 6.2, Au wt%_{MSNSH@Au} = 5.4, Table S1), which enables the comparison of their potential PTT efficacies.

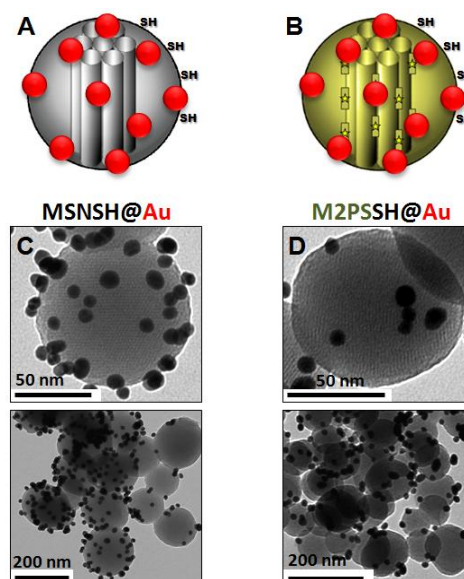


Figure 3. Schematic representation (A-B) and TEM images of MSNSH@Au (C), and M2PSSH@Au NPs (D) where the stars represent the 2PS fragments.

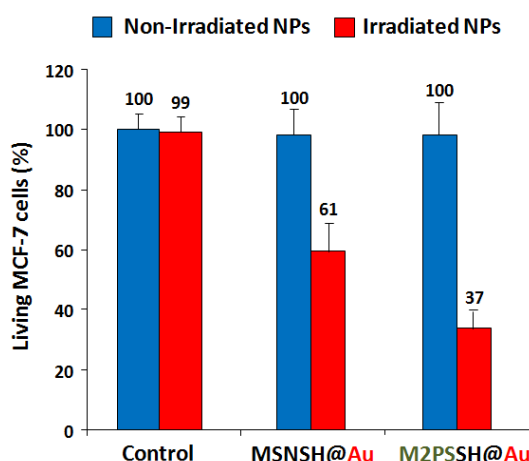


Figure 4. Two-photon-triggered cancer cell killing via MSNSH@Au, and M2PSSH@Au NPs.

Two-photon *in-vitro* irradiation of MCF-7 incubated with MSNSH@Au and M2PSSH@Au NPs was then conducted in the same manner. Interestingly, 40% of selective cell killing was observed via two-photon PTT with MSNSH@Au (Fig. 4). It is known that spatially close AuNSs are predicted to behave like gold nanorods (AuNRs)^[23] and it is probably the reason for such a significant effect. Furthermore, a remarkable synergy was obtained with M2PSSH@Au, harnessing the two-photon PDT of the 2PS moieties as well as the PTT feature of the AuNSs decorated on their external surface. Multifunctional two-photon-sensitive M2PSSH@Au NPs caused 63% of cancer cell killing. Note that, AuNRs obtained by a reported seed-growth method^[24] (ESI, see UV-visible spectra Fig. S8) were also grafted on the MSNSH and M2PSSH NPs to control the influence of the gold NPs shape (Fig. S9-12). Unfortunately, the resulting NPs were highly toxic though washed extensively (Fig. S13), which is attributed to residual CTAB molecules from the synthetic process,^[25] as shown

with the FTIR spectra of MSNSH@AuNRs (Fig. S14). Furthermore, given to the fact that Au@M2PS and M2PSSH@Au were found to have similar gold content (4.7 and 5.4 wt% respectively), the cell survival suggests that the two-photon hyperthermia is more efficient when AuNSs are placed on the silica surface. Indeed, Au@M2PS produced 50% of selective cell killing, whereas M2PSSH@Au caused more than 60% with a lower amount of 2PS moieties. Such an observation is consistent with the thermal diffusion through the organosilica matrix in Au@M2PS, which would lower the photothermal impact on the cells.

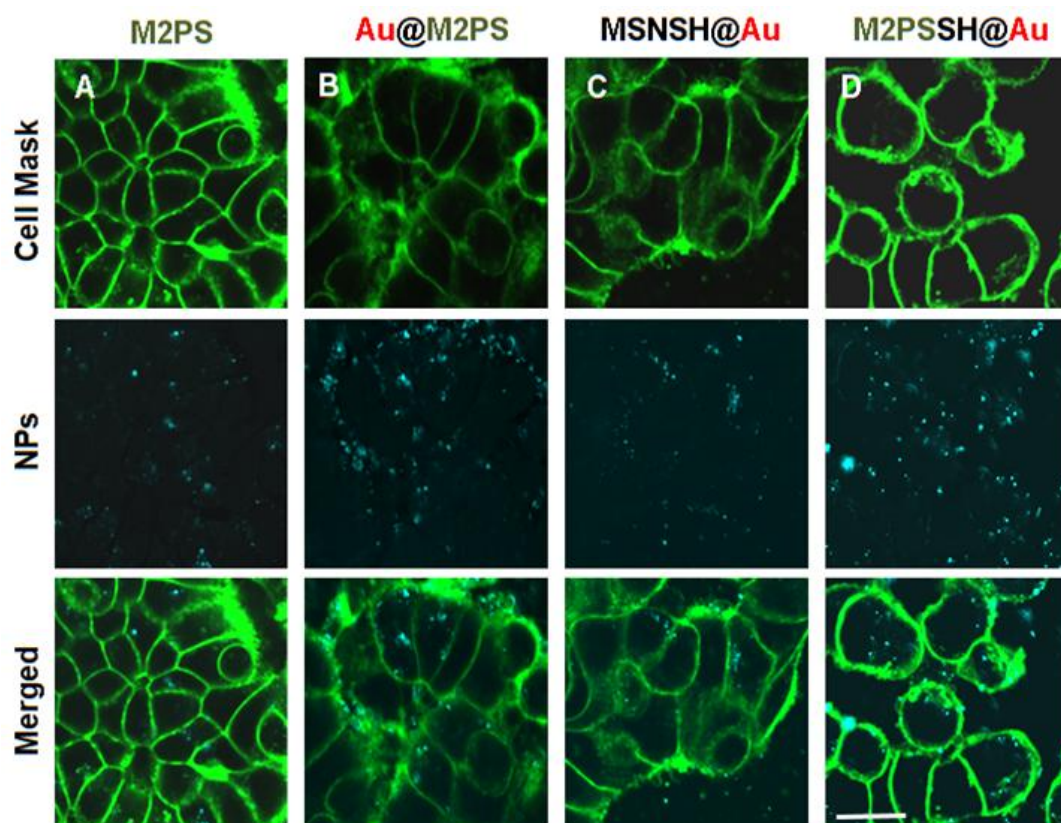


Figure 5. Two-photon fluorescence imaging of M2PS (A), MSNSH@Au (B), M2PSSH@Au (C), and Au@M2PS NPs in MCF-7 cells. Scale bar of 10 μ m.

Two-photon in-vitro fluorescence imaging on MCF-7 cells was finally studied with the various nanoplateforms (Fig. 5). All the NPs were readily visible through two-photon imaging, which demonstrated the successful cellular uptake of the NPs. Besides, it was found that MSNSH@Au also led to bright imaging (see Fig. 5B), which further suggests the nanorod-like behavior of spatially close AuNSs (bioimaging of MSNSH@AuNRs and M2PSSH@AuNRs is displayed in Fig. S13). The usefulness of gold nanospheres was further illustrated by the higher imaging capabilities of Au@M2PS and M2PSSH@Au NPs, when compared to M2PS NPs (see Fig. 5B,D, and 5A respectively). Thus, the 2PS imaging properties can be combined with the scattering feature of AuNSs to synergistically enhance the diagnostic function of M2PS NPs.

Conclusion

In summary, a two-photon synergistic cancer cell killing via PDT and PTT is reported for the first time for mesoporous organosilica NPs combined with AuNPs. Multifunctional M2PS, Au@M2PS, and M2PSSH@Au nanoplateforms were designed and fully characterized. The M2PS and various AuNSs core-shells nanostructures were found to be biocompatible on MCF-7 breast cancer cell line. Moreover, the bright two-photon intracellular imaging of the NPs demonstrated the cellular uptake of the NPs. Spatially close AuNSs were found to behave like AuNRs on the M2PSSH surface, which is of particular interest since the M2PSSH@AuNRs were cytotoxic. The properties of AuNSs were harnessed to produce 40% of selective cell killing through hyperthermia with MSNSH@Au, and the synergy with the 2PS-induced PDT caused up to 63% of cancer cell death. The drug delivery application of these theranostic nanovehicles with high surface areas is under investigation in our group.

REFERENCES

- [1] M. Pawlicki, H. A. Collins, R. G. Denning, H. L. Anderson, *Angewandte Chemie International Edition* **2009**, *48*, 3244.
- [2] Y. Chen, Y. Zhang, W. Liang, X. Li, *Nanomedicine: Nanotechnology, Biology and Medicine* **2012**, *8*, 1267.
- [3] D. Gao, R. R. Agayan, H. Xu, M. A. Philbert, R. Kopelman, *Nano Letters* **2006**, *6*, 2383.
- [4] J.-L. Li, H.-C. Bao, X.-L. Hou, L. Sun, X.-G. Wang, M. Gu, *Angewandte Chemie International Edition* **2012**, *51*, 1830.
- [5] T. Zhao, X. Shen, L. Li, Z. Guan, N. Gao, P. Yuan, S. Q. Yao, Q.-H. Xu, G. Q. Xu, *Nanoscale* **2012**, *4*, 7712.
- [6] S. S. Banerjee, D.-H. Chen, *Nanotechnology* **2009**, *20*, 185103.
- [7] H. M. Kim, B. R. Cho, *Accounts of Chemical Research* **2009**, *42*, 863.
- [8] M. Gary-Bobo, Y. Mir, C. Rouxel, D. Brevet, I. Basile, M. Maynadier, O. Vaillant, O. Mongin, M. Blanchard-Desce, A. Morere, M. Garcia, J.-O. Durand, L. Raehm, *Angewandte Chemie International Edition* **2011**, *50*, 11425.
- [9] E. Chelebaeva, L. Raehm, J. O. Durand, Y. Guari, J. Larionova, C. Guerin, A. Trifonov, M. Willinger, K. Thangavel, A. Lascialfari, O. Mongin, Y. Mir, M. Blanchard-Desce, *Journal of Materials Chemistry* **2010**, *20*, 1877.
- [10] V. Lebre, L. Raehm, J. O. Durand, M. Smaïhi, M. H. V. Werts, M. Blanchard-Desce, D. Methy-Gonnod, C. Dubernet, *Journal of Sol-Gel Science and Technology* **2008**, *48*, 32.
- [11] S.-H. Cheng, C.-C. Hsieh, N.-T. Chen, C.-H. Chu, C.-M. Huang, P.-T. Chou, F.-G. Tseng, C.-S. Yang, C.-Y. Mou, L.-W. Lo, *Nano Today* **2011**, *6*, 552.
- [12] J. Qian, D. Wang, F. Cai, Q. Zhan, Y. Wang, S. He, *Biomaterials* **2012**, *33*, 4851.
- [13] J. Croissant, A. Chaix, O. Mongin, M. Wang, S. Clément, L. Raehm, J.-O. Durand, V. Hugues, M. Blanchard-Desce, M. Maynadier, A. Gallud, M. Gary-Bobo, M. Garcia, J. Lu, F. Tamanoi, D. P. Ferris, D. Tarn, J. I. Zink, *Small* **2014**, n/a, n/a.
- [14] J. Croissant, M. Maynadier, A. Gallud, H. Peindy N'Dongo, J. L. Nyalosaso, G. Derrien, C. Charnay, J.-O. Durand, L. Raehm, F. Serein-Spirau, N. Cheminet, T. Jarroson, O. Mongin, M. Blanchard-Desce, M. Gary-Bobo, M. Garcia, J. Lu, F. Tamanoi, D. Tarn, T. M. Guardado-Alvarez, J. I. Zink, *Angewandte Chemie International Edition* **2013**, *125*, 14058.
- [15] R. E. Yanes, D. Tarn, A. A. Hwang, D. P. Ferris, S. P. Sherman, C. R. Thomas, J. Lu, A. D. Pyle, J. I. Zink, F. Tamanoi, *Small* **2013**, *9*, 697.
- [16] Z. Li, J. C. Barnes, A. Bosoy, J. F. Stoddart, J. I. Zink, *Chemical Society Reviews* **2012**, *41*, 2590.
- [17] W. X. Mai, H. Meng, *Integrative Biology* **2013**, *5*, 19.
- [18] M. W. Ambrogio, C. R. Thomas, Y.-L. Zhao, J. I. Zink, J. F. Stoddart, *Accounts of Chemical Research* **2011**, *44*, 903.
- [19] S. Kim, T. Y. Ohulchanskyy, H. E. Pudavar, R. K. Pandey, P. N. Prasad, *Journal of the American Chemical Society* **2007**, *129*, 2669.
- [20] V. Lebre, L. Raehm, J. O. Durand, M. Smaïhi, M. H. V. Werts, M. Blanchard-Desce, D. Methy-Gonnod, C. Dubernet, *Journal of Biomedical Nanotechnology* **2010**, *6*, 176.
- [21] Z. Zhang, L. Wang, J. Wang, X. Jiang, X. Li, Z. Hu, Y. Ji, X. Wu, C. Chen, *Advanced Materials* **2012**, *24*, 1418.
- [22] J. Croissant, J. I. Zink, *Journal of the American Chemical Society* **2012**, *134*, 7628.
- [23] I. Romero, J. Aizpurua, G. W. Bryant, F. J. García De Abajo, *Optics Express* **2006**, *14*, 9988.
- [24] I. Gorelikov, N. Matsuura, *Nano Letters* **2008**, *8*, 369.
- [25] A. M. Alkilany, P. K. Nagaria, M. D. Wyatt, C. J. Murphy, *Langmuir* **2010**, *26*, 9328.

APPENDIX: SUPPLEMENTARY INFORMATION

I- EXPERIMENTAL SECTION

M2PS NPs. A mixture of water (25 mL), ethanol (10 mL), and CTAB (160 mg, 4.40×10^{-1} mmol) was prepared in a three neck 50 mL round bottom flask, and stirred at 70°C. Then an aqueous solution of potassium tetrachloroaurate (13 mg, 3.45×10^{-2} mmol in 1 mL) was injected, and sodium hydroxide (100 μ L, 2 M) was added to induce the instantaneous nucleation of the nanoparticles. After 30 seconds, hydrochloric acid (18 μ L, 2 M) was added for a controlled sol-gel process. The nanoparticles growth was conducted for 20 minutes under a 600 rpm stirring speed, and the temperature was then set at 80°C. Afterwards, TEOS (450 μ L, 2.01 mmol) and the two-photon photosensitizer (89 mg, 6.45×10^{-2} mmol, in 900 μ L of anhydrous ethanol) were added dropwise to the stirring solution, and followed by sodium hydroxide (100 μ L, 2 M) to grow the porous M2PS shell onto the gold nanocrystals. The condensation process was conducted for 1 h. Afterwards, the solution was cooled at room temperature while stirring; fractions were gathered in propylene tubes, and collected by centrifugation during 15 minutes at 21 krpm. The sample was then extracted twice with an alcoholic solution of ammonium nitrate (6 g.L⁻¹), and washed three times with ethanol, water, and ethanol. Each extraction involved a sonication step of 30 minutes at 50°C in order to remove the CTAB surfactant; the collection was carried out in the same manner. The as-prepared material was dried few hours under vacuum.

Au@M2PS NPs. A mixture of water (25 mL), ethanol (10 mL), and CTAB (160 mg, 4.40×10^{-1} mmol) was prepared in a three neck 50 mL round bottom flask, and stirred at 70°C. Then, an aqueous solution of potassium tetrachloroaurate (13 mg, 3.45×10^{-2} mmol in 1 mL) was injected, and sodium hydroxide (100 μ L, 2 M) was added to induce the instantaneous nucleation of the nanoparticles. After 30 seconds, hydrochloric acid (18 μ L, 2 M) was added for a controlled sol-gel process. The nanoparticles growth was conducted for 20 minutes under a 600 rpm stirring speed, and the temperature was then set at 80°C. Afterwards, TEOS (450 μ L, 2.01 mmol) and the two-photon photosensitizer (89 mg, 6.45×10^{-2} mmol, in 900 μ L of anhydrous ethanol) were added dropwise to the stirring solution, and followed by sodium hydroxide (100 μ L, 2 M) to grow the porous M2PS shell onto the gold nanocrystals. The condensation process was conducted for 1 h. Afterwards, the solution was cooled at room temperature while stirring; fractions were gathered in propylene tubes, and collected by centrifugation during 15 minutes at 21 krpm. Extraction and following steps were identical to those of M2PS NPs.

MSNSH NPs. A mixture of CTAB (250 mg, 6.86×10^{-1} mmol), distilled water (120 mL), and sodium hydroxide (875 μ L, 2 M) was stirred at 80°C during 50 minutes at 700 rpm in a 250 mL three neck round bottom flask. Then, TEOS (1 mL) was added to the solution, and after six minutes the mercaptopropyltriethoxysilane precursor was added (100 μ L, 5.38×10^{-1} mmol), and the condensation process was conducted for 2 h. Afterwards, the solution was cooled at room temperature while stirring; fractions were gathered in propylene tubes, and

collected by centrifugation during 15 minutes at 21 krpm. Extraction and following steps were identical to those of M2PS NPs.

M2PSSH NPs. A mixture of CTAB (250 mg, 6.86×10^{-1} mmol), distilled water (120 mL), and sodium hydroxide (875 μ L, 2 M) was stirred at 80°C during 50 minutes at 700 rpm in a 250 mL three neck round bottom flask. Then, TEOS (1 mL) along with an alcoholic solution of the 2PS precursor (177 mg, 1.29×10^{-1} mol, in 500 μ L of EtOH) were added. to the solution. After six minutes, mercaptopropyltriethoxysilane was added (100 μ L, 5.38×10^{-1} mmol), and the condensation process was conducted for 2 h. Afterwards, the solution was cooled at room temperature while stirring; fractions were gathered in propylene tubes, and collected by centrifugation during 15 minutes at 21 krpm. Extraction and following steps were identical to those of M2PS NPs.

Au Nanospheres. A mixture of water (100 mL), and potassium tetrachloroaurate (55 mg, 1.38×10^{-1} mmol) was refluxed in a three neck 250 mL round bottom flask was stirred at 100°C. Then, an aqueous solution of sodium citrate (155 mg, 5.3×10^{-1} mmol in 3 mL) was quickly injected through two syringes (2×1.5 mL). The reaction was conducted for 10 minutes, and the solution was cooled at room temperature. The resulting solution of gold nanospheres was used without further modification.

MSNSH@Au NPs. A mixture of MSNSH NPs (25 mg) and deionized water (5 mL) was sonicated 5 minutes, then a fraction of the AuNSs solution (20 mL) was added. The solution was stirred 20 minutes at 60°C, and cooled down 40 minutes to room temperature before being centrifuged 15 minutes at 21 krpm. Finally, the supernatant was removed and the compound was washed twice with ethanol, and collected via centrifuging 10 minutes at 21 krpm. The as-prepared material was dried for few hours under vacuum.

M2PSSH@Au NPs. A mixture of M2PSSH NPs (25 mg) and deionized water (5 mL) was sonicated 5 minutes, then a fraction of the AuNSs solution (20 mL) was added. The solution was stirred 20 minutes at 60°C, and cooled down 40 minutes to room temperature before being centrifuged 15 minutes at 21 krpm. Finally, the supernatant was removed and the compound was washed twice with ethanol, and collected via centrifuging 10 minutes at 21 krpm. The as-prepared material was dried for few hours under vacuum.

Au Nanorods. The elaboration of gold nanorods (AuNRs) was performed via a seed-growth method reported by Gorelikov and Matsuura (*Nano Lett.*, **2008**, 8, 369-373). First, a mixture of CTAB (182 mg, 5.0×10^{-1} mmol), distilled water (2.5 mL), and potassium tetrachloroaurate (1.5 mL, 0.001 M) was stirred (1 cm stir bar at 1400 rpm) in a 5 mL round bottom flask. Afterwards, an ice-cooled aqueous solution of sodium borohydride (600 μ L, 0.01 M) was injected, and the reaction was allowed to stir 2 minutes before lowering the stirring speed to 500 rpm. The seed solution **A** was used in the following hour without further purification. Separately, a mixture of CTAB (911 mg, 2.5 mmol, SIGMA reference 6269), distilled water (24 mL), silver nitrate (700 μ L, 4 mM), and potassium tetrachloroaurate (1.250 mL, 15 mM) was stirred (2.5/0.7 cm stir bar at 1000 rpm) in a 50 mL round bottom flask at 30°C. Second, ascorbic acid was added dropwise (313 μ L, 0.08 M) to reduce Au(III) ions in Au(I) species, and gold seeds (250 μ L of solution **A**) were added in the mixture to trigger the anisotropic

growth on the seeds. The solution turned red after approximately 15 minutes and the reaction was conducted for a total of 30 minutes.

MSNSH@AuNRs NPs. A mixture of MSNSH NPs (25 mg) and deionized water (5 mL) was sonicated 5 minutes, then a fraction of the AuNRs solution (20 mL) was added, followed with sodium hydroxide (1 mL, 0.2 M). The solution was stirred 20 minutes at 60°C, neutralized with hydrochloric acid addition (0.2 M), and cooled down 40 minutes to room temperature before being centrifuged 15 minutes at 21 krpm. Finally, the supernatant was removed and the compound was washed twice in ethanol, and once with acetone, and collected via centrifuging 10 minutes at 21 krpm. The as-prepared material was dried for few hours under vacuum.

M2PSSH@AuNRs NPs. A mixture of M2PSSH NPs (25 mg) and deionized water (5 mL) was sonicated 5 minutes, then a fraction of the AuNRs solution (20 mL) was added, followed with sodium hydroxide (1 mL, 0.2 M). The solution was stirred 20 minutes at 60°C, neutralized with hydrochloric acid addition (0.2 M), and cooled down 40 minutes to room temperature before being centrifuged 15 minutes at 21 krpm. Finally, the supernatant was removed and the compound was washed twice in ethanol, and once with acetone, and collected via centrifuging 10 minutes at 21 krpm. The as-prepared material was dried under air flow for few hours.

II- NANOMATERIALS SYNTHESIS AND CHARACTERIZATIONS

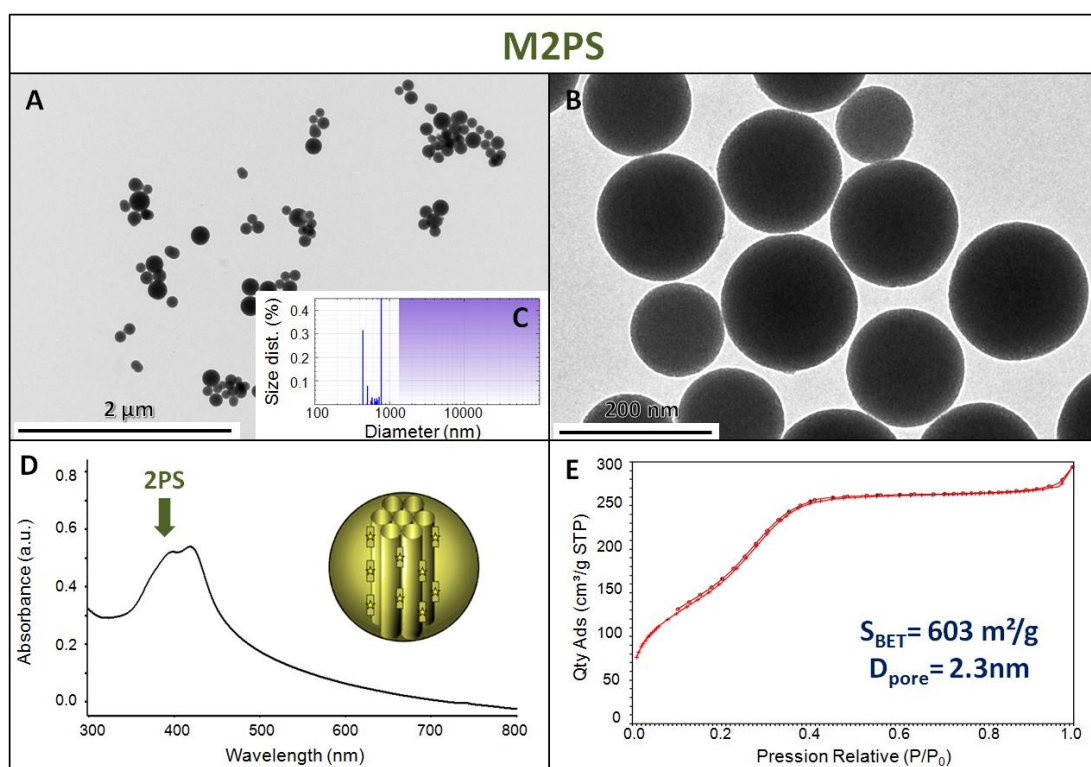


Figure S1. M2PS NPs characterization via TEM images (A-B), DLS size distribution (C), UV-visible spectroscopy (D), and N_2 -adsorption-desorption (E).

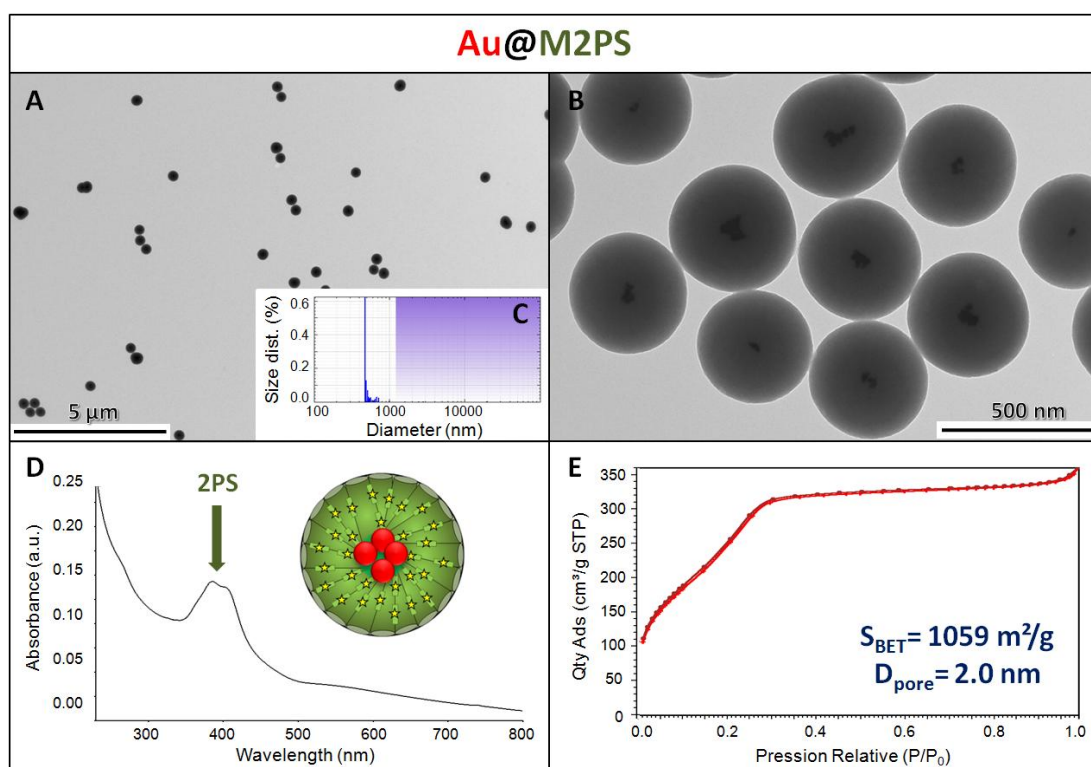


Figure S2. Au@M2PS NPs characterization via TEM images (A-B), DLS size distribution (C), UV-visible spectroscopy (D), and N_2 -adsorption-desorption (E).

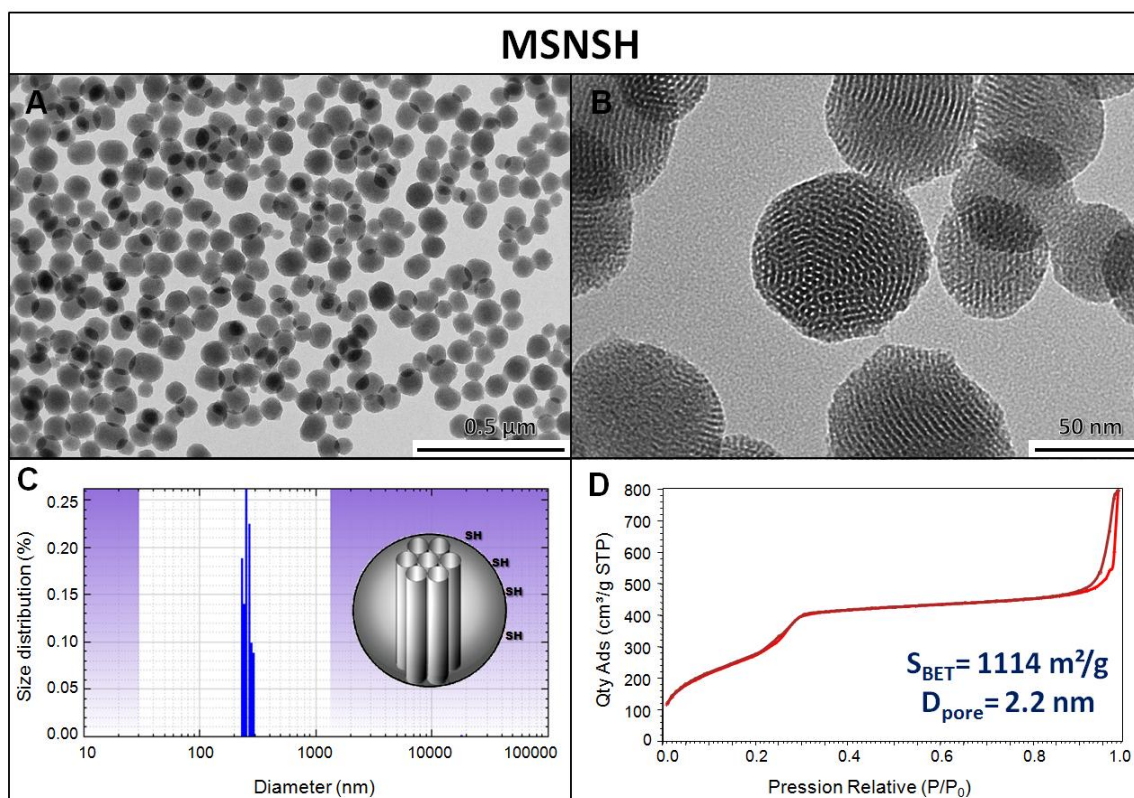


Figure S3. MSNSH NPs characterization via TEM images (A-B), N_2 -adsorption-desorption (C), and DLS size distribution (D).

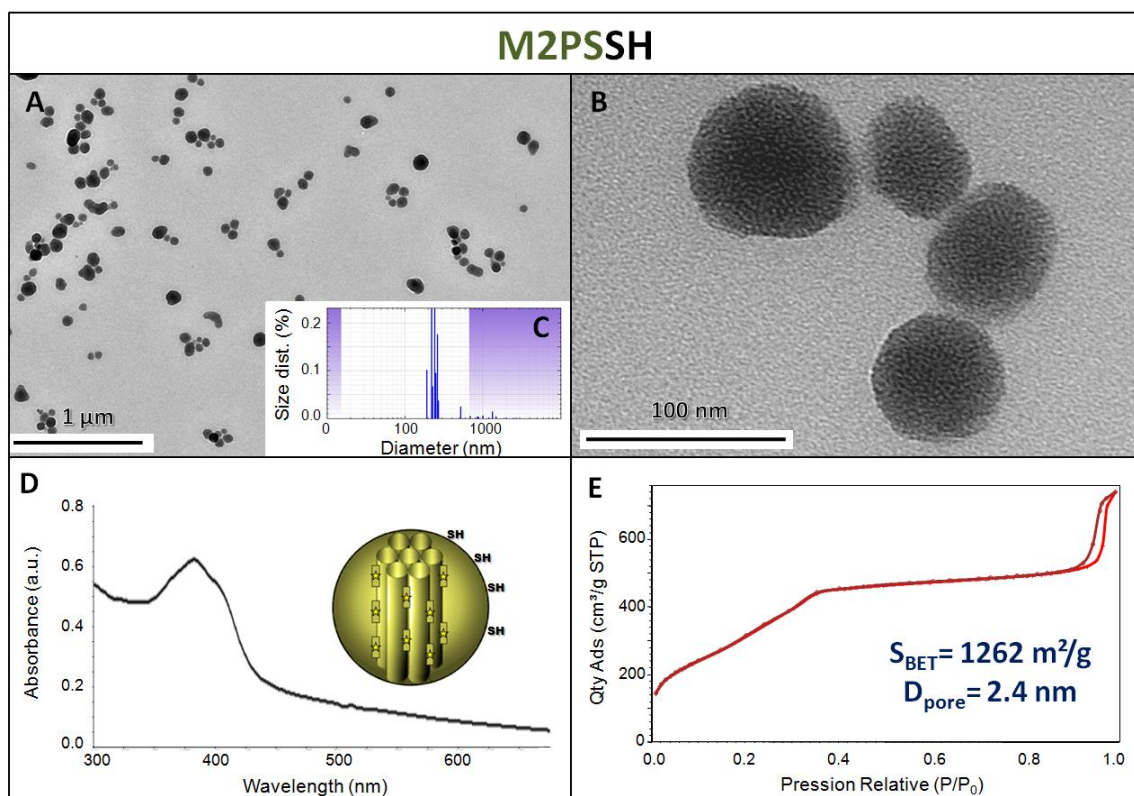


Figure S4. M2PSSH NPs characterization via TEM images (A-B), DLS size distribution (C), N_2 -adsorption-desorption (D), and UV-visible spectroscopy (E).

Table S1. Gold weight percent determination in NPs.

Sample	AuNSs wt%
Au@M2PS	4.7 ^[a]
MSNSH@Au	6.2 ^[b]
M2PSSH@Au	5.4 ^[b]

[a] Energy dispersive spectrometry analysis.

[b] Inductively coupled plasma atomic emission spectroscopy.

Table S2. 2PS weight percent determination in the NPs.

Sample	NPs N wt% ^[a]	NPs 2PS wt% ^[b]
M2PS	3.5	24.9
Au@M2PS	4.3	30.8
M2PSSH@Au	1.8	13.2

[a] Elemental analysis by combustion measurements of the NPs.

[b] Determination based on the nitrogen wt% in the 2PS molecules.

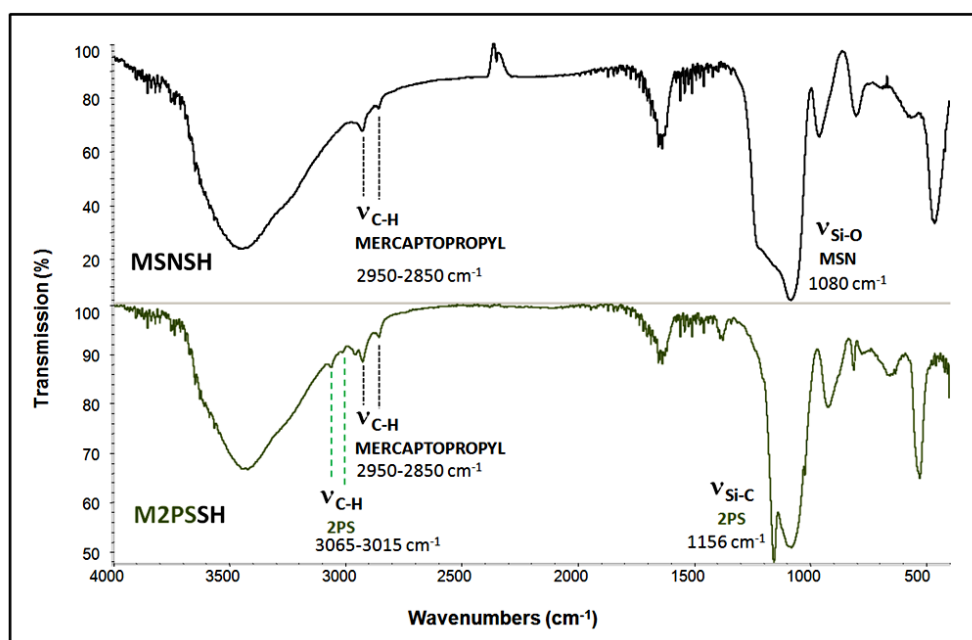


Figure S5. FTIR spectra of MSNSH and M2PSSH NPs, confirming the thiol co-condensation as well as the 2PS encapsulation.

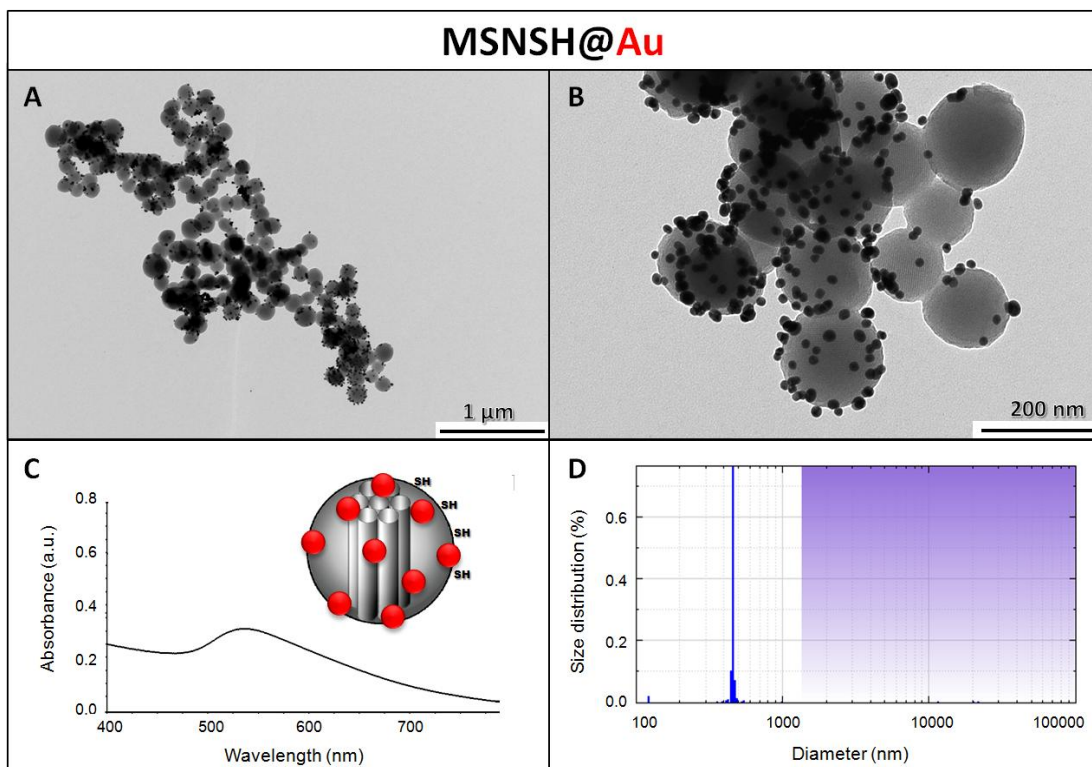


Figure S6. MSNSH@Au NPs characterization via TEM images (A-B), UV-visible spectroscopy (C), and DLS size distribution (D).

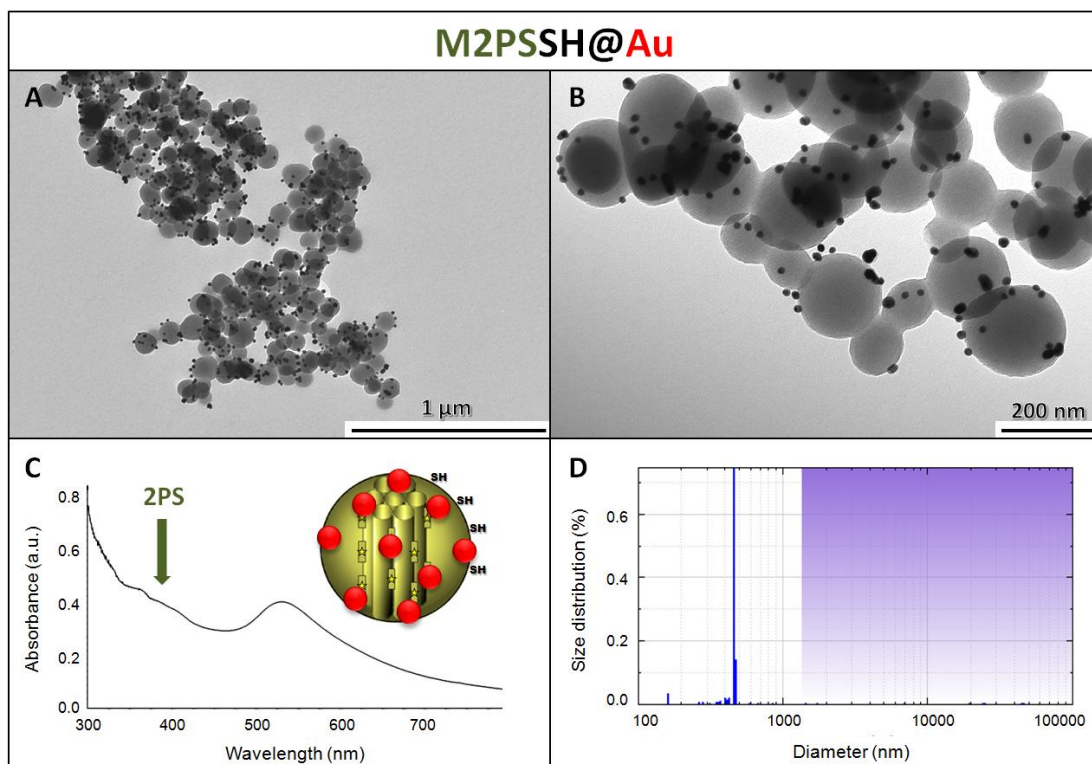


Figure S7. M2PSSH@Au NPs characterization via TEM images (A-B), UV-visible spectroscopy (C), and DLS size distribution (D).

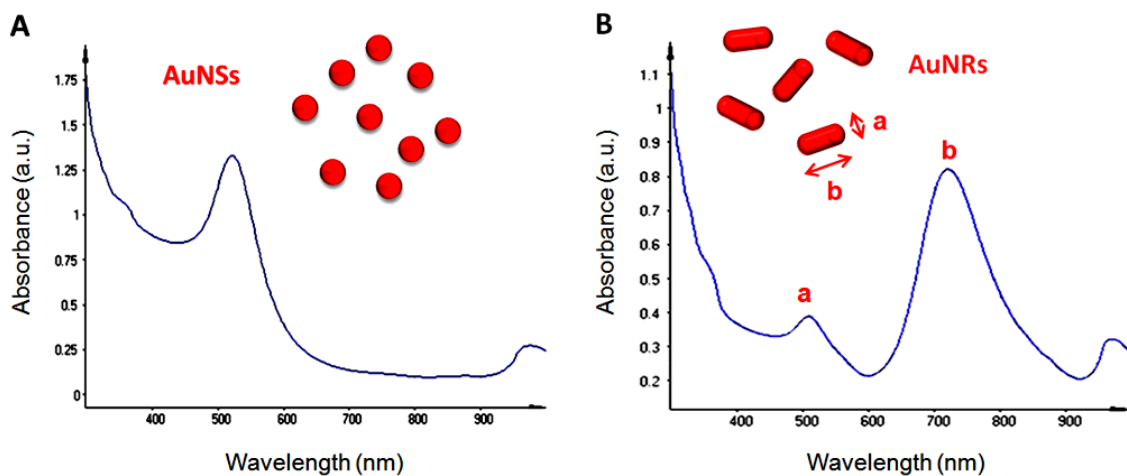


Figure S8. UV-visible spectra of gold nanospheres (A), and gold nanorods (B).

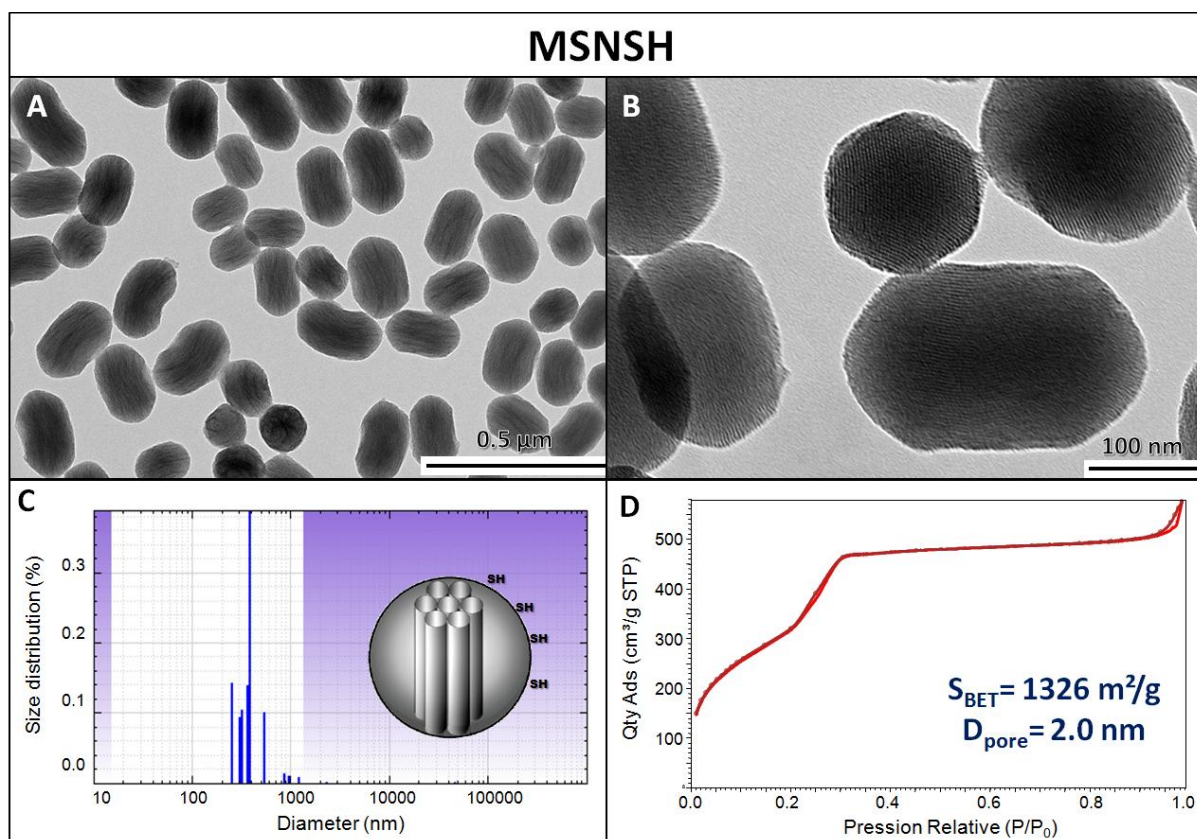


Figure S9. MSNSH NPs characterization via TEM (A-B), DLS (C), and N_2 -adsorption-desorption technique (D).

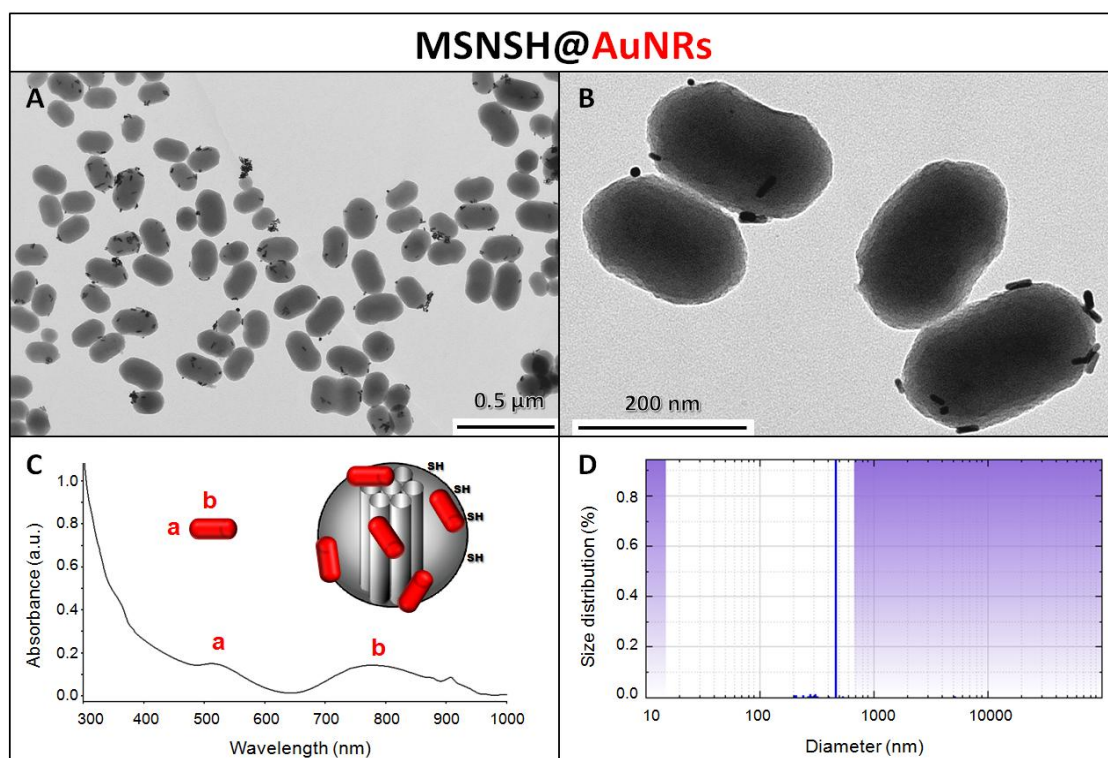


Figure S10. MSNSH@AuNRs NPs characterization via TEM (A-B), UV-visible spectroscopy (C), and DLS (D).

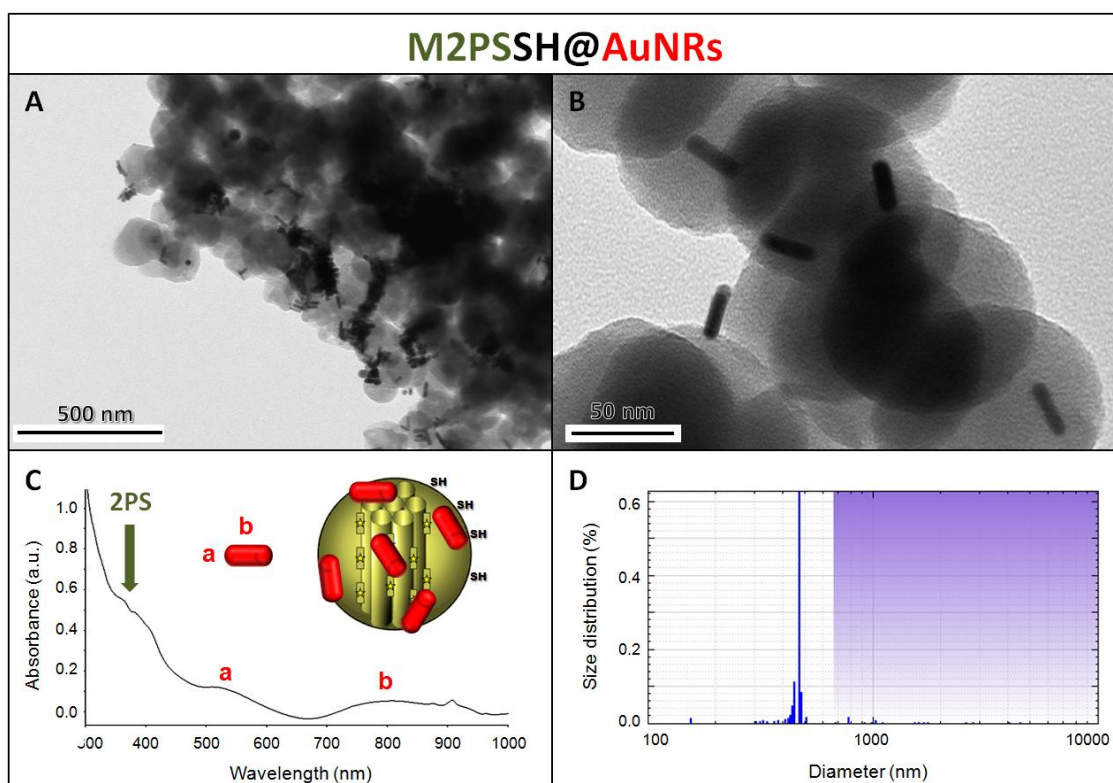


Figure S11. M2PSSH@AuNRs NPs characterization via TEM (A-B), UV-visible spectroscopy (C), and DLS (D).

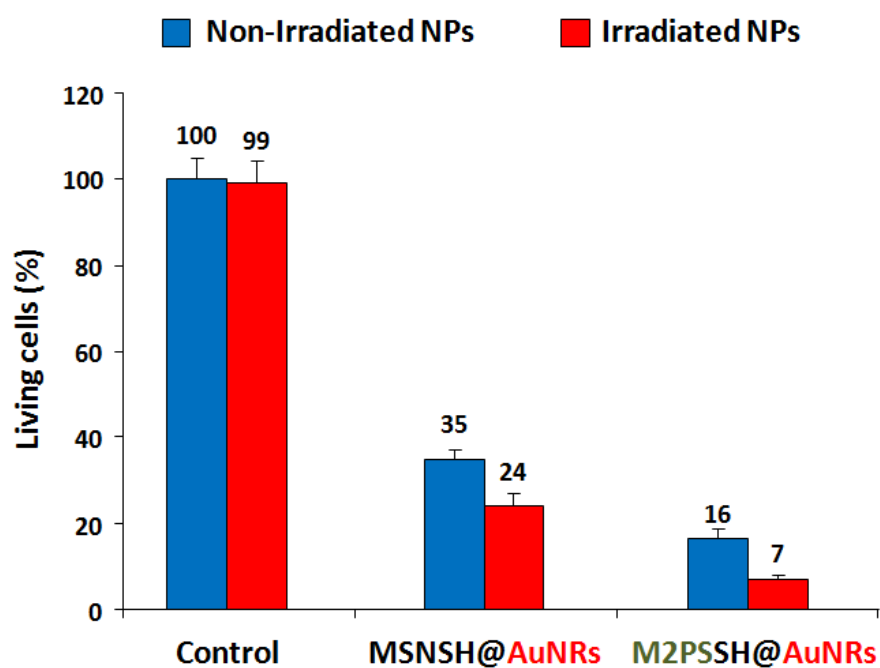


Figure S12. Cell viability study of two-photon irradiated MSNSH@AuNRs and M2PSSH@AuNRs in MCF-7 breast cancer cells at $40 \mu\text{g.mL}^{-1}$.

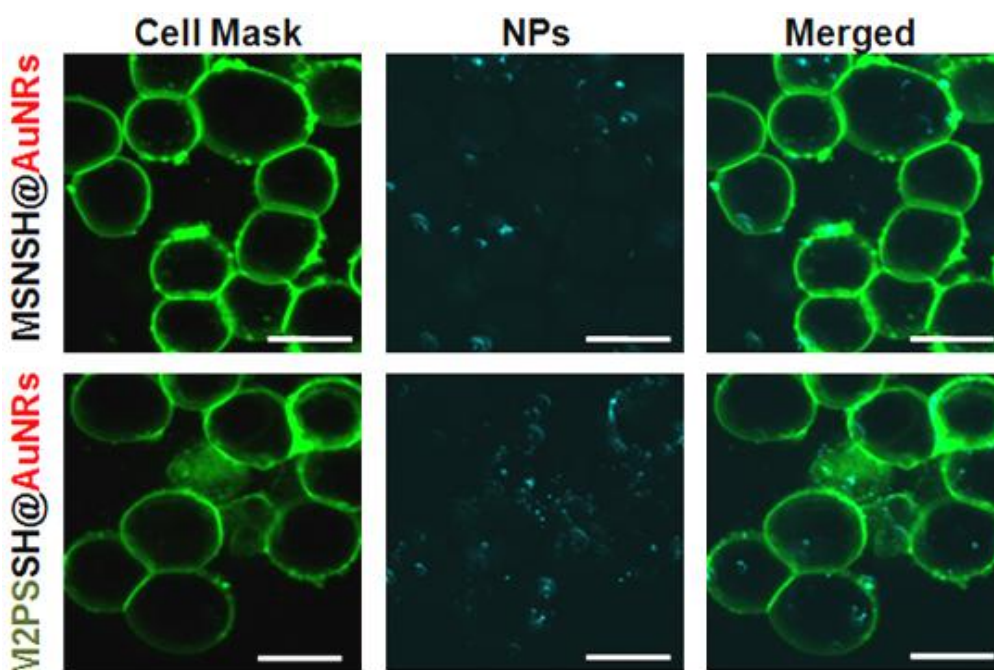


Figure S13. Two-photon fluorescence imaging of MSNSH@AuNRs and M2PSSH@AuNRs in MCF-7 breast cancer cells at $40 \mu\text{g.mL}^{-1}$ (Scale bar $10 \mu\text{m}$).

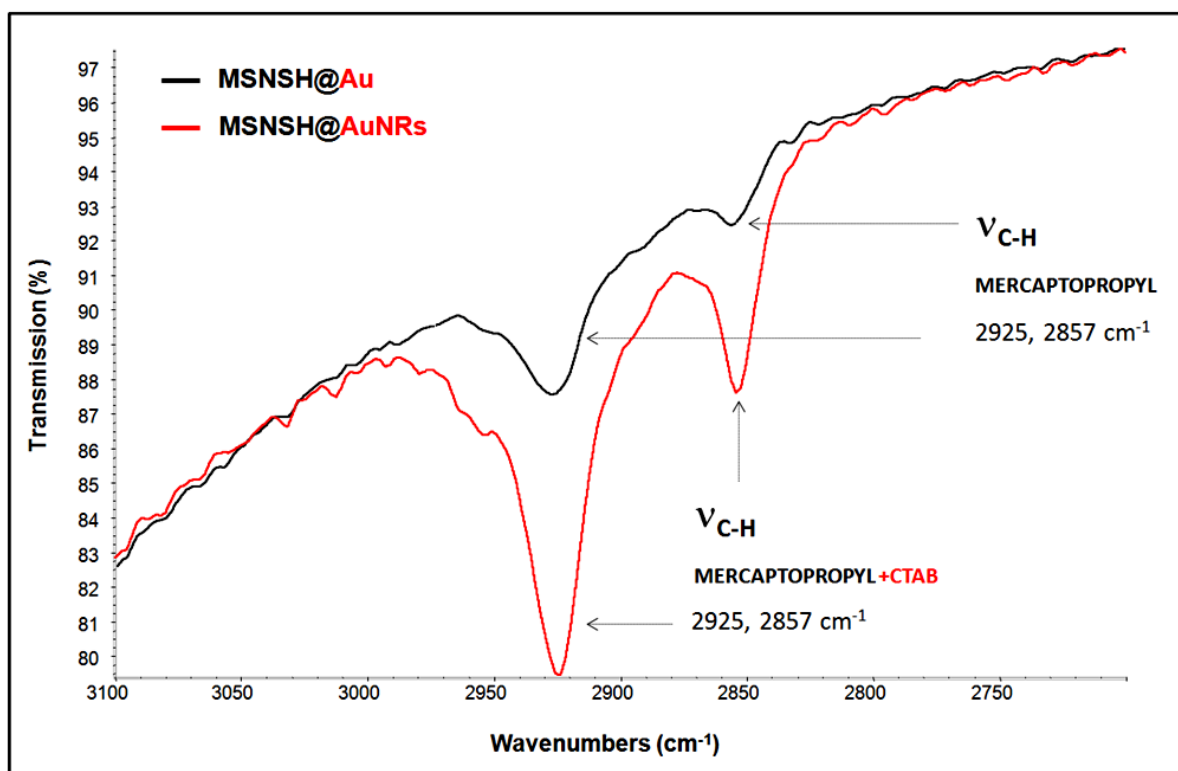
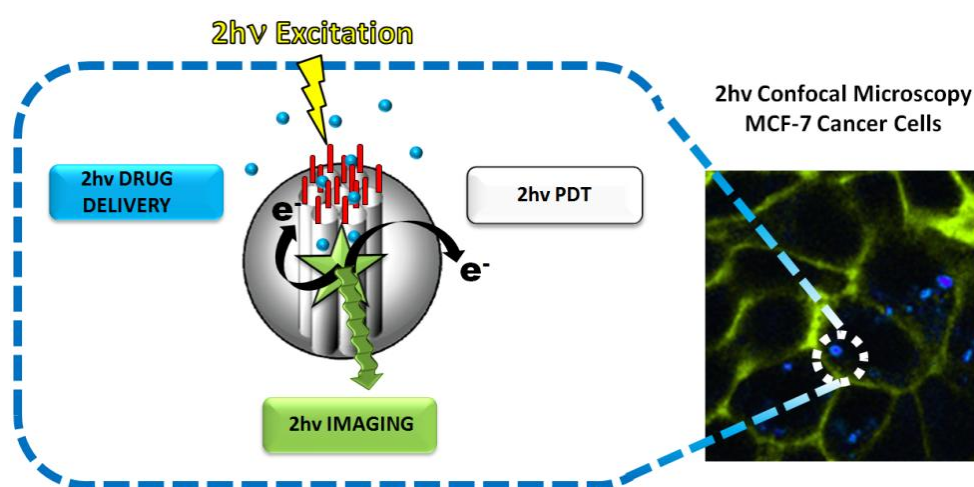


Figure S14. FTIR spectra of MSNSH@Au and MSNSH@AuNRs, validating the CTAB cytotoxicity origin postulated in MSNSH@AuNRs.

CHAPTER 5

C. Two-Photon Synergetic Cell Killing via Multifunctional Mesoporous Nanogate Theranostics



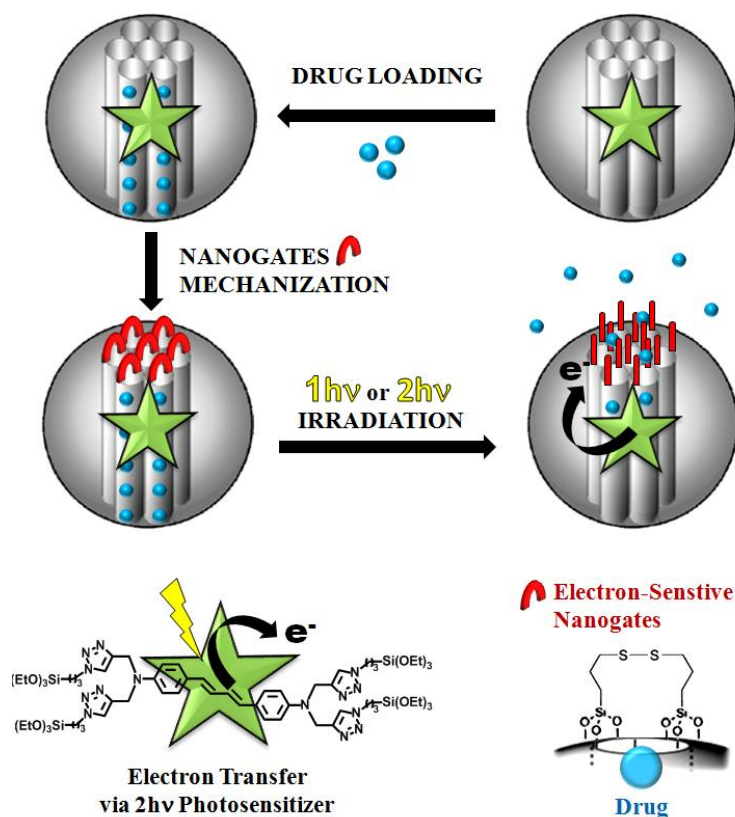
Abstract

We report a two-photon-actuated synergetic cancer cell killing via photodynamic therapy (PDT) and drug delivery through multifunctional mesoporous silica nanogates. Two-photon-sensitive mesoporous organosilica (M2PS) nanocarriers were elaborated by the co-condensation of a silica precursor and a two-photon photosensitizer. The nanogates were constructed in a fast one-pot process at room temperature on the drug-loaded M2PS nanoparticles (NPs) with the bis(3-triethoxysilylpropyl)disulfide precursor. Besides, the one and two-photon-actuated cargo releases from the M2PS nanogates were successfully monitored in aqueous solution. Finally, the cellular uptake as well as the PDT and drug delivery synergetic MCF-7 cancer cell killing were demonstrated.

Introduction

Two-photon excitation is a powerful tool to achieve the indispensable spatially and temporally-controlled drug delivery for cancer treatment via nanomedicine. Indeed, two-photon irradiation produces a 3D-dimensional spatial resolution as well as a safe and deep laser penetration in tissues (down to 2 cm).^[1] Thus, this feature provides a unique way to deliver locally a high concentration of drug necessary to both avoid the side effects of chemotherapy, and achieve an efficient treatment.^[1-3] Over the past fifteen years, mesoporous silica nanoparticles (MSN) have attracted much attention, especially as a multifunctional theranostic nanoplatforms.^[4-7] Owing to the advantage of a remote light-triggered delivery, researchers have first developed many organically modified MSN systems actuated by one-photon excitation, such as photo-cleavage,^[8-13] photoisomerizable nanoimpellers,^[14-16] up-conversion-photo-isomerization,^[17] plasmonic photothermal nanovalves,^[18] photoredox nanovalves.^[19] Unfortunately, many –though not all– of these approaches used a UV-visible light not applicable in a human model, and even for the near-infrared (NIR) actuated MSN,^[17, 20] the major drawback remains the lack of spacial accuracy due to the scattering of the one-photon irradiation. Recently, we reported the first studies of NIR two-photon-triggered drug delivery in solution,^[21, 22] and in cancer cells.^[23, 24] The most robust of these nanocarriers involved nanomachines covering the MSN pores based on supramolecular interactions between a stalk and a molecular ring. These nanomachines were usually composed of two or three moieties and require several step of elaboration. Nonetheless, the combination of various medical features is still lacking in two-photon-sensitive nanosystems. Besides, a simple and fast elaboration of a molecular machinery on the MSN framework would enhance the economic relevance of such nanomachines.

In this communication, we report the first synergetic cancer cell killing via two-photon-actuated PDT and drug delivery with multifunctional MSN. The mesoporous nanocarriers were constituted of a high content of two-photon photosensitizer covalently incorporated within a silica matrix, loaded with the doxorubicin anticancer drug, and capped by molecular gates. Such nanogates were uniquely constructed in a fast *one-pot* process on the drug-loaded M2PS nanoparticles (NPs) from the bis(3-triethoxysilylpropyl)disulfide precursor, as opposed to the multistep procedures described previously for molecular machinery.^[21, 25] The one and two-photon-actuated cargo deliveries via photoreductive cleavage of the disulfide nanogates were successfully monitored in aqueous solution (cf Scheme 1). Furthermore, we demonstrated the intracellular uptake of M2PS NPs on MCF-7 breast cancer cells, via the bright fluorescence of the incorporated two-photon photosensitizer. Hence, the multifunctionality of our nanoplatform for two-photon drug delivery, PDT, as well as intracellular imaging makes M2PS NPs valuable theranostics.



Scheme 1. M2PS nanogates design and light-actuated drug release mechanism.

Results and discussion

The M2PS nanomaterials were elaborated by co-condensation of tetraethylorthosilicate with a tetraalkoxysilylated two-photon photosensitizer (2PS, see chapter 5.A). The sol-gel process was carried out for 2 h at 80°C in an aqueous solution of the cetyltrimethylammonium bromide template with sodium hydroxide catalysis. The content of 2PS was varied by the precursor concentration in order to obtain compounds constituted of 25 and 50 wt% in photosensitizer (M2PS-25 and M2PS-50 respectively). Afterwards, the surfactant was extracted twice using an ethanolic mixture of ammonium nitrate. The nanomaterials were washed, and used without further purification (ESI).

The M2PS nanocarrier structures were first characterized via transmission electron microscopy (TEM) which revealed the presence of 80 nm monodisperse and well organized MCM-41 mesoporous nanospheres (Fig. 1A, and Fig. S1B). The narrow size distribution was observed by dynamic light scattering (DLS) measurements (Fig. 1C, Fig. S1C), as well as scanning electron microscopy (SEM, Fig. 1B, and Fig. S2). The successful incorporation of the 2PS within the silica matrix was confirmed by the absorption band ($\lambda_{\text{max}} = 384 \text{ nm}$) in the UV-visible spectra (Fig. 1D, and Fig. S1D), and solid state nuclear magnetic resonance (NMR) ^{29}Si and ^{13}C CPMAS spectra (Fig. S3). The remarkably high 2PS contents were calculated from the elemental analysis on nitrogen, knowing that the each 2PS molecule contains 14.2 wt% of this atom (see Table S1). Moreover, the N_2 -adsorption-desorption

technique indicated BET surface areas of 677 and 503 $\text{m}^2\cdot\text{g}^{-1}$ for M2PS-25 and M2PS-50 respectively, with pore diameters of about 2.5 nm (Fig. 1E, and Fig. S1E-F). These values are in agreement with the distance of 3.8 nm between pores deduced from the X-Ray diffractogram (Fig. S4).

Secondly, the photophysical properties of the nanomaterials were assessed. The fluorescence emission quantum yield of M2SP-25 was higher than for M2PS-50 NPs, with respectively of 41% and 26%. Besides, the two-photon absorption cross section was also higher in M2SP-25 than in M2PS-50, with maximum values of 200 and 180 GM at 700 nm (Table S2). These photophysical measurements suggested an aggregation of the photosensitizer in M2PS-50, which is confirmed by the red shift of the emission band observed in M2PS-50, when compared with M2PS-25 (see Fig. S5). As a result, these comparisons showed that the 2PS wt% should not be too high to retain a high surface area, and to avoid non-radiative de-excitation by chromophore-chromophore interactions.

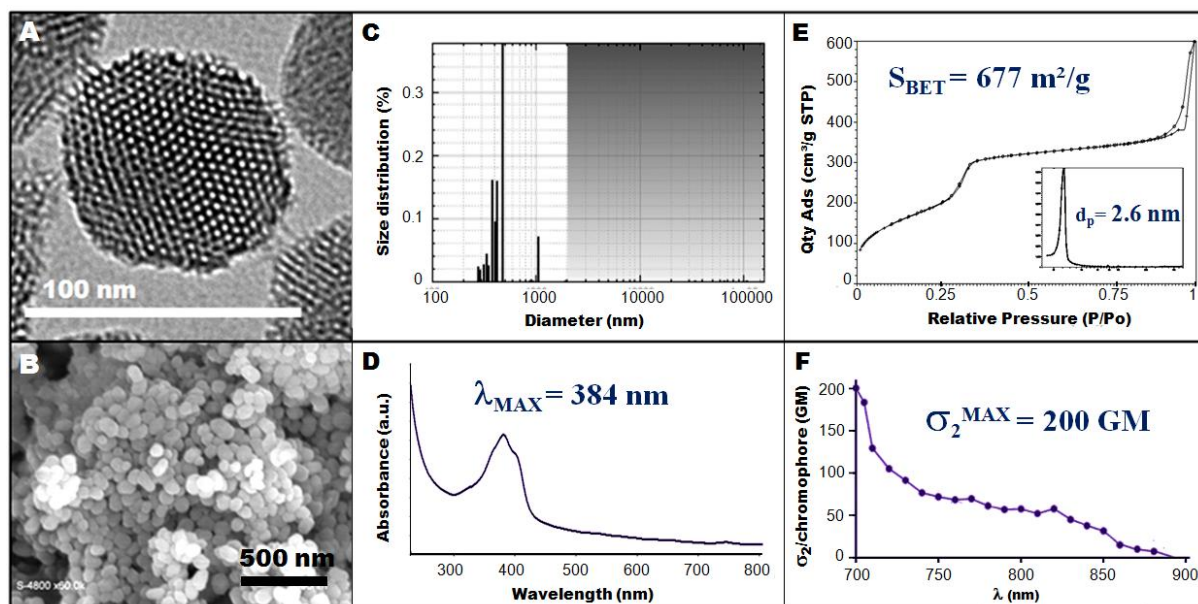


Figure 1. M2PS-25 characterization via TEM (A), SEM (B), DLS (C), UV-visible spectroscopy (D), N_2 -adsorption-desorption (E), and two-photon-emission fluorescence (F).

Thirdly, the cargo-loaded M2PS nanogates were constructed and fully characterized. The first step is the loading of the cargo placed in excess (Scheme 1). The rhodamine B (Rho B) dye and the doxorubicin (DOX) anticancer drug were used for the cargo delivery studies. Then, the nanogates were constructed on the pores with the addition of the bis(3-triethoxysilylpropyl)disulfide precursor in the loading solution. The nanogates functionalization was demonstrated by the energy dispersive spectroscopy (EDS) elemental analysis of sulfur (Table S3), as well as the solid state NMR ^{29}Si and ^{13}C CPMAS spectra of a control on MSN NPs, given that the 2PS ^{29}Si and ^{13}C signals overlap those of the nanogates (Fig. S6). Moreover, this is in accordance with the modification of the zeta potential before

and after disulfide grafting (Table S4). The DOX encapsulation in the M2PS pores was clearly visible by UV-visible spectroscopy (Fig. S7).

The one-photon-triggered cargo delivery was thus conducted with DOX-loaded M2PS nanogates (Fig. 2). First, the electron-sensitive disulfide nanogates were opened upon addition of a mercaptoethanol reducing agent, which triggered an instantaneous release of DOX and demonstrated the successful design of the molecular machinery. Second, the nanogates were irradiated with a 365 nm UV lamp while in presence of the ethylenediaminetetraacetic acid (EDTA) sacrificial agent. This light-mediated electron transfer from the excited 2PS species to the disulfides photochemically-actuated the anticancer drug release. Note that, in control experiments both the light and the EDTA stimuli were applied separately without causing the opening of the nanogates (see Fig. 2). The M2PS nanogates DOX loading capacities were of 2.5 wt% (Table S5).

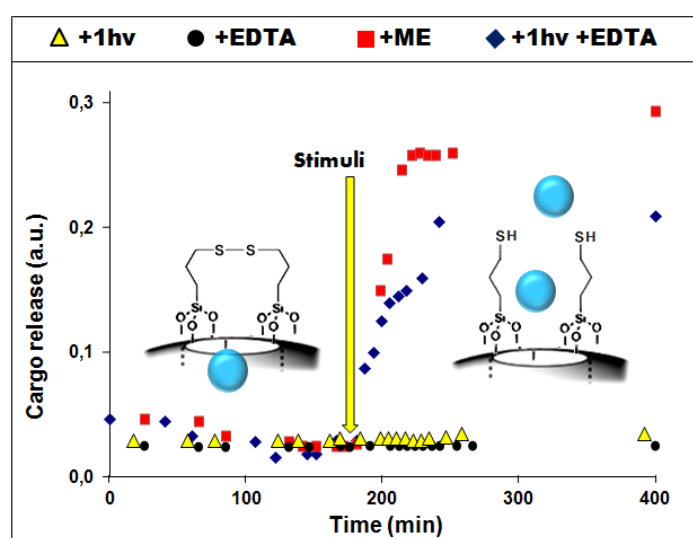


Figure 2. Release experiments from DOX-loaded M2PS nanogates and associated controls. The releases are triggered either through a one-photon actuation associated with the EDTA sacrificial agent, or with the ME reducer. The nanogates did not open in the sole presence of the light or the EDTA stimuli.

The cargo delivery in solution from M2PS nanogates was then tested using two-photon excitation. This control experiment was performed with disulfide nanogates designed in two-steps from mercaptopropyltrimethoxysilane grafted on the M2PS, and then oxidized into disulfide upon iodine addition (Scheme S1, Fig. S7). The robust Rho B dye was selected for its known resistance to photobleaching, and loaded in the M2PS nanocarriers. The electron transfer of the 2PS moieties was confirmed by the quenching of the 2PS fluorescence upon two-photon irradiation (Fig. S3A-C). The release of the cargo was followed by UV-visible analysis of the irradiated nanogates (Scheme S2), and the release profile was plotted as a function of the time (Fig. S3D). Consistently with the one-photon experiment, the laser irradiation combined with the addition of the EDTA sacrificial agent triggered the release of the cargo.

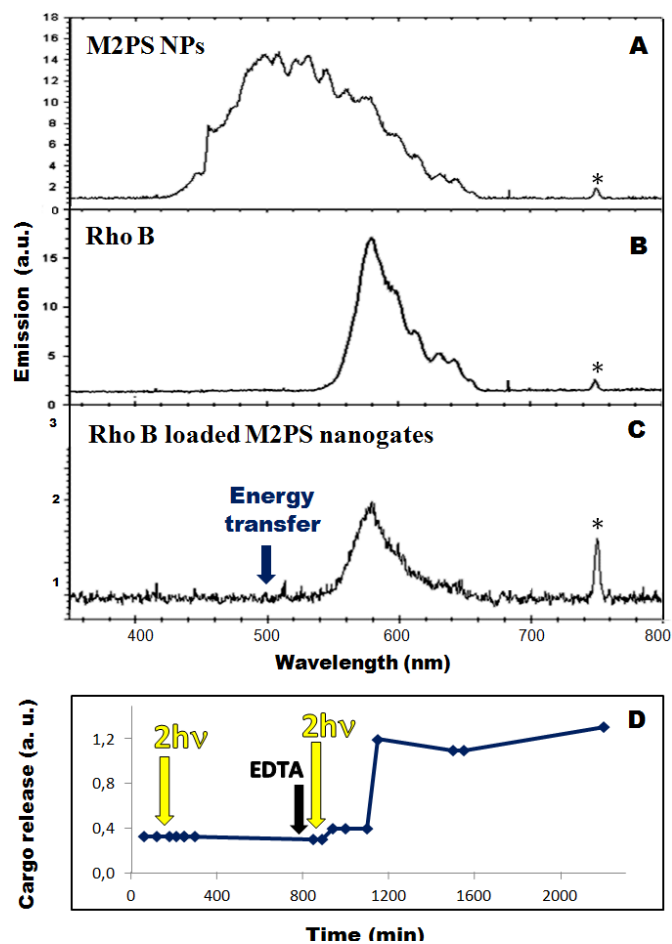


Figure 3. Demonstration of the energy transfer in M2PS-25 nanogates, through fluorescence emission spectra of bare M2PS-25 NPs (A), Rho B (B), and M2PS-25 nanogates loaded with Rho B (C). * 750 nm laser peak. Two-photon-actuated release of Rho B from M2PS-25 nanogates (D).

To assess the endocytosis of our nanocarriers, two-photon *in-vitro* imaging was then investigated with the MCF-7 breast cancer cell line. Bare M2PS-50 and M2PS-25 NPs were incubated for 24 h with cells at $40 \mu\text{g.mL}^{-1}$ in 384 multiwell glass-bottomed plate. The membranes of the cells were stained with a membrane marker (cell mask) for 15 minutes and the two-photon imaging was performed with a Carl Zeiss confocal microscope (Laser input 3W) at low power (3% of the laser input) at 760 nm. The intracellular two-photon fluorescence of the M2PS NPs confirmed the endocytosis of both nanomaterials (see Fig. 4A and B). Besides, the brighter spots of M2PS-25 correlated the higher brightness ($\sigma_2 \times \phi$) of these NPs, which makes them excellent two-photon nanoprobes.

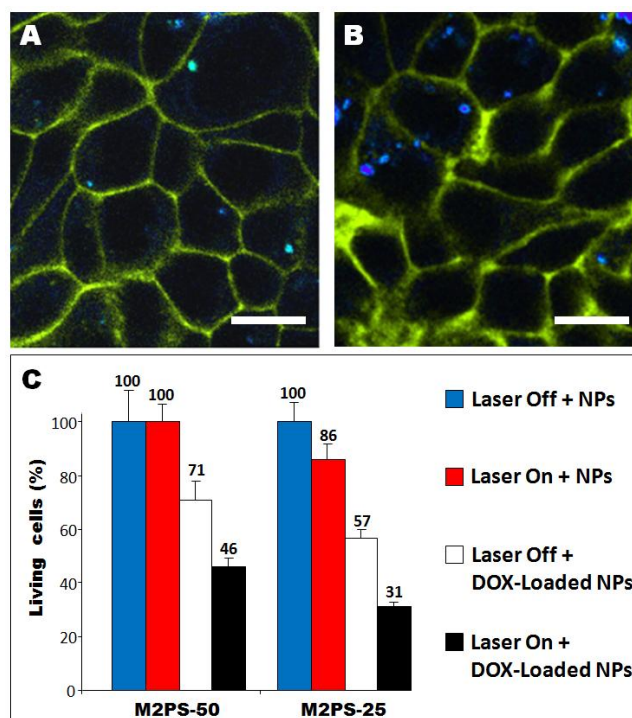


Figure 4. Two-photon fluorescence imaging of M2PS-50 (A), and M2PS-25 (B) confirming the cellular uptake of the NPs (Scale bar 10 μ m). Two-Photon triggered synergetic PDT and DOX delivery in M2PS-50, and M2PS-25 nanogates (C).

Finally, *in-vitro* two photon cancer therapy was studied on bare M2PS NPs and DOX-loaded M2PS nanogates. The two-photon excitation was performed at maximum laser power (input power of 3 W at 760 nm), the well was irradiated with three scans of 1.57 s each in four different areas without overlaps between irradiated areas with the smallest objective (Carl Zeiss 10-fold magnification/objective 0.3 EC Plan-Neofluar). This experiment led to 50% of surface irradiation. The MTT assay was performed two days after irradiation (Fig. 4C). Firstly, the photodynamic therapy was demonstrated with the 15% selective cell killing of bare M2PS-25 under two-photon excitation, whereas the M2PS-50 was non-effective. This further illustrates the threshold of the photosensitizer content for the composition-properties relationship. Note that both NPs were biocompatible without irradiation. Secondly, DOX-loaded M2PS nanogates were incubated in MCF-7 cells in order to have a synergetic cancer therapy. As expected, the autonomous delivery of DOX from the disulfide nanogates occurred before irradiation via the intracellular glutathione reducer, with 30 and 40% of cell killing for M2PS-50 and M2PS-25 respectively. This trend is in accordance with the slightly higher loading of DOX in M2PS-25 nanogates (Table S5). On the other hand, irradiated DOX-loaded M2PS-50 nanogates caused more cell killing with up to 55%, which shows the 2PS electron production upon two-photon irradiation, as initially demonstrated in solution. Furthermore, when DOX-loaded M2PS-25 nanogates were excited with the laser, the synergetic two-photon-mediated PDT and drug delivery combined with autonomous (glutathione) DOX delivery led to 70% of cancer cell killing. M2PS-25 is thus an efficient medical nanoplatform for cancer therapy.

Conclusion

In conclusion, we report the synthesis and full characterization of photosensitizer-modified MSN NPs for two-photon cancer therapy. Indeed, a maximum cross section of 200 GM as well as a fluorescence quantum yield of 41% were measured. The nanomaterials were converted into drug delivery carrier thanks to the design of disulfide nanogates via an ultrafast single step mechanization. Moreover, the one and two-photon cargo deliveries proofs of concept were monitored in aqueous solution. The design of the disulfide nanogates in two-steps from the mercaptopropyltrimethoxysilane grafting and oxidation also suggests that these nanogates are reusable nanocarriers as opposed to many reported disulfide irreversible cleavage of bulky group. Furthermore, the M2PS NPs endocytosis in MCF-7 cells was successfully demonstrated, and the M2PS-25 NPs displayed bright two-photon fluorescence imaging. Finally, the *in-vitro* synergetic cancer cell killing involving PDT and drug delivery upon two-photon irradiation were shown for the first time in such materials. These multifunctional two-photon-sensitive MSN nanogates are consequently excellent theranostic agents for cancer therapy.

REFERENCES

- [1] M. Pawlicki, H. A. Collins, R. G. Denning, H. L. Anderson, *Angewandte Chemie International Edition* **2009**, 48, 3244.
- [2] M. Gary-Bobo, Y. Mir, C. Rouxel, D. Brevet, I. Basile, M. Maynadier, O. Vaillant, O. Mongin, M. Blanchard-Desce, A. Morere, M. Garcia, J.-O. Durand, L. Raehm, *Angewandte Chemie International Edition* **2011**, 50, 11425.
- [3] V. Lebreton, L. Raehm, J. O. Durand, M. Smaïhi, M. H. V. Werts, M. Blanchard-Desce, D. Methy-Gonnod, C. Dubernet, *Journal of Biomedical Nanotechnology* **2010**, 6, 176.
- [4] J. M. Rosenholm, C. Sahlgren, M. Linden, *Nanoscale* **2010**, 2, 1870.
- [5] J. M. Rosenholm, C. Sahlgren, M. Linden, *Current Drug Targets* **2011**, 12, 1166.
- [6] C. Argyo, V. Weiss, C. BrÄuchle, T. Bein, *Chemistry of Materials* **2013**, 26, 435.
- [7] W. X. Mai, H. Meng, *Integrative Biology* **2013**, 5, 19.
- [8] C. Park, K. Lee, C. Kim, *Angewandte Chemie International Edition* **2009**, 48, 1275.
- [9] F. Tang, L. Li, D. Chen, *Advanced Materials* **2012**, 24, 1504.
- [10] J. L. Vivero-Escoto, I. I. Slowing, B. G. Trewyn, V. S. Y. Lin, *Small* **2010**, 6, 1952.
- [11] N. Z. Knezevic, V. S. Y. Lin, *Nanoscale* **2013**, 5, 1544.
- [12] J. Lai, X. Mu, Y. Xu, X. Wu, C. Wu, C. Li, J. Chen, Y. Zhao, *Chemical Communications* **2010**, 46, 7370.
- [13] Q. N. Lin, Q. Huang, C. Y. Li, C. Y. Bao, Z. Z. Liu, F. Y. Li, L. Y. Zhu, *Journal of the American Chemical Society* **2010**, 132, 10645.
- [14] J. Lu, E. Choi, F. Tamanoi, J. I. Zink, *Small* **2008**, 4, 421.
- [15] S. Angelos, M. Liong, E. Choi, J. I. Zink, *Chemical Engineering Journal* **2008**, 137, 4.
- [16] D. P. Ferris, Y. L. Zhao, N. M. Khashab, H. A. Khatib, J. F. Stoddart, J. I. Zink, *Journal of the American Chemical Society* **2009**, 131, 1686.
- [17] J. Liu, W. Bu, L. Pan, J. Shi, *Angewandte Chemie International Edition* **2013**, 52, 4375.
- [18] J. Croissant, J. I. Zink, *Journal of the American Chemical Society* **2012**, 134, 7628.
- [19] T. D. Nguyen, K. C. F. Leung, M. Liong, Y. Liu, F. Stoddart, J. I. Zink, *Advanced Functional Materials*, **2007**, 17, 2101.
- [20] X. Yang, X. Liu, Z. Liu, F. Pu, J. Ren, X. Qu, *Advanced Materials* **2012**, 24, 2890.
- [21] T. M. Guardado-Alvarez, L. Sudha Devi, M. M. Russell, B. J. Schwartz, J. I. Zink, *Journal of the American Chemical Society* **2013**, 135, 14000.
- [22] T. M. Guardado-Alvarez, L. S. Devi, J.-M. Vabre, T. A. Pecorelli, B. J. Schwartz, J.-O. Durand, O. Mongin, M. Blanchard-Desce, J. I. Zink, *Nanoscale* **2014**, 6, 4652.
- [23] J. Croissant, M. Maynadier, A. Gallud, H. Peindy N'Dongo, J. L. Nyalosaso, G. Derrien, C. Charnay, J.-O. Durand, L. Raehm, F. Serein-Spirau, N. Cheminet, T. Jarrosson, O. Mongin, M. Blanchard-Desce, M. Gary-Bobo, M. Garcia, J. Lu, F. Tamanoi, D. Tarn, T. M. Guardado-Alvarez, J. I. Zink, *Angewandte Chemie International Edition* **2013**, 125, 14058.
- [24] J. Croissant, A. Chaix, O. Mongin, M. Wang, S. Clément, L. Raehm, J.-O. Durand, V. Hugues, M. Blanchard-Desce, M. Maynadier, A. Gallud, M. Gary-Bobo, M. Garcia, J. Lu, F. Tamanoi, D. P. Ferris, D. Tarn, J. I. Zink, *Small* **2014**, n/a, n/a.
- [25] M. W. Ambrogio, T. A. Pecorelli, K. Patel, N. M. Khashab, A. Trabolsi, H. A. Khatib, Y. Y. Botros, J. I. Zink, J. F. Stoddart, *Organic Letters* **2010**, 12, 3304.

APPENDIX: SUPPLEMENTARY INFORMATION

I- EXPERIMENTAL SECTION

Materials. Tetraethoxysilane (TEOS), cetyltrimethylammonium bromide (CTAB), sodium hydroxide, and ammonium nitrate, (3-mercaptopropyl)trimethoxysilane, mercaptoethanol, rhodamine B, doxorubicin hydrochloride, iodine, tetrahydrofuran, and ethylenediaminetetraacetic acid (EDTA) were purchased from Sigma-Aldrich. Absolute ethanol was purchased from Fisher Chemicals. R. Norma Pure. Bis(3-triethoxysilylpropyl)disulfide were purchased from ABCR.

General Procedures. Absorption spectra were recorded on a Hewlett-Packard 8453 spectrophotometer and fluorescence data were collected on a Perkin-Elmer LS55 fluorimeter. Mass spectrometry was carried out at the Laboratoire de Spectrometrie de Masse (Lyon, France) with a Thermo-Finnigan MAT95 apparatus in electronic impact ionization mode. Dynamic light scattering analyses were performed using a Cordouan Technologies DL 135 Particle size analyzer instrument. ^{29}Si and ^{13}C CPMAS solid state NMR sequences were recorded with a VARIAN VNMR300, using Q8MH8 and adamantane references respectively. TEM analysis were performed on a JEOL 1200 EXII instrument. SEM analysis performed on a FEI Quanta FEG 200 instrument.

II- SYNTHESIS AND CHARACTERIZATION OF THE NANOMATERIALS

M2PS-25 NPs. A mixture of CTAB (250 mg), distilled water (120 mL), and sodium hydroxide (875 μL , 2 M) was stirred at 80°C for 50 minutes at 700 rpm in a 250 mL three neck round bottom flask. Then, tetraethylorthosilicate (1.0 mL) was added along with the two-photon photosensitizer (88 mg in 1 mL of dry THF), and the condensation process was conducted for 1 h 30 min. Afterwards, the solution was cooled to room temperature while stirring; fractions were gathered in propylene tubes and collected by centrifugation for 15 minutes at 21 krpm. The sample was then extracted twice with an ethanolic solution of ammonium nitrate (6 $\text{g}\cdot\text{L}^{-1}$, NH_4NO_3), and washed thrice with ethanol, water, and ethanol. Each extraction involved a sonication step of 30 minutes at 50 °C; the collection was carried out in the same manner. The as-prepared material was dried under air flow for few hours. Note that MSN NPs were obtained when only tetraethylorthosilicate (1.2 mL) was condensed.

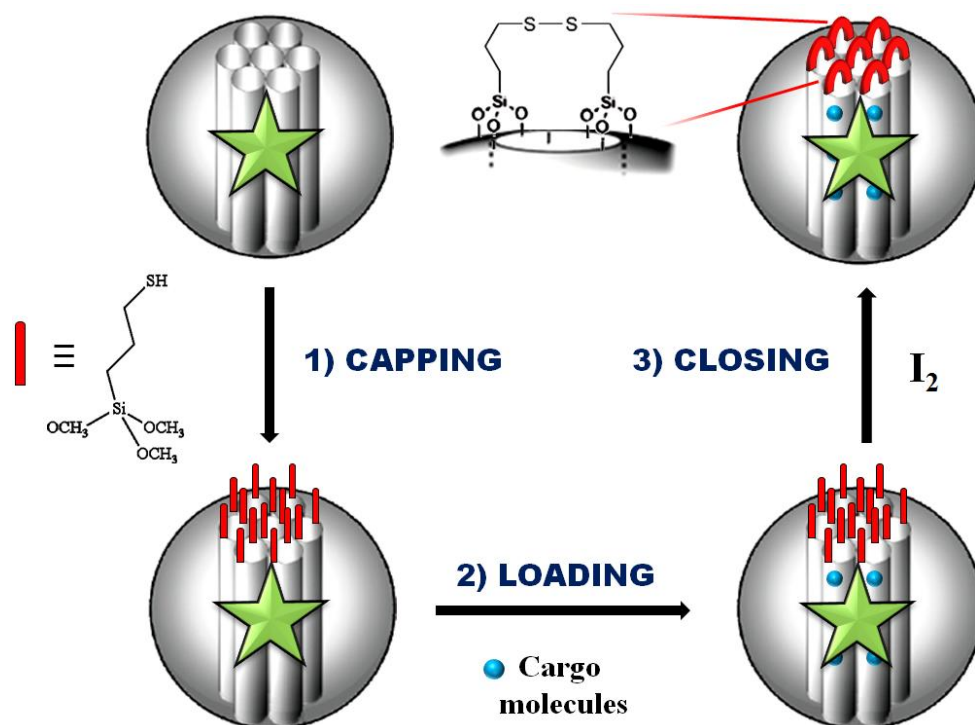
M2PS-50 NPs. A mixture of CTAB (250 mg), distilled water (120 mL), and sodium hydroxide (875 μL , 2 M) was stirred at 80°C for 50 minutes at 700 rpm in a 250 mL three neck round bottom flask. Then, TEOS (1.0 mL) was added along with the two-photon photosensitizer (267 mg in 1 mL of dry THF), and the condensation process was conducted for 1 h 30 min. Afterwards, the solution was cooled to room temperature while stirring; fractions were gathered in propylene tubes and collected by centrifugation during 15 minutes at 21 krpm. The extraction and following steps were identical of those of M2PS-25 NPs.

One-pot DOX loading and capping of M2PS NPs. A mixture M2PS NPs (20 mg), deionized water (500 μL), and DOX (2 mg) was sonicated for 10 minutes in an eppendorf tube and stirred for 2 days at room temperature. Then, bis(3-triethoxysilylpropyl)disulfide (10

μL) was added and the solution was stirred overnight. The sample was centrifuged at 10 krpm for 5 minutes and the supernatant was removed. The DOX-loaded M2PS nanogates were washed thrice with an acidic aqueous solution (1 mL, pH = 5.5) in order to removed both the surface adsorbed DOX molecules, and the potential DOX filled uncapped pores. Finally, the sample was washed twice with ethanol (1 mL), thrice with water (1 mL), and dried under vacuum for few hours.

Thiol functionalization of M2PS or MSN NPs. A mixture M2PS or MSN NPs (25 mg), anhydrous toluene (8 mL), and (3-mercaptopropyl)trimethoxysilane (12 μL) was stirred and heated at 70 $^{\circ}\text{C}$ two days. The sample was centrifuged at 10 krpm for 10 minutes, the supernatant was removed, and the material was washed once with ethanol, water, and acetone. The thiol-functionalized NPs (M2PS-SH or MSN-SH) were dried under vacuum for few hours.

Rho B loading and closing of M2PS-SH NPs. A mixture of M2PS-SH NPs (20 mg), deionized water (1 mL), and Rho B (3 mg) was sonicated 10 minutes in an eppendorf tube and stirred overnight at room temperature. Then, a saturated aqueous solution of iodine (1 mL) was poured out to form the disulfide nanogates. The sample was centrifuged at 10 krpm for 5 minutes and the supernatant was removed. Finally, the Rho B-loaded M2PS nanogates were washed twice with ethanol (1 mL), abundantly with water (1 mL), and dried under vacuum for few hours.



Scheme S1. Representation of the nanogates design from the mercaptopropyltrimethoxysilane precursor. The capping step requires the centrifugation of the NPs, while the loading and closing steps are performed in the same mixture.

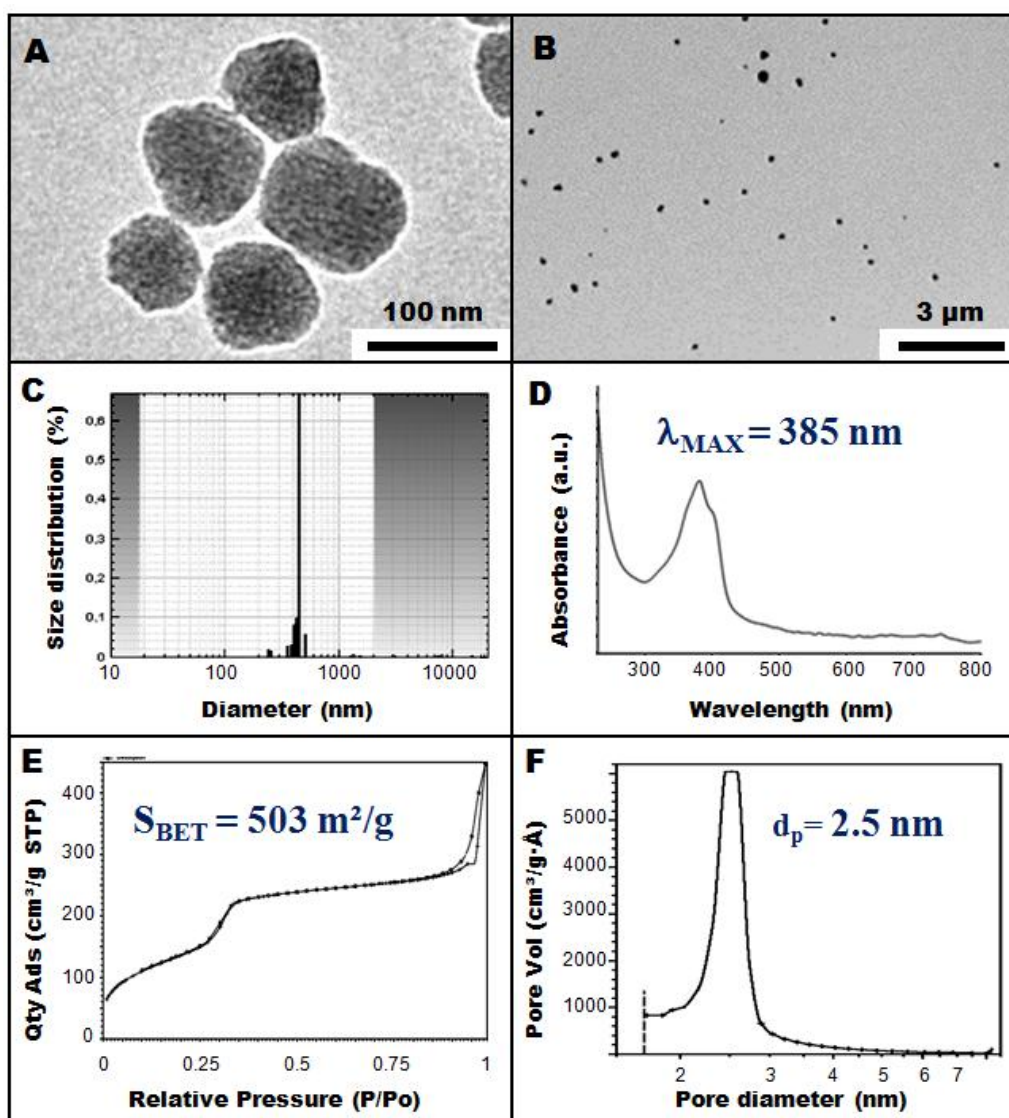


Figure S1. M2PS-50 nanogates characterization via TEM (A), SEM (B), DLS (C), UV-visible spectroscopy (D), and N_2 -adsorption-desorption isotherm (E) BJH pore size distribution (F).

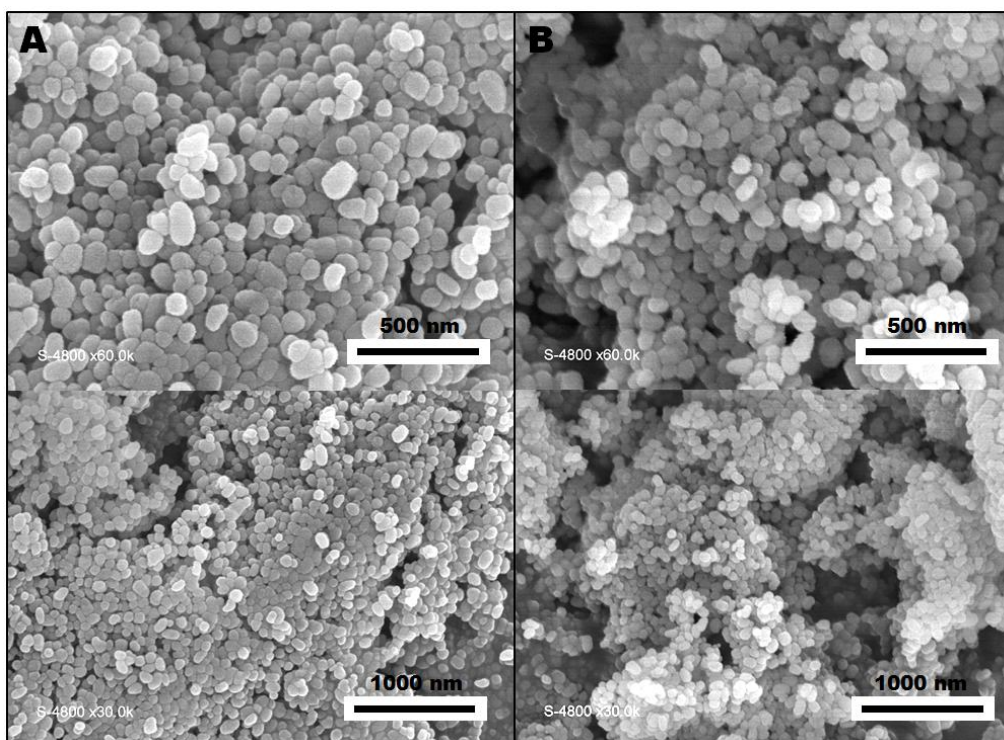


Figure S2. SEM images of M2PS-50 (A), and M2PS-25 NPs (B).

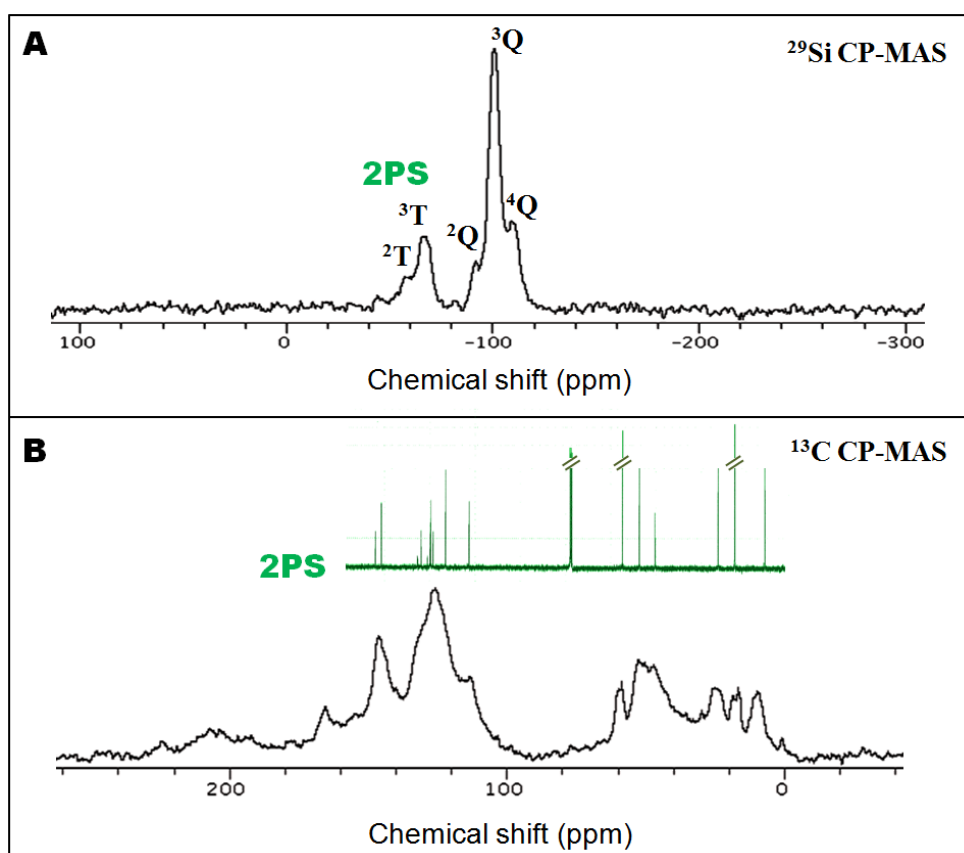


Figure S3. Solid state NMR ^{29}Si (A) and ^{13}C (B) CPMAS spectra of M2PS-50 NPs.

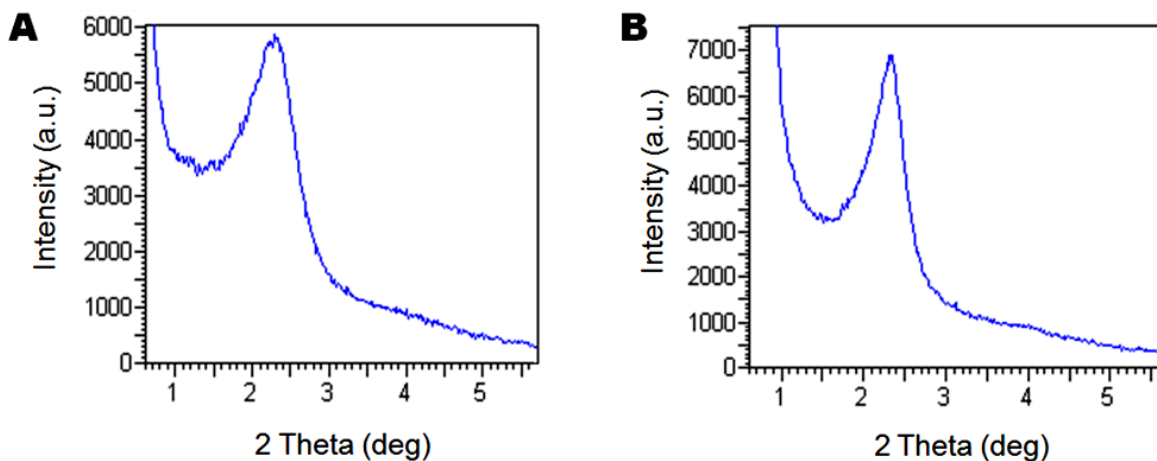


Figure S4. Small angles XRD patterns of M2PS-50 (A), and M2PS-25 NPs (B).

Sample Name	M2PS-50	M2PS-25
Nitrogen dosage (wt%)	7.27	3.36
2PS Calculations (wt%)	51.2	23.7

Table S1. 2PS weight percent (wt%) determination in the M2PS-50 and M2PS-25 nanogates. The 2PS content is calculated by combustion measurements of nitrogen in the M2PS-50, and M2PS-25 NPs.

Sample Name	M2PS-50	M2PS-25
$\lambda_{\text{abs}}/\lambda_{\text{em}}$ (nm)	385/450	384/448
Φ_{F} [a]	0.26	0.41
σ_2^{max} [b] (GM)	180	200
σ_2^{max} [b] * Φ_{F} (GM)	46	82

Table S2. Photophysical properties of M2PS-50 and M2PS-25 NPs. The wavelength absorption and emission maxima are listed ($\lambda_{\text{abs}}/\lambda_{\text{em}}$), the fluorescence quantum yield (Φ_{F}), the maximum two-photon cross sections (σ_2^{max}), and the brightness ($\sigma_2^{\text{max}} * \Phi_{\text{F}}$). [a] Quinine bisulfate standard at 0.5 M in H_2SO_4 . [b] per chromophore.

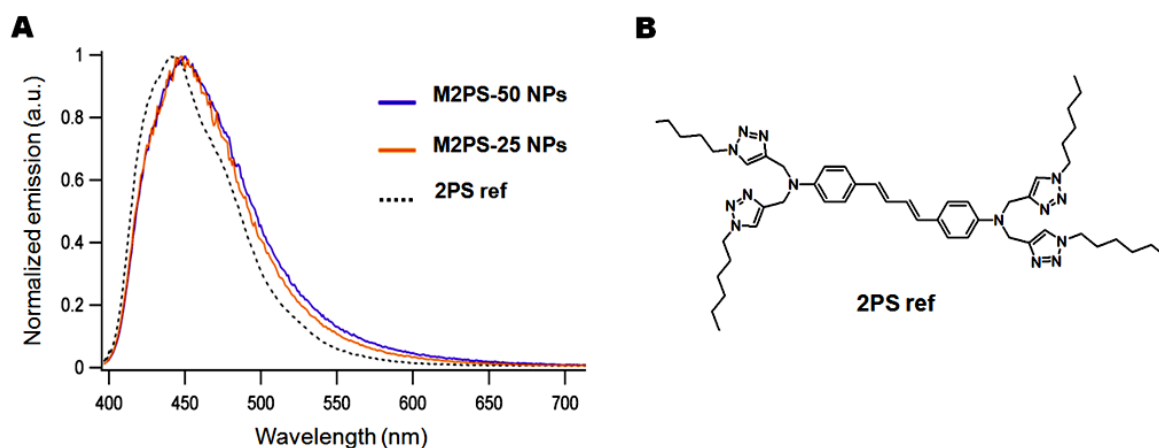


Figure S5. Normalized fluorescence emission spectra of M2PS-25 and M2PS-50 NPs (A), compared with a reference of the 2PS precursor (B). The redshift of the peak of the 2PS in the NPs indicates the aggregation of the chromophore.

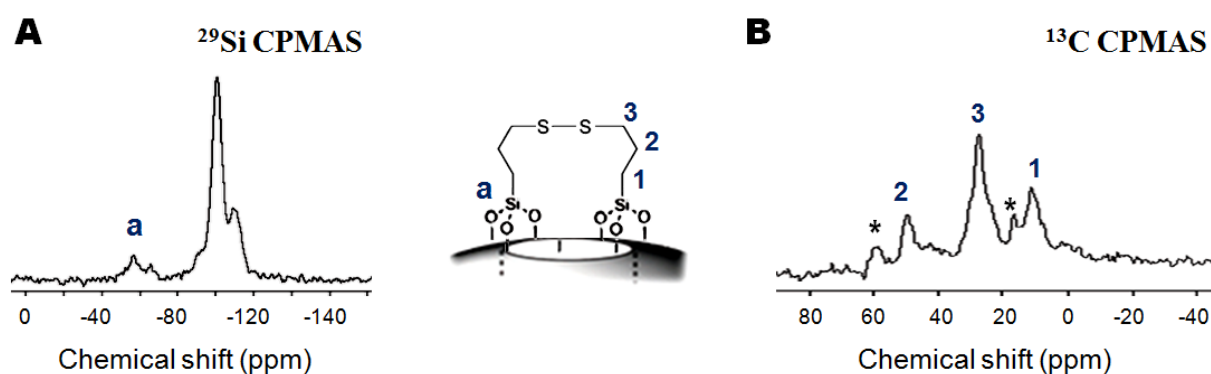


Figure S6. Solid state NMR ^{29}Si (A) and ^{13}C (B) CPMAS spectra of MSN nanogates.

Element	C	N	O	Si	S	TOTAL
M2PS Nanogates	50.12	7.36	26.31	16.05	0.16	100.00
MSN Nanogates	6.91	0.00	55.51	37.43	0.15	100.00

Table S3. EDS elemental analysis of M2PS and MSN nanogates. The presence of sulfur and carbon confirmed the nanogates surface mechanization.

Sample	Zeta Potential (mV)
MSN	-20
MSN Nanogates	-12
MSN Nanogates + ME	-27
M2PS	-23
M2PS Nanogates	-14
M2PS Nanogates + ME	-31

Table S4. Zeta potential analysis on M2PS and MSN before and after nanogates functionalization, and after disulfide cleavage via mercaptoethanol addition. The zeta potential trends correlates the activation mechanism of the disulfides.

Sample Name	M2PS-50	M2PS-25
DOX Loading capacity (wt %)	2.0	2.5

Table S5. DOX loading capacities in the M2PS-50 and M2PS-25 nanogates. The loading capacities were calculated from the UV-visible analysis of the supernatant of the mercaptoethanol-triggered release of doxorubicin in solution.

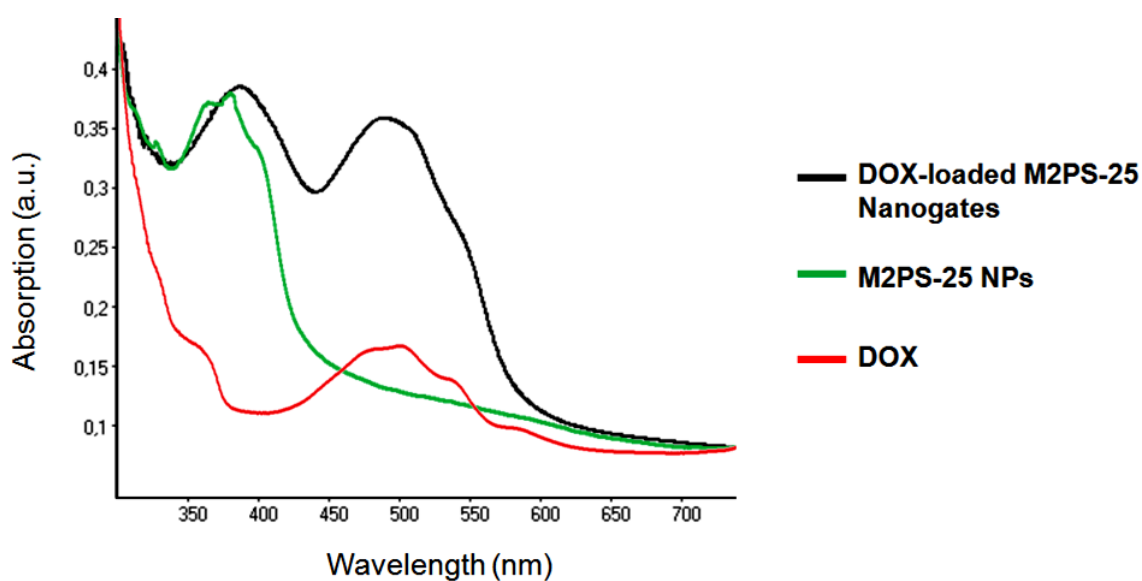


Figure S7. Absorption spectra comparison of DOX, M2PS-25, and DOX loaded M2PS-25 nanogates, depicting the DOX encapsulation in the M2PS mesopores.

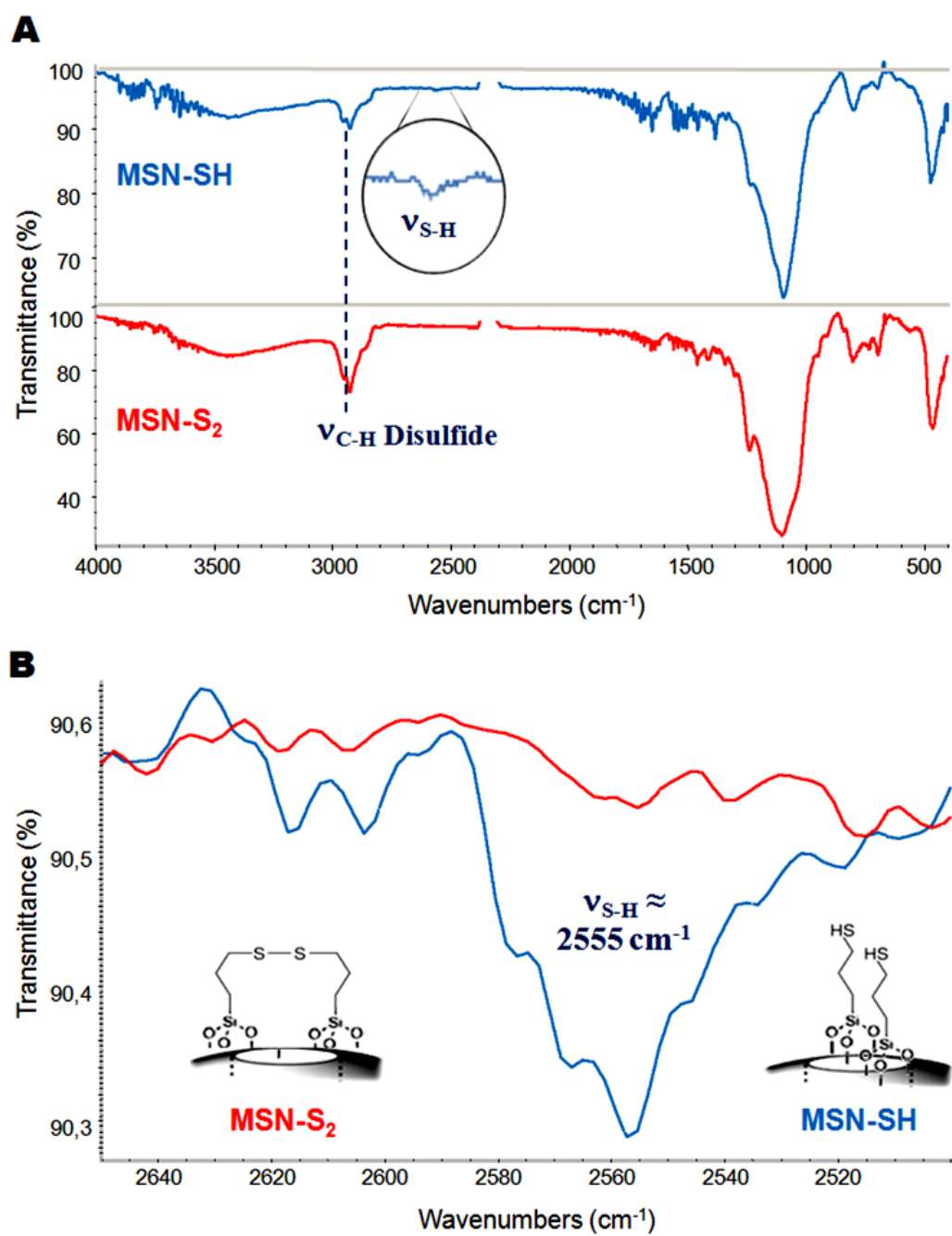
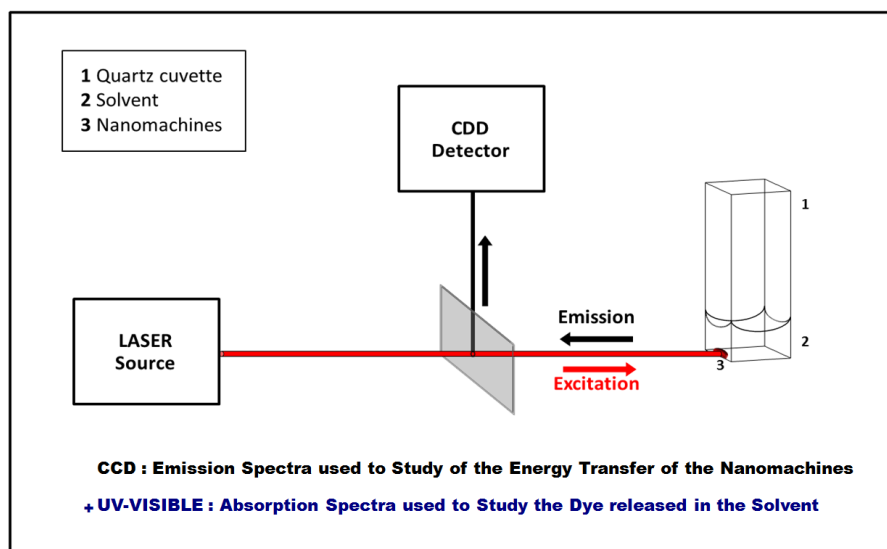


Figure S8. IR spectra comparison of MSN-SH and MSN-S₂ (after iodine addition) controls confirming the disulfide redox mechanism.

IV- TWO-PHOTON SOLUTION STUDIES



Scheme S2. Representation of the two-photon irradiation settings for the cargo release in solution. The quartz cuvette was taken out of this setting for UV-visible measurements during the experiment.

IV- TWO-PHOTON IN-VITRO STUDIES

Two-Photon Fluorescence Imaging. The day prior to the experiment, MCF7 cells were seeded onto bottom glass dishes (World Precision Instrument, Stevenage, UK) at a density of 10^6 cells. cm^{-2} . Adherent cells were then washed once and incubated in 1 mL culture medium containing nanovalves at a concentration of $40 \mu\text{g.mL}^{-1}$ for 20 h. Fifteen min before the end of incubation, cells were loaded with Cell Mask (Invitrogen, Cergy Pontoise, France) for membrane staining at a final concentration of $5 \mu\text{g.mL}^{-1}$. Before visualization, cells were washed gently with phenol red-free DMEM; then, scanned with a LSM 780 LIVE confocal microscope (Carl Zeiss, Le Pecq, France), at 760 nm with a slice depth (Z stack) of $0.62 \mu\text{m}$.

TPE-Therapy. MCF-7 human breast cancer cells were cultured in Dulbecco's modified Eagle's medium (DMEM) supplemented with 10% fetal bovine serum and $50 \mu\text{g.mL}^{-1}$ gentamycin. All cells were allowed to grow in humidified atmosphere at 37°C under 5% CO_2 . For *in vitro* phototoxicity, MCF-7 cells were seeded into a 384 multiwell glass-bottomed plate (thickness 0.17 mm), with a black polystyrene frame, 2000 cells per well in $50 \mu\text{L}$ of culture medium, and allowed to grow for 24 h. Nanoparticles were then dispersed under ultrasounds in PBS at a concentration of 1 mg.mL^{-1} and cells were then incubated for 20 h with or without nanoparticles at a final concentration of $40 \mu\text{g.mL}^{-1}$ in supplemented DMEM. After incubation with nanoparticles, cells were washed twice, maintained in fresh culture medium, and then submitted (or not) to laser irradiation; with the Carl Zeiss Microscope LSM 780 LIVE confocal microscope (laser power input 3W). Half of the well was irradiated at 760 nm by three scans of 1.57 s duration in 4 different areas of the well. The laser beam was focused by a microscope objective lens (Carl Zeiss 10x , NA 0.4). After 2 days, the MTT assay was performed and was corrected.

CHAPTER 6

Versatile Synthesis of Biodegradable Disulfide Hybrid Bridged Silsesquioxane Nanoparticles: Two-Photon Photodynamic Therapy on Cancer Cells

INTERDISCIPLINARY COLLABORATION

J. Croissant, C. Mauriello-Jimenez, X. Cattoën, M. Wong Chi Man, P. Maillard, L. Raehm, J-O. Durand: *Nanomaterial concept, synthesis, physico-chemical characterizations, and applications in solution.*

O. Mongin, V. Hugues, M. Blanchard-Desce: *Photosensitizer concept and two-photon photophysical characterizations. Nanomaterial two-photon photophysical characterizations.*

C. Mauriello-Jimenez, P. Maillard, J. Croissant: *Fluorophores synthesis and physico-chemical characterizations.*

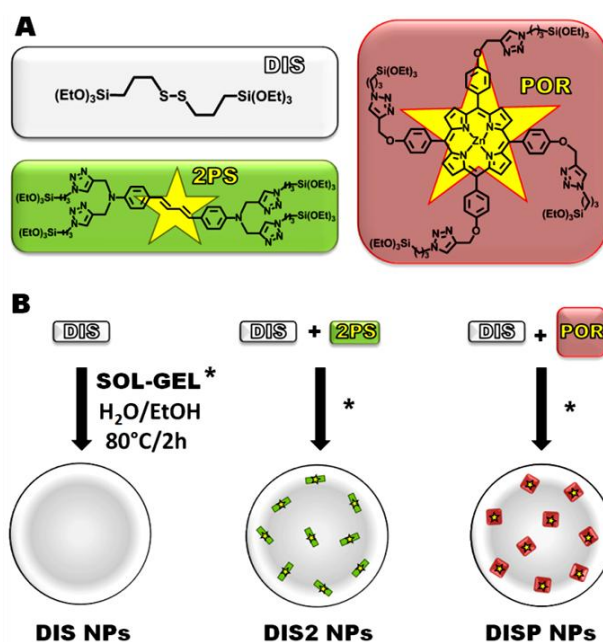
M. Maynadier, M. Gary-Bobo, M. Garcia: *Two-photon cell studies.*

Introduction

Two-photon nanomedicine is emerging as an excellent strategy to fulfill the spatiotemporal requirements of cancer therapy.^[1-3] Near-infrared (NIR) two-photon-sensitive nanodevices benefit the three-dimensional resolution and the low scattering losses of the irradiation in biological tissues, and thus safer and more selective treatments.^[4,5] Biodegradable nanoparticles (NPs) are of particular interest since they favor a safe and efficient excretion of the nanoparticles (NPs).^[6-8] Increasing number of biodegradable nanoplatforms have been reported such as porous silicon NPs,^[6] various polymeric NPs^[9-13] amongst which are poly(lactic-co-glycolic acid) (PLGA) and poly- ϵ -caprolactone (PCL) aliphatic polyesters,^[7,13] magnesium and manganous phosphate NPs,^[14] and calcium phosphate NPs.^[15]

Bridged silsesquioxane (BS) NPs is an emerging nanomaterial for applications in nanotechnology. BS compounds are produced from sol-gel processes of bis- or multi-organoalkoxysilane precursors so as to maximize the organic content of the resulting material. Up to now, very few studies have been reported on BS NPs since it is generally challenging to control the sol-gel process towards the nanoscale without the addition of silica precursors (e.g. tetraethoxysilane). Shea and co-workers pioneered BSNPs with photoresponsive,^[16,17] electrochemical,^[18] and electrochromic properties,^[19] while Hammers *et al.* used a modified Stöber synthesis to elaborate BS NPs from perylene diimide fragments as photovoltaic material.^[20] Only one study has been reported on biodegradable BS NPs with gadolinium(III)-disulfide-based material as *in-vitro* contrast agents via magnetic resonance imaging (MRI).^[21] BS NPs releasing cis-platin for targeted cancer chemotherapy were also reported.^[22] We recently studied the first BS NPs for two-photon excited (TPE) photodynamic therapy (PDT) on cancer cells from a tetraalkoxysilylated diphenylbutadiene two-photon photosensitizer (2PS) (see chapter 7).

In this communication we describe a versatile synthesis to obtain biodegradable BS NPs based on disulfide linkers. A novel tetraalkoxysilylated porphyrin photosensitizer precursor (POR) was developed via click chemistry and fully characterized. 2PS and POR precursors were then co-condensed with bis(propyl)disulfide to design two-photon-sensitive biodegradable BS NPs for nanomedical application (Scheme 1). Besides, the proof of concept of the biodegradability was demonstrated, and the designed hybrid BS NPs were biocompatible. Furthermore, *in-vitro* two-photon fluorescence imaging displayed the cellular uptake of the NPs, which also produced powerful TPE-PDT on MCF-7 breast cancer cells.



Scheme 1. Bis(3-(triethoxysilyl)propyl)disulfide (DIS), tetraalkoxysilylated two-photon photosensitizer (2PS), and porphyrine (POR) sol-gel precursors (A). Versatile synthetic process to design disulfide-based BS (DIS) NPs, and hybrid DIS/2PS (DIS2) or DIS/POR (DISP) BS NPs (B).

Results and discussion

The POR precursor and following BS nanomaterials were initially prepared. Firstly, the POR photosensitizer was designed from the reported 5,10,15,20-tetra(propargyloxyphenyl)Zn porphyrin^[23] alkoxy-silylated via a copper-catalyzed azide-alkyne cycloaddition (CuAAC) click coupling (see Scheme S1). The POR precursor was fully characterized via ¹H and ¹³C nuclear magnetic resonance (NMR), Fourier transform infrared (FTIR), and mass spectroscopies (ESI). Secondly, the elaboration of the disulfide- and photosensitizer-disulfide-based biodegradable BS NPs was carried out. A versatile sol-gel process was used for three types of material, the disulfide (DIS), the disulfide-2PS photosensitizer (DIS2), and the disulfide-POR photosensitizer (DISP) hybrid BS NPs (see Scheme 1). The reaction was carried out in a water/ethanol (5:2, v:v) mixture with sodium hydroxide catalysis at 80°C (ESI). Note that, the presence a cetyltrimethylammonium bromide was found to be necessary for the control of the NPs condensation.

The morphology and composition of the BS nanomaterials were then characterized via various techniques. Transmission electron microscopy (TEM) revealed DIS and DIS2 30 nm and 40 nm BS nearly monodisperse nanospheres respectively (See Fig. 1A and B). Besides, this synthetic route could be used to tune the size of the NPs with the variation of the alkoxy-silane concentrations. Consequently, DISP NPs of 200 and 50 nm were prepared (Fig. 1C and D respectively) by decreasing the disulfide precursor concentration of a quarter (ESI). UV-visible spectroscopy confirmed the successful encapsulation of the 2PS and POR precursors in the BS NPs as shown respectively by the absorption peak maximum at 390 nm (Fig. S1A), and the Soret bands from 403 to 461 nm along with the weak Q bands at 569 and 607 nm (Fig. S1B). In light of the fact that the Soret band at 425 nm in the precursor was split

into three bands at 403, 431, and 461 nm, it can be asserted that the aggregation of the POR precursors occurred in the DISP NPs, according to the type H (blue shift at 403) and J aggregates (red shift at 461 nm).^[24,25] The presence of the disulfide and photosensitizers functions is also supported by the IR spectra of the DIS and DIS2 NPs composed of the $\nu_{\text{C-H}}$ and $\nu_{\text{Si-C}}$ stretching vibration modes of the disulfide group at 3000-2870 and 1140 cm^{-1} respectively, and the 2PS butadiene $\nu_{\text{C=C}}$ at 1610 cm^{-1} with the aromatic $\nu_{\text{C-H}}$ and para-disubstituted bending modes at 3140-3020 and 797 cm^{-1} respectively (Fig. S2 and S3). Similar observations were made from FTIR spectra of DISP NPs depicting the $\nu_{\text{C=C}}$ (1612 cm^{-1}) and $\delta_{\text{C-H}}$ (797 cm^{-1}) typical of porphyrin derivatives.^[26] Moreover, solid state NMR ^{13}C and ^{19}Si cross-polarization magic angle spinning (CPMAS) spectra of the DIS, DIS2, and DISP NPs showed both the presence of the siloxane network by the T_3 silicon environments at -67 ppm (Fig. S4A,C, and E), with the three types of carbon found in this DIS moiety at 10, 27, and 47 ppm, and the photosensitizers carbon local environments (see Fig. S4D and F). The 2PS content in the DIS2 NPs was determined to be of 41 weight percent via elemental analysis of nitrogen atoms (14 per 2PS molecule, see Table S1). Similarly, the POR contents were respectively of 12 and 16 wt% for DISP NPs of 50 and 200 nm (16 nitrogen atoms per POR molecule, Table S1).

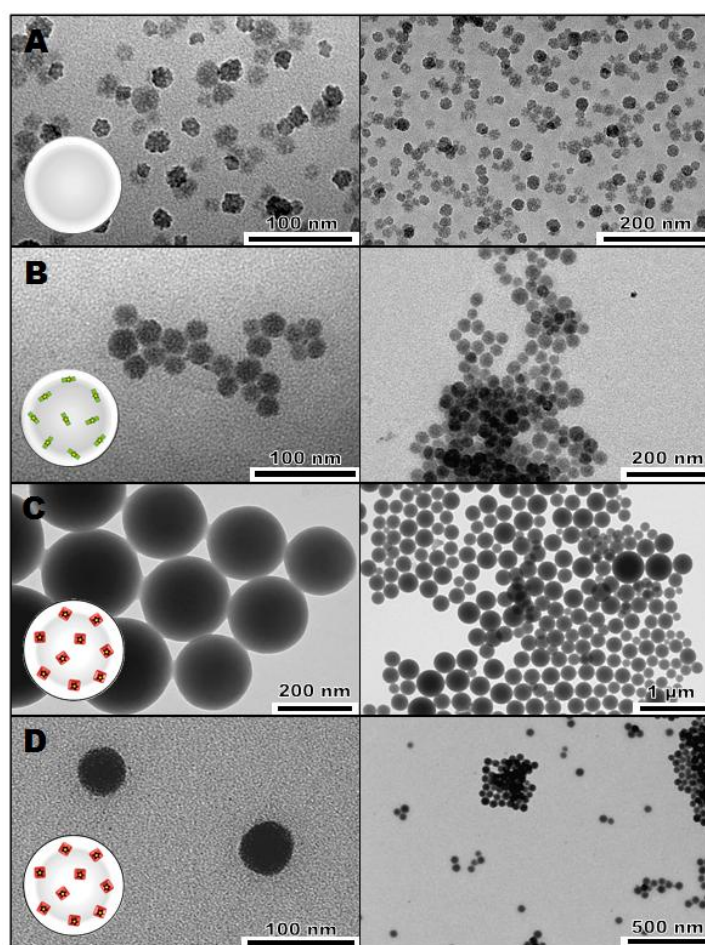
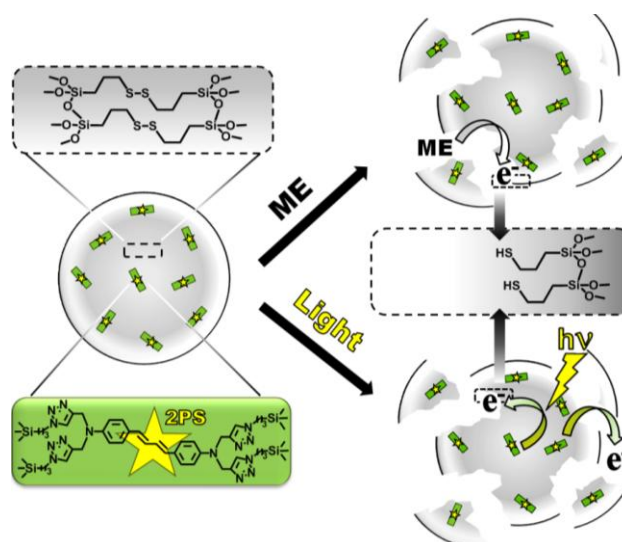


Figure 1. TEM images of DIS (A), DIS2 (B), 200 nm DISP (C), and 50 nm DISP NPs (D).

The biodegradability of the BS NPs was then assessed in near-physiological conditions. The nanomaterials were dispersed in PBS à 37°C, and an equivalent of the intracellular concentration of glutathione was added (2 nM of mercaptoethanol). TEM images of the NPs before and after 48 h of biodegradability control displayed the degradation of DIS2 and DISP NPs (Fig. 2A and B respectively). On the other hand, the electron production of the photosensitizers under irradiation^[27,28] was also expected to disrupt the BS matrix via disulfide cleavage (see Scheme 2). The proof of concept of this phenomenon was validated by TEM analysis of DIS2 after 24h of irradiation at 365 nm (Fig. 2E), which is also confirmed by



Scheme 2. Representation of the chemical and photochemical degradability of the DIS2 NPs.

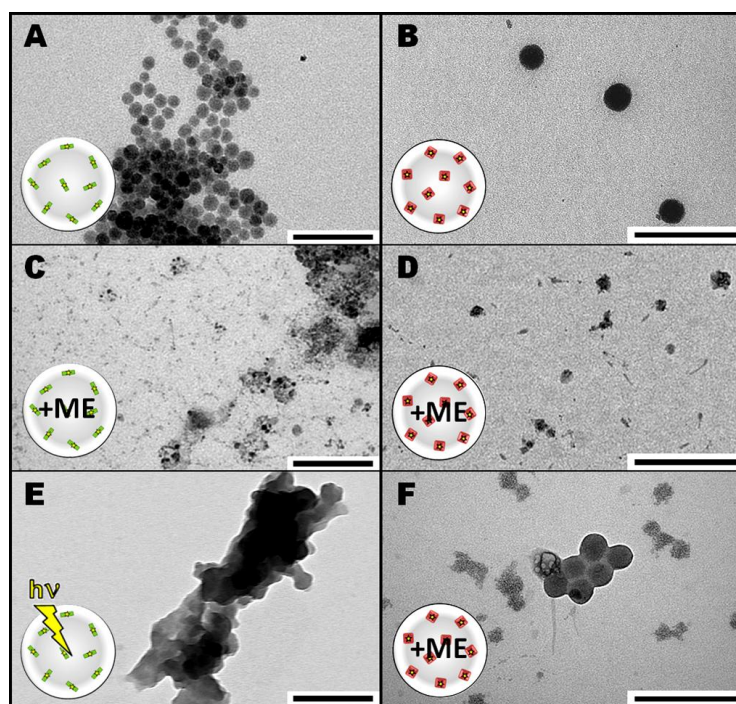


Figure 2. TEM images of DIS 2 (A, C, E) and 50 nm DISP NPs (B, D, F) before (A-B) and after 48 h of near-physiological chemical reduction (C-D, F), or 24 h of photochemical reduction (E). Scale bars 100 nm.

TEM analysis of DIS2 after 24h of irradiation at 365 nm (Fig. 2E), which is also validated by the narrow size distribution disappearance depicted by dynamic light scattering (DLS, Fig. S5). Additionally, both DIS2 and DISP BS nanospheres did not display any significant cytotoxicity up to 125 $\mu\text{g.mL}^{-1}$ (see Fig. 3A). Hence, biocompatible and biodegradable photosensitizer-disulfide hybrid BS NPs were successfully prepared.

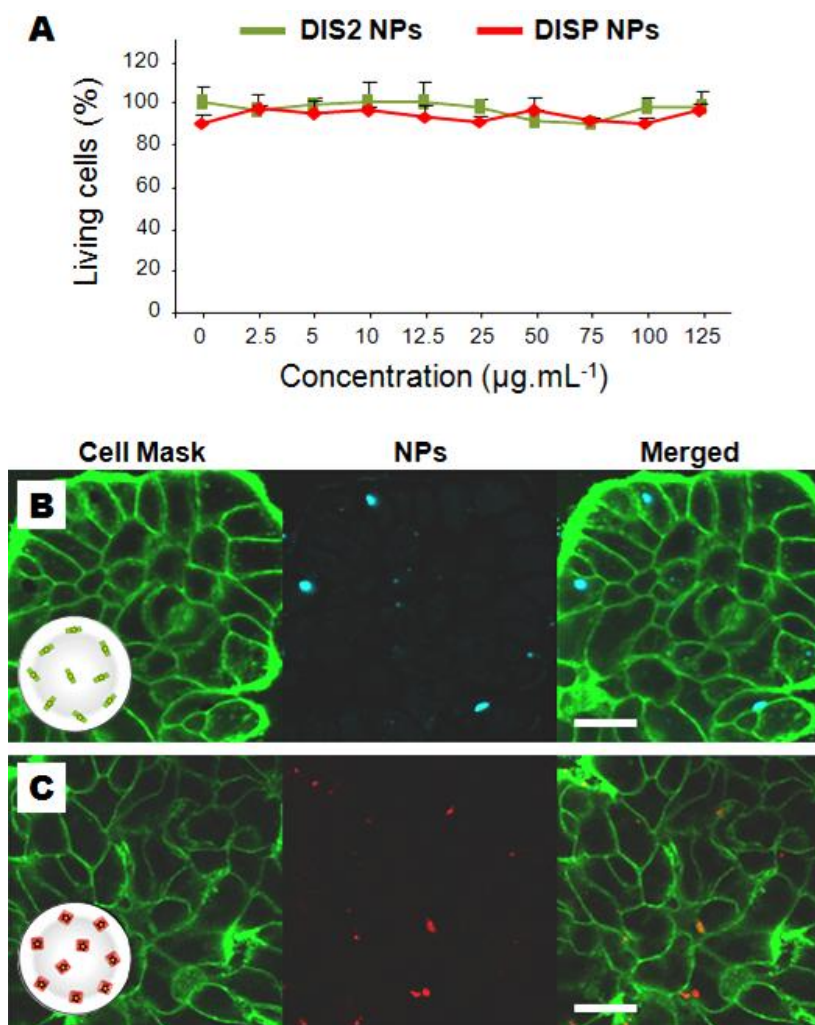


Figure 3. Cytotoxicity study of DIS2 and 50 nm DISP NPs with MCF-7 cancer cells (A). Two-photon confocal microscopy images of cells NPs incubated during 20 h with 40 $\mu\text{g.mL}^{-1}$ of DIS2 (B) and DISP (C). Scale bars of 10 μm .

Two-photon confocal *in-vitro* studies were eventually led on MCF-7 breast cancer cells incubated 20 h with 40 $\mu\text{g.mL}^{-1}$ of BS NPs. First, the two-photon imaging feature of the nanoplateforms was considered with the low-laser power irradiation of DIS2 and DISP NPs at 760 and 800 nm respectively. The endocytosis of DIS2 as well as the DISP nanospheres was clearly seen with the confocal microscopy merged images (see Fig. 3B,C). Besides, the DIS2

material displayed powerful two-photon fluorescence particularly efficient for intracellular NPs tracking.

Finally, the two-photon-triggered PDT was conducted on cancer cells incubated with DIS2 and 50 nm DISP NPs irradiated at maximum power. Figure 4 demonstrates the harmlessness of the two-photon laser on the hand (see white bars), and the great potential of the photosensitizer-disulfide-based NPs on the other (red bars). Indeed, 40% of selective cell death was obtained with irradiated DIS2 while DISP NPs caused up to 54%, which make them particularly interesting nanomedical devices for cancer therapy. Comparing BS NPs solely composed of 2PS precursor (see chapter 7), the disulfide framework was thus well-suited for the preservation of the TPE-PDT effect and the design of biodegradable nanomedical tools. Concerning DISP NPs, the surprising two-photon sensitivity of the DISP NPs arose from the H and J POR aggregates, as reported in the literature.^[5]

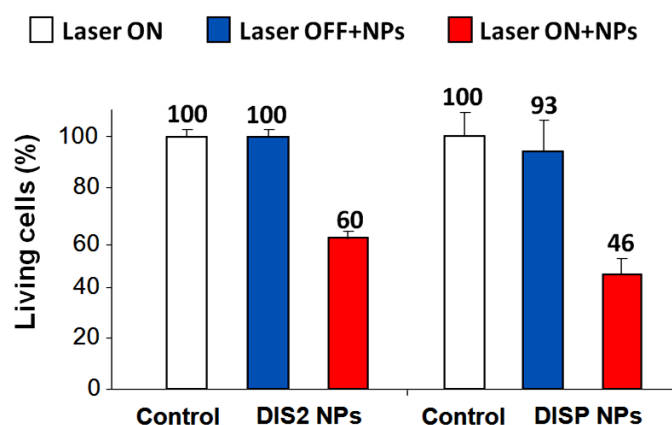


Figure 4. TPE-triggered cancer cell killing on DIS2 (irradiated at 760 nm) and 50 nm DISP NPs (irradiated at 800 nm).

Conclusion

In summary, we have designed photosensitizer-disulfide-based bridged silsesquioxane NPs via a versatile synthetic process. A novel porphyrine photosensitizer was reported and used for the preparation of hybrid BS NPs. The morphology, compositions, and functionalities of the nanomaterials were fully characterized by various techniques, which showed the encapsulation of photosensitizers in the disulfide matrices. Besides, the POR precursor was found to be aggregated in the BS NPs, which produced two-photon sensitivity for biomedical applications. The DIS2 and DISP BS NPs were both biodegradable in near-physiological media, and biocompatible in MCF-7 cancer cells. Furthermore, TPE-fluorescence imaging *in-vitro* was performed to demonstrate the NPs cellular uptake, and TPE-PDT lead to 40 to 60% of spatiotemporally-controlled cancer cell killing. It is envisioned that such organic-inorganic hybrid material could be efficient biodegradable theranostic for cancer treatment.

REFERENCES

- [1] M. Gary-Bobo, Y. Mir, C. Rouxel, D. Brevet, I. Basile, M. Maynadier, O. Vaillant, O. Mongin, M. Blanchard-Desce, A. Morère, M. Garcia, J.-O. Durand, L. Raehm, *Angewandte Chemie International Edition* **2011**, *123*, 11627.
- [2] J. Croissant, M. Maynadier, A. Gallud, H. Peindy N'Dongo, J. L. Nyalosaso, G. Derrien, C. Charnay, J.-O. Durand, L. Raehm, F. Serein-Spirau, N. Cheminet, T. Jarroson, O. Mongin, M. Blanchard-Desce, M. Gary-Bobo, M. Garcia, J. Lu, F. Tamanoi, D. Tarn, T. M. Guardado-Alvarez, J. I. Zink, *Angewandte Chemie International Edition* **2013**, *125*, Angewandte Chemie International Edition.
- [3] H. M. Kim, B. R. Cho, *Accounts of Chemical Research* **2009**, *42*, 863.
- [4] J. Croissant, A. Chaix, O. Mongin, M. Wang, S. Clément, L. Raehm, J.-O. Durand, V. Hugues, M. Blanchard-Desce, M. Maynadier, A. Gallud, M. Gary-Bobo, M. Garcia, J. Lu, F. Tamanoi, D. P. Ferris, D. Tarn, J. I. Zink, *Small* **2014**, *n/a*, n/a.
- [5] M. Pawlicki, H. A. Collins, R. G. Denning, H. L. Anderson, *Angewandte Chemie-International Edition* **2009**, *48*, 3244.
- [6] J.-H. Park, L. Gu, G. von Maltzahn, E. Ruoslahti, S. N. Bhatia, M. J. Sailor, *Nature Materials* **2009**, *8*, 331.
- [7] M. Fadel, K. Kassab, D. A. Fadeel, *Lasers in Medical Science* **2010**, *25*, 283.
- [8] M. Gaumet, R. Gurny, F. Delie, *International Journal of Pharmaceutics* **2010**, *390*, 45.
- [9] T. Uto, M. Toyama, Y. Nishi, T. Akagi, F. Shima, M. Akashi, M. Baba, *Results in Immunology* **2013**, *3*, 1.
- [10] J. Panyam, V. Labhasetwar, *Advanced Drug Delivery Reviews* **2003**, *55*, 329.
- [11] M. Keeney, S.-G. Ong, A. Padilla, Z. Yao, S. Goodman, J. C. Wu, F. Yang, *ACS Nano* **2013**, *7*, 7241.
- [12] P. K. Dutta, J. Dutta, S. Pandey, C. Haldar, D. Patel, P. Maiti, in *Advances in Polymer Science*, **2013**, *254*, 169.
- [13] J. M. Silva, M. Videira, R. Gaspar, V. Préat, H. F. Florindo, *Journal of Controlled Release* **2013**, *168*, 179.
- [14] G. Bhakta, S. Mitra, A. Maitra, *Biomaterials* **2005**, *26*, 2157.
- [15] J. Li, Y.-C. Chen, Y.-C. Tseng, S. Mozumdar, L. Huang, *Journal of Controlled Release* **2010**, *142*, 416.
- [16] L.-C. Hu, Y. Yonamine, S.-H. Lee, W. E. Van der Veer, K. J. Shea, *Journal of the American Chemical Society* **2012**, *134*, 11072.
- [17] L. Zhao, M. Vaupel, D. A. Loy, K. J. Shea, *Chemistry of Materials* **2008**, *20*, 1870.
- [18] M. Khiterer, K. J. Shea, *Nano Letters* **2007**, *7*, 2684.
- [19] V. Jain, M. Khiterer, R. Montazami, H. M. Yochum, K. J. Shea, J. R. Heflin, *ACS Applied Materials & Interfaces* **2009**, *1*, 83.
- [20] H. Rathnayake, J. Binion, A. McKee, D. J. Scardino, N. I. Hammer, *Nanoscale* **2012**, *4*, 4631.
- [21] J. L. Vivero-Escoto, W. J. Rieter, H. Lau, R. C. Huxford-Phillips, W. Lin, *Small* **2013**, *9*, 3523.
- [22] J. Della Rocca, R. C. Huxford, E. Comstock-Duggan, W. Lin, *Angewandte Chemie International Edition* **2011**, *50*, 10330.
- [23] A.-L. Wirocius, E. Ibarboure, L. Scarpantonio, M. Schappacher, N. D. McClenaghan, A. Deffieux, *Polymer Chemistry* **2013**, *4*, 1903.
- [24] N. C. Maiti, S. Mazumdar, N. Periasamy, *The Journal of Physical Chemistry B* **1998**, *102*, 1528.
- [25] M. Shirakawa, S.-i. Kawano, N. Fujita, K. Sada, S. Shinkai, *The Journal of Organic Chemistry* **2003**, *68*, 5037.
- [26] S. Tao, G. Li, *Colloid and Polymer Science* **2007**, *285*, 721.
- [27] E. Beaumont, J. C. Lambry, M. Blanchard-Desce, P. Martasek, S. P. Panda, E. E. H. van Faassen, J. C. Brochon, E. Deprez, A. Slama-Schwok, *Chembiochem* **2009**, *10*, 690.
- [28] A. C. Robin, S. Gmouh, O. Mongin, V. Jouikov, M. H. V. Werts, C. Gautier, A. Slama-Schwok, M. Blanchard-Desce, *Chemical Communications* **2007**, *13*, 1334.

APPENDIX: SUPPORTING INFORMATION

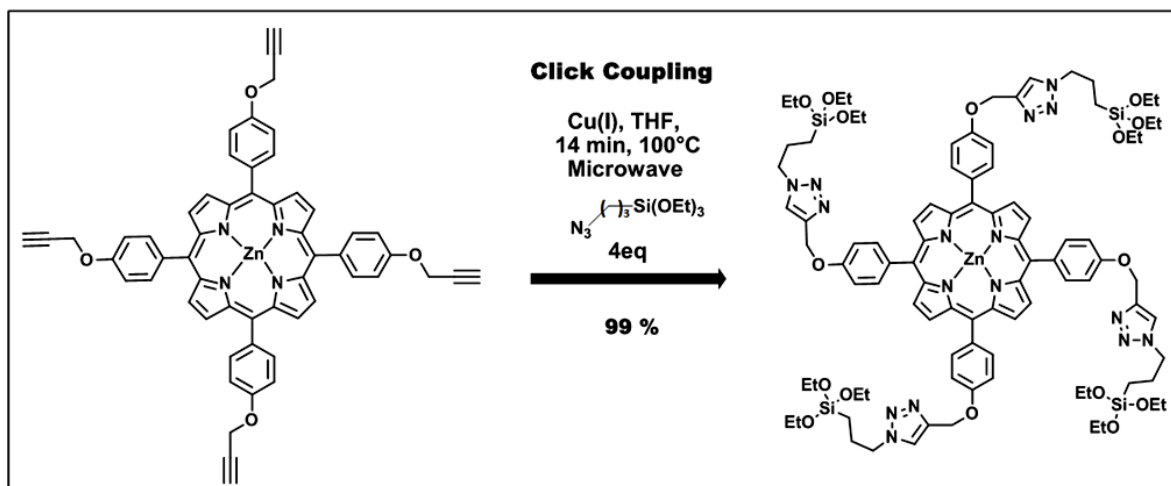
I- EXPERIMENTAL SECTION

Materials. Cetyltrimethylammonium bromide (CTAB) and sodium hydroxide were purchased from Sigma-Aldrich. Absolute ethanol was purchased from Fisher Chemicals. R. Norma Pure. Bis(3-triethoxysilylpropyl)disulfide were purchased from ABCR. (3-azidopropyl)trimethoxysilane was obtained from a reported procedure by M. Ortega-Muñoz et al (*Adv. Synth. Catal.* **2006**, 348, 2410).

General Procedures. ^1H and ^{13}C NMR spectra were recorded with a Bruker AC 400 spectrometer. Chemical shifts (in δ units, ppm) are referenced to TMS using CHCl_3 ($\delta = 7.26$ ppm) and CDCl_3 ($\delta = 77.0$ ppm) as the internal standards, respectively, for ^1H and ^{13}C NMR spectra. IR spectra were recorded on a Perkin-Elmer 100 FT spectrophotometer. Absorption spectra were recorded on a Hewlett-Packard 8453 spectrophotometer and fluorescence data were collected on a Perkin-Elmer LS55 fluorimeter. Mass spectrometry was carried out at the Laboratoire de Spectrometrie de Masse (Lyon, France) with a Thermo-Finnigan MAT95 apparatus in electronic impact ionization mode. Dynamic light scattering analyses were performed using a Cordouan Technologies DL 135 Particle size analyzer instrument. ^{29}Si and ^{13}C CPMAS solid state NMR sequences were recorded with a VARIAN VNMR5300, using Q8MH8 and adamantane references respectively. TEM analysis performed on a JEOL 1200 EXII instrument. SEM analysis performed on a FEI Quanta FEG 200 instrument.

II- PORPHYRINE PRECURSOR SYNTHESIS AND CHARACTERIZATIONS

POR Precursor. A mixture of the tetrapropargyld porphyrine derivative (100 mg, 1.12×10^{-1} mmol), bromotris(triphenylphosphine)copper(I) ($[\text{CuBr}(\text{PPh}_3)_3]$, 10 mg, 1×10^{-2} mmol), and anhydrous THF (3 mL) was placed in a 10 mL microwave sealable reactor, and (3-azidopropyl)triethoxysilane (150 mg, 0.6 mmol) was added. Then, the tube was flushed with argon and the microwave process was conducted 20 min at 100°C at 200 mW. After evaporation of the solvents, the POR precursor was quantitatively obtained as a purple solid (210 mg, 1.12×10^{-1} mmol). ^1H NMR (300 MHz, $\text{DMSO}-d_6$): δ 8.81 (s, 8H, $\text{H}_{\text{pyrrole}}$), 8.41 (s, 4H, triazole), 8.09 (d, $^3J = 8.4$ Hz, 8H, $\text{H}_{\text{Ph-pyrrole}}$), 7.44 (d, $^3J = 8.2$ Hz, 8H, $\text{H}_{\text{Ph-triazole}}$), 5.43 (s, 8H, $\text{N}-\text{CH}_2\text{-triazole}$), 4.45 (t, $^3J = 7.0$ Hz, 8H, triazole- CH_2), 3.77 (q, $^3J = 7$ Hz, 24H, $\text{O}-\text{CH}_2\text{-CH}_3$), 1.99 (t, $^3J = 7.8$ Hz, 8H, triazole- $\text{CH}_2\text{-CH}_2$), 1.16 (t, $^3J = 6.9$ Hz, 36H, $\text{O}-\text{CH}_2\text{-CH}_3$), 0.60 (t, $^3J = 7.7$ Hz, 8H, $\text{CH}_2\text{-Si}$). ^{13}C NMR (400MHz, DMSO): δ 158.8, 149.9, 143.19, 135.5, 131.8, 129, 125, 120, 113.1, 58.2, 53.3, 52.14, 24.3, 18.5, 7.3. ^{29}Si NMR (400MHz, DMSO): δ -46.4. FTIR (neat KBr) $\nu_{\text{max}}/\text{cm}^{-1} = 3116, 3032, 2977, 2932, 2882, 1596, 1563, 1502, 1435, 1391, 1346, 1296, 1268, 1240, 1174, 1107, 1068, 996, 945, 840, 789, 712, 684, 533, 422$. UV/Vis λ_{max} (EtOH): 426, 561, 604 nm. Emission (EtOH): $\lambda_{\text{max}} = 607, 660$ nm ($\lambda_{\text{excitation}} = 432$ nm). MALDI-TOF: calcd for $\text{C}_{92}\text{H}_{120}\text{N}_{16}\text{O}_{16}\text{Si}_4\text{Zn}$: 1880.690, found 1880.720.



Scheme S1. Design of the POR precursor via click CuAAC coupling.

III- NANOMATERIALS SYNTHESSES

DIS NPs. A mixture of CTAB (250 mg), distilled water (120 mL), and sodium hydroxide (875 μL , 2 M) was stirred at 80°C during 50 minutes at 700 rpm in a 250 mL three neck round bottom flask. Then, bis(3-triethoxysilylpropyl)disulfide (2.4 mL) was added to the aforementioned solution, and the condensation process was conducted for 2 h. Afterwards, the solution was cooled to room temperature while stirring; fractions were gathered in propylene tubes and collected by centrifugation during 15 minutes at 21 krpm. The sample was then washed three times with ethanol, water, and ethanol. Each washing was followed by centrifugation collection of the sample in the same manner. The as-prepared material was dried under vacuum for few hours.

DIS2 NPs. A mixture of CTAB (250 mg), distilled water (120 mL), and sodium hydroxide (875 μL , 2 M) was stirred at 80°C during 50 minutes at 700 rpm in a 250 mL three neck round bottom flask. Then, bis(3-triethoxysilylpropyl)disulfide (2.4 mL) was added to the aforementioned solution along with the two-photon photosensitizer (177 mg in 1 mL of absolute ethanol), and the condensation process was conducted for 2 h. Afterwards, the solution was cooled to room temperature while stirring; fractions were gathered in propylene tubes and collected by centrifugation during 15 minutes at 21 krpm. The sample was then washed three times with ethanol, water, and ethanol. Each washing was followed by centrifugation collection of the sample in the same manner. The as-prepared material was dried under vacuum for few hours.

200 nm DISP NPs. A mixture of CTAB (125 mg), distilled water (60 mL), and sodium hydroxide (437 μL , 2 M) was stirred at 80°C during 50 minutes at 700 rpm in a 250 mL three neck round bottom flask. Then, bis(3-triethoxysilylpropyl)disulfide (400 μL) was added to the aforementioned solution along with the two-photon photosensitizer (20 mg in 800 μL of absolute ethanol), and the condensation process was conducted for 2 h. Afterwards, the solution was cooled to room temperature while stirring; fractions were gathered in propylene

tubes and collected by centrifugation during 15 minutes at 21 krpm. The sample was then washed three times with ethanol, water, and ethanol. Each washing was followed by centrifugation collection of the sample in the same manner. The as-prepared material was dried under vacuum for few hours.

50 nm DISP NPs. A mixture of CTAB (125 mg), distilled water (60 mL), and sodium hydroxide (437 μ L, 2 M) was stirred at 80°C during 50 minutes at 700 rpm in a 250 mL three neck round bottom flask. Then, bis(3-triethoxysilylpropyl)disulfide (300 μ L) was added to the aforementioned solution along with the two-photon photosensitizer (20 mg in 800 μ L of absolute ethanol), and the condensation process was conducted for 2 h. Afterwards, the solution was cooled to room temperature while stirring; fractions were gathered in propylene tubes and collected by centrifugation during 15 minutes at 21 krpm. The sample was then washed three times with ethanol, water, and ethanol. Each washing was followed by centrifugation collection of the sample in the same manner. The as-prepared material was dried under vacuum for few hours.

Biodegradability studies. A mixture of NPs (1.5 mg), PBS (500 μ L), and mercaptoethanol (50 μ L) was stirred two days at 37°C in an eppendorf tube. Then, aliquots were taken directly to perform the TEM and DLS analyses.

IV- NANOMATERIALS CHARACTERIZATIONS

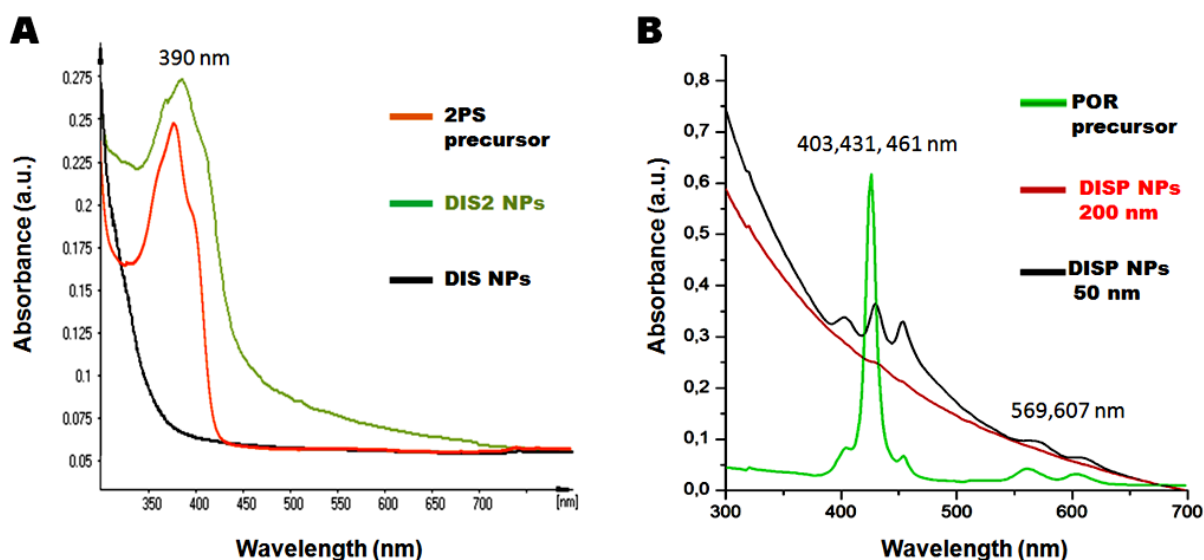


Figure S1. UV-visible spectra of the 2PS precursor, DIS, and DIS2 NPs (A), and of the POR precursor, 50 nm DISP and 200 nm DISP NPs (B), demonstrating the incorporations of both the 2PS and POR photosensitizers.

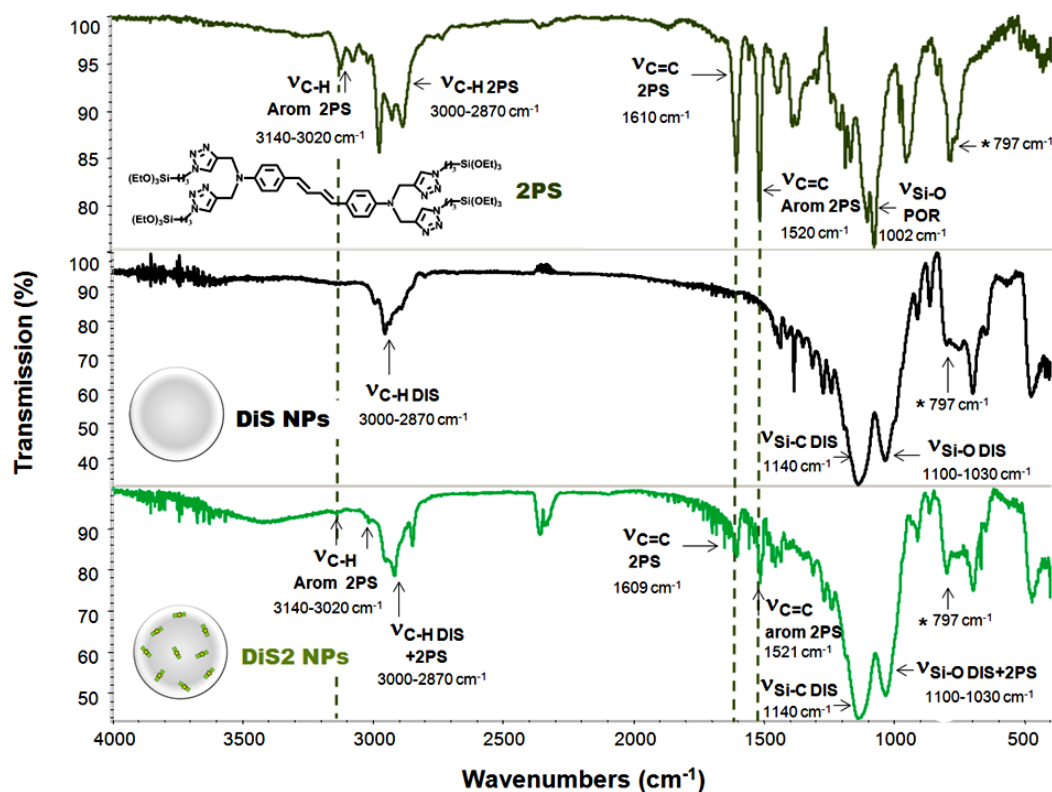


Figure S2. FTIR spectra of the 2PS precursor, DIS, and DIS2 NPs confirming the presence of the DIS and 2PS moieties in the nanomaterials framework. *Out of plan bending of para-disubstituted aromatic rings in the 2PS.

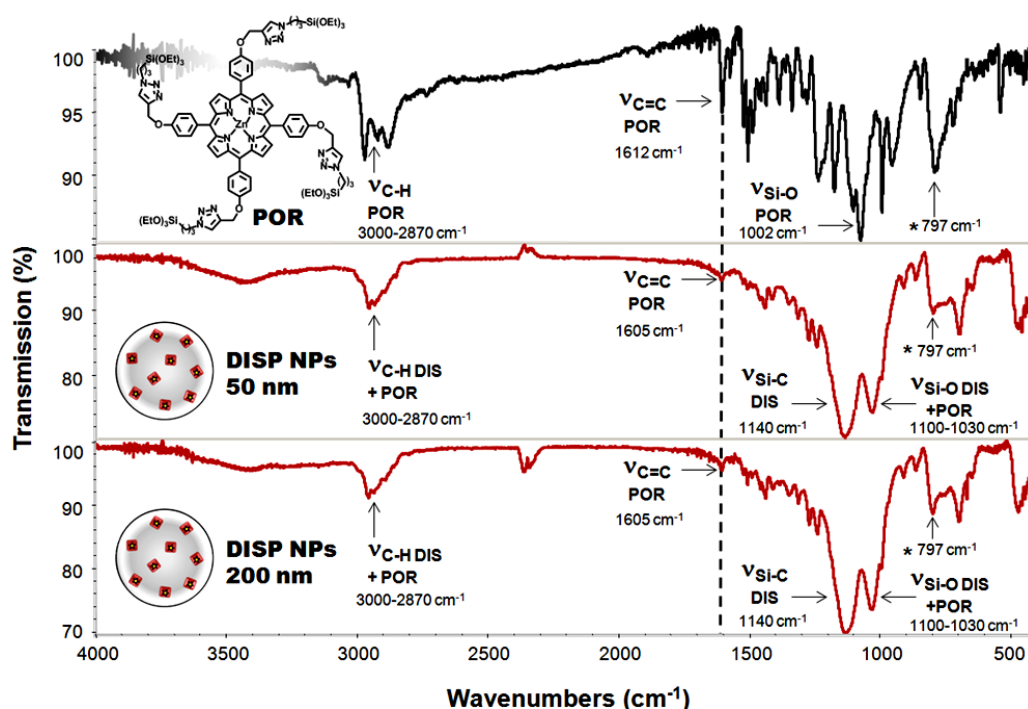


Figure S3. FTIR spectra of the POR precursor, DIS, and DISP NPs confirming the presence of the DIS and POR moieties in the nanomaterials framework. *Out of plan bending of para-disubstituted aromatic rings in the POR.

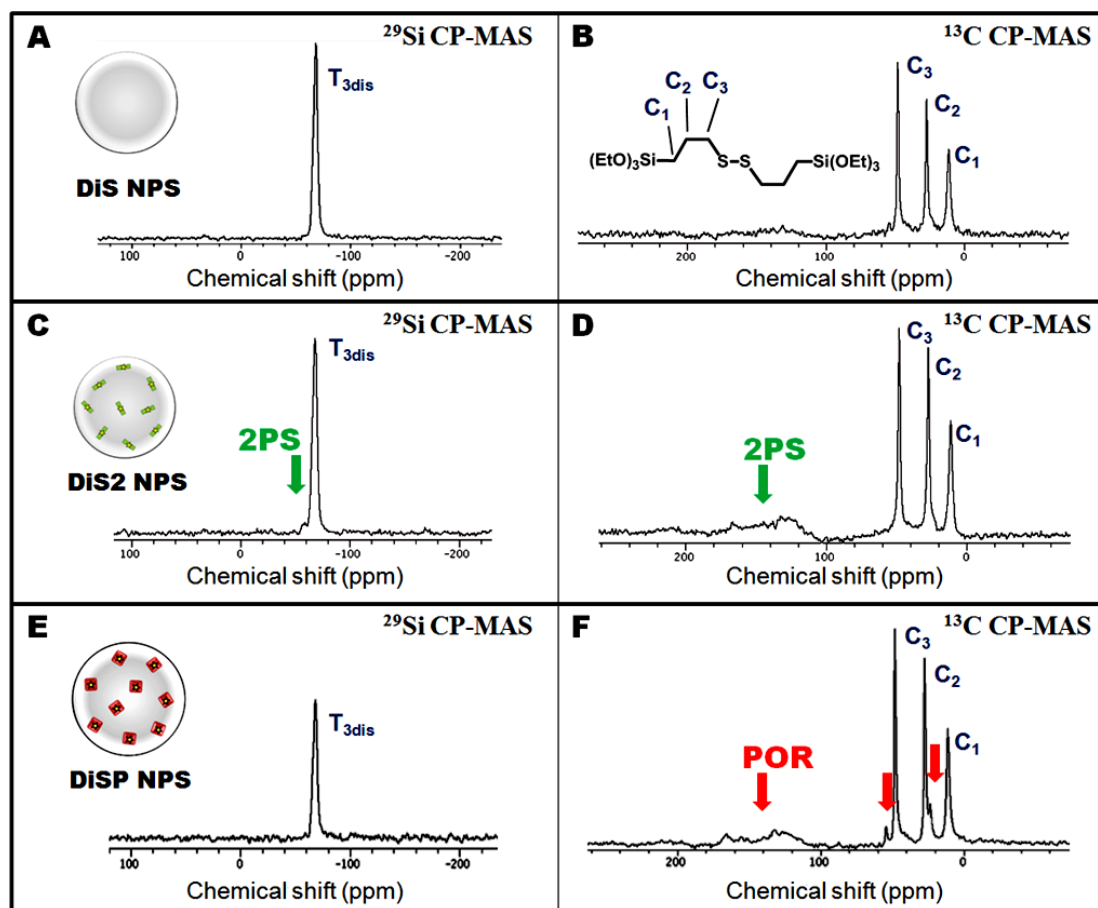


Figure S4. Solid state NMR ^{29}Si and ^{13}C CPMAS spectra of DIS (A-B), DIS2 (C-D), and DISP (E-F).

Table S1. Photosensitizers weight percent determination in the NPs.

Sample	NPs N wt% ^[a]	NPs 2PS or POR wt% ^[b]
DIS2 NPs	5.88	41
50 nm DISP NPs	1.62	12
200 nm DISP NPs	2.25	16

[a] Elemental analysis by combustion measurements of the NPs.

[b] Determination based on the nitrogen wt% in the 2PS and POR molecules.

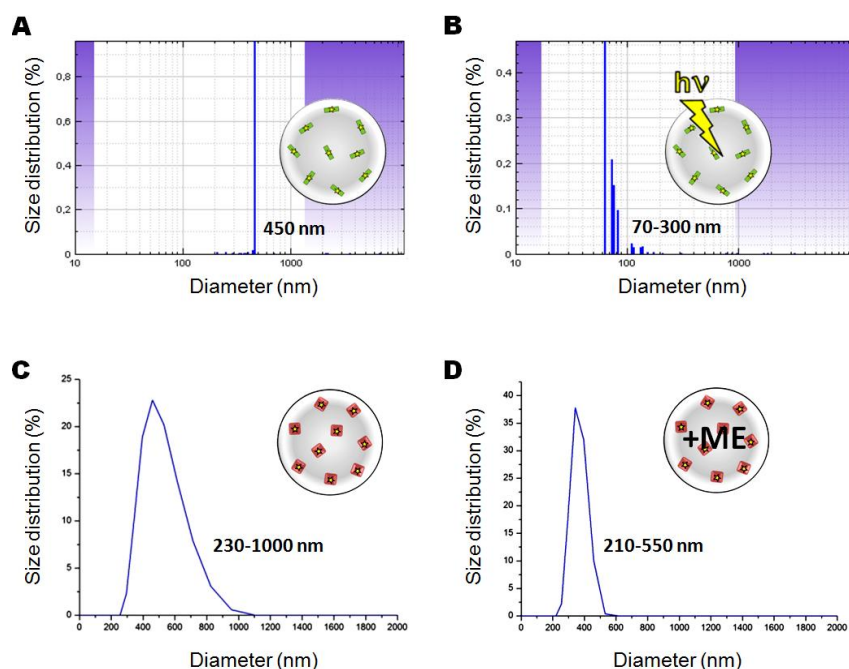


Figure S5. DLS size distributions of DIS2 NPs before and after irradiation (A and B), and of DISP NPs before and after mercaptoethanol addition (C and D), in near-physiological conditions for 24 h.

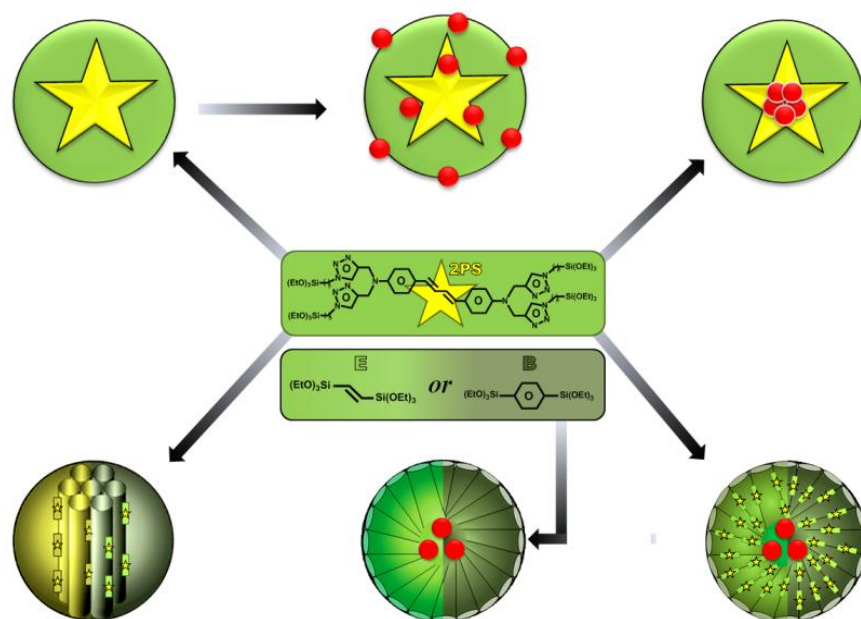
V- TWO-PHOTON IN-VITRO STUDIES

TPE-imaging. The day prior to the experiment, MCF-7 cells were seeded onto bottom glass dishes (World Precision Instrument, Stevenage, UK) at a density of 10^6 cells.cm⁻². Adherent cells were then washed once and incubated in 1 mL culture medium containing NPs at a concentration of 40 $\mu\text{g.mL}^{-1}$ for 20 h. Fifteen min before the end of incubation, cells were loaded with Cell Mask (Invitrogen, Cergy Pontoise, France) for membrane staining at a final concentration of 5 $\mu\text{g.mL}^{-1}$. Before visualization, cells were washed gently with phenol red-free DMEM. Cells were then scanned with a LSM 780 LIVE confocal microscope (Carl Zeiss, Le Pecq, France), at 760 or 800 nm with a slice depth (Z stack) of 0.62 μm .

TPE-therapy. MCF-7 human breast cancer cells were cultured in Dulbecco's modified Eagle's medium (DMEM) supplemented with 10% fetal bovine serum and 50 $\mu\text{g.mL}^{-1}$ gentamycin. All cells were allowed to grow in humidified atmosphere at 37°C under 5% CO₂. For *in vitro* phototoxicity, MCF-7 cells were seeded into a 384 multiwell glass-bottomed plate (thickness 0.17 mm), with a black polystyrene frame, 2000 cells per well in 50 μL of culture medium, and allowed to grow for 24 h. NPs were then dispersed under ultrasounds in PBS at a concentration of 1 mg.mL^{-1} and cells were then incubated for 20 h with or without nanoparticles at a final concentration of 40 $\mu\text{g.mL}^{-1}$ in supplemented DMEM. After incubation with NPs, cells were washed twice, maintained in fresh culture medium, and then submitted (or not) to laser irradiation; with the Carl Zeiss Microscope LSM 780 LIVE confocal microscope (laser power input 3W). Half of the well was irradiated at 760 or 800 nm by three scans of 1.57 s duration in 4 different areas of the well. The laser beam was focused by a microscope objective lens (Carl Zeiss 10x , NA 0.4). After 2 days, the MTT assay was performed and was corrected.

CHAPTER 7

From Two-Photon Photosensitizer to Bridged Silsesquioxane and Periodic Mesoporous Organosilica Nanoparticles: Towards Designed Cancer Theranostic



INTERDISCIPLINARY COLLABORATION

J. Croissant, X. Cattoën, M. Wong Chi Man, J-O. Durand, L. Raehm: *Nanomaterial concept, synthesis, physico-chemical characterizations, and applications in solution.*

O. Mongin, V. Hugues, M. Blanchard-Desce: *Photosensitizer concept and two-photon photophysical characterizations. Nanomaterial two-photon photophysical characterizations.*

J. Croissant: *Photosensitizer synthesis and physico-chemical characterizations.*

M. Gary-Bobo, M. Maynadier, A. Gallud, M. Garcia: *Two-photon cell studies.*

Introduction

Bridged silsesquioxanes, obtained through the sol-gel process from organo-bridged poly-trialkoxysilanes, is an emerging class of organosilicas which features the highest loading of organic groups in the material. The chemistry of bridged silsesquioxanes at the nanoscale is still in its infancy, due to the difficulties of controlling the growth of the nanoparticles from the molecular precursor. Since the pioneering work of Shea and co-workers, mainly dense bridged silsesquioxanes nanoparticles (BSNPs) have been reported, with photoresponsive,^{1, 2} electrochromic³ and electrochemical⁴ properties or for photovoltaic applications.⁵ In the field of anti-cancer therapy, two studies were reported by Lin's group⁶ using BSNPs for platinum-based chemotherapy and disulfide-based biodegradable BSNPs with high Gd(III) payloads for MRI of cancer cells.⁷ One of the most challenging tasks in the field of BSNPs is the preparation of porous systems from pure organotrialkoxysilane molecular precursors. Indeed, periodic mesoporous organosilica NPs (PMO NPs) have been recently described from simple, low-molecular-weight organosilane precursors. Using cetyltrimethylammonium bromide (CTAB) as the surfactant the groups of Kuroda⁸ and Huo⁹ prepared PMO NPs. Another strategy consists of using a silica NP core as the template and to condense the bridged organosilane precursor at the surface of the silica NP to afford hollow organosilica NPs after etching the silica core.¹⁰ This strategy enables the formation of nanovehicles for anti-cancer drug delivery.¹¹ The last strategy consists of combining a silica core with perfluorocarbon (FC4) and CTAB dual surfactant systems. Using this method, Qiao and co-workers obtained yolk-shell silica core PMO shell NPs for catalysis applications.¹² Among the next challenges in this field, the preparation of metallic core- hybrid shell systems, which have not been described yet, and the formation of PMO NPs incorporating large functional organic fragments appear very promising, notably for theranostic applications.

Here we show that an original, large molecule engineered for two-photon excitation (TPE) possessing four triethoxysilyl groups, was very versatile for the preparation of several types of nanoparticles. First of all, it could either lead to pure BSNPs, or to mixed PMOs (MPMO NPs) when co-condensed with 1,2-bis(triethoxysilyl)ethylene or 1,4-bis(triethoxysilyl)benzene in the presence of CTAB (Scheme 1). Furthermore, we succeeded in preparing core-shell NPs in a one pot reaction with a gold core and BS or MPMO shell (respectively denoted Au@BS, and Au@MPMO) respectively, and additionally BSNPs decorated with gold NPs (BS@AuNPs). Theranostic applications (combination of imaging and therapy) of these nanoparticles were studied on MCF-7 breast cancer cells with TPE, which represents a new area of investigation in nanomedicine. Indeed, TPE offers new perspectives particularly for the treatment of cancer due to the unique spatial resolution it provides and the high penetration depth of the laser beam in the near-infrared region. We

describe here the high efficiency of BSNPs on breast MCF-7 cancer cells for TPE therapy, as well as the unprecedented combination of drug delivery combined and TPE therapy thanks to the unique structure of MPMO NP.

Results and discussion

The diaminodiphenylbutadiene core structure of the two-photon photosensitizer (2PS) sol-gel precursor depicted in the center of Figure 1 was known to selectively photo-activate electron transfer in bio processes under TPE,¹³⁻¹⁵ but this property was never exploited for TPE therapy. This 2PS molecule, which exhibits four triethoxysilyl groups, was elaborated using the $[\text{CuBr}(\text{PPh}_3)_3]$ -catalyzed CuAAC click reaction with (3-azidopropyl)triethoxysilane under mild conditions (see chapter 5A). The BSNPs were prepared by a careful control of the hydrolysis and polycondensation of the 2PS precursor in a CTAB/sodium hydroxide/water/ethanol mixture at 60°C for ten minutes (Fig. 1a). The presence of ethanol in the procedure was critical to solubilize the 2PS and to slow down the reaction kinetic in order to obtain and isolate the nanoparticles with the desired size and morphology. The time and temperature of the reaction were also carefully optimized for this purpose. Notably, BSNPs could also be obtained with a triethylamine catalyst in similar conditions (ESI). Original BS@Au NPs were obtained by mixing gold NPs with these BSNPs, without the need of thiol linkers to immobilize gold NPs on the surface of BSNPs (Fig. 1b). For the preparation of Au@BSNPs, a one pot procedure was developed. First Au NPs were prepared *in-situ*¹⁶ and stabilized with a thin silica layer. The 2PS precursor was subsequently added under the same conditions as for the BSNPs affording the Au@BSNPs (Fig. 1c).

Following the successful preparation of BSNPs, Au@BSNPs, and BS@AuNPs, we intensified our efforts towards the synthesis of porous materials: PMO NPs. Thus, we decided to investigate the co-condensation of simple bridged organosilanes with 2PS, which led to the development of the following synthetic conditions to obtain MPMO NPs. 1,2-bis(triethoxysilyl)ethylene (E) or 1,4-bis(triethoxysilyl)benzene (B) were mixed with 2PS to lead to E2, or B2 MPMO NPs respectively (Fig. 1d). This synthetic process involved a mixture of water/ethanol (5/2 v/v) containing CTAB, and sodium hydroxide as the catalyst (see ESI). Besides, such a process was performed in only 2 h, which is remarkably fast compared to the few reported methodologies (2 to 6 h of reaction, plus an additional 24 h of aging).^[9,17] Core-shell Au@PMO NPs AE and AB were prepared in only 2 h at 80°C using a one-pot procedure similar to that described for Au@BS starting with bis(triethoxysilyl)ethylene (E) or bis(triethoxysilyl)benzene (B), respectively (Fig. 1e). The same procedure was used with 2PS mixed with bis(triethoxysilyl)ethylene (E) or bis(triethoxysilyl)benzene (B) to synthesize core shell gold core@ethylene-2PS-based PMO shell (AE2) or gold core@benzene-2PS-based PMO shell (AB2) respectively, which feature a gold core and a mixed PMO shell (Fig. 1f).

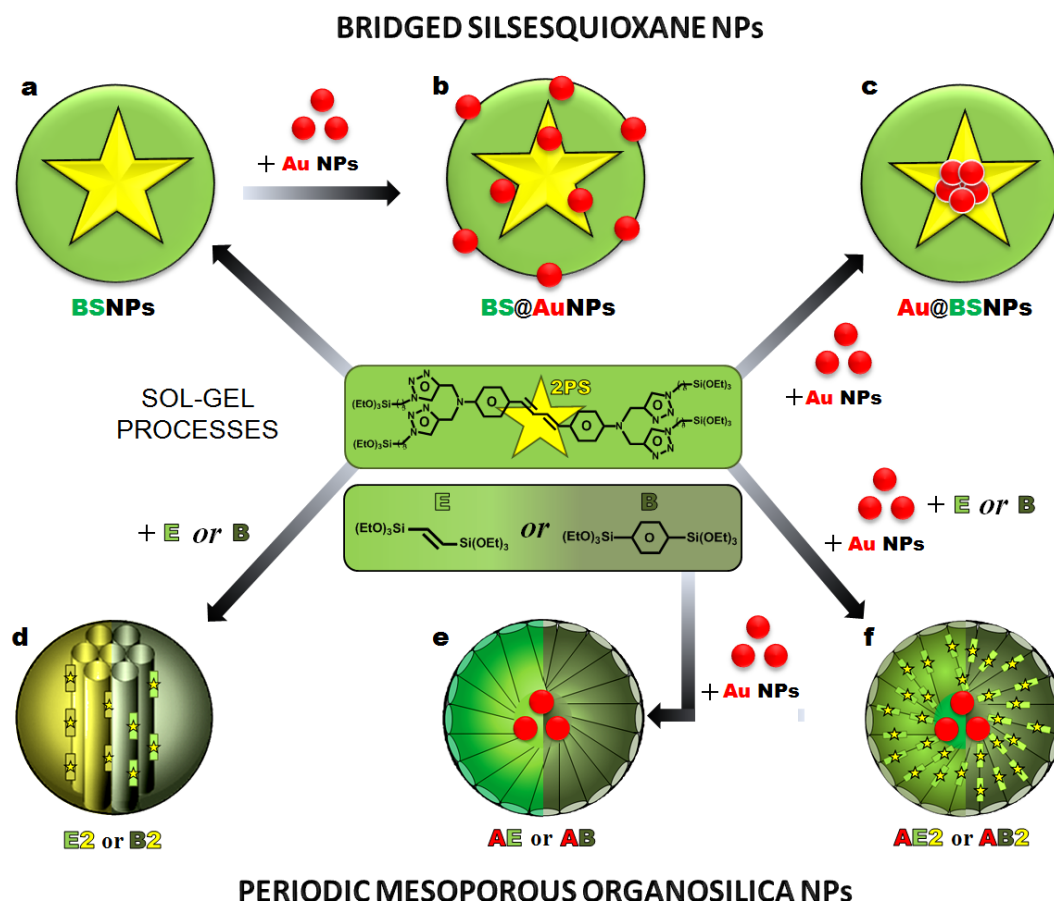


Figure 1. Synthetic design of the two-photon-sensitive bridged silsesquioxane and periodic mesoporous organosilica NPs. BSNPs obtained from the photosensitizer (2PS) (a). Post-grafting of gold NPs on BSNPs leading to BS@AuNPs (b). One-pot synthesis of core-shell Au@BSNPs (c). Preparation of E2 or B2 MPMO NPs, composed of the 2PS and either bis(triethoxysilyl)ethylene (E), or bis(triethoxysilyl)benzene (B), respectively (d). One-pot synthesis of AE or AB gold core PMO shell NPs, respectively composed of either the E or the B moiety (e). One-pot synthesis of AE2 or AB2 core-shell Au@MPMO NPs, composed of either 2PS and E (AE2), or 2PS and B (AB2 NPs) (f).

The BS, Au@BS and BS@Au nanostructures, compositions, and properties were then characterized. Transmission electron microscopy (TEM) analysis on the three types of nanomaterial revealed 150 nm nearly monodisperse spherical NPs (Fig. 1a-c), as confirmed by the scanning electron microscopy (SEM) images (Fig. 1d-e) and by dynamic light scattering (DLS) size distributions (Fig. S1). Au@BSNPs tended to be slightly smaller and aggregated. The gold nanospheres were readily visible on the surface of BS@AuNPs (Fig. 1b), or within the BS nanoshells (Fig. 1c). Moreover, ^{29}Si and ^{13}C CP-MAS NMR spectra confirmed both the formation of the siloxane inorganic network with a high condensation of the 2PS precursor and the preservation of the organic moiety, as shown by the major proportion of T^3 silicon environments (Fig. 1g,h) and the carbon environments of the 2PS (Fig. S2). This is further supported by the FTIR spectra of the BSNPs and Au@BSNPs nanomaterials with the red-shift of the $\nu_{\text{Si-O}}$ band from 1080 cm^{-1} in the 2PS precursor to 1137 cm^{-1} in the materials (Fig. S3). The gold content of Au@BSNPs and BS@AuNPs were assessed by induced-coupled plasma and energy dispersive spectroscopy respectively and were found to be of 24 and 25% in weight (Table S1).

The optical and photophysical properties of BS and Au@BS were then analyzed. To assess the optical properties of the materials, a model reference (2PS ref) was synthesized (Fig. 2i). The UV-visible absorption spectrum of BSNPs displayed the 2PS absorption band, whereas the Au@BS ones showed the gold NPs plasmon band as well (Fig. 2j). The large plasmon band is due to the gold NPs core spatial proximity within the BS structure. In the fluorescence spectra of the materials (Fig. 2e), recorded in EtOH, an important bathochromic shift was observed from the 2PS ref to the materials with a decrease of the fluorescence quantum yields (Table S2). The red shifts are consistent with the aggregation of the 2PS in the solid state with a reabsorption process; therefore the fluorescence quantum yields decreased accordingly.¹⁸ The two-photon absorption cross-section (σ_2) were determined per fluorophore and showed an increase of the σ_2 from 2PS ref (THF) to the BSNPs, BS@AuNPs and Au@BSNPs (EtOH) with a maximum value of 100, 140, 210 and 240 GM respectively at 700 nm (Fig. 2l). The enhancement of the σ_2 in the presence of gold NPs presumably arises from the plasmonic resonance of the gold NPs in the excited state.¹⁹

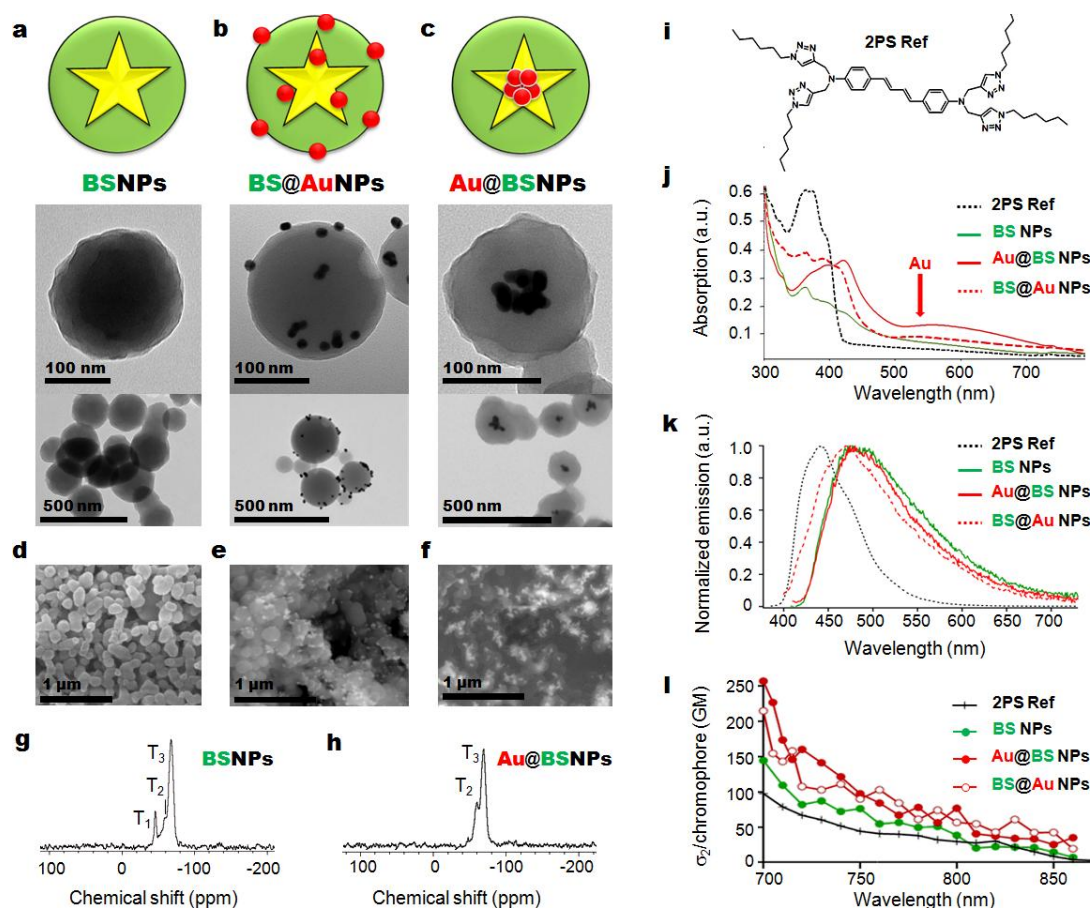


Figure 2. Schematic representations, TEM and SEM images of BSNPs, BS@AuNPs, and Au@BSNPs respectively (a-c, and d-f respectively). Solid state NMR ^{29}Si CPMAS spectra of BSNPs and Au@BSNPs respectively (g,h). Formula of the two-photon photosensitizer reference (2PS ref) used for the photophysical studies (i). Normalized emission spectra of the 2PS ref, BSNPs, Au@BSNPs, and BS@AuNPs. Excitation carried out at the wavelength of the absorption maxima (j). Uv-vis spectra of the 2PS ref, BSNPs, and Au@BSNPs (k). Two-photon absorption cross-section measurements of the 2PS ref, BSNPs, Au@BSNPs, and BS@AuNPs (l).

The structures of MPMO NPs were also readily visible with TEM (Fig. 3). E2 and B2 MPMO NPs were respectively of 200 and 100 nm in size, and monodisperse (Fig. 3a-b). Au@PMO NPs and Au@MPMO NPs were typically of a hundred nanometers in diameter, and composed of a couple of 15 nm gold nanospheres in their center (Fig. 3c-f). The mesoporous organization of the nanomaterial frameworks was further confirmed by high magnification TEM micrographs (Fig. S4a-f). SEM images as well as DLS analysis further confirmed the monodispersity of the aforementioned PMO NPs (Fig. S4g-l, and m-r respectively).

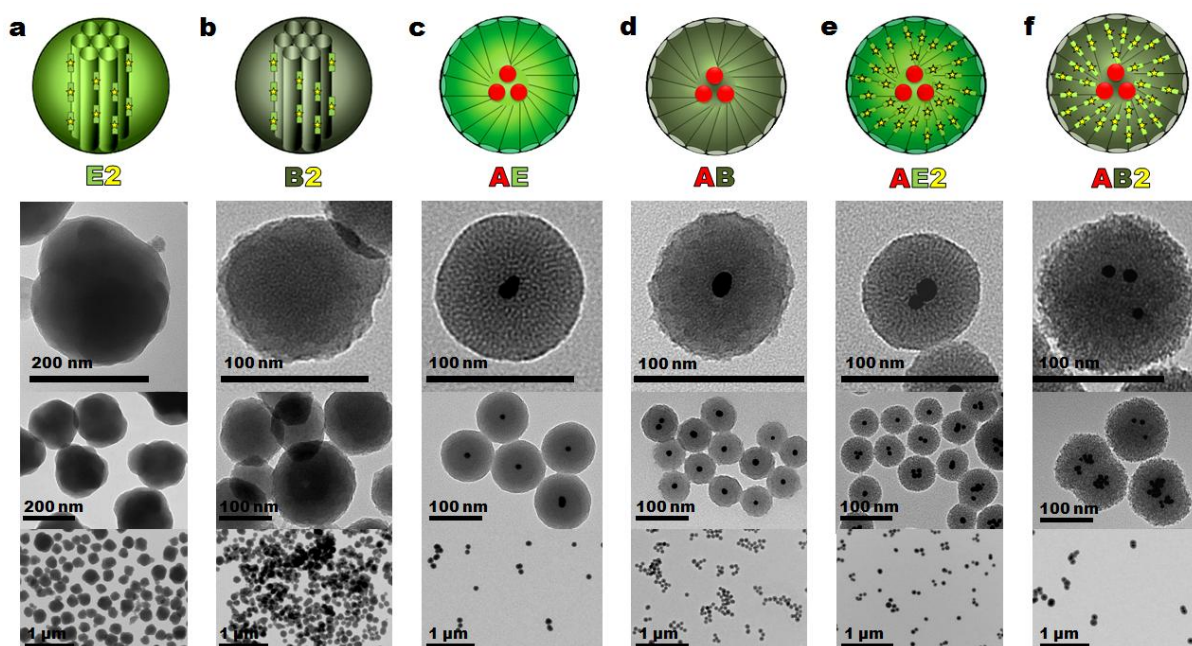


Figure 3. Characterization of the structure of the PMO NPs. a-f, Schematic representations and TEM images of E2, B2, AE, AB, AE2, AB2 NPs (a-f respectively).

Besides, the accessibility of the mesoporous structure of the MPMO NPs was demonstrated by N₂-adsorption and desorption technique, with high BET surface areas ranging from 900 to 1100 m².g⁻¹ (Fig. 4a-f). The BJH pore size distribution was generally centered at 2.5 nm, which is also confirmed with the low angle peak in the X-ray diffractograms (Fig. 4g-l). Note that E2 was structured in a 2D-hexagonal arrangement, typical of MCM-41 silica materials obtained using CTAB as surfactant, as revealed by the presence of harmonics from 4 to 5 degrees (2θ, CuKα) in the X-ray diffractograms, and by the observation of parallel channels in the TEM image (Fig. S4a). Interestingly, materials AE and AE2, synthesized from the same precursor (E) and surfactant, but in the presence of gold cores exhibited a radial porosity, whereas B2, AB and AB2 possessed a worm-like porous framework (see Fig. S4b-f). It was observed from the panel of characterization that the ethylene moiety leads to better structured materials than the benzene one. This is in agreement with the TEM images as well as the XRD measurements which display significantly more distinct peaks for materials obtained with E (Fig. 4g,i,k) than for those with B (Fig. 4h,j,l).

The chemical composition of the MPMO NPs was characterized by multiple techniques. On the one hand, the ^{29}Si CPMAS of PMO and MPMO NPs evidenced the formation of the siloxane framework with the major proportion of the T_2 and T_3 environments (Fig. S5), while the ethylene (-145 ppm), benzene (-134 ppm) and 2PS moieties were identified via ^{13}C CPMAS NMR (see Fig. S6). UV-visible spectra also showed the 2PS absorption band ($\lambda_{\text{max}} \approx 390$ nm) of MPMO NPs (Fig. S7a,b,e,f), as well as the benzene groups ($\lambda_{\text{max}} \approx 265$ nm) of B2, AB, and AB2 NPs (Fig. S7b,d,f). On the other hand, the presence of gold NPs in AE, AB, AE2, and AB2 PMO and MPMO NPs was clearly identified both by UV-visible absorption spectra (see Fig. S7c-f) and by the wide angle XRD patterns (see Fig. S7i-l), specifically the peak at 38° corresponding to the 111 crystallographic planes which is absent in E2 and B2 NPs (Fig. S7a-b). Besides, high resolution TEM images of the gold cores inside AE2 and AB2 confirmed the crystalline structure of such nanoparticles with the typical 0.22 nm interatomic distance in the gold NPs (Fig. S8). Inductively coupled plasma and energy dispersive spectrometry analyses determined 0.8 to 4.6 wt% of gold in the NPs (Table S3). Note that, the overall preparation yields of the surfactant-free PMO and MPMO NPs were generally ranging from 40 to 60% (see Table S4), though lower in AE2 (30-40%) and higher in B2 (80-95%).

The optical and photophysical properties of the MPMO NPs were then investigated. To synthesize the MPMO NPs, the 2PS precursor was co-condensed with E or B moieties. As a result, the fluorescence spectra of these particles showed only a slight bathochromic shift, less important than for the BSNPs (Fig. 4m, and S9). The quantum yields are higher in MPMO NPs than in BSNPs, in agreement with less aggregation of the fluorophore in the solid state (Table S5 and S2). The structure of the Au@MPMO NPs is different from that of the MPMO NPs and a higher bathochromic shift was observed with an important decrease of the fluorescence quantum yields (Table S5). The two-photon absorption cross-sections of the MPMO NPs were measured and an important decrease of the σ_2 compared to 2PS ref was observed for all the MPMO NPs systems from 100 GM to less than 10 GM per fluorophore (Fig. 4n). Nevertheless these materials were exploited for TPE imaging and therapy of MCF-7 breast cancer cells.

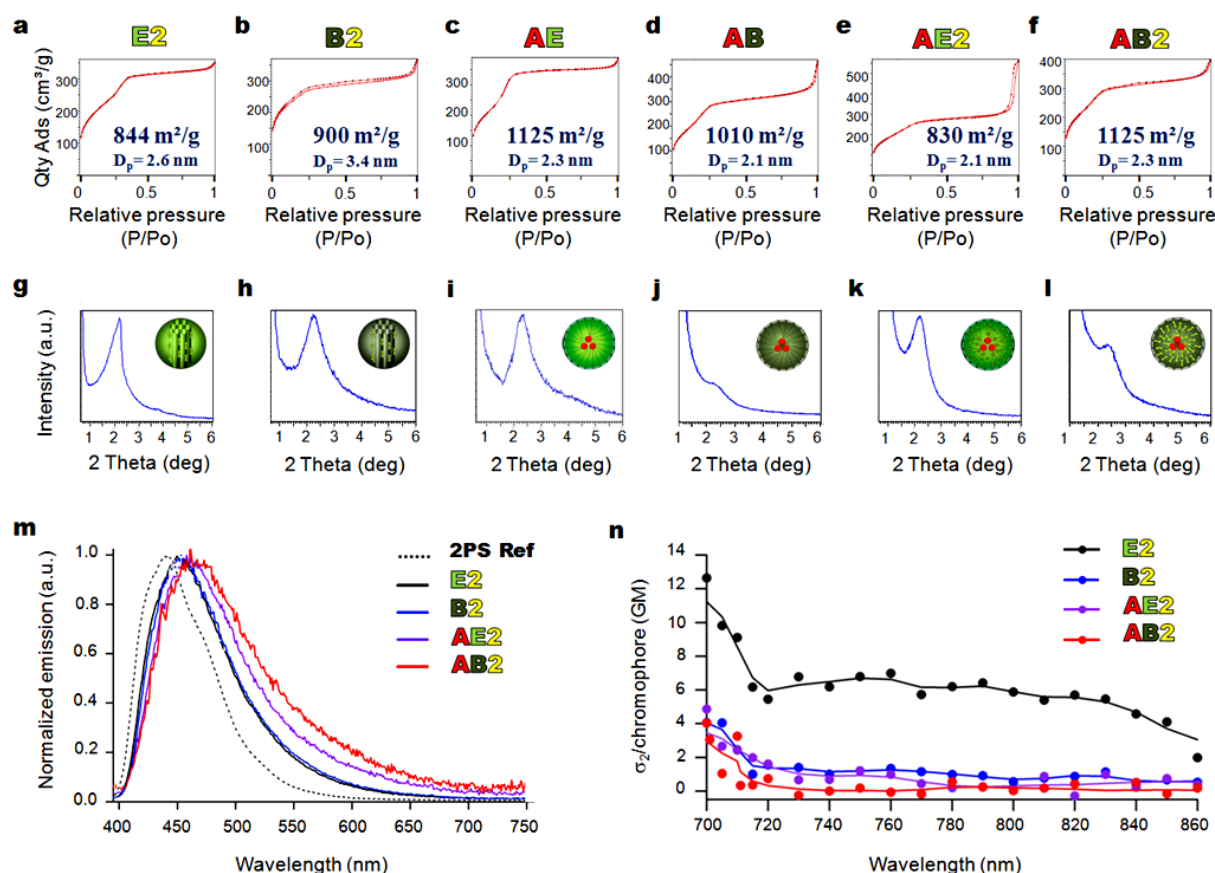


Figure 4. Physicochemical and photophysical characterizations of the PMO NPs. N₂-adsorption-desorption isotherms of E2, B2, AE, AB, AE2, AB2 NPs respectively, demonstrating the high surface areas achieved in the PMO framework (a-f). Diffraction patterns at low angles for E2, B2, AE, AB, AE2, AB2 NPs respectively (g-l). Normalized emission spectra of the 2PS reference and the MPMO NPs excited at the wavelength of the absorption maxima (m). Two-photon absorption cross-section measurements of the MPMO NPs (n).

Two-photon imaging studies on living MCF-7 breast cancer cells were then performed with BSNPs, Au@BSNPs, BS@AuNPs, MPMO and Au@MPMO NPs after 20 h of incubation, at low laser power. Cell membranes were stained with a specific membrane marker (Cell Mask) in order to enable the NPs tracking inside the cells with two-photon fluorescence. Figure 5a-i demonstrated the endocytosis of the NPs by cells. Comparing BSNPs, Au@BSNPs and BS@AuNPs, at the same laser power, a tremendous enhancement of the two-photon excited fluorescence was observed with gold-BS (Fig. 5a-c, see Fig. S10). Indeed the quantum yield and two-photon absorption cross-sections were higher with the gold systems thus enhancing the fluorescence signal. By contrast, cell imaging exhibits no enhancement of the signal with Au@MPMO NPs compared to MPMO NPs (Fig. 5d-i). This could be due to the decrease of the fluorescence quantum yield and σ_2 . Note that AB and AE NPs possessing only the gold core were also detected, showing that these NPs were efficient for TPE, probably due to the aggregation of gold NPs in the core thus leading to a plasmon resonance in the NIR.²⁰

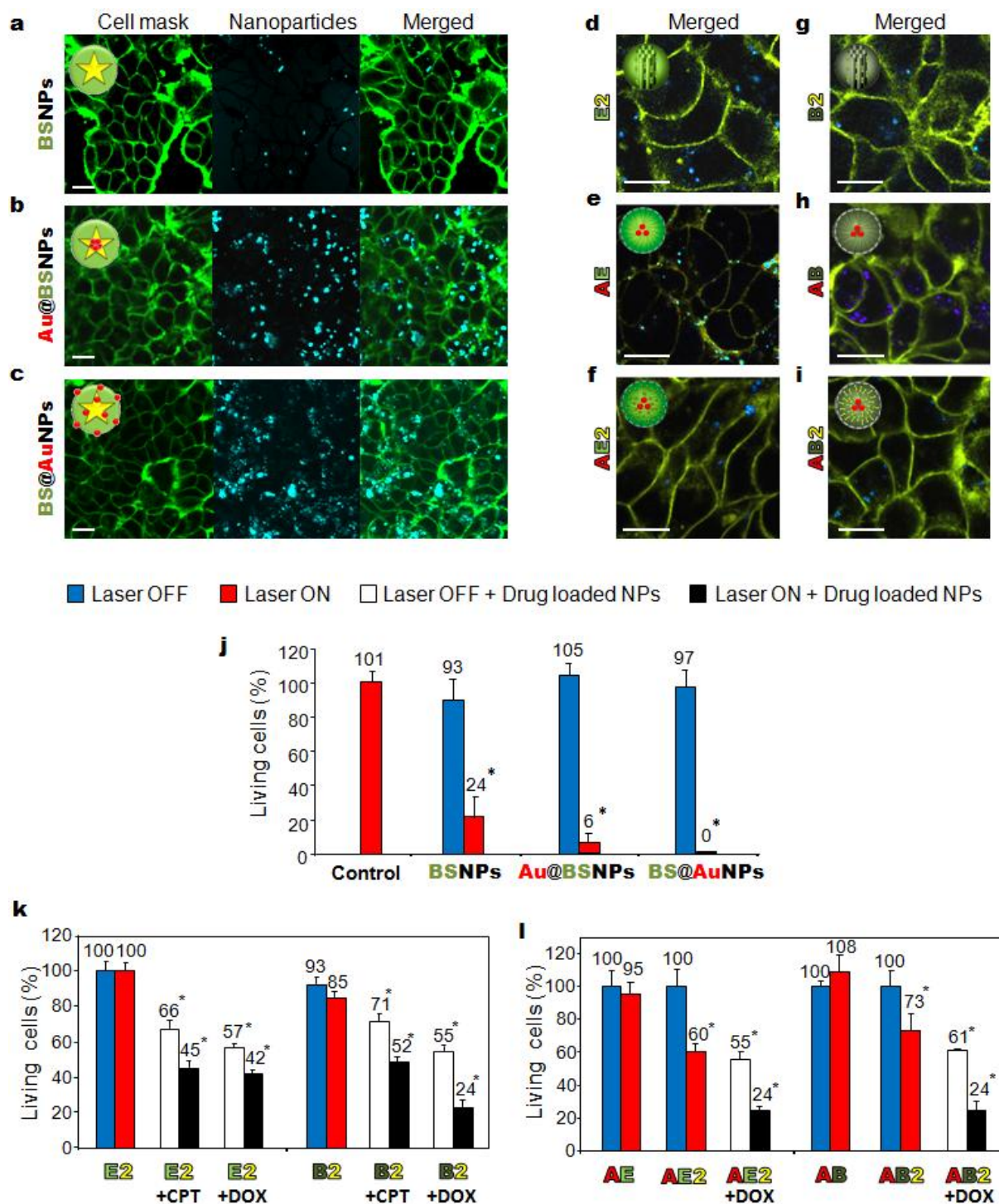


Figure 5. *In-vitro* study of the BS and PMO NPs on MCF-7 cancer cells. Two-photon confocal microscopy images of MCF-7 cells incubated during 20 h with $40 \mu\text{g.mL}^{-1}$ of NPs. Scale bar $10 \mu\text{m}$ (a-i). TPE-triggered cancer cell killing with BSNPs, BS@AuNPs, and Au@BSNPs (j). TPE-triggered cancer cell killing in drug-free and drug-loaded E2 and B2 MPMO NPs, demonstrating the synergistic effect of TPE cell killing and drug delivery (k). TPE triggered cancer cell killing in drug-free and Doxorubicin-loaded AE, AE2, AB, AB2 NPs, demonstrating the synergistic effect of TPE cell killing and drug delivery. Data are mean \pm SD from 3 experiments. * Statistically significant versus non irradiated and untreated cells ($p < 0.05$ from Student's t test) (l).

Eventually, *in-vitro* TPE therapy was performed on breast cancer cells. MCF-7 cells were incubated for 20 h in the presence of BS, Au@BS or BS@AuNPs. No cytotoxicity was observed without irradiation up to a concentration of $40\ \mu\text{g.mL}^{-1}$ (Fig. 5j) showing the biocompatibility of the prepared materials. When irradiated at 760 nm with 3 scans of 1.57 s at maximum power of the laser (input power 3W), with a focused laser beam, an important cancer cell death was observed at a concentration of $40\ \mu\text{g.mL}^{-1}$ where only 24%, 6% and 0% of cancer cells survived respectively. The presence of gold enhanced the efficiency of the Au@BS and BS@Au NPs compared to BSNPs due to a synergy between the 2PS and gold NPs. Note that 2PS ref and BS materials were not able to produce singlet oxygen under irradiation (data not shown). Therefore, we believe that a type I mechanism based on electron transfer is involved in cancer cell killing.

MPMO nanosystems were then studied for TPE therapy under the same conditions. No cancer cell killing was observed with E2 and only 15% of cancer cell death was observed with B2 (Fig. 5k). BSNPs were thus much more efficient than MPMO NPs for TPE therapy. AE and AB showed no cancer cell death under the same conditions, thus photothermal effects attributable to the gold cores are not sufficient to kill cancer cells. However, when gold NPs were encapsulated in the MPMO NPs, AE2 and AB2 showed 40% and 27% cancer cell killing respectively after irradiation (Fig. 5l). Therefore a synergy between gold nanocrystals and 2PS moieties is clearly operative, and produces an important enhancement of cancer cell death.

We then examined MPMO NPs as vectors for camptothecin (CPT) and doxorubicin (DOX) deliveries without irradiation. Drug release experiments were first carried out at pH 7 in water, with doxorubicin-loaded MPMO and Au@MPMO NPs (Fig. S11). No release of DOX was observed in these conditions showing that important hydrophobic interactions between the drug and the organosilica matrix occurred. The release was triggered at pH 5.5 (lysosomal pH) due to the protonation of DOX at such pH. All nanocarriers had high loading capacities of DOX, typically of 10 weight percent (Table S6). With non-irradiated MCF-7 cancer cells, the MPMO NPs showed efficient cancer cell killing with CPT and DOX (Fig. 5k), reaching up to 45% with DOX-loaded MPMO NPs.

Finally, the unprecedented combined action of drug delivery and TPE was studied for MPMO NPs loaded with DOX. Interestingly, an important synergy was noticed for MPMO, as more cell death was observed for all the irradiated cells than without irradiation, with up to 58 and 76% cancer cell killing with E2+DOX and B2+DOX respectively. Concerning core-shell MPMO NPs composed of inserted 2PS moieties inside the framework, the efficiency of the materials was further increased up to 76% cancer cell death with both AE2 and AB2. Hence, the most promising synergetic treatment is obtained with the AE2 nanocarrier since it provides both an efficient two-photon spatiotemporally controlled cell killing (40% without drug) and the DOX delivery to further decrease the cell survival. Thus these two-photon loaded multifunctional NPs are particularly suited for synergetic therapies.

Conclusion

In conclusion, we have engineered a versatile molecule displaying high two-photon absorption cross section and possessing four triethoxysilyl groups, which enables the synthesis of various types of hybrid nanomaterials using fast and efficient sol-gel procedures. This precursor led to the design of two-photon sensitive BSNPs, MPMO NPs or multifunctional gold core-shell systems. The main organic fragment remained unaffected during the preparation of the NPs and two-photon absorption properties were characterized. An enhancement of σ_2 with BSNPs was observed while a decrease of σ_2 occurred with MPMO NPs. The PMO NPs showed a remarkably high specific surface area, which made them suitable for drug loading. All the NPs were endocytosed by MCF-7 cancer cells, as shown by TPE fluorescence imaging at low laser power. A very efficient cancer cell killing was observed with BSNPs and gold-functionalized BSNPs, under two-photon irradiation, at high laser power. Based on these results, an unprecedented dual therapeutic approach was designed using PMO and MPMO NPs which led to synergistic cancer cell killing by two-photon excited therapy combined with drug delivery. Therefore the library of nanoparticles herein prepared are highly promising for theranostic applications. As cancer treatment should be adapted depending on the stage and type of cancer, the flexibility of our approach offers an alternative for a personalized nanomedicine.

REFERENCES

1. Hu, L.-C., Yonamine, Y., Lee, S.-H., Van der Veer, W. E. & Shea, K. J. Light-Triggered Charge Reversal of Organic-Silica Hybrid Nanoparticles. *J. Am. Chem. Soc.* **134**, 11072-11075 (2012).
2. Zhao, L., Loy, D. A. & Shea, K. J. Photodeformable Spherical Hybrid Nanoparticles. *J. Am. Chem. Soc.* **128**, 14250-14251 (2006).
3. Jain, V. *et al.* High-Contrast Solid-State Electrochromic Devices of Viologen-Bridged Polysilsesquioxane Nanoparticles Fabricated by Layer-by-Layer Assembly. *ACS Appl. Mater. Int.* **1**, 83-89 (2009).
4. Khiterer, M. & Shea, K. J. Spherical Monodisperse Functional Bridged Polysilsesquioxane Nanoparticles. *Nano Lett.* **7**, 2684-2687 (2007).
5. Rathnayake, H., Binion, J., McKee, A., Scardino, D. J. & Hammer, N. I. Perylenediimide Functionalized Bridged-Siloxane Nanoparticles for Bulk Heterojunction Organic Photovoltaics. *Nanoscale* **4**, 4631-4640 (2012).
6. Della Rocca, J., Huxford, R. C., Comstock-Duggan, E. & Lin, W. Polysilsesquioxane Nanoparticles for Targeted Platin-Based Cancer Chemotherapy by Triggered Release. *Angew. Chem. Int. Ed.* **50**, 10330-10334 (2011).
7. Vivero-Escoto, J. L., Rieter, W. J., Lau, H., Huxford-Phillips, R. C. & Lin, W. Biodegradable Polysilsesquioxane Nanoparticles as Efficient Contrast Agents for Magnetic Resonance Imaging. *Small* **9**, 3523-3531 (2013).
8. Urata, C. *et al.* Aqueous Colloidal Mesoporous Nanoparticles with Ethenylene-Bridged Silsesquioxane Frameworks. *J. Am. Chem. Soc.* **133**, 8102-8105 (2011).
9. Guan, B. *et al.* Highly Ordered Periodic Mesoporous Organosilica Nanoparticles with Controllable Pore Structures. *Nanoscale* **4**, 6588-6596 (2012).
10. Koike, N., Ikuno, T., Okubo, T. & Shimojima, A. Synthesis of Monodisperse Organosilica Nanoparticles with Hollow Interiors and Porous Shells Using Silica Nanospheres as Templates. *Chem. Commun.* **49**, 4998-5000 (2013).
11. Chen, Y., Chen, H. & Shi, J. In Vivo Bio-Safety Evaluations and Diagnostic/Therapeutic Applications of Chemically Designed Mesoporous Silica Nanoparticles. *Adv. Mater.* **25**, 3144-3176 (2013).
12. Liu, J. *et al.* Yolk-Shell Hybrid Materials with a Periodic Mesoporous Organosilica Shell: Ideal Nanoreactors for Selective Alcohol Oxidation. *Adv. Funct. Mater.* **22**, 591-599 (2012).
13. Beaumont, E. *et al.* NO Formation by Neuronal NO-Synthase can be Controlled by Ultrafast Electron Injection from a Nanotrigger. *Chembiochem.* **10**, 690-701 (2009).
14. Beaumont, E. *et al.* Two Photon-Induced Electron Injection From a Nanotrigger in Native Endothelial NO-Synthase. *Chemphyschem* **9**, 2325-2331 (2008).
15. Robin, A.C. *et al.* A NADPH Substitute for Selective Photo-Initiation of Reductive Bioprocesses via Two-Photon Induced Electron Transfer. *Chem. Commun.* **13**, 1334-1336 (2007).
16. Croissant, J. & Zink, J. I. Nanovalve-Controlled Cargo Release Activated by Plasmonic Heating. *J. Am. Chem. Soc.* **134**, 7628-7631 (2012).
17. Cho, E.-B., Kim, D. & Jaroniec, M. Preparation of Mesoporous Benzene-Silica Nanoparticles. *Micro. Meso. Mater.* **120**, 252-256 (2009).
18. Natte, K. *et al.* Synthesis and Characterisation of Highly Fluorescent Core-Shell Nanoparticles Based on Alexa Dyes. *J. Nanopart. Res.* **14**, 1-10 (2012).
19. Sivapalan, S. T. *et al.* Plasmonic Enhancement of the Two Photon Absorption Cross Section of an Organic Chromophore Using Polyelectrolyte-Coated Gold Nanorods. *Langmuir* **28**, 9147-9154 (2012).
20. Jiang, C. *et al.* Two-Photon Induced Photoluminescence and Singlet Oxygen Generation from Aggregated Gold Nanoparticles. *ACS Appl. Mater. Int.* **5**, 4972-4977 (2013).

APPENDIX: SUPPLEMENTARY INFORMATION

I- EXPERIMENTAL SECTION

Materials. Tetraethoxysilane, cetyltrimethylammonium bromide (CTAB), sodium hydroxide, dimethylsulfoxide, camptothecin, doxorubicin hydrochloride, and ammonium nitrate were purchased from Sigma-Aldrich. Absolute ethanol was purchased from Fisher Chemicals. Hydrochloric acid was purchased from Anal. R. Norma Pure. 1,2-bis(triethoxysilyl)ethylene and 1,2-bis(triethoxysilyl)benzene were purchased from ABCR.

Methods. IR spectra were recorded on a Perkin-Elmer 100 FT spectrophotometer. Absorption spectra were recorded on a Hewlett-Packard 8453 spectrophotometer and fluorescence data were collected on a Perkin-Elmer LS55 fluorimeter. Dynamic light scattering analysis were performed using a Cordouan Technologies DL 135 Particle size analyzer instrument. ^{29}Si and ^{13}C CPMAS solid state NMR sequences were recorded with a VARIAN VNMR300, using Q8MH8 and adamantane references respectively. TEM images were recorded with a JEOL instrument. SEM images were recorded with a FEI instrument. Energy dispersive spectroscopy was performed *via* an FEI scanning electron microscope.

II- BRIDGED SILSESQUIOXANE NP SYNTHESSES AND CHARACTERIZATIONS

BSNPs (with NaOH catalyst). A mixture composed of water (25 mL), ethanol (10 mL), and CTAB (160 mg, $4.40 \cdot 10^{-1}$ mmol) was stirred at 80°C in a 50 mL round bottom flask. Then a solution of the 2PS precursor in anhydrous ethanol (2PS: 44.4 mg, $2.7 \cdot 10^{-2}$ mmol in 500 μL) was quickly injected. After 1 minute, sodium hydroxide (150 μL , 2 M) was added to trigger the sol-gel process. The reaction mixture was stirred for 2 minutes at 80°C, and the solution was then neutralized by addition of hydrochloric acid (*ca* 1.38 mL, 0.2 M). Then, the mixture was cooled down to 40 °C, and the nanomaterial was collected through centrifugation at 21000 rpm for 15 minutes. Each fraction was washed with ethanol (40 mL per fraction) and centrifuged for 10 minutes. This operation was repeated twice, and the compound was dried under vacuum for few hours.

BSNPs (with Et₃N catalyst). A mixture composed of water (100 mL), ethanol (40 mL), and CTAB (640 mg, 1.76 mmol) was stirred at 80°C in a 250 mL round bottom flask. Then a solution of the 2PS precursor in anhydrous ethanol (2PS: 88.8 mg, $5.4 \cdot 10^{-2}$ mmol in 1000 μL) was quickly injected. The reaction was conducted for 2 minutes at 80°C, the mixture was cooled down for ten minutes, and the nanomaterial was collected through centrifugation at 21000 rpm for 10 minutes. At this point, the NPs could be either washed and dried as described for BSNPs with NaOH catalyst, or mixed with gold nanospheres as follows.

Au@BSNPs. A mixture of water (50 mL), ethanol (20 mL), and CTAB (320 mg, $8.80 \cdot 10^{-1}$ mmol) in a 100 mL three neck round bottom flask was stirred at 70°C. Then an aqueous

solution of potassium tetrachloroaurate (26 mg, $6.90 \cdot 10^{-2}$ mmol in 2 mL) was injected. The mixture was stirred for 5 minutes. Sodium hydroxide (200 μ L, 2 M) was injected to induce the instantaneous nucleation of the nanoparticles. The nanoparticles growth was conducted for 20 minutes under a 600 rpm stirring. Afterwards, tetraethylorthosilicate (25 μ L, $1.12 \cdot 10^{-4}$ mol) and sodium hydroxide (200 μ L, 2 M) were added dropwise in order to stabilize the gold nanocrystals with a thin silica shell. After five minutes of stirring, a solution of the 2PS precursor in anhydrous ethanol (2PS: 88 mg, $6.39 \cdot 10^{-2}$ mmol, in 1 mL) was quickly injected. The reaction mixture was stirred for 10 minutes, and the solution was neutralized by adding hydrochloric acid solution (*ca* 1.38 mL, 0.2 M), and cooled to room temperature while stirring. The solid was gathered through centrifugation at 7830 rpm for 15 minutes. Each fraction was washed with ethanol (40 mL per fraction) and centrifuged for 10 minutes. This operation was repeated twice, and the compound was dried under vacuum for few hours.

BS@AuNPs. A mixture of water (25 mL), ethanol (10 mL), and CTAB (160 mg, $4.40 \cdot 10^{-1}$ mmol) in a 100 mL three neck round bottom flask was stirred at 70°C. Then an aqueous solution of potassium tetrachloroaurate (13 mg, $3.45 \cdot 10^{-2}$ mmol in 1 mL) was injected. The mixture was stirred for 5 minutes. Sodium hydroxide (100 μ L, 2 M) was injected to induce the instantaneous nucleation of the nanoparticles. After 30 seconds, hydrochloric acid (18 μ L, 2 M) was added, and the nanoparticles growth was conducted for 12 minutes under a 600 rpm stirring, and the temperature was set at 80°C. Secondly, freshly prepared BSNPs were redispersed in deionized water (25 mL) and added to the previous solution. The reaction was left for 10 minutes, then the mixture was cooled down to 40 °C and centrifuged at 21000 rpm for 10 minutes. The nanomaterial was washed with a water:ethanol mixture (5:2, v:v) and centrifuged for 10 minutes. This operation was repeated twice, and the compound was dried under vacuum for few hours.

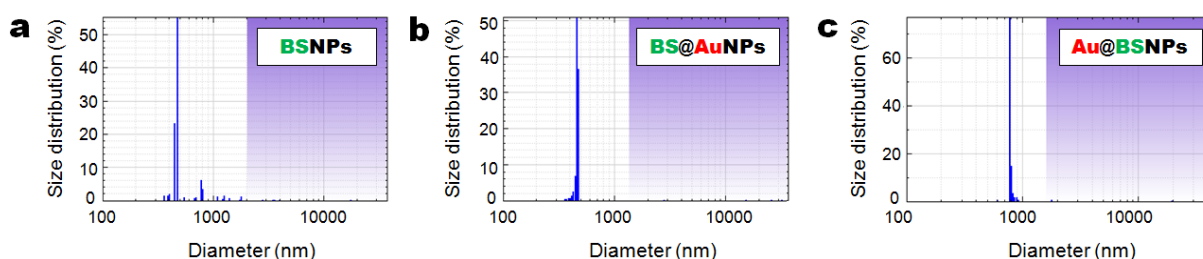


Figure S1. DLS size distributions of BSNPs (a), BS@AuNPs (b), and Au@BSNPs (c).

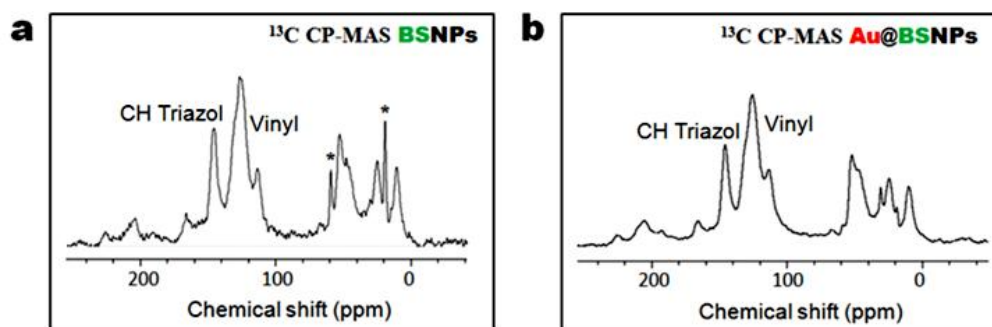


Figure S2. SSNMR ^{13}C CPMAS spectra of BSNPs (a) and Au@BSNPs (b). *Ethanol residues.

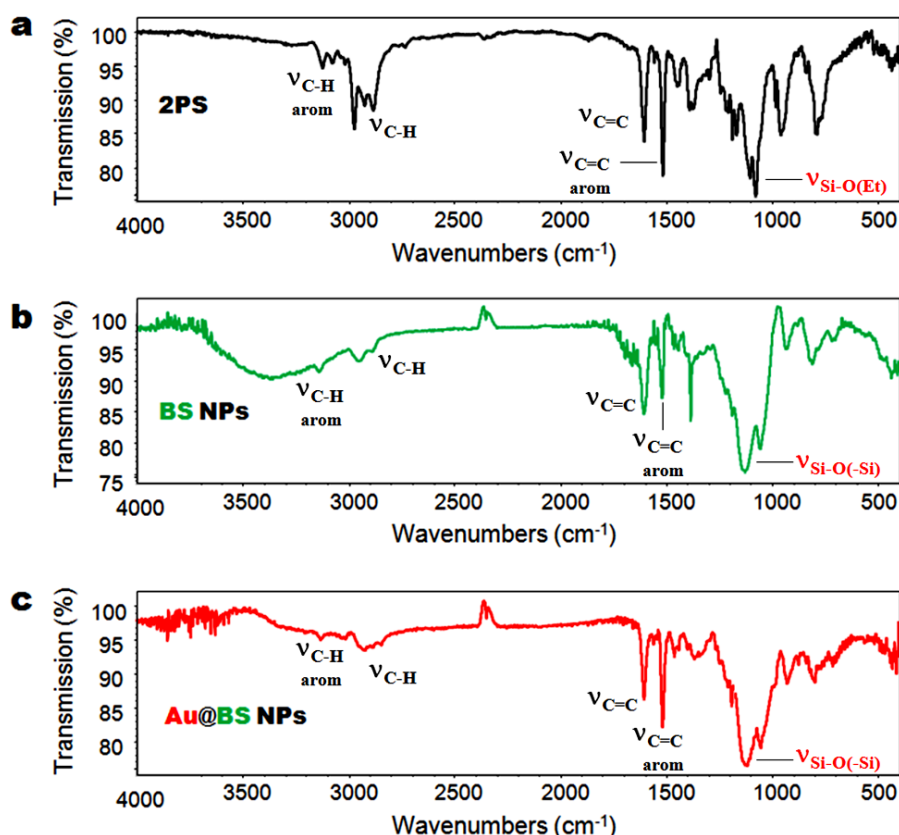


Figure S3. FTIR spectra comparison of the 2PS precursor (a), BSNPs (b), and Au@BSNPs confirming the sol-gel condensation and preservation of the organic structure of the photosensitizer.

Sample	9.0 wt% Au Control ^[a]	Au@BSNPs ^[a]	BS@AuNPs ^[b]
Gold wt %	9.76	24.12	25.10

Table S1. Gold weight percent (wt%) determination in Au@BSNPs and BS@AuNPs. [a] ICP-Atomic Emission Spectroscopy (AES) analysis. The gold control consisted of bare gold nanoparticles, made from the same procedure (but without 2PS), and mixed with a mesoporous silica powder (theoretical ratio of 9.0 wt% in gold), in order to determine the accuracy of the ICP calibration. [b] EDS measurement of the gold wt% in BS@AuNPs.

Sample	$\lambda_{\text{abs}}/\lambda_{\text{em}}$ (nm)	Φ_F ^[a]	σ_2^{max} ^[b] (GM)	$\sigma_2^{\text{max}} * \Phi_F$ (GM)
2PS Ref	378/442	0.60	100 ^[c]	60 ^[c]
BSNPs	432/477	0.033	140	5
Au@BSNPs	425/478	0.12	260	30
BS@AuNPs	394/469	0.11	210	24

Table S2. Two-photon properties of the 2PS Ref, BSNPs, Au@BSNPs, and BS@AuNPs. [a] Quinine bisulfate standard at 0.5M in H₂SO₄. [b] Per chromophore. [c] Analysis performed in THF.

III- PMO NPs SYNTHESSES AND CHARACTERIZATIONS

E2 MPMO NPs. A mixture of CTAB (250 mg, 6.86×10^{-1} mmol), distilled water (120 mL), and sodium hydroxide (875 μL , 2 M) was stirred at 80°C for 50 minutes at 700 rpm in a 250 mL three necks round bottom flask. Then, 1,4-bis(triethoxysilyl)ethylene (1 mL, 2.63 mmol) was added along with the 2PS (178 mg, 1.29×10^{-1} mmol, in 900 μL of anhydrous ethanol), and the condensation process was conducted for 2 h. Afterwards, the solution was cooled to room temperature while stirring; fractions were gathered in propylene tubes and the NPs were collected by centrifugation during 15 minutes at 21 krpm. The sample was then extracted twice with an alcoholic solution of ammonium nitrate (6 g.L⁻¹), and washed three times with ethanol, water, and ethanol. Each extraction involved a sonication step of 30 minutes at 50 °C; the collection was carried out in the same manner. The as-prepared material was dried for few hours under vacuum.

B2 MPMO NPs. A mixture of CTAB (250 mg, 6.86×10^{-1} mmol), distilled water (120 mL), and NaOH (875 μL , 2 M) was stirred at 80°C for 50 minutes at 700 rpm in a 250 mL three necks round bottom flask. Then, 1,4-bis(triethoxysilyl)benzene (1 mL, 2.52 mmol) was added along with the 2PS (178 mg, 1.29×10^{-1} mmol, in 900 μL of anhydrous ethanol), and the condensation process was conducted for 2 h. Afterwards, the solution was cooled to room temperature while stirring; fractions were gathered in propylene tubes and the NPs were collected by centrifugation during 15 minutes at 21 krpm. Extraction and the following steps were identical as those described for E2 MPMO NPs.

AE PMO NPs. A mixture of water (25 mL), ethanol (10 mL), and CTAB (160 mg, 4.40×10^{-1} mmol) in a 50 mL three neck round bottom flask was stirred at 70°C. Then an aqueous solution of potassium tetrachloroaurate (13 mg, 3.45×10^{-2} mmol in 1 mL) was injected, and NaOH (100 μL , 2 M) was injected to induce the instantaneous nucleation of the nanoparticles. After 30 seconds, hydrochloric acid (18 μL , 2 M) was added to the solution to produce 8 nm monodisperse gold nanoparticles at lower pH, suitable for a controlled sol-gel process. The nanoparticles growth was conducted for 12 minutes under a 600 rpm stirring, and the temperature was set at 80°C. Afterwards, 1,2-bis(triethoxysilyl)ethene (100 μL , 2.62×10^{-1} mmol) was added dropwise to grow the porous PMO shell on the gold nanocrystals. The condensation process was conducted for 1 h 30 minutes. Afterwards, the solution was cooled to room temperature while stirring; fractions were gathered in propylene

tubes and the NPs were collected by centrifugation for 15 minutes at 21 krpm. Extraction and the following steps were identical as those described for E2 MPMO NPs.

AB PMO NPs. A mixture of water (25 mL), ethanol (10 mL), and CTAB (160 mg, 4.40×10^{-1} mmol) in a 50 mL three neck round bottom flask was stirred at 70°C. Then an aqueous solution of potassium tetrachloroaurate (13 mg, 3.45×10^{-2} mmol in 1 mL) was injected, and NaOH (100 μ L, 2 M) was injected to induce the instantaneous nucleation of the nanoparticles. After 30 seconds, hydrochloric acid (18 μ L, 2 M) was added to the solution to produce 8 nm monodisperse gold nanoparticles at lower pH, suitable for a controlled sol-gel process. The nanoparticles growth was conducted for 12 minutes under a 600 rpm stirring, and the temperature was set at 80°C. Afterwards, 1,4-bis(triethoxysilyl)benzene (100 μ L, 2.52×10^{-1} mmol) was added dropwise, followed by sodium hydroxide (50 μ L, 2 M) to grow the porous PMO shell on the gold nanocrystals. The condensation process was conducted for 2 h. Afterwards, the solution was cooled at room temperature while stirring; fractions were gathered in propylene tubes and collected by centrifugation for 15 minutes at 21 krpm. Extraction and the following steps were identical as those described for E2 MPMO NPs.

AE2 MPMO NPs. A mixture of water (25 mL), ethanol (10 mL), and CTAB (160 mg, 4.40×10^{-1} mmol) in a 50 mL three neck round bottom flask was stirred at 70°C. Then an aqueous solution of potassium tetrachloroaurate (13 mg, 3.45×10^{-2} mmol in 1 mL) was injected, and NaOH (100 μ L, 2 M) was injected to induce the instantaneous nucleation of the nanoparticles. After 30 seconds, hydrochloric acid (18 μ L, 2 M) was added to the solution to produce 8 nm monodisperse gold nanoparticles at lower pH, suitable for a controlled sol-gel process. The nanoparticles growth was conducted for 12 minutes under a 600 rpm stirring, and the temperature was set at 80°C. Afterwards, 1,4-bis(triethoxysilyl)benzene (100 μ L, 2.62×10^{-1} mmol) and the 2PS (89 mg, 6.45×10^{-2} mmol, in 900 μ L of anhydrous ethanol) were added dropwise, followed by sodium hydroxide (50 μ L, 2 M) to grow the porous PMO shell on the gold nanocrystals. The condensation process was conducted for 2 h. Afterwards, the solution was cooled to room temperature while stirring; fractions were gathered in propylene tubes and collected by centrifugation during 15 minutes at 21 krpm. Extraction and the following steps were identical as those described for E2 MPMO NPs.

AB2 MPMO NPs. A mixture of water (25 mL), ethanol (10 mL), and CTAB (160 mg, 4.40×10^{-1} mmol) in a 50 mL three neck round bottom flask was stirred at 70°C. Then an aqueous solution of potassium tetrachloroaurate (13 mg, 3.45×10^{-2} mmol in 1 mL) was injected, and NaOH (100 μ L, 2 M) was injected to induce the instantaneous nucleation of the nanoparticles. After 30 seconds, hydrochloric acid (18 μ L, 2 M) was added to the solution to produce 8 nm monodisperse gold nanoparticles at lower pH, suitable for a controlled sol-gel process. The nanoparticles growth was conducted for 12 minutes under a 600 rpm stirring, and the temperature was set at 80°C. Afterwards, 1,4-bis(triethoxysilyl)benzene (100 μ L, 2.52×10^{-1} mmol) and the 2PS (89 mg, 6.45×10^{-2} mmol, in 900 μ L of anhydrous ethanol) were added dropwise, followed by sodium hydroxide (50 μ L, 2 M) to grow the porous PMO shell on the gold nanocrystals. The condensation process was conducted for 2 h. Afterwards, the solution was cooled to room temperature while stirring; fractions were gathered in propylene tubes and collected by centrifugation during 15 minutes at 21 krpm. Extraction and the following steps were identical as those described for E2 MPMO NPs.

CPT LOADING IN PMO NPs. A mixture of dimethylsulfoxide (DMSO, 1 mL), camptothecin (3 mg), and PMO NPs (25 mg) was prepared in a 5 mL round bottom flask and stirred at 40°C for two days. The preparation was centrifuged at 10000 rpm in 40 mL propylene tubes, and the supernatant was removed. Then, the nanomaterial was washed once with DMSO (without sonication), and twice with deionized water, and dried under vacuum.

DOX LOADING IN PMO NPs. A mixture of water (250 μ L), doxorubicin (1 mg), and PMO NPs (10 mg) was prepared in an eppendorf tube, sonicated for 30 minutes, and stirred overnight at room temperature. The preparation was centrifuged at 10000 rpm in 40 mL propylene tubes, and the supernatant was removed. The nanomaterial was washed twice with water (10 mL), and dried under vacuum. The loading capacities were deduced by the titration of doxorubicin in the supernatant fractions.

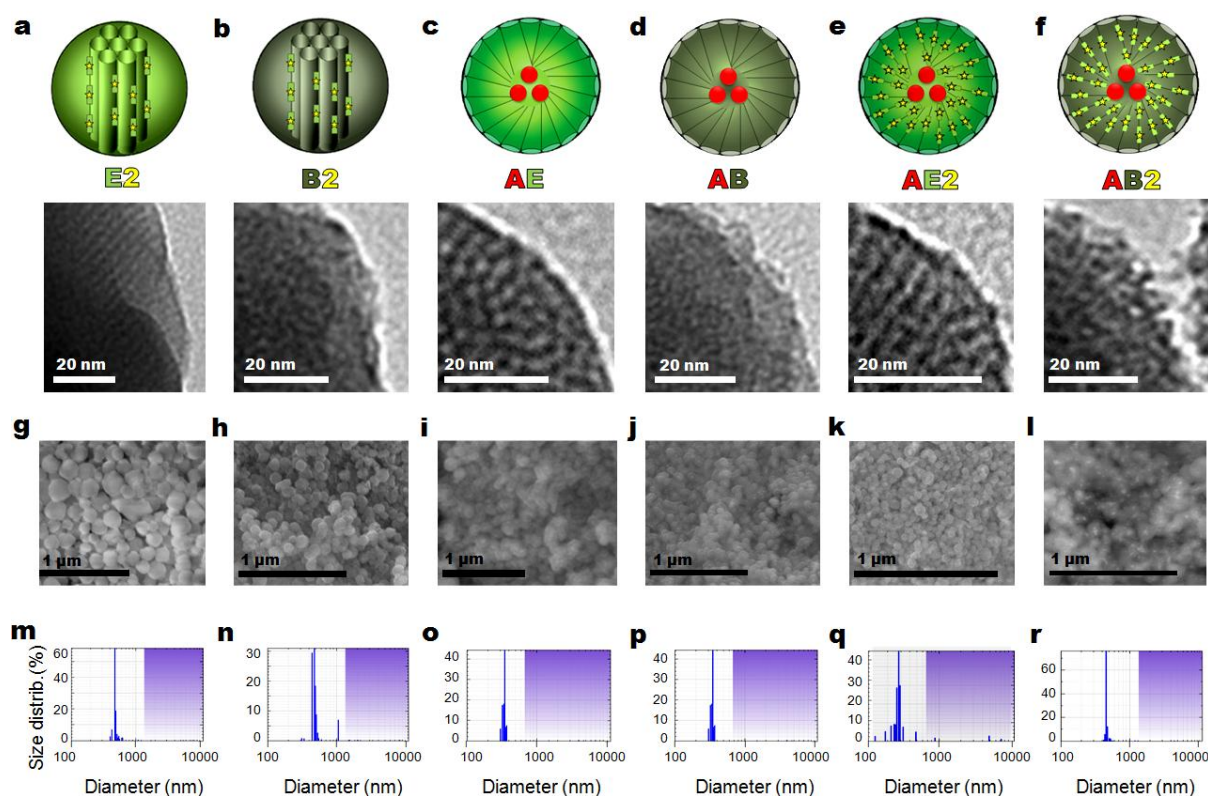


Figure S4. TEM, SEM and DLS analysis of the two-photon-sensitive PMO NPs. Schematic representations and TEM images of E2, B2, AE, AB, AE2, and AB2 NPs (a-f respectively). SEM images of E2, B2, AE, AB, AE2, AB2 NPs (g-l respectively). DLS size distributions of E2, B2, AE, AB, AE2, AB2 NPs (m-r respectively).

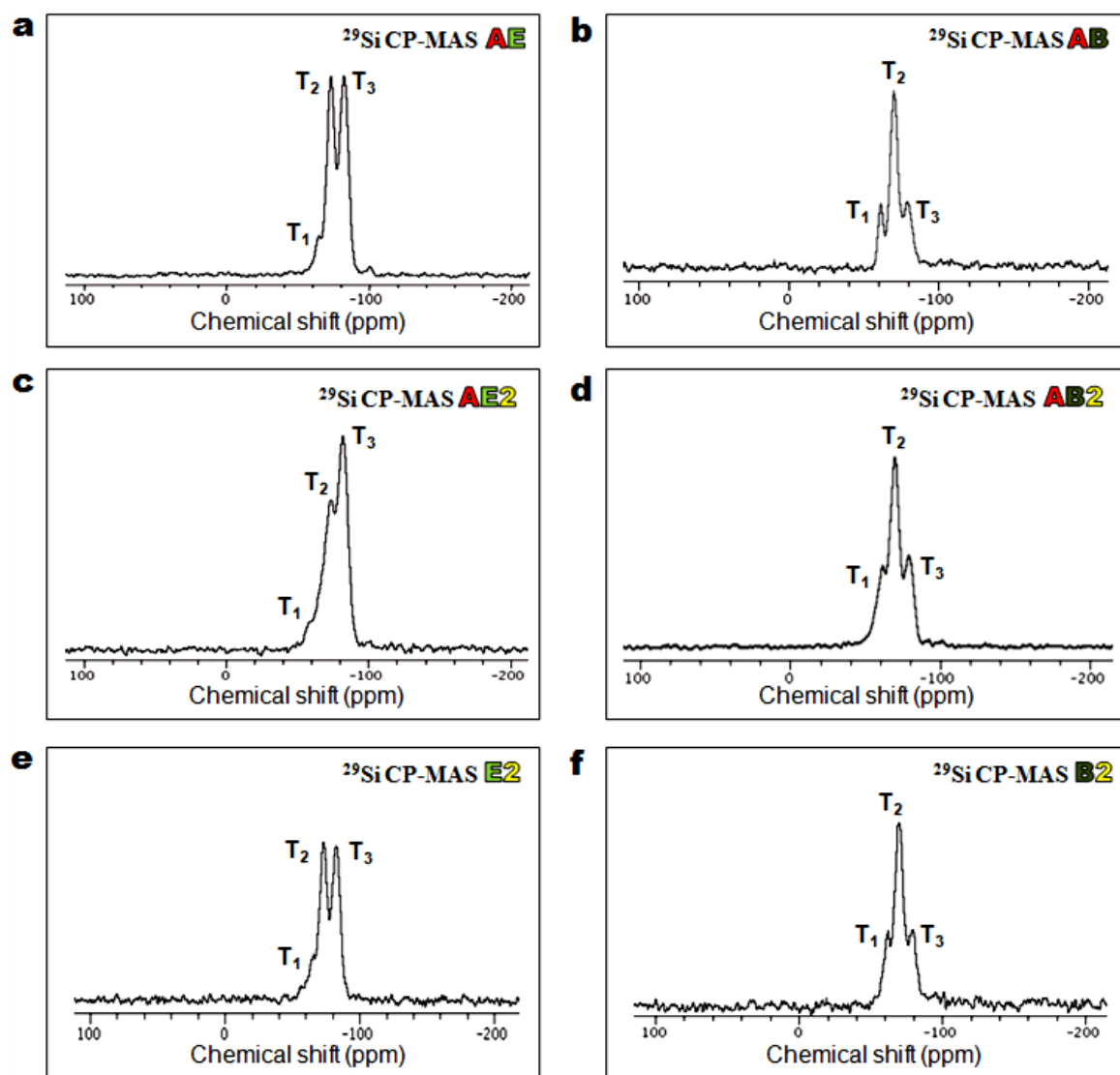


Figure S5. Solid state NMR ^{29}Si CPMAS spectra of PMO (a-b), and MPMO NPs (c-f).

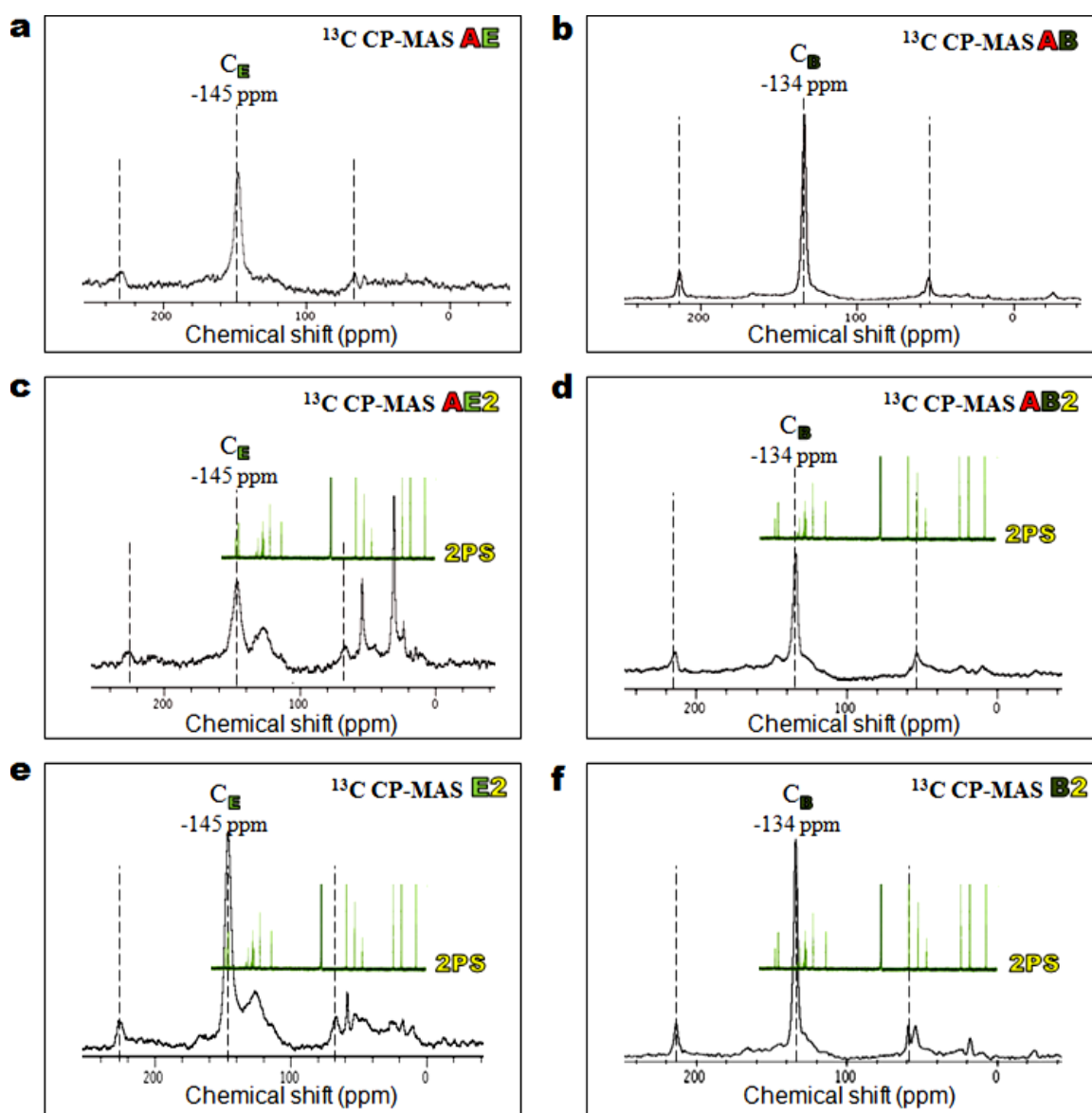


Figure S6. Solid state NMR ^{13}C CPMAS spectra of PMO (a-b), and MPMO NPs (c-f). The dashed lines show spinning side bands of the main signals of the ethylene carbon at -145 and of the benzene carbon at -134 ppm.

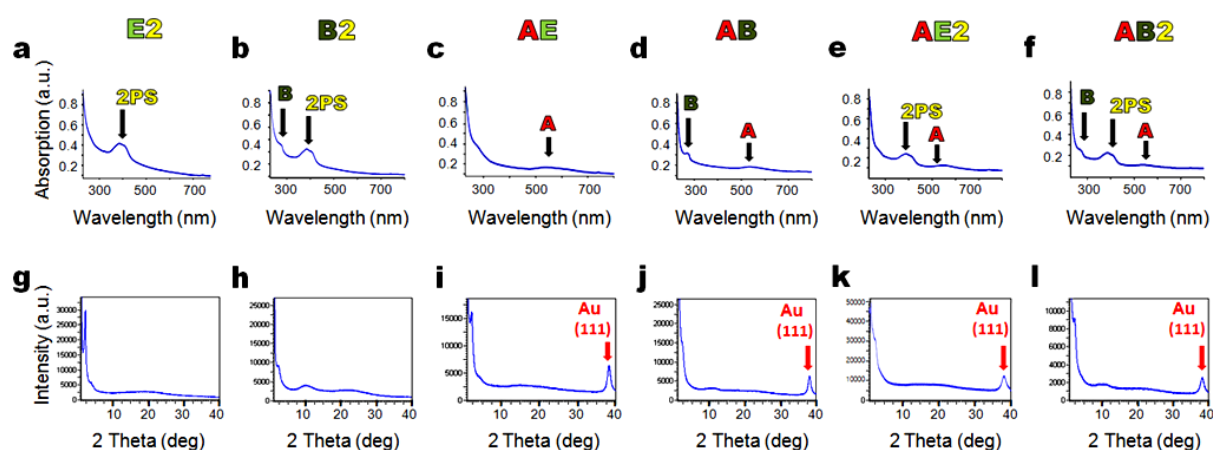


Figure S7. UV-visible spectroscopy and X-ray diffraction analysis of the two-photon-sensitive PMO NPs. UV-visible spectra of E2, B2, AE, AB, AE2, AB2 NPs (a-f respectively), demonstrating the presence of the 2PS, benzene, as well as gold component in the NPs. X-ray diffraction patterns of E2, B2, AE, AB, AE2, AB2 NPs respectively, confirming the gold encapsulation (g-l).

Sample	9.0 wt% Au Control ^[a]	AE NPs	AB NPs	AE2 NPs	AB2 NPs
Gold wt %	9.8	0.8	4.6	2.2	3.0

Table S3. Inductively coupled plasma-atomic emission spectroscopy measurement of the PMO NPs gold weight percent (wt%). [a] Bare gold nanoparticles, made from the same procedure (without organoalkoxysilane and 2PS), were mixed with a mesoporous silica powder (theoretical ratio of 9.0 wt% in gold) to determine the accuracy of the ICP calibration.

Sample	E2 NPs	B2 NPs	AE NPs	AB NPs	AE2 NPs	AB2 NPs
Total yield (%)	45-55	80-95	39-54	45-55	30-40	40-55

Table S4. Total yields of the PMO NPs elaborations calculated from the total mass of the reactants and the mass of the resulting surface-free materials dried under vacuum.

Sample	2PS ref	E2 NPs	B2 NPs	AE2 NPs	AB2 NPs
λ_{abs} (nm)	378	387	386	386	394
λ_{em} (nm)	442	451	452	459	464
Φ_F^a	0.60	0.14	0.12	0.029	0.026
$\sigma_2^{\text{max}^b}$ (GM)	100	12	4	5	4
$\sigma_2^{\text{max}} * \Phi_F$ (GM)	60	1.68	0.48	0.145	0.104

Table S5. Photophysical properties of Mixed PMOs NPs. The wavelength absorption and emission maxima are listed ($\lambda_{\text{abs}}/\lambda_{\text{em}}$), along with the fluorescent quantum yield (Φ_F), the maximum two-photon cross sections (σ_2^{max}), and the maximum brilliance ($\sigma_2^{\text{max}} * \Phi_F$) of MPMO NPs. [a] Quinine bisulfate standard at 0.5 M in H_2SO_4 . [b] per chromophore.

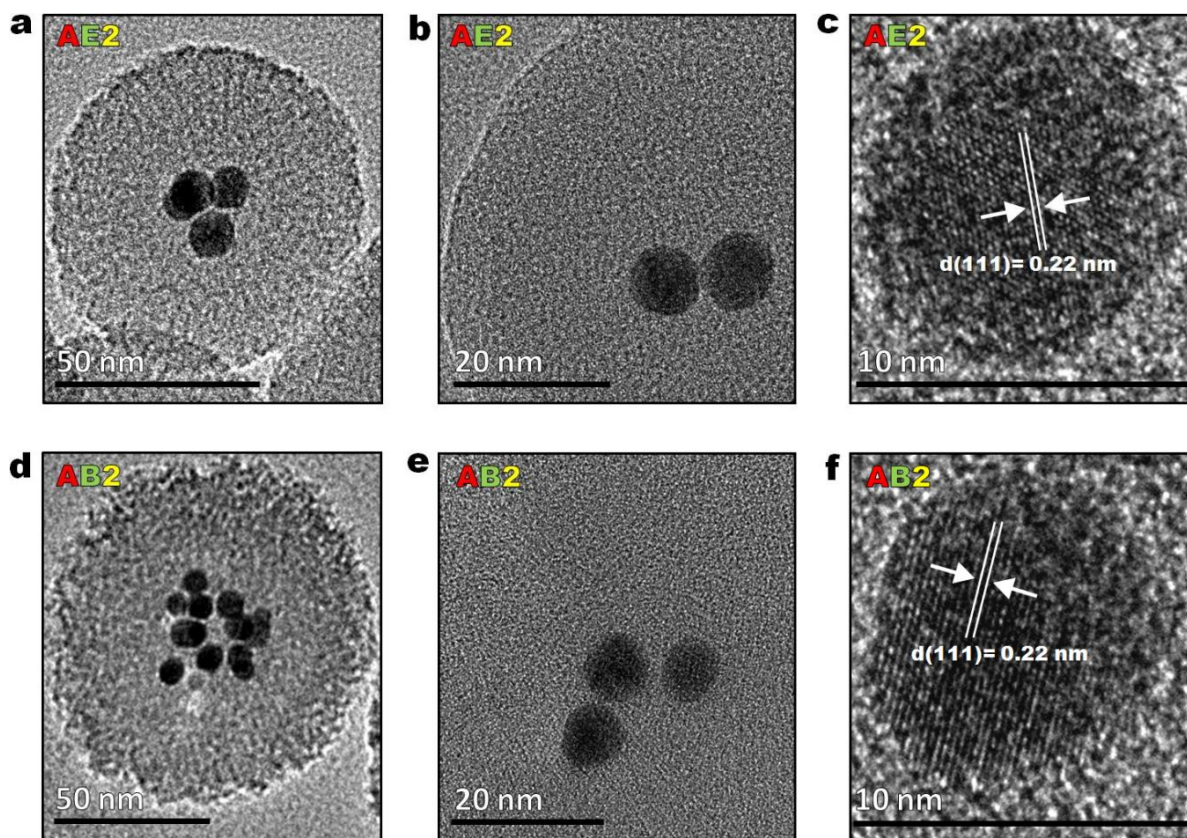


Figure S8. High Resolution TEM (HRTEM) images of AE2 and AB2 nanoPMOs. HRTEM images obtained by focusing on the radial nanopores of AE2 and AB2 NPs (a and d respectively). HRTEM images obtained by focusing on the gold NP cores of AE2 NPs (b-c). HRTEM images obtained by focusing on the gold NP cores of AB2 NPs (e-f).

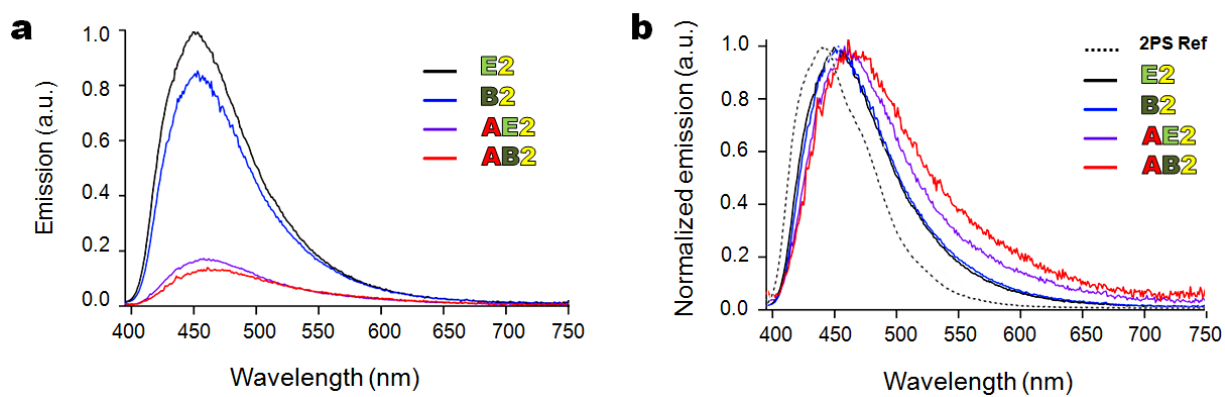


Figure S9. Fluorescence properties of mixed PMO NPs. Fluorescence emission spectra of MPMO NPs in ethanol (a), and the associated normalized spectra (b).

IV- FLUORESCENCE EMISSION OF BSNPs AND Au@BSNPs IN-VITRO

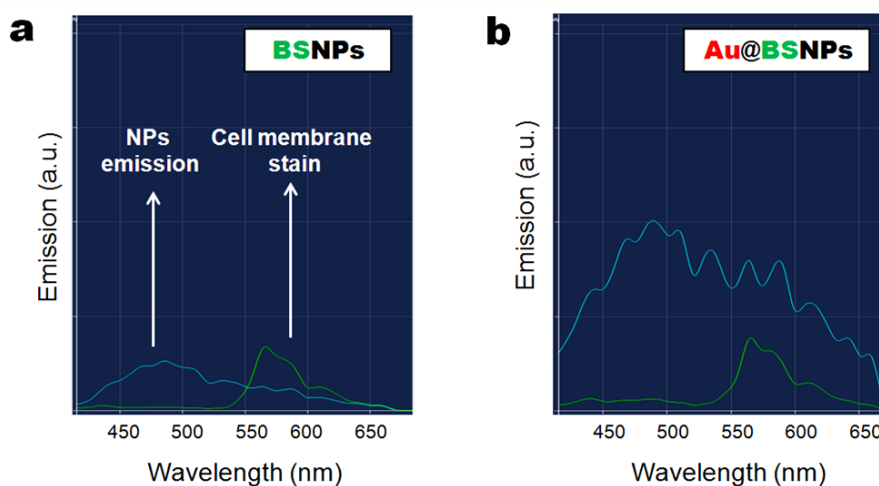


Figure S10. Fluorescent emission spectra of BSNPs and Au@BSNPs *in-vitro* (a and b respectively).

V- DRUG RELEASE CONTROL IN SIMULATED BIOLOGICAL MEDIA

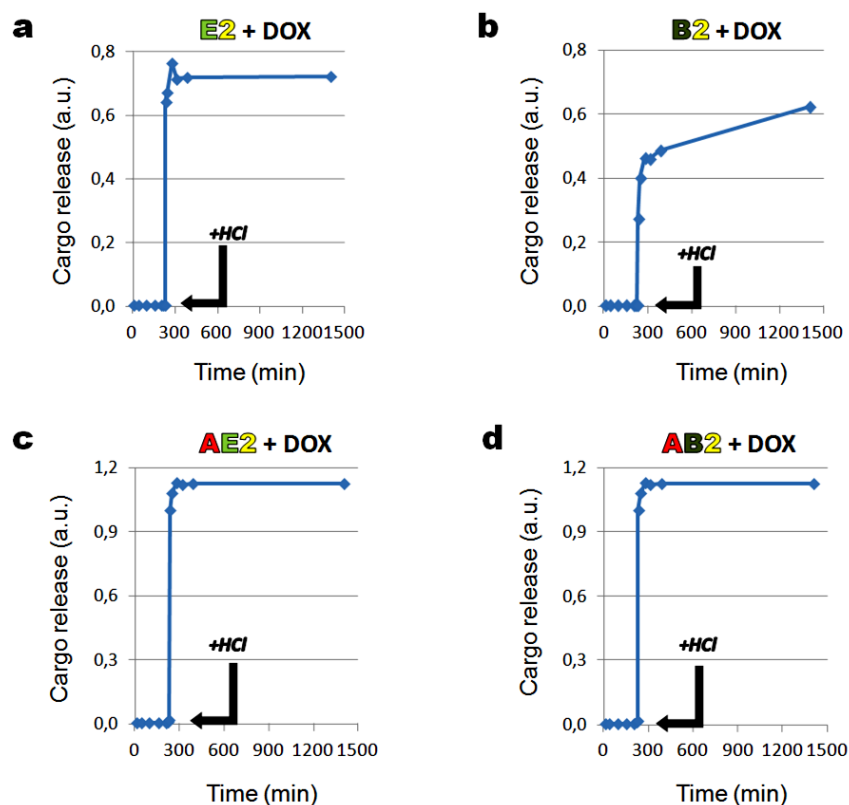


Figure S11. Doxorubicin delivery in water at pH 5.5. Release experiment on doxorubicin-loaded E2, B2, AE2, AB2 nanoPMOs (a-d respectively). The experiment is performed in ultrapure water upon addition of hydrochloric acid (0.2 M) to obtain a lysosomal pH. The release profiles are plotted from the UV-visible spectra of the released drug over time.

Sample	E2 NPs	B2 NPs	AE NPs	AB NPs	AE2 NPs	AB2 NPs
DOX (wt%)	9.2	9.8	9.5	9.6	9.7	9.7

Table S6. DOX loading capacities in the PMO NPs calculated from UV-visible spectra of the combined supernatants of the drug loading solutions, and the following washings

CHAPTER 8

Design of Periodic Mesoporous Organosilica Hybrid Nanoparticles

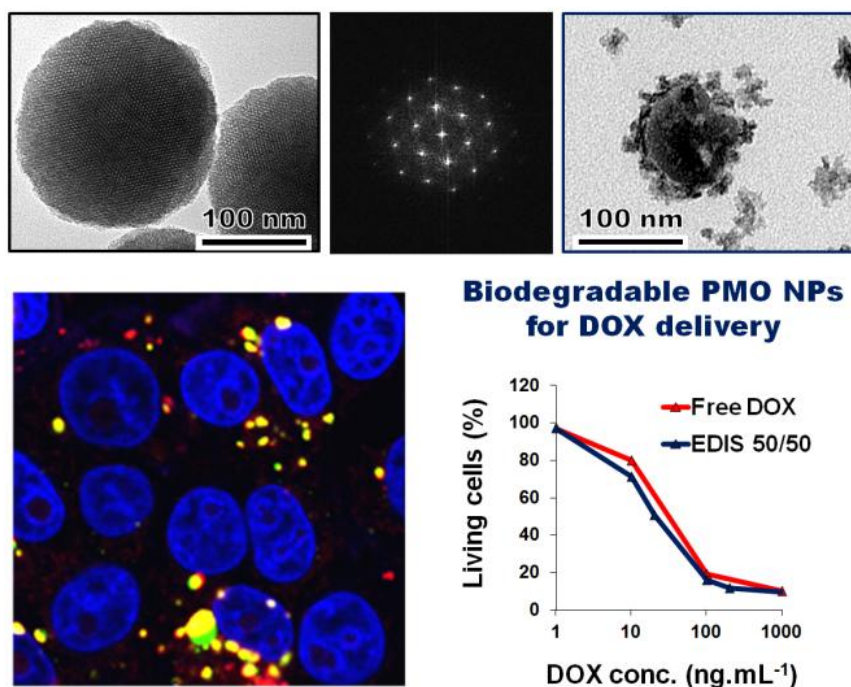
INTERDISCIPLINARY COLLABORATION

J. Croissant, X. Cattoën, M. Wong Chi Man, L. Raehm, J-O. Durand: *Nanomaterial concept, synthesis, physico-chemical characterizations, and applications in solution.*

A. Gallud, M. Maynadier: *Cell studies.*

CHAPTER 8

A. Biodegradable Ethylene-Bis(Propyl)Disulfide-Based Periodic Mesoporous Organosilica Nanorods and Nanospheres for Efficient In-Vitro Drug Delivery†



Abstract

Periodic mesoporous organosilica nanorods and nanospheres were synthesized from 1,4-bis(triethoxysilyl)ethylene and bis(3-ethoxysilylpropyl)disulfide. The nanosystems presented the long range order of hexagonal nanostructure. They were degraded in simulated physiologic conditions. The loading and release of doxorubicin with these nanosystems were both pH dependent. These nanoparticles were endocytosed by breast cancer cells and were very efficient for doxorubicin delivery.

† J. Croissant,* X. Cattoën, M. Wong Chi Man, A. Gallud, L. Raehm, M. Maynadier,* J-O. Durand,* *Adv. Mater.* 2014, adma.201401931R2.

Introduction

Periodic mesoporous organosilica (PMO) form a new class of mesoporous materials which holds great promises for a wide variety of applications such as adsorption,¹⁻⁵ catalysis,⁶⁻⁹ drug release studies in simulated biological media,^{10, 11} chromatography,¹² and enzyme immobilization.¹³ Since the pioneering independent works of Inagaki, Ozin, and Stein in 1999,^[14-16] who first described PMO materials, the size reduction of PMO to the nanoscale has been scarcely reported. In 2006, Djojoputro and co-workers used the fluorocarbon FC-4 surfactant as a vesicle templating agent to design polydisperse ethane-based hollow nanospheres of 100 to 400 nm in diameter.¹⁷ Then in 2009, Cho *et al.* reported polydisperse worm-like structured benzene-based PMO nanoparticles (NPs) from 50 to 1000 nm in diameter.¹⁸ Worm like-structured ethylene-based monodisperse PMO NPs of 20 nm were also reported by the group Kuroda as low hemolytic materials.¹⁹ Those nanoparticles were resistant to degradation in PBS compared to mesoporous silica nanoparticles of the same diameter. In 2012, Guan *et al.* have reached the nanoscale with crystal-like PMO controlled nanostructures based with methane, ethane, ethylene, and benzene bridging groups.²⁰ This work assessed the production of PMO nanospheres or nanoelipsoids from 500 to 30 nm via the variation of base concentration or co-solvent contents of the reaction media. In the same year, Lui and his coworkers published yolk-shell hybrid materials with a periodic mesoporous organosilica shell as ideal nanoreactors for selective alcohol oxidation, while Mandal and Kruk reported hollow spheres of methylene-, ethenylene-, and phenylene-bridged mesoporous organosilicas from Pluronic F127 block-copolymer template.^{21, 22} The PMO shells were composed of ethane moieties and the overall size of the NPs varied from 200 to 300 nm. Hard and soft templates were also used to prepare hollow PMO nanospheres with the ethane, ethylene, and benzene groups.²²⁻²⁵ The strategy with hard template consists of using a silica NP core and to condense the bridged organosilane precursor at the surface of the silica NP to afford hollow PMO NPs after etching the silica core.²⁴ This strategy was used very recently by J. Shi and co-workers to design monodisperse 450 nm nanocarriers with the first application of PMO NPs for drug delivery in cancer cells.²⁶

In our study we report the syntheses of biodegradable PMO 200 nm nanospheres and 450 to 130 nm nanorods based on bis(triethoxysilyl)ethylene (E) and bis(3-triethoxysilyl-propyl)disulfide (DIS) bridging groups in various weight ratios. The control of the NPs shape and size was found to be directly correlated to the ethylene over bis(propyl)disulfide ratio ($R_{E/DIS}$). Ethylene-based nanorods were obtained when only E was used whereas spherical non-porous bis(propyl)disulfide-based bridged silsesquioxane (BS) NPs were observed when the DIS precursor was used. Depending on the $R_{E/DIS}$, ethylene-disulfide (EDIS) mixed PMO (MPMO) nanorods and nanospheres of various sizes were elaborated and used as biodegradable nanocarriers of drugs in breast cancer cells. The EDIS MPMO nano-objects were very efficient in inducing cancer cell death when loaded with doxorubicin (DOX).

Results and discussion

First, the nanomaterial elaboration of ethylene-based PMO (E PMO) was studied. The synthesis was performed in water with a cetyltrimethylammonium bromide micellar template and sodium hydroxide catalysis at 80°C. The template was prepared at this temperature for 50 min with a stirring speed adjusted at 1400 rpm. Then, the sol-gel process was carefully controlled by quick addition of bis(triethoxysilyl)ethylene and the reaction was stirred for 2 h. Transmission electron microscopy (TEM) images revealed 700 nm long nanorods of 200 nm in diameter (see Fig. 1A), and their uniform morphology and size monodispersity was readily visible with scanning electron microscopy (SEM, see Fig. S1). Besides, the crystal-like 2D-hexagonal porosity visible by TEM (see Fig. S2A), was confirmed with the small angles X-ray diffraction (XRD) peaks of the hexagonal structure at 2.3, 3.9, and 4.6 degrees (Fig. S3A). The intense peak at small angle is characteristic of 2 nm mesopores, which was in accordance with the hysteresis observed in the nitrogen-adsorption-desorption isotherm (Fig. S7A). The calculations based on the BET theory resulted in a surface area of 1042 m².g⁻¹ with a pore diameter of 2.2 nm (BJH method).

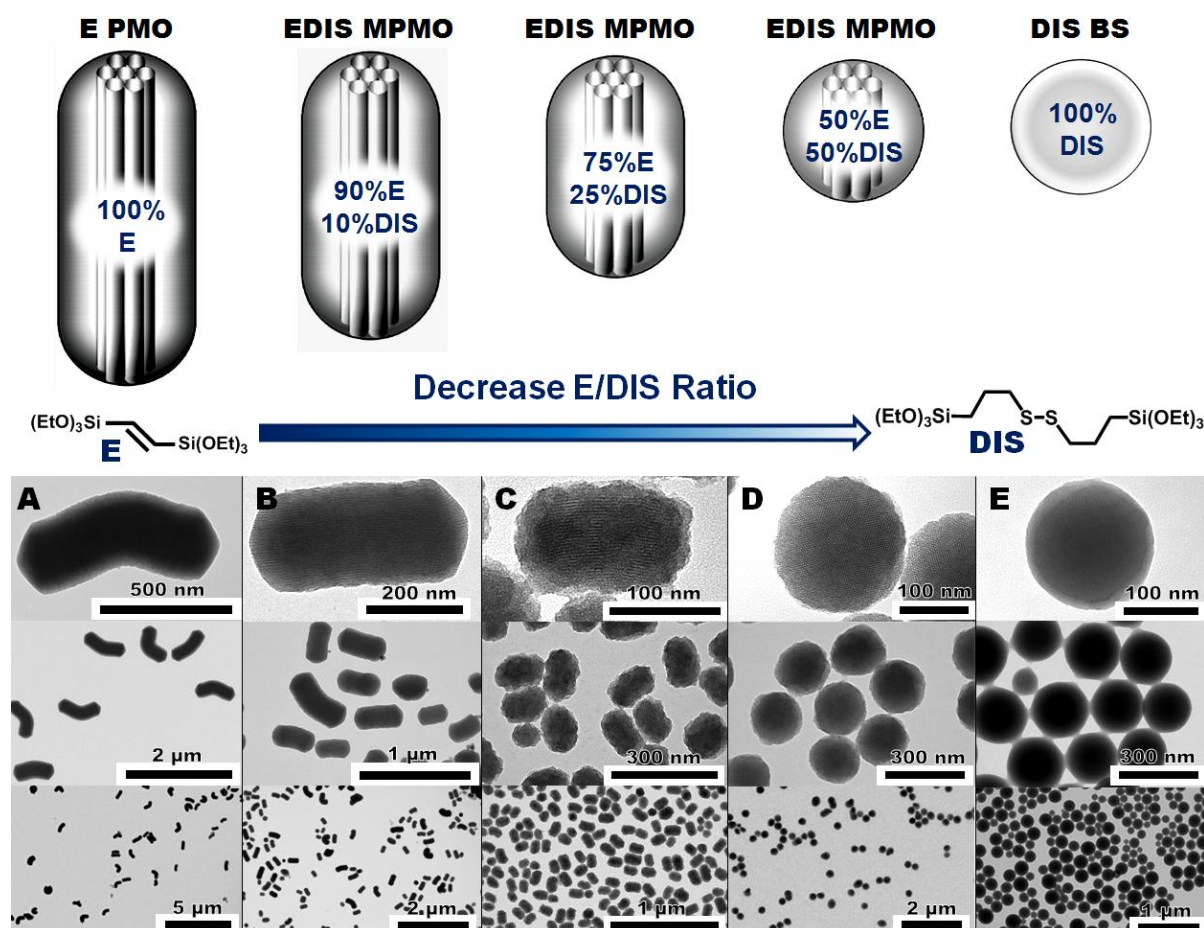


Figure 1. Schematic representation of the size and morphology control in E PMO, EDIS MPMO, and DIS BS NPs by the variation of the $R_{E/DIS}$ in the reaction media. TEM images of E PMO, EDIS MPMO constituted of $R_{E/DIS}$ of 90/10, 75/25, 50/50, and DIS BS NPs (A, B, C, D and E respectively).

Secondly, the preparation of biodegradable MPMO nanocarriers was assessed by mixing the ethylene precursor and bis(3-triethoxysilylpropyl)disulfide. The EDIS NPs syntheses were carefully controlled for 2 h at 80°C and 1400 rpm as well, with an initial quick addition of E followed by the disulfide precursor. Three different $R_{E/DIS}$ were tested: 90/10, 75/25, and 50/50 in order to study their influence on the NPs size and morphology. (see Table S1). TEM analysis showed the successful elaboration of MPMO nanorods for $R_{E/DIS} = 90/10$ and 75/25 (Fig. 1B and C respectively). EDIS 90/10 MPMO nanorods were 450 ± 100 nm long with diameter of 200 ± 50 nm; whereas EDIS 75/25 MPMO nanorods were 130 ± 25 nm long with diameter of 70 ± 10 nm (see SEM Fig. S4). Interestingly, the 50/50 ratio led to the formation of monodisperse spherical MPMO NPs of 200 ± 15 nm in diameter (Fig. 1D, see SEM Fig. S5). All the three nanomaterials were crystal-like mesoporous nanocarriers, as displayed with the XRD patterns (Fig. S3B-D), which is also supported by high magnification TEM images (Fig. S2B-D). Moreover, the long range order of the hexagonal nanostructures was demonstrated by Fast-Fourier Transform (FFT) calculation on the EDIS nanorods and nanospheres (Fig. 2). Furthermore, the materials were found to have high surface areas and pores size from 2.5 to 2 nm (Fig. S7). The specific surface area and pore size decreased when the $R_{E/DIS}$ decreased, from 1087 ($R_{E/DIS}=90/10$), to 923 ($R_{E/DIS}=75/25$), and 890 $\text{m}^2\cdot\text{g}^{-1}$ ($R_{E/DIS}=50/50$). Note that, the sole addition of the DIS precursor in a water/ethanol mixture (5:2, v:v) led to non-porous monodisperse bridged silsesquioxane nanospheres of 200 nm (Fig 1E, see SEM Fig. S6 and XRD Fig. S3E) and that an increased dilution of the E and DIS precursors in water led to smaller MPMOs nano-objects. The chemical compositions and functionalities expected in the E PMO, EDIS MPMO, and DIS BS NPs are further validated via Fourier transform infrared (FTIR) and solid state nuclear magnetic resonance (NMR) (see Fig. S8 and 9 respectively), as well as energy dispersive spectroscopies (Table S2). FTIR confirmed the presence of the E and DIS moieties in EDIS NPs with the combination of the $\nu_{C=C}$ at 1638 cm^{-1} and the ν_{Si-C} at 1164 cm^{-1} from ethylene, and the aliphatic ν_{C-H} vibration modes from 1980 to 1894 cm^{-1} , belonging to the DIS fragments (See Fig. S8). Solid state NMR ^{13}C CPMAS spectra clearly displayed the three types carbon found in this DIS moiety at 10, 27, and 47 ppm, and the ethylene carbon found at 147 ppm (Fig. S9A). The ^{29}Si CPMAS spectra depicted the presence of the T_3 environment of the DIS at -67 ppm, along with the major T_2 and T_3 of the E at -72 and -82 ppm in EDIS NPs (Fig. S9B). EDS spectroscopy correlated these observations with an increasing content of sulfur in the EDIS 90/10, 75/25, and 50/50 nanomaterials. Consequently, the $R_{E/DIS}$ variation could be used to tune the EDIS MPMO NPs shape from nanorods to nanospheres as the $R_{E/DIS}$ decreases.

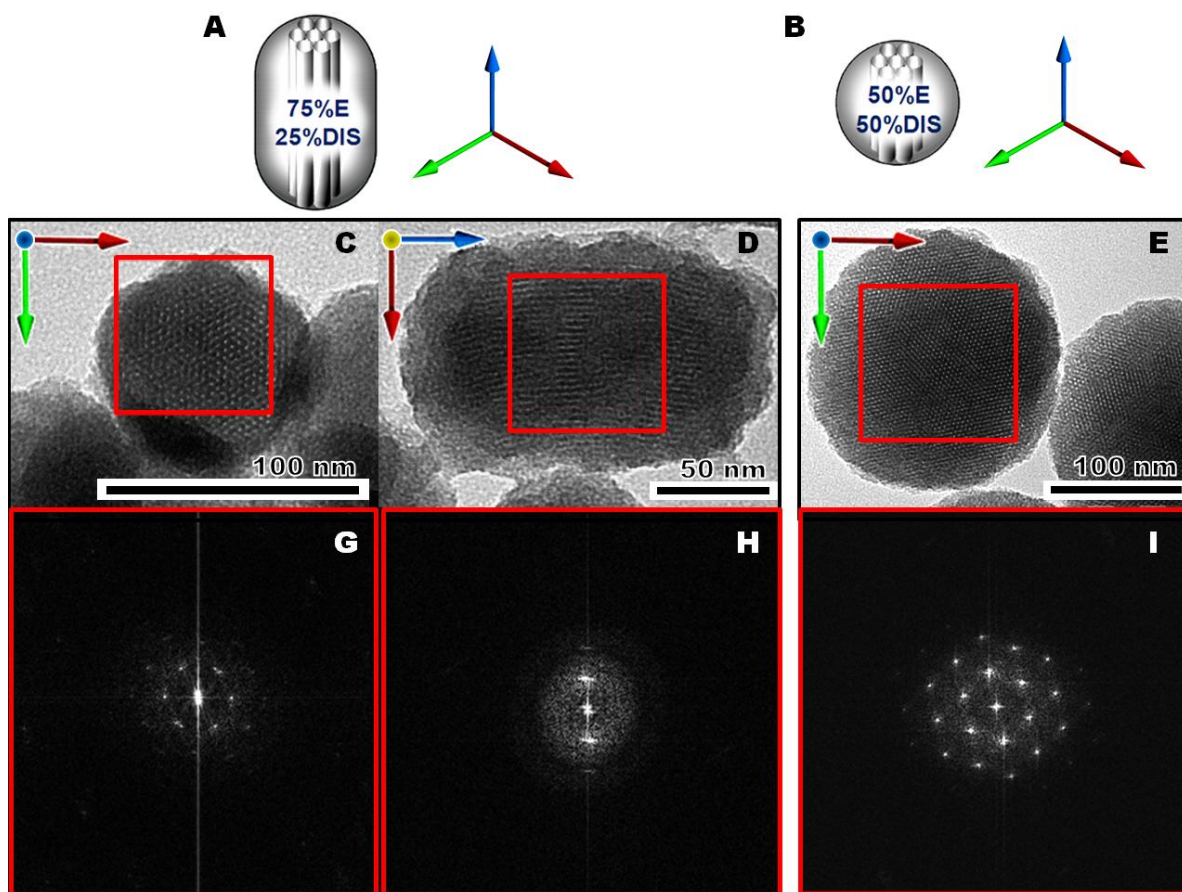


Figure 2. High magnification TEM images of EDIS MPMO nanorods (A, C, D) and nanospheres (B, E). FFT calculations carried out on the TEM red squared areas of the diameter and length dimensions of the nanorods (G and H respectively), and on the nanospheres (I).

The degradability of EDIS nanorods and nanospheres was then studied in solution. EDIS 50/50 nanospheres were dispersed in PBS (pH 7.4) at 37°C with 6 μ M or 2 mM of mercaptoethanol (ME), so as to respectively mimic the extracellular and intracellular equivalents of glutathione.²⁷ The idea was to induce the disulfide bond cleavage in order to progressively degrade the NPs in a simulated extracellular or intracellular environment. Dynamic light scattering (DLS) analysis of the EDIS 90/10, 75/25, 50/50 NPs before and after addition of 6 μ M or 2 mM mercaptoethanol (ME) for 24 and 48 h was performed (Fig. S10-11). After 24 h of simulated extracellular media (6 μ M of ME), long EDIS 90/10 nanorods were degraded as depicted by the decrease of the hydrodynamic volume maxima from 458 to 66 nm (Fig. S10A). Shorter EDIS 75/25 nanorods and EDIS nanospheres were less degraded at that point, with decreases of the hydrodynamic volumes from 278 to 222 nm and 255 to 220 nm, respectively (Fig. S10B-C). Besides, after 48 h of reaction the NPs size distributions became larger with smaller NPs from 60 to 70 nm. This conclusion is further confirmed by TEM images before and after 48 h of reaction in simulated extracellular physiological media, which clearly displayed broken EDIS nanospheres (Fig. 3) and nanorods (Fig. S12). Note that such a degradation was found to be faster and more pronounced in simulated intracellular media (2 mM of ME), as shown with the faster and higher size decreases observed by DLS analysis on EDIS nanorods and nanospheres, with

similar results after 24 and 48 h (see Fig. S11). The EDIS MPMO NPs had a negatively charged surface of -25 to -35 mV (Fig. S13), comparable to mesoporous silica nanoparticles.^{28, 29} Furthermore, cytotoxicity studies of EDIS nanospheres and nanorods revealed the biocompatibility of the nanomaterials up to 125 $\mu\text{g.mL}^{-1}$ (Fig. S14). We therefore prepared EDIS MPMO biodegradable and biocompatible nanorods and nanospheres.

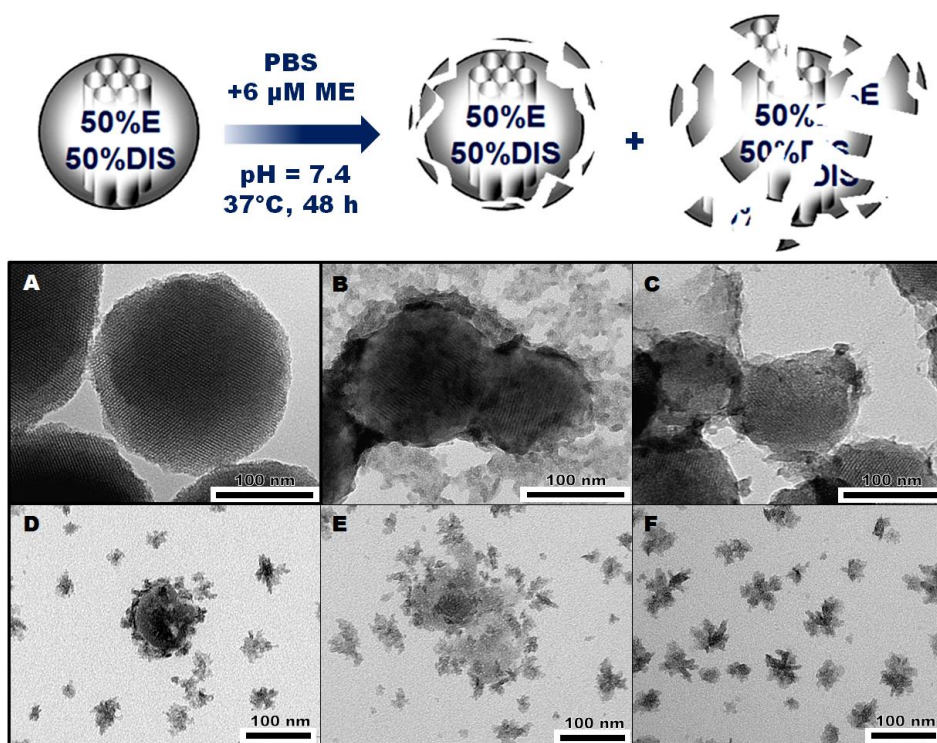


Figure 3. TEM images of EDIS 50/50 nanospheres before (A) and after 48 h of degradability control in physiological conditions (B-F).

The biodegradable MPMO nanocarriers as well as the E PMO NPs were eventually tested in solution as drug release systems. The nanomaterial powder was mixed with anticancer drug DOX in aqueous media for 48 h in neutral condition; then, the particles were washed thrice with water in order to remove the surface adsorbed drug molecules (see ESI). Dried nanomaterial powders were placed at the bottom of a plastic cuvette then filled gently with water. The absence of premature release was monitored by UV-visible spectroscopy and plotted as a function of time (see pH 7 in Fig. 4). However, as soon as the pH was lowered to 5.5 (as in the lysosomal compartment), instantaneous DOX releases occurred for all porous nanocarriers. The absence of any significant difference in the release overtime in the case of DIS BS NPs suggests that DOX is not adsorbed on the surface of the particles (Fig. 4). Besides, the trend of the release efficiencies correlated the nanomaterials surface areas and pore size: E > EDIS 90/10 > EDIS 66/64 > EDIS 50/50 (see Fig. S7). The DOX loading capacities were determined with the loading solution supernatants and ranged from 2 to 3 wt%. To increase the loading capacities of the biodegradable EDIS MPMO, the loading step was then performed at pH 5.5 instead of 7 for 48 h. Afterwards, the solution was neutralized with sodium hydroxide, stirred for 30 min, and the NPs were collected via centrifugation and

washed several times with water. Surprisingly, the payload was thus highly enhanced up to 21.5, 21.8, 22.2 wt% of DOX for EDIS 90/10, 66/43, and 50/50 respectively. The absence of premature release was also shown on these NPs, as well as the pH-mediated drug release in simulated lysosomal acidity (see Fig. S15).

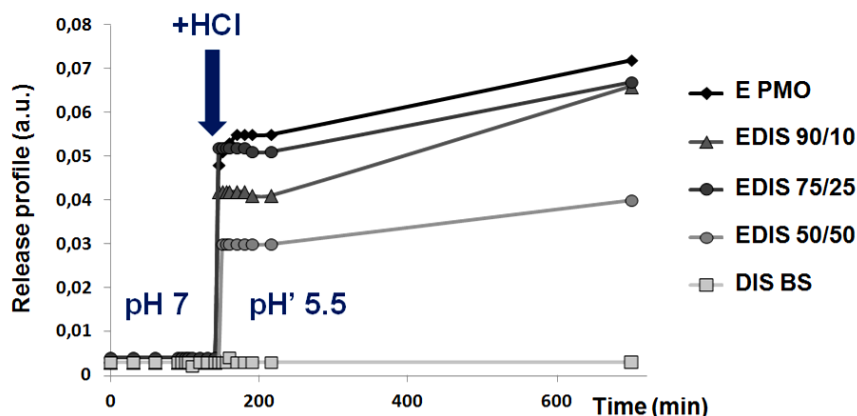


Figure 4. DOX release in solution via pH change with E PMO, EDIS MPMO, and DIS BS NPs.

The endocytosis of the EDIS nanomaterial was then studied via live confocal microscopy images of propidium iodide (PI) loaded NPs, on MCF-7 breast cancer cells. First, the PI loading of the NPs was performed in aqueous media by mixing the materials with the dye for 48 h at 25°C. Then, the mixture was centrifuged and washed four times with water; the supernatants were gathered to determine the loaded content of PI (2 wt%). The PI-loaded EDIS 90/10, 75/25, and 50/50 NPs were then incubated for 24 h at 40 $\mu\text{g.mL}^{-1}$ with MCF-7 breast cancer cells (Fig. 5A). The nuclei were stained via Hoescht 33342 and the typical blue fluorescence was seen under excitation at 405 nm. The lysosomes were revealed by the green fluorescence of LysoTracker Green DND-26 staining upon excitation at 488 nm. The NPs tracking was performed thanks to the red fluorescence of the PI cargos excited at 543 nm. The merged images clearly showed the endocytosis of all EDIS MPMO NPs. Indeed, owing to the well-known PI non-permeability of the cell membranes, the colocalization of the red and green dots signifies that EDIS MPMO NPs are endocytosed and mainly found in the lysosomes after 24 h of incubation. Furthermore, the cellular uptakes were quantitatively analyzed via flow cytometry after 4, 18, and 24 h of incubation (Fig. 5B, see Fig. S16). A small fraction of the NPs was endocytosed after 4 h of incubation and there were no significant differences between EDIS nanorods and nanospheres. On the contrary, after 18 and 24 h of incubation, the nanospheres were two-fold more efficiently internalized than the nanorods with 64 and 28-35% of cellular uptake respectively. This effect may be a combination of the NPs shape and the disulfide surface density. It is noteworthy that this trend is opposite to what was observed with mesoporous silica nanoparticles, in which long nanorods were more internalized than smaller ones and than nanospheres.^{30, 31}

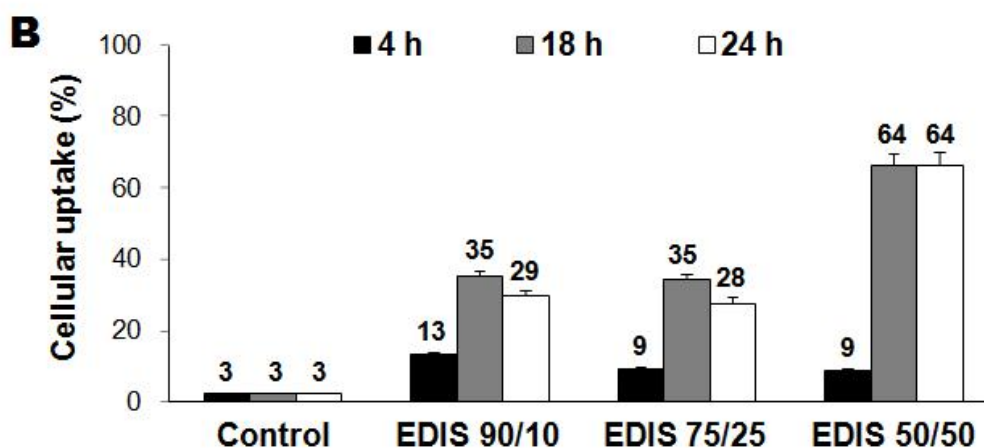
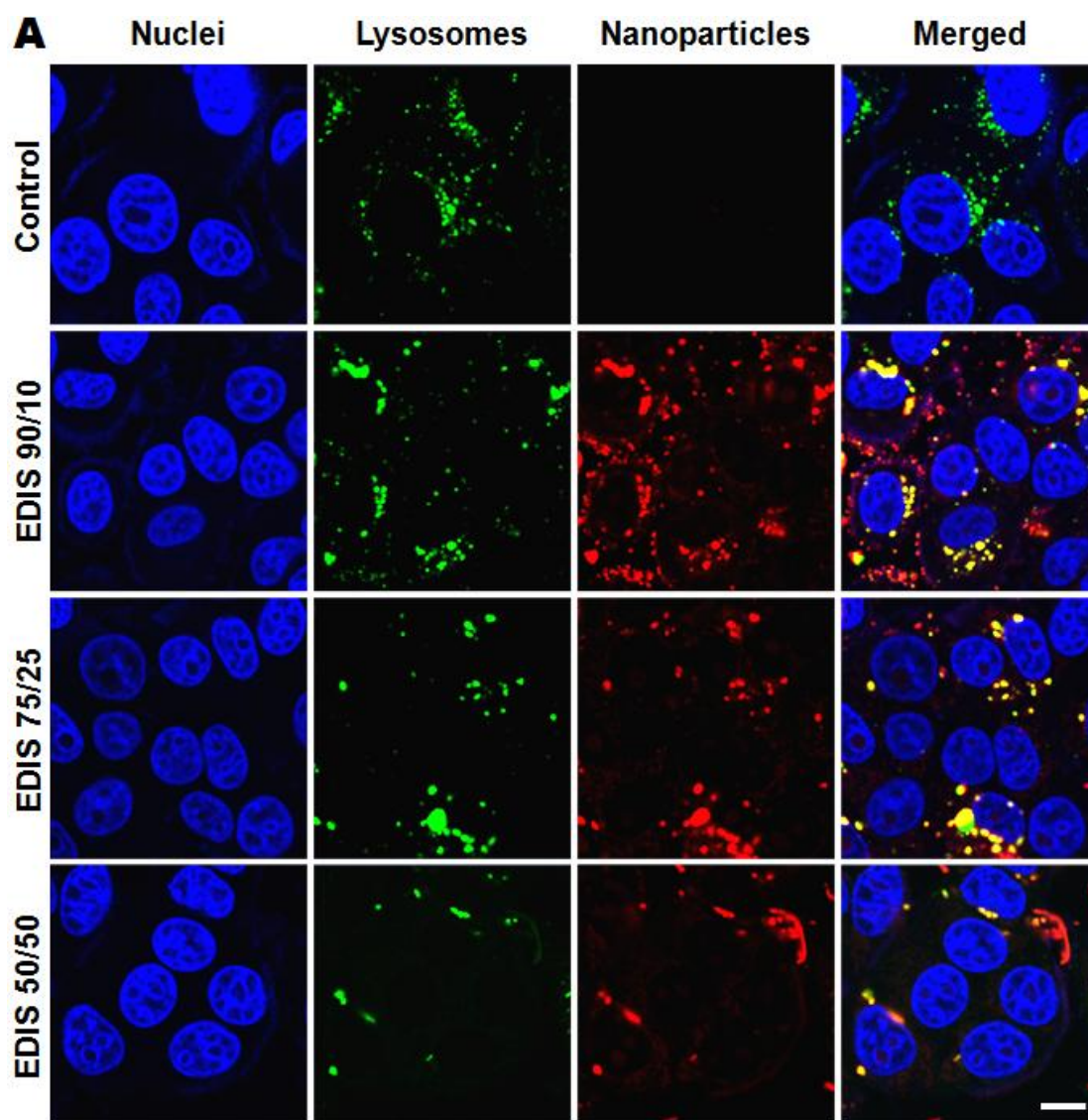


Figure 5. Confocal microscopy images of MCF-7 breast cancer cells incubated 24 h with or without EDIS nanomaterials (A). Scale bar of 10 μ m. The nuclei staining (blue fluorescence) was obtained via Hoescht 33342. The lysosomes were revealed via LysoTracker green DND-26 staining (green fluorescence). The NPs tracking was performed via PI cargos (red fluorescence). The merged images demonstrated the endocytosis of all EDIS MPMO NPs. Cellular uptake quantitative analysis determined via flow cytometry after 4, 18, and 24 h of incubation (B).

The drug delivery systems loaded with DOX were finally assessed in cancer cells *in-vitro*. DOX-loaded EDIS 90/10, 75/25, 50/50 biodegradable nano-objects were studied. MCF-7 cells were incubated with EDIS nanomaterials loaded in acidic conditions (21-22 DOX wt%) (Fig. 6A-B). First, the drug-loaded nanosystems were compared for a given incubation time of 72 h at various concentration. The DOX delivery-mediated cancer cell killing was highly efficient (Fig. 6A), with down to 12% of cell survival at only 1 $\mu\text{g.mL}^{-1}$ of nanosystems.

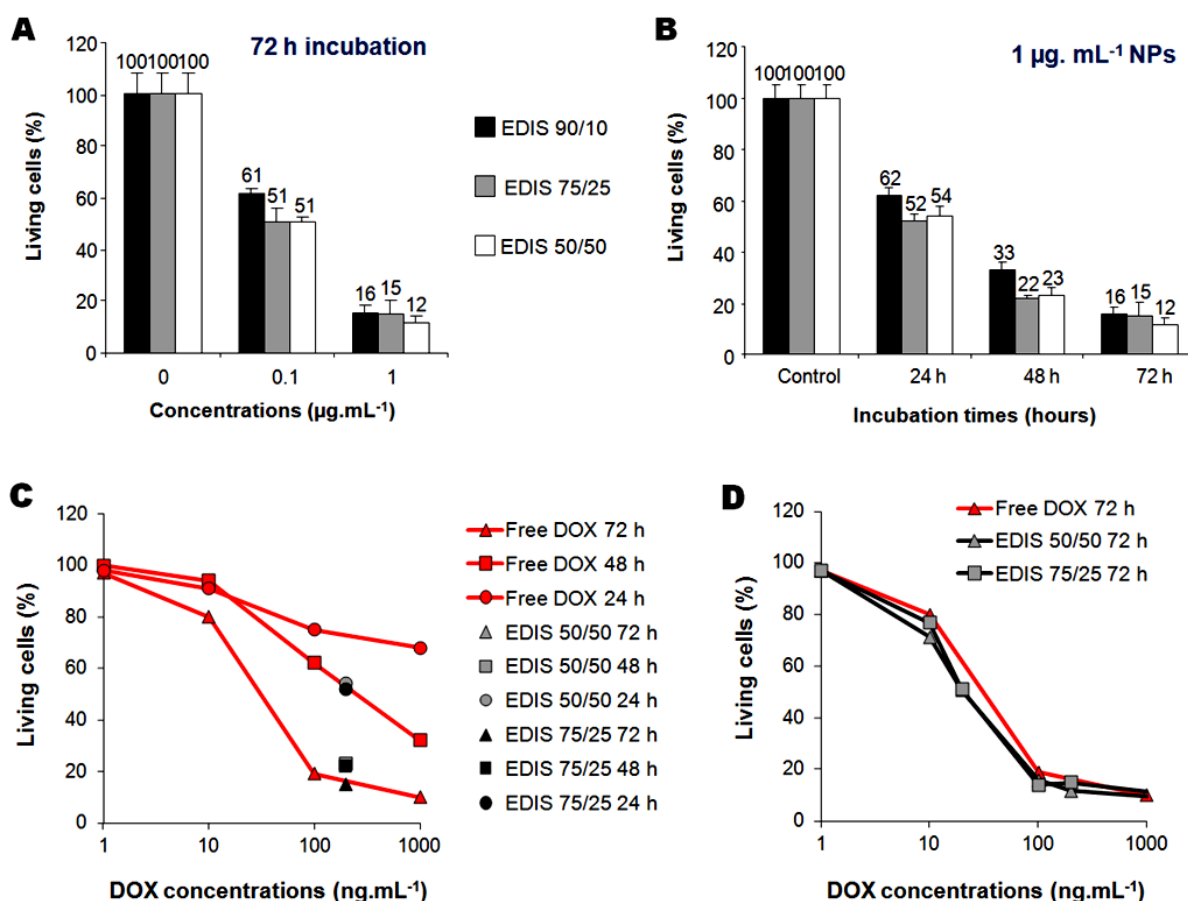


Figure 6. In-vitro cytotoxicity studies of EDIS NPs loaded with DOX in acidic conditions for a given incubation time (72 h) and various NPs concentrations (A), or for a given NPs concentration (1 $\mu\text{g.mL}^{-1}$) and various incubation times (B). DOX cytotoxicity on MCF-7 cells after 24, 48, and 72 h of incubation, compared with EDIS 75/25 and 50/50 loaded in acidic conditions at 200 ng.mL^{-1} of DOX at 24, 48 and 72 h of incubation. (C). Comparison of the DOX cytotoxicity with EDIS 75/25 and 50/50 NPs on MCF-7 cells after 72 h of incubation at various concentrations (D).

Kinetic studies of the drug delivery efficacy were secondly carried out on the EDIS nanomaterials. A fixed NPs concentration of 1 $\mu\text{g.mL}^{-1}$ was selected and the cell survival was determined according to times of incubation (Fig. 6B). Sustained drug deliveries up to 72 h were obtained. After 24, 48, and 72 h, 54, 23, and 12% cancer cells survived respectively.

Furthermore, the nanocarriers loaded in acidic conditions enhanced the kinetic of the DOX efficacy, as demonstrated by the comparison of free DOX and DOX-loaded EDIS NPs for 200 ng.mL⁻¹ of DOX (Fig. 6C). After 24 h of incubation the EDIS nanorods and nanospheres induced 50% of cell death at 200 ng.mL⁻¹ compared to 20-30% for the free DOX (Fig. 6C). Again, better results were obtained through the NPs as after 48 h of incubation, NPs were 40% more efficient than free DOX. After 72 h of incubation, the cell death, although slightly increased with NPs, was comparable to the one of free DOX (Fig. 6D). Note that the nanosystems loaded with DOX in neutral conditions (2-3 DOX wt%) were less efficient when incubated with cancer cells (Fig. S17).

Conclusion

In conclusion, we report an original size and shape controllable MPMO nanomaterial elaboration via the variation of the bis(triethoxysilyl)ethylene over bis(3-triethoxysilylpropyl)disulfide co-condensation ratio. Ethylene-based PMO nanorods were designed as well as EDIS MPMO nanorods and nanospheres. The EDIS NPs were found to be biocompatible in MCF-7 cancer cell line, and degradable in simulated physiologic conditions. The DOX NPs loading was found to be greatly enhanced in acidic aqueous media, compared to similar neutral conditions. Furthermore, DOX release was pH sensitive in aqueous media and upon acidic stimuli simulating the lysosomal compartment, DOX was released from the NPs. Furthermore the NPs were located in the lysosomes after 24 h of incubation. The EDIS NP and both EDIS nanorods and nanospheres acted as powerful biodegradable Trojan horses for efficient *in-vitro* cancer therapy. The biodegradable MPMOs NPs we prepared are as efficient as and complementary to hollow mesoporous silica nanoparticles.³²

REFERENCES

1. E. De Canck, I. Ascoop, A. Sayari and P. Van Der Voort, *Phys. Chem. Chem. Phys.*, 2013, **15**, 9792-9799.
2. S. Martens, R. Ortmann, F. J. Brieler, C. Pasel, Y. Joo Lee, D. Bathen and M. Fröba, *Z. Anorg. Allg. Chem.*, 2014, **640**, 632-640.
3. R. O. Otero, D. Esquivel, M. a. A. Ulibarri, C. S. Jiménez-Sanchidrián, F. J. Romero-Salguero and J. M. Fernández, *Chem. Eng. J.*, 2013, **228**, 205-213.
4. J. Gao, X. Zhang, S. Xu, F. Tan, X. Li, Y. Zhang, Z. Qu, X. Quan and J. Liu, *Chem. Eur. J.*, 2014, **20**, 1957-1963.
5. W. R. Grüning, G. Siddiqi, O. V. Safonova and C. Copéret, *Adv. Synth. Catal.*, 2014, **356**, 673-679.
6. J. A. Melero, J. Iglesias, J. M. Arsuaga, J. Sainz-Pardo, P. de Frutos and S. Blazquez, *J. Mater. Chem.*, 2007, **17**, 377-385.
7. B. Karimi and F. Kabiri Esfahani, *Chem. Commun.*, 2011, **47**, 10452-10454.
8. B. Karimi, H. M. Mirzaei and A. Mobaraki, *Cat. Sci. Tech.*, 2012, **2**, 828-834.
9. P. Borah, X. Ma, K. T. Nguyen and Y. Zhao, *Angew. Chem. Int. Ed.*, 2012, **51**, 7756-7761.
10. C. X. Lin, S. Z. Qiao, C. Z. Yu, S. Ismadji and G. Q. Lu, *Micro. Meso. Mater.*, 2009, **117**, 213-219.
11. H.-Y. Wu, F.-K. Shieh, H.-M. Kao, Y.-W. Chen, J. R. Deka, S.-H. Liao and K. C. W. Wu, *Chem. Eur. J.*, 2013, **19**, 6358-6367.
12. V. Rebbin, R. Schmidt and M. Fröba, *Angew. Chem. Int. Ed.*, 2006, **45**, 5210-5214.
13. W. Wang, J. E. Lofgreen and G. A. Ozin, *Small*, 2010, **6**, 2634-2642.
14. T. Asefa, M. J. MacLachlan, N. Coombs, G. A. Ozin, *Nature* **1999**, 402, 867.
15. S. Inagaki, S. Guan, Y. Fukushima, T. Ohsuna, O. Terasaki, *Journal of the American Chemical Society* **1999**, 121, 9611.
16. B. J. Melde, B. T. Holland, C. F. Blanford, A. Stein, *Chemistry of Materials* **1999**, 11, 3302.
17. H. Djojoputro, X. F. Zhou, S. Z. Qiao, L. Z. Wang, C. Z. Yu and G. Q. Lu, *J. Am. Chem. Soc.*, 2006, **128**, 6320-6321.
18. E.-B. Cho, D. Kim and M. Jaroniec, *Micro. Meso. Mater.*, 2009, **120**, 252-256.
19. C. Urata, H. Yamada, R. Wakabayashi, Y. Aoyama, S. Hirosawa, S. Arai, S. Takeoka, Y. Yamauchi and K. Kuroda, *J. Am. Chem. Soc.*, 2011, **133**, 8102-8105.
20. B. Guan, Y. Cui, Z. Ren, Z.-a. Qiao, L. Wang, Y. Liu and Q. Huo, *Nanoscale*, 2012, **4**, 6588-6596.
21. J. Liu, H. Q. Yang, F. Kleitz, Z. G. Chen, T. Yang, E. Strounina, G. Q. Lu and S. Z. Qiao, *Adv. Funct. Mater.*, 2012, **22**, 591-599.
22. M. Mandal and M. Kruk, *Chem. Mater.*, 2011, **24**, 123-132.
23. Y. Yang, J. Liu, X. Li, X. Liu and Q. Yang, *Chem. Mater.*, 2011, **23**, 3676-3684.
24. N. Koike, T. Ikuno, T. Okubo and A. Shimojima, *Chem. Commun.*, 2013, **49**, 4998-5000.
25. J. Liu, S. Bai, H. Zhong, C. Li and Q. Yang, *J. Phys. Chem. C*, 2009, **114**, 953-961.
26. Y. Chen, P. Xu, H. Chen, Y. Li, W. Bu, Z. Shu, Y. Li, J. Zhang, L. Zhang, L. Pan, X. Cui, Z. Hua, J. Wang, L. Zhang and J. Shi, *Adv. Mater.*, 2013, **25**, 3100-3105.
27. S. Mura, J. Nicolas and P. Couvreur, *Nature Mater.*, 2013, **12**, 991-1003.
28. I. Slowing, B. G. Trewyn and V. S. Y. Lin, *J. Am. Chem. Soc.*, 2006, **128**, 14792-14793.
29. C.-H. Lee, L.-W. Lo, C.-Y. Mou and C.-S. Yang, *Adv. Funct. Mater.*, 2008, **18**, 3283-3292.
30. X. L. Huang, X. Teng, D. Chen, F. Q. Tang and J. Q. He, *Biomaterials*, 2010, **31**, 438-448.
31. H. Meng, S. Yang, Z. Li, T. Xia, J. Chen, Z. Ji, H. Zhang, X. Wang, S. Lin, C. Huang, Z. H. Zhou, J. I. Zink and A. E. Nel, *ACS Nano*, 2011, **5**, 4434-4447.
32. Y. Gao, Y. Chen, X. Ji, X. He, Q. Yin, Z. Zhang, J. Shi and Y. Li, *ACS Nano*, 2011, **5**, 9788-9798.

APPENDIX: SUPPLEMENTARY INFORMATION

I- EXPERIMENTAL SECTION

Materials. Tetraethoxysilane (TEOS), cetyltrimethylammonium bromide (CTAB), sodium hydroxide, doxorubicin hydrochloride, and ammonium nitrate were purchased from Sigma-Aldrich. Absolute ethanol was purchased from Fisher Chemicals. Hydrochloric acid was purchased from Anal. R. Norma Pure. 1,2-bis(triethoxysilyl)ethylene and bis(3-triethoxysilylpropyl)disulfide were purchased from ABCR.

Methods. Dynamic light scattering analyses were performed using a Malvern Zetasizer nano ZS (ZEN 3600) instrument. ^{29}Si and ^{13}C CPMAS solid state NMR sequences were recorded with a VARIAN VNMRs300, using Q8MH8 and adamantane references respectively. TEM analysis performed on a JEOL 1200 EXII instrument. SEM and EDS analysis performed on a FEI Quanta FEG 200 instrument.

II- NANOMATERIALS SYNTHESSES AND CHARACTERIZATIONS

E PMO NPs. A mixture of CTAB (250 mg, $6.86 \cdot 10^{-1}$ mmol), distilled water (120 mL), and sodium hydroxide (875 μL , 2 M) was stirred at 80 °C for 50 min at 1000 rpm in a 250 mL three neck round bottom flask. Then, the stirring speed was enhanced to 1400 rpm and 1,4-bis(triethoxysilyl)ethylene (800 μL , 2.10 mmol) was added. The condensation process was conducted for 2 h. Afterwards, the solution was cooled to room temperature while stirring; fractions were gathered in propylene tubes and the NPs were collected by centrifugation during 15 min at 21000 rpm. The sample was then extracted twice with an alcoholic solution of ammonium nitrate (6 g.L $^{-1}$), and washed three times with ethanol, water, and ethanol. Each extraction involved a sonication step of 30 min at 50 °C; the collection was carried out in the same manner. The as-prepared material was dried for few h under vacuum. The sample was then dispersed in water (30 mL) in a propylene tube, sonicated 20 min, and allowed to sediment for 20 min. The supernatant containing the stable colloidal NPs was taken out, centrifuged 15 min at 21000 rpm and dried under vacuum few hours. Thanks to this process, 80 to 60% of the as-prepared extracted materials was collected, the best results being obtained for smaller NPs.

EDIS 90/10 MPMO NPs. A mixture of CTAB (250 mg, $6.86 \cdot 10^{-1}$ mmol), distilled water (120 mL), and sodium hydroxide (875 μL , 2 M) was stirred at 80 °C for 50 min at 1000 rpm in a 250 mL three neck round bottom flask. Then, the stirring speed was enhanced to 1400 rpm and 1,4-bis(triethoxysilyl)ethylene (900 μL , 2.34 mmol) was added, and followed by the bis(3-triethoxysilylpropyl)disulfide (100 μL , $2.0 \cdot 10^{-1}$ mmol). The condensation process was conducted for 2 h. Afterwards, the solution was cooled to room temperature while stirring; fractions were gathered in propylene tubes and the NPs were collected by centrifugation during 15 minutes at 21000 rpm. Extraction and the following steps were identical as those described for E PMO NPs.

EDIS 75/25 MPMO NPs. A mixture of CTAB (250 mg, 6.86×10^{-1} mmol), distilled water (120 mL), and sodium hydroxide (875 μ L, 2 M) was stirred at 80 °C for 50 minutes at 1000 rpm in a 250 mL three neck round bottom flask. Then, the stirring speed was enhanced to 1400 rpm and 1,4-bis(triethoxysilyl)ethylene (600 μ L, 1.58 mmol) was added, and followed by the bis(3-triethoxysilylpropyl)disulfide (200 μ L, 4.0×10^{-1} mmol). The condensation process was conducted for 2 h. Afterwards, the solution was cooled to room temperature while stirring; fractions were gathered in propylene tubes and the NPs were collected by centrifugation during 15 minutes at 21000 rpm. Extraction and the following steps were identical as those described for E PMO NPs.

EDIS 50/50 MPMO NPs. A mixture of CTAB (250 mg, 6.86×10^{-1} mmol), distilled water (120 mL), and sodium hydroxide (875 μ L, 2 M) was stirred at 80 °C for 50 minutes at 1000 rpm in a 250 mL three neck round bottom flask. Then, the stirring speed was enhanced to 1400 rpm and 1,4-bis(triethoxysilyl)ethylene (400 μ L, 2.34 mmol) was added, and followed by the bis(3-triethoxysilylpropyl)disulfide (400 μ L, 2.0×10^{-1} mmol). The condensation process was conducted for 2 h. Afterwards, the solution was cooled to room temperature while stirring; fractions were gathered in propylene tubes and the NPs were collected by centrifugation during 15 minutes at 21000 rpm. Extraction and the following steps were identical as those described for E PMO NPs.

DIS BS NPs. A mixture of cetyltrimethylammonium bromide (CTAB, 640 mg, 1.76 mmol), distilled water (100 mL), ethanol (40 mL) and sodium hydroxide (NaOH, 640 μ L (2 M)) was stirred at 80°C for 50 min at 1000 rpm in a 250 mL three neck round bottom flask. Then, the stirring speed was enhanced to 1400 rpm and bis(3-triethoxysilylpropyl)disulfide (2400 μ L, 4.8 mmol) was added. The condensation process was conducted for 2 h. Afterwards, the solution was cooled to room temperature while stirring; fractions were gathered in propylene tubes and the NPs were collected by centrifugation during 15 min at 21000 rpm. Extraction and the following steps were identical as those described for E PMO NPs.

Sample	E PMO	EDIS 90/10	EDIS 75/25	EDIS 50/50	DIS BS
E volume (μ L)	800	900	600	400	0
DIS volume (μ L)	0	100	200	400	2400
Total volume (μ L)	800	1000	800	800	2400

Table S1. Volume of the E and DIS precursors in the nanomaterial syntheses.

Biodegradability studies. A mixture of NPs (1.5 mg), PBS (500 μ L), and glutathione (3 μ L or 50 μ L) was stirred two days at 37°C in an eppendorf tube. Then, aliquots were taken directly to perform the TEM and DLS analyses.

DOX loading of the NPs in neutral conditions. A mixture of NPs (10 mg), DOX (3.2 mg), and deionized water (1 mL) was prepared in an eppendorf tube, sonicated 5 min in a bath at 45°C, and stirred overnight at 25°C. Then, the NPs were collected by centrifugation during 5 min at 10000 rpm. The sample was washed three times with water, and dried for few h under vacuum. The loading and washing solution supernatants were kept to determine the DOX payloads.

DOX loading of the NPs in acidic conditions. A mixture of NPs (10 mg), DOX (3.2 mg), and deionized water (1 mL) was prepared in an eppendorf tube, sonicated 5 min in a bath at 45°C, and 30 μ L of hydrochloric acid were added to reach pH 5.5. Then, the solution was stirred overnight at 25°C. The solution was neutralized with aliquots of sodium hydroxide and stirred for 30 minutes. Finally, the NPs were collected by centrifugation during 5 min at 10000 rpm. The sample was washed three times with water, and dried for few hours under vacuum. The loading and washing solution supernatants were kept to determine the DOX payloads.

PI loading of the NPs. A mixture of NPs (10 mg), PI (2 mg), and deionized water (1 mL) was prepared in an eppendorf tube, sonicated 5 min in a bath at 45°C, and stirred overnight at 25°C. Then, the NPs were collected by centrifugation during 5 min at 10000 rpm. The sample was washed four times with water, and dried for few h under vacuum. The loading and washing solution supernatants were kept to determine the PI payloads.

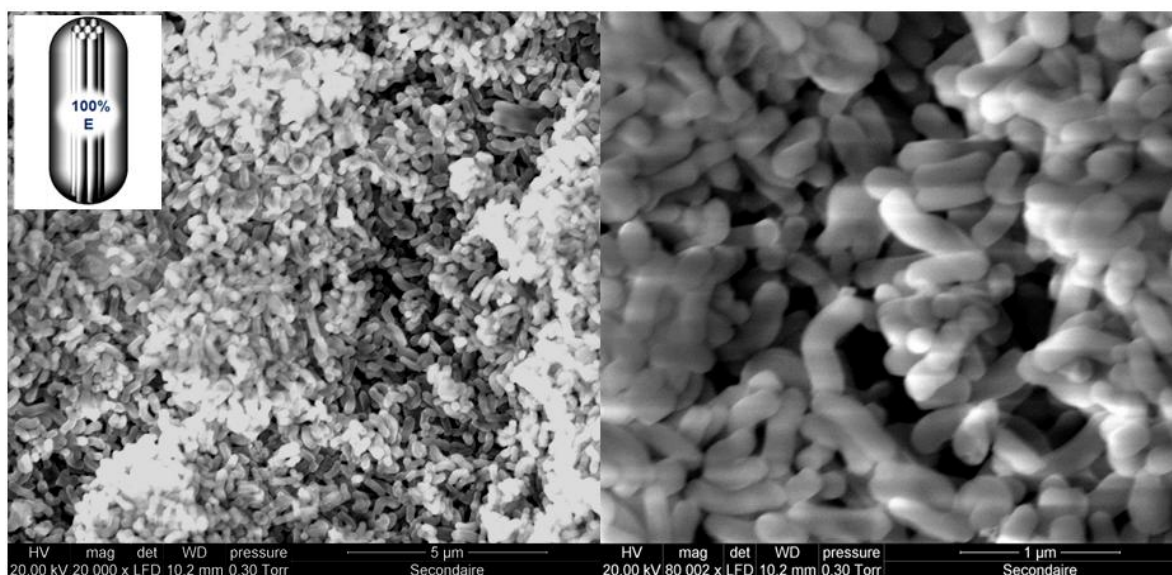


Figure S1. SEM micrographs displaying the uniform shape and size monodispersity of E PMO nanorods.

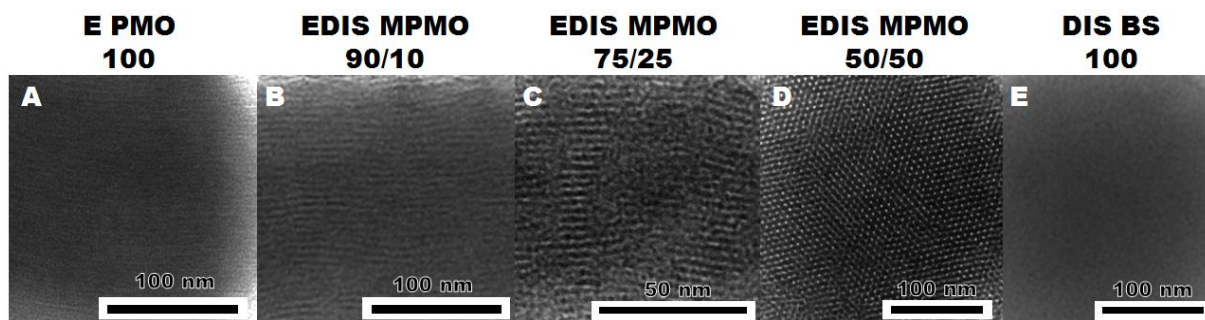


Figure S2. High magnification TEM images of E PMO, EDIS MPMO constituted of $R_{E/DIS}$ of 90/10, 75/25, 50/50, and DIS BS NPs (A, B, C, D and E respectively), demonstrating the crystal-like structure of PMO NPs.

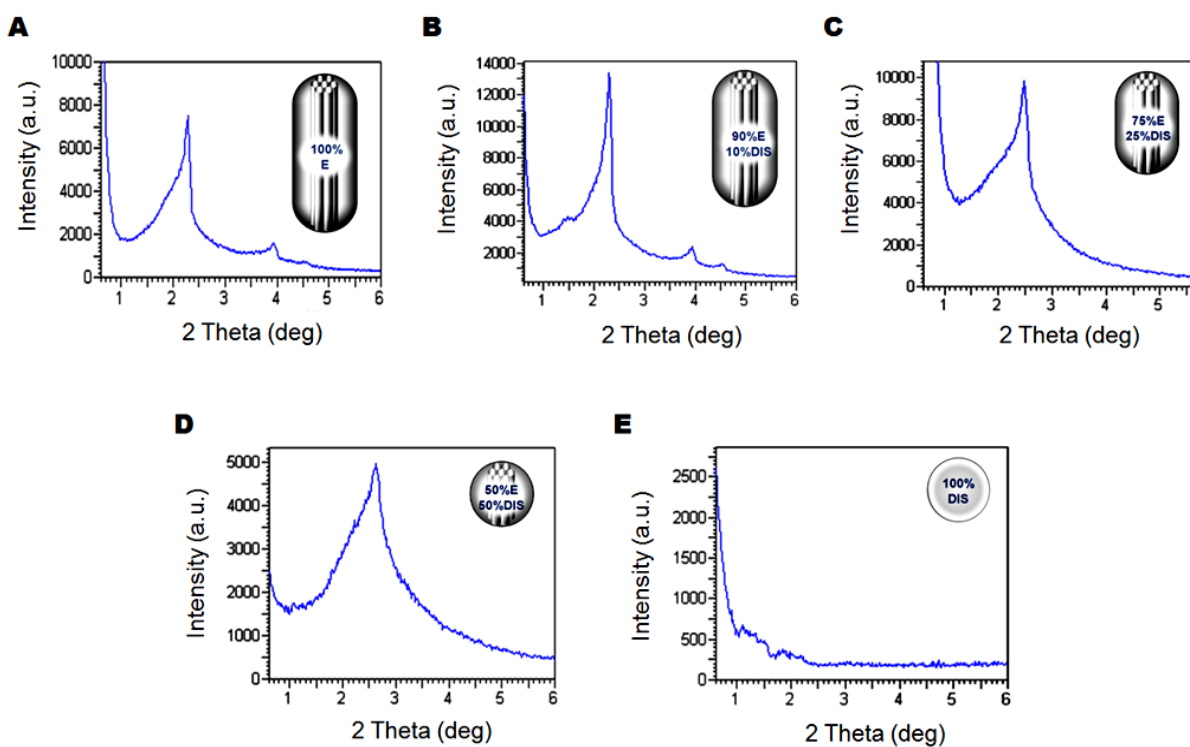


Figure S3. X-ray diffraction patterns of E PMO, EDIS MPMO constituted of $R_{E/DIS}$ of 90/10, 75/25, 50/50, and DIS BS NPs (A, B, C, D and E respectively), confirming the crystal-like structure of PMO NPs.

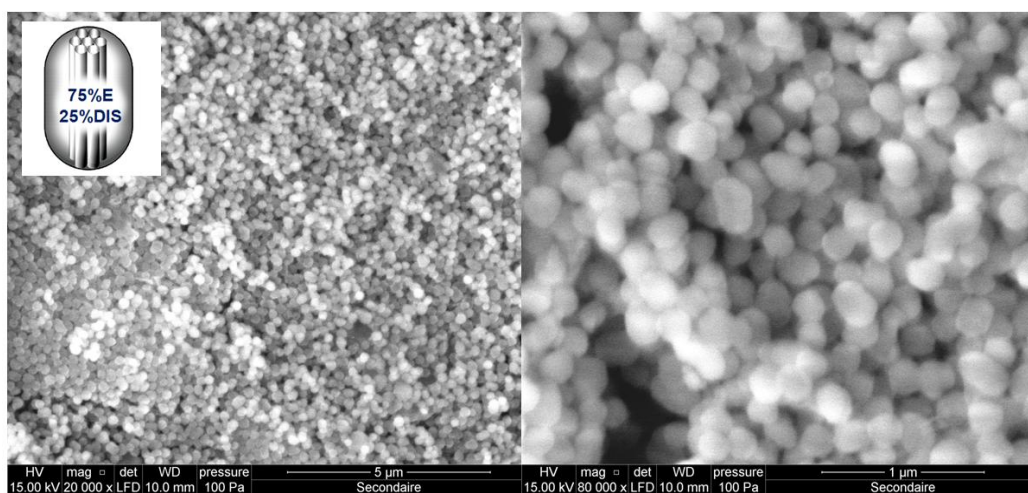


Figure S4. SEM micrographs displaying the monodispersity of EDIS PMO nanospheres.

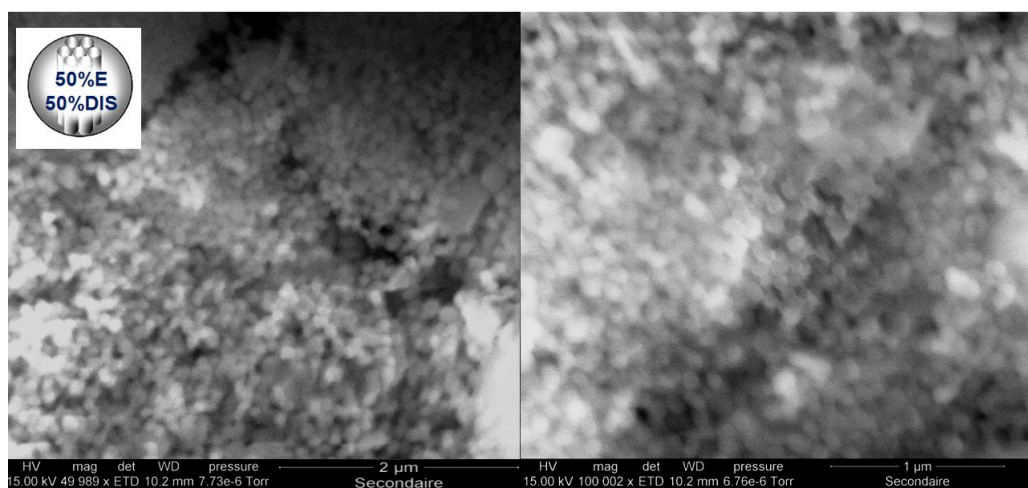


Figure S5. SEM micrographs displaying the monodispersity of EDIS PMO nanospheres.

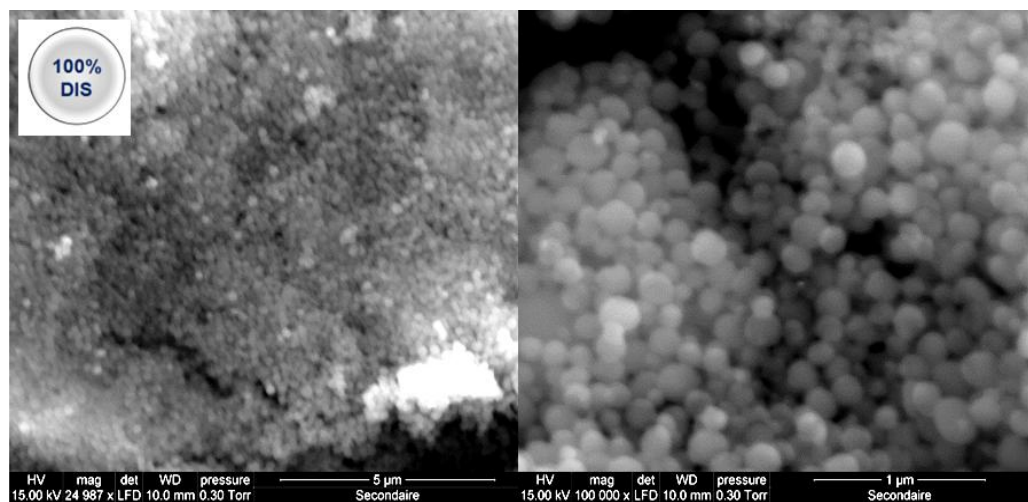


Figure S6. SEM micrographs displaying the monodispersity of DIS BS NPs.

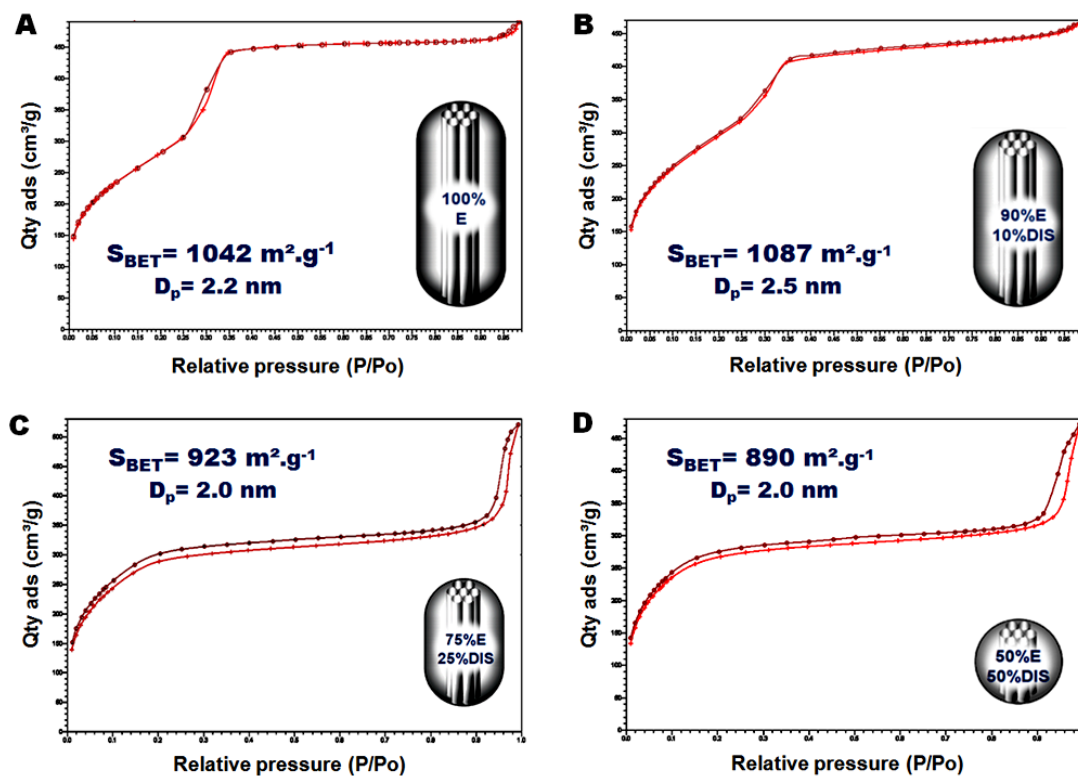


Figure S7. N_2 -adsorption-desorption isotherms of the E PMO (A) and EDIS 90/10, 75/25, 50/50 MPMO NPs (B, C, and D respectively), demonstrating the high surface areas of the compounds.

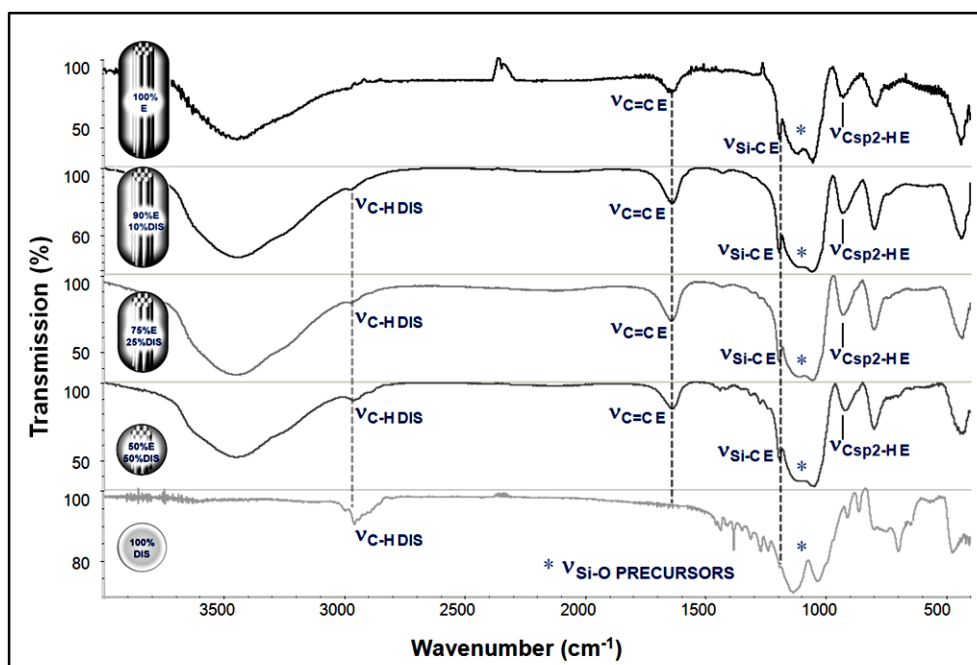


Figure S8. FTIR spectra comparison of E PMO, EDIS MPMO constituted of $R_{E/DIS}$ of 90/10, 75/25, 50/50, and DIS BS NPs (from up to down), consistent with the material compositions.

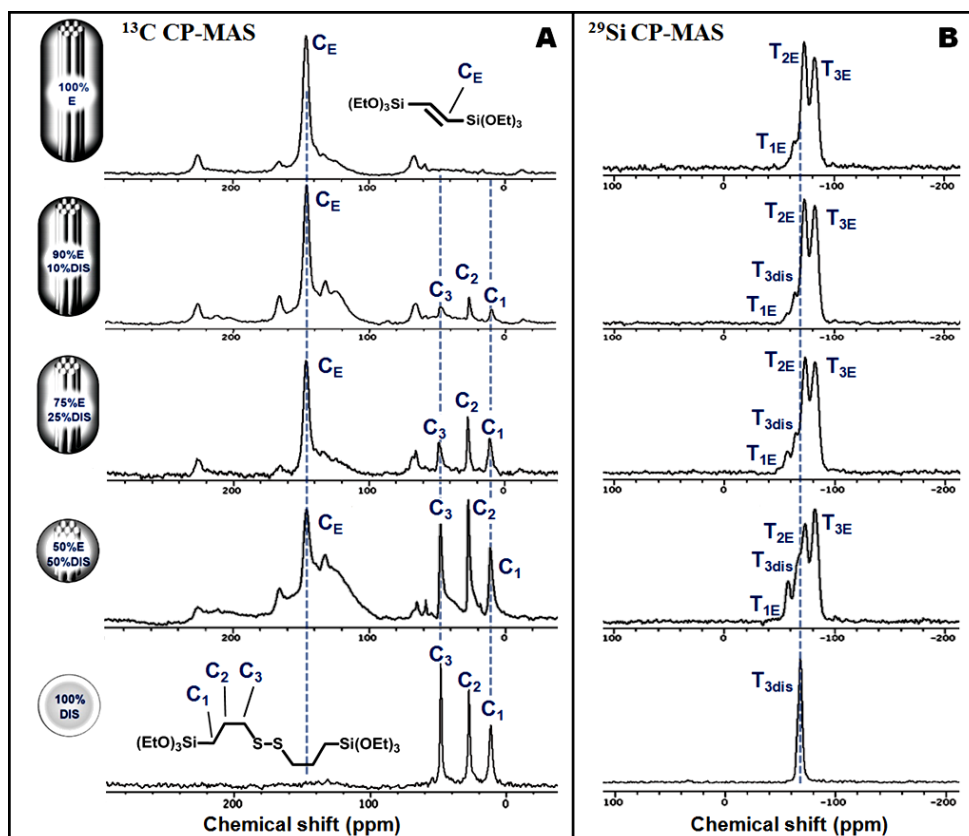


Figure S9. Solid state NMR CPMAS ^{13}C (A) and ^{29}Si (B) spectra comparison of E PMO, EDIS MPMO constituted of $R_{\text{E/DIS}}$ of 90/10, 75/25, 50/50, and DIS BS NPs (from up to down), consistent with the material compositions.

ELEMENTS	C	O	Si	S	TOTAL
E PMO	28.30	42.75	28.95	0.00	100.00
Std. deviation	1.43	1.05	1.40	0.00	
EDIS 90/10	29.70	40.90	29.30	0.10	100.00
Std. deviation	1.10	2.35	1.55	0.06	
EDIS 75/25	26.89	42.34	30.22	0.55	100.00
Std. deviation	0.66	1.07	0.48	0.09	
EDIS 50/50	28.54	38.08	32.43	0.95	100.00
Std. deviation	2.09	2.97	1.37	0.36	
DIS BS	48.04	27.59	22.52	1.84	100.00
Std. deviation	3.01	6.81	4.36	0.48	

Table S2. EDS elemental analysis of the E PMO, EDIS MPMO, and DIS BS NPs.

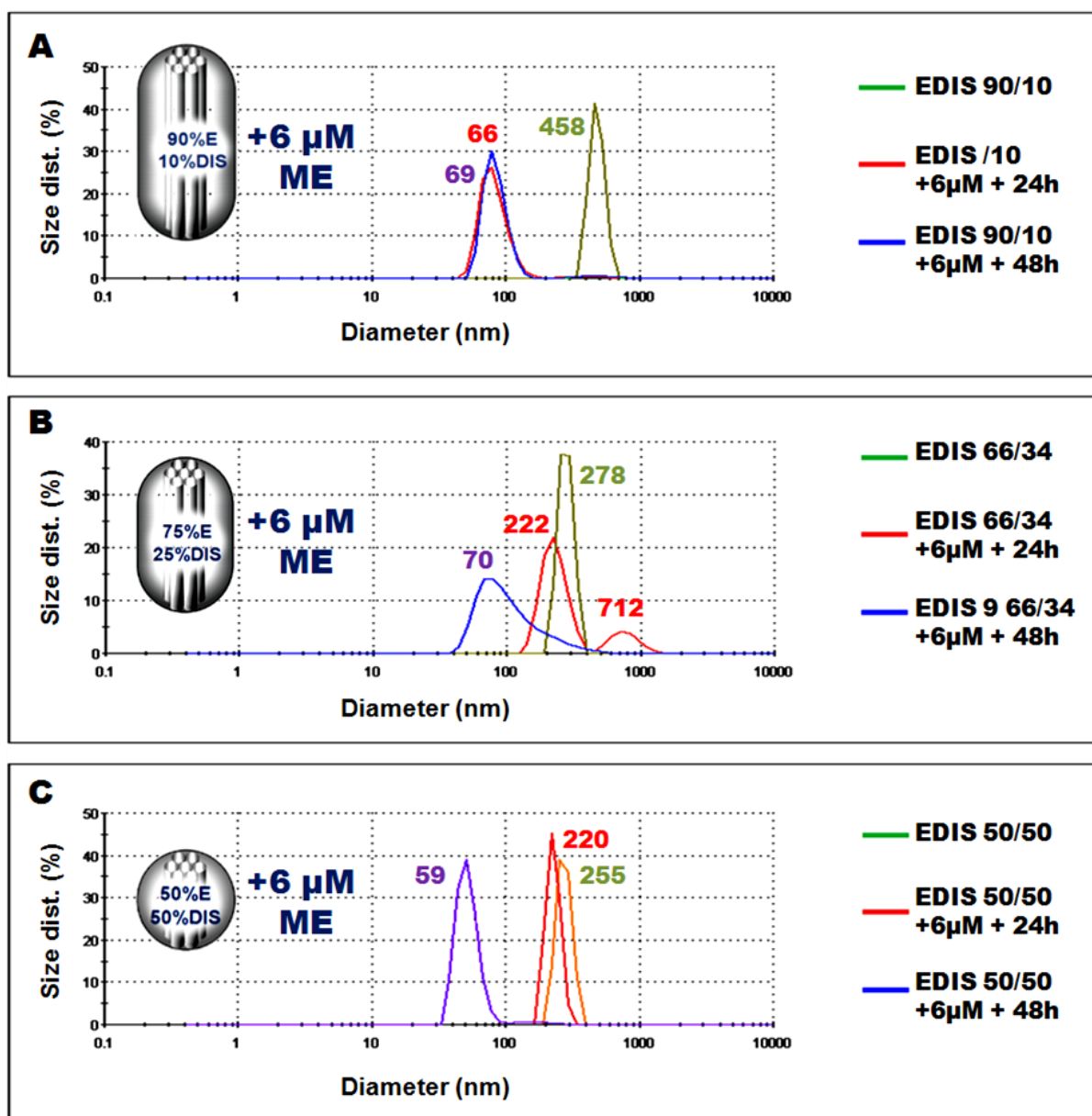


Figure S10. DLS of EDIS MPMO 90/10 (A), 75/25 (B), and 50/50 (C) in aqueous solution, before and after 24 or 48 h of simulated extracellular physiological conditions: 37°C with 6 μM of mercaptoethanol (ME).

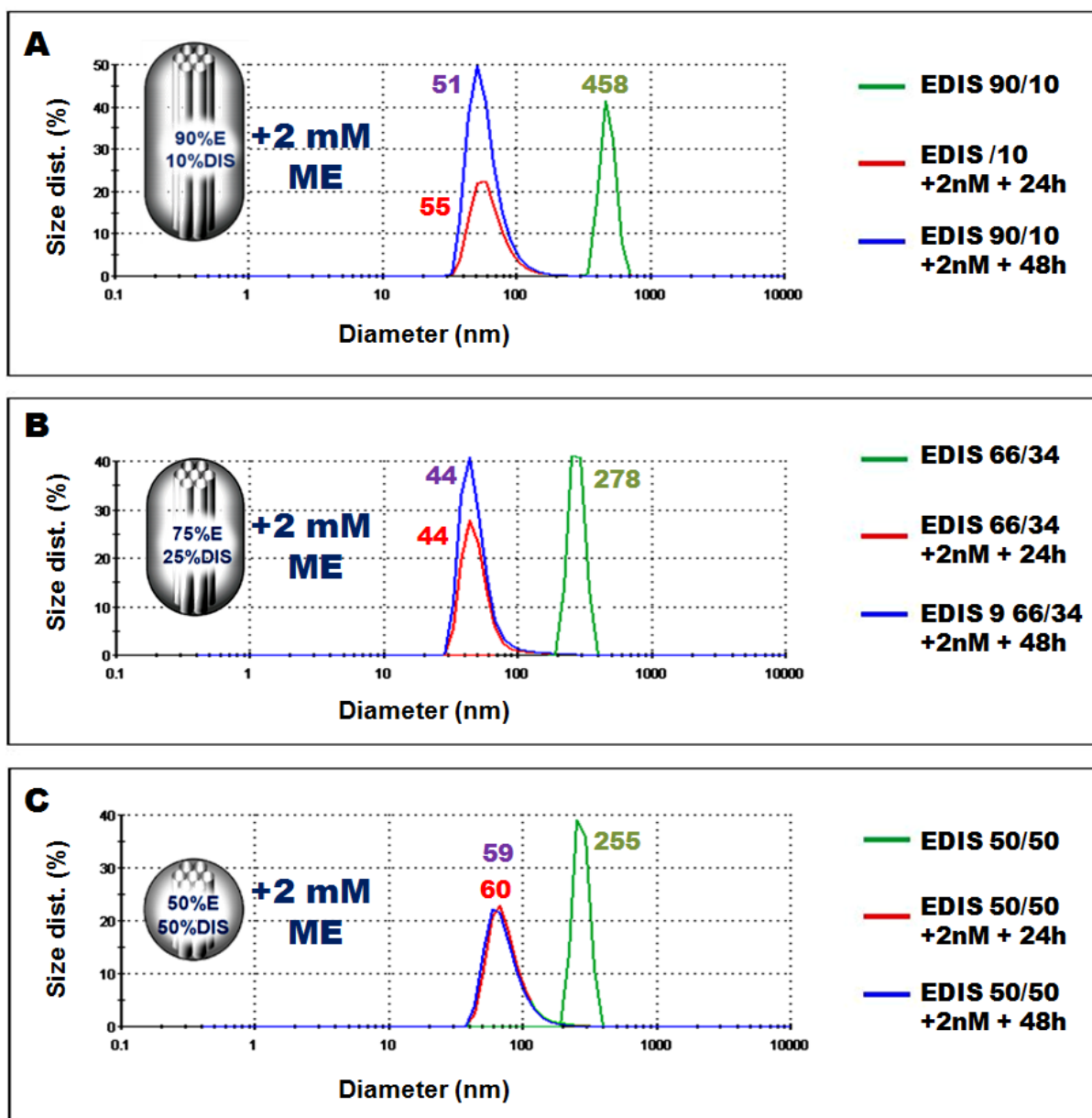


Figure S11. DLS of EDIS MPMO 90/10 (A), 75/25 (B), and 50/50 (C) in aqueous solution, before and after 24 or 48 h of simulated intracellular physiological conditions: 37°C with 2 mM of mercaptoethanol (ME).

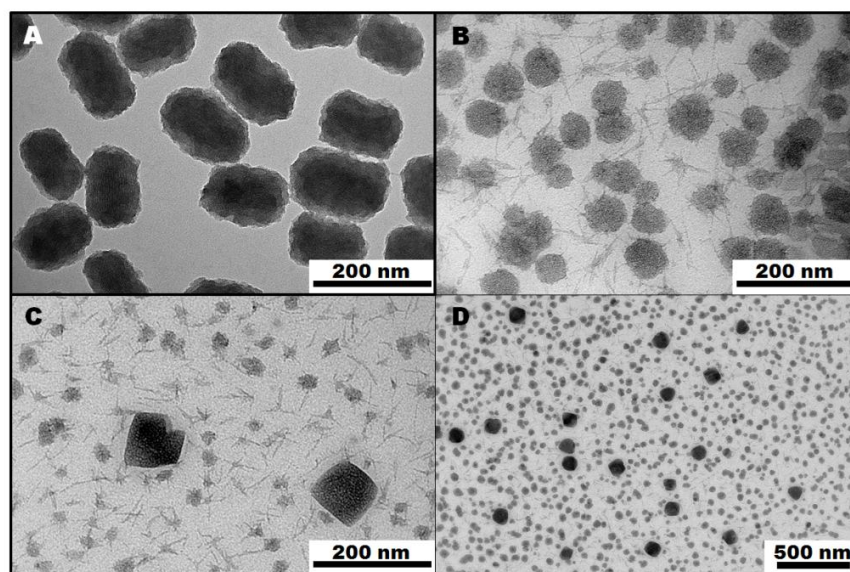


Figure S12. TEM images of EDIS 75/25 nanorods before (A) and after 48 h of degradability in simulated physiological conditions (B-D).

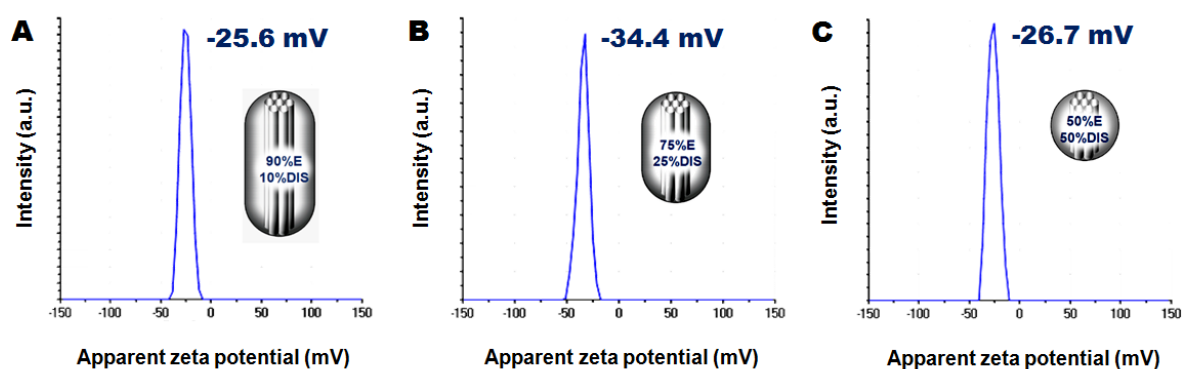


Figure S13. Zeta potential of EDIS of 90/10, 75/25, 50/50 NPs (A-C respectively).

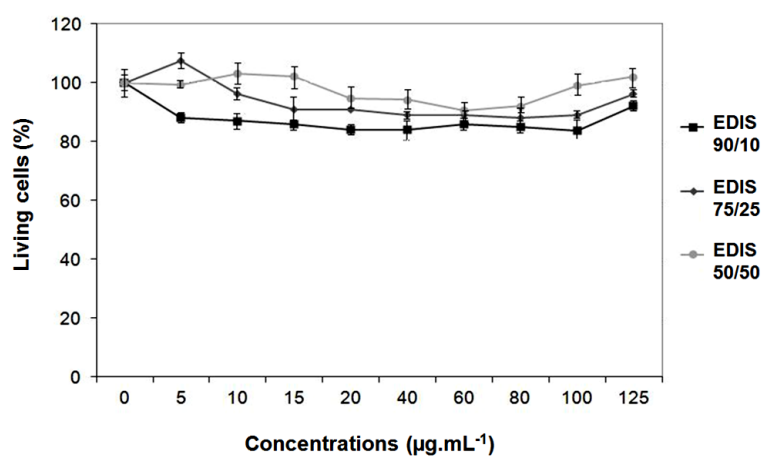


Figure S14. Cytotoxicity of EDIS PMO NPs in MCF-7 cells after 72 h of incubation.

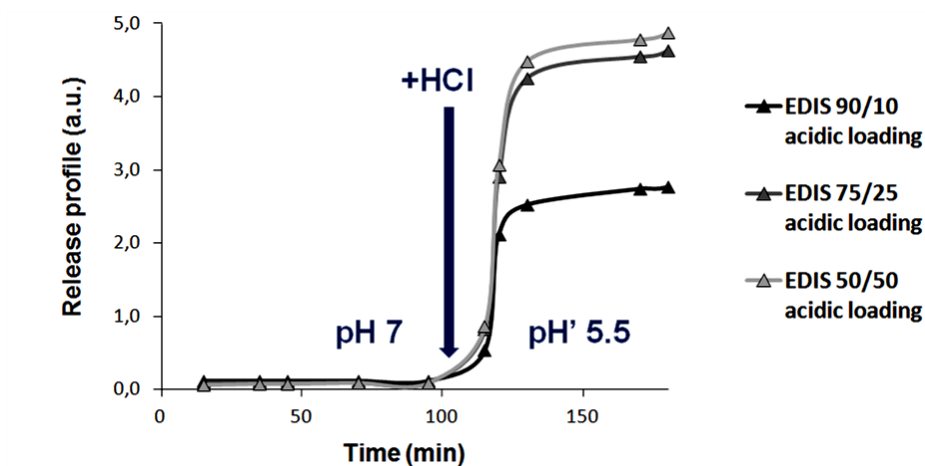


Figure S15. DOX release study in solution via pH change (from 7 to 5.5) with EDIS MPMO 90/10, 66:34, and 50/50 loaded in acidic conditions.

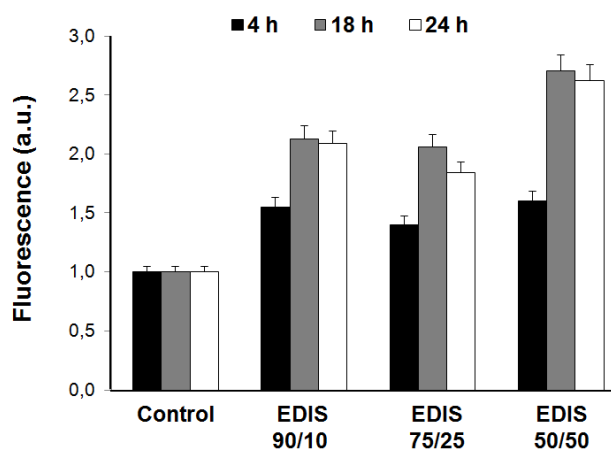


Figure S16. Flow cytometry study of EDIS MPMO NPs after 4, 18, and 24 h of incubation.

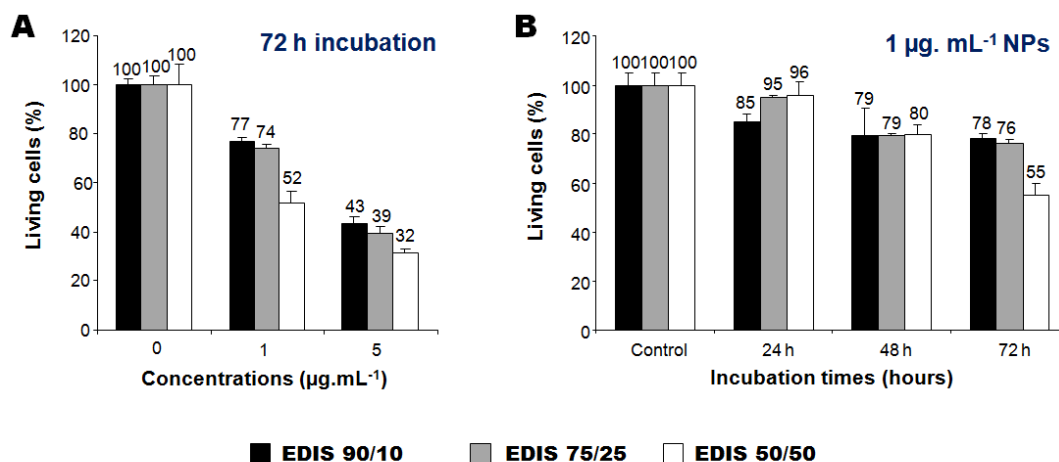
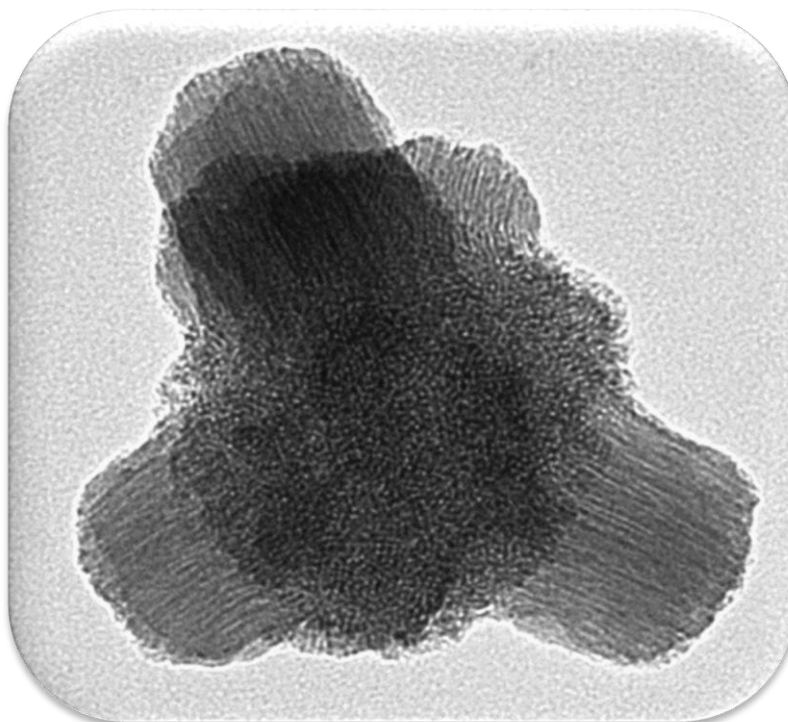


Figure S17. In-vitro cytotoxicity studies of EDIS NPs loaded with DOX in neutral conditions for a given time (72 h of incubation) and various NPs concentrations (A), or for a given concentration (1 µg.mL⁻¹) and various incubation times (B).

CHAPTER 8

B. Multipodal Hybrid Periodic Mesoporous Organosilica Nanoparticles with Crystal-Like Architectures



Abstract

Herein we describe the design of hybrid multipodal periodic mesoporous organosilica (mp-PMO) nanoparticles with crystal-like architectures elaborated in a one-pot, two steps process, involving the preparation of a benzene-based (B) spherical PMO core followed by the formation of ethylene-based (E) rod-shaped PMO pods on these cores (BE compounds). These nanomaterials possess a hierarchical organization, with $P6mm$ -mesostructured hexagonally-shaped E pods around B PMO cores periodically organized at the molecular scale, as well as very high surface areas of about 1500 m.g^{-1} . Furthermore, the synthetic process was extended to the growth of ethylene/disulfide-based PMO pods around B cores, which opens the way for versatile site-controlled functionalization of these hybrid organic-inorganic porous nanostructures for various applications.

Introduction

The design of morphological and structural complexity at the nanoscale is one of the major challenges of nanotechnology to endeavor the mimic of the highly-functional nanobjects observed in nature. Indeed, the size, shape, structure, composition, and surface functionalization of nanomaterials directly affect their optical, physico-chemical, and electrical properties.^[1-3] The control of the porosity and structure of nanomaterials has launched new areas of research in nanomedicine and catalysis.^[4, 5] Nanoparticles (NPs) with high morphological complexity have been obtained as multipodal colloidal silica clusters,^[6-8] tetrapod-shaped CdSe and CdTe NPs,^[9, 10] tri- tetra- and tree-like multipodal GaP NPs,^[11] via epitaxial connection of branched heretofore nanostructures,^[12] and various kinds of anisotropic nanoassemblies from NPs building block approaches.^[13] Multicompartment nanomaterials such as micelles obtained from block terpolymer,^[14] lipid-protein liquid-crystalline NPs,^[15] and self-assembled block copolymer were elaborated.^[16] Of particular interest is the design of multicompartment multipodal mesoporous silica nanoparticles (MSN) reported by Wiesner and coworkers in 2013 via the epitaxial growth of silica pods of 2D-hexagonal structure on silica cores of cubic porosity.^[17]

Periodic mesoporous organosilica (PMO) were first introduced independently by three research groups in 1999,^[18-20] and are constructed solely from bridged organoalkoxysilane precursors so as to maximize the organic content of the material.^[21] The controlled synthesis of PMO NPs, which constitute a valuable alternative to MSN, has recently been achieved by various groups but is still in its infancy.^[22-25] Alike MSN, macro- and nano-scaled PMO are attracting much attention due to their wide applicability arising from the versatility of organic moieties that could be periodically organized within porous frameworks, their controllable surface functionalization, and high surface areas.^[23, 26]

In this study we describe the design of hybrid multipodal PMO (mp-PMO) nanoparticles with crystal-like architectures NPs elaborated in a one-pot two steps process, involving the condensation of a benzene-based (B) spherical PMO core followed by the condensation of ethylene-based (E) rod-shaped PMO pods on these cores (BE NPs). The mp-PMO nanomaterial morphology and composition were fully characterized via versatile techniques revealing the crystallinity of the B and E compartments, the meso- and molecular organic periodicity, as well as very high surface areas of up to 1500 m.g⁻¹. Furthermore, the synthetic process was extended to the growth of ethylene-disulfide-based PMO pods on the B cores.

Results and discussion

The BE mp-PMO NPs were first prepared in a one-pot, two steps process. The sol-gel preparation was performed in an aqueous mixture of the cetyltrimethylammonium bromide (CTAB) template with sodium hydroxide catalyst at 80 °C. The addition of

bis(triethoxysilyl)benzene precursor was carefully controlled to afford B PMO nanospheres. After 50 minutes, E PMO nanorods were grown on the B cores upon addition of bis(triethoxysilyl)ethylene with an equimolar ratio. The reaction was conducted for an additional 70 minutes and the resulting BE mp-PMO were collected, and the surfactant was extracted (ESI). It is noteworthy that the reverse addition order (bis(triethoxysilyl)ethylene followed by bis(triethoxysilyl)benzene)) led to phase segregation.

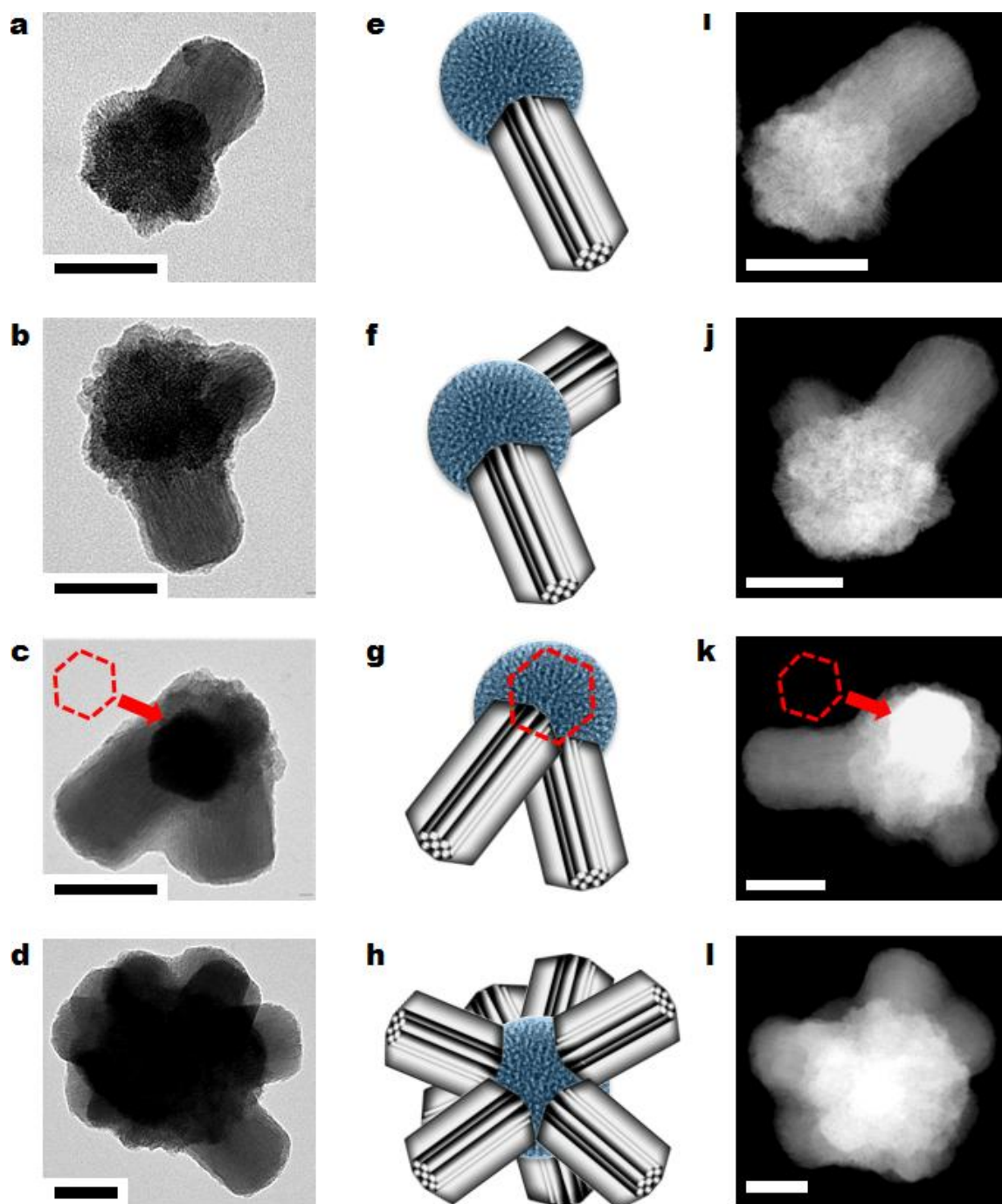


Figure 1. TEM micrographs of BE mp-PMO containing one to several pods (a-d), depicted by their schematic NPs representations (e-h). HR-STEM images BE mp-PMO NPs containing one to several pods (i-l). The red hexagons (c,k) highlight the morphology of the E PMO pods. Scale bars: 100 nm.

The morphology of the mp-PMO NPs was then characterized. Transmission electron microscopy (TEM) revealed astonishing BE mp-PMO NPs composed of one to several pods (see Fig. 1a-d, and NPs representations in Fig. 1e-h). The B PMO cores were spherical particles of 130 ± 20 nm, whereas the E PMO pods were 100 to 150 nm nanorods. High resolution scanning transmission electron microscopy (HR-STEM) imaging displayed similar conclusions as well as the expected composition-related contrast between the B core and the E pods (Fig. 1i-l). This is especially apparent in Figure 1i where the B and E compartments have comparable diameters, but the higher carbon content of the benzene-based core induces a more pronounced contrast. Besides, both TEM and HR-STEM revealed the hexagonal shape of the E PMO pods, as clearly seen when the pods were both aligned with the electron beam and situated behind the B cores (see Fig. 1c and k). Statistical analysis on nearly 180 NPs showed that the majority of the BE mp-PMO contained one or two pods (49 and 27 % respectively, see Fig. S1), the quarter left being composed of 3 to 8 pods (Fig. 1c-l).

The structure of the BE mp-PMO was then investigated. To further characterize the mp-PMO NPs, B PMO nanospheres and E PMO nanorods were prepared separately by the sol-gel processes (ESI). TEM micrographs of B and E showed, as expected, 130 nm spheres and few hundred nanometers rods, respectively (Fig. 2a and b), consistent with the multiple 100-150 nm pods of BE NPs (Fig. 2c). X-ray diffraction (XRD) patterns of BE mp-PMO, B PMO, and E PMO NPs at low angles displayed peaks at around 2° , corresponding to regular repetitions of mesopores (Fig. 2d). Broad peaks are observed in the case of B and BE NPs, which results from the radial organization of the pores (see below), while the E PMO nanorods display a 2D-hexagonal structure ($p6mm$) as shown by the intense narrow peak at 2.29° with the satellites at 3.94 and 4.55° which only appear for structures ordered on long distances. This corresponds to a d_{10} spacing of 38.8 \AA , thus to an interpore distance of 45 \AA . This pattern is also visible in the diffractogram of BE mp-PMOs (Fig. 2d and S2). In the TEM micrographs, a radial porosity is observed in the B cores (see Fig. 2a), while linear periodicity was readily visible on the E pods by fast Fourier transform (FFT, see Fig. S3) of part of the image. Moreover, a molecular-scale periodicity, first reported by Inagaki *et al.* on micron-sized materials,^[27] was found in the wide angle (5 to 40°) XRD patterns of B and BE NPs, as demonstrated by the peaks at *ca* 11.74 , 23.55 and 35.47° corresponding to a lamellar repetition of the aromatic units with a d-spacing of 7.6 \AA (Fig. 2e). Conversely, there is no molecular order in the ethylene framework. From the N_2 adsorption-desorption isotherms, BET (Brunauer-Emmett-Teller) surface areas of 979 , 1042 , $1413 \text{ m}^2\text{g}^{-1}$ were calculated for B PMO, E PMO, and BE mp-PMO, respectively, with BJH (Barrett-Joyner-Halenda) pore size distributions centered between 2.0 and 2.6 nm (Fig. S4-6). Thus, the BE mp-PMO were highly porous NPs with both meso- and molecular-scale periodicity.

The chemical composition of the NPs was then assessed by various techniques. First, the comparison of the solid state nuclear magnetic resonance (NMR) ^{13}C cross-polarization magic angle spinning (CPMAS) spectra of BE mp-PMO, B PMO, and E PMO nanomaterials demonstrated the presence of both the benzene ($\delta = 134 \text{ ppm}$) and the ethylene ($\delta = 145 \text{ ppm}$) moieties in BE NPs (Fig. 2f). Secondly, the ^{29}Si CPMAS spectra validated the formation of the siloxane network with the major proportion of T_2 and T_3 local environments (Fig. 2g). These observations were supported by the Fourier transform infrared (FTIR) spectrum of BE

NPs composed of the $\nu_{\text{C-H}}$ and $\nu_{\text{Si-C}}$ stretching vibration modes of the benzene group at 3067 and 1198 cm^{-1} respectively, and the out of plane aromatic $\delta_{\text{Csp}^2\text{-H}}$ bendings at 554 and 521 cm^{-1} , as well the ethylene modes: $\nu_{\text{Si-C}}$ and $\nu_{\text{C=C}}$ at 1193 and 1636 cm^{-1} , and the $\delta_{\text{Csp}^2\text{-H}}$ at 926 cm^{-1} (see Fig. S7 and 8). The $\nu_{\text{Si-O}}$ stretching modes of both organic fragments were also present from 1060 to 1120 cm^{-1} . Energy dispersive spectrometry validated the equimolar benzene-ethylene proportion of BE NPs when compared with B and E PMO NPs (Fig. S9, see Si/C ratios in Fig. S10). Besides, the efficiency of the CTAB template removal was correlated to the very low nitrogen content found in BE NPs (0.52 wt%, see Figure S10).

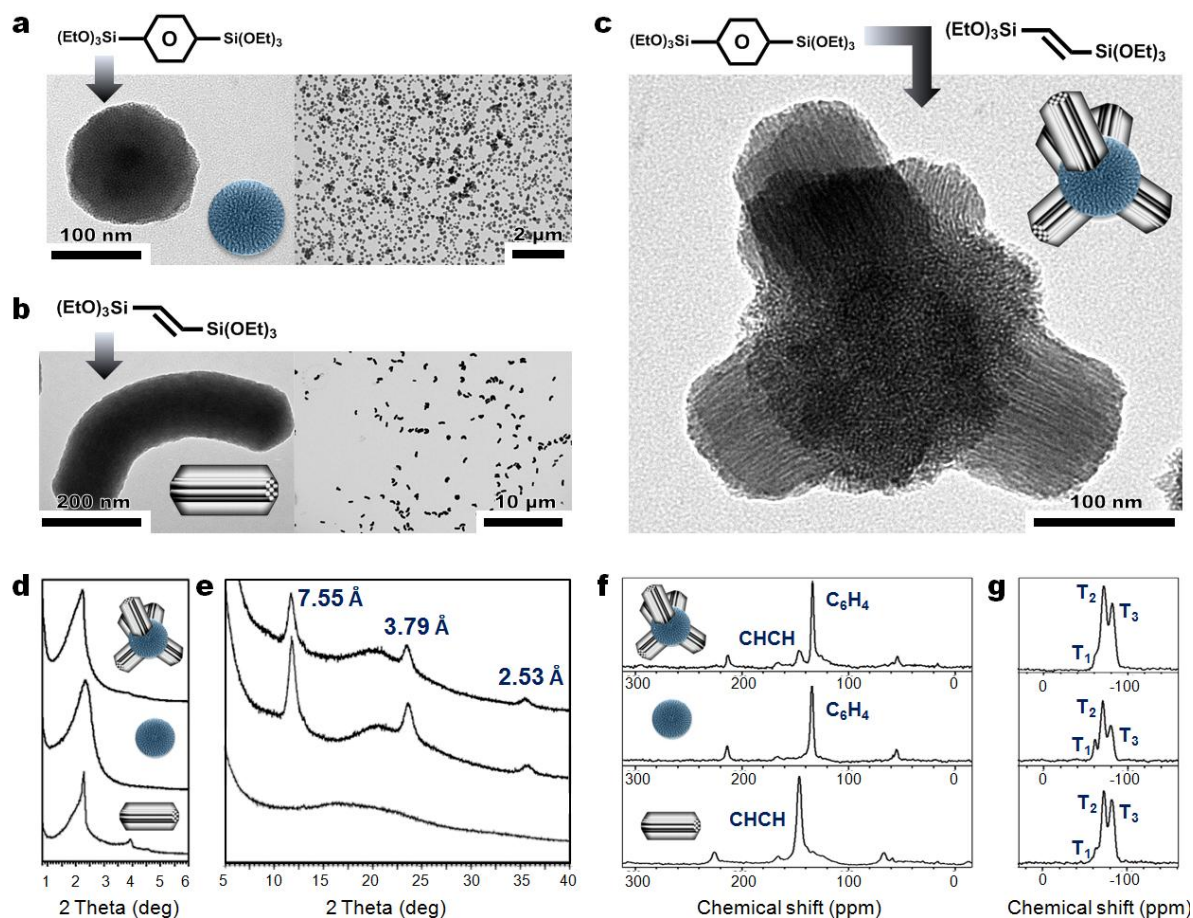


Figure 2. TEM micrographs of B PMO nanospheres and E PMO nanorods obtained solely from the bis(triethoxysilyl)benzene or bis(triethoxysilyl)ethylene precursors respectively (a and b). TEM images of multipodal BE NPs designed from the one-pot two steps condensation process (c). XRD patterns comparison of the BE mp-PMO NPs, B PMO, and E PMO, at low and wide angles (d and e respectively). Solid state NMR ^{13}C and ^{29}Si CPMAS spectra comparison of the BE mp-PMO NPs, B PMO, and E PMO (f and g respectively).

The versatility of the synthetic process was then assessed for the preparation of B PMO core ethylene-disulfide (EDIS)-based PMO pods (BEDIS) NPs. The design of such NPs involved identical reaction parameters to those used for BE mp-PMO; first the B core was prepared, and second, bis(3-triethoxysilylpropyl)disulfide was co-condensed with the bis(triethoxysilyl)ethylene precursor (see Fig. 3a). The ethylene over disulfide molar ratio

was of 2:1, favorable for the design of EDIS 130 nm nanorods in separated reactions (see chapter 8A).

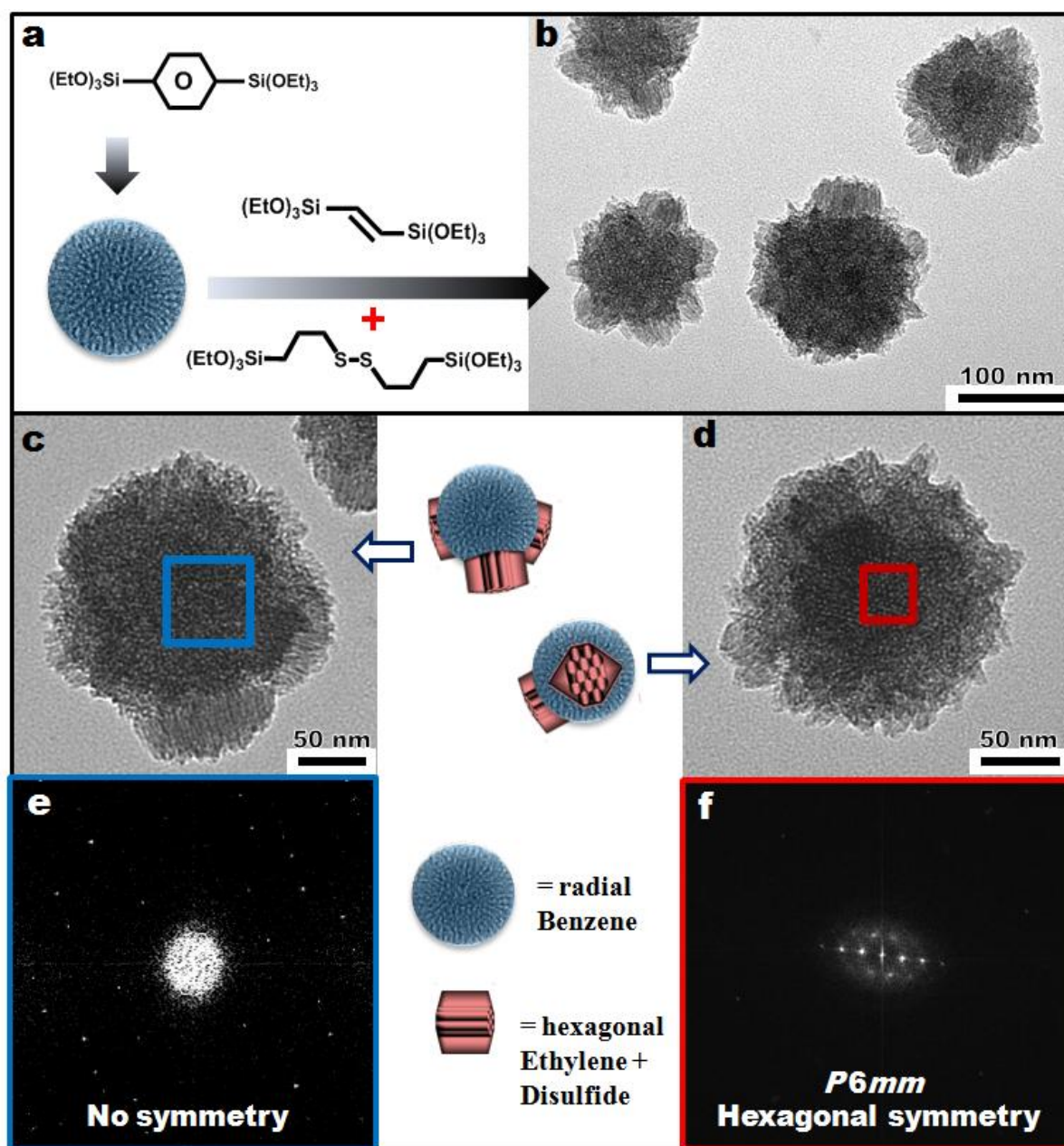


Figure 3. Formation of disulfide BEDIS mp-PMO NPs (a), and the subsequent TEM images of surfactant-free multipodal NPs (b). TEM micrographs (c-d) and the associated FFT (e-f) confirmed the expected absence of symmetry in the B core, along with the hexagonal symmetry of the mesoporous ethylene-disulfide pods.

Multipodal BEDIS NPs were readily visible by TEM micrographs, the B cores being decorated with one to six 50 nm EDIS pods (Fig. 3b-c). The hexagonal mesostructures of the pods were preserved as clearly seen by comparing the FFT transform of the image of the B core (Fig. 3c,e) with the E pods (Fig. 3d,f). The hexagonal array of the diffraction spots is

characteristic of long-distance ordered $P6mm$ structure (see Fig. 3f). Additionally, the BEDIS pods were extended to a length of 100 nm through a higher amount ethylene-disulfide mixture (ESI, see TEM in Fig. S11). N_2 -adsorption-desorption gave BET surface areas of nearly $1500 \text{ m}^2.\text{g}^{-1}$ and pore volumes up to $1.2 \text{ cm}^3.\text{g}^{-1}$ for both BEDIS mp-PMO NPs (Fig. S12 and S13), and the BJH pore size distribution of BEDIS remained in the order of 2.1 nm as for BE mp-PMO (see Fig. S14a and b respectively).

The mechanism of the multipods growth is currently under investigation. The examination of the growth of the B PMO core overtime was performed via TEM analyses. Aliquots were taken from a synthesis of B PMO every 10 minutes, and diluted in ice-cooled solutions to quench the condensation, and the NPs were analyzed by microscopy (ESI, see Fig. 4a, and S15). Interestingly, the size of the B PMO nanospheres only increased of a dozen nanometers from 10 to 50 minutes of preparation. However, TEM micrographs suggest a condensation-redissolution phenomenon overtime, cyclically leading to polygonal B PMO nanospheres of radial porosity (after 10 and 40 min Fig. 4a), and to rough-surfaced and sea-urchin-like NPs (see 20, 30 and 50 min Fig. 4a). A mechanism based on the growth of the bis(triethoxysilyl)benzene on the faces of polygonal B cores, and subsequent interstitial condensation is proposed (Fig. 4b). Consequently, the various B core shapes observed in the condensation process might favor or not the growth of E pods, particularly in the case of well-defined polygons. Besides, TEM of BE mp-PMO NPs also suggest that 150-200 nm B core are better-suited for well defined multiple E pods, while 100 nm B core often produce match-like nanostructures with a single E pod (see Fig. 1 and 2c). The influence of the core size on the ability to design complex structure was reported by S. Ravaine *et al.* for colloidal silica clusters.^[28]

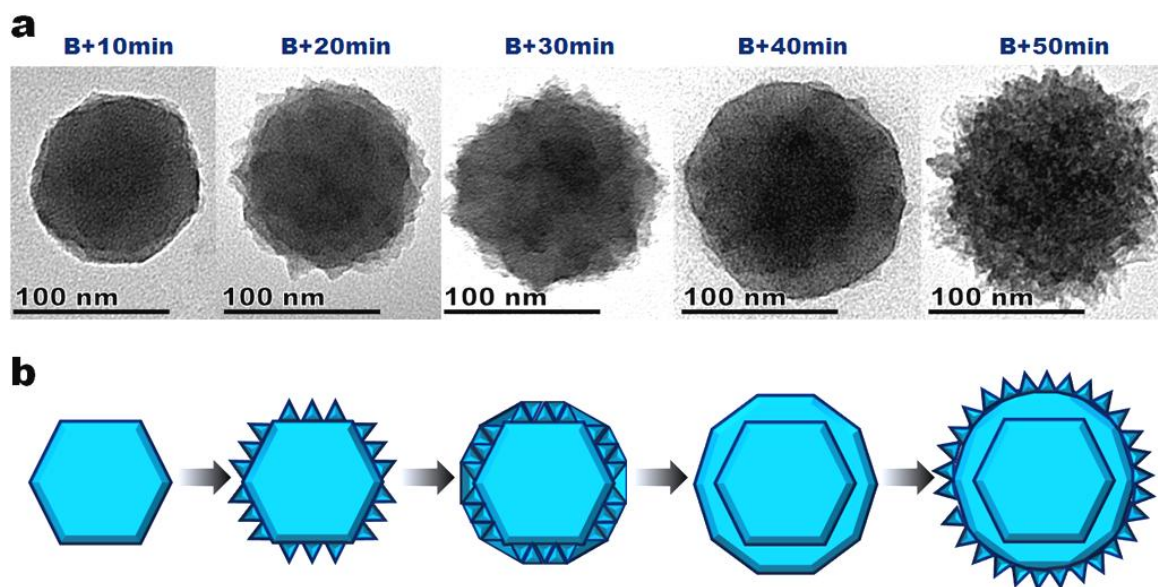


Figure 4. TEM images of the growth of B PMO nanospheres overtime (a), and the proposed growth mechanism (b). The TEM images are representative of hundreds of NPs.

Conclusion

In summary we have described original multipodal benzene core ethylene pod hybrid PMO NPs in a one-pot two steps process. The nanomaterial possessed a crystal-like organization with hexagonally-shaped E pods of $P6mm$ mesostructure, and B PMO cores periodically organized at the molecular scale. Furthermore, the procedure could be modified to design ethylene-disulfide-based PMO nanopods, which are envisioned to be biodegradable. The ability to garner various functions solely on the pods is very attractive since it would enable the morphological, structural, and functional complexities, thus paving the way to various applications. The introduction of one function in the B core, which could interact with a second function in the E pods is envisioned for catalytic, photonic and biomedical applications. Indeed, all mp-PMO NPs displayed very high surface areas and pore volumes of up to $1500 \text{ m}^2.\text{g}^{-1}$ and $1.20 \text{ cm}^3.\text{g}^{-1}$ which render them very attractive multicompartament nanocontainers. If selective adsorption could be tailored thanks to preferential drug(1)-benzene and drug(2)-ethylene interactions, the mp-PMO could be applied for multidrug delivery. Such an application could also be targeted via pro-drug strategies involving the post-functionalizations of the benzene or the ethylene groups of the mp-PMO framework. Different functionalizations in the B and E compartments might also be harnessed for sequential catalytic reaction via diffusion from the E pods to the B core. Finally, more complex mp-PMO nanostructures are under investigation with the variation of the B core size, as well as the combination of additional functions in this very promising nanoplatform.

REFERENCES

- [1] M. A. El-Sayed, *Accounts of Chemical Research* **2004**, 37, 326.
- [2] C. Burda, X. Chen, R. Narayanan, M. A. El-Sayed, *Chemical Reviews* **2005**, 105, 1025.
- [3] Y. Sun, Y. Xia, *Science* **2002**, 298, 2176.
- [4] O. C. Farokhzad, R. Langer, *ACS Nano* **2009**, 3, 16.
- [5] A. T. Bell, *Science* **2003**, 299, 1688.
- [6] A. Désert, C. Hubert, Z. Fu, L. Moulet, J. Majimel, P. Barboteau, A. Thill, M. Lansalot, E. Bourgeat-Lami, E. Duguet, S. Ravaine, *Angewandte Chemie International Edition* **2013**, 125, 11274.
- [7] A. Perro, E. Duguet, O. Lambert, J.-C. Taveau, E. Bourgeat-Lami, S. Ravaine, *Angewandte Chemie International Edition* **2009**, 48, 361.
- [8] E. Duguet, A. Desert, A. Perro, S. Ravaine, *Chemical Society Reviews* **2011**, 40, 941.
- [9] L. Manna, E. C. Scher, A. P. Alivisatos, *Journal of the American Chemical Society* **2000**, 122, 12700.
- [10] L. Manna, D. J. Milliron, A. Meisel, E. C. Scher, A. P. Alivisatos, *Nature Materials* **2003**, 2, 382.
- [11] K. A. Dick, K. Deppert, M. W. Larsson, T. Martensson, W. Seifert, L. R. Wallenberg, L. Samuelson, *Nature Materials* **2004**, 3, 380.
- [12] D. J. Milliron, S. M. Hughes, Y. Cui, L. Manna, J. Li, L.-W. Wang, A. Paul Alivisatos, *Nature* **2004**, 430, 190.
- [13] S. C. Glotzer, M. J. Solomon, *Nature Materials* **2007**, 6, 557.
- [14] Z. Li, E. Kesselman, Y. Talmon, M. A. Hillmyer, T. P. Lodge, *Science* **2004**, 306, 98.
- [15] B. Angelov, A. Angelova, S. K. Filippov, M. Drechsler, P. Štěpánek, S. Lesieur, *ACS Nano* **2014**.
- [16] H. Cui, Z. Chen, S. Zhong, K. L. Wooley, D. J. Pochan, *Science* **2007**, 317, 647.
- [17] T. Suteewong, H. Sai, R. Hovden, D. Muller, M. S. Bradbury, S. M. Gruner, U. Wiesner, *Science* **2013**, 340, 337.
- [18] S. Inagaki, S. Guan, Y. Fukushima, T. Ohsuna, O. Terasaki, *Journal of the American Chemical Society* **1999**, 121, 9611.
- [19] B. J. Melde, B. T. Holland, C. F. Blanford, A. Stein, *Chemistry of Materials* **1999**, 11, 3302.
- [20] T. Asefa, M. J. MacLachlan, N. Coombs, G. A. Ozin, *Nature* **1999**, 402, 867.
- [21] N. Mizoshita, T. Tani, S. Inagaki, *Chemical Society Reviews* **2011**, 40, 789.
- [22] E.-B. Cho, D. Kim, M. Jaroniec, *Microporous and Mesoporous Materials* **2009**, 120, 252.
- [23] B. Guan, Y. Cui, Z. Ren, Z.-a. Qiao, L. Wang, Y. Liu, Q. Huo, *Nanoscale* **2012**, 4, 6588.
- [24] J. Liu, H. Q. Yang, F. Kleitz, Z. G. Chen, T. Yang, E. Strounina, G. Q. Lu, S. Z. Qiao, *Advanced Functional Materials* **2012**, 22, 591.
- [25] H. Djojoputro, X. F. Zhou, S. Z. Qiao, L. Z. Wang, C. Z. Yu, G. Q. Lu, *Journal of the American Chemical Society* **2006**, 128, 6320.
- [26] W. Wang, J. E. Lofgreen, G. A. Ozin, *Small* **2010**, 6, 2634.
- [27] S. Inagaki, S. Guan, T. Ohsuna, O. Terasaki, *Nature* **2002**, 416, 304.
- [28] S. Reculosa, C. Mingotaud, E. Bourgeat-Lami, E. Duguet, S. Ravaine, *Nano Letters* **2004**, 4, 1677.

APPENDIX: SUPPLEMENTARY INFORMATION

I- EXPERIMENTAL SECTION

BE mp-PMO. A mixture of CTAB (250 mg, $6.86 \cdot 10^{-1}$ mmol), distilled water (120 mL), and sodium hydroxide (875 μ L, 2 M) was stirred at 80 °C for 50 minutes in a 250 mL three neck round bottom flask. First, 1,4-bis(triethoxysilyl)benzene (300 μ L, $7.54 \cdot 10^{-1}$ mmol) was added to the solution, and the condensation process was conducted for 50 minutes. Second, 1,2-bis(triethoxysilyl)ethylene (300 μ L, $7.87 \cdot 10^{-1}$ mmol) was added, and the reaction was led for an additional 70 minutes. The sample was then extracted twice with an alcoholic solution of ammonium nitrate (6 g.L⁻¹), and washed three times with ethanol, water, and ethanol. Each extraction involved a sonication step of 30 min at 50 °C; the collection was carried out in the same manner. The as-prepared material was dried under vacuum.

E PMO. A mixture of CTAB (250 mg, $6.86 \cdot 10^{-1}$ mmol), distilled water (120 mL), and sodium hydroxide (875 μ L, 2 M) was stirred at 80 °C for 50 min in a 250 mL three neck round bottom flask. 1,2-bis(triethoxysilyl)ethylene (300 μ L, $7.87 \cdot 10^{-1}$ mmol) was added to the solution, and the condensation process was conducted for 2 h. Then, the solution was cooled to room temperature while stirring; fractions were gathered in propylene tubes and the NPs were collected by centrifugation during 15 min at 21000 rpm. Extraction and the following steps were identical as those described for BE mp-PMO.

B PMO. A mixture of CTAB (250 mg, $6.86 \cdot 10^{-1}$ mmol), distilled water (120 mL), and sodium hydroxide (875 μ L, 2 M) was stirred at 80 °C for 50 minutes in a 250 mL three neck round bottom flask. 1,4-bis(triethoxysilyl)benzene (300 μ L, $7.54 \cdot 10^{-1}$ mmol) was added to the solution, and the condensation process was conducted for 2 h. Then, the solution was cooled to room temperature while stirring; fractions were gathered in propylene tubes and the NPs were collected by centrifugation during 15 min at 21000 rpm. Extraction and the following steps were identical as those described for BE mp-PMO.

BEDIS mp-PMO. A mixture of CTAB (250 mg, $6.86 \cdot 10^{-1}$ mmol), distilled water (120 mL), and sodium hydroxide (875 μ L, 2 M) was stirred at 80 °C for 50 minutes in a 250 mL three neck round bottom flask. First, 1,4-bis(triethoxysilyl)benzene (300 μ L, $7.54 \cdot 10^{-1}$ mmol) was added to the solution, and the condensation process was conducted for 50 minutes. Second, 1,2-bis(triethoxysilyl)ethylene (200 μ L, $4.72 \cdot 10^{-1}$ mmol) and bis(3-triethoxysilylpropyl)disulfide (100 μ L, $2.56 \cdot 10^{-1}$ mmol) were added, and the reaction was led for an additional 70 minutes. Then, the solution was cooled to room temperature while stirring; fractions were gathered in propylene tubes and the NPs were collected by centrifugation during 15 min at 21000 rpm. Extraction and the following steps were identical as those described for BE mp-PMO.

BEDIS mp-PMO with longer pods. The design of this NPs was identical to BEDIS mp-PMO with the exception of the following amounts: 1,2-bis(triethoxysilyl)ethylene (300 μ L, $7.87 \cdot 10^{-1}$ mmol) and bis(3-triethoxysilylpropyl)disulfide (100 μ L, $2.56 \cdot 10^{-1}$ mmol).

B PMO growth study. The B PMO reaction started, aliquots of one milliliter were taken every 10 minutes and added to eppendorf tubes filled with ice-cooled deionized water (1 mL). The samples were immediately centrifuged, washed twice with water, and dried under air. Then, the samples were analyzed by TEM.

II-NANOMATERIALS CHARACTERIZATIONS

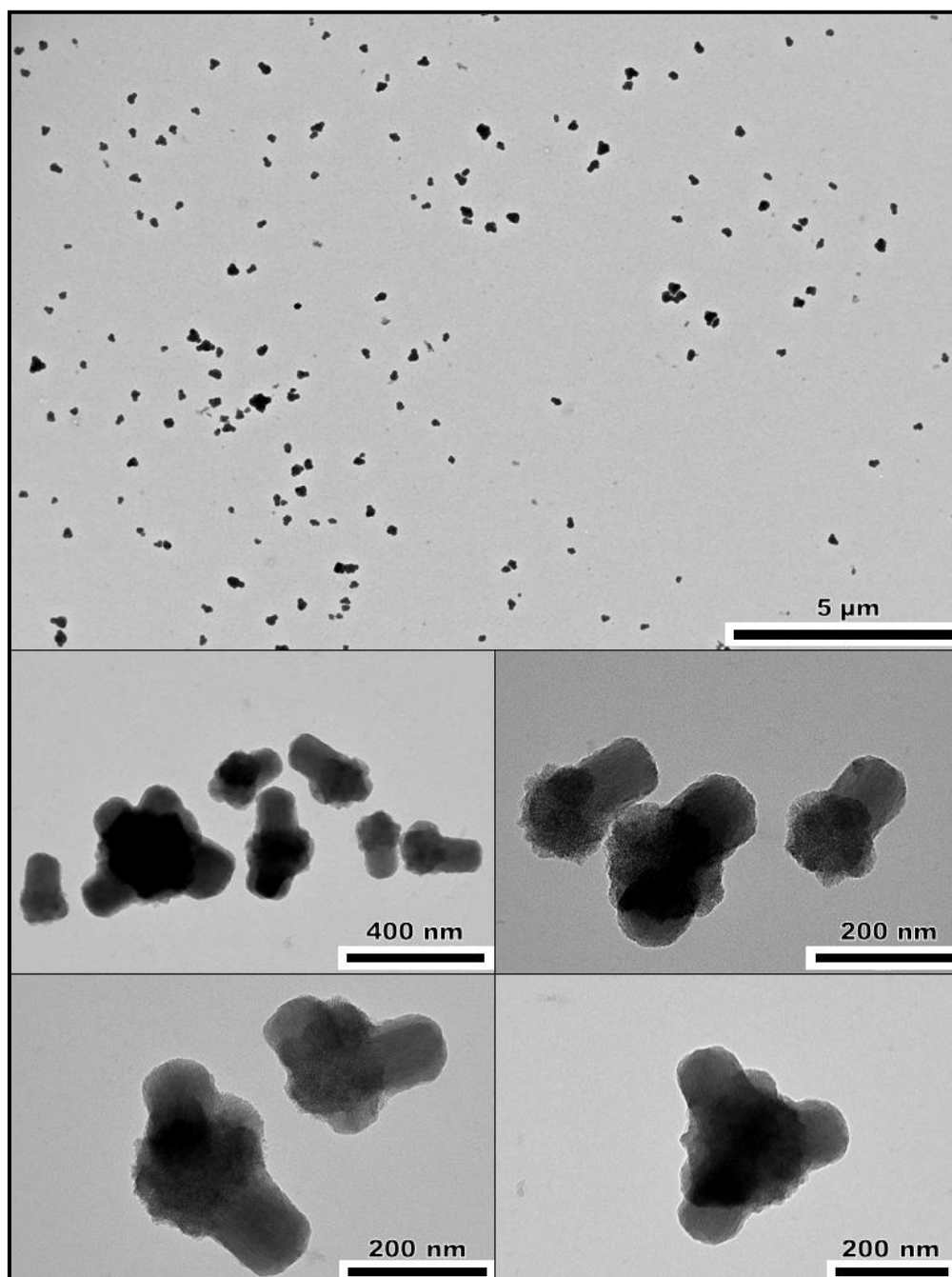


Figure S1. Additional TEM images of the BE mp-PMO NPs.

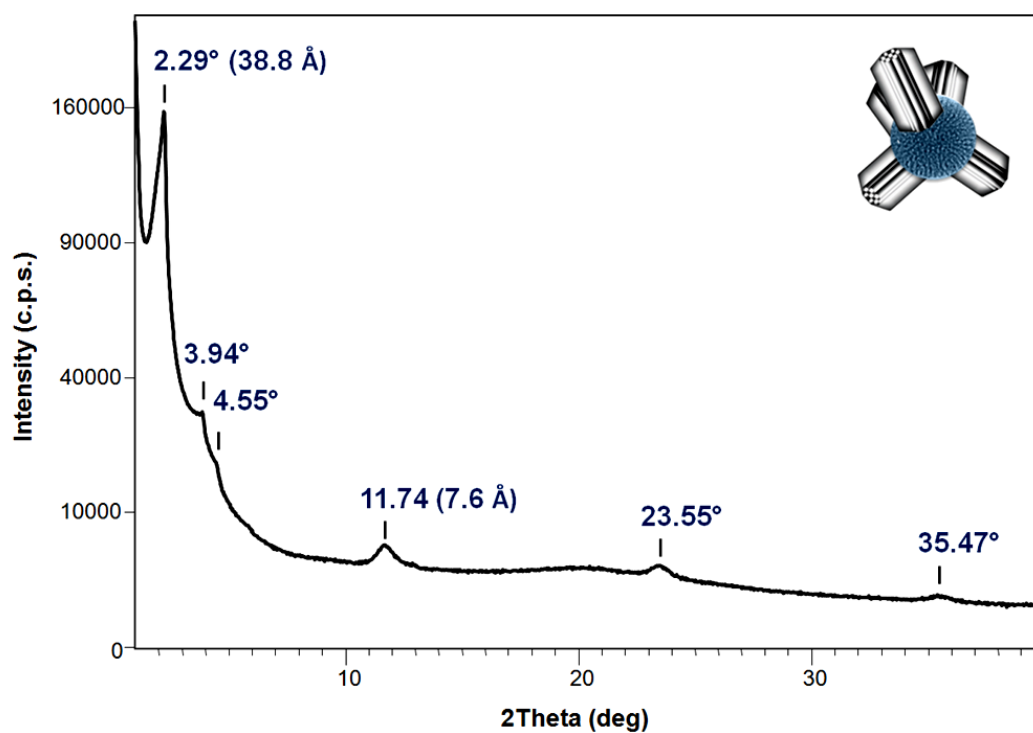


Figure S2. Additional TEM images of the BE mp-PMO NPs.

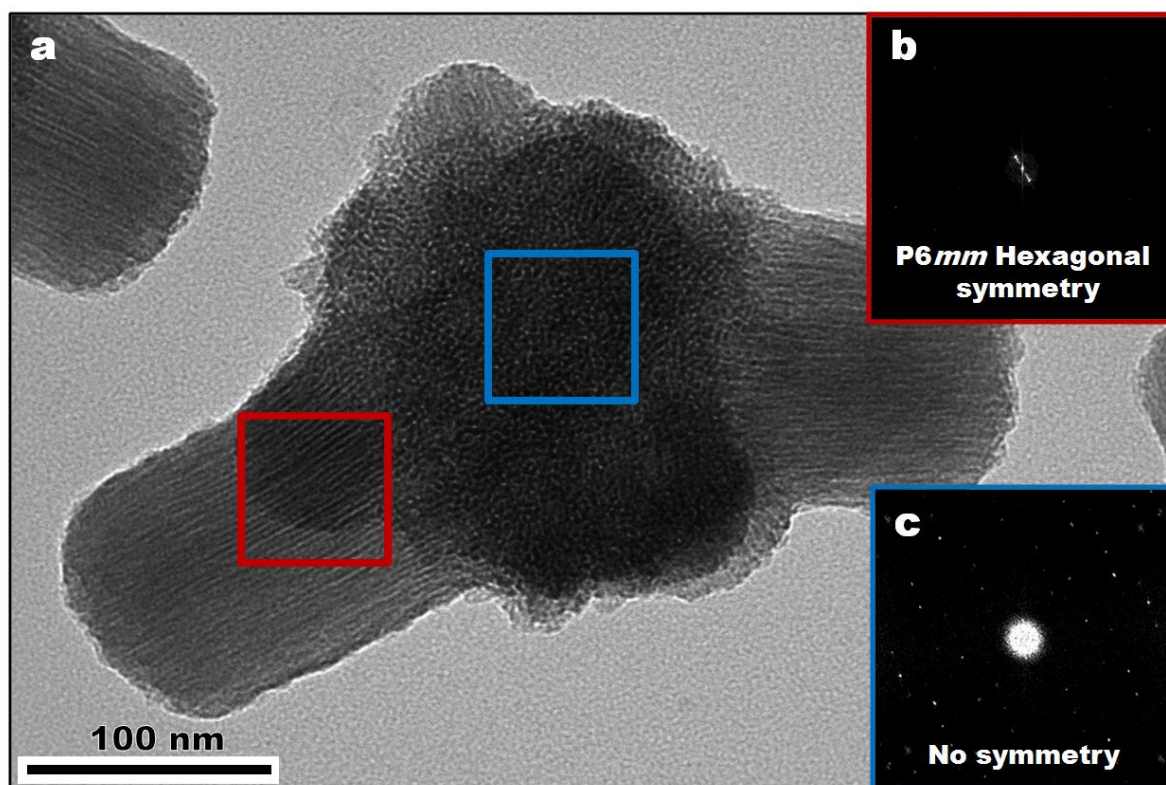


Figure S3. TEM micrograph of BE mp-PMO multipods (a) and the associated FFT calculations of the pod and core parts (b and c respectively).

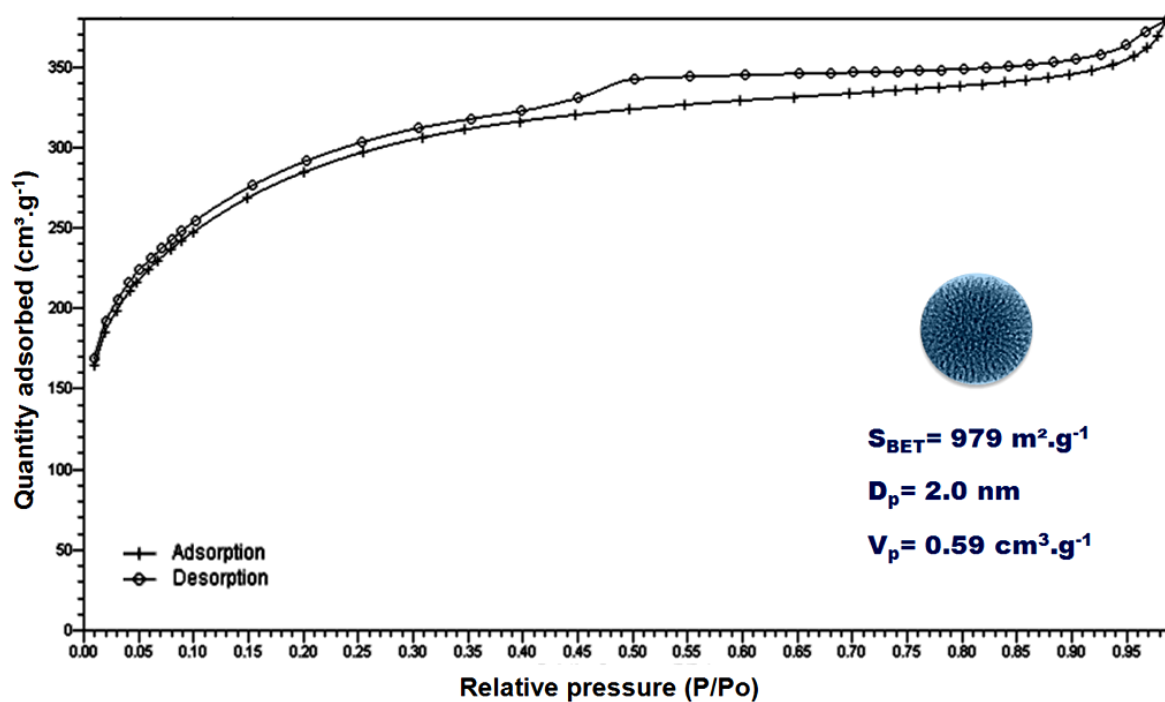


Figure S4. N_2 -adsorption-desorption isotherm of B PMO NPs.

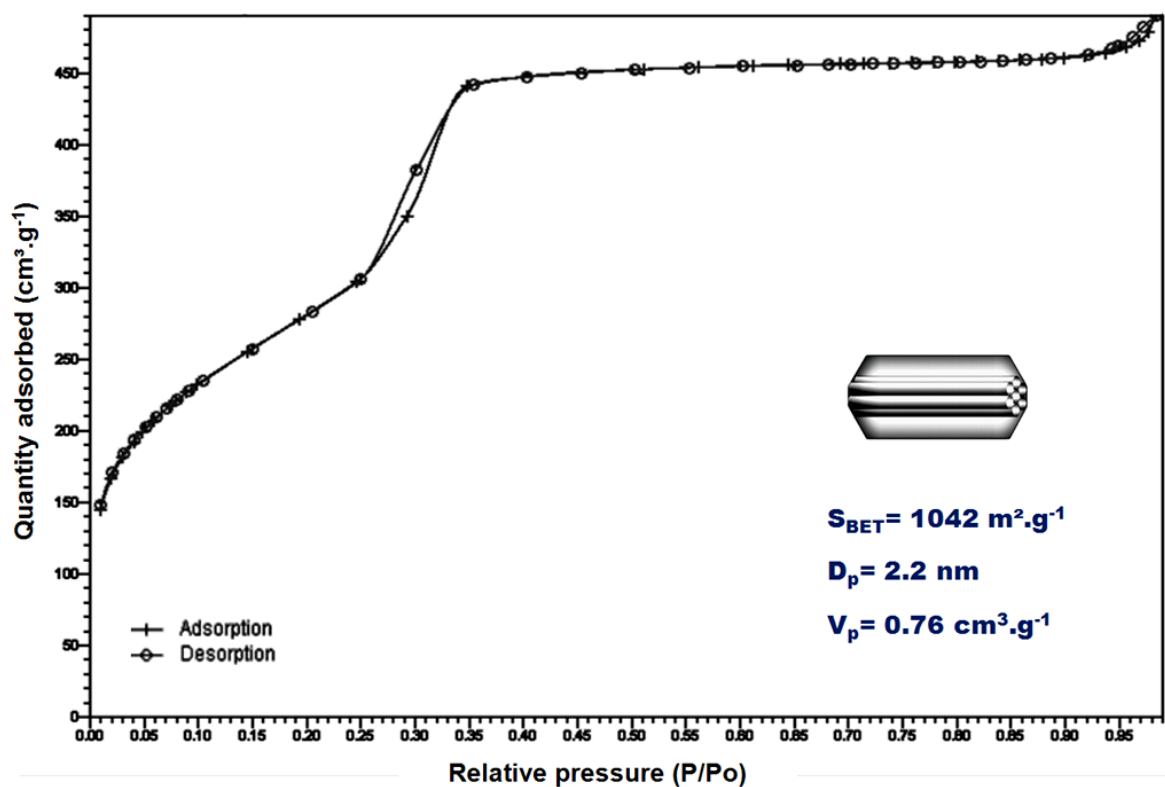


Figure S5. N_2 -adsorption-desorption isotherm of E PMO NPs.

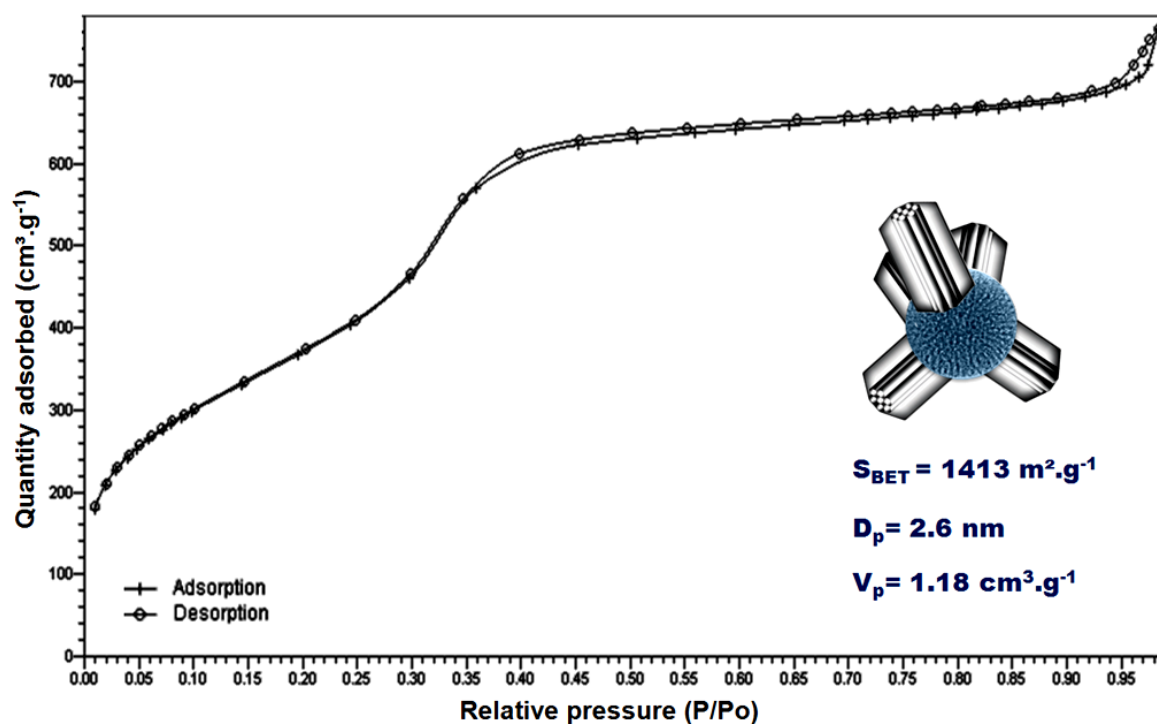


Figure S6. N_2 -adsorption-desorption isotherm of BE mp-PMO NPs.

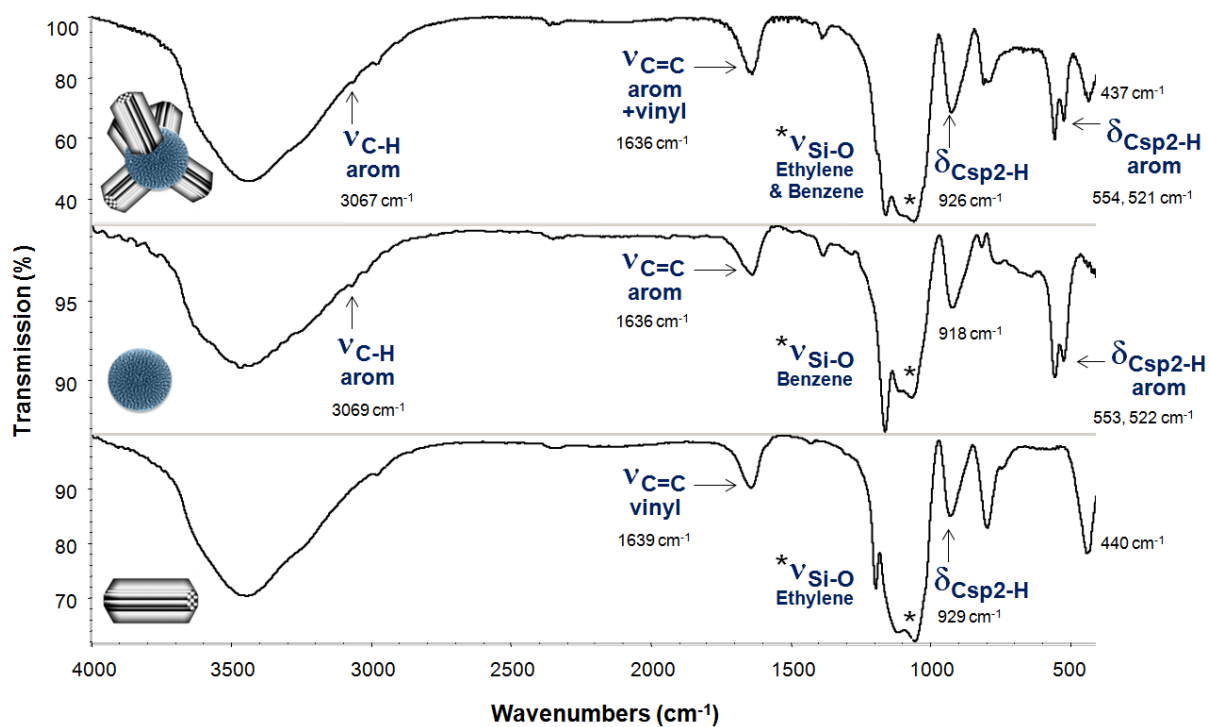


Figure S7. FTIR spectra comparison of the BE mp-PMO NPs, B PMO, and E PMO NPs.

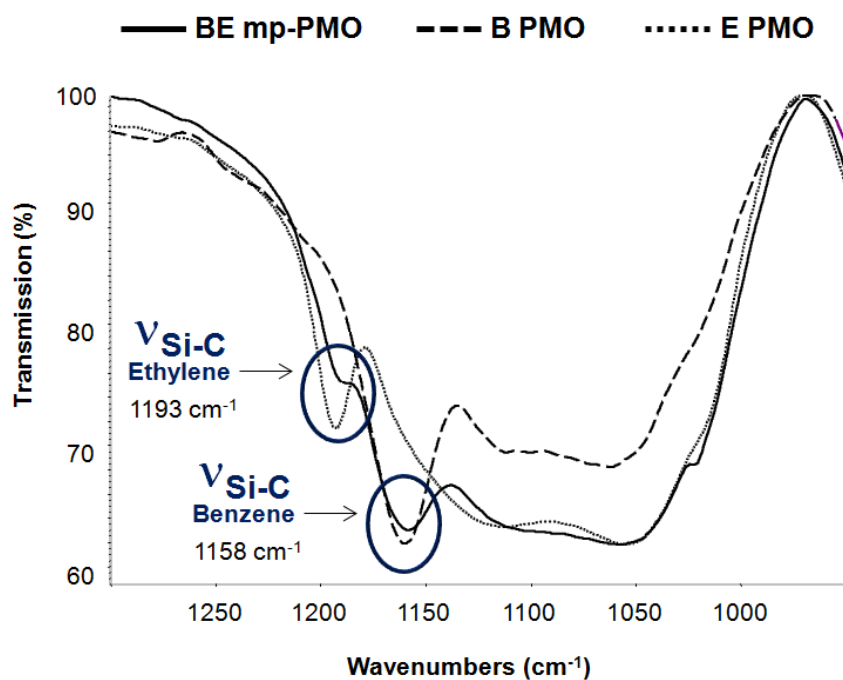


Figure S8. FTIR spectra comparison of the BE mp-PMO NPs, B PMO, and E PMO NPs, demonstrating the presence of $\nu_{\text{Si-C}}$ of both the ethylene and the benzene fragments in the BE mp-PMO.

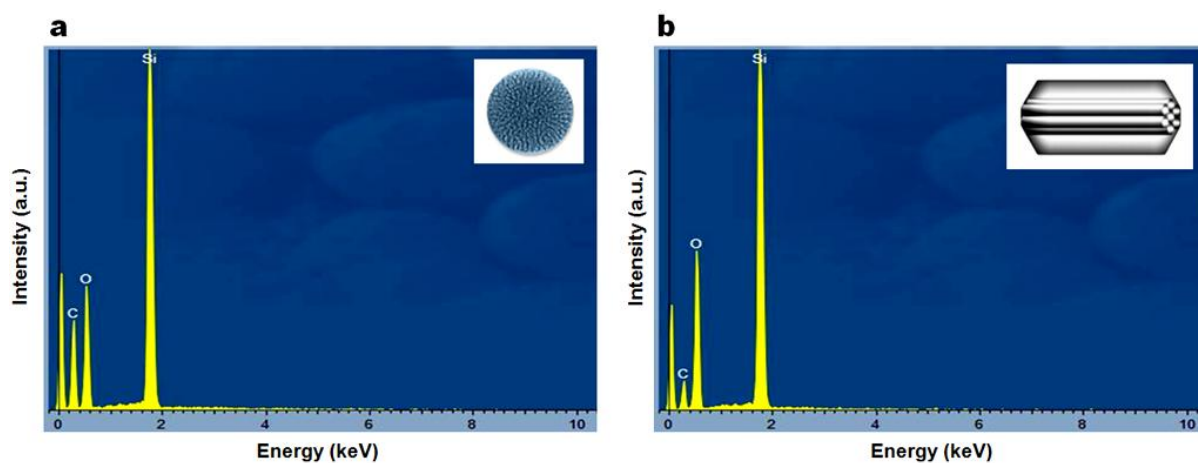


Figure S9. EDS spectra of B PMO nanospheres (a) and E PMO nanorods (b).

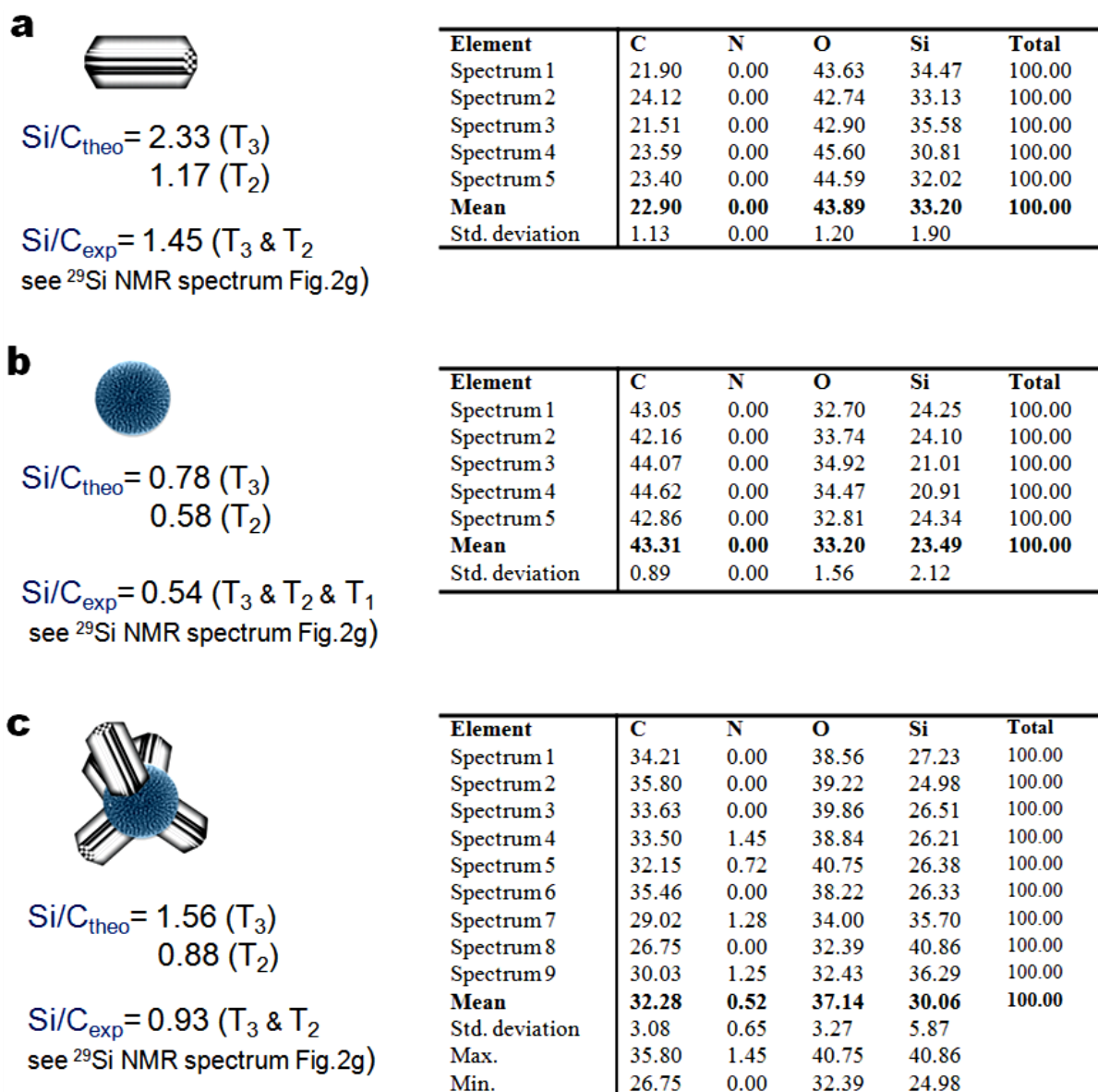


Figure S10. EDS elemental analyses of E PMO (a), B PMO (b), and BE mp-PMO NPs (c), validating the expected compositions of the nanomaterials. The theoretical Si/C ratios ($\text{Si/C}_{\text{theo}}$) are calculated for the fully and partially condensed material (T_3 and T_2 environments respectively) according to the following chemical formula: $\text{O}_{1.5}\text{-Si-R-Si-O}_{1.5}$ (T_3), and $(\text{CH}_3\text{CH}_2\text{O})_{0.5}\text{O-Si-R-Si-O}(\text{OCH}_2\text{CH}_3)_{0.5}$ (T_2) with $\text{R} = \text{C}_6\text{H}_4$ (a), CH=CH (b). The BE mp-PMO $\text{Si/C}_{\text{theo}}$ correspond to the equimolar content of B and E (c). The experimental ratios (Si/C_{exp}) correspond to the ^{29}Si NMR spectra exhibited in Fig.2g.

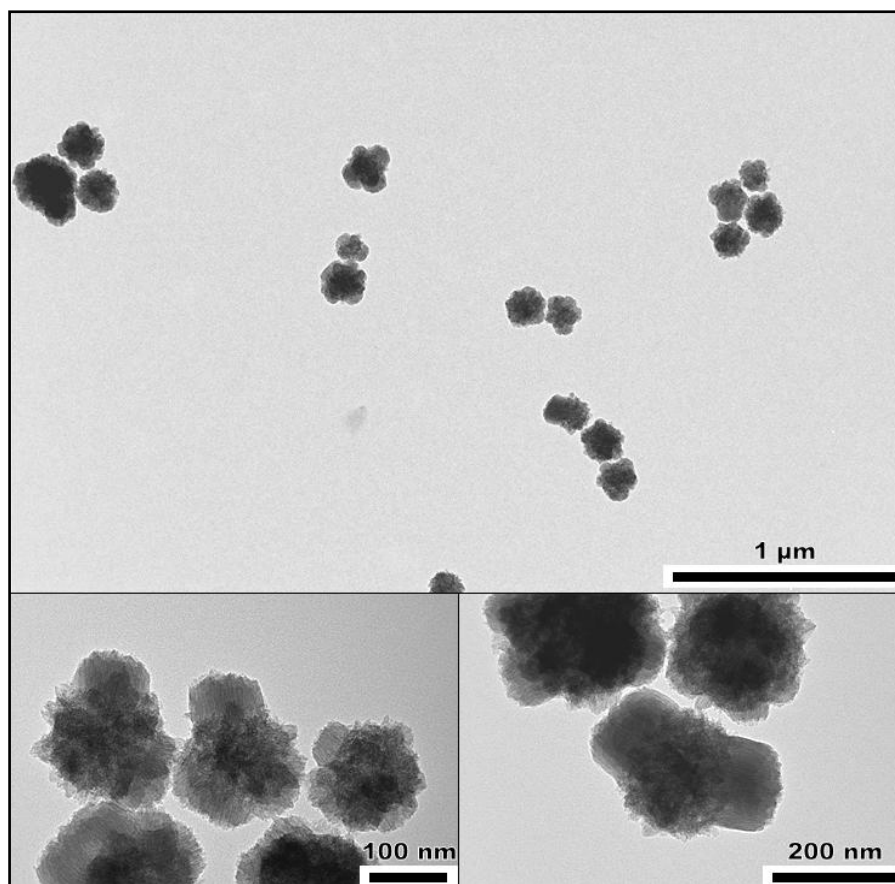


Figure S11. TEM images of the BEDIS mp-PMO NPs elaborated with longer pods.

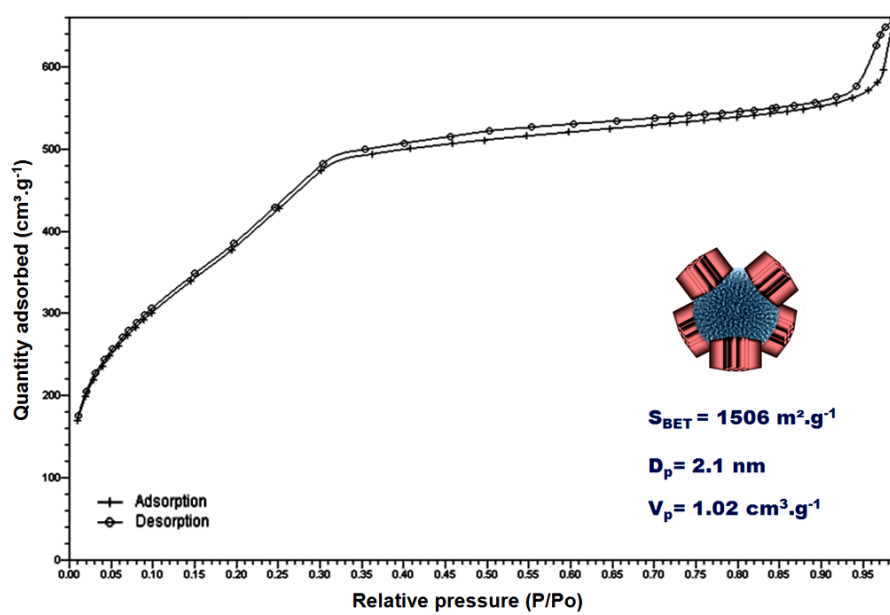


Figure S12. N_2 -adsorption-desorption isotherm of BEDIS mp-PMO NPs.

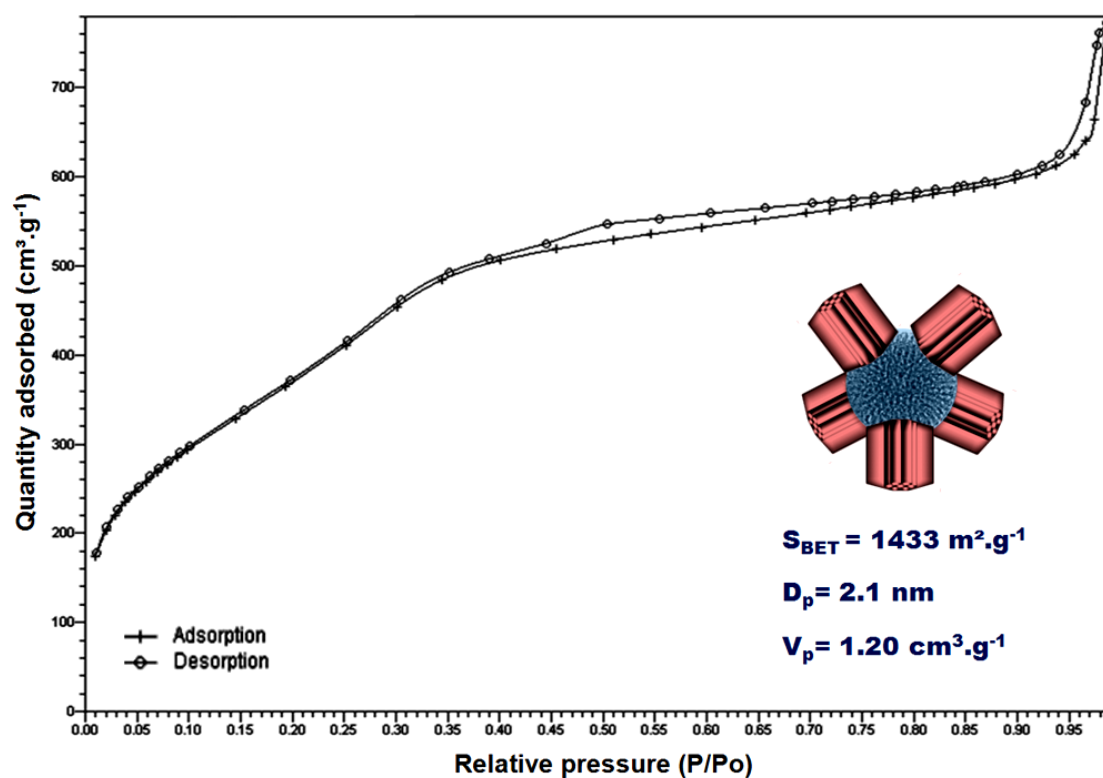


Figure S13. N_2 -adsorption-desorption isotherm of BEDIS mp-PMO with longer pods.

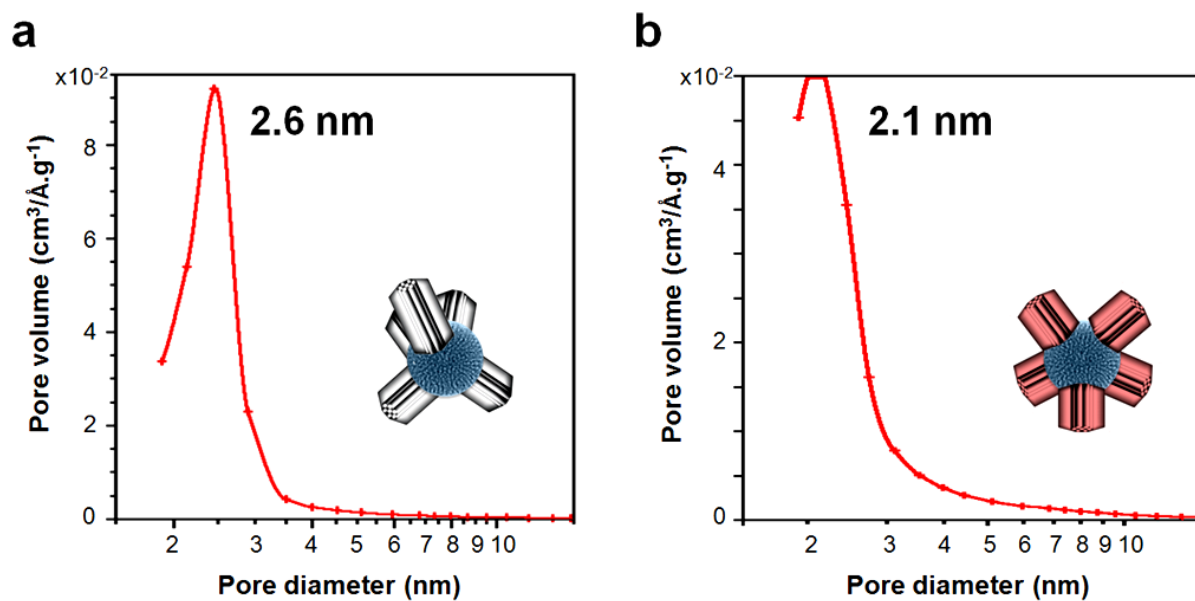


Figure S14. BJH pore size distribution of BE mp-PMO (a) and long pod BEDIS mp-PMO NPs (b).

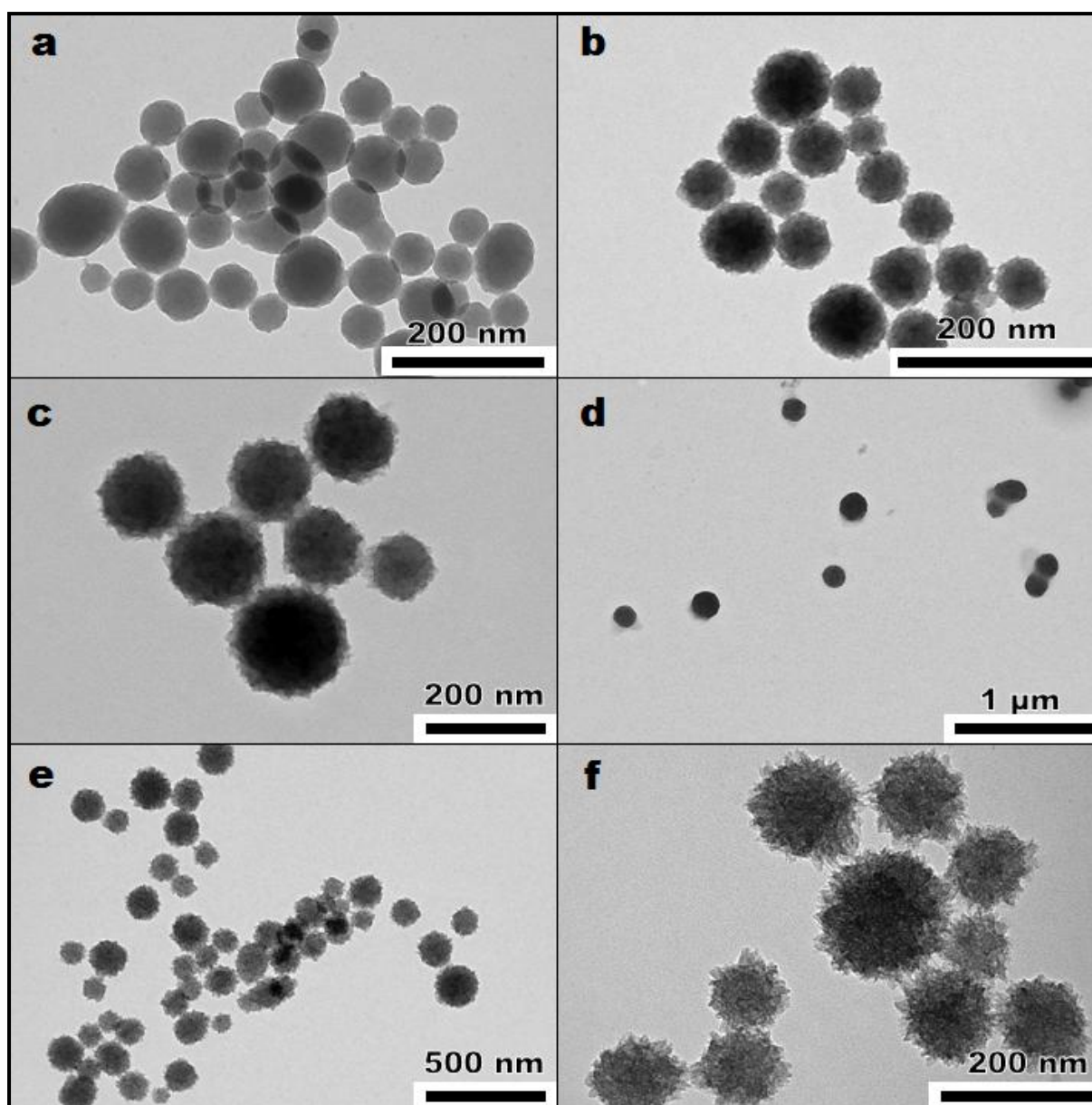
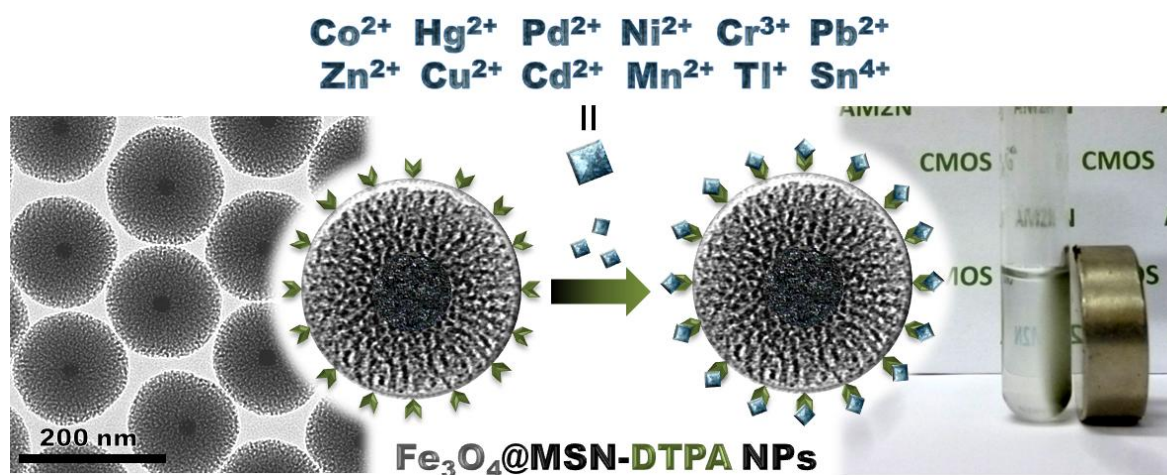


Figure S15. Additional TEM images of the B nanospheres growth after 10 (a), 20 (b), 30 (c), 40 (d), and 50 minutes of sol-gel process (e-f).

CHAPTER 9

Versatile Heavy Metals Removal via Magnetic Mesoporous Nanocontainers†



Abstract

Versatile heavy metals removal is performed via iron oxide core mesoporous silica shell nanocontainers functionalized with diethylene triamine pentaacetic acid. Magnetic separation from aqueous media is obtained for a dozen of the most toxic heavy metal ions with remarkable efficiencies. Furthermore, this study demonstrates enhancement potential of the adsorption capacities with a combination of porous and surface functionalization of the nanocontainers.

† S. Dib, M. Boufatit, S. Chelouaou, F. Sadi-Hassaine, J. Croissant,* J. Long, L. Raehm, C. Charnay, J-O. Durand, **RSC Advances**, 2014, RA-COM-02-2014-001323.R2.

INTERDISCIPLINARY COLLABORATION

J. Croissant, S. Dib, M. Boufatit, S. Chelouaou, F. Sadi-Hassaine, J. Long, C. Charnay, L. Raehm, J-O. Durand : *Nanomaterial syntheses, physico-chemical characterizations, and applications in solution.*

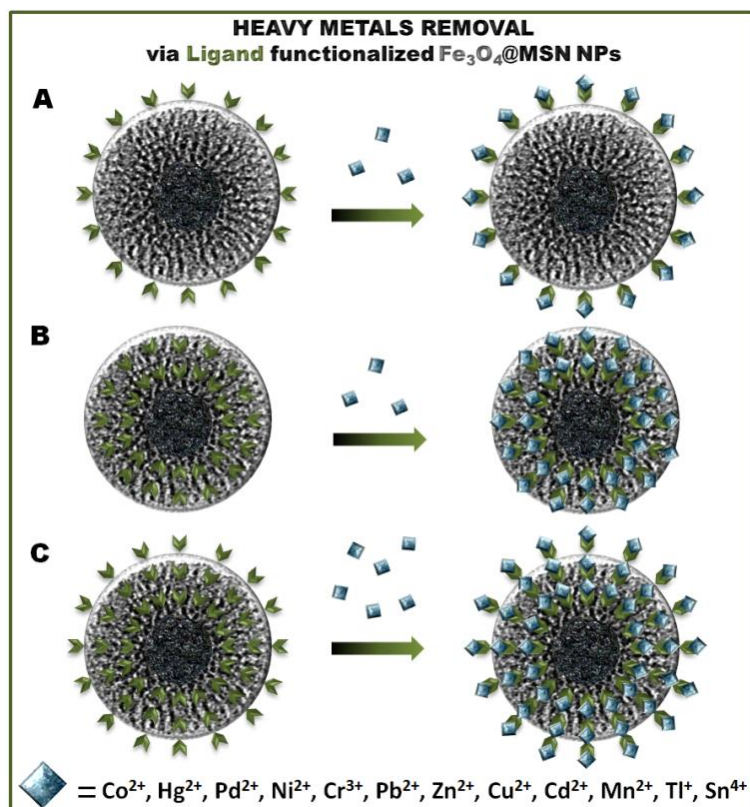
J. Croissant, J-O. Durand : *Nanomaterial concept, metal removal characterizations.*

Introduction

Heavy metal contamination from industrial processes and products has become a public health and environmental concern throughout the world.¹⁻⁶ Although there is no clear and scientific definition of heavy metals, it generally refers to metals having a specific density of more than 5 g.cm⁻³.¹ In the year 2000, the European Union has legislated that “heavy metal means any compound of antimony, arsenic, cadmium, chromium(VI), copper, lead, mercury, nickel, selenium, tellurium, thallium and tin, as well as these materials in metallic form, as far as these are classified as dangerous substances.”⁷ The toxicity for human health of heavy metal ions, among which lead, cadmium, mercury and arsenic are considered to be the most dangerous,¹ can damage mental and central nervous functions. Besides, the essentiality of metal ions transport (e.g. copper, zinc, lead) *via* proteins for cellular biochemical processes in the body, can also become the Trojan horse for toxic metal ions accumulation. As a result, various damages can be caused by heavy metal ions to vital organs such as the lungs, the kidneys, and the liver.⁸⁻¹¹ Therefore, many devices have been elaborated to remove such ions, mainly ion-exchange materials,¹²⁻¹⁴ membrane filtration and adsorption,^{5, 15-17} and colloidal adsorbents.¹⁸⁻²²

Superior efficiencies are obtained *via* adsorbents,^{18, 23-25} and porous colloids would be most appropriate due to their high surface area, and the variability of surface modifications.¹⁹ One challenge that colloidal adsorbents face is to separate the particles after ion adsorption. An efficient method utilizes the magnetic properties of iron oxide nanocrystals (Fe₃O₄NCs).^{22, 26, 27} Note that, for such an application Fe₃O₄NCs must be coated in order to avoid iron ions leaching in the waste solutions. Besides, to enhance the pollutant removal capacities of Fe₃O₄NCs, porous coatings could be tailored. Hence, micron-size Fe₃O₄NCs core mesoporous silica shell (Fe₃O₄@MSN) have been designed,^{18, 28} Fe₃O₄@MSN@chitosan microspheres,²⁹ Fe₃O₄NCs@MSN foams.³⁰ and porous magnetite-carbon nanocapsules.³¹ To our knowledge micro-sized Fe₃O₄@MSN materials were only tested with Pb²⁺, Cu²⁺, Cd²⁺, Hg²⁺, and Ag⁺.^{18, 28, 30}

In the present study, we designed Fe₃O₄@MSN nanocontainers functionalized with a tridentate chelate ligand for heavy metal ions removal. The functionalization was performed with a mono-alkoxysilylated derivative of diethylene triamine pentaacetic acid (DTPA). Thus excellent colloidal stability was obtained for an effective magnetic separation in aqueous media at neutral pH. The nanocontainers were found to be effective for twelve of the most toxic heavy metal ions, namely Pb²⁺, Cu²⁺, Zn²⁺, Cd²⁺, Tl⁺, Pd²⁺, Ni²⁺, Hg²⁺, Cr³⁺, Co²⁺, Mn²⁺, and Sn⁴⁺. Furthermore, the adsorption capacity was enhanced by taking advantage of the porosity of the mesoporous silica framework (Scheme1).

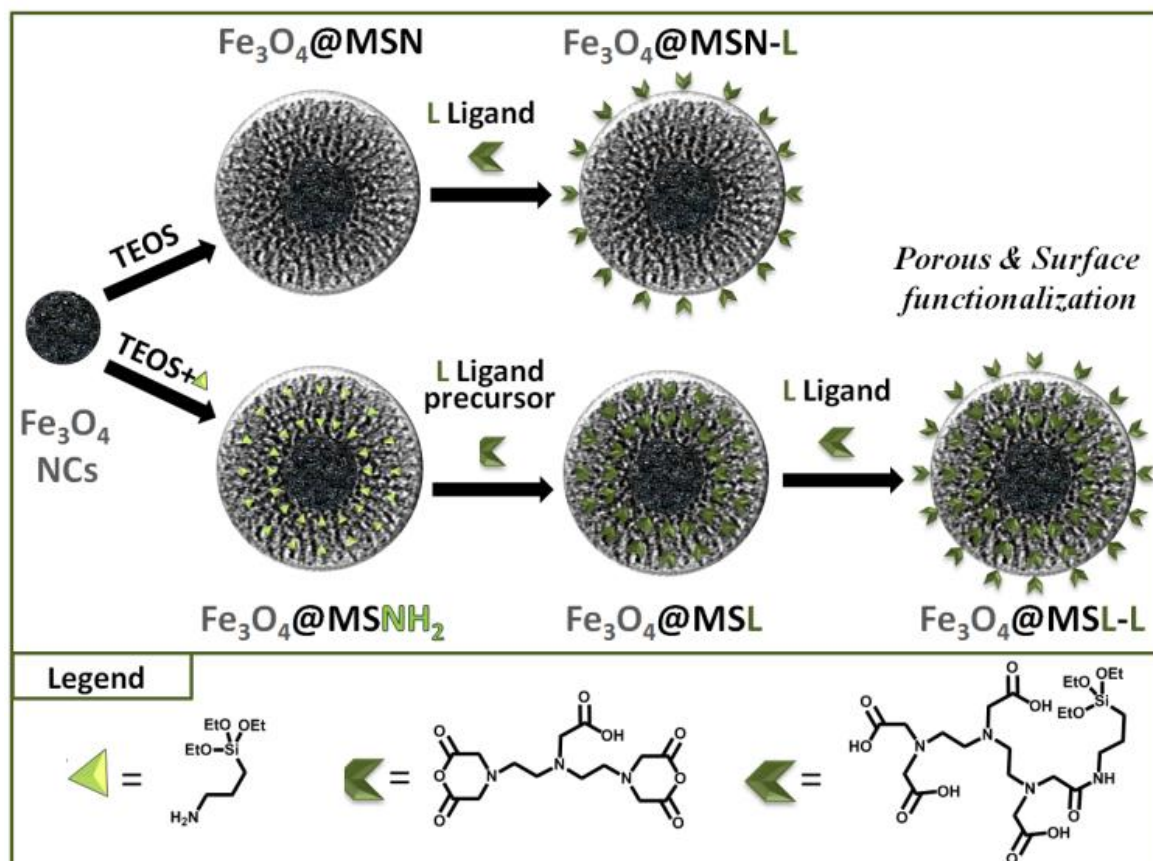


Scheme 1. Heavy metal removal strategies: surface functionalized $\text{Fe}_3\text{O}_4@\text{MSN}$ NPs (A), the porous functionalized $\text{Fe}_3\text{O}_4@\text{MSN}$ NPs (B), and surface/porous functionalized $\text{Fe}_3\text{O}_4@\text{MSN}$ NPs (C).

Results and discussion

First of all, DTPA functionalized magnetic mesoporous nanocontainers were designed with different strategies (Scheme 2). Spherical $\text{Fe}_3\text{O}_4\text{NCs}$ of 21 ± 2 nm were synthesized *via* thermal decomposition at 340°C of hydrated iron oxide with oleic acid in docosane. Then, the mesoporous silica layer was grown in 2 h by tetraethoxysilane (TEOS) addition in a sol-gel process at 80°C with a sodium hydroxide catalyst in a cetyltrimethylammonium bromide/water mixture. Three types of nanocontainers were obtained (Scheme 2), surface functionalized NPs ($\text{Fe}_3\text{O}_4@\text{MSN-L}$), porous functionalized NPs ($\text{Fe}_3\text{O}_4@\text{MSL}$), and the combined surface/porous functionalized NPs ($\text{Fe}_3\text{O}_4@\text{MSL-L}$). The $\text{Fe}_3\text{O}_4@\text{MSN-L}$ NPs were obtained through post-functionalization of $\text{Fe}_3\text{O}_4@\text{MSN}$ by the alkoxy-silylated DTPA. IR spectra demonstrated the ligand functionalization (ESI Fig. S1-2), with the apparition of $\nu_{\text{Si-C}}$ at 1204 cm^{-1} , $\nu_{\text{N-C}}$ at 1398 cm^{-1} , $\nu_{\text{C=O}}$ at 1644 cm^{-1} , and $\nu_{\text{C-C}}$ from at 1888 to 1942 cm^{-1} vibration modes corresponding to the DTPA. Solid state nuclear magnetic resonance (NMR) ^{13}C and ^{29}Si CPMAS spectra on a control of ligand functionalized MSN NPs further confirmed the surface functionalization (Fig. S3). Elemental analysis and energy dispersive spectroscopy quantitative composition determinations measured 37.8 and 31.0 wt% of ligand functionalization respectively (ESI Fig. S4). The porous functionalization of $\text{Fe}_3\text{O}_4@\text{MSL}$ was constructed in two steps. Initially, a mixture of the TEOS precursor and (3-aminopropyl)trimethoxysilane moiety was condensed on $\text{Fe}_3\text{O}_4\text{NCs}$, leading to iron oxide core mesoporous amino-silica shells ($\text{Fe}_3\text{O}_4@\text{MSNH}_2$, see Scheme 2). Then, the DTPA precursor was reacted in the pores to obtain $\text{Fe}_3\text{O}_4@\text{MSL}$ NPs. This grafting is also supported

by the IR spectra of $\text{Fe}_3\text{O}_4@\text{MSNH}_2$ and $\text{Fe}_3\text{O}_4@\text{MSL}$, with the disappearance of the sharp $\nu_{\text{N-C}}$ vibration band at 1385 cm^{-1} , and the appearance of the $\nu_{\text{C=O}}$ at 1631 cm^{-1} , and the $\nu_{\text{C-C}}$ at $1850\text{--}1961\text{ cm}^{-1}$ (ESI Fig. S5-6). Finally, $\text{Fe}_3\text{O}_4@\text{MSL-L}$ was designed *via* the grafting of the alkoxy-silylated DTPA on $\text{Fe}_3\text{O}_4@\text{MSL}$ nanocontainers.



Scheme 2. Synthetic pathways to design ligand functionalized $\text{Fe}_3\text{O}_4@\text{MSN}$ NPs.

The $\text{Fe}_3\text{O}_4@\text{MSN}$ nanocontainers were characterized *via* transmission and scanning electron microscopies (Fig. 1A-B). Spherical radial mesostructures were observed, and most nanocontainers were composed of a 20 nm iron oxide core, leading to an overall size of 130 nm. The size monodispersity of the NPs was confirmed by dynamic light scattering (DLS) measurements (Fig. 1D). The mesoporous framework was analyzed *via* nitrogen-adsorption-desorption technique, and the typical type IV isotherm profile was acquired (Fig. 1E). A surface area of $530\text{ m}^2\cdot\text{g}^{-1}$ was calculated by the BET theory, and a pore diameter of 3 nm was determined. Similarly, the $\text{Fe}_3\text{O}_4@\text{MSNH}_2$ nanocontainers were fully characterized and found to be 50 nm monodisperse and non-aggregated mesoporous NPs (ESI Fig. S7).

The heavy metal ions removal was then magnetically carried out with $\text{Fe}_3\text{O}_4@\text{MSN-L}$ NPs (Fig. 2). All the experiments were performed in aqueous media at neutral pH. The nanocontainers were mixed in deionized water with various metal salts excess to continually saturate the solution, and the solution was stirred overnight at room temperature. Afterwards, a magnet was placed on the side of the reaction tube for 10 minutes, the supernatant and the metal salts were removed. Finally, the NPs were washed thrice in water, twice in ethanol, and once in acetone, to remove the non-adsorbed metal residues (see ESI Fig. S8).

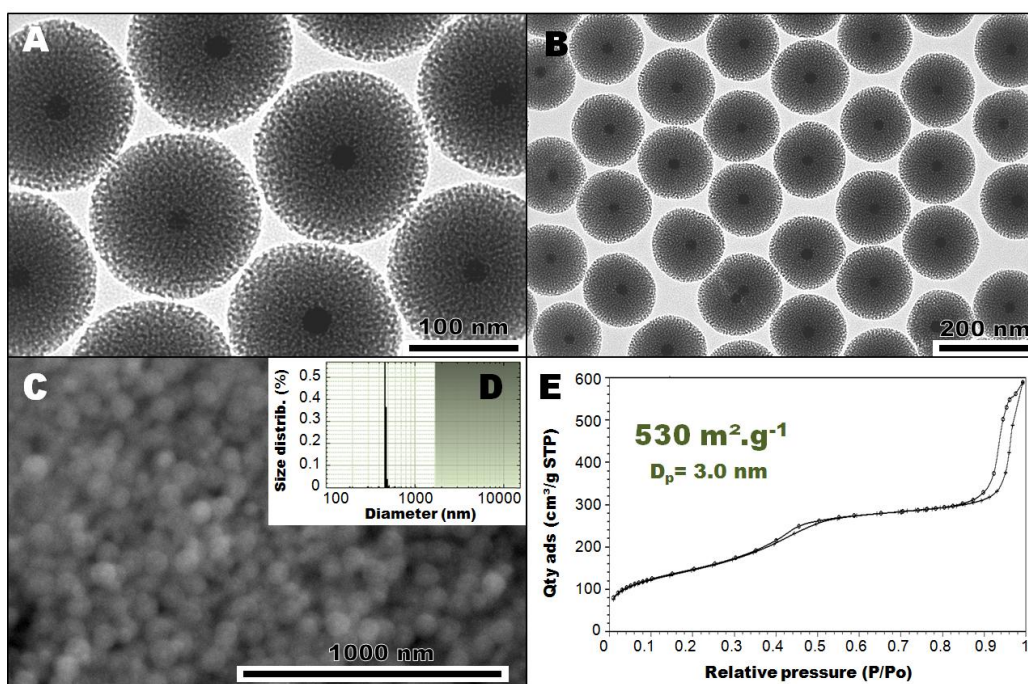


Figure 1. Transmission and scanning electron microscopy of Fe₃O₄@MSN NPs (A-B, C respectively), the DLS size distribution (D), and N₂-adsorption-desorption analysis (E).

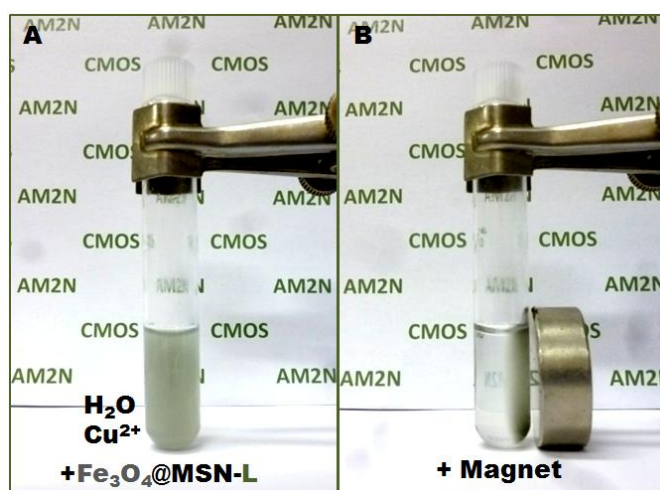


Figure 2. Nanocontainers before (A) and after magnetic separation of Fe₃O₄@MSN-L∩Cu²⁺ NPs (B).

The metal adsorption capacities (Fig. 3) were determined by statistical energy dispersive spectroscopy measurements (ESI, Fig. S9, Table S1-12). Interestingly, the ligand functionalized nanocontainers were found to be a versatile platform for many different kinds of metals. Moreover, such a separation was very efficient for certain metal ions, such as palladium(II), copper(II), chromium(III), tin (IV), nickel(II), and zinc(II), with adsorption capacities ranging from 1000 to 2400 $\mu\text{mol}\cdot\text{g}^{-1}$. Note that, the absence of chloride on the EDS spectra for most of NPs using metal chloride precursors validates the adsorption-washing procedure that was used to remove precipitated salts. Not surprisingly, the exceptions are the magnetic chromium chloride as well as the very soluble palladium chloride, probably partly accumulated in the pores. Thus, comparing solely the surface adsorption capacities of coated

iron oxide nanocontainers (to avoid iron ions pollution), our system is very competitive with the current literature. Comparing surface functionalized amino-MSN with Fe₃O₄@MSN-L nanocontainers, the adsorption of Ni²⁺, Cd²⁺, and Pb²⁺ was nearly doubled.²¹ Consequently, the DTPA ligand is most appropriated to pollutant removal green materials and nanomaterials. Moreover, the selectivity of the ion removals was studied and found to be preferential towards palladium (58%), copper (21%), and lead (7%) in a mixture of all types of metals (Fig. S10) which further illustrates the applicability of these nanocontainers.

The metal ions could then be removed *via* acidic treatment, as reported in the literature.²⁸ At pH 4.5 the efficiency of the nanocontainers regeneration was 90 and 99% for copper and zinc ions respectively after one desorption process, according to inductively-coupled plasma analysis (Fig. S11). Note that, the iron oxide weight percent remained unchanged after the acidic extraction, thus showing the stability of the core thanks to the silica protective layer. Besides, the removal was found to be reversible with 99% efficiency after 2 cycles (Fig. S12).

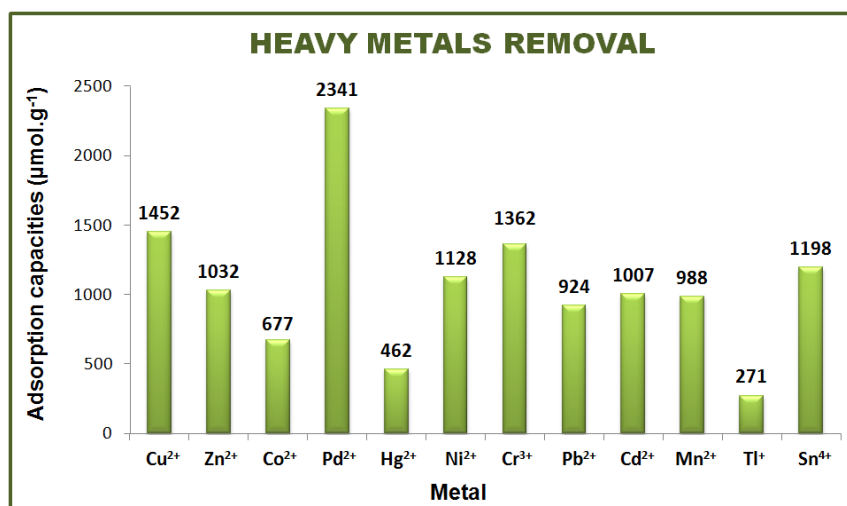


Figure 3. Heavy metal removal capacities of t Fe₃O₄@MSN-L NPs.

The enhancement of the adsorption capacities was considered for copper and zinc ions. The three types of ligand functionalized nanocontainers, Fe₃O₄@MSN-L, Fe₃O₄@MSL, and Fe₃O₄@MSL-L were compared (Fig. 4). Surprisingly, the adsorption capacities of Fe₃O₄@MSL were smaller than that of Fe₃O₄@MSN-L, with 503 and 570 μmol.g⁻¹ of zinc and copper respectively in the former, and 797 and 1122 μmol.g⁻¹ in the latter. This may be due to steric pore hindrance of amine groups which lowered the porous surface, as well as the steric effect occurring when partial metal adsorption has occurred. However, the combination of the surface and porous ligand grafting in Fe₃O₄@MSL-L led to proportional enhancement of the adsorption capacities, reaching 1363 and 1904 μmol.g⁻¹ of zinc and copper respectively. In both cases, an additional 40 percent of metal ions was adsorbed. Note that, the correlation between the amount of ligand and the adsorbed quantity of heavy metals was confirmed by varying the amount of DTPA in the pores and on the surface (ESI Fig. S13). Furthermore, the metals ions were not merely physically entrapped in the MSN framework, as suggested by the 5 to 9 cm⁻¹ shifts in the carbonyl vibration modes (ESI Fig. S14-17).

Besides, the observed increase of the intensity of the $\nu_{\text{C=O}}$ bands is in accord with conformational change associated with the DTPA- Mn^+ complex formations. That is why various colors were observed for each type of metal complexes in the NPs framework.

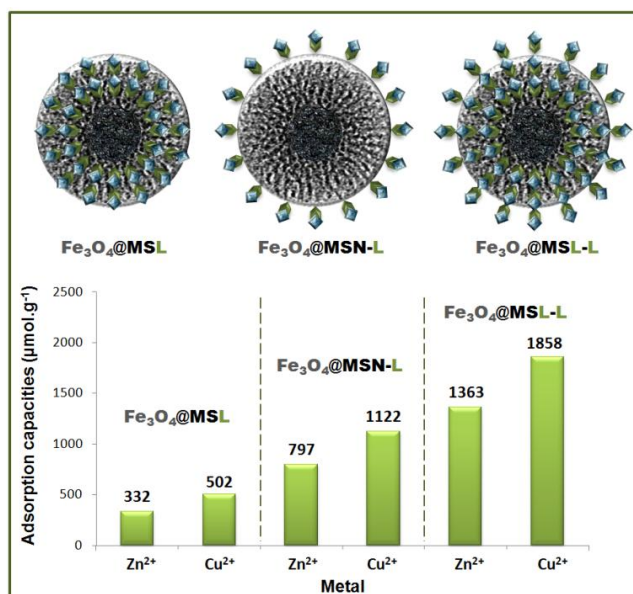


Figure 4. Heavy metal removal capacities optimization of the various nanocontainers strategies.

Conclusion

In summary, we have developed a novel diethylene triamine pentaacetic acid ligand functionalized with monodisperse $\text{Fe}_3\text{O}_4@\text{MSN}$ and $\text{Fe}_3\text{O}_4@\text{MSNH}_2$ nanocontainers. Such NPs were found to be capable of a versatile and efficient magnetic separation on a dozen of heavy metal ions. The adsorption capacities tended to be higher for the metal having high valence and electronic affinities, such as Pd^{2+} ($2341 \mu\text{mol.g}^{-1}$), Co^{2+} ($1452 \mu\text{mol.g}^{-1}$), Cr^{3+} ($1362 \mu\text{mol.g}^{-1}$), Sn^{4+} ($1198 \mu\text{mol.g}^{-1}$), and Ni^{2+} ($1128 \mu\text{mol.g}^{-1}$). Palladium(II), copper(II), and lead(II) ions were selectively removed in a mixture of all types of ions, which makes the nanocontainers selective platforms for heavy metal removal. Besides, the nanocontainers could be regenerated and reused with high efficiencies. Additionally, the adsorption capacities have been enhanced of 40 percent by the porous and surface functionalization of the nanocontainers. We are currently investigating the optimization of the adsorption capacity with larger pores and higher surface areas, in order to avoid the steric hindrance inside the mesopores. It is envisioned that such $\text{Fe}_3\text{O}_4@\text{MSL-L}$ NPs could be powerful tools to efficiently clear heavy metal liquid waste.

REFERENCES

1. L. Järup, *Br. Med. J. Bull.*, 2003, **68**, 167-182.
2. X. Liu, Q. Song, Y. Tang, W. Li, J. Xu, J. Wu, F. Wang and P. C. Brookes, *Sci. Tot. Environ.*, 2013, **463-464**, 530-540.
3. M. Pizzol, P. Christensen, J. Schmidt and M. Thomsen, *J. Clean. Prod.*, 2011, **19**, 646-656.
4. N. Malik, A. K. Biswas, T. A. Qureshi, K. Borana and R. Virha, *Environ. Monit. Assess.*, 2010, **160**, 267-276.
5. F. Fu and Q. Wang, *J. Environ. Manag.*, 2011, **92**, 407-418.
6. J. S. Barbosa, T. M. Cabral, D. N. Ferreira, L. F. Agnez-Lima and S. R. Batistuzzo de Medeiros, *Ecotox. Environ. Safe.*, 2010, **73**, 320-325.
7. T. C. O. T. E. Communities, *Off. J. Eur. Comm.*, 2000, **226**, 3.
8. S. H. Laura D. K. Thomas, Mark Nieuwenhuijsen and Lars Jarup, *Environ. Health Perspect.*, 2009, **117**, 181-184.
9. N. Johri, G. Jacquillet and R. Unwin, *BioMetals*, 2010, **23**, 783-792.
10. Q. Gu and R.-L. Lin, *J. Appl. Physiol.*, 2010, **108**, 891-897.
11. K. Gulati, B. Banerjee, S. B. Lall and A. Ray, *Ind. J. Exp. Biol.*, 2010, **48**, 710-721.
12. M. Y. Vilensky, B. Berkowitz and A. Warshawsky, *Environ. Sci. Technol.*, 2002, **36**, 1851-1855.
13. W. Plazinski and W. Rudzinski, *Environ. Sci. Technol.*, 2009, **43**, 7465-7471.
14. G. Mahajan and D. Sud, *J. Environ. Chem. Eng.*, 2013, **1**, 1020-1027.
15. M. A. Hasan, Y. T. Selim and K. M. Mohamed, *J. Haz. Mater.*, 2009, **168**, 1537-1541.
16. B. Yu, Y. Zhang, A. Shukla, S. S. Shukla and K. L. Dorris, *J. Haz. Mater.*, 2000, **80**, 33-42.
17. W. S. Wan Ngah, L. C. Teong, R. H. Toh and M. A. K. M. Hanafiah, *Chem. Eng. J.*, 2013, **223**, 231-238.
18. G. Li, Z. Zhao, J. Liu and G. Jiang, *J. Haz. Mater.*, 2011, **192**, 277-283.
19. M. Hua, S. Zhang, B. Pan, W. Zhang, L. Lv and Q. Zhang, *J. Haz. Mater.*, 2012, **211-212**, 317-331.
20. J. Wang, Y. Shao, J. Liu, Z. Xu and D. Zhu, *J. Col. Interface Sci.*, 2010, **349**, 293-299.
21. M. Najafi, Y. Yousefi and A. A. Rafati, *Sep. Purif. Technol.*, 2012, **85**, 193-205.
22. M. Chen, Y. Liu and Y. Hao, *Chem. Eng. J.*, 2013, **218**, 48-54.
23. S. Dib and M. Boufatit, *Desalination*, 2009, **5**, 106-110.
24. F. Mohammed-Azizi, S. Dib, and M. Boufatit, *Desalination*, 2013, **51**, 4447-4458.
25. H. Assameur and M. Boufatit, *Desalination*, 2012, **45**, 315-323.
26. L. Wang, J. Li, Q. Jiang and L. Zhao, *Dalton Trans.*, 2012, **41**, 4544-4551.
27. P. Xu, G. M. Zeng, D. L. Huang, C. L. Feng, S. Hu, M. H. Zhao, C. Lai, Z. Wei, C. Huang, G. X. Xie and Z. F. Liu, *Sci. Tot. Environ.*, 2012, **424**, 1-10.
28. Q. Yuan, N. Li, Y. Chi, W. Geng, W. Yan, Y. Zhao, X. Li and B. Dong, *J. Haz. Mater.*, 2013, **254-255**, 157-165.
29. Y. Ren, H. A. Abboud, F. He, H. Peng and K. Huang, *Chem. Eng. J.*, 2013, **226**, 300-311.
30. J. Chung, J. Chun, J. Lee, S. H. Lee, Y. J. Lee and S. W. Hong, *J. Haz. Mater.*, 2012, **239-240**, 183-191.
31. K. Cheng, Y.-M. Zhou, Z.-Y. Sun, H.-B. Hu, H. Zhong, X.-K. Kong and Q.-W. Chen, *Dalton Trans.*, 2012, **41**, 5854-5861.

APPENDIX: SUPPLEMENTARY INFORMATION

I- EXPERIMENTAL SECTION

Materials. Tetraethoxysilane (TEOS), cetyltrimethylammonium bromide (CTAB), diethylenetriaminepentaacetic dianhydride, sodium hydroxide, aminopropyltriethoxysilane, hydrated iron oxide, oleic acid, ammonium nitrate, triethylamine, ether, dimethylformamide, copper(II) chloride, zinc(II) chloride, cadmium(II) bromide tetrahydrate, and manganese(II) chloride tetrahydrate were purchased from Sigma-Aldrich. Anhydrous ethanol, and chloroform were purchased from Fisher Chemicals. Palladium(II) chloride, and tin(IV) chloride pentahydrate were purchased from Alfa-Aeser. Thallium(I) sulfate was purchased from Prolabo. Cobalt(II) nitrate pentahydrate, and lead(II) carbonate were purchased from Labosi. Mercury(II) acetate was purchased from Strem Chemicals. Nickel(II) chloride hexahydrate, and chromium(III) chloride were purchased from Chimica.

Methods. TEM images were recorded with a JEOL instrument. SEM images were recorded with a FEI instrument. Energy dispersive spectroscopy was performed *via* an FEI scanning electron microscope. The metal ions adsorption capacities were determined from the K_a rays. The magnetic separation was performed *via* a 1 Tesla magnet. IR spectra were recorded on a Perkin-Elmer 100 FT spectrophotometer. Absorption spectra were recorded on a Hewlett-Packard 8453 spectrophotometer. Dynamic light scattering analyses were performed using a Cordouan Technologies DL 135 Particle size analyzer instrument. ^{29}Si and ^{13}C CPMAS solid state NMR sequences were recorded with a VARIAN VNMR300, using Q8MH8 and adamantane references respectively.

II- NANOMATERIAL SYNTHESSES AND CHARACTERIZATIONS

L ligand. A mixture of diethylenetriaminepentaacetic dianhydride (DTPA, 300 mg, 8.0×10^{-1} mmol), aminopropyltriethoxysilane (177 mg, 8.0×10^{-1} mmol), triethylamine (81 mg, 8.0×10^{-1} mmol), and dimethylsulfoxide (DMF, 20 mL) was sonicated 20 minutes and stirred 3 h at room temperature. The ligand solution was then used without further purification.

$\text{Fe}_3\text{O}_4\text{NCs}$. A mixture of hydrated iron oxide ($\text{FeO}(\text{OH})$, 0.181 g), oleic acid (3.180 g), and docosane (5.016 g) was prepared in a 100 mL two neck round bottom flask, and stirred under vacuum for 30 minutes. Then, an argon atmosphere was applied and the mixture was refluxed at 340°C . As soon as the mixture reached 340°C , the reaction was conducted for 1 h 30 min. The solution was cooled down during 1 h without stirring. The resulting black solid was dissolved in pentane (14 mL), mixed with an ether/ethanol solution (30 mL, 2:1, v:v), and centrifugated 10 minutes at 21 krpm (27 krcf). The decomposed organic black solution was removed and the NCs were redispersed in pentane (2 mL), washed with the ether/ethanol solution, and centrifugated. The supernatant was removed, the NCs were stored in chloroform (15 mL), and stabilized with an addition of oleylamine (200 μL).

$\text{Fe}_3\text{O}_4\text{@MSN}$. A mixture of CTAB (250 mg), distilled water (120 mL), and sodium hydroxide (875 μL , 2 M) was stirred at 70°C during 50 minutes at 700 rpm in a 250 mL three

neck round bottom flask. Then, $\text{Fe}_3\text{O}_4\text{NCs}$ dispersed in chloroform were added stepwise ($8 \times 500 \mu\text{L}$) during 20 minutes. Note that the chloroform is quickly evaporating from the mixture at this temperature, and 40 additional minutes were used at 80°C to stabilize the NCs in the micelles. Finally, TEOS (1.2 mL) was added to the solution, and the condensation process was conducted for 2 h. Afterwards, the solution was cooled at room temperature while stirring; fractions were gathered in polypropylene tubes and collected by centrifugation during 15 minutes at 21 krpm (27 krcf). The sample was then extracted twice with an alcoholic solution of ammonium nitrate (6 g.L^{-1}), and washed three times with ethanol, water, and ethanol. Each extraction involved a sonication step of 30 minutes at 50°C in order to remove the CTAB surfactant; the collection was carried out in the same manner. The as-prepared material was dried under air flow for few hours.

$\text{Fe}_3\text{O}_4\text{@MSN-L}$. $\text{Fe}_3\text{O}_4\text{@MSN}$ NPs (100 mg) were sonicated in anhydrous ethanol (4 mL) for 10 minutes, and the ligand was added (4 mL from the DMF solution). The solution was heated to 70°C during 24 h, and centrifugated 10 minutes at 21 krpm (27 krcf). The supernatant was removed and the resulting $\text{Fe}_3\text{O}_4\text{@MSN-L}$ NPs were washed once with ethanol, twice with water, once with acetone, and dried under vacuum.

$\text{Fe}_3\text{O}_4\text{@MSN-H}_2$. A mixture of CTAB (250 mg), distilled water (120 mL), and sodium hydroxide ($875 \mu\text{L}$, 2 M) was stirred at 70°C during 50 minutes at 700 rpm in a 250 mL three neck round bottom flask. Then, $\text{Fe}_3\text{O}_4\text{NCs}$ dispersed in chloroform were added stepwise ($8 \times 500 \mu\text{L}$) during 20 minutes. Note that the chloroform is quickly evaporating from the mixture at this temperature, and 40 additional minutes were used at 80°C to stabilize the NCs in the micelles. Finally, TEOS (1 mL) and aminopropyltriethoxysilane ($200 \mu\text{L}$) were added to the solution, and the condensation process was conducted for 2 h. Afterwards, the solution was cooled at room temperature while stirring; fractions were gathered in polypropylene tubes and collected by centrifugation during 15 minutes at 21 krpm (27 krcf). Extraction and following steps were identical of those of $\text{Fe}_3\text{O}_4\text{@MSN}$.

$\text{Fe}_3\text{O}_4\text{@MSL}$. $\text{Fe}_3\text{O}_4\text{@MSN-H}_2$ NPs (50 mg) were mixed with DMF ($500 \mu\text{L}$), DTPA (5 mg), and triethylamine ($100 \mu\text{L}$), and stirred at room temperature for 5 h. The supernatant was removed and the resulting $\text{Fe}_3\text{O}_4\text{@MSL}$ NPs were washed once with ethanol, twice with water, once with acetone, and dried under vacuum.

$\text{Fe}_3\text{O}_4\text{@MSL-L}$. $\text{Fe}_3\text{O}_4\text{@MSL}$ NPs (100 mg) were sonicated in anhydrous ethanol (4 mL) for 10 minutes, and the ligand was added (4 mL from the DMF solution). The solution was heated to 70°C during 24 h, and centrifugated 10 minutes at 21 krpm (27 krcf). The supernatant was removed and the resulting $\text{Fe}_3\text{O}_4\text{@MSL-L}$ NPs were washed once with ethanol, twice with water, once with acetone, and dried under vacuum.

$\text{Fe}_3\text{O}_4\text{@MSN-L}$ metal adsorption. $\text{Fe}_3\text{O}_4\text{@MSN-L}$ NPs (4 mg) were stirred with the metallic complex (M^{n+} , 14 mg), in deionized water (1 mL) for 24 h at room temperature. The NPs were separated from the solution *via* a magnet in 10 minutes, and the solution was removed. Then, the NPs were washed thrice with water, twice in ethanol, once in acetone, and dried under vacuum.

$\text{Fe}_3\text{O}_4\text{@MSL}$ metal adsorption. $\text{Fe}_3\text{O}_4\text{@MSL}$ NPs (4 mg) were stirred with the metallic complex (M^{n+} , 14 mg), in deionized water (1 mL) for 24 h at room temperature. The NPs

were separated from the solution *via* a magnet in 10 minutes, and the solution was removed. Then, the NPs were washed thrice with water, twice in ethanol, once in acetone, and dried under vacuum.

Fe₃O₄@MSL-L metal adsorption. Fe₃O₄@MSL-L NPs (4 mg) were stirred with the metallic complex (Mⁿ⁺, 14 mg), in deionized water (2 mL) for 24 h at room temperature. The NPs were separated from the solution *via* a magnet in 10 minutes, and the solution was removed. Then, the NPs were washed thrice with water, twice in ethanol, once in acetone, and dried under vacuum.

Selectivity study of the metal adsorption. Fe₃O₄@MSL NPs (26 mg) were stirred with all the metallic complexes (Mⁿ⁺, 20 mg each), in deionized water (20 mL) for 2 h at room temperature. The NPs were separated from the solution *via* a magnet in 10 minutes, and the solution was removed. Then, the NPs were washed thrice with water, twice in ethanol, once in acetone, and dried under vacuum.

Nanocontainers metal desorption The acidic desorption of the metal ions was performed at pH 4.5, at which the DTPA ligand is protonated (pK_a values of about 5.6 and 6.1 according to *Martell and Smith, 1989*). Thirty minutes of sonication is used for an efficient desorption at 25°C. In these conditions, the DTPA-Mnⁿ⁺ complexes are not stable anymore, and the ions could be collected in the aqueous supernatant. The NPs were then washed three times in water, and the supernatant fractions were gathered for inductively-coupled plasma (ICP) measurement. According to our preliminary results with ICP measurements on the aqueous removal solution, 90 to 99 of the copper and zinc ions could be removed from the nanocontainers after one desorption process.

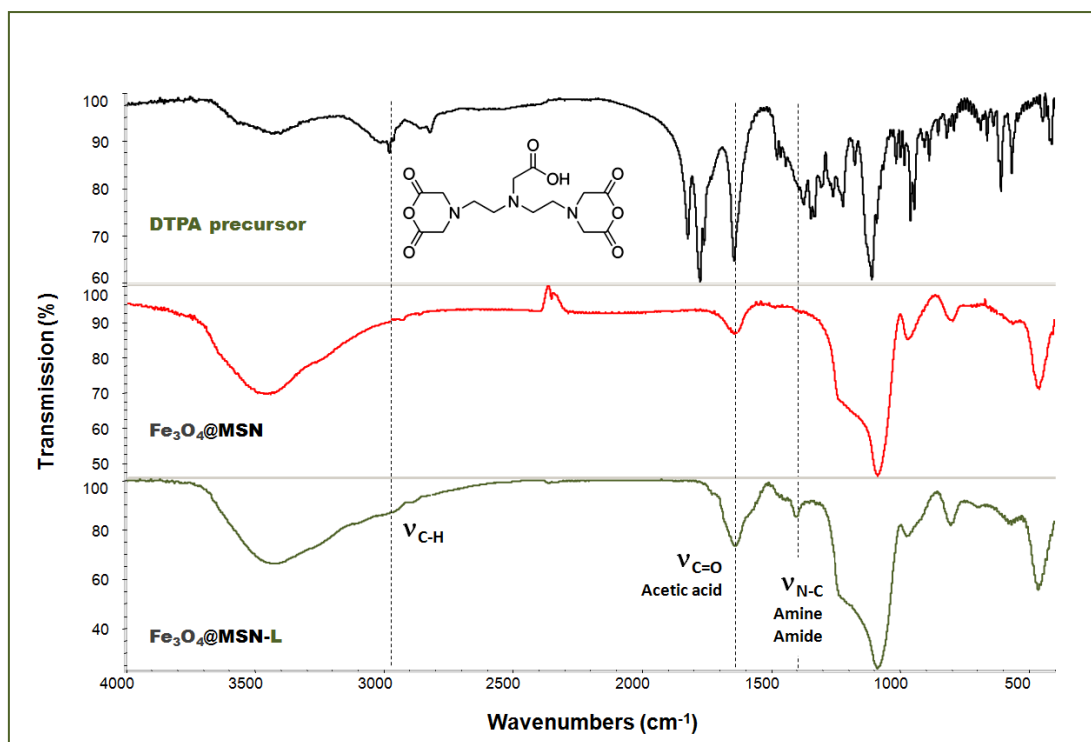


Figure S1. IR spectra of the ligand precursor, the $\text{Fe}_3\text{O}_4\text{@MSN}$ NPs, and $\text{Fe}_3\text{O}_4\text{@MSN-L}$ NPs, demonstrating the ligand functionalization.

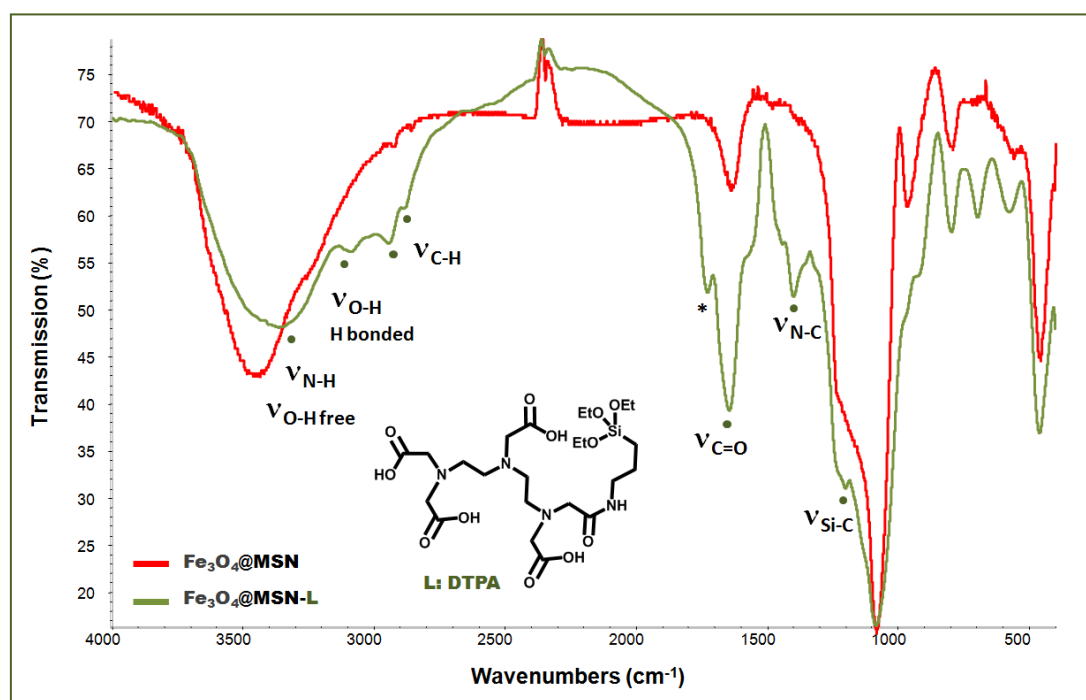


Figure S2. IR spectra of the surfactant-free $\text{Fe}_3\text{O}_4\text{@MSN}$, and $\text{Fe}_3\text{O}_4\text{@MSN-L}$ NPs with a higher ligand functionalization, further demonstrating the DTPA ligand functionalization.

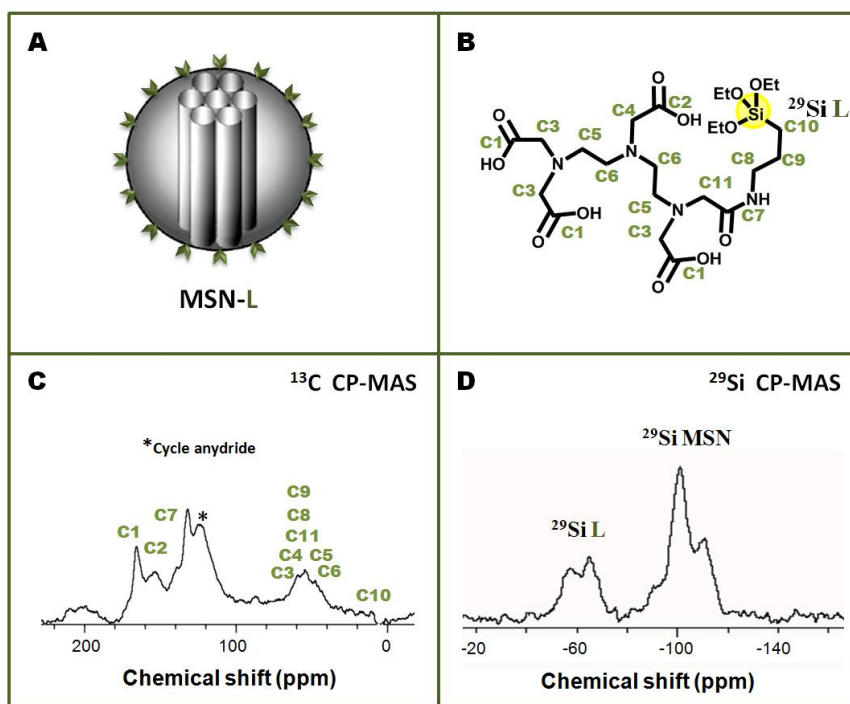


Figure S3. Solid state NMR ^{13}C and ^{29}Si CPMAS spectra (C-D) of a MSN-L NPs control (A), further confirming the alkoxylation of the ligand (B) on the MSN surface.

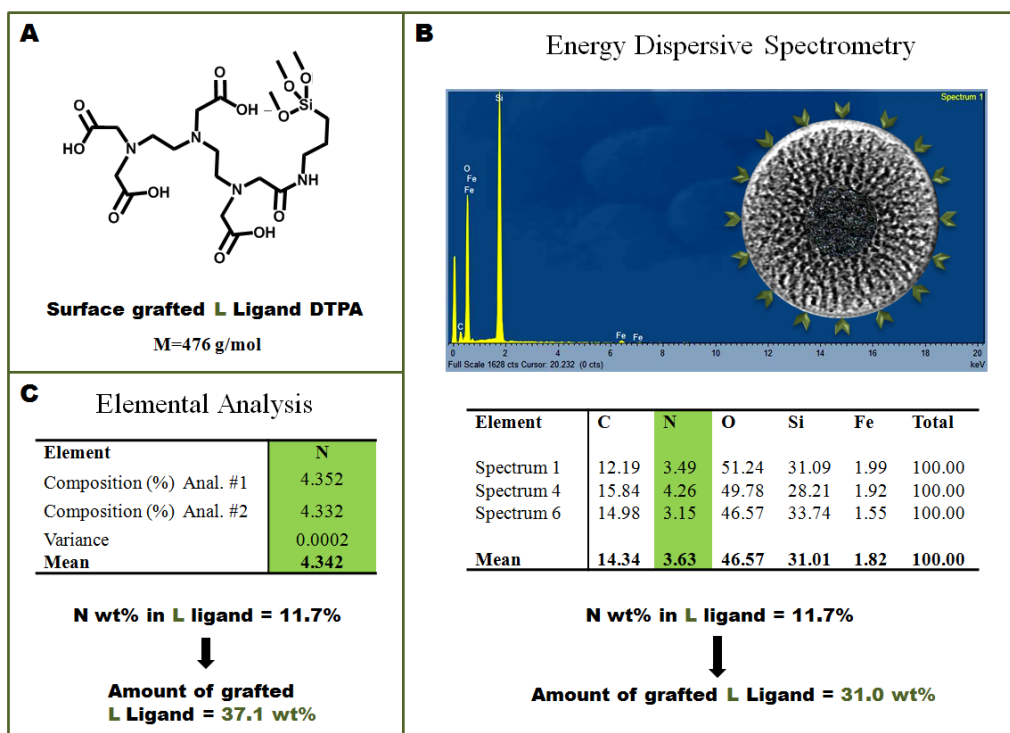


Figure S4. Molecule model used to calculate the ligand grafting on the NPs (A). EDS composition measurement of Fe_3O_4 @MSN-L (B), and the combustion elemental measurement of nitrogen (C).

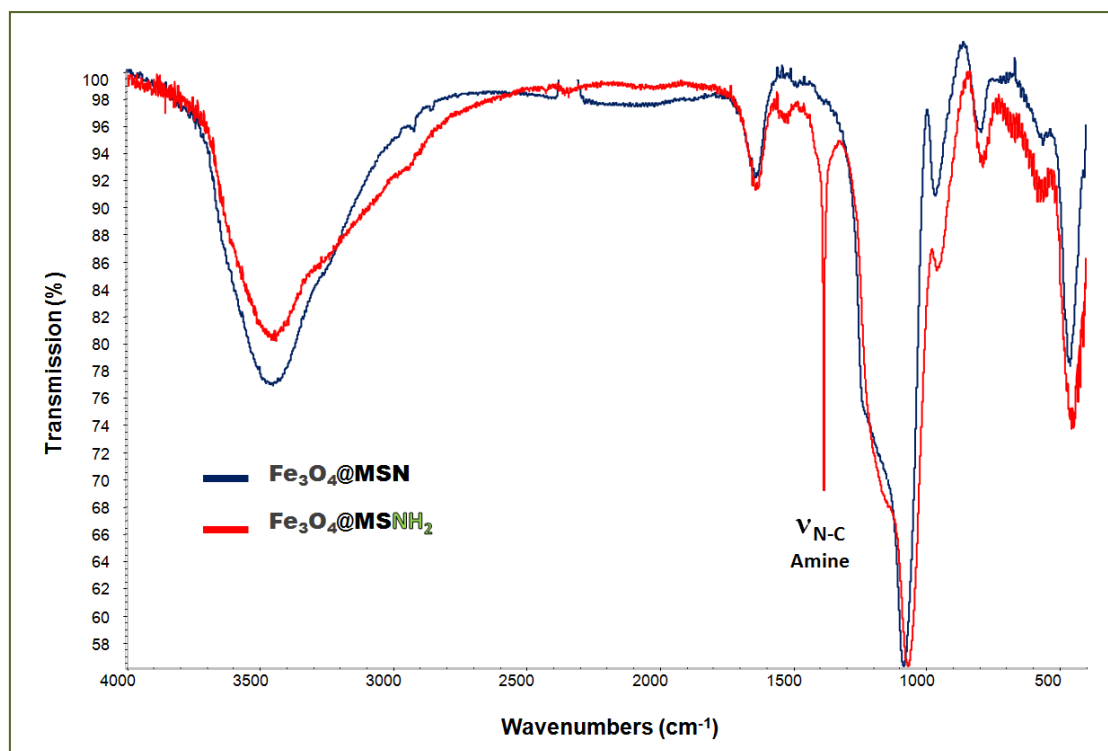


Figure S5. IR spectra of the $\text{Fe}_3\text{O}_4@\text{MSN}$ NPs, and $\text{Fe}_3\text{O}_4@\text{MSNH}_2$ NPs demonstrating the successful encapsulation of amino groups in the MSN framework.

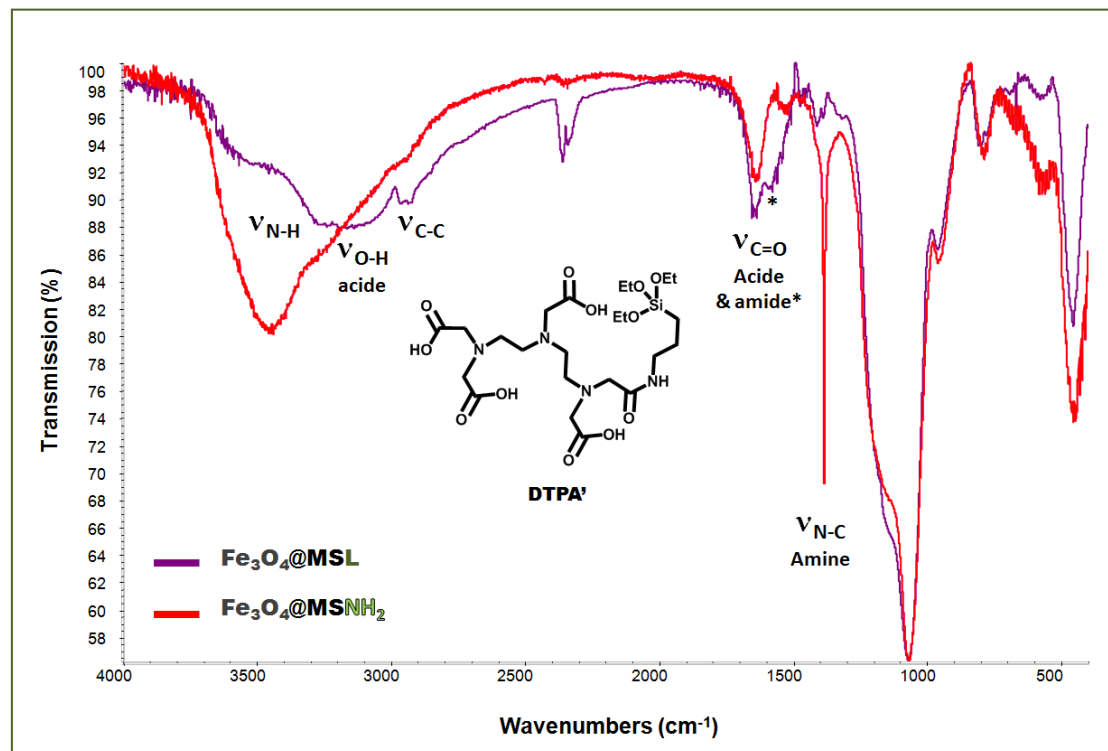


Figure S6. IR spectra of the $\text{Fe}_3\text{O}_4@\text{MSNH}_2$ NPs, and $\text{Fe}_3\text{O}_4@\text{MSL}$ NPs demonstrating the successful grafting of the ligand in the MSN framework.

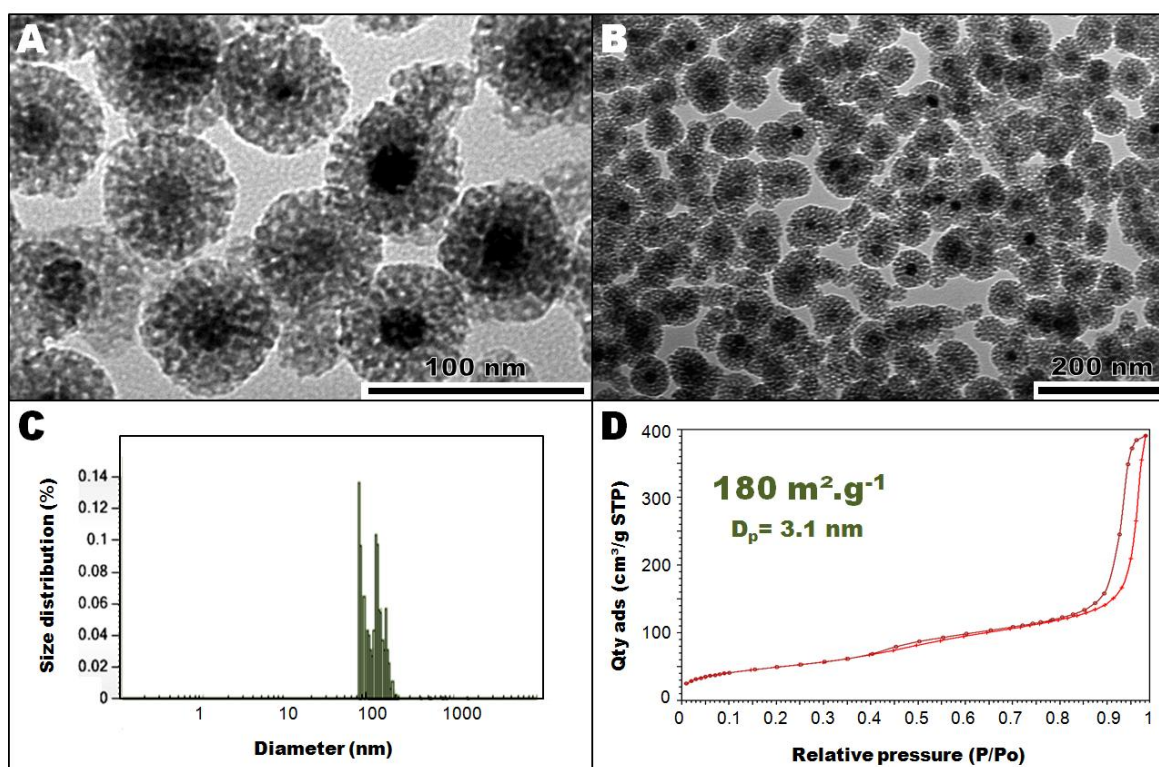


Figure S7. Transmission electron microscopy images (A-B), DLS size distribution (C), and N₂-adsorption-desorption analysis of Fe₃O₄@MSNH₂ NPs (D).

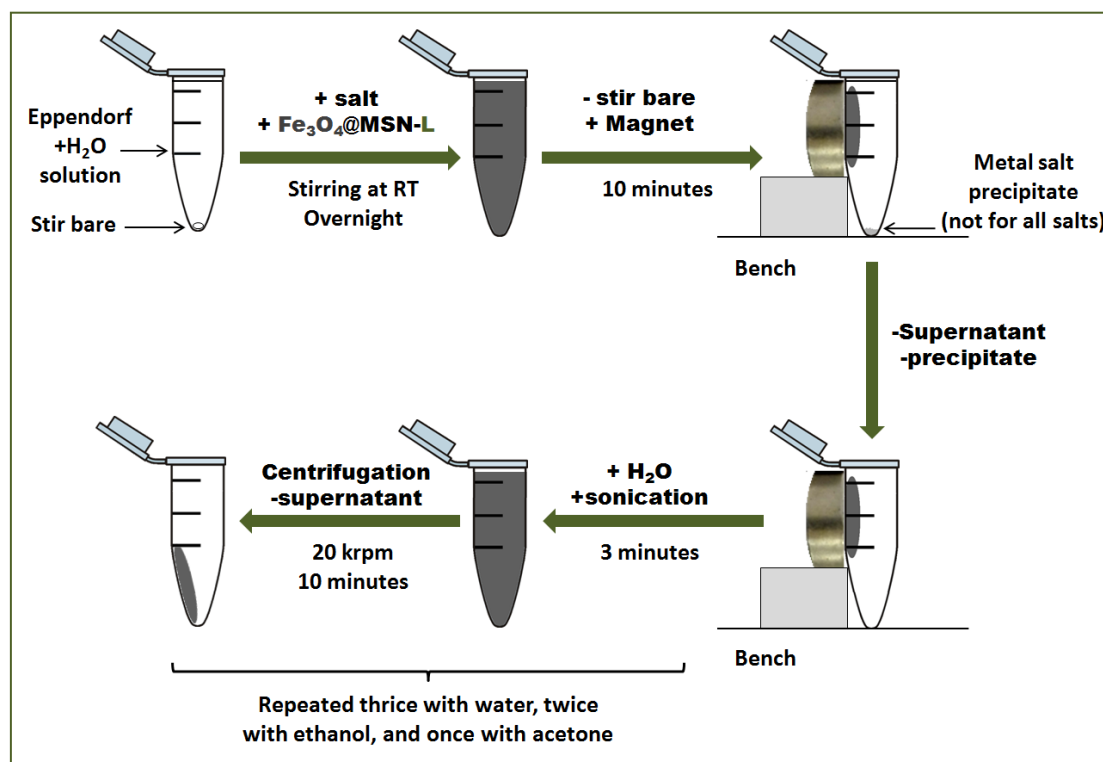


Figure S8. Schematic representation of the experimental settings of the heavy metal removal.

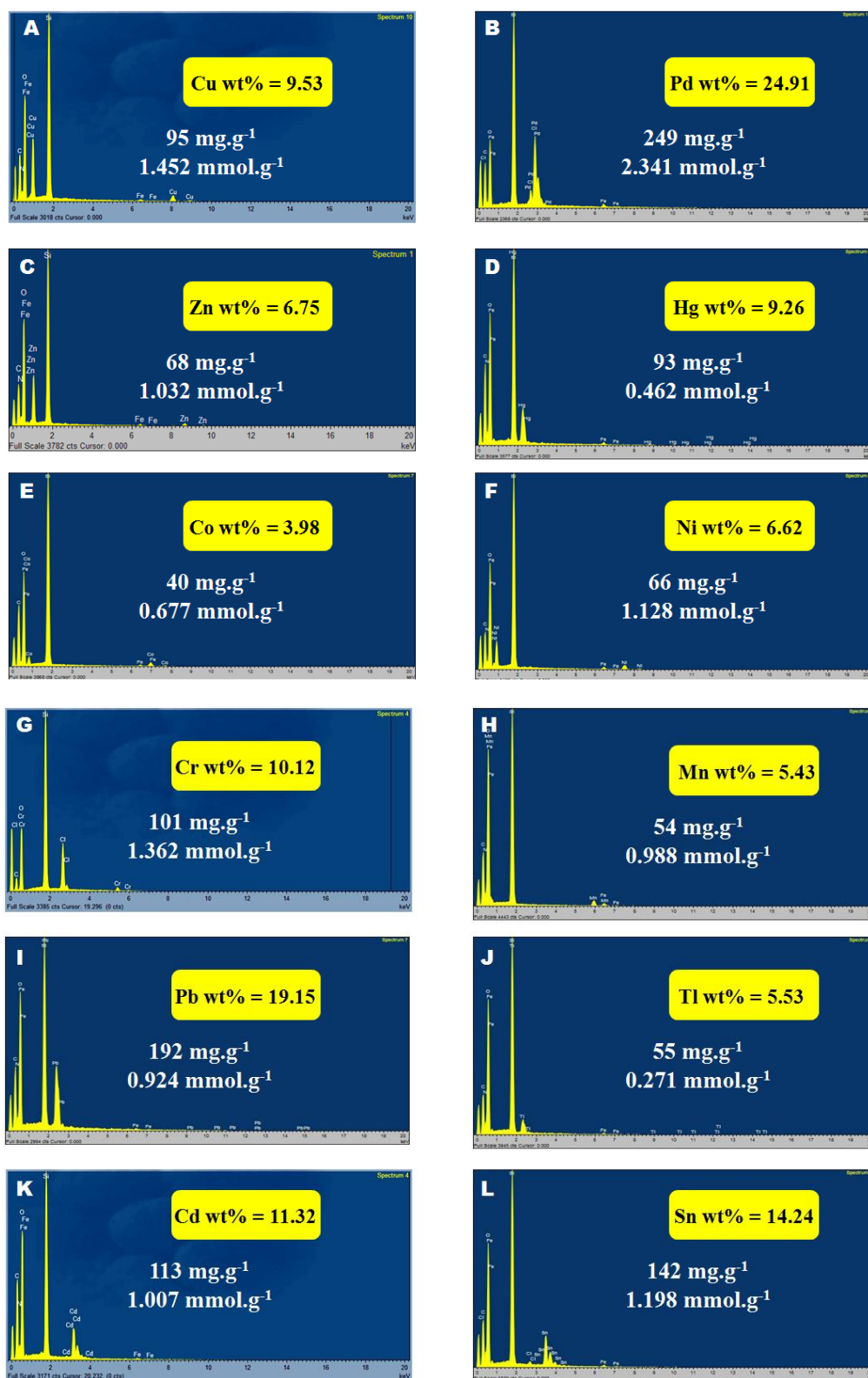


Figure S9. EDS spectra of $\text{Fe}_3\text{O}_4@\text{MSN-L}\cap\text{M}^{\text{n}+}$ and adsorption capacities (A-L).

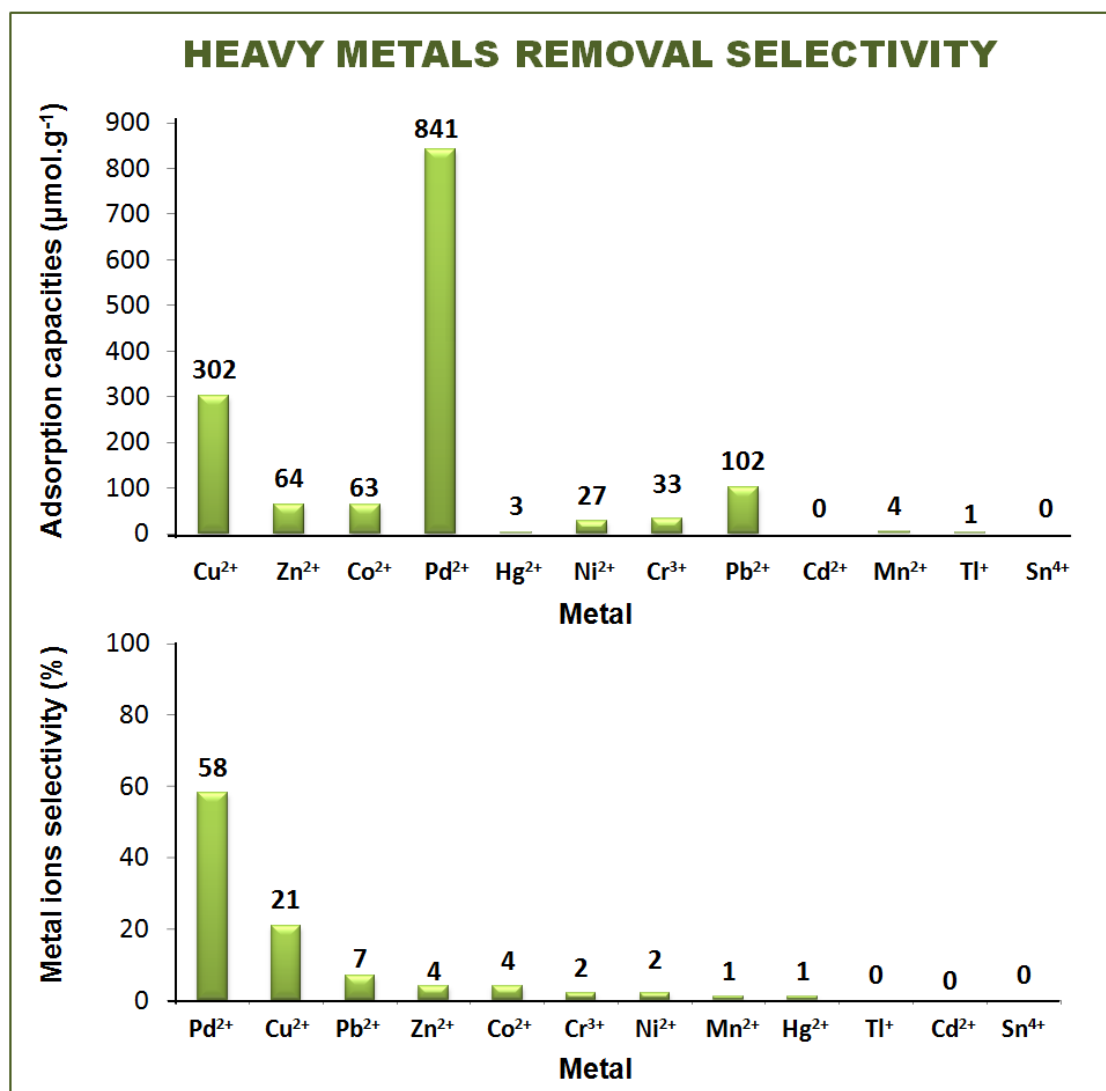


Figure S10. Selectivity of the metal ion removals by the nanocontainers. EDS was used to determine the adsorption capacities.

Table S1-11. EDS statistics of Fe₃O₄@MSN-L∩Mⁿ⁺ compositions for all metals except the magnetic chromium.

FM-L∩Cu ²⁺	C	N	O	Si	Fe	Cu	Total
Spectrum 1	23.18	6.41	31.04	27.38	2.06	9.92	100.00
Spectrum 2	25.44	7.88	41.06	17.64	1.82	6.14	100.00
Spectrum 3	22.12	6.05	33.42	26.13	2.30	9.98	100.00
Spectrum 4	28.66	6.86	34.72	20.08	1.51	8.17	100.00
Spectrum 5	26.40	9.02	40.20	16.67	1.06	6.64	100.00
Spectrum 6	27.92	8.56	31.62	17.72	0.53	13.64	100.00
Spectrum 7	24.88	6.48	32.11	22.28	1.32	12.93	100.00
Spectrum 8	25.30	5.34	34.51	19.83	1.50	13.52	100.00
Spectrum 9	31.55	5.80	33.28	19.34	1.77	8.26	100.00
Spectrum 10	24.91	7.68	40.68	17.70	2.88	6.14	100.00
Mean	26.04	7.01	35.26	20.48	1.68	9.53	100.00
Std. deviation	2.75	1.23	3.90	3.69	0.66	2.97	
Max.	31.55	9.02	41.06	27.38	2.88	13.64	
Min.	22.12	5.34	31.04	16.67	0.53	6.14	

FM-L∩Zn ²⁺	C	N	O	Si	Fe	Zn	Total
Spectrum 1	26.45	8.65	38.95	18.23	1.18	6.55	100.00
Spectrum 2	33.59	10.89	37.67	9.46	0.17	8.22	100.00
Spectrum 3	33.03	7.09	37.93	14.82	1.68	5.45	100.00
Spectrum 4	24.47	6.35	35.98	23.74	1.31	8.16	100.00
Spectrum 5	25.10	8.53	43.65	16.02	1.27	5.43	100.00
Spectrum 6	29.02	8.45	40.60	14.87	1.94	5.11	100.00
Spectrum 7	25.26	7.82	36.15	20.71	1.31	8.75	100.00
Spectrum 8	27.85	8.57	41.44	15.68	1.20	5.27	100.00
Spectrum 9	24.61	7.53	39.88	21.04	1.07	5.88	100.00
Spectrum 10	22.03	5.65	33.44	28.43	1.77	8.67	100.00
Mean	27.14	7.95	38.57	18.30	1.29	6.75	100.00
Std. deviation	3.77	1.45	2.98	5.37	0.49	1.52	
Max.	33.59	10.89	43.65	28.43	1.94	8.75	
Min.	22.03	5.65	33.44	9.46	0.17	5.11	

FM-L∩Co ²⁺	C	N	O	Si	Fe	Co	Total
Spectrum 1	28.59	13.21	40.85	11.92	0.62	4.82	100.00
Spectrum 2	28.92	10.63	42.21	12.97	0.70	4.57	100.00
Spectrum 3	25.12	5.98	34.27	26.56	2.32	5.76	100.00
Spectrum 4	33.34	7.68	39.42	15.20	1.05	3.31	100.00
Spectrum 5	29.62	7.80	42.92	15.90	0.98	2.79	100.00
Spectrum 6	26.06	7.55	45.47	17.13	1.16	2.64	100.00
Spectrum 7	36.01	4.54	34.99	19.32	1.04	4.11	100.00
Spectrum 8	28.14	6.83	44.71	16.85	0.60	2.86	100.00
Spectrum 9	35.62	4.90	27.57	22.70	3.27	5.93	100.00
Spectrum 10	32.58	9.54	41.07	12.32	1.44	3.05	100.00
Mean	30.40	7.86	39.35	17.09	1.32	3.98	100.00
Std. deviation	3.80	2.66	5.54	4.68	0.85	1.24	
Max.	36.01	13.21	45.47	26.56	3.27	5.93	
Min.	25.12	4.54	27.57	11.92	0.60	2.64	

FM-L∩Pd²⁺	C	N	O	Si	Fe	Pd	Total
Spectrum 1	20.00	6.98	33.33	14.67	0.94	24.08	100.00
Spectrum 2	25.97	5.50	30.02	16.88	0.96	20.67	100.00
Spectrum 3	22.70	7.56	32.17	12.16	0.90	24.50	100.00
Spectrum 4	22.40	7.30	30.51	13.22	0.61	25.98	100.00
Spectrum 5	16.35	4.53	29.49	15.57	1.20	32.87	100.00
Spectrum 6	31.23	5.98	27.62	11.99	1.36	21.81	100.00
Spectrum 7	20.52	7.26	36.86	15.51	1.07	18.77	100.00
Spectrum 8	19.71	7.40	36.22	15.27	1.44	19.96	100.00
Spectrum 9	16.57	4.18	25.50	16.01	4.19	33.55	100.00
Spectrum 10	19.24	5.41	28.96	17.61	1.83	26.94	100.00
Mean	21.47	6.21	31.07	14.89	1.45	24.91	100.00
Std. deviation	4.46	1.26	3.62	1.89	1.02	5.10	
Max.	31.23	7.56	36.86	17.61	4.19	33.55	
Min.	16.35	4.18	25.50	11.99	0.61	18.77	

FM-L∩Hg²⁺	C	N	O	Si	Fe	Hg	Total
Spectrum 1	31.69	6.62	33.44	13.26	1.08	13.91	100.00
Spectrum 2	22.38	7.32	39.83	17.72	1.87	10.89	100.00
Spectrum 3	22.15	6.55	43.00	19.28	1.58	7.43	100.00
Spectrum 4	18.33	4.30	43.36	26.19	1.72	6.10	100.00
Spectrum 5	21.60	4.96	45.65	21.90	1.35	4.55	100.00
Spectrum 6	29.14	8.98	36.34	13.75	1.26	10.53	100.00
Spectrum 7	22.47	7.23	36.32	14.02	1.25	18.71	100.00
Spectrum 8	30.14	8.34	38.22	15.21	1.06	7.04	100.00
Spectrum 9	19.80	4.61	44.10	22.52	1.89	7.07	100.00
Spectrum 10	19.23	4.85	39.97	27.75	1.80	6.40	100.00
Mean	23.69	6.37	40.02	19.16	1.49	9.26	100.00
Std. deviation	4.82	1.64	3.98	5.27	0.32	4.33	
Max.	31.69	8.98	45.65	27.75	1.89	18.71	
Min.	18.33	4.30	33.44	13.26	1.06	4.55	

FM-L∩Ni²⁺	C	N	O	Si	Fe	Ni	Total
Spectrum 1	22.35	7.46	40.14	22.24	1.78	6.04	100.00
Spectrum 2	26.43	6.34	41.36	17.33	1.24	7.30	100.00
Spectrum 3	27.54	6.79	34.54	16.79	3.57	10.77	100.00
Spectrum 4	23.70	3.68	46.31	20.87	1.12	4.33	100.00
Spectrum 5	25.55	7.90	38.09	20.30	1.74	6.42	100.00
Spectrum 6	24.06	6.95	40.95	21.18	1.44	5.41	100.00
Spectrum 7	22.02	6.05	32.35	26.99	2.31	10.28	100.00
Spectrum 8	25.82	7.62	42.62	18.14	1.14	4.66	100.00
Spectrum 9	26.43	8.68	43.31	15.55	1.01	5.02	100.00
Spectrum 10	24.36	5.81	43.20	19.39	1.27	5.97	100.00
Mean	24.83	6.73	40.29	19.88	1.66	6.62	100.00
Std. deviation	1.83	1.39	4.24	3.29	0.78	2.24	
Max.	27.54	8.68	46.31	26.99	3.57	10.77	
Min.	22.02	3.68	32.35	15.55	1.01	4.33	

FM-L∩Pb ²⁺	C	N	O	Si	Fe	Pb	Total
Spectrum 1	21.49	6.84	38.44	16.22	0.88	16.13	100.00
Spectrum 2	21.43	6.53	38.09	16.31	0.93	16.72	100.00
Spectrum 3	21.38	7.49	38.32	14.89	1.01	16.90	100.00
Spectrum 4	18.46	5.49	35.00	17.92	0.87	22.26	100.00
Spectrum 5	17.72	5.01	35.38	17.66	1.15	23.08	100.00
Spectrum 6	22.13	7.00	35.48	13.83	0.80	20.75	100.00
Spectrum 7	23.05	7.85	36.41	13.39	0.74	18.57	100.00
Spectrum 8	23.36	7.49	36.07	14.07	0.73	18.29	100.00
Spectrum 9	22.75	6.63	36.43	14.54	0.55	19.09	100.00
Spectrum 10	22.91	7.29	34.93	14.70	0.52	19.66	100.00
Mean	21.47	6.76	36.45	15.35	0.82	19.15	100.00
Std. deviation	1.92	0.90	1.37	1.59	0.20	2.34	
Max.	23.36	7.85	38.44	17.92	1.15	23.08	
Min.	17.72	5.01	34.93	13.39	0.52	16.13	

FM-L∩Cd ²⁺	C	N	O	Si	Fe	Cd	Total
Spectrum 1	26.81	7.83	38.55	13.14	0.55	13.13	100.00
Spectrum 2	24.99	7.19	41.09	13.38	0.78	12.57	100.00
Spectrum 3	22.68	6.77	40.63	20.76	0.32	8.84	100.00
Spectrum 4	26.00	7.78	40.20	14.29	0.49	11.23	100.00
Spectrum 5	20.04	5.42	40.60	23.46	0.49	9.98	100.00
Spectrum 6	21.32	5.49	40.77	22.47	0.37	9.58	100.00
Spectrum 7	21.18	5.37	39.93	23.20	0.32	10.00	100.00
Spectrum 8	25.97	6.84	36.26	14.61	0.61	15.71	100.00
Spectrum 9	20.57	5.06	40.90	23.44	0.22	9.80	100.00
Spectrum 10	26.22	6.46	40.82	13.60	0.55	12.35	100.00
Mean	23.58	6.42	39.98	18.24	0.47	11.32	100.00
Std. deviation	2.67	1.03	1.50	4.75	0.17	2.11	
Max.	26.81	7.83	41.09	23.46	0.78	15.71	
Min.	20.04	5.06	36.26	13.14	0.22	8.84	

FM-L∩Mn ²⁺	C	N	O	Si	Fe	Mn	Total
Spectrum 1	22.71	6.65	41.41	22.76	1.63	4.84	100.00
Spectrum 2	23.30	7.19	39.79	22.43	2.43	4.87	100.00
Spectrum 3	22.29	6.04	39.29	24.73	2.14	5.50	100.00
Spectrum 4	23.27	7.65	43.70	20.01	1.66	3.73	100.00
Spectrum 5	22.55	6.07	39.78	24.95	1.80	4.85	100.00
Spectrum 6	24.18	6.49	38.95	23.08	2.22	5.08	100.00
Spectrum 8	22.22	3.63	33.14	32.58	1.50	6.92	100.00
Spectrum 9	26.97	7.54	38.29	17.44	0.72	9.04	100.00
Spectrum 10	27.16	8.44	42.00	17.19	1.14	4.07	100.00
Mean	23.85	6.63	39.59	22.80	1.69	5.43	100.00
Std. deviation	1.92	1.37	2.95	4.64	0.54	1.63	
Max.	27.16	8.44	43.70	32.58	2.43	9.04	
Min.	22.22	3.63	33.14	17.19	0.72	3.73	

FM-L\capSn⁴⁺	C	N	O	Si	Fe	Sn	Total
Spectrum 1	14.56	0.00	42.82	27.46	1.82	13.33	100.00
Spectrum 2	16.21	0.00	43.69	25.78	1.21	13.11	100.00
Spectrum 3	24.63	5.46	43.85	11.92	0.63	13.52	100.00
Spectrum 4	24.96	5.91	44.98	12.01	0.58	11.56	100.00
Spectrum 5	21.36	0.00	44.19	16.37	1.44	16.65	100.00
Spectrum 6	19.71	2.69	43.06	16.76	1.41	16.37	100.00
Spectrum 7	21.40	0.00	44.66	16.41	1.09	16.44	100.00
Spectrum 8	20.68	4.72	41.11	18.74	1.53	13.22	100.00
Spectrum 9	20.45	6.65	41.44	17.58	1.25	12.63	100.00
Spectrum 10	22.09	0.00	43.16	18.04	1.14	15.57	100.00
Mean	20.60	2.54	43.30	18.11	1.21	14.24	100.00
Std. deviation	3.25	2.86	1.27	5.06	0.38	1.84	
Max.	24.96	6.65	44.98	27.46	1.82	16.65	
Min.	14.56	0.00	41.11	11.92	0.58	11.56	

FM-L\capTl⁺	C	N	O	Si	Fe	Tl	Total
Spectrum 1	22.63	8.37	44.00	18.52	1.12	5.37	100.00
Spectrum 2	25.78	6.17	31.77	26.16	1.77	8.35	100.00
Spectrum 3	27.47	7.39	33.04	23.59	1.62	6.89	100.00
Spectrum 4	26.45	9.03	40.84	17.30	1.49	4.89	100.00
Spectrum 5	24.65	9.21	42.40	17.34	2.10	4.30	100.00
Spectrum 6	23.51	7.38	42.26	20.74	1.05	5.06	100.00
Spectrum 7	27.88	9.24	38.27	17.61	1.28	5.72	100.00
Spectrum 8	30.24	9.92	41.55	13.14	0.98	4.17	100.00
Spectrum 9	33.57	13.07	35.85	11.73	0.72	5.07	100.00
Spectrum 10	24.06	7.17	38.58	22.58	2.11	5.51	100.00
Mean	26.62	8.69	38.86	18.87	1.42	5.53	100.00
Std. deviation	3.34	1.93	4.15	4.51	0.47	1.25	
Max.	33.57	13.07	44.00	26.16	2.11	8.35	
Min.	22.63	6.17	31.77	11.73	0.72	4.17	

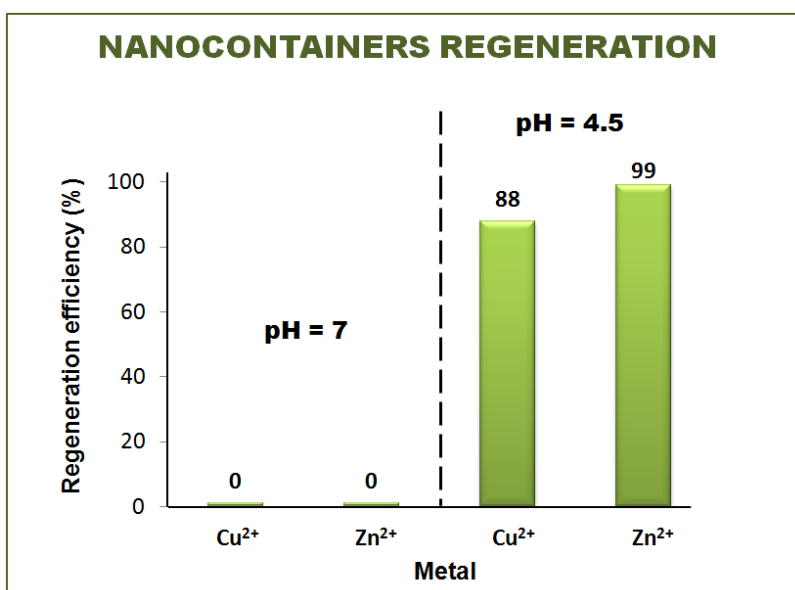


Figure S11. Nanocontainers regeneration determined by ICP measurements of the collected acidic solution used for the copper and zinc ion desorptions.

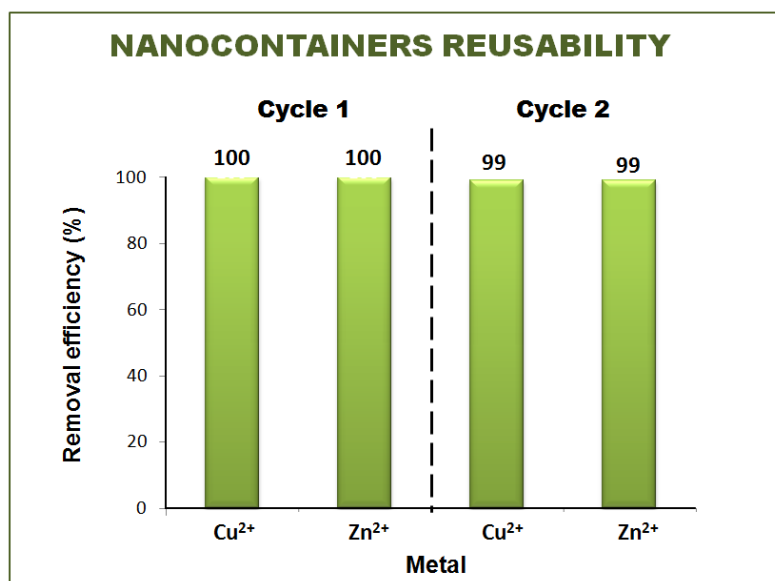


Figure S12. Reusability of the nanocontainers after regeneration for heavy metals removal.

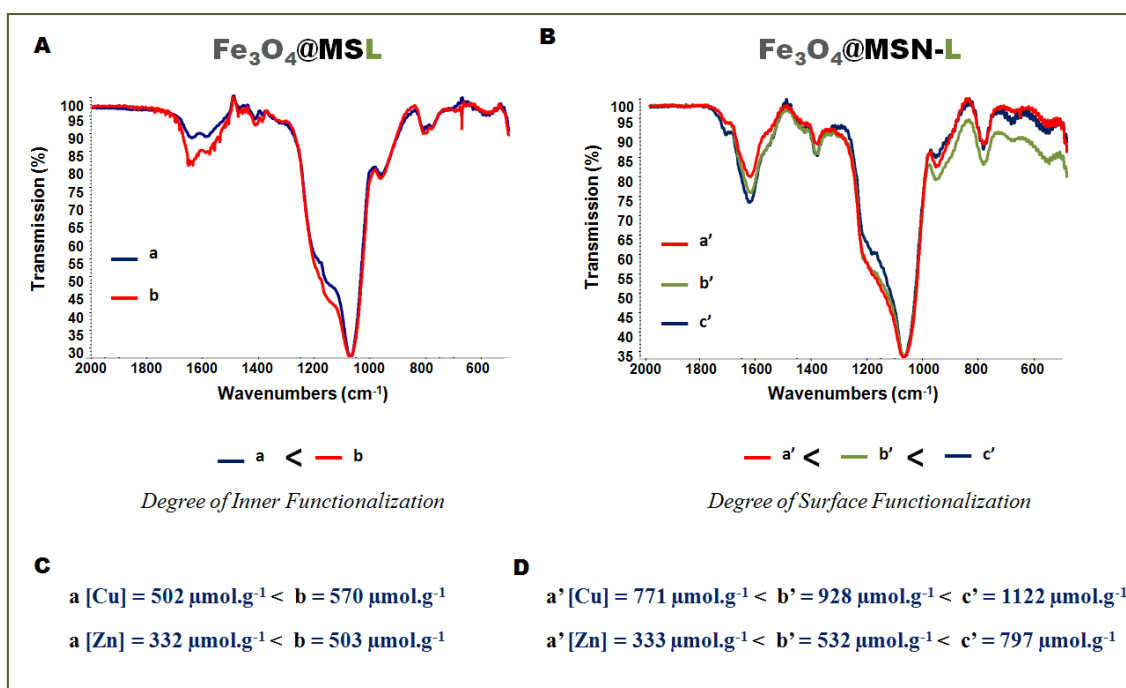


Figure S13. Study of the influence of the degree of ligand functionalization, in the pores or on the surface, on the heavy metals removal. IR spectra of the $\text{Fe}_3\text{O}_4@\text{MSL}$, and $\text{Fe}_3\text{O}_4@\text{MSN-L}$ NPs with different degrees of functionalization (A-B). EDS metal adsorption capacities of $\text{Fe}_3\text{O}_4@\text{MSL} \cap \text{Mn}^{n+}$ (C), and $\text{Fe}_3\text{O}_4@\text{MSN-L} \cap \text{Mn}^{n+}$ (D), demonstrating the influence of the ligand in the pollutant removal.

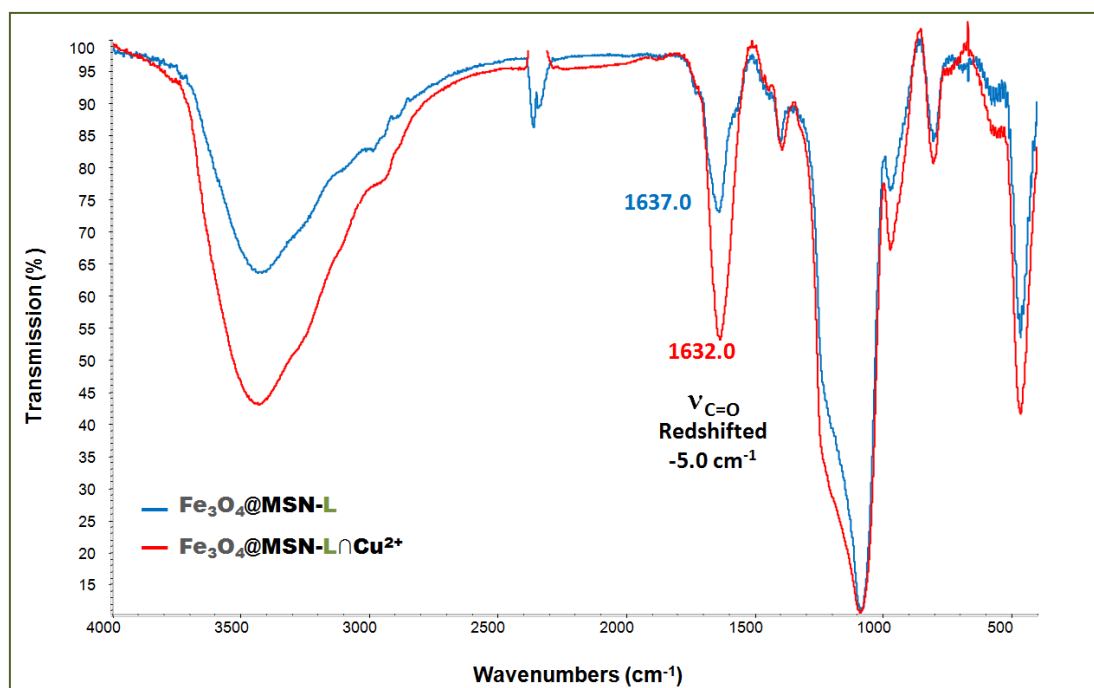


Figure S14. IR spectra of the $\text{Fe}_3\text{O}_4@\text{MSN-L}$ and $\text{Fe}_3\text{O}_4@\text{MSN-L} \cap \text{Cu}^{2+}$ NPs, confirming the successful complexation of copper ions.

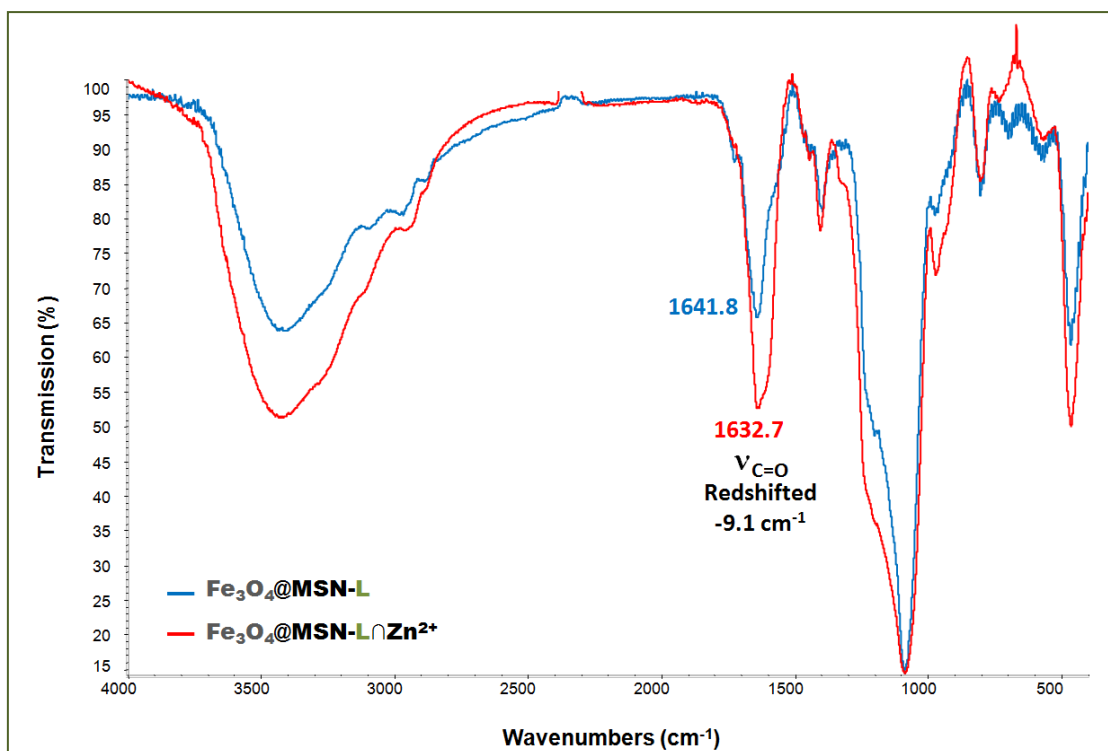


Figure S15. IR spectra of the $\text{Fe}_3\text{O}_4@\text{MSN-L}$ and $\text{Fe}_3\text{O}_4@\text{MSN-L}\cap\text{Zn}^{2+}$ NPs, confirming the successful complexation of zinc ions.

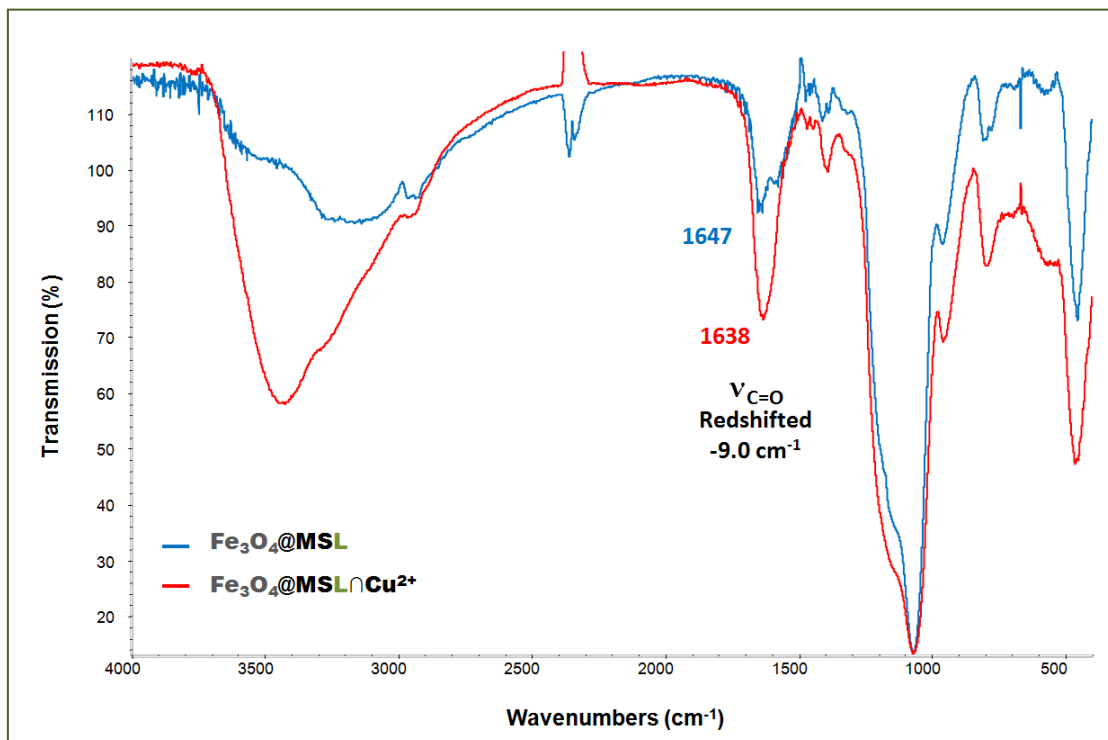


Figure S16. IR spectra of the $\text{Fe}_3\text{O}_4@\text{MSL}$ and $\text{Fe}_3\text{O}_4@\text{MSL}\cap\text{Cu}^{2+}$ NPs, confirming the successful complexation of copper ions.

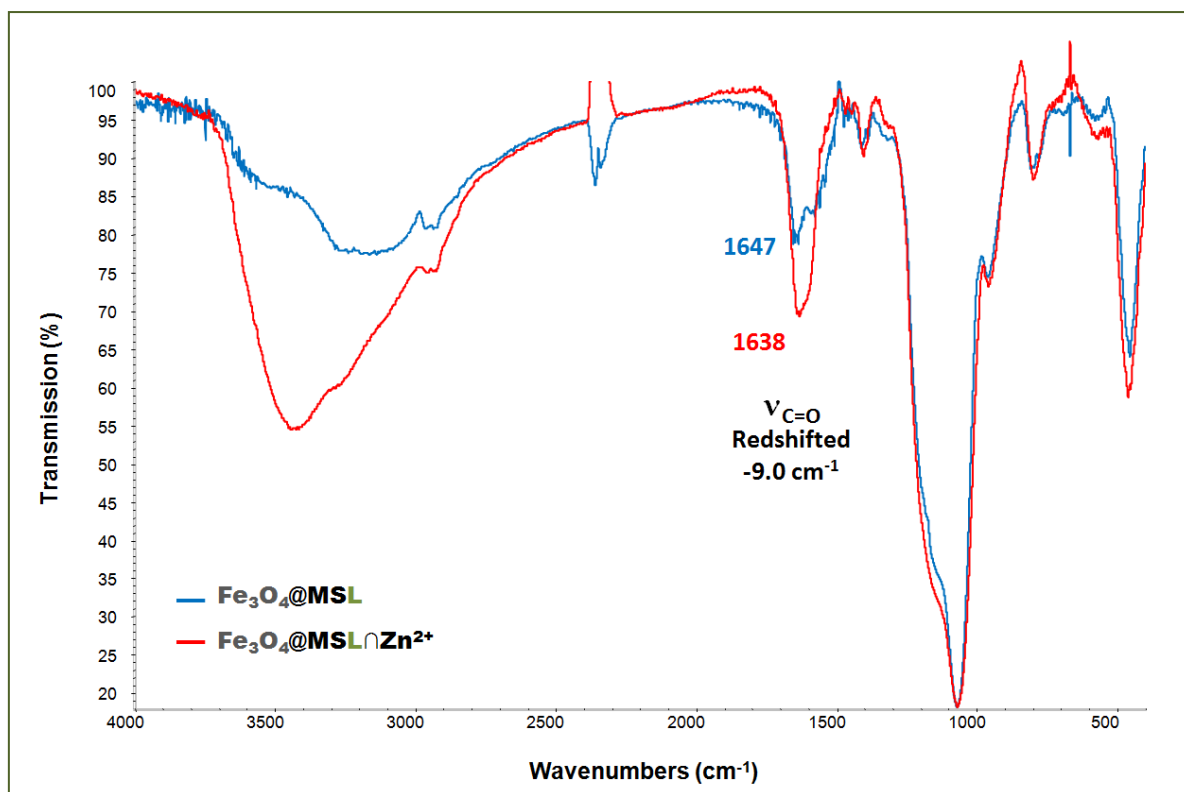


Figure S17. IR spectra of the $\text{Fe}_3\text{O}_4@\text{MSL}$ and $\text{Fe}_3\text{O}_4@\text{MSL}\cap\text{Zn}^{2+}$ NPs, confirming the successful complexation of zinc ions.

CONCLUSION

In this dissertation various nanomaterials have been designed, studied, and applied in the field of nanomedicine. The main focus of the research was aimed at two-photon theranostic nanomedicine with different therapeutic features such as photoisomerization for drug and nucleic acid deliveries, photocleavage-triggered drug delivery, and photodynamic therapy via photosensitizer-based NPs.

In chapters 2 and 3, gold core mesoporous silica shell nanoparticles were prepared by a novel one-pot method and studied as nanoplatforms for plasmonically-actuated cargo release. Nanovalves- and polymer-coated core-shell NPs were described, and the controlled-photodegradation of mesoporous silica shells was studied as a function of the laser power, wavelength, and gold core NPs size.

In chapter 4, azobenzene-functionalized MSN such as nanoimpellers and nanovalves were used for the first time as *in-vitro* two-photon-triggered drug delivery nanocarriers. Additionally, an extension of this strategy was performed with effective nucleic acid delivery on cancer cells via azobenzene-ammonium moieties, with up to 50% of gene silencing. Iron oxide core MSN or PMO shell NPs were also elaborated for nucleic acid delivery. The design of two-photon-sensitive large pore ammonium-nanoimpellers is under investigation, in order to protect siRNA strands from the biological medium.

In chapter 5, a novel two-photon photosensitizer was developed and co-condensed in MSN for photodynamic therapy and drug delivery. The photophysical properties of the resulting two-photon-sensitive MSN were compared with different synthetic approaches, and the best materials were applied as multifunctional two-photon theranostics. Hence, efficient two-photon fluorescence imaging was combined with PDT and drug delivery on MCF-7 cancer cells.

In chapter 6, bridged silsesquioxane NPs were prepared via a versatile synthetic procedure which produced disulfide- and photosensitizer-disulfide-based NPs. Such BS NPs were applied as biodegradable NPs for photodynamic therapy *in-vitro* with 60% of selective cell killing. BS NPs solely composed of photosensitizers for two-photon PDT were described for the first time in chapter 7. The two-photon properties of photosensitizer-based BS NPs were greatly enhanced by the addition of gold nanospheres within or upon the BS NPs, so that two-photon fluorescence imaging and PDT were exalted in cells. Ultrabright intracellular imaging with total cell killing were observed.

In chapter 7 and 8, various periodic mesoporous organosilica NPs were developed. PMO NPs were configured for two-photon-actuated PDT and synergistic drug delivery in cells, and gold core PMO shell nanocarriers were found to enhance the PDT effect. Besides, ethylene-disulfide-based PMO nanorods and nanospheres were studied for the first time as biodegradable PMO NPs for efficient anticancer drug delivery. Furthermore, original multipodal benzene-ethylene PMO hybrid NPs with crystal-like architectures were constructed and fully characterized. The chemical modification of the core and pod

compartments might open a wide variety of applications in nanotechnology. Another perspective would come from the ability to control a subsequent growth of benzene-silica cores on the ethylene-silica pods of the multipodal NPs, which may lead to 3D lattices of hybrid PMO NPs.

Finally in chapter 9, the knowledge acquired to design magnetic MSN and PMO for nucleic acid delivery was used for pollutant removal applications. A versatile heavy metal ion removal was performed via DTPA-functionalized Fe_3O_4 @MSN nanocontainers. The DTPA ligand was found to be an effective strategy to complex various toxic metal ions, and the porous silica framework was used to enhance the removal efficiencies.

The *in-vivo* applications of the most promising nanodevices developed during the thesis is the next challenge. Particularly, bridged silsesquioxane NPs functionalized with gold nanocrystals, and potentially with iron oxide nanocrystals, would be interesting nanomaterials to study on mice. Large pore magnetic ammonium-nanoimpellers for two-photon-triggered siRNA delivery could also be studied *in-vivo*, with PEGylation of the NPs surface to enhance circulation times and stealthiness in biological environment.

I- INTRODUCTION

1- Nanomédecine théranostique à deux-photons

La nanomédecine activée à deux-photons est devenue l'un des principaux candidats à l'accomplissement de la sélectivité spatiotemporelle nécessaire pour le traitement du cancer. En effet, la raison d'être de l'application médicale des nanotechnologies dans le domaine du traitement du cancer est de diminuer et supprimer les effets secondaires causés par les techniques actuelles telles que la chimiothérapie et la radiothérapie, à cause de leur manque de sélectivité. Parmi diverses nanoparticules (NPs), les NPs de silice mésoporeuse ont attiré une attention croissante dans la dernière décennie en raison de leur faible cytotoxicité, de leur internalisation cellulaire et excrétion, et de leur capacité à combiner de nombreuses fonctions à la fois pour la *thérapie* et le *diagnostic* de cancers via un seul nanovéhicule : la nanomédecine *théranostique*.

L'excitation à deux-photons est un phénomène rare d'optique non-linéaire impliquant la combinaison de deux photons pour ne produire qu'un seul photon. Dans la Figure 1A, une transition énergétique entre un état fondamental et un état excité, représentée par une flèche verticale pointant vers le haut, est causée par une absorption à un-photon à 380 nm. L'absorption à deux-photons implique quant à elle la somme de deux photons en général de mêmes énergies, égales à la moitié de la transition énergétique, soit dans ce cas 760 nm (Figure 1B).

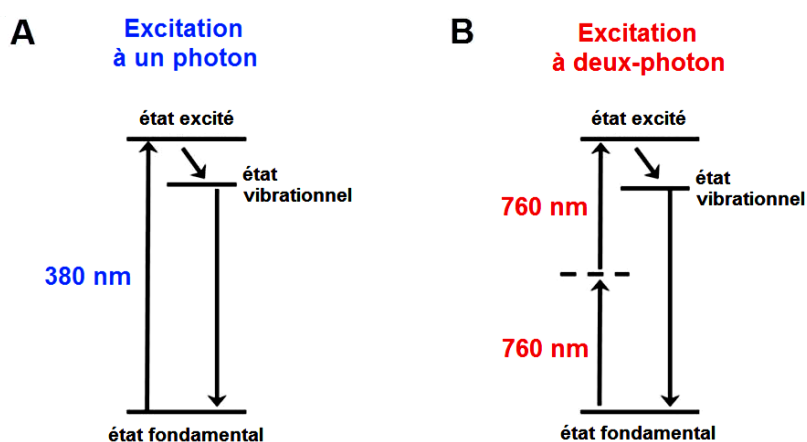


Figure 1. Excitations à un- et à deux-photons pour une même transition énergétique.

L'absorption à deux-photons est rare car la section efficace d'absorption (σ_2) à deux-photons de molécule organique est généralement très faible. De plus, les molécules à σ_2 importantes n'étant généralement pas commerciales, des connaissances poussées en photophysique et en synthèse organique sont nécessaires pour disposer de ces composés. On note que, dans la Figure 1B, l'excitation à deux-photons est réalisée dans le proche Infra-Rouge ce qui permet à la nanomédecine à deux-photons non seulement de bénéficier d'une résolution spatiale remarquable (Figure 2A-B), mais aussi du maximum de pénétration laser dans les tissus biologiques (Figure 2C), ce qui induit à la fois une meilleure efficacité optique et un traitement plus sécurisé pour l'organisme.

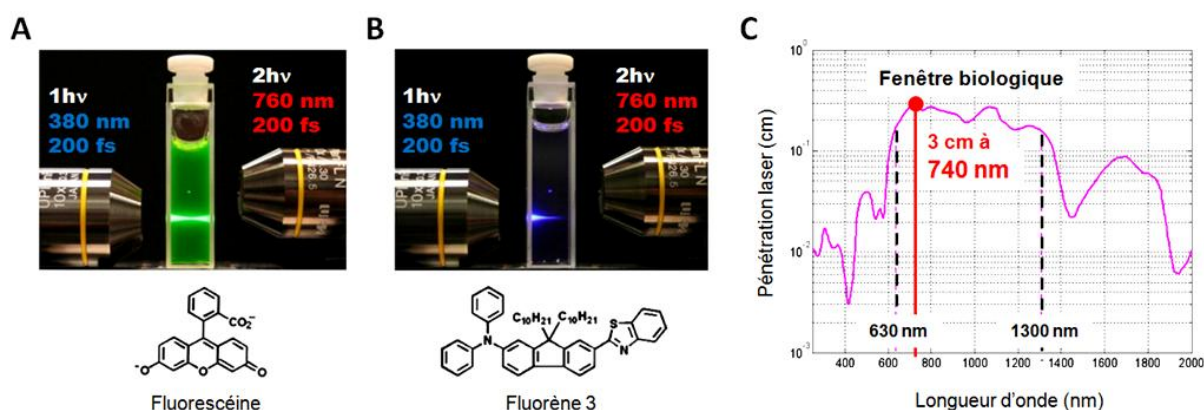


Figure 2. Comparaison de l'excitation à un- et à deux-photons pour la fluorescéine (A) et le fluorène (B). Fenêtre biologique du proche Infra-Rouge où la de pénétration laser est maximale dans les tissus biologiques.

2- Les nanomatériaux synthétisés et appliqués

Dans cette thèse, quatre types de matériaux seront étudiés : Les nanoparticules de silice mésoporeuse (MSN), les NPs d'organosilice mésoporeuse, les NPs de polysilsesquioxanes pontés (BS), et les NPs d'organosilice mésoporeuse périodique (PMO) (voir Figure 3).

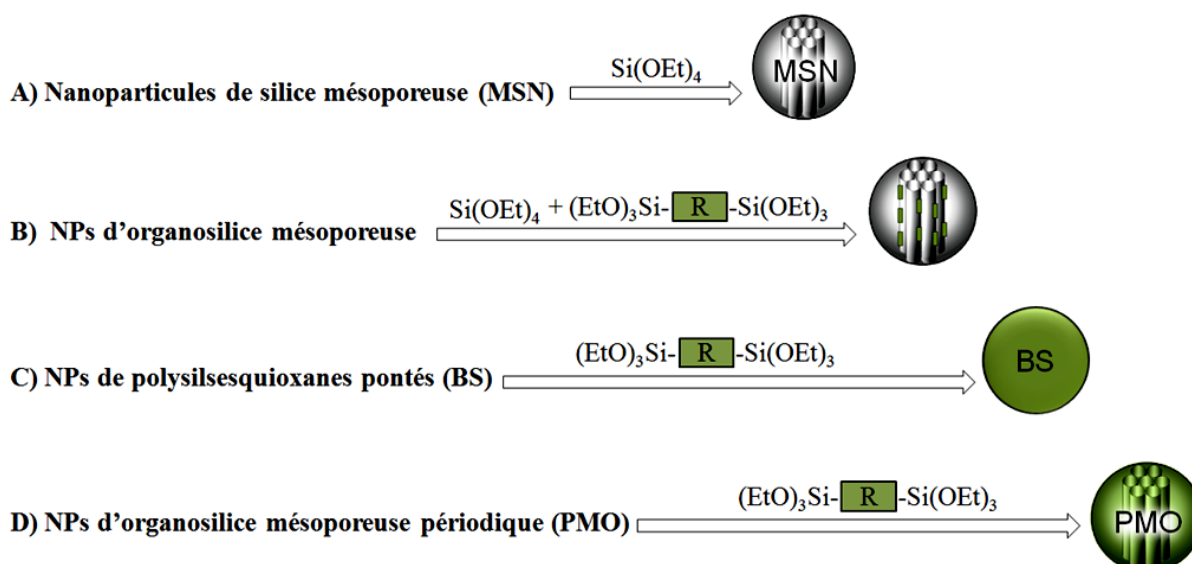


Figure 3. Différents matériaux mis en œuvre durant la thèse et leurs précurseurs de synthèse.

Premièrement, les MSN sont typiquement obtenues à partir d'un précurseur de silice tel le tétraéthoxysilane (TEOS), lequel condense dans un mélange d'eau, de catalyseur d'hydroxyde de sodium, et d'agent structurant de type bromure de cetyltriméthylammonium (CTAB) (Figure 3, stratégie A). Le template de CTAB permet l'obtention d'une structure silicique mésoporeuse hexagonale, appelée MCM-41. Les MSN ont attiré l'intérêt de multiples axes de recherches et ont conduit à de nombreuses publications ces dernières années de par leur haute surface spécifique (800-1200m²/g), notamment disponible pour la catalyse, et le transport et relargage de principe actif. Cette dernière application est rendue pertinente grâce à la faible cytotoxicité de la silice, ainsi que la stabilité suffisante en milieu biologique, l'internalisation cellulaire, et l'excrétion des MSN.

Deuxièmement, la co-condensation d'un organoalcoxysilane avec le précurseur de silice donne lieu aux NPs d'organosilice mésoporeuse (Figure 3, stratégie B). Le fragment organique d'intérêt est alors réparti aléatoirement dans la matrice de silice, il s'agit de MSN fonctionnalisées. On note, que ces NPs peuvent également être obtenues par post-fonctionnalisation de MSN via la chimie du silicium qui est couramment utilisée pour introduire un ou plusieurs groupements organiques en vue d'une application donnée. Depuis, une quinzaine d'années, des milliers de publications scientifiques ont été réalisées sur les MSN, le relargage de molécules ou de macromolécules était toujours en croissance au

commencement de la thèse en 2011, avec plus de 350 articles sur le sujet pour cette seule année.

Troisièmement, les NPs de polysilsesquioxanes pontés (BS), peuvent être synthétisées à partir de la condensation d'un bis ou multi-organoalcoxysilane sans agent structurant (Figure 3, stratégie C). En conséquence, les nanomatériaux de type BS ne sont pas poreux, et possède le plus haut contenu possible de fragment organique. Bien que les polysilsesquioxanes soient connus et étudiés depuis plusieurs dizaines d'années, l'échelle nanométrique des BS est très rarement rapportée dans la littérature (hormis les NPs polysilsesquioxanes polyédriques (POSS)), car le contrôle de la condensation est très délicat sans l'utilisation de précurseur de silice. En 2014, la préparation de NPs de BS est encore limitée à une dizaine d'études toutes applications confondues.

Quatrièmement, les NPs d'organosilice mésoporeuse périodique (PMO). Ces nano-objets sont –comme les précédentes NPs de BS- obtenues par seule condensation de bis ou multi-organoalcoxysilane, cette fois en présence d'un agent structurant (Figure 3, stratégie D). Elles sont dites « périodiques » car les fragments organiques sont périodiquement répétés dans la structure des NPs. Ces matériaux sont de loin les plus difficiles à élaborer parmi ceux mentionnés jusqu'alors, et les PMO à l'échelle nanométrique sont également très rarement rapportés, leur contrôle ne datant que de quelques années (Guan *et al. Nanoscale* **2012**, 4, 6588).

Dans le cadre de cette thèse, des NPs cœur-coquille ont également été réalisées, alliant des cœurs de nanocristaux d'or, ou d'oxyde de fer, avec des coquilles de MSN, de MSN fonctionnalisées, de BS, ou encore de PMO. La suite de ce résumé de travaux de thèse sera présentée en trois parties, l'élaboration et les applications tout d'abord de MSN et de MSN fonctionnalisées, puis celles de NPs de BS, et enfin celles des NPs de PMO.

II- ELABORATION ET APPLICATIONS DE MSN

1- Relargage contrôlé de molécules par effet plasmonique à un-photon

Des NPs cœur-coquille à base de nanocristaux d'or et de silice mésoporeuse (Au@MSN) ont été préparées par une nouvelle synthèse en une étape, et ont été caractérisées par microscopie électronique à transmission (MET, Figure 4a). L'utilisation de NPs d'or a pour but de mettre à profit l'effet de la résonance plasmon de surface (RPS) pour induire une chaleur locale lorsqu'une irradiation sur la bande de plasmon est effectuée (Figure 4b). Les pores des Au@MSN ont été chargés en molécules hôtes (rhodamine B), puis bouchés par des « nanovalves » (Figure 4c). Ces machines moléculaires appelées nanovalves sont des complexes supramoléculaires entre des chaînes aminoalkyles et des anneaux moléculaires de type cucurbit[6]uril dont la constante de liaison diminue exponentiellement avec la température de sorte qu'à 60°C les interactions sont rompues (Figure 4c).

Les Au@MSN@Nanovalves chargées en rhodamine B furent ensuite testées en solution aqueuse en tant que matériaux pour la délivrance contrôlée par effet RPS. La sensibilité thermique des nanovalves a ensuite été confirmée par une expérience de chauffage « externe » des NPs plongées dans une cuve d'eau à température ambiante, puis à 60°C. La ligne de base du profil de relargage en Figure 4d indique la bonne encapsulation des molécules cargos, tandis que le relargage instantané causé par l'élévation externe de la température confirme la réalisation du nanosystème escompté. Une élévation interne et locale de la température des Au@MSN a ensuite été réalisée par irradiation des NPs sur la bande plasmon de l'or, ce qui a induit aussi un relargage instantané (Figure 4e). Par ailleurs, l'influence de la puissance laser, de la longueur d'onde d'excitation, ainsi que la celle de la taille de nanocristaux d'or a permis un contrôle de la photodégradation de la silice (Figure 4f).

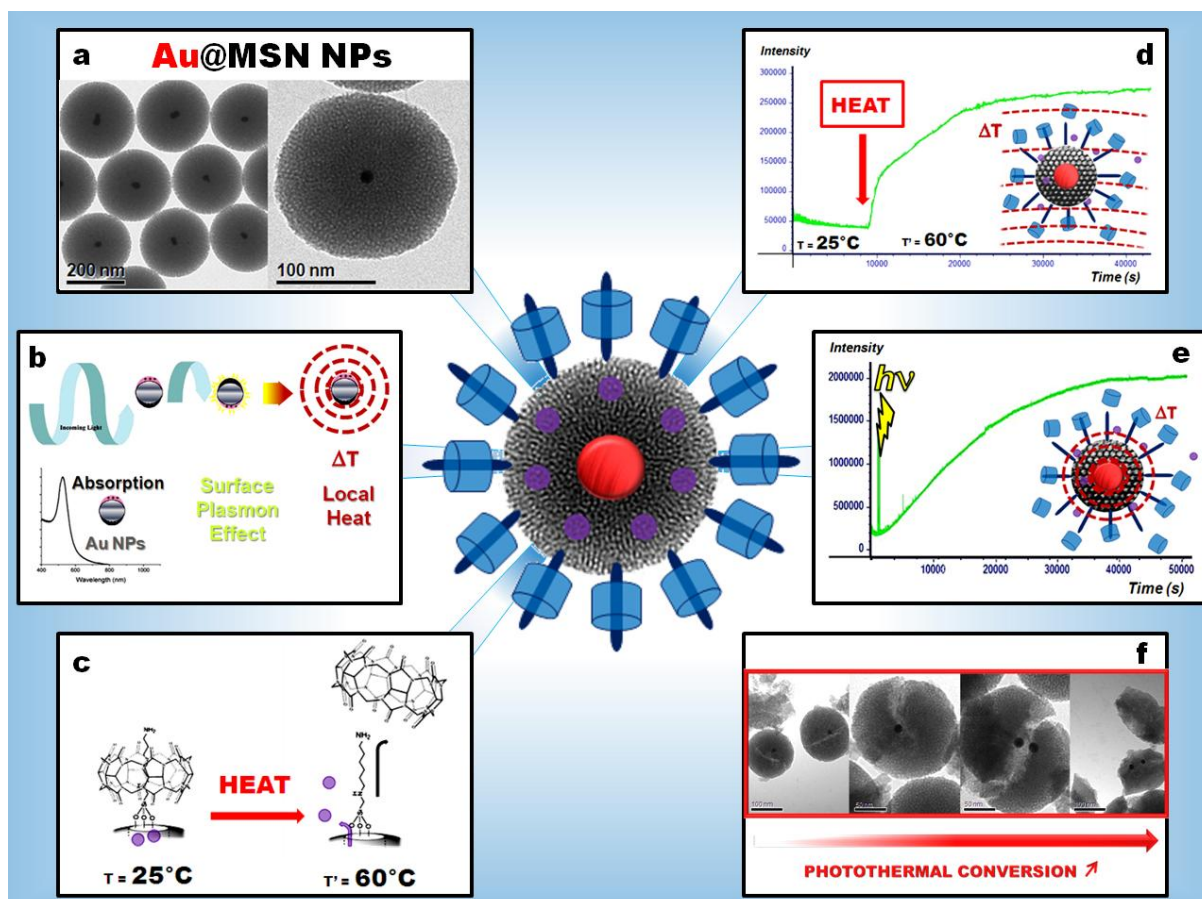


Figure 4. Images de MET des NPs Au@MSN (a). Illustration de la chaleur locale générale par effet RPS (b). Représentation des nanovalves thermosensibles greffées sur des Au@MSN chargées en molécules hôtes (c). Profil de relargage de molécules hôtes encapsulées dans les Au@MSN@Nanovalves via la chaleur externe d'un solvant chauffé (d) ou interne de l'effet RPS (e). Images de MET démontrant la photodégradation des NPs après irradiation dans des conditions spécifiques.

2- Relargage contrôlé de principe actif à deux-photons via des MSN

L'étude des MSN pour la délivrance de molécules a été ensuite étendue à l'activation biphotonique. En effet, l'irradiation à un-photon dans le domaine du visible, tel que pour les nanosphères d'or, n'est pas compatible avec des applications biologiques pour la thérapie de cancers. Des MSN-Azobenzènes –aussi appelées *nanorotors*– chargées en molécules anticancéreuse (camptothécine) ont été configurées pour une délivrance à deux-photons permettant une excellente sélectivité spatiotemporelle du traitement (Figure 5).

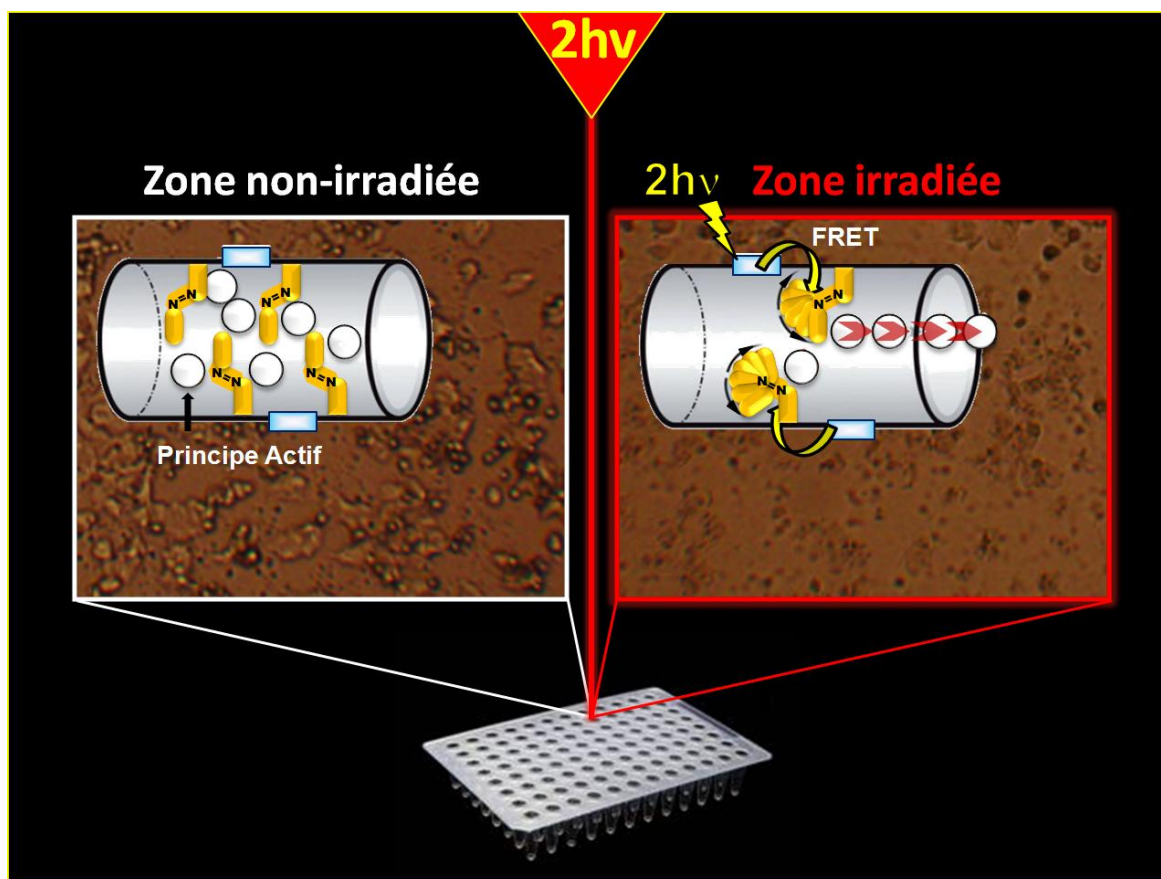


Figure 5. Sélectivité spatiale du relargage induit par excitation biphotonique des nanorotors.

Les azobenzènes absorbent dans le domaine de l'UV, il fallu donc préparer un fluorophore avec une σ_2 importante, et le co-condenser avec le TEOS et les dérivés d'azobenzènes, afin d'obtenir ces fonctions dans les pores des MSN (voir NPs « MAF » en Figure 6). Ainsi, le transfert d'énergie par résonance Förster (FRET) entre les fluorophores et les azobenzènes a permis le relargage de camptothécine *in-vitro* dans des cellules MCF-7 de cancer du sein. Le mécanisme de délivrance implique la photoisomérisation continue des diphenylazobenzènes, lesquels expulsent les molécules thérapeutiques hôtes.

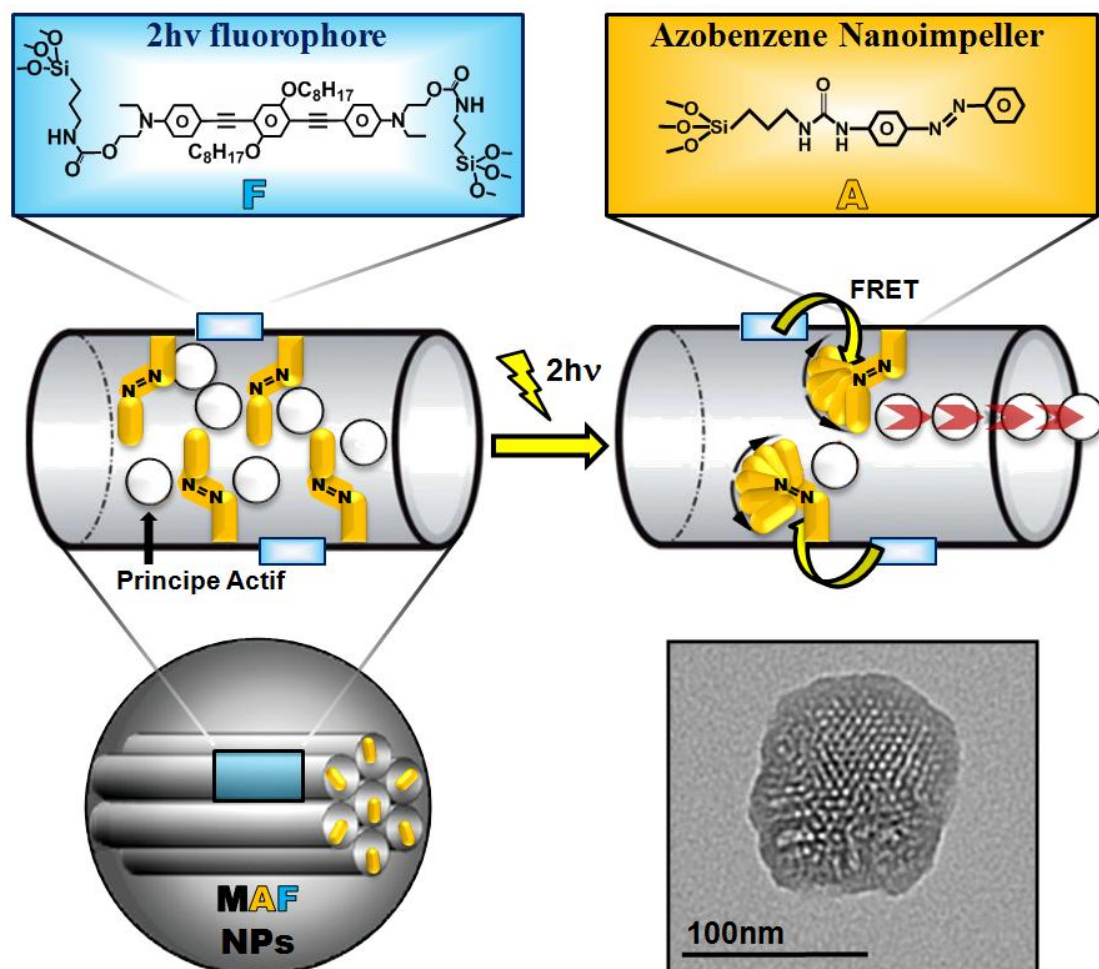


Figure 6. Structure des NPs MAF contenant les azobenzènes et les fluorophores biphotoniques pour opérer le relargage par effet FRET. Images de MET des NPs.

D'autre part, les azobenzènes ont également été fonctionnalisés en surface de MSN contenant des fluorophores sensibles à deux-photons (voir Figure 7); l'idée étant de complexer ces derniers avec des β -cyclodextrine pour former des nanovalves bouchant les pores des NPs chargés en principe actifs. Par effet FRET le relargage a aussi été induit par excitation biphotonique produisant la photoisomérisation des azobenzènes décomplexant les β -cyclodextrines pour permettre la libération des cargos (Figure 7A).

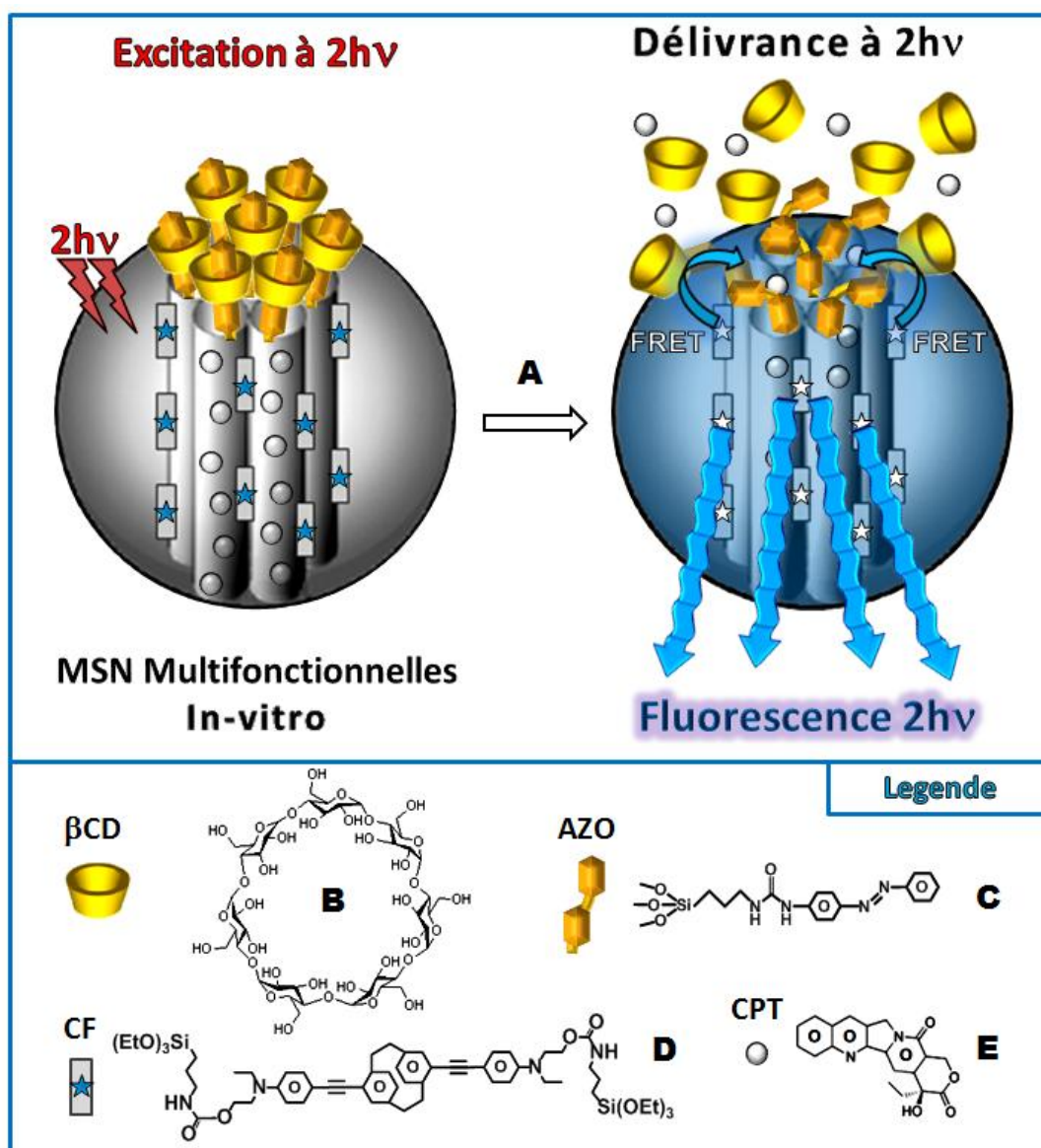


Figure 7. Relargage de camptothecin par activation à deux-photons via des MSN@Nanovalves multifonctionnelles (A). Les nanovalves sont composées de complexes azobenzènes- β -cyclodextrine (B-C), lesquels sont déstabilisés par les transferts d'énergies issus des fluorophores CF (D) dans les MSN, ce qui cause le relargage de la camptothecin (E).

Les MSN@Nanovalves multifonctionnelles ont permis un relargage contrôlé dans le temps et l'espace via les propriétés biphotoniques, ainsi qu'une fluorescence intracellulaire des nano-objets. En effet, contrairement aux nanorotors étudiés précédemment, les fluorophores ne se trouvent pas toujours à proximité des azobenzènes ce qui permet une meilleure imagerie *in-vitro* (Figure 8).

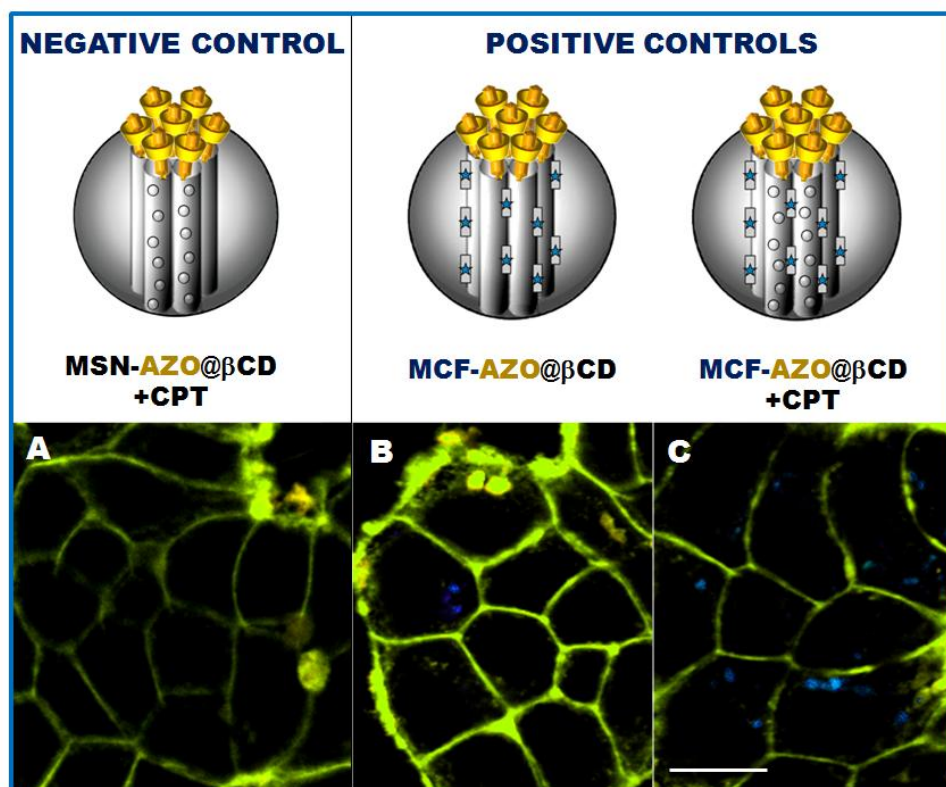


Figure 8. Fluorescence à deux-photons in-vitro via des nanovalves fonctionnalisées sur des MSN (contrôle négatif, A), et des nanovalves fonctionnalisées sur des MSN sensibles à deux-photons (MCF) (contrôles positifs, B-C).

3- Photothérapie dynamique à deux-photons via des MSN

Des MSN sensibles à deux-photons (M2PS) ont été élaborées pour opérer de la photothérapie dynamique (PTD) biphotonique. La PTD est une thérapie du cancer utilisant des molécules photosensibles (photosensibilisateurs) qui engendrent un effet cytotoxique par génération de dérivés réactifs de l'oxygène après irradiation. Les nanomatériaux ont été synthétisés à partir de co-condensation du TEOS avec un tétra-organoalcoxysilane photosensible à deux-photons (2PS) élaboré pendant la thèse (Figure 9).

Premièrement, il a été observé que la méthode de synthèse influe grandement d'une part sur le contrôle de la morphologie et de l'agrégation du matériau, et d'autre part, sur la modulation des propriétés deux-photons des M2PS (Figure 9). Cette constatation a été corrélée avec l'état d'agrégation du 2PS, ainsi que l'étude des rendements de fluorescence et des σ_2 .

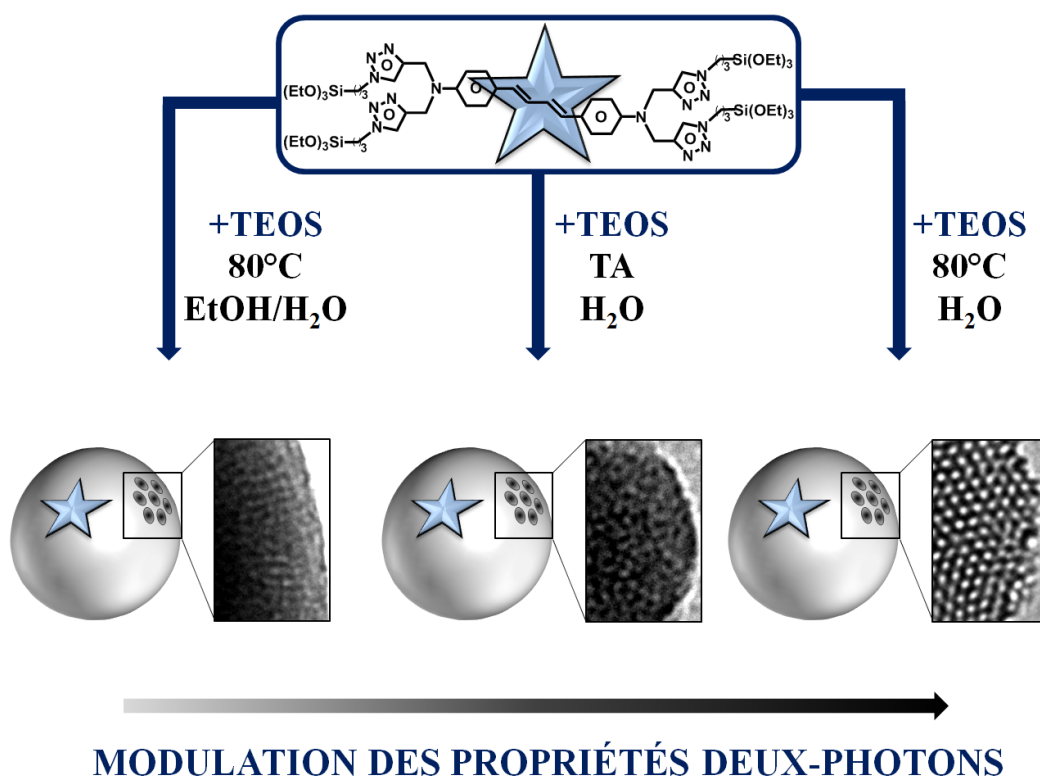


Figure 9. Influence de méthode synthèse de M2PS sur leurs propriétés deux-photons. Les NPs sont obtenues à partir de TEOS et du 2PS (encadré ci-haut).

Deuxièmement, les meilleurs nanomatériaux M2PS ont été utilisés pour l'élaboration de systèmes multifonctionnels pour la délivrance de principes actifs, l'imagerie de fluorescence, et la PTD à deux-photons (voir Figure 10). Typiquement, les M2PS possèdent une structure mésoporeuse à organisation hexagonale (voir MET Figure 11A), et sont des nanosphères monodisperses non-agrégées de 80 nm, comme l'indiquent clairement les techniques de microscopie électronique à balayage (MEB) et de diffusion dynamique de la lumière (DDL) (Figure 11B-C). De plus, la spectroscopie UV-visible a confirmé l'encapsulation du 2PS avec une bande à 384 nm (Figure 11D), et ce, avec la conservation d'une haute surface spécifique, appropriée au transport de molécules cargos (Figure 11E). La section efficace d'absorption maximale de ces matériaux a atteint 200 GM à 700 nm (Figure 11F).

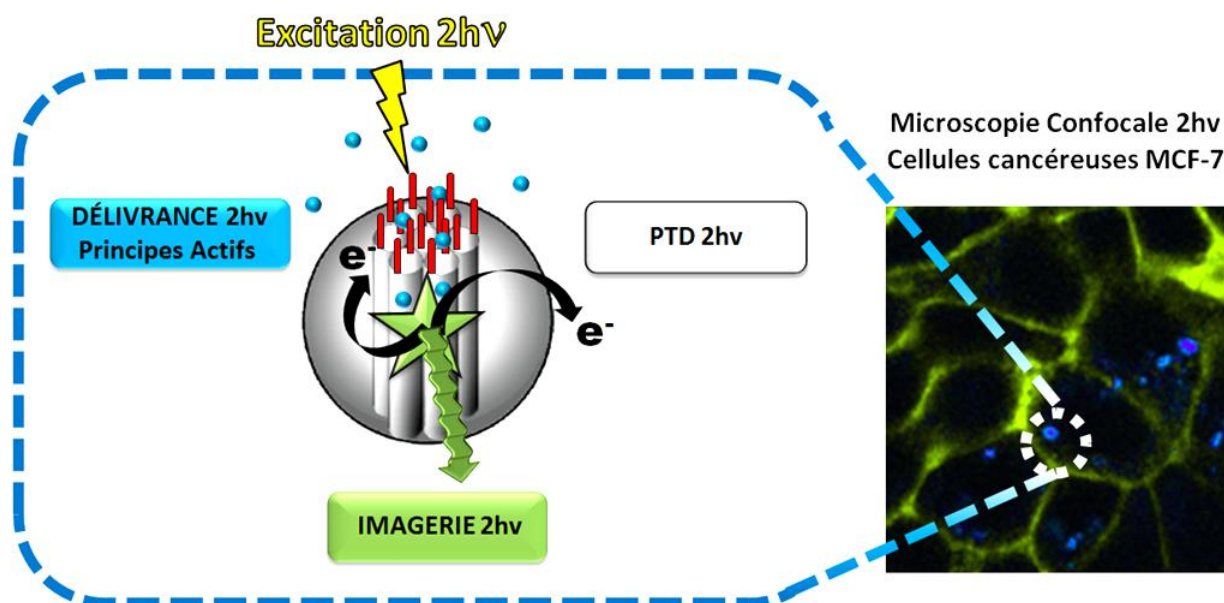


Figure 10. Multifonctionnalité des M2PS-Nanoponts pour la thérapie et le diagnostic de cancer.

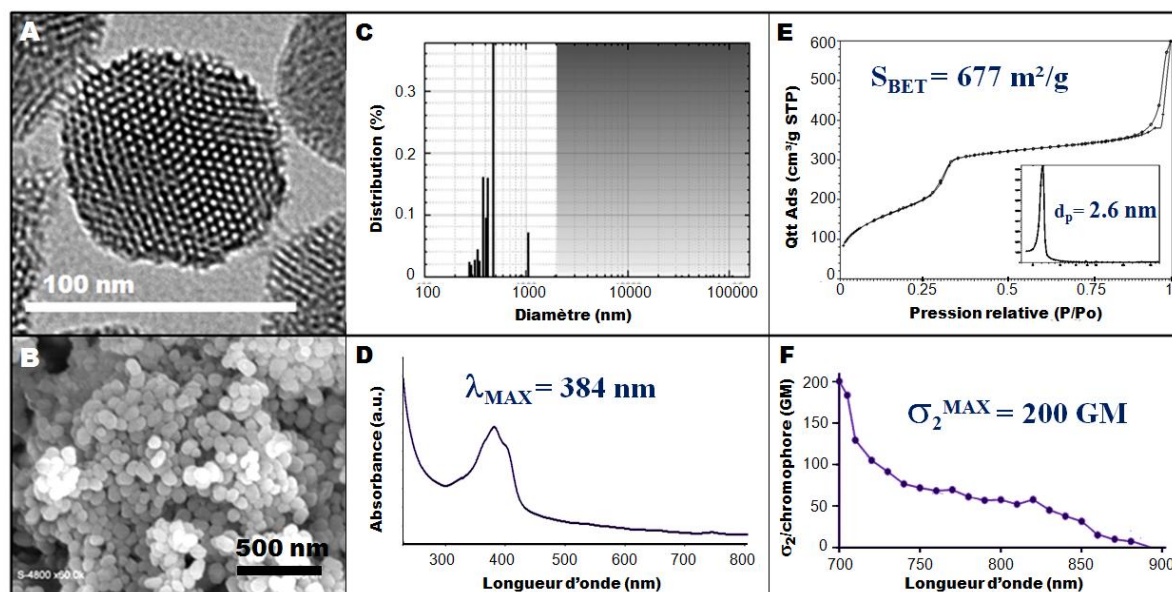


Figure 11. Image MET et MEB (A et B respectivement), distribution en taille (C), spectre UV-visible (D), isotherme d'adsorption-désorption d'azote (E), et profil de σ_2 des M2PS en fonction la longueur d'onde (F).

La fonctionnalité de délivrance a été mise au point par l'utilisation de nanoponts moléculaires afin d'encapsuler des molécules de principes actifs dans les pores des M2PS (Figure 12). Ces ponts étant à base de disulfures, le transfert électronique qu'opèrent les fragments 2PS présent dans les NPs permet l'ouverture des nanoponts à la demande par irradiation à un- ou deux-photons.

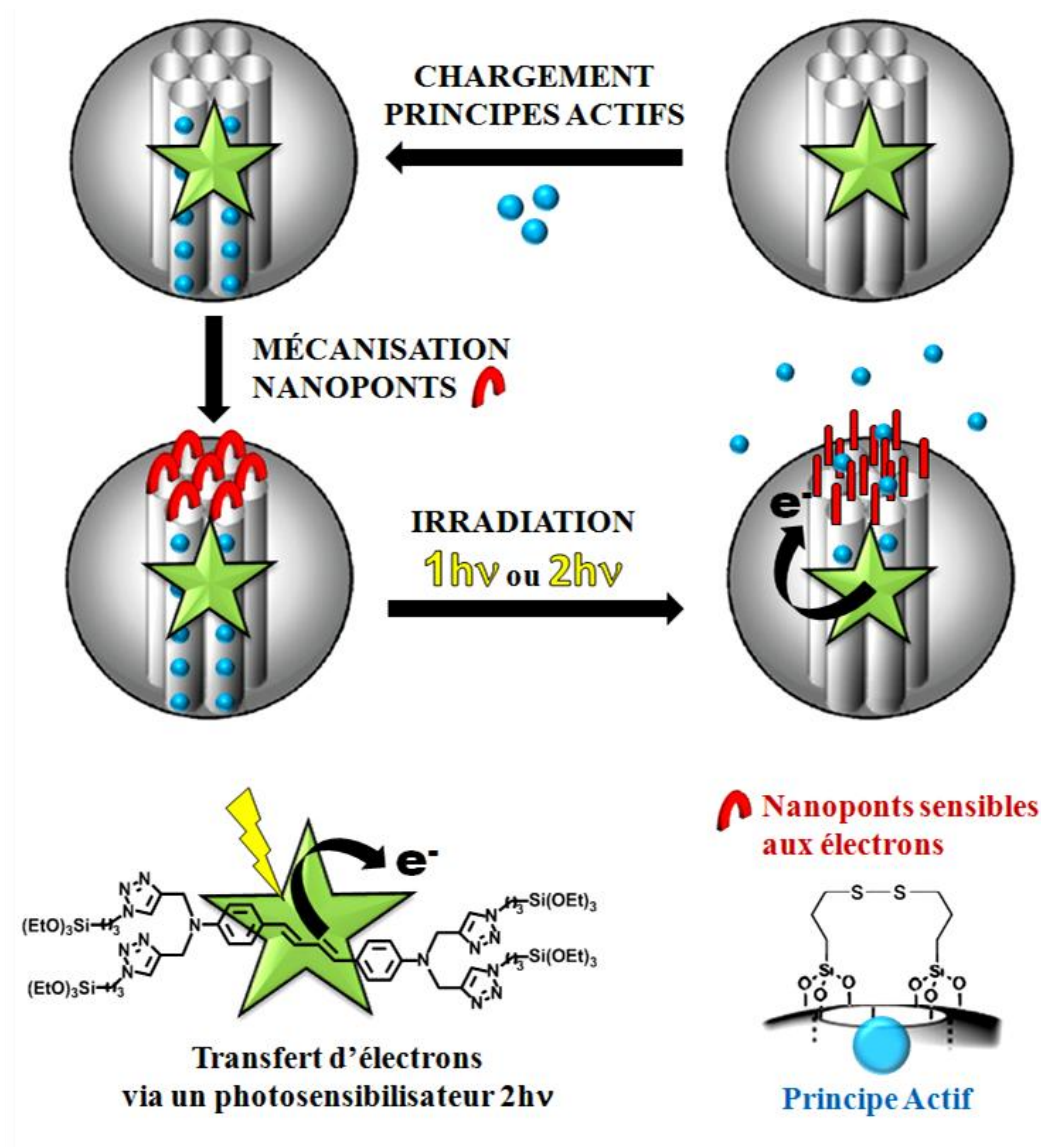


Figure 12. Etapes de préparation de M2PS-Nanoponts chargés en principes actifs pour un relargage sur commande par stimulus laser.

4- Dépollution magnétique de métaux lourds via des MSN

Des NPs cœur-coquille à base de nanocristaux d'oxyde de fer et de silice mésoporeuse ($\text{Fe}_3\text{O}_4@\text{MSN}$) ont été préparées et caractérisées par de nombreuses techniques (Figure 13). Le cœur magnétique de ces matériaux a été utilisé dans le but de réaliser une séparation magnétique de NPs en vue d'application pour la dépollution de métaux lourds.

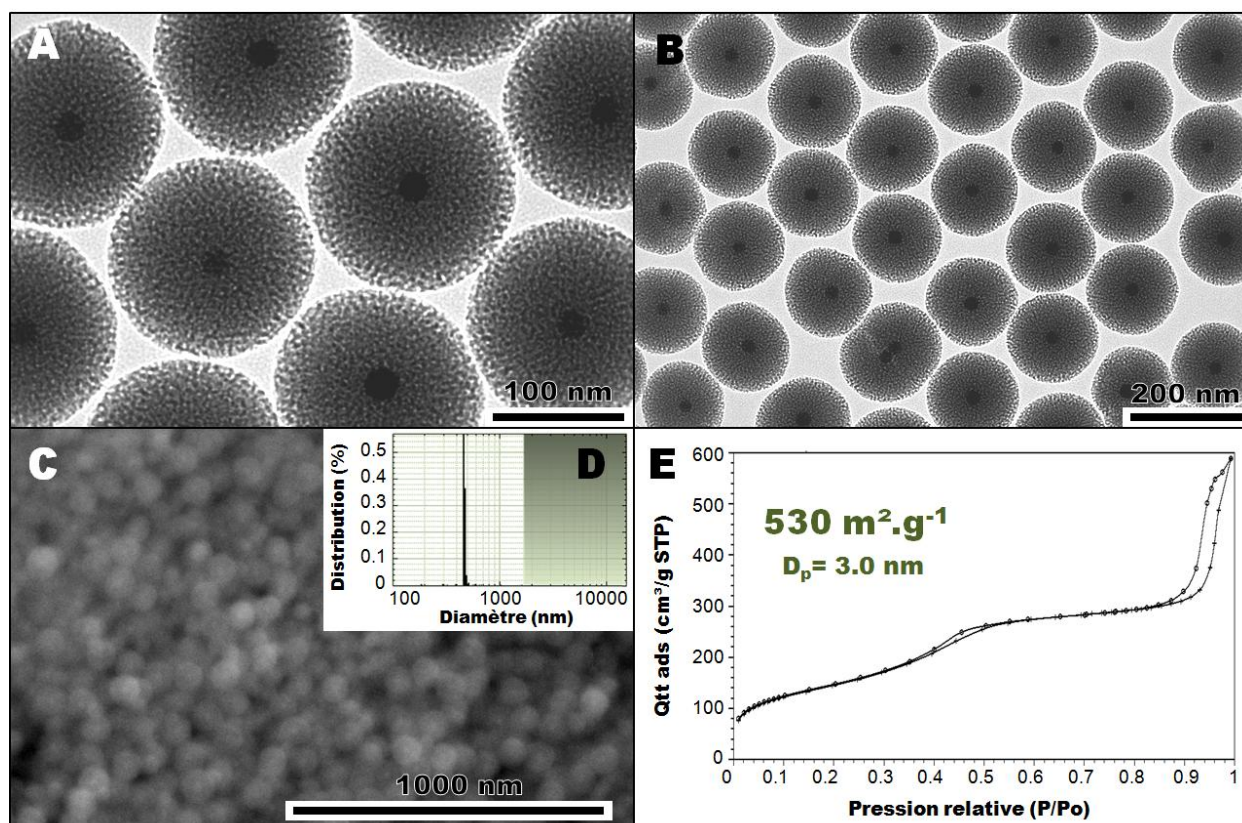


Figure 13. Images de MET et MEB des NPs de $\text{Fe}_3\text{O}_4@\text{MSN}$ (A-B et C respectivement). Distribution en taille des NPs (D), et isotherme d'adsorption-désorption d'azote (E).

Les nanomatériaux cœur-coquille ont été caractérisés par MET et MEB (voir Figure 13 A-B et C respectivement). Des NPs monodisperse d'une centaine de nm non-agrégées et possédant un cœur d'oxyde métallique ont été observées. La DDL a confirmé la distribution étroite des diamètres des NPs, et l'adsorption-désorption d'azote combinée avec les calculs BET (traitement via la théorie de Brunauer, Emmett et Teller) ont démontré la mésoporosité des objets avec 530 m^2/g de surface spécifique (Figure 13D-E).

La fonctionnalisation de surface de ces NPs avec un dérivé alcoxysilyle de type acide diéthylène triamine penta acétique (DTPA), a permis la complexation d'une douzaine de métaux lourds toxiques, ensuite séparées de la solution aqueuse par un aimant (Figure 14-15).

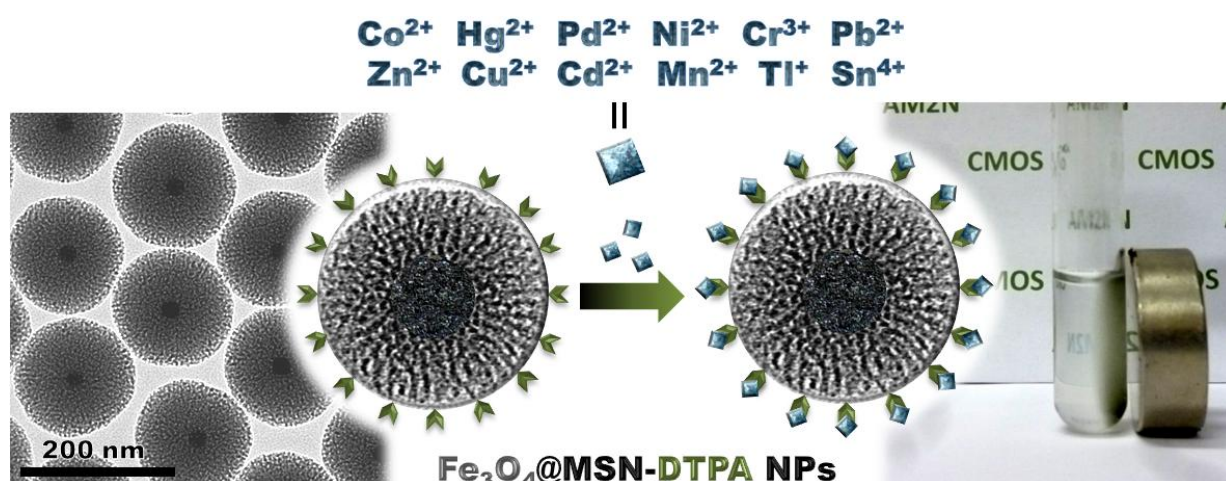


Figure 14. Dépollution magnétique d'une douzaine de métaux lourds via $\text{Fe}_3\text{O}_4\text{@MSN-DTPA}$.

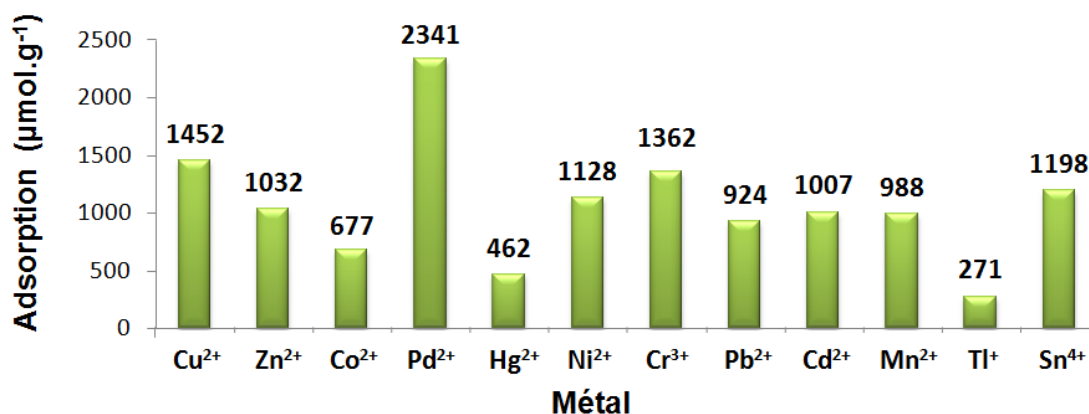


Figure 15. Capacités d'adsorption de métaux lourds avec les NPs $\text{Fe}_3\text{O}_4\text{@MSN-DTPA}$.

En outre, l'augmentation de l'efficacité de la dépollution a été étudiée par la fonctionnalisation de la surface extérieure et/ou des pores des $\text{Fe}_3\text{O}_4\text{@MSN}$. Un gain de 40% sur les capacités d'adsorption du zinc(II) et du cuivre(II) a été mesuré. On note que, la désorption des ions tout comme la réutilisation de NPs ont été mises en œuvre avec succès. Le système s'est aussi révélé plus sélectif pour les ions Pd^{2+} , Co^{2+} , Cr^{3+} , Sn^{4+} , et Ni^{2+} .

III- ELABORATION ET APPLICATIONS DES NPs DE BS

1- Photothérapie dynamique à deux-photons via des NPs de BS

Des NPs de BS ont été préparées pour opérer de la PTD à deux-photons. Les nanomatériaux BS ont été élaborés sans précurseur de silice et seulement à partir d'un tétra-organosiloxane photosensible à deux-photons utilisé précédemment (Figure 16a). Des NPs de BS et de cœur-coquille d'or-BS (Au@BS et BS@Au) ont aussi été synthétisées (Figure 16b) pour une imagerie et une PTD à deux-photons plus efficaces, propriétés qui se révélèrent exaltées par les nanosphères d'or (Figure 16c).

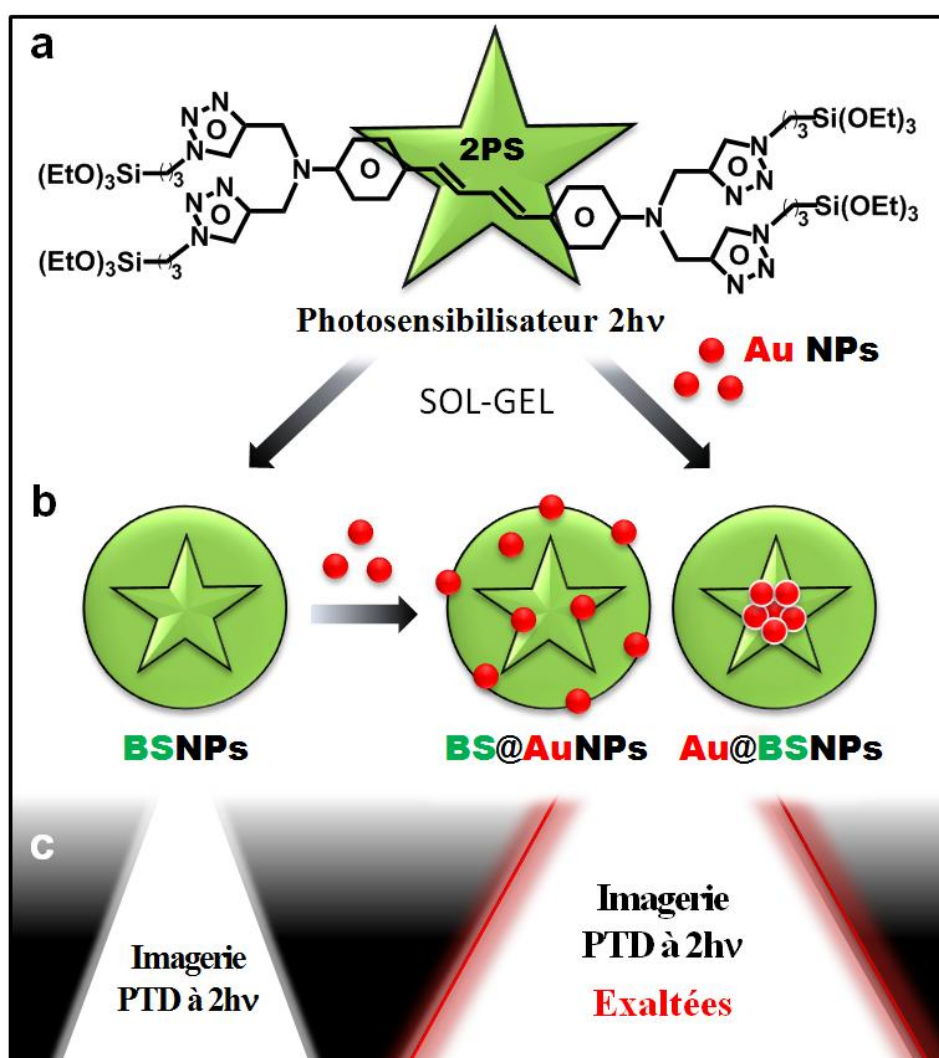


Figure 16. Photosensibilisateur deux-photons (a) précurseurs de nanomatériaux BS, BS@Au, et Au@BS (b), pour l'imagerie et la PTD biphotonique.

Les études *in-vitro* des NPs de BS et de Au@BS ont donné lieu à d'excellents résultats d'imagerie par fluorescence, remarquablement exaltée par la présence de l'or, ainsi qu'à une mort cellulaire quasi-totale de la lignée MCF-7. Les analyses de photophysiques corrélerent ces résultats avec l'augmentation des valeurs de σ_2 par chromophore dans les matériaux dotés de NPs d'or (Figure 17).

D'autres part, des NPs de BS à base de disulfure et de ce même photosensibilisateur on été synthétisées et caractérisées, et se sont révélées être des nano-outils biodégradables pour l'imagerie et la PTD à deux-photons.

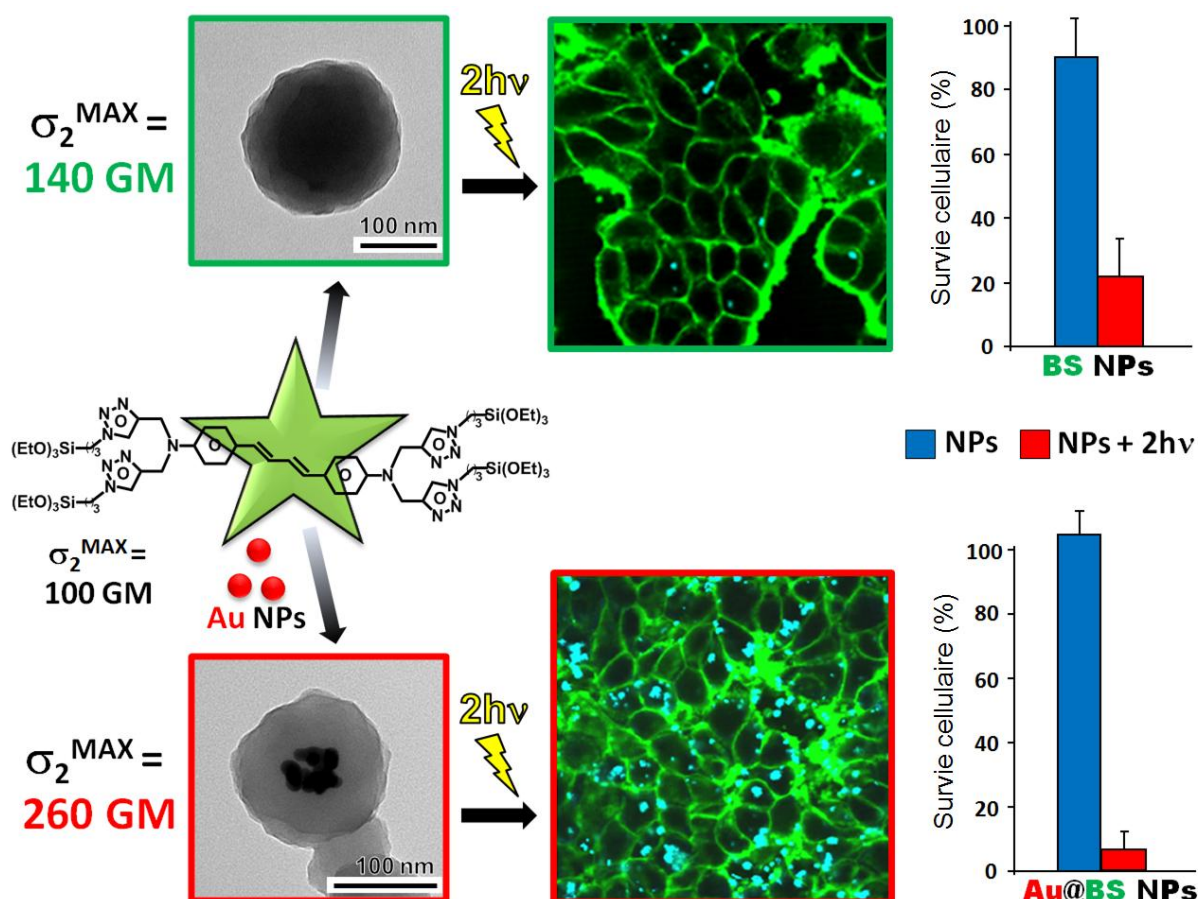


Figure 17. Augmentation des σ_2 (en Goeppert-Mayer) des photosensibilisateurs dans les BS (image MET, partie haute) et les Au@BS (image MET, partie basse) pour une exaltation des propriétés théranostiques.

IV- ELABORATION ET APPLICATIONS DES NPs DE PMO

1- NPs de PMO biodégradables pour la délivrance de principe actif

Des NPs de PMO biodégradables ont été synthétisées à partir du mélange 1,2-bis(triéthoxysilyl)éthylène (E) et de 1,2-bis(triéthoxysilylpropyl)disulfure (DIS). La décroissance du rapport E/DIS a induit d'une part la modification de la nature des matériaux, puisque la seule présence de E a conduit à la formation de nanobâtonnets de PMO (Figure 18A), tandis que la condensation du précurseur DIS mena à des nanosphères de BS (voir Figure 18E). D'autre part, la co-condensation des précurseurs E et DIS a donné lieu à la formation de NPs biodégradables de différentes formes, des nanobâtonnets pour des rapports E/DIS de 90/10 et 75/25, et des nanosphères pour le rapport 50/50 (Figure 18B-D).

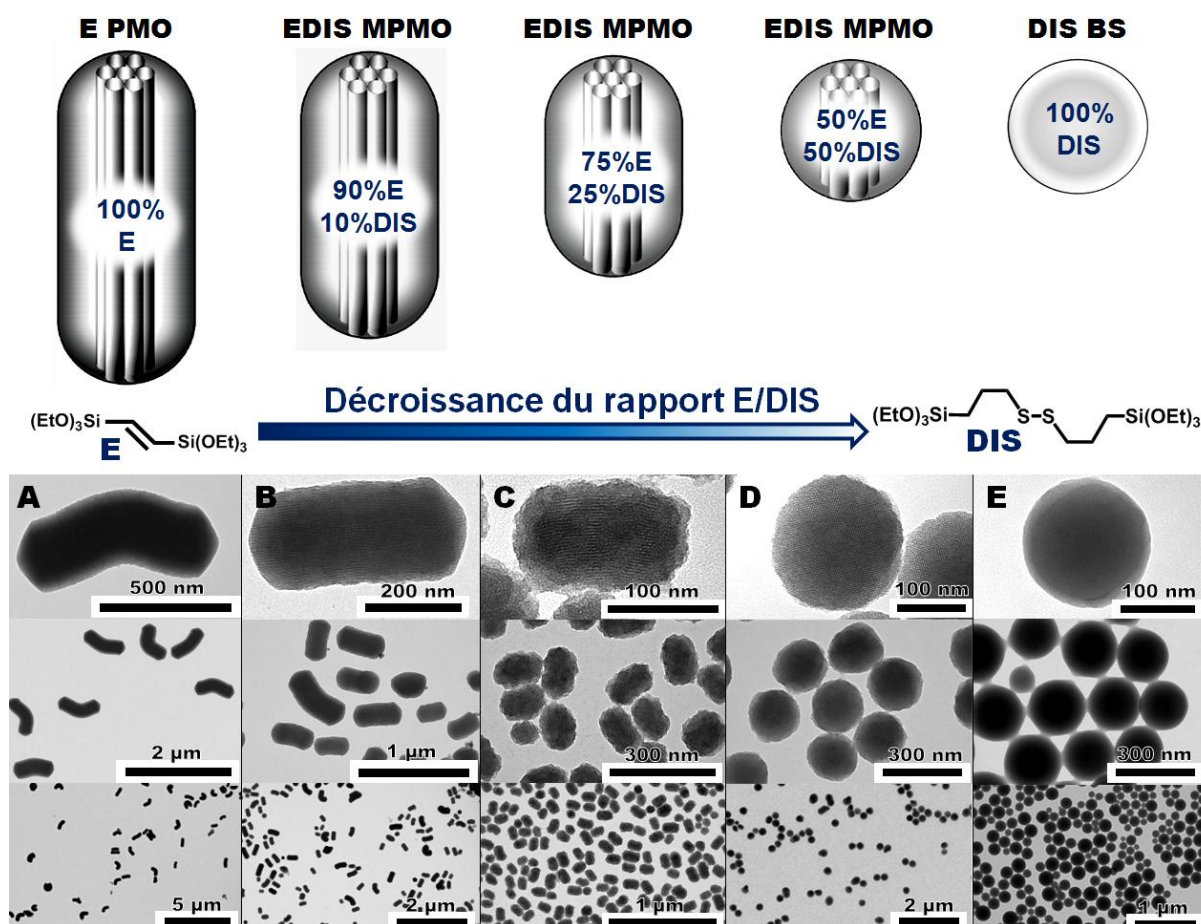


Figure 18. Représentation de l'impact du rapport E/DIS sur la structure et la morphologie de nanomatériaux, et images MET associées à chacun des rapports E/DIS (A-E).

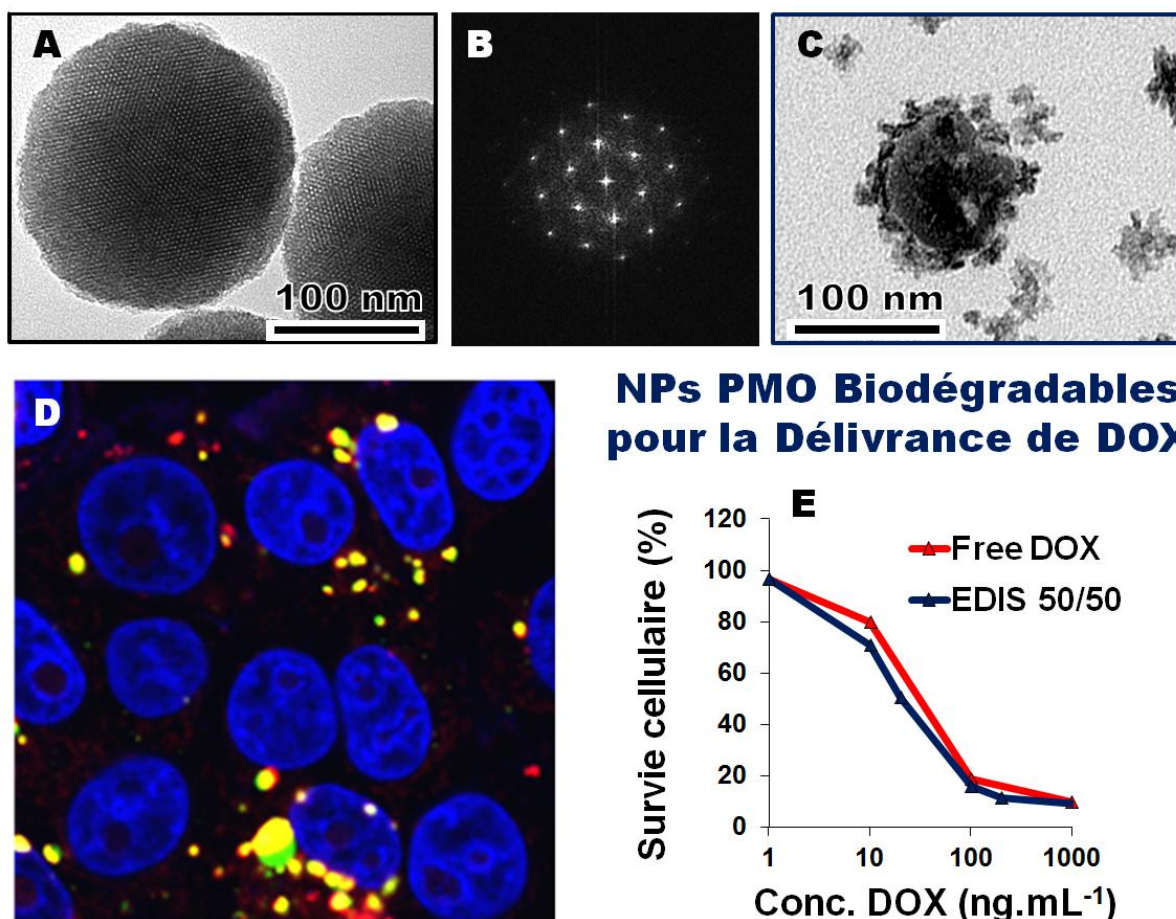


Figure 19. Image MET des nanosphères de PMO biodégradables (A) et la transformée de Fourier associée (B). Image MET des nanosphères de PMO après dégradation en conditions proches du milieu physiologique (C). Fluorescence intracellulaire des nanosphères de PMO chargées en iodure de propidium (D). Survie cellulaire de cellules MCF-7 soumises à des nanosphères de PMO chargés en DOX, ou de la DOX libre (E).

La biodégradabilité des NPs de PMO a été démontrée par diminution des volumes hydrodynamiques de nano-objets, comme l'indique l'image MET avant et après traitement en conditions proches du milieu physiologique (Figure 19A et C respectivement). On note que l'organisation à longue distance de PMO a été confirmée par diffraction de rayons X associés à la transformée de Fourier (Figure 19B).

L'application de ces nanomatériaux pour la thérapie du cancer a ensuite été étudiée. L'internalisation des NPs de PMO biodégradables dans les cellules MCF-7 a été démontrée par cytométrie de flux, grâce au chargement d'iodure de propidium (molécule imperméable aux membranes cellulaires) dans les pores des NPs (Figure 19D). Enfin, la délivrance efficace de DOX a été mise en œuvre via ces nanosystèmes (Figure 19 E).

2- NPs de PMO multipodes

Des NPs de PMO hybrides formées d'un cœur de PMO sphérique à base organique de benzène, et de un ou plusieurs nanobâtonnets de PMO à base d'éthylène (les NPs BE) ont été obtenues. Ces nanoplateformes poreuses ont été réalisées en une étape par condensations successives premièrement de bis(triéthoxysilyl)benzène (B), puis de bis(triéthoxysilyl)éthylène (E). La morphologie des NPs BE a été observée par MET et microscopie électronique à transmission et balayage haute résolution (METS-HR) (Figure 20). De plus ces nanomatériaux possèdent une très grande surface spécifique de l'ordre de 1500 m²/g (Figure 21) qui ouvre des perspectives pour la catalyse multi-étapes ou le relargage de multiples molécules hôtes.

La structure et la composition de PMO hybrides multipodes ont ensuite été caractérisées par différentes techniques. Deux contrôles ont été préparés afin d'identifier les phases des multipodes. Le premier en condensant seulement le précurseur B, ce qui a produit des nanosphères de PMO à base d'éthylène (Figure 22a). Le deuxième en condensant seulement le précurseur E, ce qui a produit des nanobâtonnets PMO à base de benzène (Figure 22b). Au contraire, la condensation séquentielle produit les NPs PMO hybrides BE (Figure 22c). Les analyses de ces trois matériaux par diffraction de rayons X (DRX) a révélé l'organisation mésoporeuse des BE avec le pic intense aux bas angles (Figure 22d), et l'organisation quasi-cristalline des cœurs de PMO benzène, grâce aux pics de diffractions caractéristiques du benzène à 7.6 angströms (Figure 22e). De plus, la résonance magnétique nucléaire (RMN) à l'état solide du ¹³C et du ²⁹Si par séquence de polarisation croisée à l'angle magique (CP-MAS) a permis de démontrer la présence des deux espèces organique dans les NPs de type BE. Les PMO BE multipodes ont donc un ordre à l'échelle moléculaire ainsi qu'une périodicité mésoscopique.

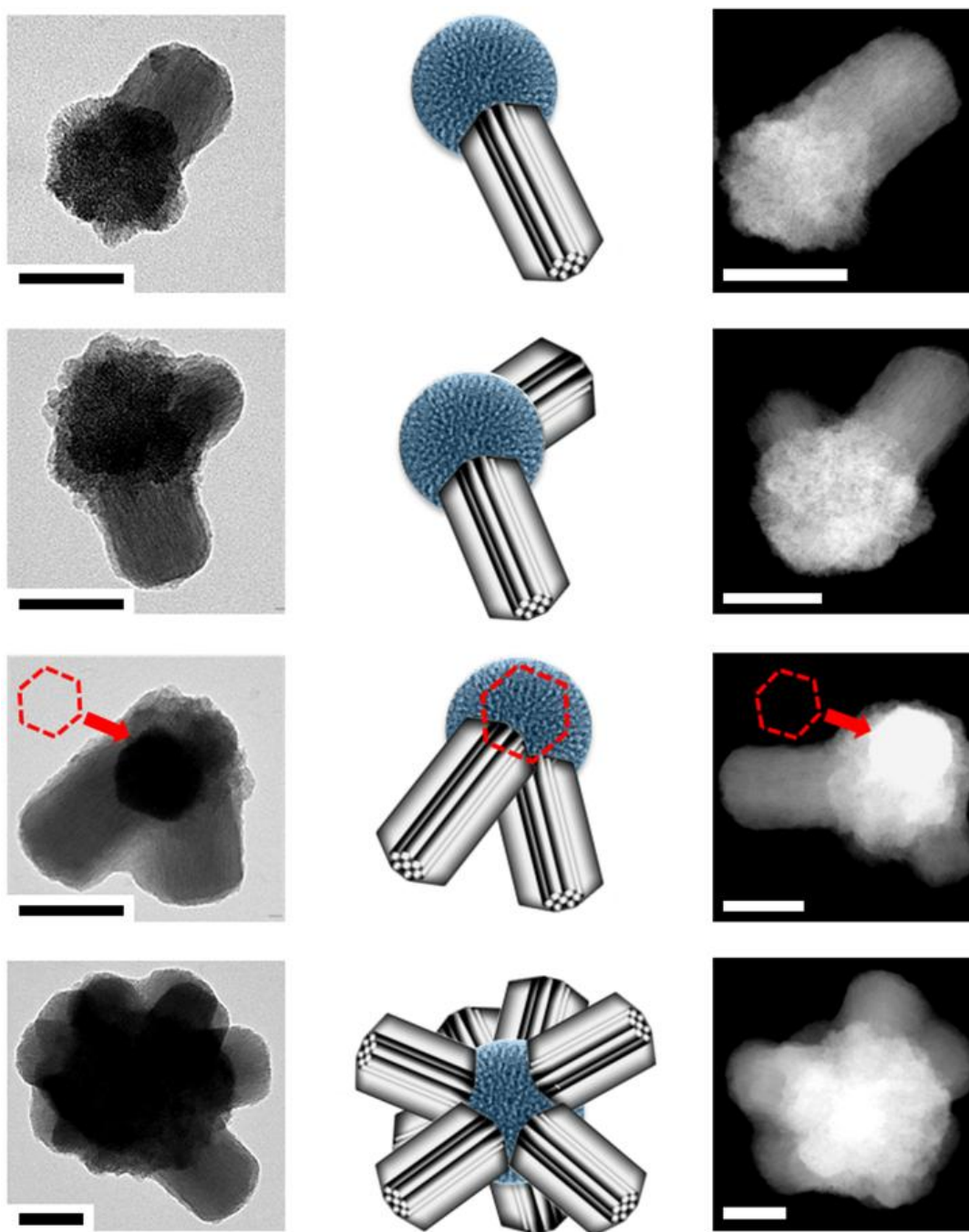


Figure 20. Images MET et de METS-HR des PMO multipodes (ci-gauche et ci-droite respectivement), les hexagones rouges indiquent la symétrie des multipodes d'éthylène.

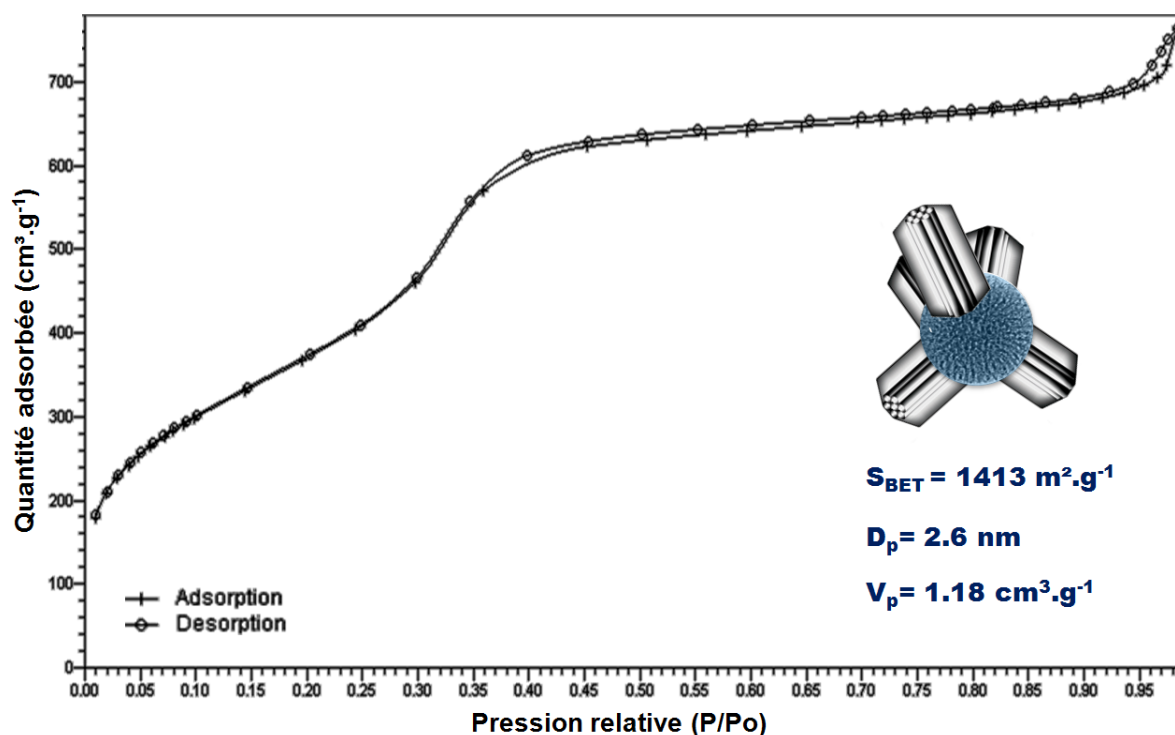


Figure 21. Isotherme d'adsorption-désorption d'azote des PMO hybrides BE.

Une extension de cette synthèse a aussi été étudiée avec la co-condensation de 1,2-bis(triethoxysilylpropyl)disulfure (DIS) pour former les NPs BEDIS, dotées de multipodes à base d'éthylènes et de disulfures (Figure 23a). Les nano-objets observés par MET possèdent 1 à 6 podes et sont de l'ordre de la centaine de nm (Figure 23b, c, d). On note que la transformée de Fourier a aussi permis de constater l'organisation hexagonale présente dans les podes EDIS (voir Figure 23e-f).

Au regard de l'étude réalisée sur les PMO biodégradables, les podes de ces NPs pourraient s'avérer être biodégradables et des relargage à cinétiques variables pourrait-être mises en œuvre. De plus, si le contrôle de la croissance de cœurs de benzène additionnels sur les podes de E ou de EDIS pouvait être obtenu, des réseaux de PMO hybrides seraient disponibles pour des applications variées, par exemple en chromatographie.

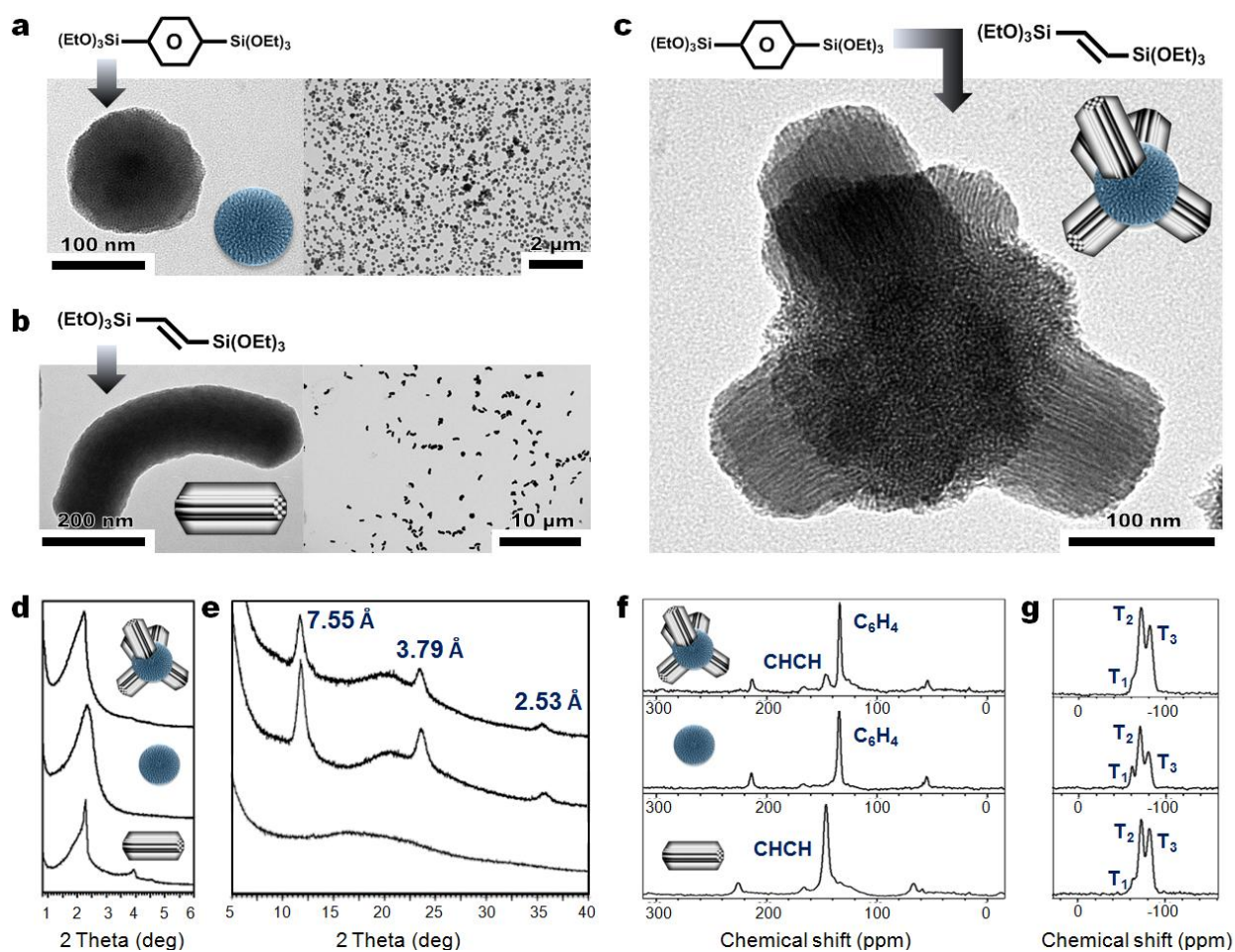


Figure 22. Images MET des PMO à base de benzène (a), d'éthylène (b), et de PMO BE (c). Comparaison DRX des contrôles de PMO et des BE aux bas et grands angles (d et e respectivement). Comparaison RMN à l'état solide pour les contrôles de PMO et des BE en CP-MAS du ^{13}C et du ^{29}Si (f et g respectivement).

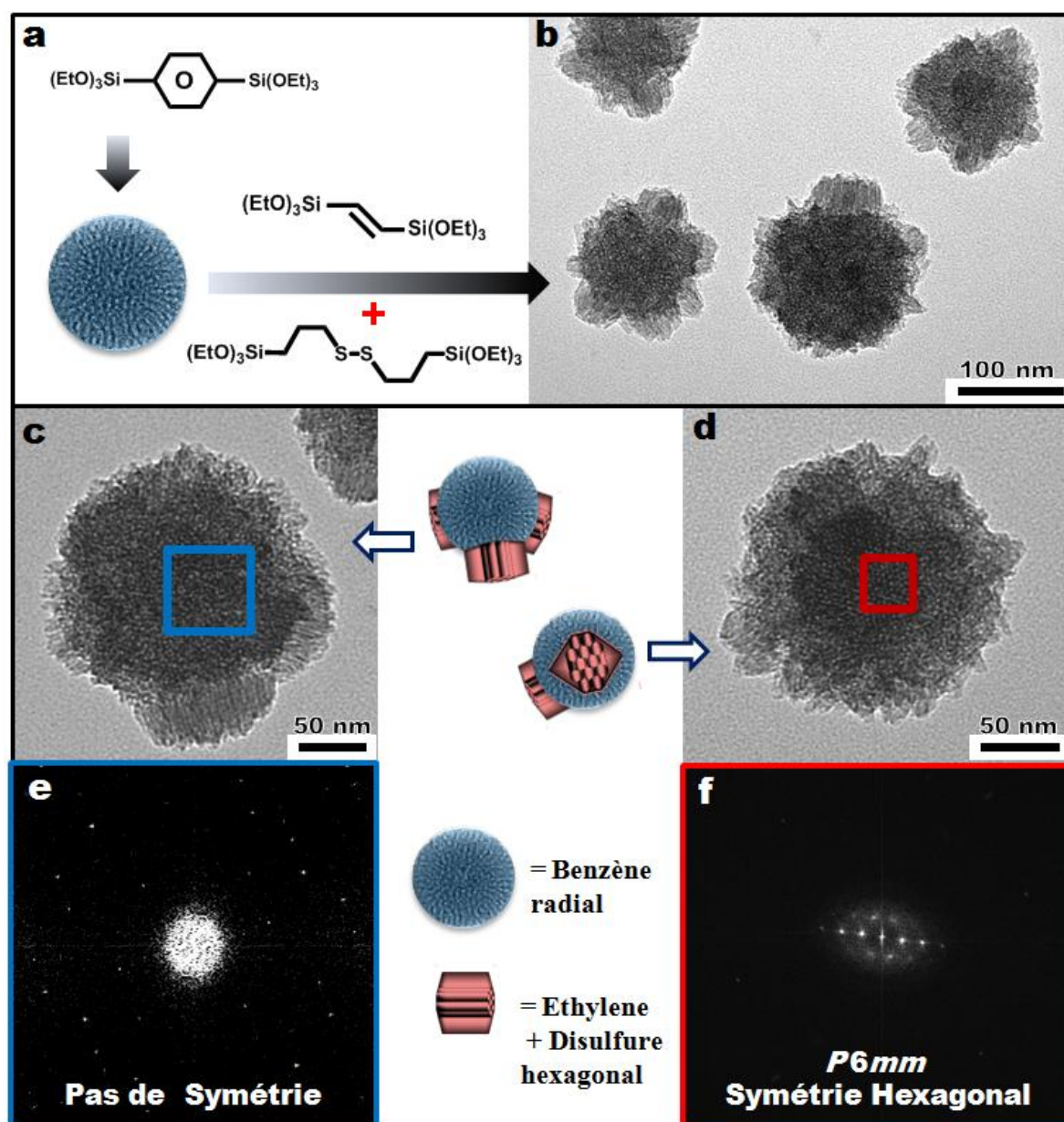


Figure 22. Stratégie de synthèse des NPs de PMO hybrides BEDIS (a), images MET de l'échantillon final après extraction du surfactant (b-d). Transformées de Fourier sur les zones colorées choisies dans les parties B (c et e), et EDIS (d et f), révélant la symétrie hexagonale des podes.

3- NPs de PMO hybrides en tant que nanosystèmes théranostiques à deux-photons

Enfin, des NPs de PMO pour des applications dans la thérapie et le diagnostic ont été préparées. La co-condensation de précurseur de bis(triéthoxysilyl)éthylène (E) ou de bis(triéthoxysilyl)benzène (B) avec du 2PS a mené aux NPs E2 ou B2 respectivement (Figure 23a). Des NPs cœur-coquille composées de nanocristaux d'or et de coquille de PMO à base d'éthylène ou de benzène (NPs AE ou AB respectivement) ont aussi été préparées. Enfin, des NPs à cœur d'or et coquille de PMO hybride E2 ou B2 (NPs AE2 et AB2 respectivement), sensibles à deux-photons ont été synthétisées en une seule étape.

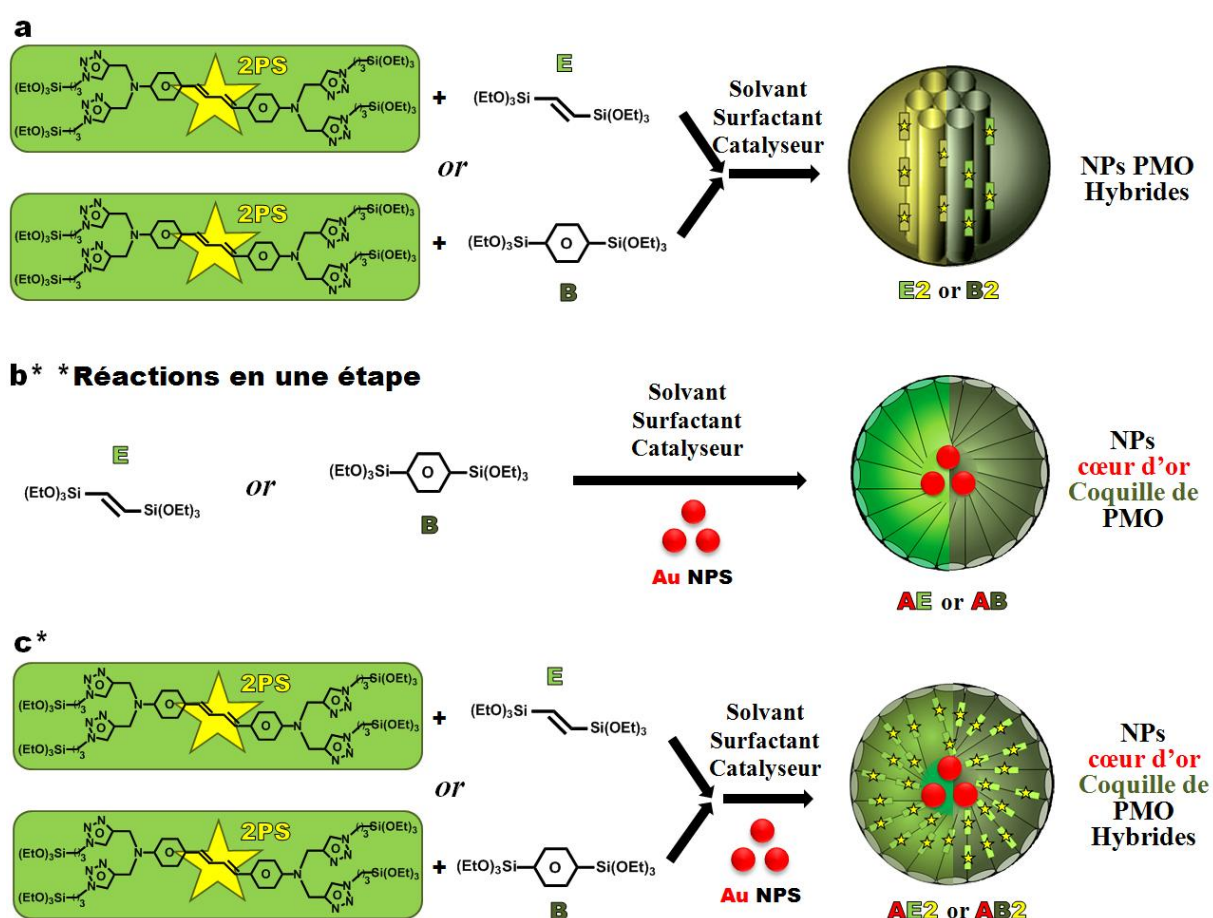


Figure 23. Stratégie de synthèses des NPs de PMO hybrides à base de E et de 2PS (E2 NPs), ou de B et de 2PS (B2 NPs) (a). Synthèses en une étape de NPs d'or à coquille de E (AE NPs) ou de B (AB NPs) (b). Synthèses en une étape de NPs d'or à coquille de E2 (AE2 NPs) ou de B2 (AB2 NPs) (c).

On note, que jusqu'alors la synthèse de NPs de PMO nécessitait plusieurs dizaines d'heure et d'étapes extraction comprise, tandis que ces synthèses (extractions comprises) ont été optimisées pour ne durer que 2 à 4 heures.

L'analyse de ces nanomatériaux par MET révéla des nanosphères entre 100 et 200 nm, non agrégées et possédant un à trois cœur d'or lors des synthèses des NPs cœur-coquille (Figure 24). Les clichés à haut grossissement ont révélés la porosité des NPs, et leur monodispersité a été confirmée par des images à plus faible grossissement (Figure 24), par MEB, et aussi par analyse DDL.

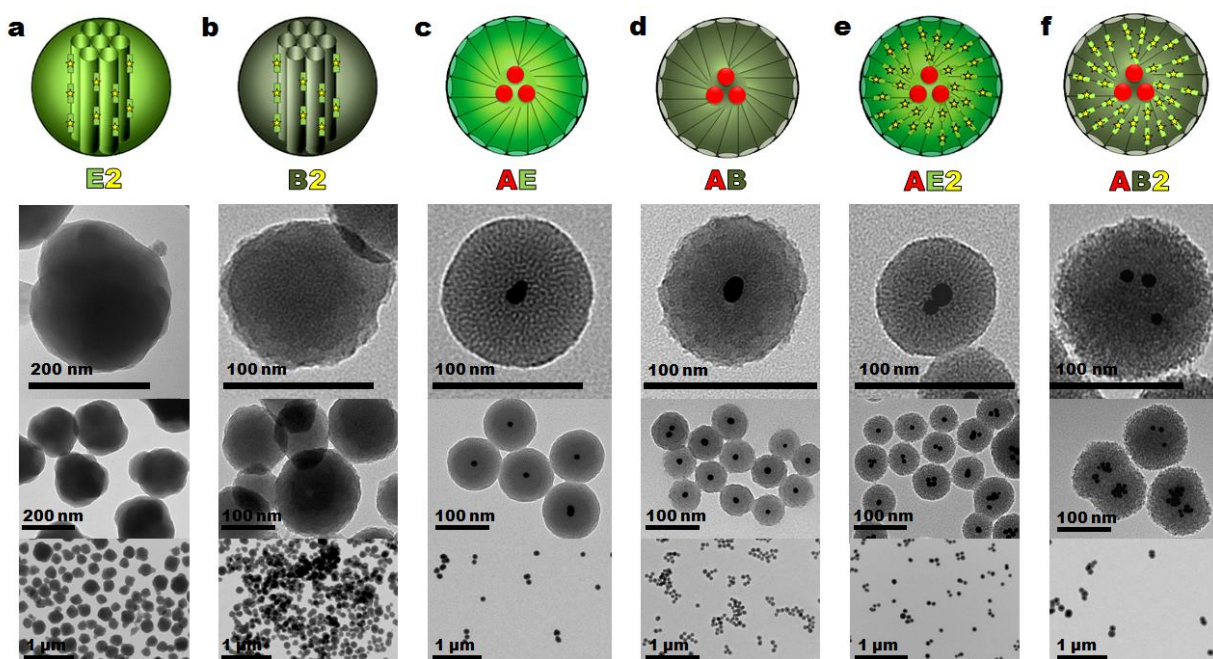


Figure 24. Images MET des NPs de E2, B2, AE, AB, AE2, et AB2 (a-f respectivement).

L'application de ces nanomatériaux a ensuite été menée pour la PTD deux-photons, ainsi que pour la délivrance de principes actifs (Figure 25). Le 2PS a produit de la PTD à deux-photons avec les NPs de PMO hybrides, ce qui a été exalté en présence de cœurs d'or. Puis, le chargement des pores avec la molécule anticancéreuse Doxorubicine (DOX) permet le relargage autonome de ces principes actifs en cellules MCF-7 (Figure 25d). Pour finir, la combinaison de la DOX avec l'irradiation à deux-photons permet un effet thérapeutique

synergétique avec ces nanomatériaux, les meilleurs résultats ayant été obtenus avec ceux à base d'éthylène.

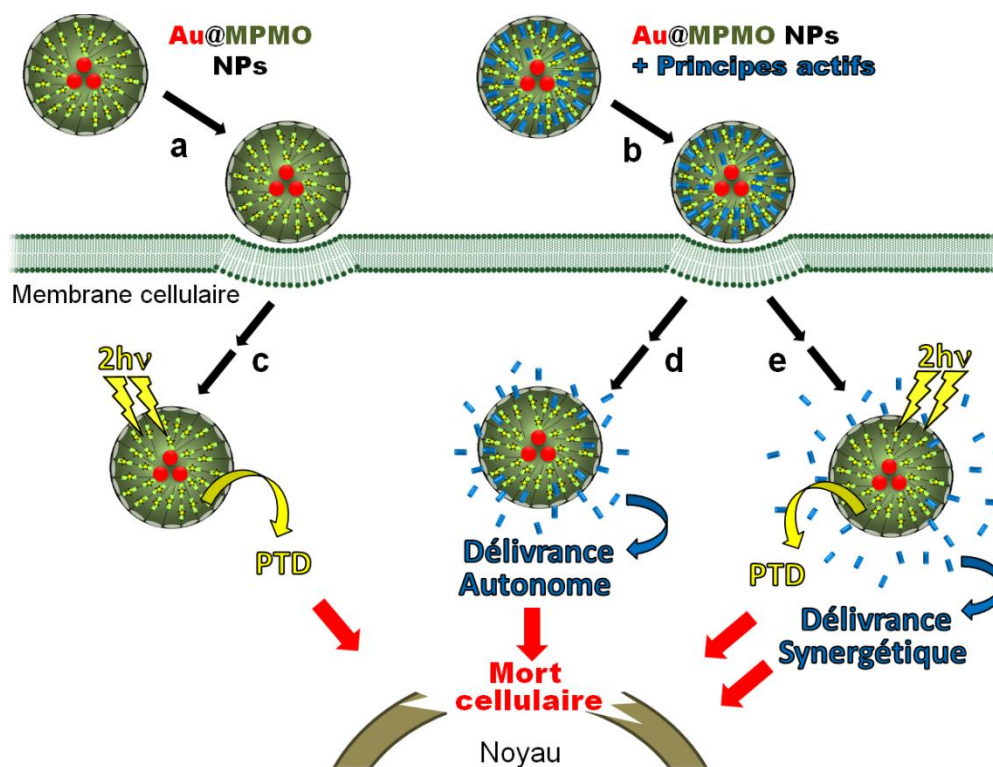


Figure 25. Représentation de l'endocytose des Au@PMO avec ou sans chargement de principe actifs (a et b respectivement), conduisant à la PDT sous irradiation deux-photons (c); à la délivrance autonome du chargement sans irradiation pour les NPs chargées (d), et à la synergie PDT et délivrance sous irradiation (e). Le laser augmente la cinétique de relargage du principe actif (e).

De plus, ces NPs ont manifesté assez de fluorescence intracellulaire pour confirmer l'endocytose de toutes les NPs (voir Figure 26). Les propriétés théranostiques de ces nanoplateformes ont donc été démontrées et appliquée *in-vitro* pour la thérapie du cancer, ouvrant des perspectives pour une nanomédecine personnalisée.

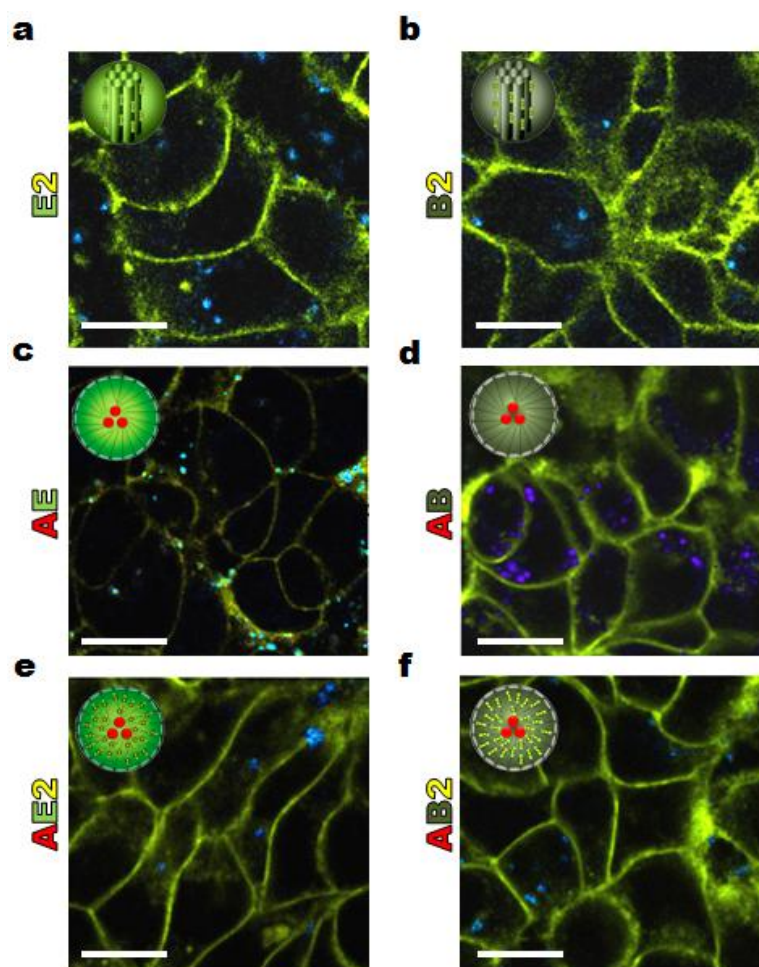


Figure 26. Fluorescence biphotonique intracellulaire des nanomatériaux PMO nus, démontrant l'endocytose de tous les types de NPs étudiés.

NANOMÉDECINE THÉRANOSTIQUE ACTIVÉE À DEUX-PHOTONS POUR LE TRAITEMENT DU CANCER

Résumé : La nanomédecine par activation biphotonique est devenue l'un des principaux candidats à l'accomplissement de la sélectivité spatiotemporelle nécessaire pour le traitement du cancer. En effet, la valeur ajoutée que peuvent apporter les nanotechnologies dans le domaine du traitement du cancer est la diminution ou la suppression des effets secondaires causés par les techniques actuelles telles que la chimiothérapie et la radiothérapie, à cause de leur manque de sélectivité. Parmi les diverses nanoparticules (NPs) étudiées, les nanoparticules de silice mésoporeuse (MSN) ont attiré une attention croissante au cours de la dernière décennie grâce à leur faible cytotoxicité, leur internalisation cellulaire et excrétion faciles, et leur capacité à combiner de nombreuses fonctions simultanément pour la *thérapie* et le *diagnostic* de cancers via un seul nanovéhicule : la nanomédecine *théranostique*.

Dans cette thèse, des MSN activées à un- ou deux-photons pour l'imagerie par fluorescence, la délivrance de principes actifs et d'acides nucléiques, et la photothérapie dynamique (PTD) seront présentées. Premièrement, le relargage contrôlé de molécules encapsulées dans des MSN fonctionnalisées avec des nanovalves est considéré par effet plasmonique. La photodégradation contrôlée de la silice soumise à l'effet photothermique de NPs d'or est ensuite étudiée. Deuxièmement, l'activation biphotonique est utilisée pour la délivrance contrôlée de molécules anticancéreuses *in-vitro* avec des nano-rotors et des nano-valves, la fonctionnalisation de surface des NPs par des dérivés d'ammonium-azobenzène permettant la délivrance d'acides nucléiques. Troisièmement, des MSN multifonctionnelles incorporant des photosensibilisateurs à deux-photons sont systématiquement étudiées pour leurs propriétés optiques et photophysiques ; la sélection du meilleur matériau est ensuite suivie par des applications biomédicales *in-vitro*.

De plus, deux types de nanomatériaux émergents sont également élaborés pour la nanomédecine activée à deux-photons, des NPs de polysilsesquioxanes pontés (BS) et d'organosilices mésoporeuses périodiques (PMO). Ces matériaux sont élaborés seulement à partir de bis- ou multi-organoalcoxysilane, sans précurseur de silice, afin d'obtenir le plus haut pourcentage de matière organique possible pour l'application ciblée. En conséquence, des NPs de BS et de PMO hybrides à base de disulfures se sont révélées être biodégradables, et les NPs à base de photosensibilisateurs ont été appliquées pour la PTD à deux-photons. Des NPs de BS et des NPs cœur-coquille or-BS ont été synthétisées pour l'imagerie et la PTD à deux-photons, tandis que des NPs de PMO ont servi de plateformes théranostiques. En outre, diverses NPs de PMO multipodes à surfaces spécifiques très élevées sont présentées comme structures nanométriques complexes.

Enfin, des nano-conteneurs de MSN contenant un cœur d'oxyde de fer ($\text{Fe}_3\text{O}_4@\text{MSN}$) sont décrits pour de multiples applications. D'une part, l'élaboration de MSN (et PMO) magnétiques activables à deux-photons est étudiée pour la délivrance de gènes en combinaison avec l'imagerie par résonance magnétique nucléaire. D'autre part, les conteneurs de $\text{Fe}_3\text{O}_4@\text{MSN}$ sont mis en œuvre et appliqués pour l'extraction de métaux lourds via la fonctionnalisation par des ligands de type acide diéthylène triamine penta acétique. L'augmentation de l'efficacité de la dépollution est étudiée par la fonctionnalisation de la surface extérieure et/ou des pores des $\text{Fe}_3\text{O}_4@\text{MSN}$.

Mots clés : Nanomédecine théranostique, deux-photons, nanoparticules de silice mésoporeuse, organosilices mésoporeuses périodiques, polysilsesquioxanes pontés.